Modelling of transient pressure waves in water distribution networks

Alexandre Bayle

▶ **To cite this version:**

Alexandre Bayle. Modelling of transient pressure waves in water distribution networks. Fluid mechanics [physics.class-ph]. Institut National Polytechnique de Toulouse - INPT, 2023. English. NNT : 2023INPT0036 . tel-04187716

HAL Id: tel-04187716
https://theses.hal.science/tel-04187716

Submitted on 25 Aug 2023

HAL is a multi-disciplinary open access archive for the deposit and dissemination of scientific research documents, whether they are published or not. The documents may come from teaching and research institutions in France or abroad, or from public or private research centers.

L'archive ouverte pluridisciplinaire **HAL**, est destinée au dépôt et à la diffusion de documents scientifiques de niveau recherche, publiés ou non, émanant des établissements d'enseignement et de recherche français ou étrangers, des laboratoires publics ou privés.

THÈSE

En vue de l'obtention du

DOCTORAT DE L'UNIVERSITÉ DE TOULOUSE

Délivré par :

Institut National Polytechnique de Toulouse (Toulouse INP)

Discipline ou spécialité :

Dynamique des fluides

Présentée et soutenue par :

M. ALEXANDRE BAYLE

le mardi 21 février 2023

Titre :

Modélisation des ondes de pression transitoires dans les réseaux de distribution d'eau.

Ecole doctorale :

Mécanique, Energétique, Génie civil, Procédés (MEGeP)

Unité de recherche :

Institut de Mécanique des Fluides de Toulouse (IMFT)

Directeur de Thèse :

M. FRANCK PLOURABOUE

Rapporteurs :

M. ARRIS TIJSSELING, TECHNISCHE UNIVERSITEIT EINDHOVEN

MME SILVIA MENICONI, UNIVERSITA DEGLI STUDI DI PERUGIA

Membres du jury :

M. OLIVIER THUAL, TOULOUSE INP, Président

M. BRUNO BRUNONE, UNIVERSITA DEGLI STUDI DI PERUGIA, Membre

M. FLORIAN NOSPELLE, Eau de Toulouse Metropole, Invité

M. FRANCK PLOURABOUE, CNRS TOULOUSE, Membre

MME CAROLE DELENNE, UNIVERSITE DE MONTPELLIER, Membre

M. ROMAIN GUIBERT, TOULOUSE INP, Invité

Acknowledgment

This PhD is supported by the collaborative ANRT Grant CIFRE 2019/1453 co-funded by SETOM, dedicated society of Veolia Water for the public drinking water service of Toulouse Métropole operating under the brand Eau de Toulouse Métropole.

Je tiens tout d'abord à remercier chaleureusement mon directeur de thèse, M. Franck Plouraboué, Directeur de recherche au CNRS, pour sa dévotion sans faille tout au long de ces trois années de recherche. Il est évident que le travail réalisé porte ta signature tant tu as su m'accompagner, me former et partager ton savoir et tes connaissances. Tes qualités humaines indiscutables allant de pair avec ton haut niveau scientifique, sache que ce fut un réel plaisir et honneur de travailler à tes côtés.

J'exprime également mes sincères remerciements à mon encadrant Veolia EAU / SETOM, M. Florian Nospelle, responsable technique et performance opérationnelle réseau. Impliqué dans la thématique des phénomènes transitoires avant même le début de cette thèse, tu as su donner à ce projet une dimension opérationnelle en apportant ton expertise sur l'analyse des modèles hydrauliques, des données capteurs ou encore en nous faisant confiance pour la réalisation d'un essai terrain grandeur nature. Tes compétences techniques ne font aucun doute et je te remercie donc d'avoir pris le temps de les partager avec moi.

Je remercie ensuite M. Romain Guibert, Docteur et Ingénieur de recherche à MFEED-IMFT. Ton remarquable niveau de compétence et ton implication dans tes missions, auront indéniablement contribués à la réussite de ce projet. Saches que nos échanges, informels ou non, ont été extrêmement enrichissants tant pour le développement de mes compétences que pour les précieux conseils que tu as su me promulguer.

J'exprime toute ma gratitude à M. Gérald Debenest, Professeur et Directeur du département MFEE de l'INP-ENSEEIHT, pour son soutien, sa bienveillance et le partage de son expertise. Tu m'as accompagné de la genèse de ce projet de recherche jusqu'à sa concrétisation et je t'en suis évidemment extrêmement reconnaissant et redevable.

Je suis également reconnaissant envers M. Oliver Sarlat, Directeur région sud activité Eau chez Veolia, pour sa disponibilité et la confiance qu'il m'a apporté dans la conduite de cette activité de recherche.

Je tiens à remercier mes correcteurs, Mme. Silvia Meniconi et M. Arris Tijsseling, respectivement Associate Professor à l'Université de Perugia en Italie et Associate Professor à l'Université de technologie de Eindhoven au Pays-Bas, pour avoir pris le temps de relire et corriger ce manuscrit de thèse. J'en profite également pour remercier tous les membres du jury pour leur temps et implication dans l'appréciation de cette thèse.

Je me dois de remercier chaleureusement les personnels SETOM et notamment Mattéo, Sandra et Cyril pour nos nombreux échanges, le partage de leur expertise et leur bonne humeur. Je remercie également Florian, Bilal, Ruming, Julien, Martin, Corentin et Pierre, Post doctorant, doctorant et stagiaire de l'IMFT, pour avoir partagé ces trois années à mes cotés. Merci également à mes anciens et anciennes camarades de l'ENSEEIHT pour leurs soutien et nos moments de partage. Hugo et Yohann, j'ai ici une pensée pour vous qui avez su être à l'écoute et m'épauler depuis nos premières années en Normandie.

Éline, je tiens par ces quelques mots à t'exprimer toute ma gratitude, admiration et affection. Ton sourire et ta tendresse auront su égailler même la plus difficile journée de ces trois dernières années. Je ne peux qu'admirer ta résilience et ton courage d'avoir fait le choix de partager ton quotidien avec un thésard stressé et en manque de sommeil, merci.

Enfin, puisqu'une thèse est à la fois un accomplissement professionnel et personnel, j'ai ici une pensée toute particulière pour mes parents Katia et Pierre. Je tiens à ce que vous sachiez que ce travail n'est que le reflet des sacrifices et des efforts que vous avez fourni tout au long de votre vie pour que, Mathilde et moi, ayons la chance de nous épanouir aujourd'hui. Aucun mot ne saurait exprimer toute ma gratitude, c'est pourquoi je vous dédie modestement cette thèse.

Résumé

Dans les zones urbaines, la disponibilité de l'eau potable repose souvent sur des systèmes de distribution complexes, dont la dynamique est encore mal comprise. La supervision des réseaux, qui s'inscrit dans le prolongement des projets de "smart city", offre de nouvelles possibilités de gestion des réseaux de distribution d'eau (RDE). Certaines technologies, comme le (SCADA), permettent déjà un contrôle et une régulation des réseaux en quasi temps réel, tandis que des techniques efficaces de gestion de la pression sont développées quotidiennement pour moderniser les installations. Ces techniques, bien qu'elles soient économiquement et opérationnellement viables, ne fournissent pas une description complète de la dynamique rapide des réseaux. Les régimes transitoires rapides, aussi incompris que dangereux, sont restés durant des décennies en marge de considérations opérationnelles. Cependant, avec la rareté des ressources et le besoin d'une gestion efficace de nos actifs vieillissants, la caractérisation des phénomènes transitoires rapides redevient un sujet d'importance. Le coup de bélier, ou la propagation d'ondes de pression émanant d'une variation de débit, peut ainsi être étudié du point de vue de la gestion patrimoniale, c.-à-d. la résilience du réseau face aux surpressions répétées, et/ou du point de vue opérationnel, c.-à-d. l'analyse de la rétropropagation des fronts d'ondes pour trouver leur générateur. Cette thèse se concentre sur le développement de modèles théoriques et numériques pour l'étude du comportement transitoire des réseaux d'eau potable par : (i) l'analyse temporelle des ondes de coup de bélier via la théorie des opérateurs, (ii) une analyse asymptotique détaillée des Interactions Fluide Structure (IFS) se produisant dans les conduites élastiques, (iii) l'extension du cadre IFS élastique aux conduites viscoélastiques, (iv) une étude numérique complète des modèles d'amortissement visqueux actuellement utilisés dans les logiciels commerciaux ou open-source par la méthode des caractéristiques, et (v) la constitution d'une nouvelle méthode de rétropropagation du premier front d'onde pour la localisation d'anomalies sur réseau. Chacun de ces points est développé dans cette étude et a conduit à plusieurs articles scientifiques également inclus dans le document. La nouveauté et la pertinence de la méthode de détection par rétropropagation des fronts d'ondes doit être soulignée pour sa conceptuelle simplicité, son efficacité numérique et sa fiabilité à géolocaliser des anomalies dans le réseau d'eau potable de Toulouse.

Mots clés: Réseau de distribution d'eau; Solutions dépendantes du temps; Interactions fluide structure; Conduites élastiques remplies de fluide; Rhéologie viscoélastique; Méthode des caractéristiques; Localisation d'anomalies; Méthode de rétropropagation.

Abstract

In urban areas, the availability of drinking water often relies on complex distribution systems, the dynamics of which is still misunderstood. Networks monitoring as part of an extension of smart city projects, nevertheless offers new management possibilities to Water Distribution Networks (WDN) shareholders. Some technologies such as the (SCADA) offers a quasi real-time control and regulation of the network, whilst efficient pressure management techniques are daily developed to modernize water facilities. Such techniques, although being economically and operationally effective, do not provide a full description of WDN fast dynamics. The WDN transient life, as misunderstood as dangerous, has remained for decades on the fringes of the operational considerations. In the context of resource scarcity and the requirement for efficient management of aging networks and assets, the transient description of hydraulic networks is moving back into focus. The water hammer phenomena, or the propagation of pressure waves due to flow-rate perturbations, can be investigated from the asset management viewpoint, i.e. the network resilience to repeated overpressure solicitations, or from a more operational one, i.e. the backtracking of the overpressure wave fronts to determine the possible hydraulic disfunctions. This PhD focuses on the development of theoretical models and numerical tools for WDN transient's analysis from: (i) time-domain operator-based water-hammer waves analysis, (ii) in-depth asymptotic analysis of Fluid-Structure Interactions (FSI) occurring in elastic liquid-filled pipes, (iii) extending current FSI-elastic-based models for visco-elastic pipes, (iv) a complete numerical study of the viscous damping model currently used in commercial or open-source software by using the Method Of Characteristic (MOC), and (v) establishing a new anomaly detection procedure in WDN from backtracking the first overpressure wave fronts. Each item is fully developed leading to several scientific papers also included in the document. The novelty and effectiveness of the herein backtracking detection method should be pointed out for its conceptual simplicity, numerical cost effectiveness and reliability to locate realistic anomalies in Toulouse's WDN.

Keywords: Water Distribution Networks; Time-dependent solutions; Fluid and Structures Interactions; Liquid-filled-elastic pipes; Visco-elastic rheology; Method of Characteristic; Anomaly localization; Backtracking methods.

Contents

List of Figures

List of Tables

Nomenclature

Physics and rheological constants		
ρ_f	Fluid density	$kg \cdot m^{-3}$
$\mathcal{K}_f$	Fluid bulk modulus	Pa
ν_f	Fluid kinematic viscosity	$m^2 \cdot s^{-1}$
ρ_s	Solid density	$kg \cdot m^{-3}$
E	Young's modulus	Pa
ν_s	Poisson's modulus	
W_0	Order of magnitude of the steady velocity	$m \cdot s^{-1}$
Characteristic velocities		
c_0	Fluid acoustic wave speed. Speed of sound in the fluid	
c_p	Modified Korteweg's wave speed / Fluid pulse wave speed	$m \cdot s^{-1}$
c_s	Solid elastic wave speed	$m \cdot s^{-1}$
$c_\pm$	Dimensionless coupled propagation modes wave speed	
Geometrical and time properties		
R_0	Inner initial tube's radius	m
r	Dimensional radial coordinate	m
R	Dimensionless radial coordinate	
e	Tube's thickness	m
L	Tube's length	m
z	Dimensional axial coordinate	m
Z	Dimensionless axial coordinate	
θ	Azimuth coordinate	m
t	Dimensional time	s
τ	Dimensionless fast time	
T	Dimensionless slow time	

s	Laplace variable	
ω	Pulsation	$rad \cdot s^{-1}$
Dimensionless numbers		
ϵ	Inner tube's radius by its length ratio	
α	Pipe's thickness by its inner radius ratio	
δ	Fluid overpressure dimensionless boundary layer	
$\mathcal{M}$	Re-scaled (on c_p) fluid Mach number	
δ_{st}	Fluid steady-state dimensionless boundary layer	
$\mathcal{C}_s$	Solid elastic by the fluid water hammer wave speed ratio	
$\mathcal{D}$	Fluid by solid density ratio	
Re	Reynolds number	
Physical fields		
W	Axial fluid velocity	$m \cdot s^{-1}$
P	Fluid pressure	Pa
$\dot{\zeta}$	Axial solid displacement velocity	$m \cdot s^{-1}$
$[\sigma_{rr}, \sigma_{\theta\theta}, \sigma_{zz}]$	Radial, azimuth and axial solid stress tensor components	Pa
τ_w	Fluid wall shear rate	Pa
τ_{qst}	Quasi-steady component of τ_w	Pa
τ_{tr}	Transient component of τ_w	Pa
f_{DW}	Darcy-Weisbach friction factor	
k_3	Boundary layer response deviation factor	
Characteristic matrices and operator		
$\mathbf{P}$	Pressure - stress vector	
$\mathbf{C}$	Speed matrix of the pressure-stress wave equation	
$\mathbf{\Pi}$	$\mathbf{C}$'s change of basis matrix	
$\boldsymbol{\mathcal{P}}$	Pressure - stress vector within $\mathbf{C}$'s diagonalization basis	
$\boldsymbol{\mathcal{C}}$	Speed matrix within $\mathbf{C}$'s diagonalization basis	
$\boldsymbol{\mathcal{N}}$, $\boldsymbol{\mathcal{M}}$, $\boldsymbol{\mathcal{Q}}$, $\boldsymbol{\mathcal{R}}$, $\boldsymbol{\mathcal{S}}$	Boundary condition matrices within the diagonalization basis	
$\mathcal{H}$	Self auto adjoint operator	
$-\lambda_k^2$	Eigenvalue of $\mathcal{H}$	
$\mathbf{\Phi}_k(Z)$	Eigenvector of $\mathcal{H}$	
$\tilde{\mathbf{\Phi}}_k(Z)$	Contracted form of $\mathbf{\Phi}_k$	

Acronyms

(BP) Bayle-Plouraboué's wall shear rate

(Bru) Brunone's wall shear rate

(DMA) District Metered Area

(DW) Darcy-Weisbach's quasi-steady wall shear rate

(FDM) Finite Difference Method

(FSI) Fluid Structures Interactions

(FVM) Finite Volume Method

(HDPE) High Density PolyEthylene

(IMAB) Instantaneous Material Acceleration-Based (wall shear rate model)

(ITA) Inverse Transient Analysis

(LDPE) Low Density PolyEthylene

(L.H.S) Left Hand Side

(MDPE) Medium Density PolyEthylene

(MOC) Method Of Characteristic

(NILT) Numerical Inverse Laplace Transform

(NRW) Non-Revenue-Water

(PE) PolyEthylene

(PM) Pressure Management

(PMA) Pressure Metered Area

(PRV) Pressure Regulation Valve

(PVC) PolyVinyl Chloride

(R.H.S) Right Hand Side

(ROI) Region Of Interest

(RPV) Reservoir-Pipe-Valve

(RTC) Real Time Control

(SCADA) Supervisory Control And Data Acquisition

(TMM) Transfer Matrix Method

(TVB) Trikha-Vardy-Brown's wall shear rate

(WDN) Water Distribution Network

(WFB) Weighting Function-Based (wall shear rate model)

(Z) Zielke's wall shear rate

Chapter 1

Introduction

Contents

1.1 The challenges of drinking water

Drinking water, also referred to as the "new oil" or "blue gold", is part of the resources we undoubtedly have to protect. Scarce at the worldwide scale, the amount of drinking water is declining with climate change. According to the last Intergovernmental Panel on Climate Change (IPPC): "*Risks in physical water availability and water-related hazards will continue to increase by the mid- to long-term in all assessed regions, with greater risk at higher global warming levels*", [IPCC Working Group II, 2022]. The World Health Organization (WHO) also follows the IPCC's assessment that: "*by 2025, half of the world's population will be living in water-stressed areas*", [World Health Organization, 2022]. In human activity areas, drinking water supply is one underlying problem of the global water-stress. The river and aquifer systems are indeed climate-dependent as depicted in Figure 1.4. With the resource's scarcity, the Water Distribution Networks (WDN) must unquestionably be operated under optimal and efficient conditions. However, the rude on-field reality brings out a striking contrast with the operative expectations.

(a) *Garonne river* **(b)** *Loire river.*

Figure 1.1: *Drought effects on the water availability of two major rivers in France during the summer of 2022: (a) Garonne river and (b) Loire river (original photo of the Poilly-sur-Loire's city).*

The Figure 1.2, extracted from the research work of [Che et al., 2021], depicts the WDN's efficiency of twenty world-wide reference cities. In France, the mean networks efficiency is close to 80% according to [EauFrance, 2022] (the French public information service on water). Despite the evident facts, water distribution

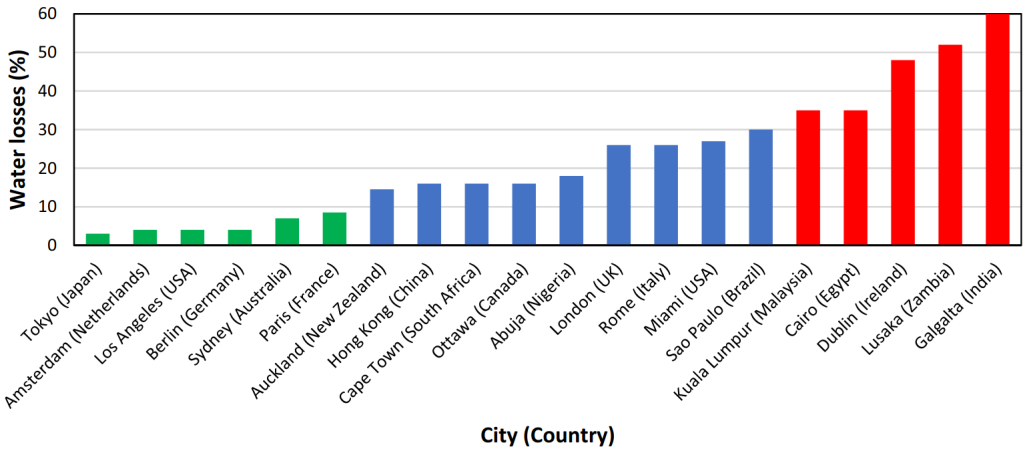

Figure 1.2: *Water losses in twenty reference cities. Original figure of [Che et al., 2021]*

networks suppliers, being public or private, are struggling to improve the operative efficiency of networks. Among all, underground leakage plays a cornerstone role in the observed poor performance. Since WDN are mainly buried, the detection, repair and prevention of such leakage are complex and costly operations to carry out. The leaks and the replacement of the pipes thus yearly cost millions of euros to water suppliers. The Non-Revenue-Water (NRW) is an economic indicator reflecting the losses of income due to faults or disturbances in WDN, e.g. leakage, pipe's burst, water theft or bad connections. In an extensive study, [Liemberger

and Wyatt, 2019] quantified the world-wide NRW value. Since the price of water may differ from location, the authors supposed a linear evolution of the water's price with respect to the Gross Domestic Product (GDP) as summed up in Figure 1.3. The leakage in WDN arises from poor pipe branch connections, structural

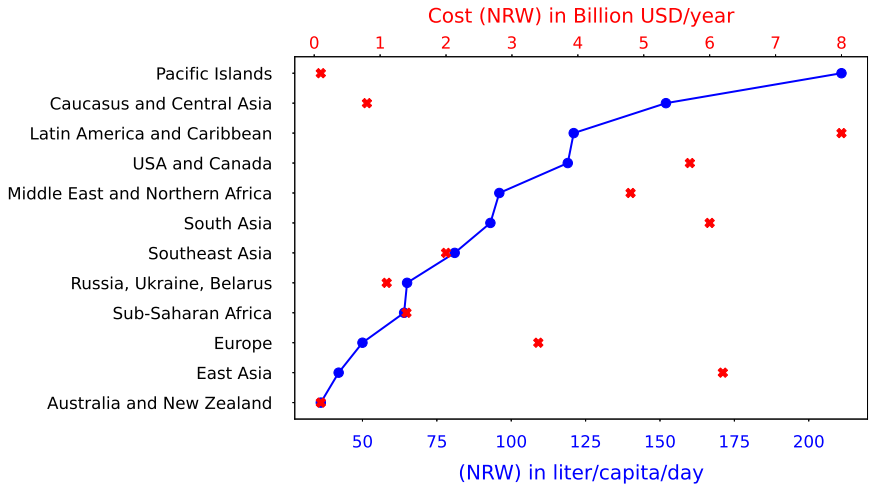

Figure 1.3: *Worldwide Non-Revenue Water (NRW) value and consecutive cost to the suppliers. Data of [Liemberger and Wyatt, 2019]*

wears, pipe erosion, ground chemical aggression or poor pressure management, to cite a few. An overall aging of the pipes also reinforces and accelerates the development of leaks and bursts, further reducing the network's efficiency. Thus, "**how current knowledge of water distribution networks could be improved in order to prevent, predict and detect faults that lead to a decrease in network performances ?**"

1.2 The concept of Pressure Management (PM)

The concept of Pressure Management (PM), encompasses all operational techniques and technologies dedicated to the search of optimum WDN's management. A poor pressure regulation is indeed known to cause leakages, reduce infrastructures lifetime, increase consumption and may lead to hazardous burst of pipes, [Vicente et al., 2016, Creaco et al., 2019]. Diminishing the pressure is usually considered useful to reduce leakage since: "*background leakage is pressure dependent, thus, controlling the excess pressure at some tactical nodes in the network is worthwhile in reducing the water losses*", [Abu-Mahfouz et al., 2019]. From an operational viewpoint, WDN are sub-divided into Pressure Metered Area (PMA) or District Metered Area (DMA), the consequence of which increases the management of pressure flux across the distinct sectors. However, the selection of such supervised area is a strenuous task and results into a multi-parameters minimization problem, [Laucelli et al., 2017]. Once sectorized, the PM is operationally

carried-out via the use of a valves, usually pressure regulator valves, or hydraulic devices such as pumps. The DMA approach is depicted in Figure 1.4a. A more ad-

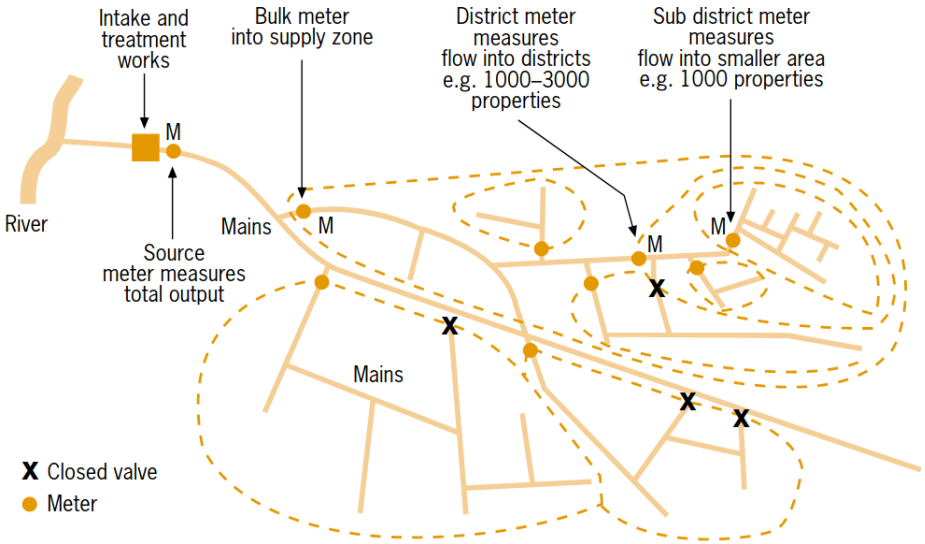

(a) *Metering hierarchy in WDN. Source [Farley, 2001]*

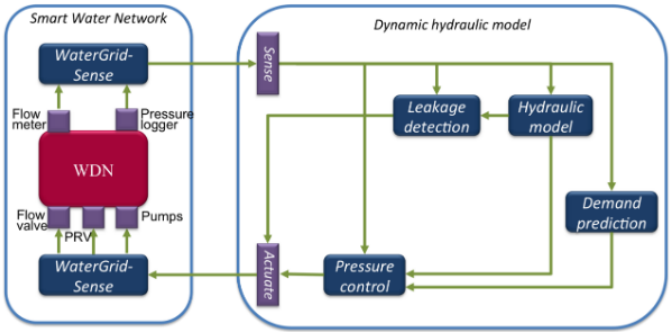

(b) *Real time control (RTC) of WDN. Source [Fontana et al., 2018]*

Figure 1.4: *Pressure Management (PM) of Water Distribution Networks (WDN).*

vanced level of efficiency is achieved through the development of hydraulic network control loop or Real Time Control (RTC) devices. The RTC monitoring methods deal with the measurement of physical fields of interest (e.g. pressure, flow-rate, temperature) in a non-continuous manner over time intervals of the order of one to fifteen minutes, [Creaco et al., 2019]. These on-field monitoring techniques are now cost effective for water suppliers due to the decreasing cost of sensors along with the development of effective telemetry technologies such as the Supervisory Control And Data Acquisition, (SCADA). The RTC concept is sketched in Figure 1.4b. The on-field measurements are broadcast to a distant control room where data are analyzed automatically (e.g. using servo control), or manually (e.g. detection of anomaly), depending on the encountered configuration. A corrective

order is then broadcasted back to the actuators scattered in the network. Such network monitoring, at the WDN's scale, is relevant for the dynamic management of the regulation valves, [Campisano et al., 2016, Creaco and Walski, 2018, Fontana et al., 2018].
The DMA, while optimal in terms of pressure and flow-rate management, may have negative counterparts. The recent work of [Armand et al., 2018] indeed pointed out the possible negative impact of the network sectorization on the overall water quality (e.g. water age, particle accumulation mechanism or bio-film behavior). The authors noticed, for the UK-based WDN investigated, an increase in water age and dead-end-like hydraulic behaviors resulting in a decreasing number of pipes with self-cleaning flow-rate. Even if PM is a robustness concept allowing to deal with large-scale slow operative issues occurring in WDN, it remains limited in scope. The reduction of background leakage is in fact allowed by PM, although leakages remain. Furthermore, PM does not significantly reduce the occurrence of new leakages or bursts. Finally, PM only protects from slow pressure trends, occurring at minute scale, whereas it is known that significant pressure variations happen at much lower time-scale, the impact of which can be more hazardous.
Thus, new elements related to strategic management of WDN may hold from transient life. A transient event in a pipeline, also referred to as Water Hammer phenomena, is related to any overpressure (or underpressure) arising from sudden flow-rate perturbations. The overpressure generated propagates in the networks, giving rise to complex hydraulic interactions. As depicted in Figure 1.5, for a simple pipe connected to an iso-pressure reservoir upstream and to an instantaneous closure valve downstream, the phenomena can be simplified. Let us suppose an instantaneous downstream closure occurring at the time $t = T_c$. If the pipe of length L is initially filled with a fluid having a pressure P_i, denoting the shock wave speed c_p, the following pressure trend is found:

- At $t = T_c$, an overpressure arises in the system due to the valve closure.
- For $t \in \left[T_c, T_c + \frac{2L}{T_c}\right[$, the shock wave propagates up to the reservoir. Once reached, the wave is fully reflected and an under-pressure propagates backwards.
- At $t = T_c + \frac{2L}{T_c}$, the under-pressure hits the closed valve.
- For $t \in \left[T_c + \frac{2L}{T_c}, T_c + \frac{4L}{T_c}\right[$, the wave propagates once again up to the reservoir. The wave is then reflected and an overpressure propagates backwards.

The sudden overpressure shocks are detrimental to the network's durability. The under-pressure phases being the more critical ones. The pressure shocks are indeed sufficient to destroy a whole hydraulic plant, as depicted in Figure 1.6, and then represent a risk that the PM methods cannot handle. Even worst, the network regulation devices induce flow-rate perturbations that may generate detrimental shock waves. On the other hand from a more optimistic standpoint, the propagating overpressure shock waves embed crucial topographic information, useful for

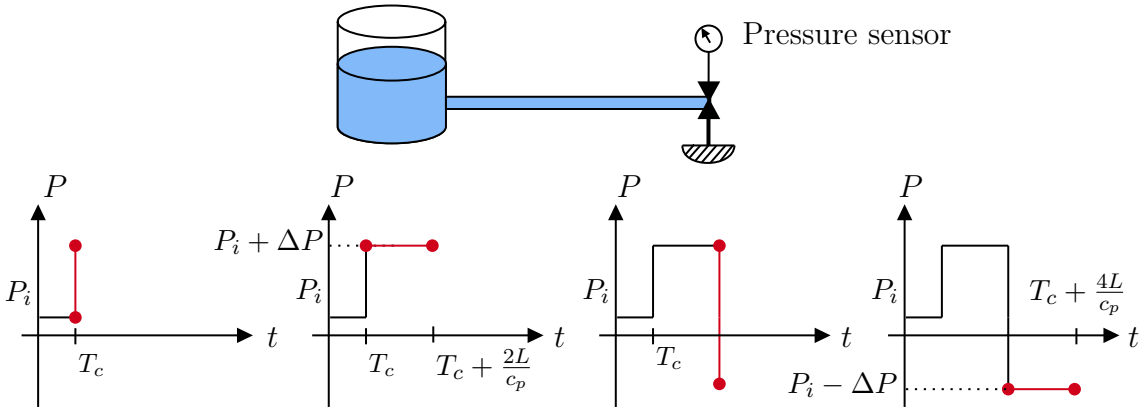

Figure 1.5: *Water hammer cycle for the reservoir-pipe-anchored valve system.*

(a) *Collapsing of a water supply pipe in Puerto Rico, source [Abuiziah et al., 2013]*

(b) *Burst of a steam pipe in Manhattan (USA) in 2007.*

Figure 1.6: *Water hammer accidents. (b): Photo credit to TIMOTHY A. CLARY/Agence France-Presse/Getty Images.*

asset management (e.g. characterization of the pipe thickness by measuring the shock propagation speed). Furthermore, since a pipe burst generates a flow-rate disturbance, it is conceivable to record the associated overpressure/under-pressure flow in several network locations, by analogy with the RTC analysis, and thus intend to locate it, [Che et al., 2021]. These considerations are a topic of interest for this PhD.

1.3 Motivation of the study

This PhD is supported by the collaborative ANRT Grant CIFRE 2019/1453 co-funded by SETOM, dedicated society of Veolia Water for the public drinking water service of Toulouse Métropole operating under the brand Eau de Toulouse Métropole. Several objectives are targeted:

- Understand and develop the currently existing knowledge framework on hy-

draulic transients.

- Develop a numeric operational tool for the prediction (e.g. infrastructure designing) of transient phenomena in WDN.
- Integrate the signals transmitted by high-frequency sensors deployed in the Toulouse Métropole WDN into a processing code able to localize (possibly approximately) the transient origin.

The Toulouse's WDN is interesting for the study of hydraulic transients for its topographical complexity and its length ($\approx$ 1200 km). State of the art of hydraulic transients in pipe, along with their consequences in terms of the WDN asset management, is now discussed.

1.4 State of the art

1.4.1 Early contributions to the water hammer research

The problem of liquid hammer occurs in any system that requires the pressurized transport of fluids through pipes. The liquid hammer problematic emerges in the second industrial revolution, in the early 20^{th} century, with the development of steam machines. The research on the subject then began with an engineers viewpoint, motivated by devices to suppress/attenuate overpressure effects. The first noteworthy contribution can be credited to the Italian engineer, [Menabrea, 1858]. In his notes, L. Menabrea underlined the importance of physical parameters such as the fluid bulk modulus $\mathcal{K}_f$, and the pipe elasticity modulus or Young's modulus E, to describe the liquid hammer phenomena. Subsequently, [Michaud, 1878] presented a guideline for the design of protection devices for hydraulic plans. He focused on the sizing of safety valves or water hammer balloons. For the latter, he provided the following relationship to determine the useful volume of the balloon

$$\frac{1}{2} m W_i^2 = \mathcal{V} P_i \log\left(\frac{P_i + \Delta P}{P_i}\right) - (\mathcal{V}_e - \mathcal{V})\, P_i, \tag{1.1}$$

where m is the mass of fluid in the pipe, $P_i, \Delta P$ and W_i stand for the initial pressure, increase pressure amplitude and velocity condition, respectively, whilst $\mathcal{V}, \mathcal{V}_e$ hold for the compressed and initial balloon air volume, respectively. These protection devices are depicted in the Figure 1.7. The same year as [Michaud, 1878], [Korteweg, 1878] theoretically derived one of the first known expressions for the propagation speed of water hammer waves, c_p. Relying on the work of [Résal, 1876] and by considering the pipe as a succession of concentric axially independent elastic rings, the author reached the following expression

$$c_{p,Korteweg} = \frac{c_0}{\sqrt{1 + \frac{2\mathcal{K}_f}{\alpha E}}}, \tag{1.2}$$

$$c_0^2 = \frac{\mathcal{K}_f}{\rho_f}, \tag{1.3}$$

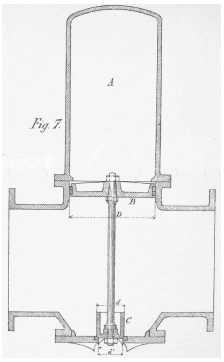

(a) *Water hammer balloon*

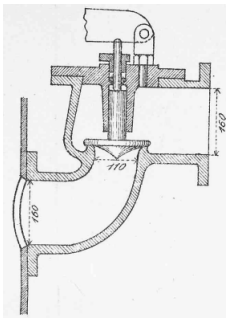

(b) *Safety valves*

Figure 1.7: *Water hammer protection devices introduced in the work of [Michaud, 1878]*

where ρ_f, is the fluid density and $\alpha \equiv \frac{e}{R_0}$, stands for the ratio of the pipe thickness e, by its inner radius R_0. [Korteweg, 1878] thus pointed out the cornerstone role play by both, the ratio of the pipe elasticity modulus by the liquid's bulk modulus, i.e. $\frac{E}{\mathcal{K}_f}$, and the α ratio, when describing the hydraulic transient pulse wave speed. The denominator of (1.2) being higher than one, it turns out that the overpressure wave speed has a lower value than the wave speed of sound in an unconstrained medium, c_0. It is worthwhile to contrast the D.J. Korteweg's work with his contemporary [Résal, 1876]. By reorganizing (1.2), it leads to, [Tijsseling, 1993, Tijsseling and Anderson, 2012]

$$\frac{1}{c^2_{p,Korteweg}} = \frac{1}{c_0^2} + \frac{1}{c^2_{p,Résal}}, \tag{1.4}$$

$$c^2_{p,Résal} = \frac{\alpha E}{2\rho_f}. \tag{1.5}$$

The herein pulse wave speed structure is obviously reminiscent with the expression of the equivalent resistance in parallel electrical circuits. In other words, the [Korteweg, 1878]'s wave velocity can be analyzed as the equivalent wave speed of an unconstrained acoustic phenomenon c_0, in parallel with an elastic response $c_{p,Résal}$. An in-depth presentation of the above expressions can be found in the work of [Tijsseling and Anderson, 2012]. Few years after the D.J. Korteweg's work, [Joukowsky, 1904] focused on the mass equilibrium occurring during an hydraulic transient event, and yielded to an analytical expression of the maximal reachable overpressure ΔP, versus the corresponding velocity variation ΔW

$$\Delta P = \rho_f c_p \Delta W. \tag{1.6}$$

This fundamental relationship permitted to increase the effectiveness and efficiency of the design criteria, thus enhancing the resilience of water plants. The derivation outlines of (1.6) are now briefly discussed. Let us consider the mass balance

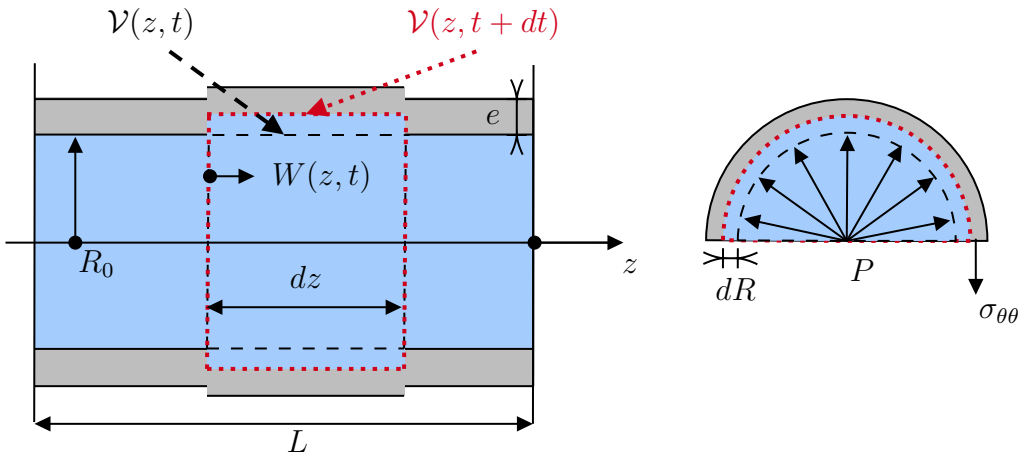

Figure 1.8: *Fluid mass conservation during a hydraulic transient*

occurring over a time step dt, in the elementary volume $\mathcal{V}$, of surface S, as defined in Figure 1.8

$$\begin{aligned}[\rho_f(z,t+dt)S(z,t+dt) - \rho_f(z,t)S(z,t)]\,dz = \\ [\rho_f(z,t)S(z,t)W(z,t) - \rho_f(z+dz,t)S(z+dz,t)W(z+dz,t)]\,dt.\end{aligned} \quad (1.7)$$

It thus follows

$$\partial_t\left(\rho_f S\right) = -\partial_z\left(\rho_f S W\right), \quad (1.8)$$

or otherwise introducing the particular derivative $D_t \equiv \partial_t + W\partial_z$

$$\underbrace{\frac{1}{\rho_f}D_t\rho_f}_{\text{Liquid compression}} + \underbrace{\frac{1}{S}D_t S}_{\text{Pipe dilatation}} + \underbrace{\partial_z W}_{\text{Velocity gradient}} = 0. \quad (1.9)$$

Whilst the fluid density gradients are related to the pressure ones, through the thermodynamic compression law, [Lighthill, 2001]

$$\frac{1}{\rho_f}D_t\rho_f = \frac{1}{\mathcal{K}_f}D_t P, \quad (1.10)$$

the pipe dilatation requires further investigations. If the solid is supposed to instantaneously respond to pressure solicitations, an equilibrium can be achieved between the hoop stress $\sigma_{\theta\theta}$, and the fluid pressure

$$\sigma_{\theta\theta} = \frac{1}{\alpha}P. \quad (1.11)$$

The theory of elasticity then relates the relative strain of the pipe with its stress

$$d\sigma_{\theta\theta} = \frac{E}{R}dR, \quad (1.12)$$

or otherwise since $S = \pi R^2$

$$\frac{1}{S} D_t S = \frac{2}{\alpha E} D_t P. \tag{1.13}$$

Finally, by combining (1.10) and (1.13) with (1.9), it yields to the following mass conservation equation

$$\frac{1}{\rho_f} D_t P + \underbrace{\frac{c_0^2}{1 + \frac{2\mathcal{K}_f}{\alpha E}}}_{\equiv c^2_{p,Korteweg}} \partial_z W = 0. \tag{1.14}$$

It turns out this relation reconcile both the [Korteweg, 1878]'s and [Joukowsky, 1904]'s works. Last but not least, it is worthwhile to highlight the major contributions of the Italian engineer [Allievi, 1913], who in the context of railway activities developed sizing methods for pipes transporting steam under pressure, or those of the French physicist [Camichel et al., 1917], who carried out a large series of experimental measurements of water hammer.
Although sufficient for many engineering applications, these theoretical outlines remain too limited in scope as they do not provide an in-depth comprehensive understanding of hydraulic transients. The relation (1.12) highlights the weaknesses of these early models. The solid rheology is highly simplified which results in a poor representation of shear and strain distribution in the pipe. Furthermore, the fluid is supposed inviscid and the long time dynamic of the pressure trend thereby remains unknown. The liquid-filled pipe problem is therefore a dual phenomena, at the border of two research frameworks being: (i) Fluid Structures Interactions (FSI) and, (ii) the fluid viscous dissipation in the pipe.

1.4.2 Water hammer, a dual phenomena

As mentioned earlier, water hammer involves different physical mechanisms. From the hydraulic standpoint and by analogy with the analysis of permanent flows in pipes, the liquid-filled pipe system is subjected to energy losses arising from viscous friction or wall shear stress. Furthermore, from a mechanical viewpoint, any pipe's degree of freedom is expected to interact with the fluid dynamics, then generating non-trivial couplings, [Wiggert and Tijsseling, 2001]. Interactions can have a plenty of origins depending on the regarded framework (e.g. cavitation, geometrical vibrations, column separation) and are classified by [Tijsseling and Lavooij, 1990] into three categories:

- *Poisson's coupling* refers to solid axial vibrations arising from radial ones. These interactions depend on the rheology used to describe the solid (*breathing phenomena*),
- *Junction couplings* emerge at pipe's connections, (e.g. dead-ends, elbows, tees),

- *Friction couplings* refer to the shear stress couplings between the fluid and the solid, i.e. viscous friction coupling, and between the solid and the surrounding medium, e.g. dry Coulomb's friction if the pipe is buried.

According to [Wiggert and Tijsseling, 2001], the Poisson and Junction couplings have a meaningful impact upon the system dynamics, i.e. the resonance structure of the solutions, whilst the friction couplings traduce the slow pressure trend attenuation due to energetic losses.

Fluid and Structure Interactions (FSI) perspectives

The FSI approach embeds the couplings occurring in a liquid-filled pipe system. The pipe is hereby supposed homogeneous, elastic and isotropic having a density ρ_s, a radial displacement ξ and an axial displacement ζ. This subsection aims to provide a review of notorious contributions dealing with FSI in liquid-filled pipes. In many cases, the acoustic hypothesis , i.e. neglecting fluid inertial contributions, is used for the fluid, [Courant and Friedrichs, 1999, D'Souza and Oldenburger, 1969, Wylie et al., 1993, Ghidaoui et al., 2005].

One of the first major contribution to overpressure wave propagation studies in pipes taking into account FSI, can be attributed to [Lamb, 1898]. The author extends the work of [Korteweg, 1878] by taking into account the Poisson's coupling effect. Based on the second Newton's law for the solid equilibrium, and a radial dependent pressure wave for the fluid, his theory achieves as follows

$$\underbrace{\rho_s e \partial_t^2 \zeta}_{\text{Axial inertia}} = \underbrace{\frac{\alpha E}{1-\nu_s^2}\left(\nu_s \partial_z \xi + R_0 \partial_z^2 \zeta\right)}_{\text{Axial tension}}, \tag{1.15}$$

$$\underbrace{\rho_s e \partial_t^2 \xi}_{\text{Radial inertia}} = \underbrace{-\frac{\alpha E}{1-\nu_s^2}\left(\frac{\xi}{R_0} + \nu_s \partial_z \zeta\right)}_{\text{Radial tension}} + \underbrace{P}_{\text{Dynamic loading}}, \tag{1.16}$$

$$\partial_t^2 P = c_0^2 \left(\partial_z^2 + \frac{\partial_r}{r}(r\partial_r)\right) P. \tag{1.17}$$

Under the plane-wave framework assumption, Lamb determines the radial pressure variation with Bessel function. Furthermore, ensuring the kinematic continuity conditions at the pipe's inner wall, he spells out a cubic (in c^2) dispersion relation for the wave speeds

$$\frac{c^2 - c_0^2}{c_0^2} \underbrace{\left[c^4 - \left(1 + \frac{\lambda^2}{4\pi^2 R_0^2}\right)\frac{E}{\rho_s\left(1-\nu_s^2\right)}c^2 + \frac{\left(1-\nu_s^2\right)\lambda^2}{4\pi^2 R_0^2}\left(\frac{E}{\rho_s\left(1-\nu_s^2\right)}\right)^2\right]}_{\text{Dispersion equation for } P=0 \text{ in (1.16)}}$$
$$- \frac{2\mathcal{D}}{\alpha}\frac{\lambda^2 c^2}{4\pi^2 R_0^2}\left(c^2 - \frac{E}{\rho_s\left(1-\nu_s^2\right)}\right) = 0, \tag{1.18}$$

with the density ratio

$$\mathcal{D} = \frac{\rho_f}{\rho_s}, \tag{1.19}$$

λ being the wavelength. The cubic structure of the dispersion relation thus provides a set of three modes of propagation, being in increased order of frequency (decreasing order of wavelength) comparable to corrections upon the acoustic fluid wave speed (i.e. c_0), solid axial wave speed (i.e. $c_s = E/\rho_s$) and dispersive solid radial wave speed (i.e. $c_{s,r}(\lambda) = \frac{\lambda}{2\pi R_0} c_s / \sqrt{1-\nu_s^2}$), respectively. Under the long wavelength hypothesis framework, i.e. $\lambda \gg R_0$, H. Lamb finds an important set of results. If the dynamic loading term is neglected in (1.16), i.e. P is set to zero, the author finds the expression of compressible axial wave speed in solid (Cf. terms between brackets in (1.18))

$$c_s^2 = \frac{E}{\rho_s} \quad , \text{(Hyp: } P = 0\text{)}. \tag{1.20}$$

Furthermore, if the solid instantaneously responds to the fluid dynamic load, i.e. neglecting time derivatives in (1.15)-(1.16), H. Lamb proves that his theory leads to [Korteweg, 1878]'s one (Cf. (1.2)) so that no proper FSI occurs then

$$c_{p,Lamb}^2 \equiv c_{p,Korteweg}^2 \quad , \text{(Hyp: } \partial_t^2 [\zeta, \xi] = 0\text{)}. \tag{1.21}$$

If one considers a highly deformable tube, i.e. $\mathcal{K}_f \gg E$, Lamb's theory merges with the [Résal, 1876]'s one (Cf. (1.5))

$$c_{p,Lamb}^2 \equiv c_{p,Résal}^2 \quad \text{, and, } \quad c_{s,Lamb}^2 = \frac{E}{\rho_s (1-\nu_s^2)} \quad \text{, (Hyp: } \mathcal{K}_f \gg E\text{)}. \tag{1.22}$$

Finally, Taylor-expanding the dispersion relation (1.18) with respect to the radius per wavelength ratio, i.e. R_0/λ, H. Lamb finds an analytical formulation for the fluid and axial solid wave speed corrections due to FSI

$$c_{\pm,Lamb}^2 = \frac{1}{2}\left[\bar{c}_{Lamb}^2 \pm \sqrt{\bar{c}_{Lamb}^4 - \frac{4\left(c_0 c_s\right)^2}{1 + \frac{2(1-\nu_s^2)\mathcal{K}_f}{\alpha E}}}\right], \tag{1.23}$$

$$\bar{c}_{Lamb}^2 = \frac{c_s^2 + c_0^2\left(1 + \frac{2\mathcal{D}}{\alpha}\right)}{1 + \frac{2(1-\nu_s^2)\mathcal{K}_f}{\alpha E}}, \tag{1.24}$$

where the negative mode holds for the fluid pulse wave speed correction, whilst the positive mode stands for the axial solid wave speed correction one. [Skalak, 1954, Skalak, 1956] extends the brilliant contribution of [Lamb, 1898]. In a sterling paper, Skalak derives an in-depth analysis of the coupling mechanisms occurring between an elastic shell pipe and the liquid. He considers both rotatory radial inertia and the bending moment of the solid. The author shell model (hereby slightly re-organized) achieves as follows, [Flügge, 1960, Paidoussis, 2003]

$$\underbrace{\rho_s e \partial_t^2 \zeta}_{\text{Axial inertia}} = \underbrace{\frac{\alpha E}{1-\nu_s^2}\left(\nu_s \partial_z \xi + R_0 \partial_z^2 \zeta\right)}_{\text{[Lamb, 1898]'s axial tension}} - \underbrace{\frac{\alpha e^2 E}{12\left(1-\nu_s^2\right)} \partial_z^3 \xi}_{\text{Bending axial tension}}, \tag{1.25}$$

and

$$\underbrace{\rho_s e \partial_t^2 \xi}_{\text{Radial inertia}} - \underbrace{\frac{\rho_s e^3}{12}\partial_z^2\partial_t^2\xi}_{\text{Rotatory inertia}} = \underbrace{-\frac{\alpha E}{1-\nu_s^2}\left[\left(1+\frac{\alpha^2}{12}\right)\frac{\xi}{R_0}+\nu_s\partial_z\zeta\right]}_{\text{[Lamb, 1898]'s modified radial tension}} - \underbrace{\frac{\alpha e^2 E}{12\left(1-\nu_s^2\right)}\partial_z^2\left[R_0\partial_z^2\xi-\partial_z\zeta\right]}_{\text{Bending}} + \underbrace{P}_{\text{Dynamic loading}} . \quad (1.26)$$

The continuity conditions at the fluid solid interface were ensured and the author overcomes the system resolution by performing a conjugate Fourier (upon space) and Laplace (upon time) analysis. The in-depth investigations of the radial solid displacement field reveals a discrete infinite set of resonance frequencies governed by a transcendental equation. As H. Lamb, [Skalak, 1954, Skalak, 1956] then analyzes the solution in the infinite limit wavelength, i.e. when frequency goes to zero. In this limit, two propagating modes remain and: "*a physical interpretation of this fact is that only these two lowest modes have finite phase velocities as the wave-length increases indefinitely.* The two wave speeds, in the infinite wavelength framework, then converges in the [Lamb, 1898]'s one

$$\lim_{\lambda\to\infty} c^2_{\pm,Skalak} \equiv c^2_{\pm,Lamb}. \quad (1.27)$$

R. Skalak is nevertheless the first to introduce the key notion of: "*precursor wave*" to describe the impact of the axial pipe dynamic upon the overall movement. Aware of using the shell approximation for practical analysis, [Skalak, 1954, Skalak, 1956] made drastic simplifications of his model. Whereas the effects of precursor wave still remain, this new model neglects the wave speed dispersion arising from radial inertia. R. Skalak thus achieved the derivation of one of the first known four-FSI equations to describe the liquid-filled pipe coupled dynamic

$$\frac{1}{\mathcal{K}_f}\partial_t P + \partial_z W = -\frac{2}{R_0}\partial_t\xi, \quad (1.28)$$

$$\rho_f \partial_t W + \partial_z P = 0, \quad (1.29)$$

$$\underbrace{\rho_s e \partial_t^2 \zeta}_{\text{Axial inertia}} = \underbrace{\frac{\alpha E}{1-\nu_s^2}\left(\nu_s\partial_z\xi + R_0\partial_z^2\zeta\right)}_{\text{[Lamb, 1898]'s axial tension}} \quad (1.30)$$

$$\underbrace{\frac{\alpha E}{1-\nu_s^2}\left[\frac{\xi}{R_0}+\nu_s\partial_z\zeta\right]}_{\text{[Lamb, 1898]'s radial tension}} = P, \quad (1.31)$$

or otherwise considering the coupled wave form

$$\left[\partial_t^2 - \begin{pmatrix} c^2_{p,Skalak} & 0 \\ 0 & c_s^2 \end{pmatrix}\partial_z^2 - \begin{pmatrix} 0 & 2\nu_s\rho_f c^2_{p,Skalak} \\ \frac{\nu_s c_s^2}{\alpha E} & 0 \end{pmatrix}\partial_z\partial_t\right]\begin{pmatrix} P \\ \partial_t\zeta \end{pmatrix} = \mathbf{0}, \quad (1.32)$$

with

$$c^2_{p,Skalak} = \frac{c_0^2}{1 + \frac{2\mathcal{K}_f(1-\nu_s^2)}{\alpha E}}. \tag{1.33}$$

Two years after, [Lin and Morgan, 1956] followed up [Skalak, 1954, Skalak, 1956]'s analysis by both: (i) integrating a transverse shear force contribution to the radial solid momentum conservation (1.26) and, (ii) considering the movement along the direction of revolution of the pipe. In the long wavelength assumption framework, they also carried out a frequency analysis upon both fluid and solid systems and converged in the results of [Lamb, 1898] and [Skalak, 1954, Skalak, 1956]. Although precursor waves has been theoretically accepted for a long time, it was experimentally confirmed by [Thorley, 1969] in 1969 only. Thorley conducted a series of water hammer experiments in elastic steel (aluminum alloyed) and visco-elastic (PE) pipes, and focused on the measurement of coupled wave propagation velocities. Whilst the predictive trend for the wave propagation speeds was inconclusive for visco-elastic materials, the order of magnitude for elastic solids was consistent. The author attributed these discrepancies to the temperature sensitivity of visco-elastic rheology as illustrated in Figure 1.9. [DeArmond and Rouleau,

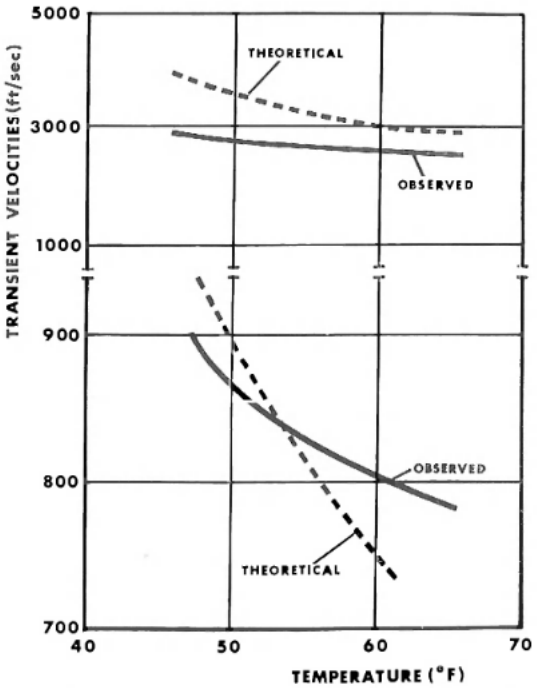

Figure 1.9: *Experimental results of [Thorley, 1969]. The upper curve represents the investigated elastic material whilst the lower curve holds for the visco-elastic material.*

1972] carried out a complete study extending the analysis of [Lin and Morgan, 1956] viscous fluid. The kinematic continuity conditions at the pipe's wall were spelled out and ensured, whilst the set of constitutive equations was analyzed un-

der the scope of the plane wave framework. The authors then concluded that the: "'*frequency dependence of the zeroth mode phase velocity is primarily a result of the tube constraint at high frequencies and viscosity at low frequencies.*" Finally, [DeArmond and Rouleau, 1972] were able to propose an order of magnitude of the transverse solid shear force q, versus the fluid wall shear-stress τ_w

$$q \equiv \frac{D}{\alpha}\left(\frac{c_0}{c_s}\right)^2 \tau_w. \tag{1.34}$$

[Williams, 1977] carried out experimental tests similar to those of [Thorley, 1969] on ABS, plasticized PVC and steel materials for flexible and rigid configurations, i.e. unstressed and axially stressed pipes. Despite the author encountered difficulties in discarding the effects of the junction coupling arising from his downstream solenoid valve, he clearly observed and identified the presence of precursor perturbations resulting from Poisson's coupling. [Williams, 1977] further noted: "*that mechanical damping can be more important for water-hammer decay than viscous friction*". This remark is meaningful when the radial inertia of the pipe is preponderant or when the rheology is inelastic, as is the case for visco-elastic materials. [Rubinow and Keller, 1971, Rubinow and Keller, 1978] delivered a complete work emphasizing the previous contributions from [Lamb, 1898] to [Bürmann, 1975]. The authors considered the rigid, elastic and visco-elastic behavior of a pipe together with the viscous, or inviscid, behavior of the fluid. Their pipe model furthermore accounts for the radial thickness influence. The authors derived a complete set of dispersion relations and studied the frequency dependence of the propagation wave speeds.

[Kuiken, 1984a, Kuiken, 1984b, Kuiken, 1984c] carried out an outstanding and complete work emphasizing rheology, thermal and fluid viscosity effects. The work of [Kuiken, 1984c] provides a comprehensive overview of the main models, assumptions and results of the early researches on hydraulic transients in pipes. For the solid, the momentum conservation equation are r-integrated yielding to an axial dependent problem, whilst the bending effects were neglected. [Tijsseling, 1993] work represents a breakthrough in the liquid-filled pipe research area. The author combined both the Navier-Stokes equations, averaged over the pipe's section, with the solid momentum conservation equations, also denoted Lamé-Clapeyron equations, [Thual, 1997]. In the long wavelength assumptions framework, the radial dependence of the physical fields were neglected, and [Tijsseling, 1993] derives a set of four-FSI hyperbolic equations

$$\left[\begin{pmatrix} \frac{1}{\mathcal{K}_f}\left(\frac{c_0}{c_{p,Tij}}\right)^2 + \frac{4\nu_s^2}{\alpha(2+\alpha)E} & 0 \\ 0 & 1 \end{pmatrix}\partial_t + \begin{pmatrix} 0 & 1 \\ \frac{1}{\rho_f} & 0 \end{pmatrix}\partial_z\right]\begin{pmatrix} P \\ W \end{pmatrix} = \frac{2\nu_s}{E}\begin{pmatrix} \partial_t\sigma_{zz} \\ 0 \end{pmatrix} - \begin{pmatrix} 0 \\ \frac{2\tau_w}{\rho_f R_0} \end{pmatrix}, \tag{1.35}$$

$$\left[\partial_t - \begin{pmatrix} 0 & E \\ \frac{1}{\rho_s} & 0 \end{pmatrix}\partial_z\right]\begin{pmatrix} \sigma_{zz} \\ \dot{\zeta}, \end{pmatrix} = \frac{2\nu_s}{\alpha(2+\alpha)}\begin{pmatrix} \partial_t P \\ 0 \end{pmatrix} + \begin{pmatrix} 0 \\ \frac{2\tau_w}{\rho_s e(2+\alpha)} \end{pmatrix} \tag{1.36}$$

$$c_{p,Tij}^2 = \frac{c_0^2}{1 + \frac{2\mathcal{K}_f}{\alpha E}\left(\frac{2(1-\nu_s^2)}{2+\alpha} + \alpha(1+\nu_s)\right)} \tag{1.37}$$

By analogy with the work of [Lamb, 1898, Skalak, 1956, Lin and Morgan, 1956] a set of two coupled wave speeds can be spelled out from (1.35)-(1.36) and results

as follows

$$c^2_{\pm,Tij} = \frac{1}{2}\left[\bar{c}^2_{Tij} \pm \sqrt{\bar{c}^4_{Tij} - 4c_s^2 c^2_{p,Tij}}\right], \tag{1.38}$$

$$\bar{c}^2_{Tij} = c_s^2 + \left(1 + \frac{4\nu_s^2 \mathcal{D}}{\alpha\,(2+\alpha)}\right) c^2_{p,Tij}. \tag{1.39}$$

A simplified derivation but neglecting the influence of transverse shear τ_w, can also be found in [Tijsseling, 2007]. Further information on the development of liquid-filled pipe models during the 20^{th} century can also be gathered from the review of [Tijsseling, 1996]. The pulse wave speeds and the corresponding corrective coupled wave speeds, are depicted in Figure 1.10. The Skalak's pulse wave speed

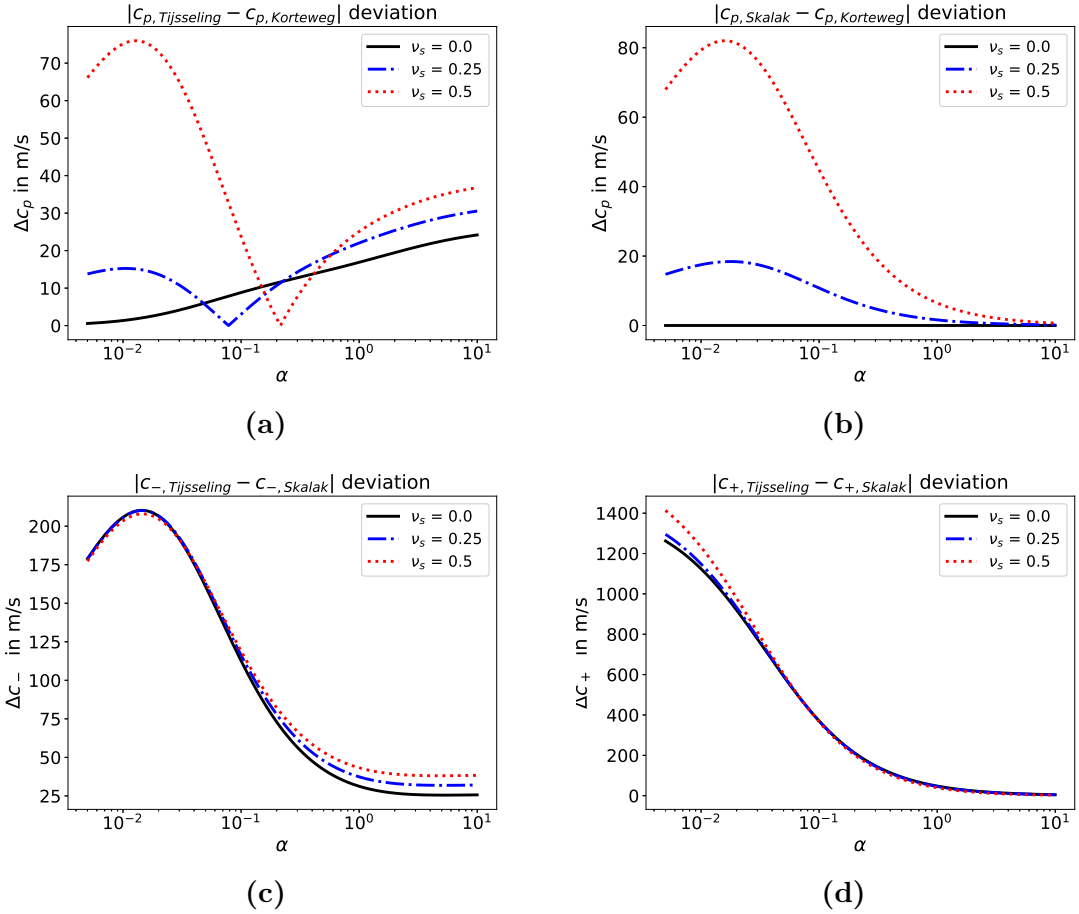

Figure 1.10: *Pulse and FSI-corrective wave speeds absolute deviation analysis for the models of [Korteweg, 1878, Skalak, 1956, Tijsseling, 2007].*

model converges, in the limit α tends to one, to the D. Korteweg's one, whilst as expected, the A.S. Tijsseling's model differs for thick tubes (Cf. Fig. 1.10a&1.10b). In addition, for very thin pipes, the models strongly differ in the prediction of the coupled wave speeds as depicted in Figure 1.10d.

Despite the hereby PhD is restricted to the analysis of four-FSI equations system, i.e. ignoring radial inertia and radial bending, it is important to point out that depending on the system's degree of freedom, several additional vibrations must be taken into account (e.g. torsion, bending etc.). The recent works of review of [Li et al., 2015, Ferras et al., 2018] provide insight into this modeling when all pipe's degree of freedom are considered. The four-FSI equations system (1.35)-(1.36) nevertheless requires a closure wall shear stress model, [Budny et al., 1991]. Some wall shear stress models emerged from the hydraulic analysis of viscous flow in pipes, ignoring FSI effects.

Hydraulic standpoint

The hydraulic approach for the water hammer analysis focuses on the energetic viscous losses, but ignores FSI effects. Precisely, only the instantaneous response of the radial solid deformation is considered, then recovering the framework provided in section 1.4.1, whilst Poisson's coupling is discarded. In such a limit, the set of four-FSI equations introduced in (1.35)-(1.36), simplifies into a set of two coupled hyperbolic equations upon both fluid pressure and velocity variables, [Chaudhry, 2014, Martins et al., 2017]

$$\left[\partial_t + \begin{pmatrix} 0 & \rho_f c_p^2 \\ \frac{1}{\rho_f} & 0 \end{pmatrix} \partial_z\right] \begin{pmatrix} P \\ W \end{pmatrix} = -\frac{2\tau_w}{\rho_f R_0} \begin{pmatrix} 0 \\ 1 \end{pmatrix}. \tag{1.40}$$

When a viscous fluid is considered, the above equation set is unclosed and a wall shear stress model is needed. A first intuitive modeling approach is to extend the steady-state framework provided by the Darcy-Weisbach's friction law (Cf. [Brown, 2002]), to the hydraulic transient one, [Tijsseling, 1993]. The use of the redesigned quasi-steady wall shear rate τ_{qst}

$$\tau_{qst}(z,t) = \frac{\rho_f f_{DW} W(z,t)|W(z,t)|}{8}, \tag{1.41}$$

through the Darcy-Weisbach coefficient f_{DW}, is nevertheless questionable for transient investigations. Poor experimental agreement is sometimes found using this dissipation model [Vardy and Hwang, 1991, Bergant et al., 2001, Adamkowski and Lewandowski, 2006].

The model was then enriched to better predict the experimental attenuation. Several classes of model, [Duan et al., 2020] have been established: (i) instantaneous material acceleration-based (IMAB) models and, (ii) weighting function-based (WFB). Although conceptually different, these two approaches seek to account for the same physical observation, that the near-wall dynamics does not instantaneously respond to the core velocity variations. The energetic dissipation emerges from the time response delay between the central part of the flow and its boundary layer. Finally, these models are based on a decomposition of the total wall shear rate into a quasi-steady component, via the use of the Darcy-Weisbach model

(1.41), and a transient one τ_{tr}, [Ghidaoui et al., 2005]

$$\tau_w = \tau_{qst} + \tau_{tr}. \tag{1.42}$$

The τ_{tr} component is then expected to fill the gaps between the model predictions and the experimental observations, when only a quasi-steady wall shear stress model is considered.

Instantaneous material acceleration-based (IMAB) model relies on semi-empirical observations and assumes a linear variation of the transient wall shear stress τ_{tr}, with respect to the mean flow acceleration $\partial_t W$. These models arise from the experimental work of [Daily et al., 1955]. The author analyzed the turbulence structure in a pressurized flow with or without orifices. [Daily et al., 1955] highlighted the time delay between the response of boundary lines with respect to the mean flow variations. He then proposed the following transient wall shear stress model

$$\tau_{tr} = \frac{\rho_f k_3 R_0}{2} \partial_t W, \tag{1.43}$$

where k_3 account for the boundary response deviation. When re-injecting the above transient wall shear stress expression into the hyperbolic constitutive equation set (1.40), it turns out that no energetic damping arises, [Vítkovský et al., 2006]. Indeed, the time-derivatives of both (1.40) and (1.43) can be factorized so that no source term remains in the hyperbolic system r.h.s. However, the structure of the hyperbolic system, i.e. its eigenvalues and eigenvectors, are modified by k_3. The wave speed is thus modified by the prefactor, $\frac{1}{\sqrt{1+k_3}}$. To account for energetic losses, the IMAB model was then latter completed by [Brunone et al., 1991, Bergant et al., 2001, Pezzinga, 2000]. The authors added a convective term to the transient shear stress (1.43) and found

$$\tau_{tr}(z,t) = \frac{\rho_f k_3 R_0}{2} \left(\partial_t W + c_p sgn(W) \left| \partial_z W \right| \right), \tag{1.44}$$

where $sgn(W)$ informs on the accelerating or decelerating transient flow phase. This inertial contribution, similar to the Navier's inertial terms, creates a source term in the hyperbolic system (1.40). Consequently, the IMAB model intents to model both the attenuation and the phase shift of overpressure waves. Some authors, [Vitkovsky et al., 2000, Ramos et al., 2004, Storli and Nielsen, 2011], also developed a slightly distinct model by using a second semi-empirical parameter k_3'

$$\tau_{tr}(x,t) = \frac{\rho_f R_0}{2} \left(k_3 \partial_t W + k_3' c_p sgn(W) \left| \partial_z W \right| \right) \tag{1.45}$$

and then distinguished the phenomena of wave speed deviation from the damping one, [Vítkovský et al., 2006]. When the single coefficient model is used in (1.44), an approximation arising from theoretical arguments is used to estimate the Reynolds

number dependence of k_3, [Vardy and Brown, 1995]

$$k_3 = \frac{\sqrt{0.00476}}{2} \text{ , if, } Re \leq 2000, \tag{1.46}$$

$$k_3 = \frac{1}{2}\sqrt{\frac{7.41}{Re^{\log\left(\frac{14.3}{Re^{0.05}}\right)}}} \text{ , else,} \tag{1.47}$$

where $Re = W_0 R_0/\nu_f$ is the Reynolds number, W_0 is a reference axial fluid velocity magnitude and ν_f is the fluid kinematic viscosity. The k_3 Reynolds dependence is depicted in Figure 1.11. The review of [Ghidaoui et al., 2005] provides an excellent

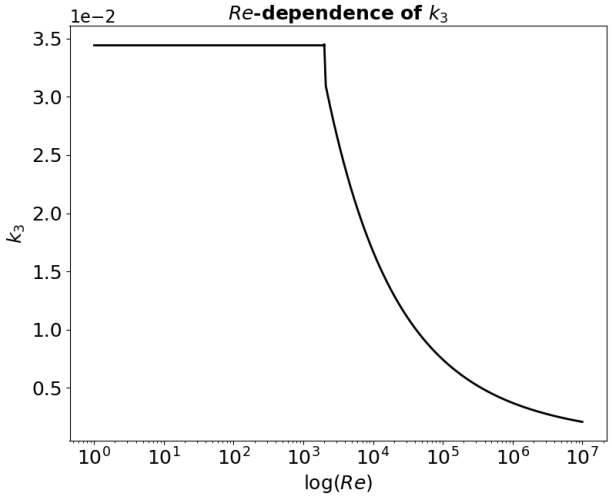

Figure 1.11: *Reynolds dependence of the deviation parameter k_3.*

state-of-the-art of IMAB models. In addition to the use of semi-empirical models, some analytical developments relying on a weighting function-based approach, have also been carried out.

Weighting function-based (WFB) model seeks for an analytical description of the viscous shear energetic losses. One of the first noteworthy contribution was given by [Holmboe and Rouleau, 1967]. In the low-Mach number acoustic framework, i.e. neglecting Navier's inertial terms and decomposing the fluid variables into steady and perturbed components, the authors performed a Laplace domain analysis of the fluid mass and momentum conservation equations. They achieved the derivation of a radial- Bessel-dependent solution for the axial fluid velocity. The transient wall shear stress was then derived, using the axial fluid velocity radial-dependence

$$\tau_{tr} = \rho_f \nu_f \partial_r W \Big|_{r=R_0}. \tag{1.48}$$

This theoretical approach is also convergent with that of [Joukowsky, 1904] in the prediction of the maximum overpressure. Furthermore, the authors highlighted the relevance of a dimensionless parameter associated with the damping trend of the pressure waves

$$\delta^2 = \frac{\nu_f L}{c_p R_0^2} \equiv \frac{1}{\epsilon Re_p}, \tag{1.49}$$

where $\epsilon = R_0/L$ is the inner pipe's radius to its length ratio and $Re_p = R_0 c_p/\nu_f$ is the pulse re-scaled Reynolds number. [Zielke, 1966, Zielke, 1968] delivered an in-depth analysis of the hydraulic problem. The author addressed a fully developed laminar boundary layer problem and theoretically analyzed both the mass conservation equation and the diffusion equation, i.e. momentum conservation equation, governing the axial fluid velocity, the which is forced by the longitudinal pressure gradient

$$\partial_t P + \rho_f c_p^2 \partial_z W = 0, \tag{1.50}$$

$$\left[\partial_t - \nu_f \frac{\partial_r}{r}(r\partial_r)\right] W = -\frac{1}{\rho_f}\partial_z P. \tag{1.51}$$

The resolution of (1.51) was overcome in the Laplace domain, whilst performing an inverse Laplace transform (by the Cauchy's residue theorem) yielded to a convoluted expression of the wall shear stress

$$\tau_w = \underbrace{\frac{4\rho_f\nu_f}{R_0}W}_{\tau_{qst}} + \underbrace{\frac{2\rho_f\nu_f}{R_0}\int_0^t \Theta_{Zielke}(t-\tau)\partial_\tau W d\tau}_{\tau_{tr}}, \tag{1.52}$$

where $\Theta_{Zielke}(t)$ is the convolution kernel provided by the following relations

$$\Theta_{Zielke} = \sum_{i=0}^{5} m_i \left(\frac{\nu_f t}{R_0^2}\right)^{\frac{i-1}{2}} \text{, if, } \frac{\nu_f t}{R_0^2} \leq 0.02, \tag{1.53}$$

$$\Theta_{Zielke} = \sum_{i=0}^{4} e^{-n_i \frac{\nu_f t}{R_0^2}} \text{, if, } \frac{\nu_f t}{R_0^2} > 0.02, \tag{1.54}$$

$$n_i = [26.3744, 70.8493, 135.0198, 218.9216, 322, 5544], \tag{1.55}$$

$$m_i = \left[\frac{1}{2\sqrt{\pi}}, -1.25, \frac{15}{16\Gamma\left(\frac{3}{2}\right)}, \frac{15}{16}, \frac{135}{256\Gamma\left(\frac{5}{2}\right)}, -\frac{45}{64\Gamma(3)}\right], \tag{1.56}$$

and Γ is the Gamma function. The presence of the τ_{qst} term in (1.52) arises form the fact that W. Zielke did not decompose his fluid velocity and pressure fields into steady and perturbed components as its classically done in the low Mach number acoustic framework. This point is highlighted here and will be discussed in more detail later in §3. It is noteworthy to point out that the W. Zielke's kernel is convoluted with the fluid mean acceleration. It then reflects that the underlying physical phenomena governing the energetic damping in the

WFB models and in the IMAB ones is the same (Cf. (1.43)), and relies on the non-instantaneous response of the boundary layer with respect to the core acceleration. Whilst the IMAB assumes a direct linear relation between the wall shear stress and the mean acceleration using k_3, the WFB embeds all the historic mean flow variations through a time convolution with $\Theta_{Zielke}(t)$. The scaling of the W. Zielke convolution kernel is obtained regarding both the first term of (1.53) and by setting up the characteristic advective time scale $\tau_c = \frac{L}{c_p}$, thus leading to

$$\Theta_{Zielke} \equiv O\left(\frac{1}{\delta}\right), \tag{1.57}$$

with δ is introduced in (1.49). The convolution kernel scaling thereby merges with the conclusion of [Holmboe and Rouleau, 1967]. Finally, the author confronted his theory to the experimental data of [Holmboe and Rouleau, 1967] and a very close agreement was found as revealed in Figure 1.12. [Wood and Funk, 1970] extended

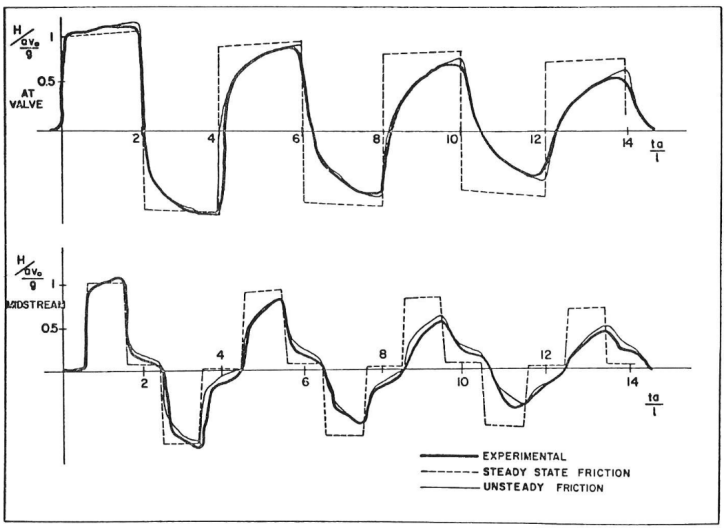

Figure 1.12: *[Zielke, 1968]'s theoretical predictions compared to [Holmboe and Rouleau, 1967]'s experimental data. The following notation are used: H the hydraulic head line, a the pulse wave speed.*

the W. Zielke's work and supposed a near wall concentrated laminar boundary layer, or a skin friction model. The flow in the core area, or bulk region, was assumed inviscid. The Figure 1.13a provides a schematic representation of the [Wood and Funk, 1970]'s model. During a transient event, the authors supposed that: "*the fluid remains divided into a turbulent core and laminary boundary layer and that, the boundary-layer thickness remains constant.*" The boundary layer thickness, and hence its dynamic, are thus governed by the preexisting flow regime. The dimensionless steady boundary layer thickness δ_{st}, follows from the equilibrium of steady state viscous terms with the initial the pressure gradient

$$\delta_{st} = \frac{4}{f_{DW} Re}. \tag{1.58}$$

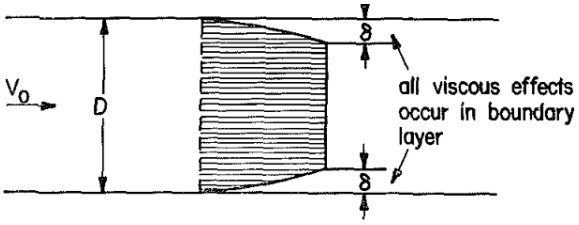

(a) *Laminar boundary layer concept, [Wood and Funk, 1970].*

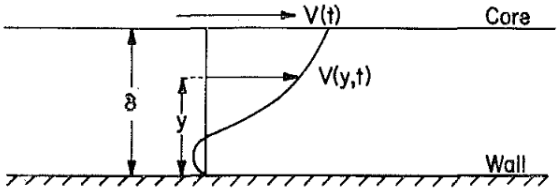

(b) *Axial velocity matching at the fluid boundary layer interface, [Wood and Funk, 1970].*

Figure 1.13: *[Wood and Funk, 1970] boundary layer model for pressure waves energetic damping.*

Two approaches were finally presented to determine the attenuation of pressure waves. The first one focused on the resolution of the diffusion equation upon the axial velocity in the boundary layer. A velocity matching at the boundary layer interface is then performed to ensure kinematic continuity conditions (Cf. Fig.1.13b). The second method involved an energy balance band takes into account the energetic losses via the quadratic integral of the wall shear stress over the boundary layer thickness. [Vardy and Hwang, 1991] designed a two-dimensional model to describe the viscous losses in both the laminar and turbulent flow regimes. By considering the pipe as an in-extensible solid, i.e. without radial dilatation, they decomposed the fluid into a succession of interconnected concentric rings of small thicknesses. Each layer of fluid is coupled to others via momentum transfers, radial kinematic and shear stress continuity, as depicted in the Figure 1.14. Finally,

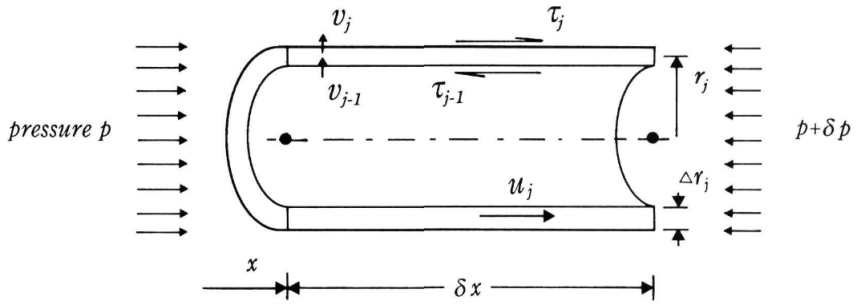

Figure 1.14: *Momentum balance on a cylinder element, [Vardy and Hwang, 1991]*

by ensuring the mass and momentum conservations in each rings, the authors derived a coupled hyperbolic system forced by the radial transfer terms. For

turbulent flow regimes, a five-region model was adopted to model the shear rate. The authors found: "*pleasantly surprising that Zielke's expression is so successful even through his assumed (laminar) initial velocity profile differs markedly from reality*". [Vardy and Hwang, 1993] extended the laminar framework of [Wood and Funk, 1970] by taking into account the Reynolds-dependence of the flow in its convolution kernel. The flow was divided into two zones: (i) the acoustic zone (*bulk*) where the velocity fields are radially uniform and, (ii) the boundary layer (*annulus*) where viscous effects are concentrated. The dimensionless boundary layer thickness is once again set up to match with the preexisting flow conditions. The authors, relying on the experimental work of [Artl, 1993], highlighted the effects of the initial Reynolds number upon the convolution kernel structure as depicted in Figure 1.15. In the boundary layer, a diffusion equation was derived,

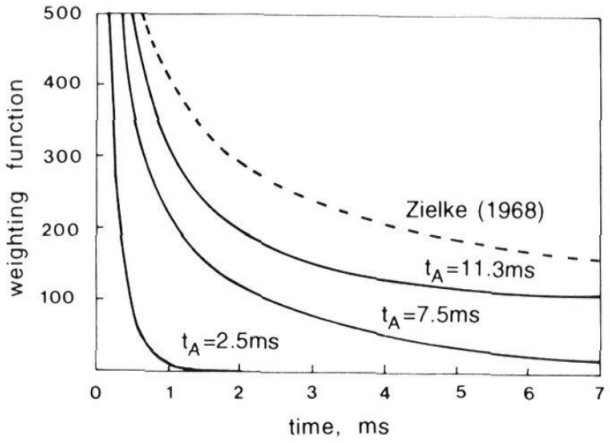

Figure 1.15: *[Vardy and Hwang, 1993] discussion on the convolution kernel Reynolds-dependence according to the experimental work of [Artl, 1993].*

the which merges with both [Zielke, 1968, Wood and Funk, 1970] theories. The difficulty and elegance of [Vardy and Hwang, 1993]'s model lies in performing an *asymptotic matching* between the axial inner, i.e. in the skin friction, and outer, i.e. in the bulk, velocities at the boundary layer interface. The authors finally yielded to the derivation of a Reynolds-dependent (via the δ_{st} parameter) transient wall shear stress kernel expression

$$\Theta_{\text{Vardy et al. (1993)}}(t) \approx \frac{1}{\delta_{st}} \sum_{k \in \mathbb{N}^*} e^{-\left(\frac{k\pi}{\delta_{st}}\right)^2 \frac{\nu_f t}{R_0^2}} \equiv O\left(\frac{1}{\delta_{st}}\right). \tag{1.59}$$

The experimental contributions of [Laufer, 1953, Ohmi and Usui, 1976] on the turbulent kinematic viscosity distribution in pipes, permitted to [Vardy and Brown, 1995] to extend the previous framework of [Vardy and Hwang, 1993] by accounting for higher Reynolds numbers ($Re \gg 10^5$). This new model, valid in a smooth pipe, is based on an idealized radial distribution of the turbulent kinematic viscosity in the boundary layer as shown in Figure 1.16a. The core viscosity ν_c, per the wall

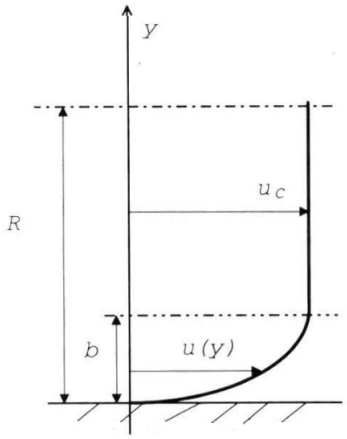

(a) *Skin friction axial velocity distribution, [Vardy and Brown, 1995]*

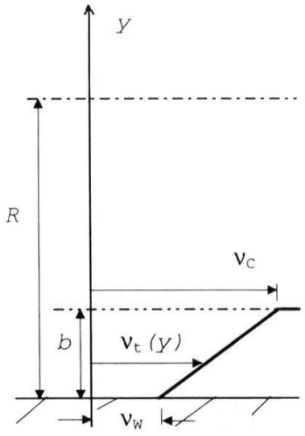

(b) *Idealized distribution of turbulent kinematic viscosity, [Vardy and Brown, 1995]*

Figure 1.16: *Idealized velocity and viscosity distribution for the skin friction model of [Vardy and Brown, 1995].*

viscosity ν_w, ratio is introduced and used to characterize the turbulent kinematic distribution

$$\frac{\nu_c}{\nu_w} \equiv \sigma_{\text{Vardy et al.}} \approx 0.173 \left(f_{DW} Re\right)^{1.12}, \tag{1.60}$$

whilst a new dimensionless boundary layer thickness is set up to scale in

$$\frac{b}{R_0} = \delta_{st} \frac{u_c}{U} \frac{\sigma_{\text{Vardy et al.}} - 1}{\ln\left(\sigma_{\text{Vardy et al.}}\right)}, \tag{1.61}$$

where u_c is the uniform core velocity, U the mean flow velocity per section and b is the dimensional boundary layer thickness. In the limit $\sigma_{\text{Vardy et al.}}$ tends to unity, the dimensionless boundary layer thickness of [Vardy and Hwang, 1993], presented in (1.58), is recovered. A similar asymptotic analysis to the one of [Vardy and Hwang, 1993] was carried out and yielded to the derivation of a modified convolution kernel

$$\Theta_{\text{Vardy et al. (1995)}}(t) = \frac{A^* e^{-B^* \frac{\nu_f t}{R_0^2}}}{\sqrt{\frac{\nu_f t}{R_0^2}}}, \quad A^* = \frac{1}{2\sqrt{\pi}}, \quad B^* = 0.135 Re^{\log_{10}\left(\frac{14.3}{Re^{0.05}}\right)}, \tag{1.62}$$

and then for $t \equiv O\left(\frac{L}{c_p}\right)$

$$\Theta_{\text{Vardy et al. (1995)}} \equiv O\left(\frac{1}{\delta}\right). \tag{1.63}$$

Under the hypothesis framework of constant acceleration transients, i.e. $\partial_t W = cst$ in (1.52), the authors derived a straightforward relation between the semi-empirical

deviation constant k_3, and their inertial shear coefficient B^*

$$k_3 \approx \frac{1}{2\sqrt{B^*}}. \tag{1.64}$$

This relation provides a brief explanation for the derivation of the system (1.46)-(1.47). They thus pointed out the Reynolds-dependence of the parameter k_3. Additional elements on the relations between the [Vardy and Brown, 1995]'s model and the IMAB ones lie in the work of [Brunone et al., 1991]. Finally, it is important to mention that many expressions exist to model A^* and B^*, the which are derived from several approximations. [Vardy and Brown, 2003] extended their previous model by modifying both: (i) their idealized turbulent viscosity distribution (until then considered as infinite in the acoustic core) and, (ii) by considering the boundary layer thickness as Reynolds non dependent. They thus reached a new convolution kernel via a modification of the B^* coefficient

$$B^* = \frac{Re^{\log_{10}\left(\frac{15.29}{Re^{0.0567}}\right)}}{12.86}, \tag{1.65}$$

which is valid over a wide range of Reynolds numbers, $Re \in [2 \cdot 10^3, 10^8]$. Finally, this theory was one more time extended by [Vardy and Brown, 2004] in order to take into account the pipe's roughness.
It is noteworthy here to discuss the assumptions used by [Vardy and Brown, 2003, Vardy and Brown, 2004] in the derivation of their models. The authors indeed supposed that the idealize turbulent eddy viscosity profile does not instantaneously respond to the mean flow variations. Quoting the authors: "*The change in the effective viscosity occurs during the period when the shape of the velocity profile is changing, not during the earlier period when the velocity amplitude increases uniformly. That is, there is a phase lag between the step change in mean velocity and the resulting change in the effective viscosity.*" This assumption is known in the subject literature as the "*frozen viscosity*" model and was analyzed by [Ghidaoui et al., 2002, Ghidaoui et al., 2005]. The authors validated the "*frozen viscosity*" approach as long as the shear pulse diffusion through the viscous sub-layer time scale, i.e. $\tau_{diff,sublayer} \equiv \frac{\sqrt{2}R_0}{u_\star}$ with $u_\star^2 = \frac{f_{DW}W_0^2}{8}$ the friction velocity, is smaller than the advective wave time scale, i.e. $\tau_{adv} \equiv \frac{L}{c_p}$. The condition of validity then follows

$$\frac{4R_0c_p}{\sqrt{f_{DW}}LW_0} \gg 1, \tag{1.66}$$

or otherwise, invoking the definition of δ and δ_{st} in (1.49) and (1.58), respectively

$$\delta^2 \ll \sqrt{f_{DW}}\delta_{st}, \tag{1.67}$$

It obviously follows from the condition (1.67), that it should not be expected close agreement between the [Vardy and Brown, 2003, Vardy and Brown, 2004] model predictions and the experimental data, for observation times upper than $\tau_{diff,subayer}$. The relevance of the viscosity distribution, along with the relevance

of the "*frozen viscosity*" was also addressed by [Vardy et al., 2015]. The authors focused on constant acceleration flows and concluded that: "*no frozen-viscosity distribution performs well for large times after the commencement of an acceleration. However, even the simplest approximation (laminar) performs well for short durations*" and that "*very simple assumed distributions yield acceptable outcomes, provided only that the assumed value in the wall region is the molecular viscosity (or nearly so).*" To confirm or refute some models, comparisons

Friction Model Category	Model Name	Equation
Steady and quasisteady friction	Darcy Weisbach	$f_s = \frac{8fL}{\pi^2 g D^5} Q^2$
Instantaneous mean flow velocity	Hino	$f_u = 0.188 \left(V \sqrt{\frac{4L}{v\pi a}} \right)^{-\frac{1}{2.85}}$
Instantaneous mean flow velocity and local acceleration	Daily	$\frac{f_u}{f_s} = 1 + c_2 \frac{2D}{f_s V^2} \frac{dV}{dt}$
Instantaneous mean flow velocity, local acceleration, and convective acceleration	Brunone	$f_u = \frac{kD}{V\|V\|} \left(\frac{\partial V}{\partial t} - a \frac{\partial V}{\partial x} \right)$
Instantaneous mean flow velocity, local acceleration, and convective acceleration	Vítkovský	$f_u = \frac{kD}{V\|V\|} \left(\frac{\partial V}{\partial t} - a.sign(V) \left\| \frac{\partial V}{\partial x} \right\| \right)$
Instantaneous mean flow velocity and past velocity changes weights	Convolutional model	$f_u = \frac{16\mu}{\rho D^2 A} \left(\frac{\partial Q}{\partial t} * W(\tau) \right)$
	Vardy and Brown weighting function	$W(\tau) = \frac{A^{\times} e^{-B^{\times}\tau}}{\sqrt{\tau}}$

Figure 1.17: *Friction coefficient f_u, i.e. $\tau_{tr} \equiv \frac{\rho_f f_u W|W|}{4}$ for the characterization of transient overpressure waves damping in pipes. Original chart of [Abdeldayem et al., 2021].*

between theoretical/semi-empirical predictions and experimental data were carried out by [Bergant et al., 2001]. The authors found excellent agreement for all the model herein presented. Other experimental validation was accomplished by [Adamkowski and Lewandowski, 2004, Adamkowski and Lewandowski, 2006]. The authors performed a series of experiment in an elastic copper pipe of length $L = 98m$, inner radius $R_0 = 8 \cdot 10^{-3}m$ and wall thickness $e = 10^{-3}m$ for a wide Reynolds number range, $R_e \in [1100, 15800]$. Despite their conclusions merge those of [Bergant et al., 2001], they highlighted that WFB models: "*have to be singled out. These models predict almost superbly the wave front shape and preserve the frequency. However, it is symptomatic that for higher Reynolds number (over approx. 10,000) the damping effect observed in the calculated courses is greater than in the experimental ones*". An observation also shared recently by [Duan et al., 2017, Ferrari and Vento, 2020]. An overview of all damping models can be gathered from the work of [Abdeldayem et al., 2021] from which Figure 1.17 is taken. The development of both unsteady wall shear stress and FSI models lead to a better understanding of the key mechanisms governing the transient life of liquid-filled pipe systems. If a sufficient accurate model is established, it is then thinkable to detect any fault in the network by a direct comparison between the numerical

and/or theoretical predictions and the on-field observed dynamic. The following section thus aims to provide a brief overview on fault detection in water distribution networks WDN by pressure transient analysis. The forthcoming sections largely refer to the impressive reviews of [Duan et al., 2020, Che et al., 2021].

1.4.3 Standard signal processing methods

This short subsection brings out some insights of standard signal processing methods used for leak detection in (WND). Some additional elements on signal processing methods for pipe faults detection can be found in [Covas, 2003, Datta and Sarkar, 2016, Kousiopoulos et al., 2020]. In the following, it will be considered two recorded signals P_1, P_2 of N samples each.

The Fourier transform $\mathcal{F}$ is used to provide the frequency signature of a time (or space) dependent signal. The signal is decomposed into a Fourier basis (e.g. cosine and sine basis) which allows the determination of the signal frequency properties such as its resonant frequencies. If $\mathcal{P}_1$ represents the Fourier transform of the time dependent pressure signal P_1, it follows the discrete Fourier transform

$$\mathcal{P}_1[k] \quad =_{\mathcal{F}} \quad \sum_{n=0}^{N-1} P_1[n] e^{-\frac{2i\pi kn}{N}}, \tag{1.68}$$

$$P_1[n] \quad =_{\mathcal{F}^{-1}} \quad \frac{1}{N} \sum_{k=0}^{N-1} \mathcal{P}_1[k] e^{\frac{2i\pi kn}{N}}. \tag{1.69}$$

The wavelet transform consists, by analogy with Fourier transform, in decomposing the measured signal into a strategic function basis (also called *mother wavelet*). Following the statement of [Ferrante and Brunone, 2003]: "*wavelets are often compared to a microscope, for their ability to reveal particular aspects of the signal at different scales just by adjusting the focus.* These adjustments are made by the introduction of both a scale χ, and a translation t_r, parameters such that

$$WT(\chi, t_r) = \frac{1}{\sqrt{\chi}} \int_{-\infty}^{\infty} P_1(t) \Phi \left(\frac{t - t_r}{\chi} \right) dt, \tag{1.70}$$

with Φ the wavelet mother. In contrast to the Fourier transform which loses the time information by transforming it into frequency, the wavelet transform approach allows a time-frequency localization of the signal. Quoting [Daubechies, 1992], the wavelet transform: "*is similar to music notation, for example, which tells the player which note (= frequency information) to play at any given moment.*". The method is also well suited to detect the signal singularities (i.e. the presence of pressure wave rebounds), [Ferrante and Brunone, 2003]. The knowledge of the wavelet transform map (i.e. for each $(\chi - t_r)$ couple) of both the intact and the altered systems then allows to distinguish the singular effect of an anomaly, the time-arrival of which can be localized in time thought the use of translation parameter t_r, [Ferrante and Brunone, 2003, Avitia and Deniss, 2011, Bentoumi et al., 2017].

The cross correlation technique provides an estimation of the time reception delay between sensors, the delay being related to the fault location through the pressure wave speed. The normalized cross correlation follows

$$CC[n] \quad \frac{\sum_{m=0}^{N-1} P_1[m]P_2[m-n]}{\sqrt{\sum_{m=0}^{N-1} P_1^2[m] \sum_{m=0}^{N-1} P_2^2[m]}}, \text{ with, } \quad n \in [-N, N]. \tag{1.71}$$

Its maximum position argument n_{max}, i.e. $R[n_{max}] = \max(R[n])$, is a direct measure of the time delay between the sensors according to the relation,

$$\Delta t = \frac{n_{max}}{f_N}, \tag{1.72}$$

where f_N is the sampling frequency. The knowledge of the pulse propagation speed (here the simplest speed model of [Korteweg, 1878], Cf. 1.2) then makes it possible to determine the potential location of the fault. The recorded pressure signals used in the method are not proper water hammer ones but arise from leak induce-vibrations, the amplitude of which are small, sensitive to damping, and may be diluted into the WDN's surrounding noise. This methods thus appears to be noise-dependent and restricted to the DMA scope despite noise effects can be reduced by conducting the measurement by night and repeatedly over several days. Nevertheless, the daily repetitiveness implies some constancy of the hydraulic parameters in the DMA, which is rarely verified as pointed out by [Marsili et al., 2021, Meniconi et al., 2022].

The cepstrum method is by definition the inverse Fourier transform of the logarithm of the signal Fourier transform

$$CP(t) = \mathcal{F}^{-1}\left(\log\left[\mathcal{F}\left(P_1(t)\right)\right]\right). \tag{1.73}$$

The cepstrum is hence a time dependent function and is made up of the sharp signal discontinuity peaks. These peaks have temporal locations which can be converted on graph length via the knowledge of the pulse wave speed.

The impulse response function I corresponds to the output response of a linear system perturbed by an input Dirac function $\delta(t)$. For a linear time invariant system, any output signal may be expressed as a function of $\mathcal{I}$ and the input signal H as follows

$$P_1(t) = \int_{-\infty}^{\infty} I(t-\tau)H(\tau)dt. \tag{1.74}$$

Depending on the input signature, e.g. periodic forcing, a strategic output indicating the location of the fault can be obtained.

The frequency response function is a extension of the impulse response method to the frequency domain analysis. The convolution theorem indeed achieves as follows

$$\mathcal{P}_1(t) =_{\mathcal{F}} \mathcal{I}(f)\mathcal{H}(f). \tag{1.75}$$

The signal processing is an allied tool for network fault detection as it will now be discussed.

1.4.4 Water distribution networks WDN fault detection

The decrease in operational performance of a hydraulic system is the result of several factors:

- Corrosion, mainly present in carbonaceous pipes (i.e. cast iron or steel pipes), locally degrades the surface properties and may lead, in the most severe cases, to local decreases in pipe thicknesses.
- Blockages, whether partial or total, locally obstruct the pipe. This type of disturbance can be found, for example, in a damaged valve that remains partially open.
- Deposits (e.g. limestone), unlike corrosion, add material to the inner wall of the pipe, increasing its thickness.
- Leakages

The hydraulic transients, as they propagate through the network, incorporate several topographic information, which informs on the network condition. The Figure 1.18, an original chart of [Che et al., 2021], illustrates the idea. There are many

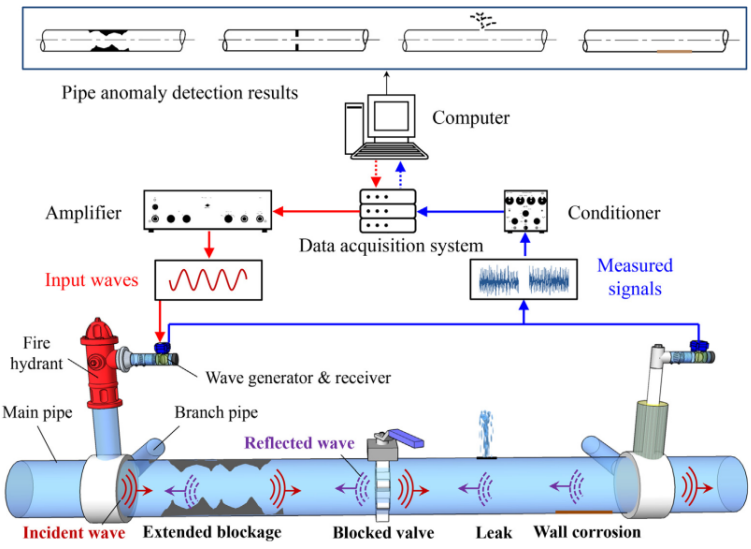

Figure 1.18: *Faults in water distribution networks WDN. Original chart of [Che et al., 2021].*

techniques for detecting singularities in networks that do not require the study of hydraulic transients. Thus, passive acoustic or hydro-acoustic techniques have

focused on the study of the noise emerging from the presence of an anomaly. A direct approach consists in analyzing the resulting noise emitted by the source via a sensor, [Lockwood et al., 2005]. The fault is located at the maximum noise level. This kind of monitoring is commonly used by WDN's shareholders due to its low cost of implementation. Nevertheless, this method is limited to a single pipe analysis, is subjected to the surrounding noise, and is not automated. Another solution is to simultaneously record the noise emitted by a fault, at several locations, in the network. An operator can perform a cross-correlation and then observes the time delay between noise signal patterns, [Kousiopoulos et al., 2020, Bakhtawar and Zayed, 2021]. This method has the advantages of being reliable, non-intrusive, and sufficiently automatic that an operator is not present full-time on the measurement sites. The impact of surrounding noise can also be reduced by carrying out measurements at night. However, these detection techniques may be less accurate for high density WDN and are subject, in terms of sensor positioning, to the available network access points (e.g. tap, fire hydrant, valve). Numerous steady-state-based detection techniques are reported in the review of [Liu and Kleiner, 2013, Zaman et al., 2020]. Steady-state analyses methods are by definition local detection methods, at best on the scale of the hydraulic sector or the district metered area (DMA, Cf. section 1.2). Hydraulic transients, due to their greater amplitudes ($\approx 10^5 Pa$) and their speed of transmission ($10^2 m/s$ to $10^3 m/s$), can therefore be considered to locate a rupture, a leak or a blockage. The search for faults by the means of hydraulic pressure transients can be summarized in two sub-groups, one taking into account of a specific characteristic of the signal (*Local feature-based method*), while the other integrates all the temporal or frequency information available (*Global feature-based method*), [Che et al., 2021]. The set of transient detection techniques are depicted, and classified, in Figure 1.19. All are subsequently described and discussed.

Local feature-based method

Detection by signal characterization, or local feature-based method, uses only part of all the measured information to find the potential location of a fault in the network. The strength of these techniques lies in their simplicity of implementation, although the selection of information makes them sensitive to noise, [Wang et al., 2021]. Furthermore, these methods require an idealized or benchmarked solution, i.e. without faults, to compare with the experimental signals. However, in real life WDN, it is unthinkable to obtain such a benchmark (even numerically) due to the network relative complexity. A simple cross section variation, a very common singularity, may indeed result in a eigenfrequency shift or a different signal signature, [Meniconi et al., 2012, Louati and Ghidaoui, 2017]. Such method thus relies on our ability to model the non trivial behavior of WDN, [Meniconi et al., 2012, Riedelmeier et al., 2014, Malesińska et al., 2021].

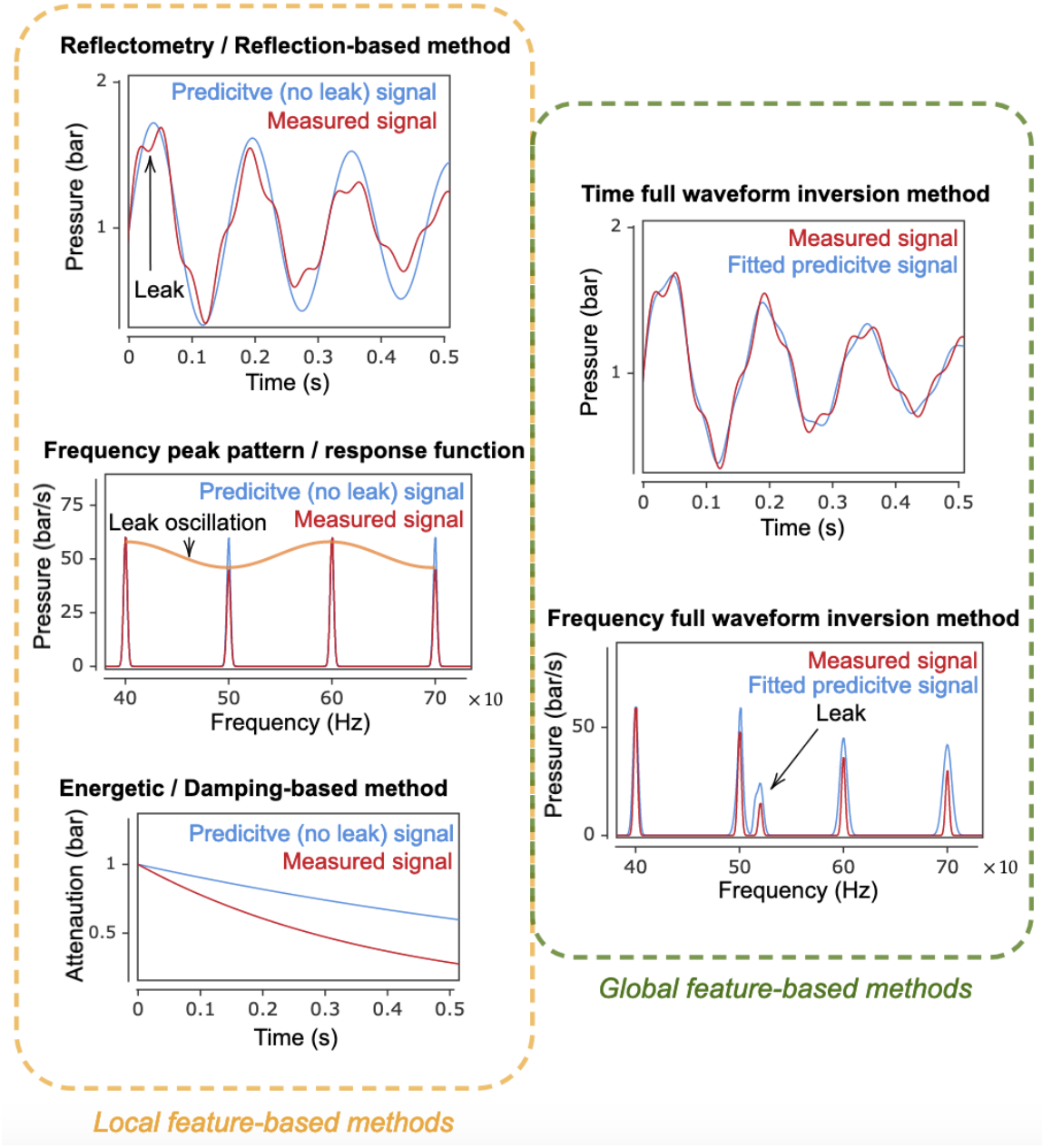

Figure 1.19: *Overview of WDN leak detection techniques.*

Reflectometry / Reflection-based methods consist in observing the characteristic pressure reflection induced by the presence of a leak (or a blockage) during the first instance of a transient event. When the water hammer waves pass through a pipe's default, its signature will be perturbed. Namely, a leak will be characterized by the presence of a pressure drop whilst a blockage is expected to increase the pressure, [Jönsson and Larson, 1992]. The method was experimentally investigated and validated on a drilled (PE) outfall pipe by [Brunone, 1999]. [Taghvaei et al., 2006] then successfully used the cepstrum method to locate leak

on T-branched experimental setup. [Lee et al., 2007] used the impulse response function method to locate leak in a single 37.53m long copper pipe. The authors focused on the measurement of the impulse function response I (Cf. (1.74)) by using a de-convolution procedure of the output by input signals ratio (Cf. (1.75)). They reached an experimental expression of I and were able to distinguish the additional fault contributions. The authors furthermore pointed out the importance of the input signal bandwidth to avoid high frequency perturbations. Focusing on a single pipe, [Ferrante et al., 2009a] validated the relevance of the wavelet transform approach to analyze the reflections induced by a leak. The authors performed a multi-scale wavelet analysis, i.e. consider the product of wavelet function with distinct scaling parameters (Cf. (1.70)), to reduce the noise impact on the detection method and were able to point out the source location with a relative error of 1.4% (pipe's length of 352m). The authors previous contribution was remarkably extended in [Ferrante et al., 2009b]. The authors experimentally analyzed the pressure response of an Y-connected test pipe network in the presence of leaks using both a Lagrangian model approach and a wavelet transform analysis. Both models show a close agreement to each other (a relative percentage error of less than 2.5%) and permit a fault localization. A realistic field test was hence carried out on the main trunk of the Lintrahen's (Scotland) water distribution network, which has exactly the same Y-shaped configuration. Using a cepstrum signal analysis process, [Shucksmith et al., 2012] conducted a series of experiments on the Bradford (Yorkshire, UK) water distribution network. Echo leakage location was studied over a large range of pipe materials and network connectivity. Although locations were found, the method showed relative sensitivity to ambient noise and is highly dependent on the value of the wave velocity. Irrelevant for a WDN full-scale analysis, this detection method is nevertheless effective when dealing with the district metered area DMA scales as performed by [Meniconi et al., 2015]. The authors carried out a similar analysis than [Ferrante et al., 2009b], i.e. wavelet analysis and Lagrangian approach, to examine one of the main supply line of the Milan's (Italy) water distribution network. Recently [Nguyen et al., 2018] extended the [Lee et al., 2007]'s work by performing an additional least-square minimization procedure for noise reduction during the de-convolution procedure of the impulse function response method. Recently, [Meniconi et al., 2021] focused on the reflection method based deeds and misdeeds by running transient investigations in the Trento (Italy) transmission main trunk. The authors concluded on the relevance of the method to investigate long transmission trunk due to the method low intrusiveness and its cost efficiency but addressed several issues. First, the authors reminded: "*how important is the knowledge of the transient response of the intact pipe system*" since errors in the initial and boundary conditions, poor water consumption description or topological incertitude may have a massive impact on the expected WDN's transient response (Cf. [Meniconi et al., 2018]). Then, the authors suggested to improve the transient wave generation by taking care of its bandwidth: "*the smaller the duration, the sharper the generated pressure wave and, then, the smaller the length of the pipe obscured by the maneuver, and the more*

precise the fault location", and its localization within the WDN: "*the effectiveness of a pressure wave to detect a defect depends strongly on the number of the singularities it interacts with along its path. As a consequence, for a given transient generation point, a related length of the pipe can be explored viably*".

Resonant frequency pattern methods use the spectrum information of the frequency response function (Cf. (1.75)) to detect the presence of a fault in a pipe. For a single pipe, [Lee et al., 2005] developed a robust method to locate multi-leaks. They highlighted that a leakage induces a sinusoidal oscillation of the resonant frequency peak amplitudes as depicted in Figure 1.20a. The amplitude

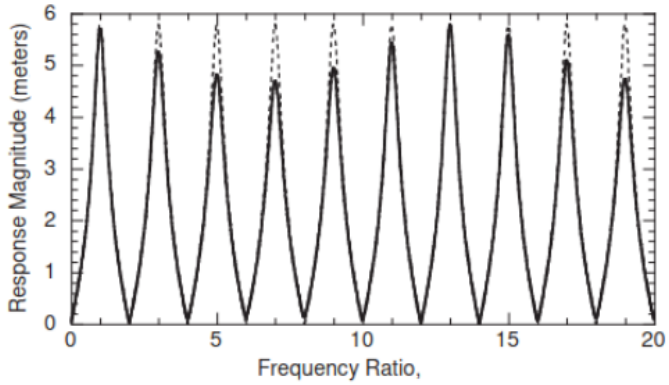

(a) *Frequency response function oscillation due to the presence of a leak in a single pipe, [Lee et al., 2005]. The continuous lines represents a leaky pipe spectrum whilst the dashed signal holds for an intact pipe frequency response.*

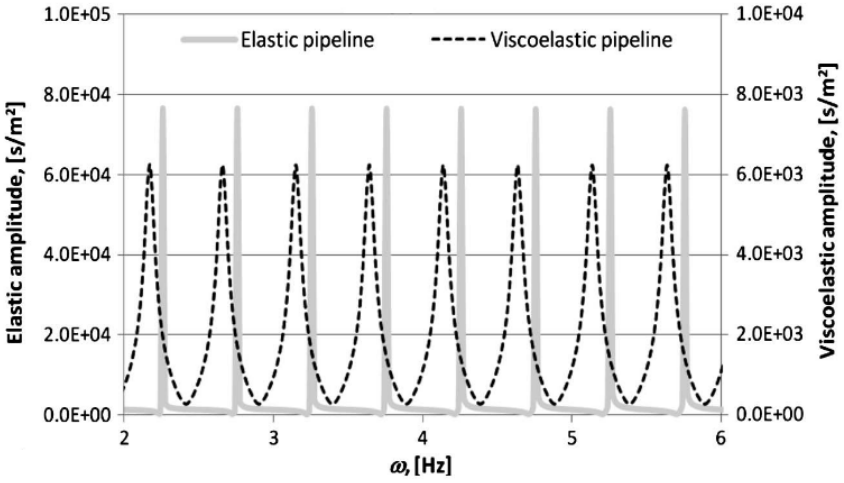

(b) *Frequency response function shift induces by visco-elastic rheology in a single intact pipe, [Duan et al., 2012b].*

Figure 1.20: *Frequency response function phase and amplitude description with respect to the pipe rheology and the presence of faults.*

of these oscillations are related to the leakage size whilst the phase is a function of its position. This approach, performed under the scope of a single elastic pipe, allows to find a leak without the need of an idealize reference case. [Lee et al., 2006] thus experimentally confirmed the relevance of the method on a 37.53m long copper pipe. [Lee et al., 2008] transferred [Lee et al., 2005]'s approach to the study of discrete blockages, i.e. blockages of short length with respect to the pipe's one. [Duan et al., 2011] further extended [Lee et al., 2005]'s framework by considering a complex system composed a heterogeneous diameter pipes branched in series. The authors successfully analyzed the leak-induced frequency response oscillation pattern for this non-trivial configuration. The authors hence concluded: "*that internal junctions in complex series pipelines can modify the system resonant frequencies but has a small effect on the leak-induced information*". [Duan et al., 2012a] focused on the detection of extended blockages, i.e. with length comparable to the pipe's length, detection in a set of N in-line branched pipes. The authors carried out an analytical derivation (using the Transfer Matrix Method (TMM), Cf. §2.1) of a transcendental equation that governs the resonant frequency behavior of the frequency response function

$$\sum_{j=0}^{\left(2^{N-1}\right)-1} \left[C_j \cos\left(\lambda_j \omega_r\right)\right] = 0, \tag{1.76}$$

with

$$C_j = (-1)^{\sum_{i=1}^{N-1} J_i} \left[Y_1 + (-1)^{J_1} Y_2\right] \prod_{k=2}^{N-1} \left[Y_k (-1)^{J_{k-1}} + (-1)^{J_k} Y_{k+1}\right], \tag{1.77}$$

$$Y_j = -\frac{c_{p,j}}{\pi g R_{0,j}^2} \sqrt{1 - \frac{i\pi g R_{0,j}^3}{\omega}}, \tag{1.78}$$

$$\lambda_j = \frac{L_1}{c_{p,1}} + \sum_{k=2}^{N} (-1)^{J_k} \left(\frac{L_k}{c_{p,k}}\right), \tag{1.79}$$

and $J_k = 0$ or 1 represents the number at k^{th} binary position of k (e.g. for $k = 5$ then the binary expression is $(0, 0, 1, 0, 1)$ and $J_{k=5} = 0$). [Duan et al., 2012a] pointed out that extended blockage may lead to frequency shift in the frequency response function. Through the definition of an optimization problem upon the transcendental equation (1.76) and the experimentally measured resonant frequencies, the extended blockage geometrical properties can be found. [Duan et al., 2013] then experimentally confirmed the relevance of the previous developments for a set of three-pipes in-line. A first order approximation of the transcendental equation (1.76) was provided to simplify the model, i.e. by supposing a small variation of the blockage's impedance with respect to the initial system one. It was shown that this approximation leads to reduce the method accuracy ($\approx 30\%$ of relative error in estimating the blockage diameter) which supposes a non linear dependence variation to the frequency shift with respect to the impedance variations. [Duan et al., 2012b] extended the frequency response method to the analysis of single

visco-elastic pipes. The authors concluded that: "*pipe-wall visco-elasticity effect has significant impact on amplitude damping and phase shift of the pressure wave trace, but little influence on leak-induced patterns of pressure head peaks in transient system frequency responses*". The Figure 1.20b depicts the pressure response frequency shift induced by visco-elastic pipe rheology. [Duan et al., 2014] provided new theoretical elements to overcome the difficulties encountered in [Duan et al., 2013] for the prediction of frequency shift induced by extended blockages. The authors considered a Reservoir-Pipe-anchored Valve system (RPV) of length L, with a radially small spread extended blockage of length L_2. A schematic representation is provided in Figure 1.21. The authors carried out an analytical investigation of

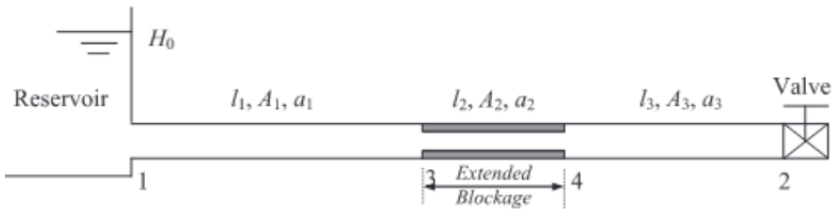

Figure 1.21: *Schematic representation of an extended blockage. Original chart of [Duan et al., 2014].*

the hereby problem (by assuming a pulsating forcing term at the valve) and yielded to an theoretical expression for the pressure (for $x > 0.5L_2$) in the time domain

$$P(z,t) = P_0 \left[e^{\frac{i\omega_0(z-0.5L_2)}{c_p}} + \underbrace{\left(e^{\frac{2i\omega_0 L_2}{c_{p,2}}} - 1 \right)}_{\text{Frequency shifting term}} \mathcal{B}_A e^{-\frac{i\omega_0(z-0.5L_2)}{c_p}} \right] e^{-i\omega_0 t}, \qquad (1.80)$$

where $\mathcal{B}_A = \frac{1-\frac{c_{p,2}R_2^2}{c_p R_0^2}}{1+\frac{c_{p,2}R_2^2}{c_p R_0^2}}$ is the amplitude modulation due to the blockage, (ω_0, P_0) are the forcing pulsation and amplitude, respectively, $(c_p, c_{p,2})$ are the pulse wave speed of the pipe without and with fault, respectively, (R_0, R_2) are the radius of the pipe without and with fault, respectively. To follow the authors' reasoning, in the limit L_2 tends to zeros (i.e. when the fault tends to be a spatial singularity), the frequency shifting term vanishes and only the amplitude modification remains. This is consistent with the previous work of [Lee et al., 2005, Duan et al., 2011]. On the other hand, the transcendental spectrum equation (1.76), also derived in [Duan et al., 2012a], was linearized by assuming small variations of the blockage pulse wave speed with respect to the intact configuration. [Duan et al., 2014] thus delivered an analytical explicit relation to describe the resonant frequency shift $\Delta\omega_{rf}$

$$\Delta\omega_{rf} = \frac{\epsilon_A}{2-\epsilon_A}\frac{c_p}{L}\left[\sin\left(\frac{2L_1\omega_{rf,0}}{c_p}\right) - \sin\left(\frac{2L_3\omega_{rf,0}}{c_p}\right) - \frac{\epsilon_A}{2-\epsilon_A}\sin\left(\frac{2L_2\omega_{rf,0}}{c_p}\right)\right], \qquad (1.81)$$

with

$$\epsilon_A = \frac{A_0 - A_2}{A_0}, \tag{1.82}$$

$$\epsilon_L = \frac{L_2}{L}, \tag{1.83}$$

and where $w_{rf,0}$ are the resonant frequencies without blockage, L is the total pipe's length and L_j are the sub-pipe's lengths defined in Figure 1.21. [Lee et al., 2013] carried out a complete study on the frequency response by integrating the impact of fault effects, friction and pipe wall visco-elasticity. [Duan and Lee, 2016] then extended the frequency response function pattern to the detection of dead-end side branch in networks. [Louati and Ghidaoui, 2017] carried out an extended energetic analysis of the resonant frequency shift induced by blockage. The authors defined a threshold value for the area of pipe obstruction allowing the problem to be treated either as local (less than 30% blockage) or extended (more than 30%). Furthermore, their modal energetic analysis concluded that a modification of a resonant mode total energy, by an increase or a decrease, results in a resonant frequency shift, in the negative of positive direction, respectively. An in-depth understanding of the eigenfrequency shift, i.e. positive negative or zero, in function of the blockage size and location was delivered by [Louati and Ghidaoui, 2018]. The authors pointed out that any blockage of length being multiple of a mode's half wavelength, will not produce frequency shift. A similar zero shift is furthermore observed if the blockage mid-length is located at a position of equal pressure and flow magnitudes. Finally, a maximum mode frequency shift is observed if the blockage mid-length is located at a pressure stagnation, i.e. at zero pressure harmonics' magnitudes, point. More recently, [Pan et al., 2021] dealt with the leak detection, using the frequency function method, in visco-elastic pipes. An experimental system consisting of a HDPE pipe of length 166.28m was used to validate both the visco-elastic parameters estimation and the leak location.

Energetic damping-based methods consist in analyzing the damping of the pressure Fourier modes. [Wang et al., 2002] introduced the method. The authors performed an acoustic, low-Mach number, analysis of the fluid mass and momentum conservation equations, (1.40), but added a source term being representative of the leak magnitude and position. The resulting wave equation was solved and a modal exponential damping trend was found, the latter depending on both the Darcy-Weisbach damping coefficient, i.e. $O\left(\frac{f_{DW} L W_0}{4 c_p R_0}\right)$, and the leak-damping factor component

$$R_{nL} = \frac{C_d A_L}{A} \frac{c_p}{\sqrt{2 g H_{L0}}} \sin^2\left(n \pi x_L^*\right), \tag{1.84}$$

where C_d is the leak coefficient discharge, A_L, A are the leak and pipe surfaces, respectively, H_{L0} is the steady-state hydraulic charge at the leak and x_L^* is the leak dimensionless position. Thus, the leak position is a function of the R_{nL} damping coefficient and can be obtained by performing the ratio between the pressure harmonics. Once the leak location is determined, the leak size can be easily obtained

according to (1.84). The herein method was then successfully confronted with an experimental setup consisting of a 37.2m copper pipe in the University of Adelaide (Australia). [Wang et al., 2005] then extended the method of [Wang et al., 2002] to investigate partial blockages in single pipes. It turned out that a similar derivation of the problem could be performed. The trigonometric sine of (1.84) being replaced by a cosine function whereas its prefactor became $\frac{K_b W_0}{2c_p}$, with K_b the blockage head loss coefficient. The models of [Wang et al., 2002, Wang et al., 2005] nevertheless suggest a quasi-steady model of viscous shear rate despite experimental investigations reveal the need to account for unsteady damping, [Bergant et al., 2001, Adamkowski and Lewandowski, 2006]. [Nixon et al., 2006] addressed these interrogations stating that: "*the quasi-steady and small amplitude assumptions do not limit the applicability of the method provided that the pipeline is simple and wall friction is correctly represented in the mathematical model used to estimate modal damping rates. That is, should a mathematical model be needed to generate the head trace data for the case without the leak, this model needs to incorporate unsteady friction so that the damping rates are correctly estimated*". Furthermore, the method suffers from the non-uniqueness determination of the leak position due to the periodicity of the sine and cosine functions. The localization non-uniqueness was recently highlighted by both the numerical analysis of [Brunone et al., 2018] and the experimental contribution of [Capponi et al., 2020].

Global feature-based method

Unlike the fault detection methods discussed up to now, the full waveform inversion methods, or the Inverse Transient Analysis (ITA), rely on all the signal characteristics to locate the fault. Such method is consequently more robust to environmental noises. The ITA, in the time of frequency domain, are based on the same framework. First a theoretical expression has to be derived, embedded free fitting parameters (e.g. leak location or blockage dimensions), to predict the pressure signatures at sensors locations. Then, the pressure signal is experimentally/on-field measured. Finally, an optimization problem is set up, the result of which provides the optimal value of the fault fitting parameters.

The ITA in time domain was firstly investigated by [Liggett and Chen, 1994]. The author defined a merit function

$$E = \int_z \int_t (h_m - h_c)^2 \, dxdt, \tag{1.85}$$

the which have to be minimized. Here, h_m denotes the measured hydraulic head whereas h_c stands for the computed one. An optimization problem, i.e. minimization of the E-gradients or the Levenberg-Marquardt (LM) method, was then set up regarding both the identification of optimal Darcy-Weisbach friction factors and leakage locations. In order to apply such detection strategy, the leaks are nevertheless assumed to occur at network's nodes, the which is a strong assumption. [Vítkovský et al., 2000] used a genetic algorithm (GA) to reach an

optimal distribution of the leak discharges and quasi-steady Darcy-Weisbach friction factors whereas [Kapelan et al., 2003] used an hybrid method combining GA and LM methods. [Covas and Ramos, 2001] pursued experimental investigation on a leaky test network at the Laboratory of Hydraulics of Civil Engineering of Lisbon (Portugal). The authors concluded on the relevance of the ITA method for known small networks but also pointed out numerous limitations to a large scale development: *"(i) the accuracy of the transient simulator to reproducing the behaviour of the system, (ii) the uncertainty of collected data, (iii) measurements synchronization in respect to time and to datum level, (iv) the accuracy of the estimation of the main water hammer parameters, such wave speed, pipe roughness and closure manoeuvre that generated the transient"*. [Stephens et al., 2002] conducted on-field experimental investigation of the ITA, on the Willunga (South Adelaide, Australia), to locate blockage in pipeline. [Vítkovský et al., 2007] also conducted laboratory experiments in a copper pipe for the localization and sizing of single and multiple leaks. The works of [Covas and Ramos, 2010, Soares et al., 2011] furthermore extended the existing framework by taking into account the pipe solid visco-elastic rheology in the optimization process. Numerous similar studies can then be found in [Al-Khomairi, 2008, Shamloo and Haghighi, 2009, Stephens et al., 2013, Zhang et al., 2018, Sarkamaryan et al., 2018]. Whereas the previous inverse transient analysis were performed in time domain, some authors focused on the extension of the method in the frequency domain.

The ITA in frequency domain consists in searching for a maximum correspondence between the numerical or theoretical signal predictions and the observed experimental one in the Fourier domain. The method was brilliantly presented by [Wang and Ghidaoui, 2018a]. In the frequency domain and for each of the selected frequencies, ω_j with $j \in [1, \ddots, J]$ and J the number of samples, the authors reached an analytic expression (Cf. §2) of the transient head distribution $\tilde{h}_j^M$ as a function of the non-leaky head distribution $\tilde{h}_j^{NL}(\omega_j, z^M)$, the leak perturbation impedance $\tilde{G}(\omega_j, z^L, z^M)$, the characteristic leak size s^L, and a white noise component n_j

$$\underbrace{\begin{pmatrix} \tilde{h}_1(\omega_1, z^M) - \tilde{h}^{NL}(\omega_1, z^M) \\ \vdots \\ \tilde{h}_J(\omega_J, z^M) - \tilde{h}^{NL}(\omega_J, z^M) \end{pmatrix}}_{\Delta\tilde{\mathbf{h}}} = s^L \underbrace{\begin{pmatrix} \tilde{G}(\omega_1, z^L, z^M) \\ \vdots \\ \tilde{G}(\omega_J, z^L, z^M) \end{pmatrix}}_{\tilde{\mathbf{G}}} + \underbrace{\begin{pmatrix} n_1 \\ \vdots \\ n_J \end{pmatrix}}_{\mathbf{n}}, \tag{1.86}$$

where the superscripts M, NL, L refer to the measurement location, the non-leak solution and the leak location, respectively. The leak perturbation impedance vector $\tilde{\mathbf{G}}$ is a know analytical, frequency-dependent, function. The leak location and size are obtained thought a matched-field processing method (here comparable

to a maximum likelihood estimation method) then leading to

$$\hat{z}^L = \underset{z^L}{\operatorname{argmax}} \left(\frac{\Delta\tilde{\mathbf{h}}^H \tilde{\mathbf{G}}\left(z^L\right) \tilde{\mathbf{G}}^H\left(z^L\right) \Delta\tilde{\mathbf{h}}}{\tilde{\mathbf{G}}^H\left(z^L\right) \tilde{\mathbf{G}}\left(z^L\right)} \right), \tag{1.87}$$

$$\hat{s}^L = \frac{\tilde{\mathbf{G}}^H\left(\hat{z}^L\right) \Delta\tilde{\mathbf{h}}}{\tilde{\mathbf{G}}^H\left(\hat{z}^L\right) \tilde{\mathbf{G}}\left(\hat{z}^L\right)}, \tag{1.88}$$

where the superscript H refers to the conjugate transpose. The method hereby proposed can furthermore be extended to deal with multiple leaks, [Wang and Ghidaoui, 2018b], due to the problem linearity. If several leakage are investigated, the leaks nevertheless have to be separated by a distance: *"larger than minimum half-wavelength"*, in order to be correctly detected. The detection method was experimentally studied by [Wang et al., 2019] in an HDPE pipe of length $144m$. Several leak positions were analyzed and located by the method. To account for visco-elastic solid rheology, the pulse wave speed expression (1.2) was slightly modified by the use of a complex creep function instead of the elastic Young modulus, [Suo and Wylie, 1990] (Cf. §4). More recently, [Keramat and Duan, 2021] brilliantly extended the [Wang and Ghidaoui, 2018a]'s frequency detection approach to account for both FSI couplings and proper visco-elastic effects. The five detection methods here introduced only represent a tiny fraction of the whole fault detection methods in water distribution networks. Out of the herein scope, it is nevertheless noteworthy to present the impressive work review of [Datta and Sarkar, 2016], the Figure 1.22 of which is extracted.

1.5 Dissertation process

The liquid-filled pipe problem, despite of being a long standing problem, still suffers from several lack of understandings. A large amount of research have indeed focused on either the development of unsteady wall shear stress models, or on the in-depth analysis of fluid and structure interactions FSI. It is nevertheless not known by the author, any tentative to reconcile both approaches. Not to mention the derivation of a consistent equation model for the liquid-filled pipe system, the theoretical framework for the resolution of existing models is also limited in scope. Whilst some analytical solutions of the four-FSI equations exist in the frequency domain, time-dependent solutions are scarce or non-existent. The lack of understanding is obviously detrimental to the accuracy of transient fault detection methods and reduce their effectiveness as it was highlighted by the subject literature.

The hereby research project thus aims to provide an in-depth understanding of the liquid-filled pipe problem by embedding Poisson's coupling, unsteady wall shear stress and visco-elastic wall behavior. This project is also dedicated to the development of numerical operational tools allowing both: (i) the predictive analysis of the propagation pressure waves in networks and, (ii) the detection of anomalies in WDN. The PhD is organized as follows:

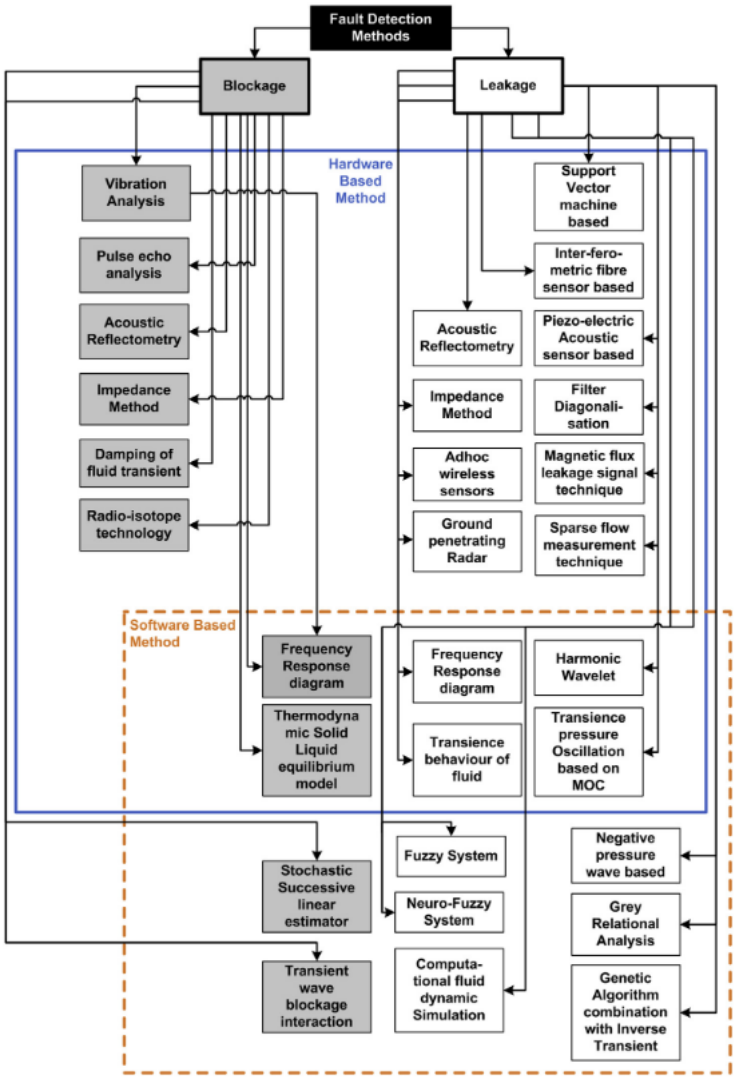

Figure 1.22: *Overview of transient and steady fault detection methods. Original chart of [Datta and Sarkar, 2016].*

- A first chapter is dedicated to the presentation of the frequency Transfer Matrix Method (TMM). In a second time, a new time domain analytical approach is set up relying on both spectral and self adjoint operator theories.
- Then, a second chapter focuses on the asymptotic derivation of a consistent theoretical model, embedded both unsteady wall shear stress effects and FSI couplings, to describe the liquid-filled pipe dynamic in elastic thick pipes. The resolution of this new theoretical model is overcome relying on analytical development spelled out in the first chapter.
- Since the use of visco-elastic materials in water distribution networks is getting common, a third chapter is dedicated to the extension of pre-existing model to account for solid visco-elastic effects.

- A fourth chapter deals with the development of a numerical tool to model water hammer pressure waves in WDN. The pressure wave model is solved using the Method Of Characteristics (MOC) formalism and several unsteady wall shear stress damping models are analyzed and confronted to an on-field test case.
- Finally, a fifth chapter presents a new approach for the fault detection in water distribution networks by the use of time reversal of first event detection.

Chapter 2

Time- and frequency- dependent liquid filled pipe analysis.

Contents

This chapter aims at providing a new analytical time-domain approach for the liquid-filled pipe problem resolution relying on both spectral and operators theory. This new approach reconciles known results obtained though frequency analysis, which are thereafter presented.

2.1 Frequency analysis and Transfer Matrix Method (TMM)

In the forthcoming, the Laplace transform of a causal function $f(t)$, i.e. $\forall t \leq 0, \quad f(t) = 0$, is denoted $\tilde{f}(s)$ and achieves as follows

$$\tilde{f}(s) = \int_0^\infty f(t)e^{-st}dt, \tag{2.1}$$

with $s \in \mathbb{C}$ the Laplace variable. Theoretical methods have been developed to analytically describe the behavior of hyperbolic-governed systems. The transfer matrix method (TMM) is a frequency-based theoretical method which consists in deriving the transmission matrix associated with an acoustic system. Classically, a Laplace (or Fourier) transform is performed upon the set of equations which simplifies them into a set of space-dependent ODE. In the case of liquid-filled pipe system where the spacial gradient are simple derivative, the propagation operator then displays an exponential space-frequency dependence. A solution of the

coupled ODE system is then searched into its diagonal basis. Finally, the application of axial boundary condition at the pipe's dead-ends constrains the overall dynamic and specify its resonant frequencies, also denoted spectrum. The method basic concept is hereafter provided following the work of [Zhang et al., 1999]. Let us consider the homogeneous, perturbed (i.e. with at rest initial condition) hyperbolic system

$$\left(\partial_t + \mathbf{C}^2\partial_Z\right)\mathbf{P}(Z,t) = \mathbf{0}. \tag{2.2}$$

Performing a Laplace transform of (2.2) then yields

$$\left(\mathbf{C}^2\partial_Z + s\right)\tilde{\mathbf{P}}(Z,s) = \mathbf{0}. \tag{2.3}$$

A solution of this ODE is now searched in the diagonal basis of $\mathbf{C}^2$. Let us respectively set up $(\mathcal{C}^2, \mathbf{\Pi})$ being the diagonal matrix of $\mathbf{C}^2$ and its associated change of basis matrix. The $\mathbf{P}$ vector is denoted by $\boldsymbol{\mathcal{P}} = \mathbf{\Pi}^{-1}\mathbf{P}$, in the $\mathbf{C}^2$-diagonal basis. The (2.2) thus achieves as follows

$$\left(\partial_Z + s\boldsymbol{\mathcal{C}}^{-2}\right)\tilde{\boldsymbol{\mathcal{P}}}(Z,s) = \mathbf{0}. \tag{2.4}$$

Hence, a straightforward relation is established between the pipe's upstream condition and any downstream point following

$$\tilde{\mathcal{P}}_i(Z,s) = \tilde{T}_i(s)e^{-s\mathcal{C}_i^{-2}}\tilde{\mathcal{P}}_i(0,s), \tag{2.5}$$

whilst changing basis leads to

$$\tilde{P}_i(Z,s) = \underbrace{\Pi_{ij}\tilde{T}_j(s)e^{-s\mathcal{C}_j^{-2}}}_{\text{Transfer matrix}}\tilde{P}_j(0,s), \tag{2.6}$$

where the Einstein's index notation have been used and $\tilde{T}_i(s)$, is an unknown amplitude. Finally, when regarding (2.6) at $Z = L$, a linear system in $\tilde{T}_i$, emerges between the pipe's upstream and downstream conditions. Setting the axial boundary conditions thus constrains the solution and specifies both its spectrum and amplitudes.

The TMM is widely used in the liquid-filled pipe problem community for its efficiency and easy implementation. We only provide here some references using it to investigate FSI water-hammer problems. [Lesmez, 1989, Lesmez et al., 1990] carried-out an impressive study from analyzing the FSI occurring in a U-bend pipe configuration. The authors dealt with both Poisson and junction couplings. [Zhang et al., 1999] delivered a complete work and provided significant theoretical insights on TMM. The authors indeed theoretically analyzed the flexural and axial vibrations of a fluid-filled pipe induced by discrete impacts. For each configurations, they spelled out the frequency-dependent solutions along with their spectrum as depicted in Figure 2.1. [Li et al., 2002] then used the TMM to depict the behavior of a set of axially connected pipes in a row. The authors dealt with diameter heterogeneity and in-depth analyzed the harmonic response of their system, which

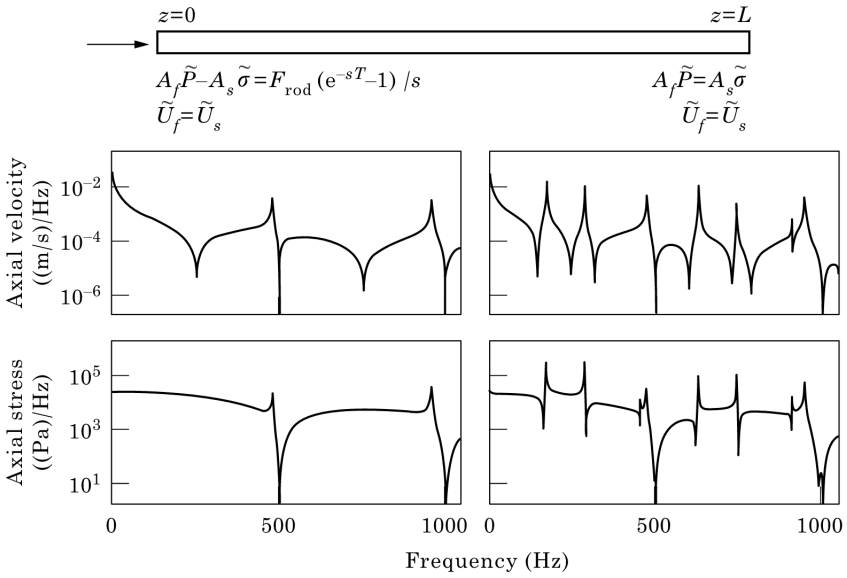

Figure 2.1: *Frequency-response of an axially, discrete, impacted free hanging pipe, [Zhang et al., 1999].*

is similar to the experimental setup of [Vardy and Fan, 1986]. [Yang et al., 2004] investigated the FSI-response of a multi-spanned pipe along with the downstream inertial perturbations induced by the valve's movement in a reservoir-pipe-valve (RPV) system. By varying the Poisson's modulus values ($\nu_s \in [0, 0.3]$), the authors thus quantified the impact of the Poisson couplings upon both the overall dynamic and the resonant frequencies. [Kim, 2005] used the impedance method, which is similar to the TMM but with the distinction of defining explicitly the acoustic system impedance, to deal with leak location in single pipes. [Kim, 2007] transposes the impedance method to looped hydraulic networks and then generalized the concept as matrix impedance method. As TMM, the application of network nodes boundary conditions yields to a linear system dependent upon each pipe acoustic impedance Z_i, and the node's degree, the resolution of which prescribes the system spectrum and amplitudes. The looped network along with its spectrum, i.e. linear boundary condition system, for the [Kim, 2007]'s analysis is depicted in Figure 2.2. The excellent contributions of [Zecchin, 2010, Zecchin et al., 2012] should be distinguished. The author considerably expands the matrix impedance method from combining it with graph theory. The authors then develop a Numerical Inverse Laplace Transform (NILT) procedure allowing a time-domain analysis of complex distribution networks, as depicted in Figure 2.3. In the last few years, the [Zecchin, 2010]'s NILT method was successfully used by [Capponi et al., 2018] to investigate the transient behavior of an Y-pipe experimental setup. Others TMM or impedance matrix contributions can be found in [Liu and Li, 2011], whose analyzed the impact of pipe's elastic supports, [Dai et al., 2012] whose performed a multidimensional space frequency analysis or [Li et al., 2014] whose investigated the FSI-waves propagation in elbows. The latter also focused on the junction cou-

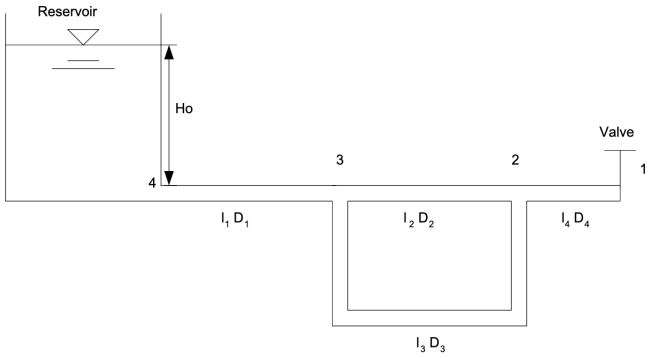

$$\begin{bmatrix} Z_{c2}\sinh\gamma_2 l_2 & 0 & 0 & 0 & 1 & 0 \\ \cosh\gamma_2 l_2 & 0 & -1 & 0 & 0 & 0 \\ 0 & Z_{c3}\sinh\gamma_3 l_3 & 0 & 0 & 1 & 0 \\ 0 & \cosh\gamma_3 l_3 & 0 & -1 & 0 & 0 \\ 1 & 1 & 0 & 0 & 0 & 0 \\ 0 & 0 & 1 & 1 & 0 & -1 \end{bmatrix} \cdot \begin{bmatrix} Q_{3l_2}/Q_{3l_1} \\ Q_{3l_3}/Q_{3l_1} \\ Q_{2l_2}/Q_{3l_1} \\ Q_{2l_3}/Q_{3l_1} \\ H_2/Q_{3l_1} \\ Q_{2l_4}/Q_{3l_1} \end{bmatrix} = \begin{bmatrix} Z_3\cosh\gamma_2 l_2 \\ Z_3\sinh\gamma_2 l_2/Z_{c2} \\ Z_3\cosh\gamma_3 l_3 \\ Z_3\sinh\gamma_3 l_3/Z_{c3} \\ 1 \\ 0 \end{bmatrix}$$

Figure 2.2: *Hydraulic looped network and its associated linear boundary condition system, [Kim, 2007].*

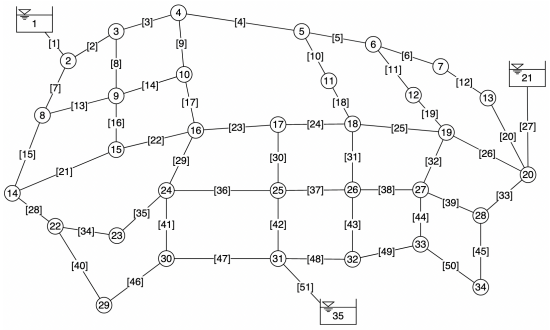

(a) *51-pipes test network, [Zecchin et al., 2012]*

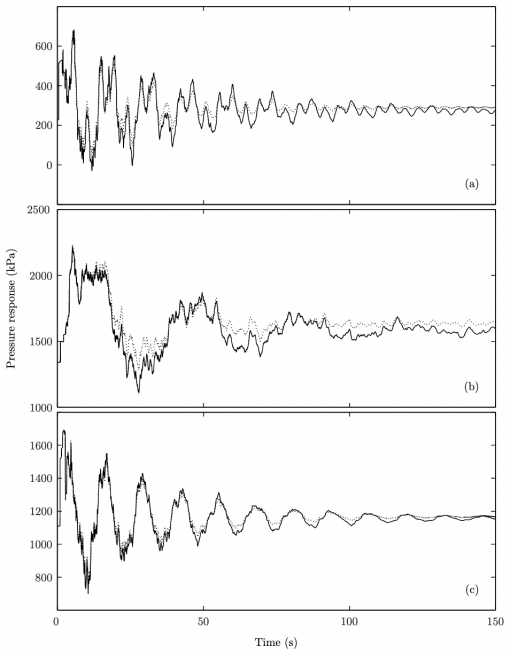

(b) *Example of pressure signature for the NILT method, in dotted line, compared with the Method Of Characteristic (MOC) predictions, in continuous lines.*

Figure 2.3: *Investigation of a complex network by the numerical inverse Laplace transform NILT procedure, [Zecchin, 2010, Zecchin et al., 2012]*

plings interaction emerging from pipe clamping. [Duan et al., 2012a, Duan et al., 2013] used TMM to derive a transcendental spectrum equation for a set of pipes axially connected in a row. Their theory was then experimentally validated. [Li et al., 2014] extended the method to a set a fourteen hyperbolic equations, each governing a FSI-induced vibration mode. Additional contributions can be found in the excellent review of [Li et al., 2015].
While the treatment in the frequency domain is trivial, performing a Laplace (or Fourier) transform inversion is usually challenging and stands as a limitation of the TMM. Despite their interest in parametric estimations, sensitivity analyses or numerical validations, few analytical time-dependent solutions exist in the literature. As part of this research project, a set of basic FSI-configurations are hereafter investigated so as to detail their time-domain respective solutions. The spectrum of each configurations is derived, which provides the resonant frequencies of the system. First, we focus on performing the analytical Laplace inverse transform resulting from the TMM. Then, relying on operator theory, the TMM is revisited into a new time-domain framework for the resolution of liquid-filled pipe systems.

2.2 Fluid structure interactions analytical analysis for the liquid filled pipes problem: Proceedings to 14^{th} *conference on pressure surge, BHR group*

Fluid structure interactions analytical analysis for the liquid filled pipes problem

A. Bayle[1] and *F. Plouraboué*[*1]

[1] *Institut de Mécanique des Fluides de Toulouse, IMFT, Université de Toulouse, CNRS, Toulouse, 31400, France*

Abstract

In this contribution we derive new analytical solutions for the coupled wave equation system resulting from Fluid Structure Interactions (FSI) occurring in liquid filled pipes. After diagonalizing the wave operator in the Laplace domain, we bring out a transcendental spectrum equation and conduct an in-depth spectral analysis for various configuration sets: (i) reservoir-pipe-anchored valve (ii) reservoir-pipe-free valve (iii) steel rod impacted pipe. A general formulation for the inverse Laplace procedure is proposed relying on spectral arguments. Numerical convergence resulting from mode truncation and numerical error on eigenvalues is checked. The present theory is validated by comparison with numerical benchmarks found in the literature and a very close agreement is found.
Keywords: Fluid Structure Interaction (FSI), Liquid filled pipe, Wave operator, Time-domain solutions, Frequency-domain solutions, Spectral analysis

1 INTRODUCTION

Wave propagations in liquid-filled pipe systems has been investigated for a long time [1, 3, 4, 7, 8, 11, 16, 17] as discussed in exhaustive and sagacious review papers [6, 14, 19]. Furthermore, it can also be applied to defect/leak localization [5, 9, 10] parameter identification and boundary condition de-convolution inside liquid-filled pipes. In this context, analytical solutions are helpful to deepen understanding and/or, more pragmatically, to provide reference test cases. We hereby considered the pressure-stress wave equation operator derived from the classical four FSI-equation system, [18]. By following the approach of [23] and for a large set of boundary conditions, we handled the resolution of the wave equation in the Laplace domain leading to a frequency-dependent solution. A general inverse Laplace formulation is thereafter managed invoking spectral arguments from [2] and resulting in a time-dependent solution. The theoretical analysis of this paper concludes by highlighting the modal convergence behavior of the proposed solutions.

2 THEORETICAL FRAMEWORK

In this section we mainly focus on the spectrum, the resonant frequencies of FSI solutions.

*Corresponding author: fplourab@imft.fr

2.1 Dimensionless parameters

Let us consider a cylindrical tube having inner radius R_0, wall thickness e, length L, so that parameter α can be defined as

$$\alpha = \frac{e}{R_0}. \tag{1}$$

The tube is entirely filled with a fluid having density ρ_f, bulk modulus $\mathcal{K}_f$. The elastic solid response is associated with Young's modulus E, Poisson's modulus ν_s, and density ρ_s. Reference [18] derived the classical pulse wave speed within the fluid, c_p, distinct from the elastic pulse wave speed within the solid, c_s

$$c_p^2 = \frac{\frac{1}{\rho_f}}{\frac{1}{\mathcal{K}_f} + \frac{2}{\alpha E}\left(\frac{2(1-\nu_s^2)}{2+\alpha} + \alpha(1+\nu_s)\right)}, \quad c_s^2 = \frac{E}{\rho_s}, \tag{2}$$

their respective ratio being

$$\mathcal{C}_s = \frac{c_s}{c_p}. \tag{3}$$

In the forthcoming, the perturbed fluid pressure P^*, and axial solid stress σ^*, will be scaled on the [8]'s overpressure, i.e. $O\left(\rho_f c_p W_0\right)$ with W_0 the flow perturbation amplitude imposed to the system, so that their dimensionless counterparts follow from

$$P = \frac{P^*}{\rho_f c_p W_0} \quad \text{, and,} \quad \sigma = \frac{\sigma^*}{\rho_f c_p W_0}. \tag{4}$$

The physical time t is furthermore regarded with respect to the fluid acoustic advective time scale, i.e. $\tau = t\frac{L}{c_p}$, while the axial coordinate is rescaled with respect to the tube's length, i.e. $Z = z/L$. Finally, the dimensionless density ratio is introduced as

$$\mathcal{D} = \frac{\rho_f}{\rho_s}. \tag{5}$$

2.2 Governing wave-vector equation

The derivation of the wave-vector equation governing the space-time distribution of the dimensionless perturbed pressure P and dimensionless axial stress σ has been provided in [2] so that it is not repeated here. It results in the following wave-operator acting on the pressure/stress 2D-vector:

$$\left(\partial_\tau^2 - \mathbf{C}_\mathbf{P}^2 \partial_Z^2\right)\mathbf{P} = \mathbf{0}, \tag{6}$$

where

$$\mathbf{C}_\mathbf{P}^2 = \begin{pmatrix} 1 & 2\nu_s\mathcal{D} \\ \frac{2\nu_s}{\alpha(2+\alpha)} & \frac{4\nu_s^2\mathcal{D}}{\alpha(2+\alpha)} + \mathcal{C}_s^2 \end{pmatrix} \quad \text{, and,} \quad \mathbf{P} = \begin{pmatrix} P \\ \sigma \end{pmatrix}. \tag{7}$$

The fluid pressure and the axial solid stress as well as their respective time-derivatives will be assumed initially at rest so that

$$\mathbf{P}(Z,0) = \mathbf{0} \quad , \partial_\tau \mathbf{P}(Z,0) = \mathbf{0}. \tag{8}$$

The vector homogeneous wave-equation resolution will be handled within the eigenvectors basis of $\mathbf{C}_\mathbf{P}^2$ as in [23]. The eigenvalues of $\mathbf{C}_\mathbf{P}^2$, denoted $c_\pm^2 > 0$, associated with diagonalized matrix $\boldsymbol{\mathcal{C}}_\boldsymbol{\mathcal{P}}^2$ correspond to the wave speed mode

propagation. They are the solution of the following polynomial characteristic problem

$$c_{\pm}^4 - \left[1 + \mathcal{C}_s^2 + \frac{4\nu_s^2\mathcal{D}}{\alpha(2+\alpha)}\right] c_{\pm}^2 + \mathcal{C}_s^2 = 0, \tag{9}$$

the solutions of which are

$$c_{\pm}^2 = \frac{1 + \mathcal{C}_s^2 + \frac{4\nu_s^2\mathcal{D}}{\alpha(2+\alpha)} \pm \sqrt{\left(1 + \mathcal{C}_s^2 + \frac{4\nu_s^2\mathcal{D}}{\alpha(2+\alpha)}\right)^2 - 4\mathcal{C}_s^2}}{2}. \tag{10}$$

The dimensionless wave-equation system (6) with initial condition (8) expressed in the eigenvector base finally reads

$$\left(\partial_\tau^2 - \boldsymbol{\mathcal{C}}_{\boldsymbol{\mathcal{P}}}^2 \partial_Z^2\right) \boldsymbol{\mathcal{P}} = \mathbf{0} \quad \text{, with,} \quad \boldsymbol{\mathcal{P}}(Z,0) = \partial_\tau \boldsymbol{\mathcal{P}}(Z,0) = \mathbf{0}, \tag{11}$$

where the change of basis relations

$$\boldsymbol{\Pi} = \begin{pmatrix} \frac{2\nu_s\mathcal{D}}{c_-^2 - 1} & \frac{2\nu_s\mathcal{D}}{c_+^2 - 1} \\ 1 & 1 \end{pmatrix}, \quad \boldsymbol{\mathcal{C}}_{\boldsymbol{\mathcal{P}}}^2 = \begin{pmatrix} c_-^2 & 0 \\ 0 & c_+^2 \end{pmatrix} \equiv \boldsymbol{\Pi} \mathbf{C}_{\mathbf{P}}^2 \boldsymbol{\Pi}^{-1} \quad \text{, and,} \quad \boldsymbol{\mathcal{P}} = \boldsymbol{\Pi}^{-1}\mathbf{P}, \tag{12}$$

have been used. The initially coupled pressure/stress wave propagation problem now looks decoupled into two distinct wave propagation modes associated with 2D-vector $\boldsymbol{\mathcal{P}}$. Nevertheless the coupling persists from the resulting coupled upstream and downstream boundary conditions associated with $\boldsymbol{\mathcal{P}}$. For the sake of simplification let us introduce four 2×2 matrices $\boldsymbol{\mathcal{N}}$, $\boldsymbol{\mathcal{M}}$, $\boldsymbol{\mathcal{Q}}$, $\boldsymbol{\mathcal{R}}$ and $\boldsymbol{\mathcal{S}}\delta(\tau)$ as a four-dimensional column vector corresponding to the perturbation with respect to the imposed steady-state ($\delta(\tau)$ being Dirac distribution). Boundary conditions can be formally written as a rectangular 8×4 linear system

$$\begin{pmatrix} \boldsymbol{\mathcal{N}} & \boldsymbol{\mathcal{M}} & \mathbf{0} & \mathbf{0} \\ \mathbf{0} & \mathbf{0} & \boldsymbol{\mathcal{Q}} & \boldsymbol{\mathcal{R}} \end{pmatrix} \cdot \begin{pmatrix} \boldsymbol{\mathcal{P}}(0,\tau) \\ \partial_Z \boldsymbol{\mathcal{P}}(0,\tau) \\ \boldsymbol{\mathcal{P}}(1,\tau) \\ \partial_Z \boldsymbol{\mathcal{P}}(1,\tau) \end{pmatrix} = \boldsymbol{\mathcal{S}}\delta(\tau), \tag{13}$$

where $\boldsymbol{\mathcal{S}}\delta(\tau)$ is a source term exciting the system. Specific sets of boundary conditions will hereafter be investigated and corresponding resolution using diagonalized vector wave-equation system (11), will be handled in the Laplace domain.

2.3 Laplace resolution of the FSI wave equation

Let us introduce $\mathcal{L}$, the Laplace transform operator, s its Laplace variable and $\tilde{\boldsymbol{\mathcal{P}}}$ the Laplace transform of $\boldsymbol{\mathcal{P}}$:

$$\tilde{\boldsymbol{\mathcal{P}}}(Z,s) = \mathcal{L}\left(\boldsymbol{\mathcal{P}}(Z,t)\right). \tag{14}$$

The Laplace transform of (11) then leads to

$$\left(s^2 - \boldsymbol{\mathcal{C}}_{\boldsymbol{\mathcal{P}}}^2 \partial_Z^2\right) \tilde{\boldsymbol{\mathcal{P}}} = \mathbf{0}, \tag{15}$$

$\boldsymbol{\mathcal{C}}_{\boldsymbol{\mathcal{P}}}^2$ being diagonal (Cf (12)). A solution can be found for the spatial ODE system leading to

$$\tilde{\boldsymbol{\mathcal{P}}}(Z,s) = \mathbf{E}(Z,s)\tilde{\boldsymbol{\mathcal{P}}}^{\mathcal{D}}(s) + \mathbf{F}(Z,s)\tilde{\boldsymbol{\mathcal{P}}}^{\mathcal{N}}(s), \tag{16}$$

with 2×2 diagonal matrices

$$\mathbf{E}(Z,s) = \begin{pmatrix} \cos\left(\frac{is}{c_-}Z\right) & 0 \\ 0 & \cos\left(\frac{is}{c_+}Z\right) \end{pmatrix}, \quad \mathbf{F}(Z,s) = \begin{pmatrix} \sin\left(\frac{is}{c_-}Z\right) & 0 \\ 0 & \sin\left(\frac{is}{c_+}Z\right) \end{pmatrix}, \quad (17)$$

and $\tilde{\boldsymbol{\mathcal{P}}}^{\mathcal{D}}(s), \tilde{\boldsymbol{\mathcal{P}}}^{\mathcal{N}}(s)$ 2D-vectors yet to be found. $\tilde{\boldsymbol{\mathcal{P}}}^{\mathcal{D}}(s), \tilde{\boldsymbol{\mathcal{P}}}^{\mathcal{N}}(s)$ provide the mode-dependent amplitude of $\tilde{\boldsymbol{\mathcal{P}}}(Z,s)$ respectively associated with the Dirichlet or the Neumann boundary condition imposed at location $Z = 0$. This is a transposition of the transfer matrix method [14, 20, 23, 12], to the wave operator problem. Combining the expression of (16) and (17) with the Laplace transform of the boundary condition system (13), leads to

$$\begin{pmatrix} \tilde{\boldsymbol{\mathcal{P}}}^{\mathcal{D}} \\ \tilde{\boldsymbol{\mathcal{P}}}^{\mathcal{N}} \end{pmatrix}(s) = \boldsymbol{\mathcal{B}}^{-1}(s)\boldsymbol{\mathcal{S}}, \quad (18)$$

with

$$\boldsymbol{\mathcal{B}} = \begin{pmatrix} \boldsymbol{\mathcal{N}} & is\boldsymbol{\mathcal{M}}\boldsymbol{\mathcal{C}}_{\boldsymbol{\mathcal{P}}}^{-1} \\ \boldsymbol{\mathcal{Q}}\mathbf{E}(1) - is\boldsymbol{\mathcal{R}}\boldsymbol{\mathcal{C}}_{\boldsymbol{\mathcal{P}}}^{-1}\mathbf{F}(1) & \boldsymbol{\mathcal{Q}}\mathbf{F}_k(1) + is\boldsymbol{\mathcal{R}}\boldsymbol{\mathcal{C}}_{\boldsymbol{\mathcal{P}}}^{-1}\mathbf{E}(1) \end{pmatrix} \quad (19)$$

In the following development, the inverse of (19) is needed to bring out the pole of $\tilde{\boldsymbol{\mathcal{P}}}$. By introducing the adjugate matrix of $\boldsymbol{\mathcal{B}}$, namely $\mathbf{adj}\,[\boldsymbol{\mathcal{B}}]$ one can formally see that

$$\boldsymbol{\mathcal{B}}^{-1}(s) = \frac{\mathbf{adj}\,[\boldsymbol{\mathcal{B}}(s)]}{\det \boldsymbol{\mathcal{B}}(s)}, \quad (20)$$

Let us furthermore introduce the two matrices

$$\mathbf{e}_1 = \begin{pmatrix} 1 & 0 & 0 & 0 \\ 0 & 1 & 0 & 0 \end{pmatrix}, \text{ and, } \mathbf{e}_2 = \begin{pmatrix} 0 & 0 & 1 & 0 \\ 0 & 0 & 0 & 1 \end{pmatrix}, \quad (21)$$

vector $\tilde{\boldsymbol{\mathcal{P}}}(s,Z)$ can then be found using (16), (18) and (20) to reach

$$\tilde{\boldsymbol{\mathcal{P}}}(s,Z) = \frac{\boldsymbol{\Phi}(s,Z)}{\det \boldsymbol{\mathcal{B}}(s)}, \quad (22)$$

with

$$\boldsymbol{\Phi}(s,Z) = \left[\mathbf{E}(Z)\mathbf{e}_1 + \mathbf{F}(Z)\mathbf{e}_2\right]\left(\mathbf{adj}\,[\boldsymbol{\mathcal{B}}]\,\boldsymbol{\mathcal{S}}\right). \quad (23)$$

2.4 Laplace inversion and time-dependent solution

The pole of (16) are investigated in order to perform the inverse Laplace transform using Cauchy's theorem. Regarding the structure of (16), it immediately appears that the poles are located within the expressions of $\tilde{\boldsymbol{\mathcal{P}}}^{\mathcal{D}}(s)$ and $\tilde{\boldsymbol{\mathcal{P}}}^{\mathcal{N}}(s)$ and, consequently using (18)-(20), within the root of $\det \boldsymbol{\mathcal{B}}(s)$. The adjugate matrix, by definition, does not contribute to the pole set of $\tilde{\boldsymbol{\mathcal{P}}}^{\mathcal{D}}(s)$ and $\tilde{\boldsymbol{\mathcal{P}}}^{\mathcal{N}}(s)$. The condition $\det(\boldsymbol{\mathcal{B}}(s)) = 0$ is similar to the spectrum condition derived in [2] and leads to

$$\mathcal{S}_{\mathcal{P}} = \{s \in \mathbb{C} \;\; | \det \boldsymbol{\mathcal{B}}(s) = 0\}. \quad (24)$$

The resulting transcendental equation for root s_k is specific to each boundary condition set and has to be computed numerically. In the following, three configurations are considered for which, in each case, the root s_k is purely imaginary, i.e.

$$s_k = i\lambda_k \quad \text{, with,} \quad \lambda_k \in \mathbb{R}. \quad (25)$$

It is interesting to mention that purely imaginary poles are found for the three specific considered configurations examined in section 3, without stating it is a general result. This remark goes along with the consideration obtained for the operator spectrum in [2]. The pole set of $\tilde{\boldsymbol{\mathcal{P}}}(Z,s)$, $\mathcal{S}_{\mathcal{P}}$, being found, Cauchy's residue theorem is used to derive a time-domain solution for vector wave problem (11), leading to

$$\boldsymbol{\mathcal{P}}(\tau,Z)=\mathcal{R}_e\left(\sum_{\mathcal{S}_{\mathcal{P}}}\lim_{s\to i\lambda_k}\left((s-i\lambda_k)\frac{\boldsymbol{\Phi}(s,Z)}{\det\left(\boldsymbol{\mathcal{B}}(s)\right)}e^{s\tau}\right)\right). \tag{26}$$

and using the classical Taylor expansion of $\det\boldsymbol{\mathcal{B}}(s)$ at poles $s_k=i\lambda_k$,

$$\boldsymbol{\mathcal{P}}(\tau,Z)=\mathcal{R}_e\left(\sum_{\mathcal{S}_{\mathcal{P}}}\frac{\boldsymbol{\Phi}(i\lambda_k,Z)}{\partial_s\det\left(\boldsymbol{\mathcal{B}}(i\lambda_k)\right)}e^{i\lambda_k\tau}\right). \tag{27}$$

The previous expression completes the frequency-domain analysis for the time-domain solution of (11). A variety of spatial boundary conditions is then investigated. The associated spectrum will be described and analyzed in detail. Natural frequencies, f_k, found from transcendental spectrum equation roots, s_k, read

$$f_k(Hz)=\frac{s_kc_p}{2\pi iL}=\frac{\lambda_kc_p}{2\pi L}, \tag{28}$$

where L is the pipe's length introduced in §1.

3 SETS OF SPATIAL BOUNDARY CONDITIONS

Three sets of boundary conditions are analyzed: (i) the reservoir-pipe-anchored valve system (Cf Fig. 1a), (ii) the reservoir-pipe-free valve system (Cf Fig. 1b), (iii) pipe impacted by a rod (Cf Fig. 1c).

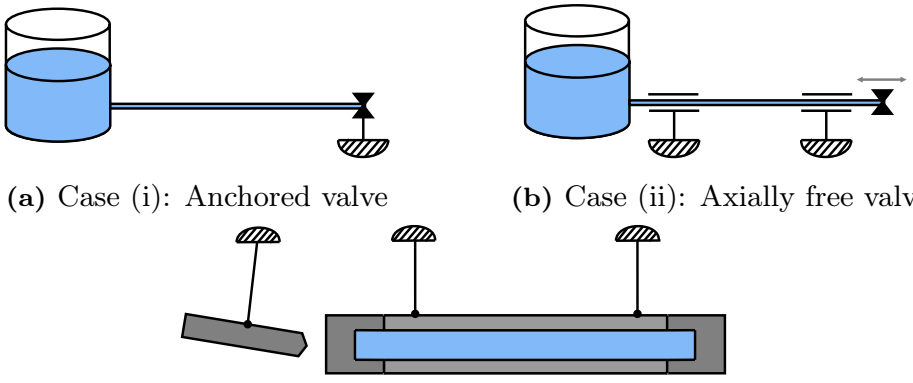

(a) Case (i): Anchored valve

(b) Case (ii): Axially free valve

(c) Case (iii): Impacting rod

Figure 1: Boundary condition sets investigated for the liquid-filled pipe problem.

3.1 The reservoir-pipe-anchored valve system: : case (i)

In the following configuration (Cf Fig. 1a), the pipe is supposed perfectly anchored both upstream and downstream. One thereby supposes an homogeneous

Anchored and free valve systems (i) & (ii) (Cf Fig. 1a & 1b)

Fluid (water)	Solid (steel)
$\rho_f = 1000\ kg \cdot m^3$	$\rho_s = 7900\ kg \cdot m^{-3}$
$\mathcal{K}_f = 2.1\ GPa$	$E = 210\ GPa$
	$\nu_s = 0.3$
	$R_0 = 0.395\ m$
	$e = 0.008\ m$
	$L = 20\ m$

(a) Physical properties and configuration for case (i) & (ii)

Impacting rod system (iii) (Cf Fig. 1c)

Fluid (water)	Solid (steel)	rod & sleeves (steel)
$\rho_f = 999\ kg \cdot m^3$	$\rho_s = 7985\ kg \cdot m^{-3}$	$M_0 = 1.312\ kg$
$\mathcal{K}_f = 2.14\ GPa$	$E = 168\ GPa$	$M_L = 0.3258\ kg$
	$\nu_s = 0.29$	$F_{rod} = 9.4\ kN$
	$R_0 = 0.02601\ m$	$V_{rod} = 0.1175\ m/s$
	$e = 0.003945\ m$	
	$L = 4.502\ m$	

(b) Physical properties and configuration for case (iii)

Table 1: Identification of the parameters necessary for the study of the three configurations shown in Figure 1.

Neumann condition for the axial stress at $Z = 0$ & $Z = 1$. Furthermore the reservoir impedes any pressure fluctuation upstream which can be interpreted as an homogeneous Dirichlet condition for the pressure field. Finally, downstream, the instantaneous valve closure is modeled with a Dirac distribution $\delta(\tau)$ acting on the axial pressure spatial gradient. The four boundary conditions thereby read

$$P(0,\tau) = 0 \quad , \partial_Z P(1,\tau) = \delta(\tau), \quad \partial_Z \sigma(0,\tau) = \partial_Z \sigma(1,\tau) = 0. \tag{29}$$

Invoking the change-of-basis relationships (12) whilst introducing

$$\beta = \frac{c_+}{c_-}\frac{c_-^2 - 1}{c_+^2 - 1}, \tag{30}$$

the boundary condition matrices (13) can then be determined:

$$\boldsymbol{\mathcal{N}} = \begin{pmatrix} 1 & \frac{\beta c_-}{c_+} \\ 0 & 0 \end{pmatrix}, \ \boldsymbol{\mathcal{M}} = \begin{pmatrix} 0 & 0 \\ 1 & 1 \end{pmatrix}, \ \boldsymbol{\mathcal{Q}} = \mathbf{0}, \ \boldsymbol{\mathcal{R}} = \boldsymbol{\mathcal{N}} + \boldsymbol{\mathcal{M}}, \ \boldsymbol{\mathcal{S}} = \frac{(c_-^2 - 1)}{2\nu_s \mathcal{D}} \begin{pmatrix} 0 \\ 0 \\ 1 \\ 0 \end{pmatrix}. \tag{31}$$

The boundary condition matrices are useful to derive an expression for cornerstone matrix $\boldsymbol{\mathcal{B}}$. Invoking the definition of the latter in (19), one finds

$$\boldsymbol{\mathcal{B}} = \begin{pmatrix} 1 & \frac{\beta c_-}{c_+} & 0 & 0 \\ 0 & 0 & \frac{is}{c_-} & \frac{is}{c_+} \\ -is\frac{\sin\left(\frac{is}{c_-}\right)}{c_-} & -is\frac{\beta c_-}{c_+}\frac{\sin\left(\frac{is}{c_+}\right)}{c_+} & is\frac{\cos\left(\frac{is}{c_-}\right)}{c_-} & is\frac{\beta c_-}{c_+}\frac{\cos\left(\frac{is}{c_+}\right)}{c_+} \\ -is\frac{\sin\left(\frac{is}{c_-}\right)}{c_-} & -is\frac{\sin\left(\frac{is}{c_+}\right)}{c_+} & is\frac{\cos\left(\frac{is}{c_-}\right)}{c_-} & is\frac{\cos\left(\frac{is}{c_+}\right)}{c_+} \end{pmatrix}. \tag{32}$$

The determinant of $\boldsymbol{\mathcal{B}}(s)$ can be easily found leading to

$$\det\left(\boldsymbol{\mathcal{B}}(s)\right) = -is^3\frac{c_-\beta - c_+}{c_+^3 c_-}\left[\beta\sin\left(\frac{is}{c_-}\right)\cos\left(\frac{is}{c_+}\right) - \sin\left(\frac{is}{c_+}\right)\cos\left(\frac{is}{c_-}\right)\right], \quad (33)$$

and,

$$\partial_s \det\left(\boldsymbol{\mathcal{B}}(s)\right) = 3\frac{\det\left(\boldsymbol{\mathcal{B}}(s)\right)}{s}$$
$$+ s^3\left(\frac{c_-\beta - c_+}{c_+^2 c_-}\right)^2\left[\frac{c_+\beta - c_-}{c_-\beta - c_+}\cos\left(\frac{is}{c_-}\right)\cos\left(\frac{is}{c_+}\right) - \sin\left(\frac{is}{c_+}\right)\sin\left(\frac{is}{c_-}\right)\right]. \quad (34)$$

Let $s_k = i\lambda_k$, with $\lambda_k \in \mathbb{R}$, be a root of (33). The spectrum associated with the reservoir-pipe-anchored valve configuration arises from λ_k transcendental equation

$$\mathcal{S}_{\mathcal{P}} = \left\{\lambda_k \in \mathbb{R},\quad \beta\sin\left(\frac{\lambda_k}{c_-}\right)\cos\left(\frac{\lambda_k}{c_+}\right) = \sin\left(\frac{\lambda_k}{c_+}\right)\cos\left(\frac{\lambda_k}{c_-}\right)\right\}. \quad (35)$$

It remains to establish the expression of $\boldsymbol{\Phi}(s, Z)$ in (23) to provide $\boldsymbol{\mathcal{P}}$ in (27). Since the determination of $\mathbf{adj}\left[\boldsymbol{\mathcal{B}}(s)\right]\boldsymbol{\mathcal{S}}$ can be tedious, the resolution is performed via symbolic computation (using **Maple** software) leading to

$$\mathbf{adj}\left[\boldsymbol{\mathcal{B}}(s)\right]\boldsymbol{\mathcal{S}} = \frac{s^2\left(c_-^2 - 1\right)}{2\nu_s\mathcal{D}}\begin{pmatrix} \frac{\beta}{c_+^2}\left(\cos\left(\frac{is}{c_-}\right) - \cos\left(\frac{is}{c_+}\right)\right) \\ -\frac{1}{c_+c_-}\left(\cos\left(\frac{is}{c_-}\right) - \cos\left(\frac{is}{c_+}\right)\right) \\ \frac{1}{c_+^2}\left(\beta\sin\left(\frac{is}{c_-}\right) - \sin\left(\frac{is}{c_+}\right)\right) \\ -\frac{1}{c_+c_-}\left(\beta\sin\left(\frac{is}{c_-}\right) - \sin\left(\frac{is}{c_+}\right)\right) \end{pmatrix}. \quad (36)$$

At this stage, the solution of the vector wave equation (11) can be expressed in either frequency-domain, combining (33) and (36) in (22), or time-domain, combining (34) and (36) in (27). When evaluating in $i\lambda_k$, the derivative of the determinant (34) turns out to be purely imaginary while the term $\mathbf{adj}\left[\boldsymbol{\mathcal{B}}(s)\right]\boldsymbol{\mathcal{S}}$ in (36) turns out to be real, as do matrix $\mathbf{E}(Z, s)$ and $\mathbf{F}(Z, s)$ in (17). In other words, when performing the inverse Laplace transform over $\tilde{\boldsymbol{\mathcal{P}}}$ only the temporal sinus mode in (27) contributes. Figures 2 & 3 illustrate this solution and its spectrum

$$\boldsymbol{\mathcal{P}}(Z,\tau) = \frac{\left(c_-^2 - 1\right)\sum_{\lambda_k\in\mathcal{S}_{\mathcal{P}}}\sin\left(\lambda_k\tau\right)}{2\nu_s c_+^2\,\mathcal{D}\lambda_k\left(\frac{c_-\beta - c_+}{c_+^2 c_-}\right)^2\left[\frac{c_+\beta - c_-}{c_-\beta - c_+}\cos\left(\frac{\lambda_k}{c_-}\right)\cos\left(\frac{\lambda_k}{c_+}\right) - \sin\left(\frac{\lambda_k}{c_+}\right)\sin\left(\frac{\lambda_k}{c_-}\right)\right]}$$
$$\left[\left(\cos\left(\frac{\lambda_k}{c_-}\right) - \cos\left(\frac{\lambda_k}{c_+}\right)\right)\begin{pmatrix}\beta\cos\left(\frac{\lambda_k Z}{c_-}\right) \\ -\frac{c_+}{c_-}\cos\left(\frac{\lambda_k Z}{c_+}\right)\end{pmatrix} + \left(\beta\sin\left(\frac{\lambda_k}{c_-}\right) - \sin\left(\frac{\lambda_k}{c_+}\right)\right)\begin{pmatrix}\sin\left(\frac{\lambda_k Z}{c_-}\right) \\ -\frac{c_+}{c_-}\sin\left(\frac{\lambda_k Z}{c_+}\right)\end{pmatrix}\right]. \quad (37)$$

3.2 The reservoir-pipe-free valve system : case (ii)

A second configuration is analyzed when the valve is free to move axially (Cf Fig. 1b). Upstream, the same conditions (29) are applied, with homogeneous Neumann condition for the axial stress and homogeneous Dirichlet condition for

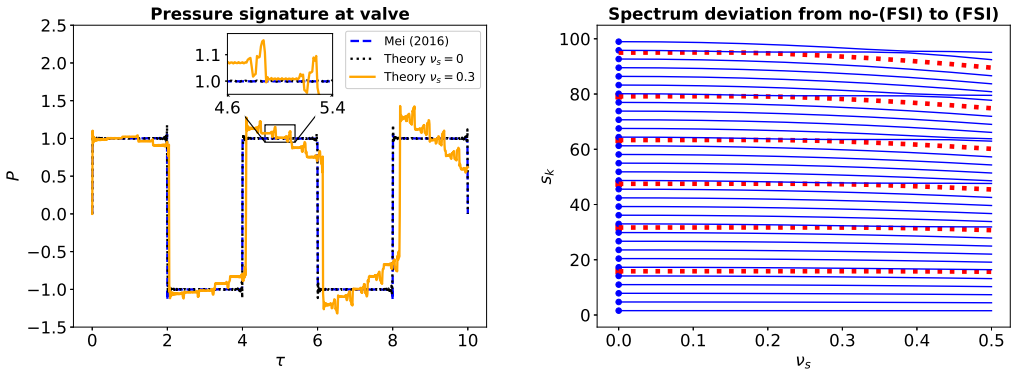

(a) **(b)**

Figure 2: Time-domain result and spectrum of test case (i). (a) Pressure response with FSI ($\nu_s = 0.3$ continuous brown lines) and without FSI modeling ($\nu_s = 0$ black dotted lines) versus [15]'s theoretical solution (the which does not account for FSI effects, i.e. $\nu_s \equiv 0$). (b) Spectrum (43 first eigenvalues) associated with Dirichlet/Dirichlet boundary conditions (29) versus the Poisson modulus ν_s (blue dots for $\nu_s = 0$ are [15]'s spectrum and red dots are the pure elastic modes the union of which are being the spectrum (35). As ν_s varies, some eigenvalues come close to one-another, but a careful inspection shows no cross-over between the depicted eigenvalues.

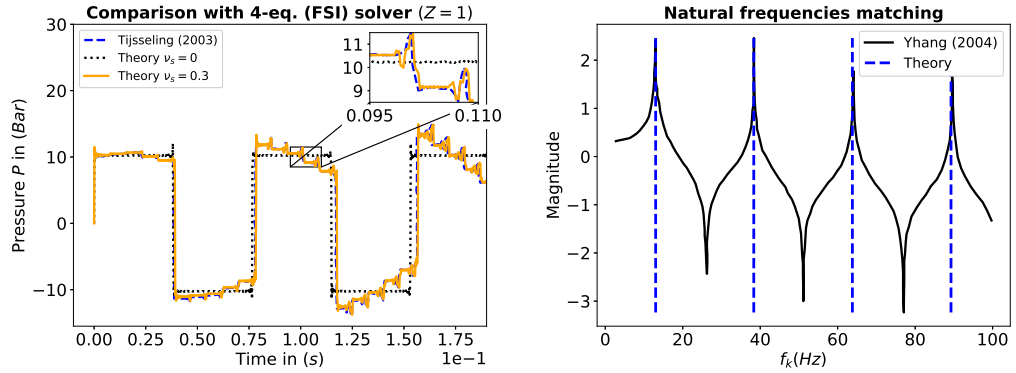

(a) **(b)**

Figure 3: Time-domain and frequency-domain results of test case (i). (a) Comparison between pressure field analytical solution at valve location (continuous brown lines) with MOC solutions provided by [20] (dashed blue lines). Non-FSI solutions (i.e $\nu_s = 0$) are provided for illustration in black dotted lines. Insets provide a zoom for detailed check. (b) Comparison between [22]'s pressure prediction at valve eigenvalues obtained from transcendental equation (35)

the pressure. Downstream, the static equilibrium of forces at the valve location combined with velocity continuity leads to

$$\alpha(2+\alpha)\sigma(1,\tau) = P(1,\tau), \tag{38}$$

$$\partial_Z P(1,\tau) + \mathcal{D}\partial_Z \sigma(1,\tau) = \delta(\tau). \tag{39}$$

Considering change of basis (12) whilst introducing parameters

$$\kappa_{\pm} = \mathcal{D} + \frac{2\nu_s \mathcal{D}}{c_{\pm}^2 - 1}, \tag{40}$$

$$\gamma = \frac{\alpha(2+\alpha) - \frac{2\nu_s \mathcal{D}}{c_+^2 - 1}}{\alpha(2+\alpha) - \frac{2\nu_s \mathcal{D}}{c_-^2 - 1}}, \tag{41}$$

the boundary condition matrices (13) can be found leading to

$$\boldsymbol{\mathcal{N}} = \begin{pmatrix} 1 & \frac{\beta c_-}{c_+} \\ 0 & 0 \end{pmatrix}, \quad \boldsymbol{\mathcal{M}} = \begin{pmatrix} 0 & 0 \\ 1 & 1 \end{pmatrix}, \quad \boldsymbol{\mathcal{Q}} = \begin{pmatrix} 0 & 0 \\ 1 & \gamma \end{pmatrix}, \quad \boldsymbol{\mathcal{R}} = \begin{pmatrix} \kappa_- & \kappa_+ \\ 0 & 0 \end{pmatrix}, \quad \boldsymbol{\mathcal{S}} = \begin{pmatrix} 0 \\ 0 \\ 1 \\ 0 \end{pmatrix}. \tag{42}$$

Using definition (19), $\boldsymbol{\mathcal{B}}$ can be found as

$$\boldsymbol{\mathcal{B}} = \begin{pmatrix} 1 & \frac{\beta c_-}{c_+} & 0 & 0 \\ 0 & 0 & \frac{is}{c_-} & \frac{is}{c_+} \\ -is\frac{\kappa_-}{c_-}\sin\left(\frac{is}{c_-}\right) & -is\frac{\kappa_+}{c_+}\sin\left(\frac{is}{c_+}\right) & is\frac{\kappa_-}{c_-}\cos\left(\frac{is}{c_-}\right) & is\frac{\kappa_+}{c_+}\cos\left(\frac{is}{c_+}\right) \\ \cos\left(\frac{is}{c_-}\right) & \gamma\cos\left(\frac{is}{c_+}\right) & \sin\left(\frac{is}{c_-}\right) & \gamma\sin\left(\frac{is}{c_+}\right) \end{pmatrix} \tag{43}$$

Noticing that

$$\frac{\kappa_-}{\gamma\kappa_+} = \frac{c_+}{\beta c_-}, \tag{44}$$

the determinant of $\boldsymbol{\mathcal{B}}(s)$ and its derivative with respect to s are

$$\det \boldsymbol{\mathcal{B}}(s) = -\frac{2s^2\beta\kappa_-}{c_+^2} + s^2\frac{\kappa_+}{c_+^2}\left[\beta\cos\left(\frac{is}{c_+}\right)\cos\left(\frac{is}{c_-}\right)\left(1+\left(\frac{\kappa_-}{\kappa_+}\right)^2\right) + \sin\left(\frac{is}{c_+}\right)\sin\left(\frac{is}{c_-}\right)\left(1+\left(\frac{\beta\kappa_-}{\kappa_+}\right)^2\right)\right], \tag{45}$$

$$\partial_s \det \boldsymbol{\mathcal{B}}(s) = is^2\left(\chi_+\sin\left(\frac{is}{c_-}\right)\cos\left(\frac{is}{c_+}\right) + \chi_-\cos\left(\frac{is}{c_-}\right)\sin\left(\frac{is}{c_+}\right)\right) + \frac{2\det\boldsymbol{\mathcal{B}}(s)}{s}, \tag{46}$$

with

$$\chi_{\pm} = \frac{\kappa_+}{c_+^2}\left(\frac{1}{c_{\pm}}\left[1+\left(\frac{\beta\kappa_-}{\kappa_+}\right)^2\right] - \frac{\beta}{c_{\mp}}\left[1+\left(\frac{\kappa_-}{\kappa_+}\right)^2\right]\right), \tag{47}$$

Let $s = i\lambda_k$, with $\lambda_k \in \mathbb{R}$, be a root of (33). The spectrum associated with the reservoir-pipe-free valve configuration is governed by the following λ_k transcendental equation,

$$\beta\cos\left(\frac{\lambda_k}{c_+}\right)\cos\left(\frac{\lambda_k}{c_-}\right)\left(1+\left(\frac{\kappa_-}{\kappa_+}\right)^2\right) + \left(1+\left(\frac{\beta\kappa_-}{\kappa_+}\right)^2\right)\sin\left(\frac{\lambda_k}{c_+}\right)\sin\left(\frac{\lambda_k}{c_-}\right) = \frac{2\kappa_-}{\kappa_+}. \tag{48}$$

Again the tedious determination of $\mathbf{adj}\left(\boldsymbol{\mathcal{B}}(s)\right)\boldsymbol{\mathcal{S}}$ is performed using symbolic computation and leads to

$$\mathbf{adj}\left[\boldsymbol{\mathcal{B}}(s)\right]\boldsymbol{\mathcal{S}} = -is\begin{pmatrix} \frac{\beta}{c_+^2}\left(c_-\sin\left(\frac{is}{c_-}\right) - \gamma c_+\sin\left(\frac{is}{c_+}\right)\right) \\ -\frac{1}{c_-c_+}\left(c_-\sin\left(\frac{is}{c_-}\right) - \gamma c_+\sin\left(\frac{is}{c_+}\right)\right) \\ -\frac{1}{c_+^2}\left(\beta c_-\cos\left(\frac{is}{c_-}\right) - \gamma c_+\cos\left(\frac{is}{c_+}\right)\right) \\ \frac{1}{c_-c_+}\left(\beta c_-\cos\left(\frac{is}{c_-}\right) - \gamma c_+\cos\left(\frac{is}{c_+}\right)\right) \end{pmatrix}. \tag{49}$$

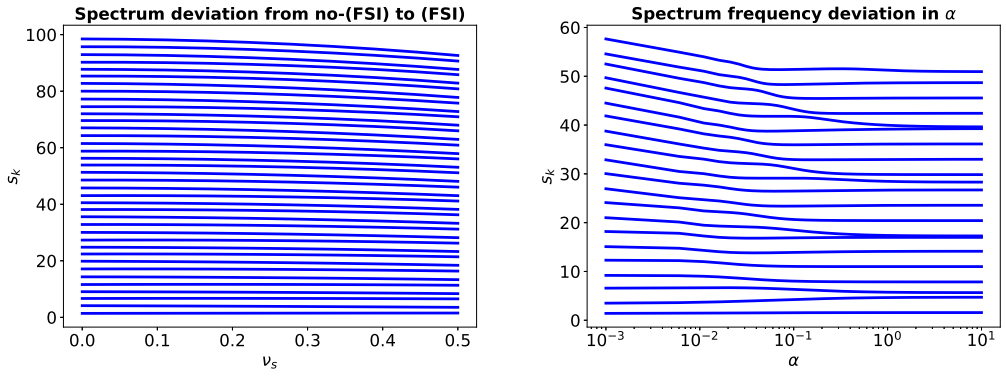

(a) **(b)**

Figure 4: Spectrum of case (ii). (a) first 40 eigenvalues evaluated from (48) versus the Poisson modulus ν_s. (b) first 24 eigenvalues versus the pipe's thickness / radius ratio α. As α varies, some eigenvalues come close to one-another, but a careful inspection shows no cross-over between the depicted eigenvalues.

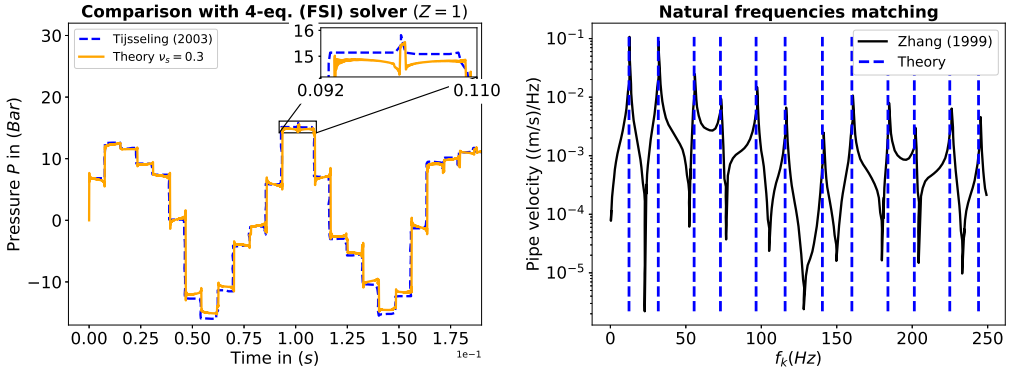

(a) **(b)**

Figure 5: Time-domain and frequency-domain results of test case (ii). (a) Comparison between pressure field analytical solution at valve location (continuous brown lines) with MOC solutions provided by [20] (dashed blue lines). Insets provide a zoom for detailed check. (b) Comparison between [23]'s pipe velocity spectrum at valve and eigenvalues obtained from transcendental equation (48)

The solution of the vector wave equation (11) can once again be expressed in either frequency-domain, combining (45) and (49) in (22), or time-domain, combining (46) and (49) in (27). Figures 4 & 5 illustrate this solution and its spectrum

$$\boldsymbol{\mathcal{P}}(Z,\tau) = -\sum_{\lambda_k \in \mathcal{S}_{\mathcal{P}}} \frac{\left(c_- \sin\left(\frac{\lambda_k}{c_-}\right) - \gamma c_+ \sin\left(\frac{\lambda_k}{c_+}\right)\right)\begin{pmatrix} \beta \cos\left(\frac{\lambda_k Z}{c_-}\right) \\ -\frac{c_+}{c_-}\cos\left(\frac{\lambda_k Z}{c_+}\right)\end{pmatrix}}{\lambda_k c_+^2\left(\chi_+ \sin\left(\frac{\lambda_k}{c_-}\right)\cos\left(\frac{\lambda_k}{c_+}\right) + \chi_- \cos\left(\frac{\lambda_k}{c_-}\right)\sin\left(\frac{\lambda_k}{c_+}\right)\right)} \sin(\lambda_k \tau)$$
$$+\sum_{\lambda_k \in \mathcal{S}_{\mathcal{P}}} \frac{\left(\beta c_- \cos\left(\frac{\lambda_k}{c_-}\right) - \gamma c_+ \cos\left(\frac{\lambda_k}{c_+}\right)\right)\begin{pmatrix} \sin\left(\frac{\lambda_k Z}{c_-}\right) \\ -\frac{c_+}{c_-}\sin\left(\frac{\lambda_k Z}{c_+}\right)\end{pmatrix}}{\lambda_k c_+^2\left(\chi_+ \sin\left(\frac{\lambda_k}{c_-}\right)\cos\left(\frac{\lambda_k}{c_+}\right) + \chi_- \cos\left(\frac{\lambda_k}{c_-}\right)\sin\left(\frac{\lambda_k}{c_+}\right)\right)} \sin(\lambda_k \tau)\,. \quad (50)$$

3.3 The impact induced water hammer : case (iii)

In this third configuration, the over-pressure occurs from the impact of a steel rod on a closed liquid-filled pipe system. This ingenious experiment was designed by [21] to reveal intrinsic FSI coupling occurring in liquid-filled pipes while minimizing external disturbing contributions. This system has been analytically investigated in [12, 13]. At the upstream pipe end, a steel rod impacts the pipe sleeve producing an over-stress which propagates within the fluid/solid system. While the impact time of the rod over the upstream sleeve is supposed negligible, one nevertheless considers the sleeve's inertia. The dynamic equilibrium of forces along with the velocity continuity at both pipe's upstream and downstream ends leads to

$$
\begin{aligned}
m_0 \mathcal{D}\partial_Z \sigma_{zz}(0,\tau) &= \mathcal{F}_r \delta(\tau) + \alpha(2+\alpha)\sigma_{zz}(0,\tau) - P(0,\tau), && (51)\\
\mathcal{D}\partial_Z \sigma_{zz}(0,\tau) + \partial_Z P(0,\tau) &= 0, && (52)\\
-m_L \mathcal{D}\partial_Z \sigma_{zz}(1,\tau) &= \alpha(2+\alpha)\sigma_{zz}(1,\tau) - P(1,\tau), && (53)\\
\mathcal{D}\partial_Z \sigma_{zz}(1,\tau) + \partial_Z P(1,\tau) &= 0. && (54)
\end{aligned}
$$

where

$$
\begin{aligned}
m_{\substack{0\\L}} &= \frac{M_{\substack{0\\L}}}{\pi \rho_f R^2 L}, && (55)\\
\mathcal{F}_r &= \frac{F_{rod}}{\pi \rho_f c_p V_{rod} R^2}. && (56)
\end{aligned}
$$

Considering change of basis relations (12) and introducing parameters

$$
\begin{aligned}
\eta_{\substack{0\\L}} &= \frac{m_{\substack{0\\L}} \mathcal{D}}{\alpha(2+\alpha) - \frac{2\nu_s \mathcal{D}}{c_-^2 - 1}}, && (57)\\
\mathcal{F} &= \frac{\mathcal{F}_r}{\alpha(2+\alpha) - \frac{2\nu_s \mathcal{D}}{c_-^2 - 1}}, && (58)
\end{aligned}
$$

the boundary conditions matrices (13) can be determined

$$
\boldsymbol{\mathcal{N}} = -\begin{pmatrix} 0 & 0 \\ 1 & \gamma \end{pmatrix}, \quad \boldsymbol{\mathcal{M}} = \begin{pmatrix} \kappa_- & \kappa_+ \\ \eta_0 & \eta_0 \end{pmatrix}, \quad \boldsymbol{\mathcal{Q}} = -\boldsymbol{\mathcal{N}}, \quad \boldsymbol{\mathcal{R}} = \begin{pmatrix} \kappa_- & \kappa_+ \\ \eta_L & \eta_L \end{pmatrix}, \quad \boldsymbol{\mathcal{S}} = \begin{pmatrix} 0 \\ \mathcal{F} \\ 0 \\ 0 \end{pmatrix}. \quad (59)
$$

Cornerstone matrix $\boldsymbol{\mathcal{B}}$ can now be evaluated using (19)

$$
\boldsymbol{\mathcal{B}} = \begin{pmatrix}
0 & 0 & is\frac{\kappa_-}{c_-} & is\frac{\kappa_+}{c_+} \\
-1 & -\gamma & \frac{is\eta_0}{c_-} & \frac{is\eta_0}{c_+} \\
-is\frac{\kappa_- \sin\left(\frac{is}{c_-}\right)}{c_-} & -is\frac{\kappa_+ \sin\left(\frac{is}{c_+}\right)}{c_+} & is\frac{\kappa_- \cos\left(\frac{is}{c_-}\right)}{c_-} & is\frac{\kappa_+ \cos\left(\frac{is}{c_+}\right)}{c_+} \\
\mathcal{B}_{41}(s) & \mathcal{B}_{42}(s) & \mathcal{B}_{43}(s) & \mathcal{B}_{44}(s)
\end{pmatrix}, \quad (60)
$$

with

$$
\begin{aligned}
&\mathcal{B}_{41}(s) = \cos\left(\frac{is}{c_-}\right) - \frac{is\eta_L}{c_-}\sin\left(\frac{is}{c_-}\right), \quad \mathcal{B}_{42}(s) = \gamma\cos\left(\frac{is}{c_+}\right) - \frac{is\eta_L}{c_+}\sin\left(\frac{is}{c_+}\right),\\
&\mathcal{B}_{43}(s) = \sin\left(\frac{is}{c_-}\right) + \frac{is\eta_L}{c_-}\cos\left(\frac{is}{c_-}\right), \quad \mathcal{B}_{44}(s) = \gamma\sin\left(\frac{is}{c_+}\right) + \frac{is\eta_L}{c_+}\cos\left(\frac{is}{c_+}\right). \quad (61)
\end{aligned}
$$

Hence introducing

$$\psi = \beta \left(\frac{\kappa_-}{\kappa_+} \right)^2, \tag{62}$$

the determinant of $\boldsymbol{\mathcal{B}}(s)$ and its derivative follows

$$\begin{aligned}
\det \boldsymbol{\mathcal{B}}(s) = {} & s^2 \frac{\eta_0 \eta_L \left(\kappa_- - \kappa_+\right)^2 s^2 + c_-^2 \kappa_+^2 \left(1 + \psi^2\right)}{c_-^2 c_+^2} \sin\left(\frac{is}{c_-}\right) \sin\left(\frac{is}{c_+}\right) \\
& + is^3 \frac{\kappa_+ \left(\kappa_- - \kappa_+\right) \left(\eta_0 + \eta_L\right)}{c_- c_+^2} \left(\psi \cos\left(\frac{is}{c_+}\right) \sin\left(\frac{is}{c_-}\right) - \cos\left(\frac{is}{c_-}\right) \sin\left(\frac{is}{c_+}\right) \right) \\
& + 2s^2 \frac{\psi \kappa_+^2}{c_+^2} \left(\cos\left(\frac{is}{c_-}\right) \cos\left(\frac{is}{c_+}\right) - 1 \right)
\end{aligned} \tag{63}$$

$$\begin{aligned}
\partial_s \det \boldsymbol{\mathcal{B}}(s) = {} & \frac{2 \det \boldsymbol{\mathcal{B}}(s)}{s} - s^3 \cos\left(\frac{is}{c_-}\right) \cos\left(\frac{is}{c_+}\right) \frac{\kappa_+ \left(\kappa_- - \kappa_+\right) \left(\eta_0 + \eta_L\right)}{c_- c_+^2} \left[\frac{\psi}{c_-} - \frac{1}{c_+} \right] \\
& + \frac{is^2}{c_- c_+^2} \cos\left(\frac{is}{c_+}\right) \sin\left(\frac{is}{c_-}\right) \left[\psi \kappa_+ \left(\left(\kappa_- - \kappa_+\right) \left(\eta_0 + \eta_L\right) - 2\kappa_+ \right) + \frac{\eta_0 \eta_L \left(\kappa_- - \kappa_+\right)^2 s^2 + c_-^2 \kappa_+^2 \left(1 + \psi^2\right)}{c_- c_+} \right] \\
& + \frac{is^2}{c_+^2} \cos\left(\frac{is}{c_-}\right) \sin\left(\frac{is}{c_+}\right) \left[\frac{\eta_0 \eta_L \left(\kappa_- - \kappa_+\right)^2 s^2 + c_-^2 \kappa_+^2 \left(1 + \psi^2\right)}{c_-^3} - \kappa_+ \left(\frac{\left(\kappa_- - \kappa_+\right) \left(\eta_0 + \eta_L\right)}{c_-} + \frac{2\psi\kappa_+}{c_+} \right) \right] \\
& + s^3 \sin\left(\frac{is}{c_-}\right) \sin\left(\frac{is}{c_+}\right) \frac{\kappa_- - \kappa_+}{c_- c_+^2} \left[\frac{2\eta_0 \eta_L \left(\kappa_- - \kappa_+\right)}{c_-} - \kappa_+ \left(\eta_0 + \eta_L\right) \left(\frac{1}{c_-} - \frac{\psi}{c_+} \right) \right]
\end{aligned} \tag{64}$$

The spectrum associated with this configuration is found from (63) since it is

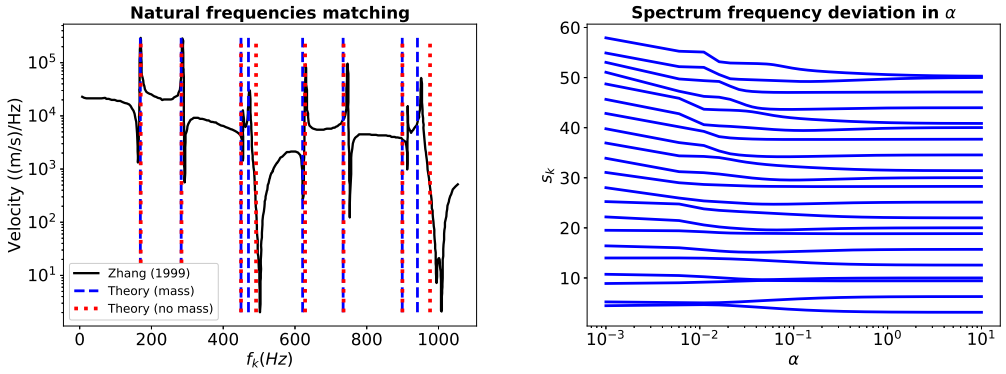

(a) **(b)**

Figure 6: Spectrum of case (iii). (a) Comparison between [23]'s pipe velocity spectrum at valve and eigenvalues obtained from the root of (63). Investigation of natural frequencies with (blue dashed line) or without (red dotted line) considering the sleeves masses is depicted. (b) first 24 eigenvalues versus the pipe's thickness / radius ratio α. As α varies, some eigenvalues come close to one-another, but a careful inspection shows no cross-over between the depicted eigenvalues.

the set of roots of: $\det \boldsymbol{\mathcal{B}}(s) = 0$. Once again $\mathbf{adj}\left[\boldsymbol{\mathcal{B}}(s)\right]\boldsymbol{\mathcal{S}}$ is evaluated and reads

$$\mathbf{adj}\left[\boldsymbol{\mathcal{B}}(s)\right]\boldsymbol{\mathcal{S}} = -s^2\mathcal{F}\begin{pmatrix} \frac{\left[-is\eta_L\kappa_+\left(\kappa_- - \kappa_+\right)\sin\left(\frac{is}{c_+}\right)+c_-\kappa_+^2\psi\cos\left(\frac{is}{c_+}\right)\right]\cos\left(\frac{is}{c_-}\right)+c_-\kappa_+^2\left[\sin\left(\frac{is}{c_-}\right)\sin\left(\frac{is}{c_+}\right)-\psi\right]}{c_-c_+^2} \\ \frac{\kappa_-}{\kappa_+}\frac{\left[is\eta_L\kappa_+\left(\kappa_- - \kappa_+\right)\sin\left(\frac{is}{c_-}\right)+c_-\kappa_+^2\cos\left(\frac{is}{c_-}\right)\right]\cos\left(\frac{is}{c_+}\right)+c_-\kappa_+^2\left[\sin\left(\frac{is}{c_-}\right)\sin\left(\frac{is}{c_+}\right)\psi-1\right]}{c_+c_-^2} \\ \frac{\left[-is\eta_L\kappa_+\left(\kappa_- - \kappa_+\right)\sin\left(\frac{is}{c_+}\right)+c_-\kappa_+^2\psi\cos\left(\frac{is}{c_+}\right)\right]\sin\left(\frac{is}{c_-}\right)-c_-\kappa_+^2\sin\left(\frac{is}{c_+}\right)\cos\left(\frac{is}{c_-}\right)}{c_-c_+^2} \\ -\frac{\kappa_-}{\kappa_+}\frac{\left[-is\eta_L\kappa_+\left(\kappa_- - \kappa_+\right)\sin\left(\frac{is}{c_+}\right)+c_-\kappa_+^2\psi\cos\left(\frac{is}{c_+}\right)\right]\sin\left(\frac{is}{c_-}\right)-c_-\kappa_+^2\sin\left(\frac{is}{c_+}\right)\cos\left(\frac{is}{c_-}\right)}{c_-^2c_+} \end{pmatrix}. \tag{65}$$

A parametric analysis is carried-out to investigate the shift of natural frequencies caused by the geometrical parameter α in Fig. 6b. The natural frequencies are then compared in Fig. 6a with the ones found by [23]. This brings out the importance of considering the sleeve masses in such systems. The fourth and eighth frequencies are considerably affected by the oscillations of the pipe's end masses.

3.4 Modal convergence analysis

The mode truncation convergence of our analytical solution is checked by evaluating the quadratic error E

$$E = \frac{1}{N_Z N_\tau}\int_0^1\int_0^{\tau=5}\left(\mathcal{P}_{M_{tr}}(z,t) - \mathcal{P}_{ref}(z,t)\right)^2 dzdt, \tag{66}$$

where $(N_Z, N_\tau) \equiv (1000, 5000)$ are the space and time numerical uniform grid point number whereas $\mathcal{P}_{ref}(Z,\tau)$ is a reference solution with very-high mode truncation (2000 modes). For each configuration analyzed the analytical solution is truncated to M_{tr} modes (with $M_{tr} \ll 2000$) and in each case a $1/M_{tr}$ convergence is found in Fig. 7.

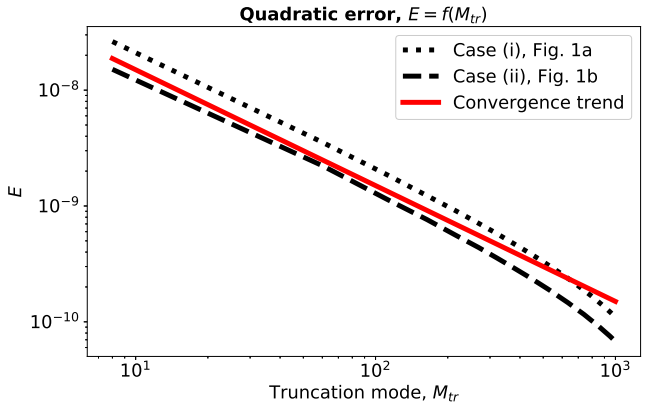

Figure 7: Mode truncation convergence of the analytical solutions.

4 CONCLUSION

The paper has presented analytical solutions for FSI wave propagation in liquid-filled pipes. By considering three sets of boundary conditions, the diagonalized pressure-stress wave equation has been analyzed by a frequency-domain Laplace transform approach. For all configurations investigated, a transcendental spectrum equation was described and detailed analysis was carried out with respect to constitutive parameters such as the Poisson modulus or the pipe's thickness radius ratio α. The determined natural frequencies were successfully compared with previous contributions found in the subject literature. For the pipe-reservoir-valve (free or not) system, a straightforward time dependent solution was derived and compared to numerical benchmarks. The solutions was found to be identical to those derived in [2]. For brevity, no time dependent solution was explicitly provided for the third configuration. This can nevertheless be accomplished by the use of the theoretical and calculus elements of this paper. We discussed and demonstrated the modal convergence of the time dependent solutions provided and highlighted the polynomial convergence behavior of the latter.

ACKNOWLEDGEMENT

This work was supported by the collaborative ANRT Grant CIFRE 2019/1453 co-funded by SETOM, dedicated society of Veolia for the public drinking water service of Toulouse Métropole operating under the brand Eau de Toulouse Métropole.
The authors have no competing interests to declare.

REFERENCES

[1] L. Allievi. Teoria del colpo d'ariete, atti collegio ing. arch.(english translation by Halmos E.E. 1929), The theory of waterhammer. *Trans. ASME*, 1913.

[2] A. Bayle and F. Plouraboué. Spectral properties of Fluid Structure Interaction pressure/stress waves in liquid filled pipes. *Wave Motion*, 116:103081, 2023.

[3] D. D. Budny, D. C. Wiggert, and F. J. Hatfield. The Influence of Structural Damping on Internal Pressure During a Transient Pipe Flow. *J. Fluids Eng.*, 113(3):424–429, Sept. 1991.

[4] W. Burmann. Water hammer in coaxial pipe systems. *J. Hydraul. Eng.*, 101(6):699–715, 1975.

[5] T. C. Che, H. F. Duan, and P. J. Lee. Transient wave-based methods for anomaly detection in fluid pipes: A review. *Mech Syst Signal Process*, 160:107874, Nov. 2021.

[6] D. Ferras, P. Manso, A. Schleiss, and D. Covas. One-dimensional fluid-structure interaction models in pressurized fluid-filled pipes: A review. *Appl. Sci.*, 8(10):1844, Oct. 2018.

[7] E. L. Holmboe and W. T. Rouleau. The Effect of Viscous Shear on Transients in Liquid Lines. *J. Basic Eng.*, 89(1):174–180, March. 1967.

[8] N. Joukowski. Memoirs of the imperial academy society of st. petersburg [Über den hydraulischen stoss in wasserleitungsröhren]. 1898.

[9] A. Keramat and H. F. Duan. Spectral based pipeline leak detection using a single spatial measurement. *Mech Syst Signal Process*, 161:107940, Dec. 2021.

[10] A. Keramat, B. Karney, M. S. Ghidaoui, and X. Wang. Transient-based leak detection in the frequency domain considering fluid-structure interaction and viscoelasticity. *Mech Syst Signal Process*, 153:107500, May 2021.

[11] D. Korteweg. Ueber die fortpflanzungsgeschwindigkeit des schalles in elastischen röhren (on the speed of sound propagation in elastic tubes). *Ann. Phys.*, 241(12):525–542, 1878.

[12] Q. Li, K. Yang, L. Zhang, and N. Zhang. Frequency domain analysis of fluid–structure interaction in liquid-filled pipe systems by transfer matrix method. *INT J MECH SCI*, 44:2067–2087, Oct. 2002.

[13] Q. S. Li, K. Yang, and L. Zhang. Analytical Solution for Fluid-Structure Interaction in Liquid-Filled Pipes Subjected to Impact-Induced Water Hammer. *Journal of Engineering Mechanics*, 129(12):1408–1417, Dec. 2003.

[14] S. Li, B. W. Karney, and G. Liu. FSI research in pipeline systems – A review of the literature. *J Fluids Struct*, 57:277–297, Aug. 2015.

[15] C. C. Mei and H. Jing. Pressure and wall shear stress in blood hammer - Analytical theory. *Mathematical Biosciences*, 280:62–70, Oct. 2016.

[16] H. Résal. Note sur les petits mouvements d'un fluide incompressible dans un tuyau élastique. *Journal de Mathematiques Pures et Appliquées*, 2:342–344, 1876.

[17] R. Skalak. An extension of the theory of waterhammer. *Transactions of the ASME*, 78:105–116, 1956.

[18] A. Tijsseling. Water hammer with fluid-structure interaction in thick-walled pipes. *Comput Struct*, 85:844–851, June 2007.

[19] A. S. Tijsseling. Fluid structure interaction in liquid filled pipe systems: a review. *J Fluids Struct*, 10(2):109–146, Feb. 1996.

[20] A. S. Tijsseling. Exact solution of linear hyperbolic four-equation system in axial liquid-pipe vibration. *J Fluids Struct*, 18(2):179–196, Sept. 2003.

[21] A. Vardy and D. Fan. Water hammer in a closed tube. pages 123–137, Hanover, Germany. Proceedings of the Fifth International Conference on Pressure Surge, BHRA.

[22] K. Yang, Q. S. Li, and L. Zhang. Longitudinal vibration analysis of multi-span liquid-filled pipelines with rigid constraints. *J. Sound Vib.*, 273(1):125–147, May 2004.

[23] L. Zhang, A. Tijsseling, and A. Vardy. FSI analysis of liquid-filled pipes. *J. Sound Vib.*, 224:69–99, July 1999.

2.3 Spectral properties of Fluid Structure Interaction pressure/stress waves in liquid filled pipes: Article to *Wave Motion*

Highlights

Spectral properties of Fluid Structure Interaction pressure/stress waves in liquid-filled pipes

A.Bayle, F.Plouraboué

- Research highlight 1: Explicit analytical solutions for Fluid Structure Interaction (FSI) waves propagation occurring in liquid-filled pipes are developed
- Research highlight 2: Convoluted behavior of time dependent solutions is spelled out.
- Research highlight 3: These theoretical solutions perfectly match with previous published numerical results
- Research highlight 4: The hereby theoretical framework applies to a broad range of boundary conditions
- Research highlight 5: The spectrum sensitivity is theoretically and numerically investigated.

Spectral properties of Fluid Structure Interaction pressure/stress waves in liquid-filled pipes

A.Bayle, F.Plouraboué

[a]*Institut de Mécanique des Fluides de Toulouse, IMFT, Université de Toulouse, CNRS, Toulouse, 31400, France*

Abstract

We hereby develop a theoretical framework for analyzing Fluid Structure Interaction (FSI) waves propagation occurring in liquid filled pipes to manage a large family set of boundary conditions (e.g. junctions coupling effects). A self-adjoint operator theory framework leads to the analytical derivation of a transcendental equations for operator's spectrum. The latter provides the system's natural resonant frequencies as well as permit to find the discrete mode orthogonal basis decomposition. This theoretical framework also permits to demonstrate that the spectrum is uniquely composed into simple eigenvalues enabling explicit time-domain solutions from inverse-Laplace transform. The analysis is directly conducted in the time-domain but the obtained spectrum also applies to Fourier transformed frequency analysis. The obtained analytical solutions are successfully confronted with numerical simulation obtained using the Method of characteristic (MOC) for the same four equations FSI model on the very same configurations. The spectrum sensitivity matrix is also explicitly evaluated.

Keywords: Fluid Structure Interaction (FSI), Liquid-filled pipes, Junction coupling, Operator's spectrum, Time domain solution, Method of characteristics (MOC)

1. Introduction

Wave propagation in liquid-filled pipe systems have been investigated for a long time [1, 2, 3, 4, 5, 6, 7] to cite only a few, possibly seminal, contributors. The phenomenology is now well understood as fully discussed in exhaustive and sagacious review papers [8, 9, 10]. Fluid Structure Interaction

(FSI) arising between pressure/stress propagation have been recognized as one major modeling pathway, leading to four coupled hyperbolic equations in the case of axi-symmetric compressive planar waves modes propagation [5, 11, 12, 7, 13]. The long wavelength approximation is a widely established and validated framework [3, 14, 15, 7]. It permits to neglect secondary FSI effects associated with rotatory vibration modes or radial inertia (e.g. bending, twisting, etc.), the analysis of which needs a more complex set of equations. Considering an averaged formulation both in solid and fluid for mass and momentum conservation equations, [7] derive a set of four coupled hyperbolic equations highlighting the overriding role of the Poisson's coupling effects, namely the axial transmission of the radial stresses and strains via the Poisson's modulus, on the whole dynamic. In [16] two other major coupling mechanisms were spelled out: (i) the junction occurring at edge conditions and, (ii) the friction coupling resulting from viscous effects in boundary layers and/or pipe's supports. Whereas (i) is precisely analyzed in this study, on the contrary, (ii) is not considered. Pipe's support coupling effects has nevertheless been thoroughly analyzed in [6, 17, 18].

Recent and active motivations to analyze the FSI vibrations in pipes lies from the use of water-hammer waves in defect/leak detection and localization [19, 20, 21, 22, 23]. Since in common practice "localized" pipe anomaly, such as a leak and a discrete blockage leads to a modification of the Fourier peaks of the signal, a spectral-based diagnostic signal processing has been sough for [19, 21, 22, 23]. In this context, the ability to obtain an explicit derivation of the traveling waves system spectral properties can pave the way to elaborate spectral diagnostic signal processing strategies among which the spectral sensitivity matrix is a central one [24, 25]. As spectral sensitivity matrix is a time-consuming and noise-sensitive quantity, a purely numerical estimate of this quantity, e.g. based upon finite-difference estimate, is sometimes not precise enough or too demanding (in case of high-dimensionality of parameter space). This is why it is either interesting to lower the parameter space dimensions and/or to find analytical estimate of this spectral sensitivity matrix, as performed here. Many contributions relying on the Laplace/frequency-domain numerical resolution of the four-FSI equations using transfer matrix method (TMM) can be found [9, 26, 27, 28, 29, 30, 20]. Nevertheless, to our knowledge, no fully explicit time-domain solutions nor explicit spectrum have been previously obtained except in [31], which has ignored Poisson's coupling and therefore FSI. In the following, we thereby focus on developing a new analytical framework using operator's theory, for pressure/stress wave

operator. We derive a straightforward real transcendental equation for the spectrum and successfully spelled out an orthogonal projection basis for the uncoupled diagonalized wave operator. The separation of variables technique is used to handle the derivation of a pressure–stress solution in time-domain (a Fourier transform may thereafter easily be managed, if required, to find the corresponding frequency domain solution). The paper is organized as follow. Section 2.1 describes the dimensionless constitutive four-FSI equations model, boundary conditions sets, parametric description, proper wave dimensional and dimensionless velocity propagation, and the resulting diagonalized 2-waves equations reminiscent of [28]'s solution strategy. Section 3 provides the theoretical framework defining the self-adjoint operator for the separable waves solutions decomposition. Section 4 illustrates the comparison between the obtained analytical solutions and previously published numerical or theoretical results for specific sets of boundary conditions. Section 5 then provides the spectrum sensitivity matrix for each boundary condition set.

2. Governing equations

2.1. Dimensionless constitutive model

Let us consider a cylindrical tube having inner radius R_0, wall thickness e, and length L, which defines the following aspect and geometrical parameters

$$\alpha = \frac{e}{R_0} \quad \text{, and,} \quad \epsilon = \frac{R_0}{L}. \tag{1}$$

The tube is supposed to be entirely filled with a fluid having density ρ_f, bulk modulus K, perturbed pressure P^* and velocity W^*. Considering low-Mach waves, the fluid density is considered as constant and equal to the reference density ρ_f as in [32, 33]. The elastic solid response is associated with Young's modulus, E, Poisson's modulus ν_s, perturbed axial stress, σ^*, perturbed axial strain ζ^*, and density ρ_s supposed constant. [7] derived the classical pulse wave speed within the fluid, c_p, distinct from the elastic pulse wave speed within the solid, c_s, the ratio of which is denoted $\mathcal{C}_s$

$$c_p^2 = \frac{\frac{K}{\rho_f}}{1 + \frac{2K}{\alpha E}\left(\frac{2(1-\nu_s^2)}{2+\alpha} + \alpha(1+\nu_s)\right)}, \quad c_s^2 = \frac{E}{\rho_s}, \quad \mathcal{C}_s = \frac{c_s}{c_p}. \tag{2}$$

The coupled system is furthermore described through the dimensionless density ratio

$$\mathcal{D} = \frac{\rho_f}{\rho_s}, \tag{3}$$

so that the dimensionless four-FSI equations derived in [7] achieves as follows

$$\begin{aligned} \partial_\tau W &= -\partial_Z P, && (4)\\ \partial_\tau P + \partial_Z W &= 2\alpha\nu_s \partial_Z \dot{\zeta}, && (5)\\ \partial_\tau \dot{\zeta} &= \frac{\mathcal{D}}{\alpha}\partial_Z \sigma, && (6)\\ \partial_\tau \sigma - \frac{\alpha \mathcal{C}_s^2}{\mathcal{D}}\partial_Z \dot{\zeta} &= \frac{2\nu_s}{\alpha(2+\alpha)}\partial_\tau P. && (7) \end{aligned}$$

where W, P, $\dot{\zeta}$, σ are dimensionless quantities referring to the fluid longitudinal velocity, the fluid pressure, the longitudinal solid deformation velocity and the longitudinal stress, respectively. The physical time t is scaled on the advective fluid pulse one, i.e. $\tau \equiv \frac{c_p}{L}t$, whilst the longitudinal coordinate z is scaled on the tube's length, i.e. $z \equiv LZ$. More details on the hereby dimensionless derivation is provided in Appendix B. (4)-(7) represents a set of two coupled hyperbolic equations. While the first part (4)-(5) is associated with the acoustic waves propagation in the fluid, the second part (6)-(7) describes the propagation of axial compressible waves in the solid tube. Poisson's coupling is highlighted by the presence of the Poisson's modulus in both source terms of (5) and (7).
It is noteworthy to point-out that (4)-(7) are the leading order contributions regarding small parameter ϵ [34]. [3, 35, 14] in-depth analyzed the secondary FSI occurring in liquid-filled pipe systems, revealing their significant impact at very high-frequencies only, the cut-off of which f_{Kc}, is known as the Korteweg's stop band, [36]

$$f_{Kc} = \frac{\mathcal{C}_s}{\epsilon} f_0 \quad \text{, with,} \quad f_0 = \frac{c_p}{2\pi L}. \tag{8}$$

For $f_{Kc} > f > f_0$, the axial dynamics prevails over the radial one and despite simplifications (4)-(7) is relevant to investigate several configurations [37, 7, 38, 39]. This frequency cut-off f_{Kc} nevertheless stands as a frequency limitation of the proposed analysis and will be thereafter discussed. Last but not least, it is known from [31, 40] that viscous shear dissipation occurring at the fluid and solid interface may have a significant impact on the coupling dynamic. Even though of physical interest, this issue is herein discarded but in-depth analyzed in [41]. Considering the acoustic framework for the fluid whilst using the linearity of the FSI-governing equations, only the perturbed

component of the physical field are investigated so that the initial conditions are

$$\mathbf{Y}(Z,0) = \partial_\tau \mathbf{Y}(Z,0) = \mathbf{0}, \tag{9}$$

with $\mathbf{Y}(Z,\tau)$ a four column vector,

$$\mathbf{Y}(Z,\tau) = \Big(P(Z,\tau), \sigma(Z,\tau), W(Z,\tau), \dot{\zeta}(Z,\tau)\Big)^T, \tag{10}$$

where subscript T holds for the conjugate transpose.

2.2. Vectorial two-waves system of FSI four-equations

The four coupled hyperbolic (4)-(7) are hereby re-organized to bring-up a d'Alembert operator upon the time–space dependent variable $\mathbf{Y}$

$$\left(\partial_\tau^2 - \mathbf{C}_\mathbf{Y}^2 \partial_Z^2\right) \mathbf{Y}(Z,\tau) = \mathbf{0}, \tag{11}$$

where,

$$\mathbf{C}_\mathbf{P}^2 = \begin{pmatrix} 1 & 2\nu_s\mathcal{D} \\ \frac{2\nu_s}{\alpha(2+\alpha)} & \frac{4\nu_s^2\mathcal{D}}{\alpha(2+\alpha)} + \mathcal{C}_s^2 \end{pmatrix}, \quad \mathbf{C}_\mathbf{W}^2 = \begin{pmatrix} 1 & -2\alpha\nu_s \\ -\frac{2\nu_s\mathcal{D}}{\alpha^2(2+\alpha)} & \frac{4\nu_s^2\mathcal{D}}{\alpha(2+\alpha)} + \mathcal{C}_s^2 \end{pmatrix} \tag{12}$$

and

$$\mathbf{C}_\mathbf{Y}^2 = \begin{pmatrix} \mathbf{C}_\mathbf{P}^2 & \mathbf{0} \\ \mathbf{0} & \mathbf{C}_\mathbf{W}^2 \end{pmatrix}. \tag{13}$$

Eigenvalues of the $\mathbf{C}_\mathbf{P}^2$ and $\mathbf{C}_\mathbf{W}^2$ matrices correspond to coupled vibrating modes wave speeds propagation. Both matrices have identical eigenvalues, $c_\pm^2$, the solutions of the polynomial characteristic problem

$$c_\pm^4 - \left[1 + \mathcal{C}_s^2 + \frac{4\nu_s^2\mathcal{D}}{\alpha(2+\alpha)}\right] c_\pm^2 + \mathcal{C}_s^2 = 0, \tag{14}$$

then achieves as follows

$$c_\pm^2 = \frac{1 + \mathcal{C}_s^2 + \frac{4\nu_s^2\mathcal{D}}{\alpha(2+\alpha)} \pm \sqrt{\left(1 + \mathcal{C}_s^2 + \frac{4\nu_s^2\mathcal{D}}{\alpha(2+\alpha)}\right)^2 - 4\mathcal{C}_s^2}}{2}. \tag{15}$$

(15) stands for the dimensionless version of coupled wave speed modes derived in [6, 7, 28]. The choice for denoting $\mathbf{C}_\mathbf{P}^2$ and $\mathbf{C}_\mathbf{W}^2$ matrices with a square as well as its eigenvalues $c_\pm^2$, now becomes clear since $c_\pm$ describes the wave

speed of each propagating mode, each governed by their specific D'Alembert operator. Dimensionless wave speed, c_-, has a value close to one, whilst c_+ is found close to $\mathcal{C}_s$. In Appendix E a systematic asymptotic analysis provides the Poisson coupling corrections to these quantities as $\nu_s \ll 1$. The mode c_- is thus associated with the fluid pulse mode while, c_+ is associated with the solid elastic one. Furthermore, it is noteworthy to point-out that the negative mode of (15) is always real in the Korteweg's frequency range since for real $\mathcal{C}_s^2$ parameter

$$\left(1-\mathcal{C}_s^2\right)^2 > -\frac{4\nu_s^2\mathcal{D}}{\alpha(2+\alpha)}\left[\frac{4\nu_s^2\mathcal{D}}{\alpha(2+\alpha)}+2\left(1+\mathcal{C}_s^2\right)\right], \tag{16}$$

is always satisfied. This property nevertheless vanishes as $f > f_{Kc}$, in which case the radial contributions leads to a dispersive waves, the propagating velocity of which can be complex [3, 36]. The D'Alembert wave propagation operator is hereby regarded within the diagonal base of $\mathbf{C}_\mathbf{Y}^2$ as classically performed in coupled hyperbolic systems [21, 28, 29]. The transition matrices $\mathbf{\Pi_Y}$ of the diagonal base change can easily be deduced from $\mathbf{C}_\mathbf{P}^2$ and $\mathbf{C}_\mathbf{W}^2$ eigenvectors

$$\mathbf{\Pi_Y}=\begin{pmatrix}\mathbf{\Pi_P} & \mathbf{0}\\ \mathbf{0} & \mathbf{\Pi_W}\end{pmatrix}\ ,\mathbf{\Pi_P}=\begin{pmatrix}\frac{2\nu_s\mathcal{D}}{c_-^2-1} & \frac{2\nu_s\mathcal{D}}{c_+^2-1}\\ 1 & 1\end{pmatrix}\ ,\mathbf{\Pi_W}=\begin{pmatrix}\frac{2\alpha\nu_s}{c_-^2-1} & \frac{2\alpha\nu_s}{c_+^2-1}\\ 1 & 1\end{pmatrix}, \tag{17}$$

such as the transition relations

$$\boldsymbol{\mathcal{C}}_{\boldsymbol{\mathcal{Y}}}^2=\mathbf{\Pi}_\mathbf{Y}^{-1}\mathbf{C}_\mathbf{Y}^2\mathbf{\Pi_Y}=\begin{pmatrix}\boldsymbol{\mathcal{C}}_{\boldsymbol{\mathcal{P}}}^2 & \mathbf{0}\\ \mathbf{0} & \boldsymbol{\mathcal{C}}_{\boldsymbol{\mathcal{W}}}^2\end{pmatrix}\ \text{, and, }\ \boldsymbol{\mathcal{Y}}=\mathbf{\Pi}_\mathbf{Y}^{-1}\mathbf{Y}, \tag{18}$$

where

$$\boldsymbol{\mathcal{C}}_{\boldsymbol{\mathcal{P}}}^2=\mathbf{\Pi}_{\boldsymbol{\mathcal{P}}}^{-1}\mathbf{C}_\mathbf{P}^2\mathbf{\Pi}_{\boldsymbol{\mathcal{P}}}=\begin{pmatrix}c_-^2 & 0\\ 0 & c_+^2\end{pmatrix}\ \text{, and, }\ \boldsymbol{\mathcal{C}}_{\boldsymbol{\mathcal{W}}}^2=\mathbf{\Pi}_{\boldsymbol{\mathcal{W}}}^{-1}\mathbf{C}_\mathbf{W}^2\mathbf{\Pi}_{\boldsymbol{\mathcal{W}}}=\begin{pmatrix}c_-^2 & 0\\ 0 & c_+^2\end{pmatrix}. \tag{19}$$

The dimensionless wave-equations system (11) and its initial conditions (9) expressed in the eigenvector base finally reads

$$\left(\partial_\tau^2-\boldsymbol{\mathcal{C}}_{\boldsymbol{\mathcal{Y}}}^2\partial_Z^2\right)\boldsymbol{\mathcal{Y}} = \mathbf{0}, \tag{20}$$

$$\boldsymbol{\mathcal{Y}}(Z,0)=\partial_\tau\boldsymbol{\mathcal{Y}}(Z,0) = \mathbf{0}. \tag{21}$$

The operator (11) diagonalization has indeed simplified the mode propagation now described by two independent D'Alembert propagating waves

but obviously not suppressed their coupling. The coupling is now recast in the resulting upstream and downstream boundary conditions. Boundary conditions for $\boldsymbol{\mathcal{Y}}$ can be deduced from the mechanical boundary conditions associated with $\mathbf{Y}$ using change-basis relations (19). For the sake of notation simplification let us introduce four 4×4 matrices $\boldsymbol{\mathcal{N}}$, $\boldsymbol{\mathcal{M}}$, $\boldsymbol{\mathcal{Q}}$, $\boldsymbol{\mathcal{R}}$ and $\boldsymbol{\mathcal{S}}(\tau)$ a eight-dimensional column vector. Boundary conditions can formally be written as a rectangular 8×16 linear system

$$\begin{pmatrix} \boldsymbol{\mathcal{N}} & \boldsymbol{\mathcal{M}} & \mathbf{0} & \mathbf{0} \\ \mathbf{0} & \mathbf{0} & \boldsymbol{\mathcal{Q}} & \boldsymbol{\mathcal{R}} \end{pmatrix}_{(8\times16)} \begin{pmatrix} \boldsymbol{\mathcal{Y}}(0,\tau) \\ \partial_Z \boldsymbol{\mathcal{Y}}(0,\tau) \\ \boldsymbol{\mathcal{Y}}(1,\tau) \\ \partial_Z \boldsymbol{\mathcal{Y}}(1,\tau) \end{pmatrix}_{(16\times1)} = \boldsymbol{\mathcal{S}}_{(8\times1)}(\tau). \tag{22}$$

Specifics set of boundary conditions are later on considered in section 4. The resolution of this vector waves equation is usually handled by Laplace transform, combined with usual transfer matrix method [28, 9, 29]. Some analytical difficulties are sometimes nevertheless encountered when performing the inverse Laplace transform. Thereafter a new analytical derivation for solution of (20), having initial conditions (21) and spatial boundary conditions (22), relying on variable separation, spectral analysis and self-adjoint operator theory is proposed.

3. Analytical framework

3.1. Self-adjoint operator theory

Let us define the operator $\mathcal{H}$, acting on the square-integrable real four dimensional column vector field $\boldsymbol{\Psi}(Z)$,

$$\forall \boldsymbol{\Psi}(Z) \in L^4(\mathbb{R}) \times L^4(\mathbb{R}), \quad \boldsymbol{\Psi}(Z) \to \mathcal{H}\boldsymbol{\Psi}(Z) = \boldsymbol{\mathcal{C}}_{\boldsymbol{\mathcal{Y}}}^2 \cdot \partial_Z^2 \boldsymbol{\Psi}(Z), \tag{23}$$

with the homogeneous associated set of spatial boundary conditions,

$$\begin{pmatrix} \boldsymbol{\mathcal{N}} & \boldsymbol{\mathcal{M}} & \mathbf{0} & \mathbf{0} \\ \mathbf{0} & \mathbf{0} & \boldsymbol{\mathcal{Q}} & \boldsymbol{\mathcal{R}} \end{pmatrix}_{(8\times16)} \begin{pmatrix} \boldsymbol{\Psi}(0) \\ \partial_Z \boldsymbol{\Psi}(0) \\ \boldsymbol{\Psi}(1) \\ \partial_Z \boldsymbol{\Psi}(1) \end{pmatrix}_{(16\times1)} = \mathbf{0}. \tag{24}$$

Let us set up the general scalar product,

$$\forall \boldsymbol{\Psi}, \boldsymbol{\Psi}' \in L^4(\mathbb{R}) \times L^4(\mathbb{R}), \quad \langle \boldsymbol{\Psi}', \boldsymbol{\Psi} \rangle = \sum_{j=1}^{4} \eta_j \int_0^1 \Psi_j'(Z) \Psi_j(Z) dZ, \tag{25}$$

with $j = 1, 2, 3, 4$ referring to the j^{th} components of vector $\boldsymbol{\eta} \equiv (\eta_1, \eta_2, \eta_3, \eta_4) \in \mathbb{R}^4$, a yet unknown real vector which is adapted to each specific problem. Invoking the definition of $\mathcal{H}$ in (23), the search for self-adjoint condition for operator $\mathcal{H}$, equipped with scalar product (25), performing a double integration by parts leads to

$$\langle \mathcal{H}\boldsymbol{\Psi}, \boldsymbol{\Psi}^{'} \rangle = \langle \boldsymbol{\mathcal{C}}^2_{\boldsymbol{\mathcal{Y}}} \cdot \partial^2_Z \boldsymbol{\Psi}, \boldsymbol{\Psi}^{'} \rangle = \langle \boldsymbol{\Psi}, \boldsymbol{\mathcal{C}}^2_{\boldsymbol{\mathcal{Y}}} \cdot \partial^2_Z \boldsymbol{\Psi}^{'} \rangle + \sum_{j=1}^{4} \eta_j c_j^2 \left(\left[\partial_Z \Psi_j(Z) \Psi_j^{'}(Z) - \Psi_j(Z) \partial_Z \Psi_j^{'}(Z) \right]_0^1 \right), \quad (26)$$

where c_j^2 are the j^{th} diagonal terms of $\boldsymbol{\mathcal{C}}^2_{\boldsymbol{\mathcal{Y}}}$. Self-adjoint property $\langle \mathcal{H}\boldsymbol{\Psi}, \boldsymbol{\Psi}^{'} \rangle = \langle \boldsymbol{\Psi}, \mathcal{H}\boldsymbol{\Psi}^{'} \rangle$, is thus obtained from condition

$$\sum_{j=1}^{4} \eta_j c_j^2 \left[\partial_Z \Psi_j(Z) \Psi_j^{'}(Z) - \Psi_j(Z) \partial_Z \Psi_j^{'}(Z) \right]_0^1 = 0. \quad (27)$$

In the following, the scalar-product weight parameter $\boldsymbol{\eta}$ is adjusted with given boundary conditions set so as to ensure relation eq.(27), and thus self-adjointness.

3.2. Eigenfunction base and spectrum condition

The self-adjoint operator $\mathcal{H}$ spectrum $\mathcal{S}_{\mathcal{P}}$, is composed of real discrete eigenvalues having a related discrete orthogonal basis [42]. This property obviously remains for frequency up to the Korteweg's band stop. Denoting $-\lambda_k^2$ the k^{th} eigenvalue, then being real negative in accordance with the well known eigenvalues of the Laplacian , $\boldsymbol{\Phi}_k$ its related eigen-function, the eigenvalue problem reads

$$\mathcal{H}\boldsymbol{\Phi}_k(Z) = -\lambda_k^2 \boldsymbol{\Phi}_k(Z), \quad (28)$$

so that using (23), one gets

$$\partial^2_Z \boldsymbol{\Phi}_k(Z) = -\lambda_k^2 \boldsymbol{\mathcal{C}}^{-2}_{\boldsymbol{\mathcal{Y}}} \boldsymbol{\Phi}_k(Z), \quad (29)$$

where we have introduced notation $\boldsymbol{\mathcal{C}}^{-2}_{\boldsymbol{\mathcal{Y}}} \equiv [\boldsymbol{\mathcal{C}}^2_{\boldsymbol{\mathcal{Y}}}]^{-1}$ for the inverse of matrix $\boldsymbol{\mathcal{C}}^2_{\boldsymbol{\mathcal{Y}}}$ defined in (18). The solution of (29) then achieves as follows

$$\begin{pmatrix} \boldsymbol{\Phi}_k(Z) \\ \partial_Z \boldsymbol{\Phi}_k(Z) \end{pmatrix} = \boldsymbol{\mathcal{T}}_k(Z) \begin{pmatrix} \boldsymbol{\Phi}_k(0) \\ \partial_Z \boldsymbol{\Phi}_k(0) \end{pmatrix}_{(8\times 1)}, \quad (30)$$

with

$$\boldsymbol{\mathcal{T}}_k(Z) = \begin{pmatrix} \partial_Z \mathbf{T}(Z) & \mathbf{T}(Z) \\ \partial_Z^2 \mathbf{T}(Z) & \partial_Z \mathbf{T}(Z) \end{pmatrix}, \quad \mathbf{T}(Z) = \begin{pmatrix} \mathbf{T}_s(Z) & \mathbf{0} \\ \mathbf{0} & \mathbf{T}_s(Z) \end{pmatrix}, \tag{31}$$

and

$$\mathbf{T}_s(Z, \lambda_k) = \frac{1}{\lambda_k} \begin{pmatrix} c_- \sin\left(\frac{\lambda_k Z}{c_-}\right) & 0 \\ 0 & c_+ \sin\left(\frac{\lambda_k Z}{c_+}\right) \end{pmatrix}. \tag{32}$$

This formulation is a modal time-domain version of the popular transfer matrix method, (TMM), developed in the frequency domain for coupled hyperbolic problems in [9, 21, 22, 26, 27, 28, 29, 30] but for the adaption to the need for a Laplacian operator of two boundary conditions to be specified. Combining (30) and (32) in boundary condition set (24) provides the following linear condition to be fulfilled by mode amplitudes $[\mathbf{\Phi}_k(0), \partial_Z \mathbf{\Phi}_k(0)]$

$$\begin{pmatrix} \boldsymbol{\mathcal{N}} & \boldsymbol{\mathcal{M}} \\ \boldsymbol{\mathcal{Q}} \partial_Z \mathbf{T}(1) + \boldsymbol{\mathcal{R}} \partial_Z^2 \mathbf{T}(1) & \boldsymbol{\mathcal{Q}} \mathbf{T}(1) + \boldsymbol{\mathcal{R}} \partial_Z \mathbf{T}(1) \end{pmatrix} \begin{pmatrix} \mathbf{\Phi}_k(0) \\ \partial_Z \mathbf{\Phi}_k(0) \end{pmatrix} = \mathbf{0}. \tag{33}$$

The trivial zero solution of (33) being irrelevant, the non-trivial solution necessitates a one-dimensional non-empty kernel of (33)'s matrix, i.e. a zero eigenvalue of the matrix acting on $[\mathbf{\Phi}_k(0), \partial_Z \mathbf{\Phi}_k(0)]$ vector. This condition is equivalent to set a zero determinant of (33)'s matrix, i.e.

$$\begin{vmatrix} \boldsymbol{\mathcal{N}} & \boldsymbol{\mathcal{M}} \\ \boldsymbol{\mathcal{Q}} \partial_Z \mathbf{T}(1) + \boldsymbol{\mathcal{R}} \partial_Z^2 \mathbf{T}(1) & \boldsymbol{\mathcal{Q}} \mathbf{T}(1) + \boldsymbol{\mathcal{R}} \partial_Z \mathbf{T}(1) \end{vmatrix} = \mathbf{0}. \tag{34}$$

(34) is met for specific values of λ_k, providing the spectrum $\mathcal{S}_\mathcal{P}$ of operator $\mathcal{H}$. It leads to a transcendental equation for λ_k specific to each boundary condition set, to be computed numerically, as done in section 4. The spectrum provides each resonant frequency of the system, which should lie in the frequency range given in (8), i.e. $\lambda_k \in [-f_{Kc}/f_0, f_{Kc}/f_0]$. It remains to determine the modal-dependent amplitudes of $\mathbf{\Phi}_k(Z)$. From (34) one can realize that the amplitude vector $[\mathbf{\Phi}_k(0), \partial_Z \mathbf{\Phi}_k(0)]$ is defined up to any arbitrary multiplicative constant, as the kernel of (33)'s matrix is non-empty. Hence, among the eight amplitude parameters of eight-dimensional vector $[\mathbf{\Phi}_k(0), \partial_Z \mathbf{\Phi}_k(0)]$, one can be kept to any arbitrary value, which is equivalent to chose a unitary eigenfunction $\mathbf{\Phi}_k(Z)$ such as

$$\begin{pmatrix} \mathbf{\Phi}_k(Z) \\ \partial_Z \mathbf{\Phi}_k(Z) \end{pmatrix} = \frac{1}{\|\tilde{\mathbf{\Phi}}_k(Z)\|} \begin{pmatrix} \tilde{\mathbf{\Phi}}_k(Z) \\ \partial_Z \tilde{\mathbf{\Phi}}_k(Z) \end{pmatrix}, \tag{35}$$

where $\tilde{\mathbf{\Phi}}_k(Z)$ stands as the generator of the solution space associated with the linear system (33).

3.3. Solution for 2D-vector homogeneous wave equation

The solution of the two-waves equations (20) associated with the initial boundary conditions (21) are searched under decomposition

$$\boldsymbol{\mathcal{Y}}(Z,\tau) = \boldsymbol{\mathcal{Y}}_h(Z,\tau) + \boldsymbol{\mathcal{Y}}_p(Z,\tau), \tag{36}$$

where subscript h refers to homogeneous solution whilst subscript p refers to particular one associated with non-homogeneous boundary conditions. The latter is regarded as a separated variable time–space function. The Z behavior is furthermore decomposed into the first order polynomial

$$\boldsymbol{\mathcal{Y}}_p(Z,\tau) = Z\boldsymbol{\mathcal{Y}}_p^1(\tau) + \boldsymbol{\mathcal{Y}}_p^0(\tau). \tag{37}$$

Since the previous expression should ensures the boundary condition system spelled out in (22), it consequently results

$$\begin{pmatrix} \boldsymbol{\mathcal{N}} & \boldsymbol{\mathcal{M}} \\ \boldsymbol{\mathcal{Q}} & \boldsymbol{\mathcal{Q}} + \boldsymbol{\mathcal{R}} \end{pmatrix}_{(8\times 8)} \begin{pmatrix} \boldsymbol{\mathcal{Y}}_p^0(\tau) \\ \boldsymbol{\mathcal{Y}}_p^1(\tau) \end{pmatrix}_{(8\times 1)} = \boldsymbol{\mathcal{S}}_{(8\times 1)}(\tau). \tag{38}$$

The resolution of (38) then provides $\boldsymbol{\mathcal{Y}}_p$. The homogeneous component, $\boldsymbol{\mathcal{Y}}_h$, is hereby decomposed over the eigenvector base of the self-adjoint operator $\mathcal{H}$ so that

$$\boldsymbol{\mathcal{Y}} = \sum_{\mathcal{S}_p} a_k(\tau)\mathbf{\Phi}_k(Z) + \boldsymbol{\mathcal{Y}}_p(Z,\tau), \tag{39}$$

or, using $\tilde{\mathbf{\Phi}}_k(Z)$ in (35)

$$\boldsymbol{\mathcal{Y}}(Z,\tau) = \sum_{\mathcal{S}_p} \frac{a_k(\tau)\tilde{\mathbf{\Phi}}_k(Z)}{\|\tilde{\mathbf{\Phi}}_k(Z)\|} + \boldsymbol{\mathcal{Y}}_p(Z,\tau), \tag{40}$$

where $a_k(\tau)$ is the k^{th} mode time-dependent amplitude. Invoking the initial rest conditions (21), with definition of $\tilde{\mathbf{\Phi}}_k(Z)$ in (35), leads to,

$$a_k(0) = -\frac{\langle \boldsymbol{\mathcal{Y}}_p(Z,0), \tilde{\mathbf{\Phi}}_k(Z)\rangle}{\|\tilde{\mathbf{\Phi}}_k(Z)\|} \text{ , and, } \partial_\tau a_k(0) = -\frac{\langle \partial_\tau \boldsymbol{\mathcal{Y}}_p(Z,0), \tilde{\mathbf{\Phi}}_k(Z)\rangle}{\|\tilde{\mathbf{\Phi}}_k(Z)\|}. \tag{41}$$

The proposed decomposition of $\boldsymbol{\mathcal{Y}}(Z,\tau)$ in (40) must hereby satisfy the wave equation system (20). Regarding the definition of $\mathcal{H}$ in (23) with the spatial polynomial decomposition of $\boldsymbol{\mathcal{Y}}_p$ in (37) it achieves as follows

$$\mathcal{H}\boldsymbol{\mathcal{Y}}_p = \mathbf{0}, \tag{42}$$

so that

$$\left(\partial_\tau^2 - \mathcal{H}\right) \sum_{\mathcal{S}_\mathcal{P}} \frac{a_k(\tau)\tilde{\boldsymbol{\Phi}}_k(Z)}{\|\tilde{\boldsymbol{\Phi}}_k(Z)\|} = -\partial_\tau^2 \boldsymbol{\mathcal{Y}}_p. \tag{43}$$

Now projecting over $\tilde{\boldsymbol{\Phi}}_k(Z)$ leads to,

$$\left(\partial_\tau^2 + \lambda_k^2\right) a_k(\tau) = -\partial_\tau^2 \frac{\langle \boldsymbol{\mathcal{Y}}_p, \tilde{\boldsymbol{\Phi}}_k(Z)\rangle}{\|\tilde{\boldsymbol{\Phi}}_k(Z)\|}. \tag{44}$$

This ordinary differential equation, having initial conditions (41), is solved leading to (Further details provided in Appendix C)

$$a_k(\tau) = \lambda_k \int_0^\tau \frac{\langle \boldsymbol{\mathcal{Y}}_p, \tilde{\boldsymbol{\Phi}}_k(Z)\rangle(t)}{\|\tilde{\boldsymbol{\Phi}}_k(Z)\|} \sin\left(\lambda_k(\tau - t)\right) dt - \frac{\langle \boldsymbol{\mathcal{Y}}_p, \tilde{\boldsymbol{\Phi}}_k(Z)\rangle}{\|\tilde{\boldsymbol{\Phi}}_k(Z)\|}. \tag{45}$$

Finally, combining the (45) with the $\boldsymbol{\mathcal{Y}}$'s definition in (40) results in

$$\begin{aligned}\boldsymbol{\mathcal{Y}}(Z,\tau) = \sum_{\mathcal{S}_\mathcal{P}} \lambda_k \left(\int_0^\tau \frac{\langle \boldsymbol{\mathcal{Y}}_p, \tilde{\boldsymbol{\Phi}}_k(Z)\rangle(t)}{\|\tilde{\boldsymbol{\Phi}}_k(Z)\|^2} \sin\left(\lambda_k(\tau - t)\right) dt \right) \tilde{\boldsymbol{\Phi}}_k(Z) \\ - \sum_{\mathcal{S}_\mathcal{P}} \frac{\langle \boldsymbol{\mathcal{Y}}_p, \tilde{\boldsymbol{\Phi}}_k(Z)\rangle}{\|\tilde{\boldsymbol{\Phi}}_k(Z)\|^2} \tilde{\boldsymbol{\Phi}}_k(Z) + \boldsymbol{\mathcal{Y}}_p(Z,\tau).\end{aligned} \tag{46}$$

In the following, (46) is used to cross-check/validate predictions of two well-known configurations of liquid-filled pipes problem: (i) a constant pressure tank with a fixed instantaneous closing valve (Cf Fig. 1a), (ii) a constant pressure tank with a free instantaneous closing valve (Cf Fig. 1b). The related upstream and downstream boundary conditions are analyzed in depth in [32]. It is important to mention that, in the special case of boundary conditions having no pressure/velocity coupling, the previous general framework associated with four coupled waves equations boils down into two decoupled two-waves propagation, not only sharing the same spectrum, but also the same modes and amplitudes. In other words, in the absence of coupling

between pressure and velocity in the boundary conditions, the four-waves equations set degenerates into a two-waves one. In the next section, we consider this simplified degenerate case for two classes of boundary conditions.

4. Application to specific boundary conditions

4.1. Constant pressure tank with a fixed instantaneous closing valve

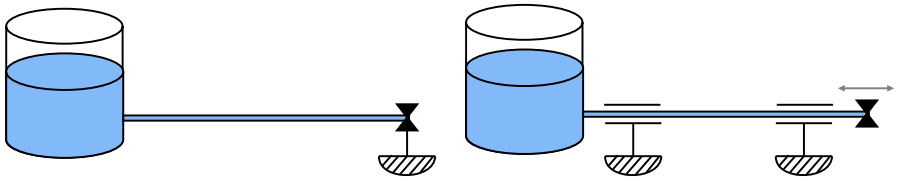

(a) First configuration : anchored valve (b) Second configuration : axially free valve

Figure 1: Boundary condition set investigated for the liquid-filled pipe problem

Fluid (water)	Solid (steel)
$\rho_f = 1000\ kg \cdot m^3$	$\rho_s = 7900\ kg \cdot m^{-3}$
$\mathcal{K} = 2.1\ GPa$	$E = 210\ GPa$
$\nu_f = 9.493 \cdot 10^{-7}\ m^2 s^{-1}$	$\nu_s = 0.3$
	$R_0 = 0.395\ m$
	$e = 0.008\ m$
	$L = 20\ m$

Table 1: Physical and geometrical properties for the analysis of the reservoir-pipe-valve system (anchored and free). The parameter values are extracted from [27].

All comparisons and analysis are based upon the parameter set introduced in Table 1. The natural fluid-pulse frequency of both configurations is found equal to $f_0 \approx 8Hz$, whereas the cutoff frequency is $f_{Kc} \approx 2060Hz$. The λ_k should then lie in the range $\lambda_k \in [-247.6, 247.6]$ in order to fulfill the modeling assumptions (Cf. section 2.1).

4.1.1. Analytical solution

In the first configuration (Cf. Figure 1a), the pipe is supposed perfectly anchored, both upstream and downstream. Thus, no solid axial movement

occurs at both pipe dead-ends which can be modeled as a Dirichlet–Dirichlet condition on the axial solid displacement acceleration. Furthermore, the reservoir does not impede any upstream pressure fluctuation which can be interpreted as an homogeneous Dirichlet condition for the pressure. Finally, an instantaneous valve closure downstream is modeled by a Dirac distribution, $\delta(\tau)$ (i.e. singular perturbation), acting on the axial fluid acceleration. The four boundary condition thereby achieves as follows

$$P(0,\tau)=0 \quad ,\partial_\tau W(1,\tau)=-\delta(\tau), \quad \partial_\tau\dot{\zeta}(0,\tau)=\partial_\tau\dot{\zeta}(1,\tau)=0, \tag{47}$$

or otherwise regarding (4)&(6)

$$P(0,\tau)=0 \quad ,\partial_Z P(1,\tau)=\delta(\tau), \quad \partial_Z\sigma(0,\tau)=\partial_Z\sigma(1,\tau)=0. \tag{48}$$

The initial Dirichlet conditions upon both fluid and solid acceleration quantities thus turn into Neumann conditions for the fluid pressure and solid stress fields. Invoking base-change (17)-(19), whilst introducing

$$\beta=\frac{c_+}{c_-}\frac{c_-^2-1}{c_+^2-1}, \tag{49}$$

the matrices introduced in (22) describing boundary conditions in the diagonalized basis can be found explicitly

$$\boldsymbol{\mathcal{N}}=\begin{pmatrix}1 & \frac{\beta c_-}{c_+}\\ 0 & 0\end{pmatrix}, \quad \boldsymbol{\mathcal{M}}=\begin{pmatrix}0 & 0\\ 1 & 1\end{pmatrix}, \quad \boldsymbol{\mathcal{Q}}=\mathbf{0}, \quad \boldsymbol{\mathcal{R}}=\boldsymbol{\mathcal{N}}+\boldsymbol{\mathcal{M}}, \tag{50}$$

and,

$$\boldsymbol{\mathcal{S}}(\tau)=\frac{\left(c_-^2-1\right)\delta(\tau)}{2\nu_s\mathcal{D}}\left(0,0,1,0\right)^T, \tag{51}$$

The determination of the scalar-product weight parameter $\boldsymbol{\eta}\equiv(\eta_1,\eta_2)$, introduced in (27), is hereby overcame. Injecting boundary conditions (48) within self-adjointness one (27) for the couple of two 2D unknown column vectors

$$\left(\boldsymbol{\Psi}(Z),\boldsymbol{\Psi}^{'}(Z)\right)=\left(\left(\psi_1(Z),\psi_2(Z)\right)^T,\left(\psi_1^{'}(Z),\psi_2^{'}(Z)\right)^T\right), \tag{52}$$

yields

$$\left[\partial_Z\Psi_1(0)\Psi_1^{'}(0)-\Psi_1(0)\partial_Z\Psi_1^{'}(0)\right]\left(\eta_1+\eta_2\frac{c_+^3}{\beta c_-^3}\right)=0, \tag{53}$$

so that the relation between η_1 & η_2 can be found

$$\eta_2 = -\eta_1 \beta \left(\frac{c_-}{c_+}\right)^3. \tag{54}$$

Scalar product (25) then results in

$$\langle \mathbf{\Psi}, \mathbf{\Psi}^{'} \rangle = \eta_1 \int_0^1 \left[\Psi_1(z) \Psi_1^{'}(z) - \beta \left(\frac{c_-}{c_+}\right)^3 \Psi_2(z) \Psi_2^{'}(z) \right] dz. \tag{55}$$

The λ_k are hence solutions of the formal relation (34). Using $\boldsymbol{\mathcal{C}}^2_{\boldsymbol{\mathcal{P}}}$ in (19), boundary condition matrices (50) and $\mathbf{T}_s(Z)$ in (32), leads to the explicit (and simplified) transcendental equation

$$\beta \sin\left(\frac{\lambda_k}{c_-}\right) \cos\left(\frac{\lambda_k}{c_+}\right) - \sin\left(\frac{\lambda_k}{c_+}\right) \cos\left(\frac{\lambda_k}{c_-}\right) = 0. \tag{56}$$

The particular component of $\boldsymbol{\mathcal{P}}(Z,\tau)$, $\boldsymbol{\mathcal{P}}_p(Z,\tau)$, follows from the spatial polynomial decomposition (37) and the resolution of the linear system (38), whilst $\tilde{\mathbf{\Phi}}_k(Z)$ determination is found combining transfer matrix formulation (30), linear boundary condition system (33) and the associated boundary condition matrices (50)

$$\tilde{\mathbf{\Phi}}_k(Z) = \begin{pmatrix} \cos\left(\frac{\lambda_k}{c_-} Z\right) + \tan\left(\frac{\lambda_k}{c_-}\right) \sin\left(\frac{\lambda_k}{c_-} Z\right) \\ -\frac{c_+}{\beta c_-} \left[\cos\left(\frac{\lambda_k}{c_+} Z\right) + \tan\left(\frac{\lambda_k}{c_+}\right) \sin\left(\frac{\lambda_k}{c_+} Z\right) \right] \end{pmatrix}, \tag{57}$$

$$\boldsymbol{\mathcal{P}}_p(Z,\tau) = \frac{\delta(\tau) Z}{\det\left(\mathbf{\Pi}_{\mathbf{P}}\right)} \begin{pmatrix} 1 \\ -1 \end{pmatrix}. \tag{58}$$

Further details on the derivation are provided in Appendix D. The combination of $\tilde{\mathbf{\Phi}}_k(Z)$ and $\boldsymbol{\mathcal{P}}_p(Z,\tau)$ vectors in (57)-(58) fulfill the expression $\boldsymbol{\mathcal{P}}(Z,\tau)$ in (46)

$$\boldsymbol{\mathcal{P}}(Z,\tau) - \boldsymbol{\mathcal{P}}_p(Z,\tau) = \sum_{\mathcal{S}_{\mathcal{P}}} \frac{\langle Z \begin{pmatrix} 1 \\ -1 \end{pmatrix}, \tilde{\mathbf{\Phi}}_k(Z) \rangle}{\det\left(\mathbf{\Pi}_{\mathbf{P}}\right) \| \tilde{\mathbf{\Phi}}_k(Z) \|^2} \tilde{\mathbf{\Phi}}_k(Z) \left[\lambda_k \sin\left(\lambda_k \tau\right) - \delta(\tau) \right], \tag{59}$$

with,

$$\|\tilde{\mathbf{\Phi}}_k(Z)\|^2 = \frac{c_+\beta\cos^2\left(\frac{\lambda_k}{c_+}\right) - c_-\cos^2\left(\frac{\lambda_k}{c_-}\right)}{2c_+\beta\cos^2\left(\frac{\lambda_k}{c_+}\right)\cos^2\left(\frac{\lambda_k}{c_-}\right)}, \tag{60}$$

$$\langle Z\begin{pmatrix}1\\-1\end{pmatrix}, \tilde{\mathbf{\Phi}}_k(Z)\rangle = \frac{c_-^2\left(\cos\left(\frac{\lambda_k}{c_+}\right) - \cos\left(\frac{\lambda_k}{c_-}\right)\right)}{\lambda_k^2\cos\left(\frac{\lambda_k}{c_-}\right)\cos\left(\frac{\lambda_k}{c_+}\right)}. \tag{61}$$

4.1.2. ν_s parametric analysis

Since the Poisson coupling, relies on the Poisson modulus, it is relevant to investigate the ν_s dependency of the previous analytical expressions. By performing an asymptotic analysis, without considering FSI effects, [31, 43] found the spectrum associated with the pressure waves in the fluid. It is interesting to point out that the solution (59) converges toward the [31]'s leading-order one, as $\nu_s \to 0$. The [31]'s leading-order solution is

$$\lambda_k = \pi\left(1+\frac{k}{2}\right), \quad \forall k \in \mathbb{N}, \tag{62}$$

$$P(Z,\tau) = 2\sum_{k=0}^{\infty}(-1)^k\frac{\sin\left(\lambda_k Z\right)\sin\left(\lambda_k\tau\right)}{\lambda_k}. \tag{63}$$

A more detailed derivation of this result is provided in Appendix E. The ν_s dependence of both spectrum and pressure waves compared with no-FSI solutions (i.e $\nu_s = 0$ case) is further illustrated in Figure 2. Figure 2b shows that the spectrum of the first configuration can be interpreted as the union between the fluid vibration modes (continuous blue lines) and the pure elastic ones (red squared lines). The solid and fluid contributions to the spectrum are easily identified from the analysis of the no-FSI configuration, as theoretically detailed in Appendix E (Cf. (E.10)). In Figure 2a the (59) solution for $\nu_s = 0$ is confronted with the [31]'s leading order one and, for comparison with the $\nu_s = 0.3$ case, all other parameters being equals. One can observed that high-frequency pressure oscillations progressively growing in time are revealed by the FSI coupling. These high-frequency oscillations are nevertheless expected to be damped by the viscous fluid friction or some structural energetic losses. In the $\nu_s \to 0$ limit, [31]'s pointed-out that fluid viscous friction exponentially damps each resonant mode. This feature remains when considering FSI, as analyzed in [41]. When dealing with time-scale of the order of the advective

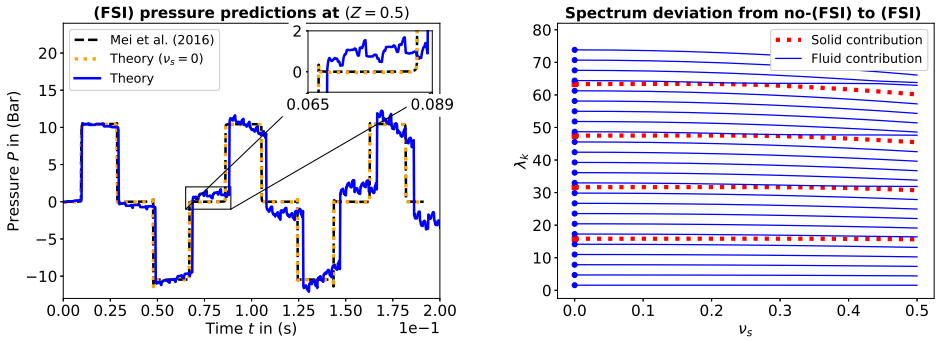

(a) Pressure response at $Z = 0.5$

(b) Spectrum (28 first eigenvalues) versus the Poisson modulus ν_s in the Korteweg's frequency range.

Figure 2: Impact of the FSI on the expected: (a) pressure response and, (b) spectrum for the first case configuration (Cf. Fig. 1a). In (a), the [31]'s leading order solution is provided, in black dashed lines, as to point out the convergence of the models. In (b), as ν_s vary, some eigenvalues come close one-another, but a careful inspection shows no cross-over between the depicted eigenvalues.

pulse wave speed one, i.e. $O\left(L/c_p\right)$, the energetic losses are shown [6, 31] to have a negligible impact on the overall coupled dynamic.

4.2. Constant pressure tank with free instantaneous closing valve

A second configuration, depicted in Figure 1b, is hereby analyzed whereby the downstream valve is free to move axially. Hence, upstream, the same conditions as in (48) are applied, with homogeneous Neumann condition for the axial stress and homogeneous Dirichlet condition for the pressure field set as

$$P(0,\tau) = 0 \quad \text{, and,} \quad \partial_Z \sigma(0,\tau) = 0. \tag{64}$$

Downstream, the boundary condition strongly differs from the previous configuration from valve longitudinal motion. Since $\alpha(2+\alpha)$ is equal to the ratio of solid surface (i.e. $\pi e R_0\left(2+\alpha\right)$) to the fluid one (i.e. πR_0^2), the static equilibrium of forces at valve location, in the absence of valve's inertia, reduces to

$$\alpha(2+\alpha)\sigma(1,\tau) = P(1,\tau). \tag{65}$$

The axial solid and fluid acceleration matching at the valve further imposes

$$\partial_\tau W(1,\tau) - \alpha \partial_\tau \dot{\zeta}(1,\tau) = -\delta(\tau), \tag{66}$$

or otherwise regarding relations (4) & (6)

$$\partial_Z P(1,\tau) + \mathcal{D}\partial_Z \sigma(1,\tau) = \delta(\tau). \tag{67}$$

The α constant in (66) arises from dimensionless arguments and can be obtained regarding the Appendix B. As the valve is now free to move, the downstream boundary condition slightly differs form the one provided in (47). Indeed, the acceleration perturbation is now applied to the relative acceleration of the fluid with respect to the tube motion, [32]. Considering change-basis (17)-(18) and introducing parameters

$$\kappa_\pm = \mathcal{D} + \frac{2\nu_s \mathcal{D}}{c_\pm^2 - 1} \quad \text{, and,} \quad \frac{\beta c_- \kappa_-}{c_+ \kappa_+} = \frac{1 - \frac{2\nu_s \mathcal{D}}{\alpha(2+\alpha)(c_+^2-1)}}{1 - \frac{2\nu_s \mathcal{D}}{\alpha(2+\alpha)(c_-^2-1)}}, \tag{68}$$

yields

$$\boldsymbol{\mathcal{N}} = \begin{pmatrix} 1 & \frac{\beta c_-}{c_+} \\ 0 & 0 \end{pmatrix}, \quad \boldsymbol{\mathcal{M}} = \begin{pmatrix} 0 & 0 \\ 1 & 1 \end{pmatrix}, \quad \boldsymbol{\mathcal{Q}} = \begin{pmatrix} 0 & 0 \\ 1 & \frac{\beta c_- \kappa_-}{c_+ \kappa_+} \end{pmatrix}, \quad \boldsymbol{\mathcal{R}} = \begin{pmatrix} \kappa_- & \kappa_+ \\ 0 & 0 \end{pmatrix}, \tag{69}$$

with the forcing term

$$\boldsymbol{\mathcal{S}}(\tau) = \delta(\tau)\,(0,0,1,0)^T \tag{70}$$

The non-trivial parametric relation (68) is established in Appendix F. The same footsteps are hereby applied to overcome the resolution of $\boldsymbol{\mathcal{P}}(Z,\tau)$. The self-adjoint condition (27) leads to

$$\left(\eta_1 + \left(\frac{c_+}{c_-}\right)^3 \frac{\eta_2}{\beta}\right) \left[\partial_Z \Psi_1(Z)\Psi_1'(Z) - \Psi_1(Z)\partial_Z \Psi_1'(Z)\right]_0^1 = 0, \tag{71}$$

so that

$$\eta_2 = -\eta_1 \beta \left(\frac{c_-}{c_+}\right)^3. \tag{72}$$

Thereby, scalar product defined in (25) remains identical to (55). A combination boundary condition matrices (69), the spectrum condition (34) and transfer matrices (31)-(32) expressions, leads to the following (simplified) transcendental equation

$$\left(1 + \left(\frac{\kappa_-}{\kappa_+}\right)^2\right) \cos\left(\frac{\lambda_k}{c_+}\right) \cos\left(\frac{\lambda_k}{c_-}\right) + \frac{1}{\beta}\left(1 + \left(\frac{\beta\kappa_-}{\kappa_+}\right)^2\right) \sin\left(\frac{\lambda_k}{c_+}\right) \sin\left(\frac{\lambda_k}{c_-}\right) = \frac{2\kappa_-}{\kappa_+}. \tag{73}$$

Finally, one can find $\tilde{\boldsymbol{\Phi}}_k(Z)$ and $\boldsymbol{\mathcal{P}}_p(Z,\tau)$ vectors fields using boundary condition system (22) and boundary condition matrices (69), leading to (detailed derivation provided in Appendix G),

$$\tilde{\boldsymbol{\Phi}}_k(Z) = \begin{pmatrix} \cos\left(\frac{\lambda_k}{c_-}Z\right) + \xi_k \sin\left(\frac{\lambda_k}{c_-}Z\right) \\ -\frac{c_+}{\beta c_-}\left[\cos\left(\frac{\lambda_k}{c_+}Z\right) + \beta\xi_k \sin\left(\frac{\lambda_k}{c_+}Z\right)\right] \end{pmatrix}, \tag{74}$$

$$\boldsymbol{\mathcal{P}}_p(Z,\tau) = \frac{\delta(\tau)}{\kappa_- - \kappa_+}\left[\begin{pmatrix} 1 \\ -1 \end{pmatrix} Z - \gamma \begin{pmatrix} 1 \\ -\frac{c_+}{\beta c_-} \end{pmatrix}\right], \tag{75}$$

with,

$$\xi_k = \frac{\sin\left(\frac{\lambda_k}{c_-}\right) - \frac{\kappa_+}{\beta\kappa_-}\sin\left(\frac{\lambda_k}{c_+}\right)}{\cos\left(\frac{\lambda_k}{c_-}\right) - \frac{\kappa_+}{\kappa_-}\cos\left(\frac{\lambda_k}{c_+}\right)} \text{ , and, } \gamma = \frac{\kappa_- c_- \beta - c_+\kappa_+}{c_+\left(\kappa_- - \kappa_+\right)}. \tag{76}$$

Since, according to the scalar product (55) and (72)

$$\|\tilde{\boldsymbol{\Phi}}_k(Z)\|^2 = -\frac{c_- + c_-\beta^2\xi_k^2 - c_+\beta\left(\xi_k^2+1\right)}{2c_+\beta} + c_-\xi_k\frac{\cos^2\left(\frac{\lambda_k}{c_+}\right) - \cos^2\left(\frac{\lambda_k}{c_-}\right)}{\lambda_k} + c_-\frac{\frac{\beta^2\xi_k^2-1}{\beta}\sin\left(\frac{2\lambda_k}{c_+}\right) - \left(\xi_k^2-1\right)\sin\left(\frac{2\lambda_k}{c_-}\right)}{4\lambda_k}, \tag{77}$$

and

$$\langle \boldsymbol{\mathcal{P}}_p(Z,\tau), \tilde{\boldsymbol{\Phi}}_k(Z)\rangle = \frac{c_-\delta(\tau)}{\kappa_- - \kappa_+}\left(\mathcal{F}_- - \frac{c_-\mathcal{F}_+}{c_+} - \gamma\left[\mathcal{G}_+ - \mathcal{G}_-\right]\right) \tag{78}$$

$$\mathcal{F}_\pm = \frac{\cos\left(\frac{\lambda_k}{c_\pm}\right)\left[c_\pm - \theta_\pm\lambda_k\xi_k\right] + \sin\left(\frac{\lambda_k}{c_\pm}\right)\left[\lambda_k + c_\pm\theta_\pm\xi_k\right] - c_\pm}{\lambda_k^2}, \tag{79}$$

$$\mathcal{G}_\pm = \frac{\theta_\pm\xi_k\left(\cos\left(\frac{\lambda_k}{c_\pm}\right) - 1\right) - \sin\left(\frac{\lambda_k}{c_\pm}\right)}{\theta_\pm\lambda_k}, \tag{80}$$

$$\theta_- = 1, \quad \theta_+ = \beta, \tag{81}$$

the expression of $\boldsymbol{\mathcal{P}}(Z,\tau)$ in (46) pursues

$$\boldsymbol{\mathcal{P}}(Z,\tau) - \boldsymbol{\mathcal{P}}_p(Z,\tau) = c_-\sum_{\mathcal{S}_\mathcal{P}} \frac{\mathcal{F}_- - \frac{c_-\mathcal{F}_+}{c_+} - \gamma\left[\mathcal{G}_+ - \mathcal{G}_-\right]}{\left(\kappa_- - \kappa_+\right)\|\tilde{\boldsymbol{\Phi}}_k(Z)\|^2}\tilde{\boldsymbol{\Phi}}_k(Z)\left[\lambda_k\sin\left(\lambda_k\tau\right) - \delta(\tau)\right]. \tag{82}$$

The above expressions (77)-(81) have been cross-checked using formal calculus softwares.

4.3. Comparisons and illustrations

We now discuss quantitative illustrations of the provided analytical solutions so as to demonstrate their matching with previously published numerical results. Since many previous contributions have considered Fourier representation of test cases, our theoretical predictions for the discrete spectrum associated with discrete frequency peaks are first analyzed. The spectrum formally given by general relation (34) and more specifically by explicit simple transcendent relations (56) and (73) are compared to the Fourier transform peaks in Figure 3. The determinant's zeros, λ_k, are classically related to the natural frequencies accordingly to the following linear law, [28]

$$f_k = \lambda_k f_0, \tag{83}$$

where f_k is the k^{th} natural frequency expressed in Hz and f_0 is the natural acoustic fluid frequency introduced in (8). A perfect matching of the predicted peaks (dotted lines) with the numerical one can be observed in Figure 3 . More precisely, Figure 3a compares [44]'s results with our prediction for boundary conditions (i) (Cf Fig. 1a) whereas Figure 3b consider [28]'s prediction for boundary conditions (ii) (Cf Fig. 1b). These theoretical predictions are matched to numerical results without any adjusted parameters. More quantitative comparison between the numerical peaks and their theoretical predictions are provided in table 2 with excellent agreement.
Temporal predictions are also compared with MOC numerical results so as to test every details of the analytical solutions, i.e. not only the spectrum but also the eigenmodes and their amplitudes. Figure 4 provides this comparison with [27]'s MOC solutions for the set of parameters presented in Table 1. In each case a nearly perfect matching between the theoretical prediction and the numerical computation can be observed. Zoom are provided for high-frequency fidelity check. The resulting mismatch might be attributable to the inaccuracy of data collection from [27]. No parameter adjustment have been used.

5. Sensitivity matrix evaluation

5.1. Wave speed, $c_\pm$, deviations

From the analytical expressions of $c_\pm$ in (15), the respective derivation of the dimensionless wave speeds are deduced upon dimensionless variables describing the fluid structure interactions. The parametric dependence of

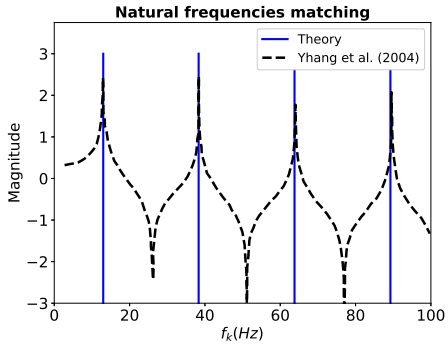

(a) First configuration (Cf Fig. 1a)

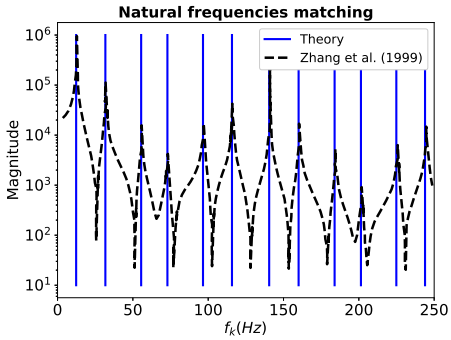

(b) Second configuration (Cf Fig. 1b).

Figure 3: Continuous black-lines : Fourier transform of the pressure field at valve location within the pipe versus frequency f. Blue dotted lines : spectrum eigenvalues. (a) Comparison between [44]'s prediction at the valve location with eigenvalues obtained from transcendental equation (56). (b) comparison between [28]'s pressure prediction at the valve location with prediction from transcendental equation (73).

First boundary condition (i) (Cf Fig. 1a)			Second boundary condition (ii) (Cf Fig. 1b)		
[44] (Hz)	Theoretical (Hz)	Δ (%)	[28] (Hz)	Theoretical (Hz)	Δ (%)
13.1	13.00	0.8	12	12.4	3.2
38.5	38.3	0.5	32	31.8	0.6
64.0	63.8	0.3	56	55.5	0.9
89.6	89.3	0.3	73	72.9	0.1
115.1	114.6	0.4	97	96.6	0.4
131.8	131.7	0.08	116	115.8	0.2
141.3	140.8	0.3	141	140.5	0.4
166.6	165.9	0.4	161	160.0	0.6
192.1	191.4	0.4	185	183.9	0.6
			202	201.4	0.3
			226	224.9	0.5
			245	243.9	0.5

Table 2: Comparative analysis of natural frequencies for the two study configurations. For each encountered frequency, the relative error $\Delta(\%)$ is estimated.

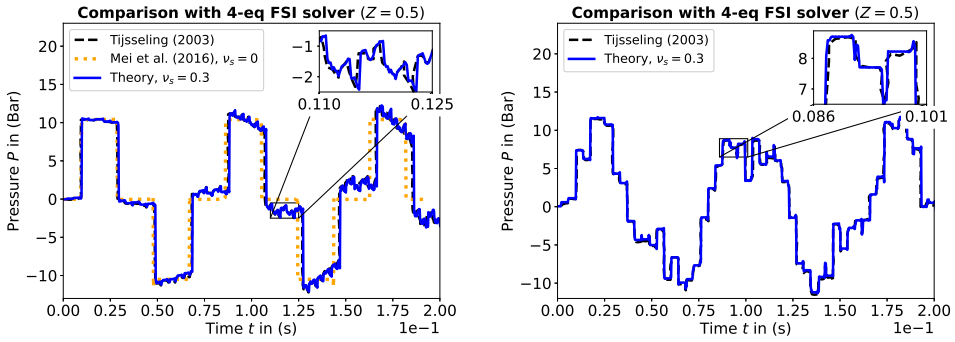

(a) First configuration (Cf Fig. 1a)

(b) Second configuration (Cf Fig. 1b).

Figure 4: Comparison between pressure field analytical solution at middle pipe location (continuous blue lines) with MOC solutions (dotted black lines). Non-FSI solutions (i.e $\nu_s = 0$) are provided for illustration in brown dotted lines. Insets provide a zoom for careful check.

$c_\pm\left(\frac{E}{K}, \nu_s, \mathcal{D}, \alpha\right)$ is known so that any derivative $\frac{\partial c_\pm}{\partial X}$ (X being any structural parameter embedded in parameters $\frac{E}{K}$, ν_s, $\mathcal{D}$ in (3) and α) in (1) is possible to compute analytically. In order to simplify the algebraic expressions the squared wave speeds (15) derivatives are evaluated

$$\frac{\partial c_\pm^2}{\partial \alpha} = \mu_c \frac{1+\alpha}{\alpha\,(2+\alpha)}\left[1 + \pm\frac{2\nu_s^2 - 1 + 2\nu_s\mathcal{D} + \mu_a}{\sqrt{\left(c_+^2 + c_-^2\right)^2 - 4\mathcal{C}_s^2}}\right], \tag{84}$$

$$\frac{\partial c_\pm^2}{\partial\left(\frac{E}{K}\right)} = \frac{\mathcal{D}}{2}\left[1 \pm \frac{\mu_a + 2\nu_s\mathcal{D} - 1}{\sqrt{\left(c_+^2 + c_-^2\right)^2 - 4\mathcal{C}_s^2}}\right] \tag{85}$$

$$\frac{\partial c_\pm^2}{\partial \nu_s} = \frac{1}{2}\left[2\mathcal{D} \pm \frac{4\nu_s\left(\mathcal{D}^2 - \mu_c\right) + 4\mathcal{D}\left(\frac{\mu_a - 1}{2} - 1\right)}{\sqrt{\left(c_+^2 + c_-^2\right)^2 - 4\mathcal{C}_s^2}}\right], \tag{86}$$

$$\frac{\partial c_\pm^2}{\partial\left(\frac{E}{K}\right)} = \frac{\mathcal{D}}{2}\left[1 \pm \frac{\mu_a + 2\nu_s\mathcal{D} - 1}{\sqrt{\left(c_+^2 + c_-^2\right)^2 - 4\mathcal{C}_s^2}}\right], \tag{87}$$

$$\frac{\partial c_\pm^2}{\partial \mathcal{D}} = \frac{1}{2\mathcal{D}}\left[\mu_a + 2\nu_s\mathcal{D} \pm \frac{\left(1 + \mu_a + 2\nu_s D\right)\left(\mu_a + 2\nu_s\mathcal{D}\right) - 2\mathcal{C}_s^2}{\sqrt{\left(c_+^2 + c_-^2\right)^2 - 4\mathcal{C}_s^2}}\right], \tag{88}$$

where $\mu_a = \mathcal{D}\left(2 + \frac{E}{K} + \frac{4}{\alpha(2+\alpha)}\right)$ and, $\mu_c = -\frac{4\mathcal{D}}{\alpha(2+\alpha)}$ are defined in (E.2)-(E.4). From (84)-(88) the velocity derivatives can easily be deduced from

$$\partial_X c_\pm = \frac{1}{2c_\pm}\partial_X c_\pm^2. \tag{89}$$

5.2. Sensitivity matrix for boundary condition (i)

From (56) it is possible to find an analytical expression of the sensitivity of the eigenvalues λ_k with respect to the parameters set $(\nu_s\alpha, E/K, \mathcal{D})$. Using (49) one gets

$$\frac{\partial\beta}{\partial X} = \frac{\partial\beta}{\partial c_-}\frac{\partial c_-}{\partial X} + \frac{\partial\beta}{\partial c_+}\frac{\partial c_+}{\partial X}, \tag{90}$$

$$\frac{\partial\beta}{\partial c_\pm} = \mp\frac{\beta}{c_\pm}\frac{c_\pm^2+1}{c_\pm^2-1}, \tag{91}$$

whilst from (56) one gets

$$\frac{\partial\lambda_k}{\partial X} = \frac{-c_-\partial_X\beta\tan\left(\frac{\lambda_k}{c_-}\right) + \frac{\lambda_k}{c_-}\left(\beta\partial_X c_- - \left(\frac{c_-}{c_+}\right)^2\partial_X c_+ + \tan\left(\frac{\lambda_k}{c_-}\right)\tan\left(\frac{\lambda_k}{c_+}\right)\left[\partial_X c_- - \beta\left(\frac{c_-}{c_+}\right)^2\partial_X c_+\right]\right)}{\beta - \frac{c_-}{c_+} + \tan\left(\frac{\lambda_k}{c_-}\right)\tan\left(\frac{\lambda_k}{c_+}\right)\left[1 - \beta\frac{c_-}{c_+}\right]}. \tag{92}$$

The spectrum sensitivity of the first configuration (Cf. Fig. 1a) is depicted in Figures 5a-5d, for the first five eigenmodes. The sensitivity analysis of the first configuration reveals an increased parametric dependence for higher modes. The higher the mode, the more sensitive it is to the dimensionless parameters variation. Furthermore, this analysis highlights a high sensitivity of the first five eigenmodes with respect to the density ratio $\mathcal{D}$ as depicted on Figure 5d, whilst the system is found weakly dependent on the E/K ratio, as illustrated in Figure 5c.

5.3. Sensitivity matrix for boundary condition (ii)

A similar footpath is hereby provided for the reservoir-pipe-free valve configuration. The spectrum transcendental equation derived in (73), which holds for the second configuration (Cf Fig. 1b), is found dependent upon a set of four dimensionless parameters namely $c_\pm$, β and

$$\kappa(c_\pm, \nu_s) = \frac{\kappa_-}{\kappa_+} \equiv \frac{c_+}{\beta c_-}\frac{c_-^2 - (1-2\nu_s)}{c_+^2 - (1-2\nu_s)}. \tag{93}$$

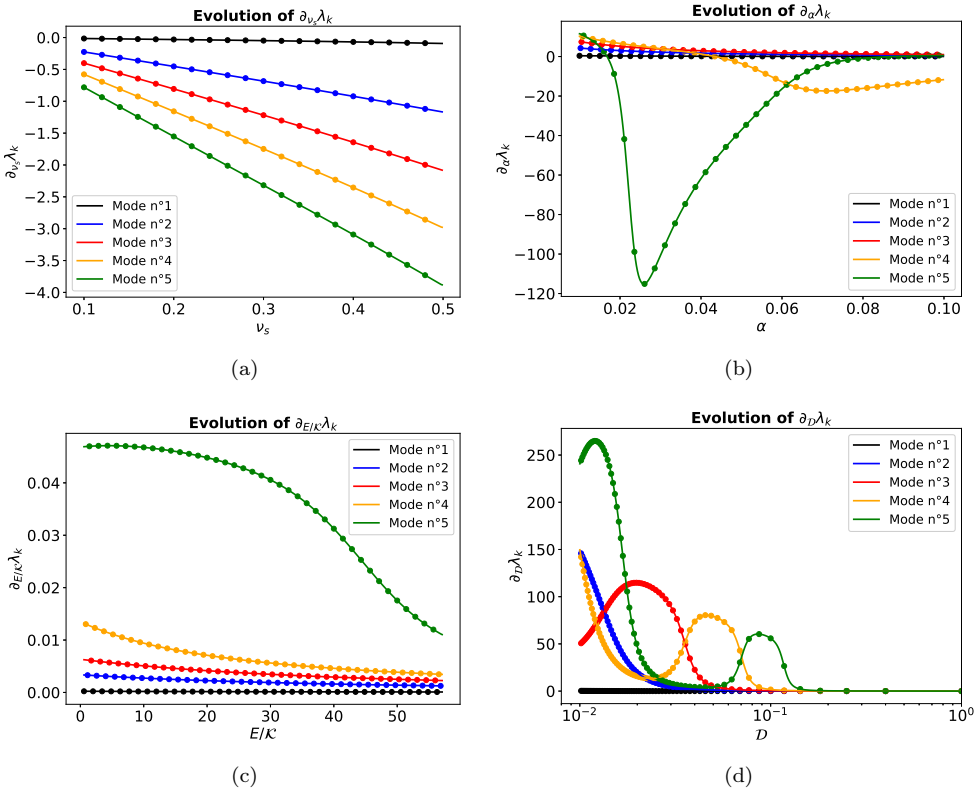

Figure 5: Sensitivity analysis of the first five resonant eigenmodes associated with the spectrum equation (56). (a) $\partial_{\nu_s}\lambda_k$. (b) $\partial_\alpha\lambda_k$. (c) $\partial_{(E/\mathcal{K})}\lambda_k$. (d) $\partial_{\mathcal{D}}\lambda_k$. The numerical gradients are depicted in continuous lines whereas the analytical expressions are represented by dotted lines.

The derivative of κ with respect to the dimensionless quantity $X \equiv (\nu_s, \alpha, E/\mathcal{K}, \mathcal{D})$ thus achieves as follows

$$\partial_X \kappa = \frac{c_+}{c_- \beta}\left[\partial_X \kappa_r + \kappa_r\left(\frac{1}{c_+}\partial_X c_+ - \frac{1}{c_-}\partial_X c_- - \frac{1}{\beta}\partial_X \beta\right)\right] \tag{94}$$

$$\kappa_r = \frac{c_-^2 - (1-2\nu_s)}{c_+^2 - (1-2\nu_s)}, \tag{95}$$

$$\partial_X \kappa_r = \frac{2}{c_+^2 - (1-2\nu_s)}\left(c_- c_+\left(\frac{1}{c_+}\partial_X c_- - \frac{\kappa_r}{c_-}\partial_X c_+\right) + \partial_X \nu_s\,(1-\kappa_r)\right), \tag{96}$$

whereas from (73) one gets

$$\partial_X \lambda_k = -\frac{2\kappa \partial_X \kappa}{\tan\left(\frac{\lambda_k}{c_+}\right)\left[\frac{1+(\beta\kappa)^2}{\beta c_-} - \frac{1+\kappa^2}{c_+}\right] + \tan\left(\frac{\lambda_k}{c_-}\right)\left[\frac{1+(\beta\kappa)^2}{\beta c_+} - \frac{1+\kappa^2}{c_-}\right]}$$
$$+ \frac{\tan\left(\frac{\lambda_k}{c_+}\right)\tan\left(\frac{\lambda_k}{c_-}\right)\left(\frac{1+(\beta\kappa)^2}{\beta^2}\partial_X\beta - 2\kappa\left[\beta\partial_X\kappa + \kappa\partial_X\beta\right]\right)}{\tan\left(\frac{\lambda_k}{c_+}\right)\left[\frac{1+(\beta\kappa)^2}{\beta c_-} - \frac{1+\kappa^2}{c_+}\right] + \tan\left(\frac{\lambda_k}{c_-}\right)\left[\frac{1+(\beta\kappa)^2}{\beta c_+} - \frac{1+\kappa^2}{c_-}\right]}$$
$$+ 2\frac{\partial_X \kappa}{\cos\left(\frac{\lambda_k}{c_-}\right)\cos\left(\frac{\lambda_k}{c_+}\right)\left(\tan\left(\frac{\lambda_k}{c_+}\right)\left[\frac{1+(\beta\kappa)^2}{\beta c_-} - \frac{1+\kappa^2}{c_+}\right] + \tan\left(\frac{\lambda_k}{c_-}\right)\left[\frac{1+(\beta\kappa)^2}{\beta c_+} - \frac{1+\kappa^2}{c_-}\right]\right)}$$
$$+\lambda_k \frac{\tan\left(\frac{\lambda_k}{c_+}\right)\left[\frac{1}{c_-}\partial_X c_- \frac{1+(\beta\kappa)^2}{\beta c_-} - \frac{1}{c_+}\partial_X c_+ \frac{1+\kappa^2}{c_+}\right] + \tan\left(\frac{\lambda_k}{c_-}\right)\left[\frac{1}{c_+}\partial_X c_+ \frac{1+(\beta\kappa)^2}{\beta c_+} - \frac{1}{c_-}\partial_X c_- \frac{1+\kappa^2}{c_-}\right]}{\tan\left(\frac{\lambda_k}{c_+}\right)\left[\frac{1+(\beta\kappa)^2}{\beta c_-} - \frac{1+\kappa^2}{c_+}\right] + \tan\left(\frac{\lambda_k}{c_-}\right)\left[\frac{1+(\beta\kappa)^2}{\beta c_+} - \frac{1+\kappa^2}{c_-}\right]}. \tag{97}$$

The derivative of the five first eigenmodes is once again investigated and their related variations with respect to $(\nu_s, \alpha, E/\mathcal{K}, \mathcal{D})$ are depicted in Figure 6a-6d. A very same sensitivity ordering is found for the second configuration. The density ratio variations remain the most sensitive parameter whereas the $\frac{E}{\mathcal{K}}$ ratio has little impact on the coupled dynamic. It is interesting to point-out that the higher eigenmodes are no longer the most sensitive in this second case, as illustrated in Figures 6a-6b. The boundary condition couplings, or junction couplings, occurring in the second configuration, then reshape the eigenmode structure and their sensitivity.

6. Conclusion

This contribution provide a theoretical framework for the analysis of analytical solutions for FSI pulsed waves propagation inside liquid-filled tubes. This framework leads to an explicit spectrum derivation and analytical eigenmode decomposition. It favorably compares with previously published results. The spectrum sensitivity matrix has been computed explicitly with respect to (dimensionless) parameter derivatives, as well as wave velocity derivatives. The provided solutions might be used in various contexts associated with signal processing interpretation, parameter identification or boundary condition de-convolution inside liquid-filled pipes.

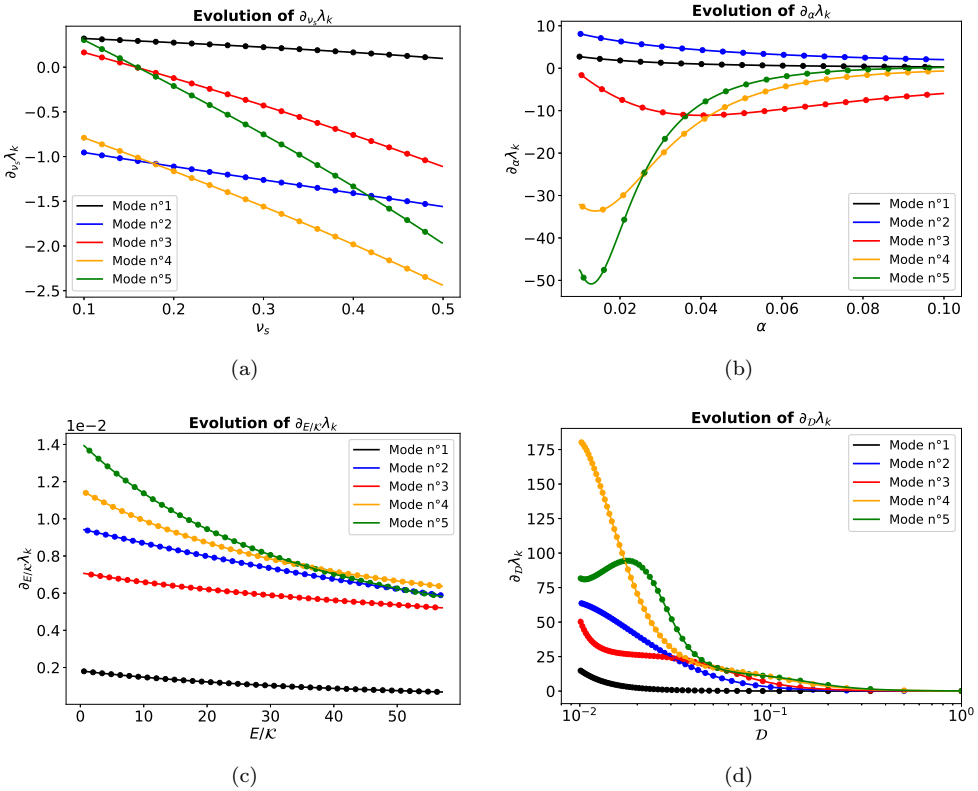

Figure 6: Same conventions as Figure 5 for spectrum equation (73). (a) $\partial_{\nu_s}\lambda_k$. (b) $\partial_\alpha\lambda_k$. (c) $\partial_{(E/\mathcal{K})}\lambda_k$. (d) $\partial_\mathcal{D}\lambda_k$.The numerical gradients are depicted in continuous lines whereas the analytical expressions are represented by dotted lines.

Acknowledgement

This work was supported by the collaborative ANRT Grant CIFRE 2019/1453 co-funded by SETOM, dedicated society of Veolia for the public drinking water service of Toulouse Métropole operating under the brand Eau de Toulouse Métropole.
The authors have no competing interests to declare.

References

[1] N. Joukowsky, Uber den hydraulischen Stoss in Wasserleitungsro hren.(On the hydraulic hammer in water supply pipes) Mémoires de

l'Académie Impériale des Sciences de St.-Petersbourg., English translation, partly, by Simin 9 (1904).

[2] D. Korteweg, Ueber die fortpflanzungsgeschwindigkeit des schalles in elastischen rohren, on the speed of sound propagation in elastic tubes, Annalen der Physik 241 (12) (1878) 525–542.

[3] R. Skalak, An extension of the theory of waterhammer, Transactions of the ASME 78 (1956) 105–116.

[4] E. L. Holmboe, W. T. Rouleau, The Effect of Viscous Shear on Transients in Liquid Lines, J. Basic Eng. 89 (1) (1967) 174–180.

[5] W. Burmann, Water hammer in coaxial pipe systems, J. Hydraul. Eng. 101 (6) (1975) 699–715.

[6] D. D. Budny, D. C. Wiggert, F. J. Hatfield, The Influence of Structural Damping on Internal Pressure During a Transient Pipe Flow, J. Fluids Eng. 113 (3) (1991) 424–429.

[7] A. Tijsseling, Water hammer with fluid-structure interaction in thick-walled pipes, Computers & Structures 85 (2007) 844–851.

[8] A. S. Tijsseling, Fluid structure interaction in liquid filled pipe systems: a review, J Fluids Struct 10 (2) (1996) 109–146.

[9] S. Li, B. W. Karney, G. Liu, FSI research in pipeline systems – A review of the literature, J Fluids Struct 57 (2015) 277–297.

[10] D. Ferras, P. A. Manso, A. J. Schleiss, D. I. C. Covas, One-Dimensional Fluid–Structure Interaction Models in Pressurized Fluid-Filled Pipes: A Review, Applied Sciences 8 (10) (2018) 1844.

[11] S. Čanić, J. Tambača, G. Guidoboni, A. Mikelić, C. J. Hartley, D. Rosenstrauch, Modeling viscoelastic behavior of arterial walls and their interaction with pulsatile blood flow, SIAM J. Appl. Math. 67 (1) (2006) 164–193.

[12] T. J. Plona, B. K. Sinha, S. Kostek, S. Chang, Axisymmetric wave propagation in fluid-loaded cylindrical shells. II: Theory versus experiment, J. Acoust. Soc. Am. 92 (2) (1992) 1144–1155.

[13] B. K. Sinha, T. J. Plona, S. Kostek, S. Chang, Axisymmetric wave propagation in fluid-loaded cylindrical shells. i: Theory, J. Acoust. Soc. Am. 92 (2) (1992) 1132–1143.

[14] J. S. Walker, J. W. Phillips, Pulse Propagation in Fluid-Filled Tubes, Journal of Applied Mechanics 44 (1) (1977) 31–35.

[15] N. Kizilova, Pressure wave propagation in liquid-filled tubes of viscoelastic material, Fluid Dyn. 41 (2006) 434–446. doi:10.1007/s10697-006-0060-9.

[16] A. S. Tijsseling, C. S. W. Lavooij, Waterhammer with fluid-structure interaction, Applied Scientific Research 47 (3) (1990) 273–285.

[17] G. Liu, Y. Li, Vibration analysis of liquid-filled pipelines with elastic constraints, J. Sound Vib. 330 (13) (2011) 3166–3181.

[18] A. Keramat, M. Fathi-Moghadam, R. Zanganeh, M. Rahmanshahi, A. S. Tijsseling, E. Jabbari, Experimental investigation of transients-induced fluid–structure interaction in a pipeline with multiple-axial supports, J. Fluids Struct. 93 (2020) 102848. doi:10.1016/j.jfluidstructs.2019.102848.

[19] X. Wang, J. Lin, A. Keramat, M. S. Ghidaoui, S. Meniconi, B. Brunone, Matched-field processing for leak localization in a viscoelastic pipe: An experimental study, Mech Syst Signal Process 124 (2019) 459–478.

[20] X. Wang, D. Palomar, L. Zhao, M. Ghidaoui, R. Murch, Spectral-based methods for pipeline leakage localization, Journal of Hydraulic Engineering, ASCE 145 (3) (2019) 04018089.

[21] A. Keramat, B. Karney, M. S. Ghidaoui, X. Wang, Transient-based leak detection in the frequency domain considering fluid-structure interaction and viscoelasticity, Mech Syst Signal Process 153 (2021) 107500.

[22] A. Keramat, H. F. Duan, Spectral based pipeline leak detection using a single spatial measurement, Mech Syst Signal Process 161 (2021) 107940.

[23] T. C. Che, H. F. Duan, P. J. Lee, Transient wave-based methods for anomaly detection in fluid pipes: A review, Mech Syst Signal Process 160 (2021) 107874.

[24] H. F. Duan, P. J. Lee, Transient-based frequency domain method for dead-end side branch detection in reservoir pipeline-valve systems, J. Hydraul. Eng 142 (2) (2016) 04015042.

[25] H. F. Duan, Accuracy and sensitivity evaluation of tfr method for leak detection in multiple-pipeline water supply systems, Water Resour. Manage. 32 (2018) 2147–2164.

[26] M. W. Lesmez, D. C. Wiggert, F. J. Hatfield, Modal Analysis of Vibrations in Liquid-Filled Piping Systems, J. Fluid Eng. 112 (3) (1990) 311–318.

[27] A. S. Tijsseling, Exact solution of linear hyperbolic four-equation system in axial liquid-pipe vibration, J Fluids Struct 18 (2) (2003) 179–196.

[28] L. Zhang, A. Tijsseling, E. Vardy, FSI Analysis of Liquid-Filled Pipes, J. Sound Vib. 224 (1999) 69–99.

[29] Q. Li, K. Yang, L. Zhang, N. Zhang, Frequency domain analysis of fluid–structure interaction in liquid-filled pipe systems by transfer matrix method, INT J MECH SCI 44 (2002) 2067–2087.

[30] S. J. Li, G. M. Liu, W. t. Kong, Vibration analysis of pipes conveying fluid by transfer matrix method, Nuclear Engineering and Design 266 (2014) 78–88.

[31] C. C. Mei, H. Jing, Pressure and wall shear stress in blood hammer - Analytical theory, Mathematical Biosciences 280 (Oct. 2016).

[32] A. Tijsseling, Fluid-structure interaction in case of waterhammer with cavitation, Ph.D. thesis, Delft University of Technology (1993).

[33] M. H. Chaudhry, Applied Hydraulic Transients, 3rd Edition, Springer-Verlag, 2014.

[34] S. Li, B. W. Karney, G. Liu, FSI research in pipeline systems – a review of the literature, J. Fluids Struct. 57 (2015) 277–297. doi:10.1016/j.jfluidstructs.2015.06.020.

[35] T. C. Lin, G. W. Morgan, Wave Propagation through Fluid Contained in a Cylindrical, Elastic Shell, J. Acoust. Soc. Am. 28 (6) (1956) 1165–1176.

[36] F. Gaultier, J. Gilbert, J. Dalmont, R. Picó, Wave propagation in a fluid filled rubber tube: Theoretical and experimental results for korteweg's wave, Acta Acust. United Ac. 93 (2007) 333–344.

[37] M. S. Ghidaoui, M. Zhao, D. A. McInnis, D. H. Axworthy, A review of water hammer theory and practice, Appl. Mech. Rev. 58 (1) (2005) 49–76. doi:10.1115/1.1828050.

[38] A. Keramat, A. Tijsseling, Q. Hou, A. Ahmadi, Fluid–structure interaction with pipe-wall viscoelasticity during water hammer, J. Fluids Struct. 28 (2011) 434–455. doi:10.1016/j.jfluidstructs.2011.11.001.

[39] H. K. Aliabadi, A. Ahmadi, A. Keramat, Frequency response of water hammer with fluid-structure interaction in a viscoelastic pipe, Mech Syst Signal Process 144 (2020) 106848. doi:10.1016/j.ymssp.2020.106848.

[40] C. C. Mei, H. Jing, Effects of thin plaque on blood hammer—An asymptotic theory, Eur. J. Mech. B Fluids 69 (2018) 62–75. doi:10.1016/j.euromechflu.2018.01.004.

[41] A. Bayle, F. Plouraboué, Low Mach number theory of pressure waves inside an elastic tube, submitted (2022).

[42] M. Lewin, Eléments de théorie spectrale : le laplacien sur un ouvert borné, Master's thesis, CNRS & CEREMADE, Université Paris-Dauphine, PSL Research University (2017).

[43] G. D. C. Kuiken, Amplification of pressure fluctuations due to fluid-structure interaction, J Fluids Struct 2 (5) (1988) 425–435.

[44] K. Yang, Q. S. Li, L. Zhang, Longitudinal vibration analysis of multi-span liquid-filled pipelines with rigid constraints, J. Sound Vib. 273 (1) (2004) 125–147.

Appendix A. Nomenclature

Physics Constants		
ρ_f	Fluid density	$kg \cdot m^{-3}$
$\mathcal{K}$	Fluid bulk modulus	Pa
ρ_s	Solid density	$kg \cdot m^{-3}$
E	Young's modulus	Pa
ν_s	Poisson's modulus	
W_0	Order of magnitude of the steady velocity	$m \cdot s^{-1}$
Characteristic velocities		
c_p	Modified Korteweg's wave speed / Fluid pulse wave speed	$m \cdot s^{-1}$
c_s	Solid elastic wave speed	$m \cdot s^{-1}$
$c_\pm$	Dimensionless coupled propagation modes wave speed	
Geometrical properties		
R_0	Inner initial tube's radius	m
e	Tube's thickness	m
L	Tube's length	m
z	Dimensional axial coordinate	m
Z	Dimensionless axial coordinate	
Dimensionless numbers		
ϵ	Ratio of the inner tube's radius by the tube's length	
α	Ratio of the tube's thickness by the inner tube's	
$\mathcal{C}_s$	Ratio of the solid elastic wave speed by the fluid pulse wave speed	
$\mathcal{D}$	Ratio of fluid density by the solid density	
Theoretical elements		
$W(Z, \tau)$	Perturbed axial fluid velocity	

$P(Z,\tau)$	Perturbed fluid pressure
$\sigma(Z,\tau)$	Perturbed axial fluid stress tensor
$\dot{\zeta}(Z,\tau)$	Perturbed axial solid displacement velocity
$\mathcal{H}$	Self auto adjoint operator
$-\lambda_k^2$	Eigenvalue of $\mathcal{H}$
$a_k(\tau)$	Temporal amplitude of $\boldsymbol{\mathcal{Y}}_h$
f_k	Natural frequencies

Characteristic matrices

$\mathbf{Y}(Z,\tau)$	Perturbed dimensionless fluid and solid pressure–velocity vector
$\mathbf{P}(Z,\tau)$	Perturbed dimensionless pressure–stress vector
$\mathbf{C_P}$	Speed matrix of the pressure–stress wave equation
$\mathbf{C_W}$	Speed matrix of the velocity–displacement velocity wave equation
$\mathbf{C_Y}$	Speed matrix coupled fluid and solid pressure–velocity wave equation
$\boldsymbol{\mathcal{Y}}$	Perturbed dimensionless fluid and solid pressure–velocity vector within the diagonalization basis
$\boldsymbol{\mathcal{Y}}_p(Z,\tau)$	Particular part of $\boldsymbol{\mathcal{Y}}$
$\boldsymbol{\mathcal{Y}}_h(Z,\tau)$	Homogeneous part of $\boldsymbol{\mathcal{Y}}$
$\boldsymbol{\mathcal{P}}$	Perturbed dimensionless pressure–stress vector within the diagonalization basis
$\boldsymbol{\mathcal{P}}_h(Z,\tau)$	Homogeneous part of $\boldsymbol{\mathcal{P}}$
$\boldsymbol{\mathcal{P}}_p(Z,\tau)$	Particular part of $\boldsymbol{\mathcal{P}}$
$\boldsymbol{\mathcal{C}}_{\boldsymbol{\mathcal{P}}}$	Speed matrix within the diagonalization basis
$\boldsymbol{\mathcal{C}}_{\boldsymbol{\mathcal{W}}}$	Speed matrix within the diagonalization basis
$\boldsymbol{\mathcal{C}}_{\boldsymbol{\mathcal{Y}}}$	Speed matrix coupled fluid and solid pressure–velocity wave equation

$\boldsymbol{\mathcal{N}}$, $\boldsymbol{\mathcal{M}}$, $\boldsymbol{\mathcal{Q}}$, $\boldsymbol{\mathcal{R}}$, $\boldsymbol{\mathcal{S}}$ Boundary condition matrices within the diagonalization basis

$\mathbf{\Phi}_k(Z)$ Eigenvector of $\mathcal{H}$

$\tilde{\mathbf{\Phi}}_k(Z)$ Contracted form of $\mathbf{\Phi}_k$

Notations

$\langle\cdot\rangle$ Scalar product

η_1, η_2 Constant of the scalar product

$\cdot^*$ Dimensional field

$\hat{\cdot}$ Laplace transform

s Laplace variable

t Dimensional time

τ Dimensionless time

β, $\kappa_\pm$, γ, ξ_k Constants

$\kappa = \frac{\kappa_-}{\kappa_+}$ Constant ratio

Appendix B. Dimensionless FSI four equations

[7] provides a derivation of well-known four-FSI equations system. From averaged mass and momentum conservation equations within fluid and solid, [7] founds the coupled hyperbolic equations for longitudinal fluid velocity W^*, pressure P^*, longitudinal solid deformation velocity $\dot{\zeta}^*$ and longitudinal stress σ^*,

$$\partial_t W^* = -\frac{1}{\rho_f}\partial_z P^*, \tag{B.1}$$

$$\partial_z W^* + \frac{1}{\rho_f c_p^2}\partial_t P^* = 2\nu_s \partial_z \dot{\zeta}^*, \tag{B.2}$$

$$\partial_t \dot{\zeta}^* = \frac{1}{\rho_s}\partial_z \sigma^*, \tag{B.3}$$

$$\partial_t \sigma^* - E\partial_z \dot{\zeta}^* = \frac{2\nu_s}{\alpha\,(2+\alpha)}\partial_t P^*, \tag{B.4}$$

where subscript * refers to dimensional quantities. The velocity perturbation W^* reference amplitude is set as W_0, so that as $W^* = W_0 W$. The pressure

perturbation P^*, is known from [1]'s theory to match the dynamic pulse overpressure so that $P^* = \rho_f c_p W_0 P$. From stress continuity at the tube wall, the axial perturbed stress, σ^* is prescribed having the same order of magnitude as P^*, i.e. $\sigma^* = \rho_f c_p W_0 \sigma$. The axial displacement field, ζ^*, is set as $\zeta^* = \alpha \frac{\mathcal{M}}{\epsilon} R_0 \zeta$ in order to ensure both axial velocity matching at the tube's wall and the small strain and small displacement hypothesis framework. Furthermore, the physical time, t, is scaled on the advection time, $t = \frac{L}{c_p}\tau$ whilst axial longitudinal scale is set as $z = LZ$. Using these scaling within (B.1)-(B.4), leads to (7).

Appendix C. Resolution of the constitutive ODE in $a_k(\tau)$

Let us consider the ODE

$$\left(\partial_\tau^2 + \lambda_k^2\right) a_k(\tau) = -\frac{\langle \partial_\tau^2 \boldsymbol{\mathcal{Y}}_p, \tilde{\boldsymbol{\Phi}}_k(Z)\rangle}{\|\tilde{\boldsymbol{\Phi}}_k\|}, \tag{C.1}$$

and its initial conditions

$$a_k(0) = -\frac{\langle \boldsymbol{\mathcal{Y}}_p(Z,0), \tilde{\boldsymbol{\Phi}}_k(Z)\rangle}{\|\tilde{\boldsymbol{\Phi}}_k\|}, \text{ and, } \partial_\tau a_k(0) = -\frac{\langle \partial_\tau \boldsymbol{\mathcal{Y}}_p(Z,0), \tilde{\boldsymbol{\Phi}}_k(Z)\rangle}{\|\tilde{\boldsymbol{\Phi}}_k\|}. \tag{C.2}$$

A Laplace transform, hereby denoted $\mathcal{L}$, approach is employed to solve (C.1). Introducing s, the conjugate variable of t and setting up hat notation for Laplace variables yields

$$\begin{aligned}\left(s^2 + \lambda_k^2\right) \hat{a}(s) - s a_k(0) - \partial_\tau a_k(0) = -s^2 \frac{\langle \hat{\boldsymbol{\mathcal{Y}}}_p, \tilde{\boldsymbol{\Phi}}_k(Z)\rangle}{\|\tilde{\boldsymbol{\Phi}}_k\|} \\ + \frac{s\langle \boldsymbol{\mathcal{Y}}_p(Z,0), \tilde{\boldsymbol{\Phi}}_k(Z)\rangle + \langle \partial_\tau \boldsymbol{\mathcal{Y}}_p(Z,0), \tilde{\boldsymbol{\Phi}}_k(Z)\rangle}{\|\tilde{\boldsymbol{\Phi}}_k\|}.\end{aligned} \tag{C.3}$$

Invoking (C.2) reads to

$$\hat{a}_k(s) = \lambda_k^2 \frac{\langle \hat{\boldsymbol{\mathcal{Y}}}_p, \tilde{\boldsymbol{\Phi}}_k(Z)\rangle}{\left(s^2 + \lambda_k^2\right)\|\tilde{\boldsymbol{\Phi}}_k\|} - \frac{\langle \hat{\boldsymbol{\mathcal{Y}}}_p, \tilde{\boldsymbol{\Phi}}_k(Z)\rangle}{\|\tilde{\boldsymbol{\Phi}}_k\|}. \tag{C.4}$$

Since $\mathcal{L}\left(\sin\left(\lambda_k \tau\right)\right) = \frac{\lambda_k}{s^2+\lambda_k^2}$, the use of convolution theorem finally results in

$$a_k(\tau) = \lambda_k \int_0^\tau \frac{\langle \boldsymbol{\mathcal{Y}}_p, \tilde{\boldsymbol{\Phi}}_k(Z)\rangle(t) \sin\left(\lambda_k\left[\tau - t\right]\right) dt}{\|\tilde{\boldsymbol{\Phi}}_k\|} - \frac{\langle \boldsymbol{\mathcal{Y}}_p, \tilde{\boldsymbol{\Phi}}_k(Z)\rangle}{\|\tilde{\boldsymbol{\Phi}}_k\|}. \tag{C.5}$$

Appendix D. Derivation of $\tilde{\mathbf{\Phi}}_k(Z)$ in configuration (i)

Let us focus on the first configuration boundary matrices (50) along with the homogeneous system upon $\left(\mathbf{\Phi}_k(0), \partial_Z \mathbf{\Phi}_k(0)\right)^T$ in (33). Introducing the fourth unknown column vector

$$\begin{pmatrix} \mathbf{\Phi}_k(0) \\ \partial_Z \mathbf{\Phi}_k(0) \end{pmatrix} = \left(\phi_k^-, \phi_k^+, \partial_Z \phi_k^-, \partial_Z \phi_k^+\right)^T \tag{D.1}$$

yields

$$\begin{pmatrix} 1 & \frac{\beta c_-}{c_+} & 0 & 0 \\ 0 & 0 & \frac{1}{c_-} & \frac{1}{c_+} \\ -\frac{\lambda_k \sin\left(\frac{\lambda_k}{c_-}\right)}{c_-} & -\frac{\lambda_k \beta c_- \sin\left(\frac{\lambda_k}{c_+}\right)}{c_+^2} & \frac{\cos\left(\frac{\lambda_k}{c_-}\right)}{c_-} & \frac{\beta c_- \cos\left(\frac{\lambda_k}{c_+}\right)}{c_+^2} \\ -\frac{\lambda_k \sin\left(\frac{\lambda_k}{c_-}\right)}{c_-} & -\frac{\lambda_k \sin\left(\frac{\lambda_k}{c_+}\right)}{c_+} & \frac{\cos\left(\frac{\lambda_k}{c_-}\right)}{c_-} & \frac{\cos\left(\frac{\lambda_k}{c_+}\right)}{c_+} \end{pmatrix} \begin{pmatrix} \phi_k^- \\ \phi_k^+ \\ \partial_Z \phi_k^- \\ \partial_Z \phi_k^+ \end{pmatrix} = \mathbf{0}. \tag{D.2}$$

A non homogeneous solution of this linear system follows from re-organizing the last two lines of (D.2) and achieves in

$$\begin{pmatrix} \phi_k^+ \\ \partial_Z \phi_k^- \\ \partial_Z \phi_k^+ \end{pmatrix} = \phi_k^- \begin{pmatrix} -\frac{c_-}{\beta c_-} \\ \frac{\lambda_k}{c_-} \tan\left(\frac{\lambda_k}{c_-}\right) \\ -\frac{c_+}{\beta c_-} \frac{\lambda_k}{c_+} \tan\left(\frac{\lambda_k}{c_+}\right) \end{pmatrix}. \tag{D.3}$$

The use of (D.3) within the equations set (30)-(32) in case of a separate pressure–velocity boundary conditions (i.e. $\mathbf{T} \equiv \mathbf{T}_s$ such as transfer matrices order are divided by two) results in

$$\mathbf{\Phi}_k(Z) = \phi_k^- \begin{pmatrix} \cos\left(\frac{\lambda_k Z}{c_-}\right) + \tan\left(\frac{\lambda_k}{c_-}\right) \sin\left(\frac{\lambda_k Z}{c_-}\right) \\ -\frac{c_+}{\beta c_-} \left(\cos\left(\frac{\lambda_k Z}{c_+}\right) + \tan\left(\frac{\lambda_k}{c_+}\right) \sin\left(\frac{\lambda_k Z}{c_+}\right)\right) \end{pmatrix}, \tag{D.4}$$

so that the reduced eigenfunction form $\tilde{\mathbf{\Phi}}_k(Z)$ in (35), follows

$$\tilde{\mathbf{\Phi}}_k(Z) = \begin{pmatrix} \cos\left(\frac{\lambda_k Z}{c_-}\right) + \tan\left(\frac{\lambda_k}{c_-}\right) \sin\left(\frac{\lambda_k Z}{c_-}\right) \\ -\frac{c_+}{\beta c_-} \left(\cos\left(\frac{\lambda_k Z}{c_+}\right) + \tan\left(\frac{\lambda_k}{c_+}\right) \sin\left(\frac{\lambda_k Z}{c_+}\right)\right) \end{pmatrix}. \tag{D.5}$$

Appendix E. $\nu_s = 0$ limit of the first configuration (Cf. Fig.1a)

We hereby consider the $\nu_s = 0$ limit of our solution and compare it with the one of [31] (only its leading order).

Appendix E.1. Wave speed mode $c_\pm$ for $\nu_s \ll 1$

Using c_p^2, c_s^2 and $\mathcal{C}_s^2$ definitions (2), one can find

$$\mathcal{C}_s^2 = \mu_a + \mu_b \nu_s + \mu_c \nu_s^2, \tag{E.1}$$

with

$$\mu_a = \mathcal{D}\left(2 + \frac{E}{K} + \frac{4}{\alpha(2+\alpha)}\right), \tag{E.2}$$

$$\mu_b = 2\mathcal{D}, \tag{E.3}$$

$$\mu_c = -\frac{4\mathcal{D}}{\alpha(2+\alpha)}. \tag{E.4}$$

Furthermore, accordingly to (15), the wave speed $c_\pm$ reads

$$c_\pm^2 = \frac{1 + \mu_a + \nu_s\mu_b \pm (\mu_a - 1)\sqrt{1 + \frac{\nu_s\mu_b}{\mu_a - 1} + \frac{\nu_s^2(\mu_b^2 + 4\mu_c)}{(\mu_a-1)^2}}}{2}, \tag{E.5}$$

so that Taylor expanding (E.5) in the $\nu_s \ll 1$ results in

$$\left(c_+^2 - c_-^2\right) = (\mu_a - 1) + \frac{\mu_b}{2}\nu_s + O(\nu_s^2), \tag{E.6}$$

$$c_+ = \sqrt{\mu_a} + \frac{3\mu_b}{8\sqrt{m u_a}}\nu_s + O(\nu_s^2), \tag{E.7}$$

$$c_- = 1 + \frac{\mu_b}{8}\nu_s + O(\nu_s^2). \tag{E.8}$$

Appendix E.2. Spectrum of configuration (i) in the $\nu_s = 0$ limit

Using β definition (49) and regarding (E.7)-(E.8) in the limit $\nu_s \to 0$, the spectrum transcendental equation (56) reduces to,

$$\cos(\lambda_k)\sin\left(\frac{\lambda_k}{\sqrt{\mu_a}}\right) = 0. \tag{E.9}$$

The solution of which are [31]'s spectrum union pure elastic-wave eigenvalues,

$$\lambda_k = \left\{\pi\left(\frac{1}{2} + k\right)\right\} \cup \left\{\pi\sqrt{\mu_a}\,(1+k)\right\}. \tag{E.10}$$

Appendix E.3. Pressure solution of configuration (i) in the $\nu_s = 0$ limit

The pressure field for configuration (i) is obtained combining (59) with the change of basis (17)-(19) and achieves in

$$P(Z,\tau) = \frac{c_+^2 - 1}{(c_+^2 - c_-^2)} \sum_{\mathcal{S}_\mathcal{P}} \frac{\langle Z \begin{pmatrix} 1 \\ -1 \end{pmatrix}, \tilde{\mathbf{\Phi}}_k(Z) \rangle}{\|\tilde{\mathbf{\Phi}}_k(Z)\|^2} \left(\tilde{\mathbf{\Phi}}_k(Z) \cdot \mathbf{e}_1 \right) \lambda_k \sin(\lambda_k \tau) + \frac{c_-^2 - 1}{(c_+^2 - c_-^2)} \sum_{\mathcal{S}_\mathcal{P}} \frac{\langle Z \begin{pmatrix} 1 \\ -1 \end{pmatrix}, \tilde{\mathbf{\Phi}}_k(Z) \rangle}{\|\tilde{\mathbf{\Phi}}_k(Z)\|^2} \left(\tilde{\mathbf{\Phi}}_k(Z) \cdot \mathbf{e}_2 \right) \lambda_k \sin(\lambda_k \tau). \quad \text{(E.11)}$$

Using β in (49), $\tilde{\mathbf{\Phi}}_k(Z)$ in (57), $\|\tilde{\mathbf{\Phi}}_k(Z)\|^2$ in (60) and $\langle Z \binom{1}{-1}, \tilde{\mathbf{\Phi}}_k(Z) \rangle$ in (61) leads to

$$\begin{aligned} &\frac{c_\pm^2 - 1}{(c_+^2 - c_-^2)} \frac{\langle Z \binom{1}{-1}, \tilde{\mathbf{\Phi}}_k(Z) \rangle}{\|\tilde{\mathbf{\Phi}}_k(Z)\|^2} \left(\tilde{\mathbf{\Phi}}_k(Z) \cdot \mathbf{e}_{\frac{1}{2}} \right) = \\ &\pm \frac{c_-^2 - 1}{(c_+^2 - c_-^2)} \frac{2c_+^2 \cos\left(\frac{\lambda_k}{c_+}\right) \cos\left(\frac{\lambda_k}{c_-}\right) \left(\cos\left(\frac{\lambda_k}{c_+}\right) - \cos\left(\frac{\lambda_k}{c_-}\right) \right)}{\lambda_k^2 \left(\frac{c_+^2}{c_-^2} \frac{c_-^2 - 1}{c_+^2 - 1} \cos^2\left(\frac{\lambda_k}{c_+}\right) - \cos^2\left(\frac{\lambda_k}{c_-}\right) \right)} \cos\left(\frac{\lambda_k}{c_\mp} Z\right) \\ &\pm \frac{c_-^2 - 1}{(c_+^2 - c_-^2)} \frac{2c_+^2 \cos\left(\frac{\lambda_k}{c_\pm}\right) \left(\cos\left(\frac{\lambda_k}{c_+}\right) - \cos\left(\frac{\lambda_k}{c_-}\right) \right)}{\lambda_k^2 \left(\frac{c_+^2}{c_-^2} \frac{c_-^2 - 1}{c_+^2 - 1} \cos^2\left(\frac{\lambda_k}{c_+}\right) - \cos^2\left(\frac{\lambda_k}{c_-}\right) \right)} \sin\left(\frac{\lambda_k}{c_\mp}\right) \sin\left(\frac{\lambda_k}{c_\mp} Z\right), \end{aligned} \quad \text{(E.12)}$$

where upper/lower symbols $\pm$ & $\mp$ are combined with upper $\mathbf{e}_1 \equiv \binom{1}{0}$ /lower $\mathbf{e}_2 \equiv \binom{0}{1}$ symbol $\mathbf{e}_{\frac{1}{2}}$. The $\nu_s = 0$ spectrum limit (E.10) is the union of two distinct subsets, the contribution of which in (E.11) is now discussed separately.

- Fluid spectrum contribution

When $\nu_s = 0$ the fluid spectrum is $\lambda_{kF} = \pi\left(\frac{1}{2} + k\right)$. Furthermore, when $\nu_s \ll 1$, using (E.8), one finds $\cos^2\left(\frac{\lambda_{kF}}{c_-}\right) \sim O(\nu_s^2)$ and $\left(\frac{c_+^2}{c_-^2} \frac{c_-^2 - 1}{c_+^2 - 1} \cos^2\left(\frac{\lambda_{kF}}{c_+}\right)\right) \sim O(\nu_s)$. The $\nu_s \ll 1$, asymptotic behavior of (E.12) can be obtained using

(E.6), (E.7) and (E.8) and results in

$$\frac{c_+^2-1}{\left(c_+^2-c_-^2\right)}\frac{\langle Z\left(\begin{smallmatrix}1\\-1\end{smallmatrix}\right),\tilde{\mathbf{\Phi}}_k(Z)\rangle}{\|\tilde{\mathbf{\Phi}}_k(Z)\|^2}\left(\tilde{\mathbf{\Phi}}_k(Z)\cdot\mathbf{e}_1\right) = (-1)^k\frac{2\sin\left(\lambda_{kF}Z\right)}{\lambda_{kF}^2}+O\left(\nu_s\right), \quad \text{(E.13)}$$

$$\frac{c_-^2-1}{\left(c_+^2-c_-^2\right)}\frac{\langle Z\left(\begin{smallmatrix}1\\-1\end{smallmatrix}\right),\tilde{\mathbf{\Phi}}_k(Z)\rangle}{\|\tilde{\mathbf{\Phi}}_k(Z)\|^2}\left(\tilde{\mathbf{\Phi}}_k(Z)\cdot\mathbf{e}_2\right) = O\left(\nu_s\right). \quad \text{(E.14)}$$

- Solid spectrum contribution

When $\nu_s = 0$ the solid spectrum is $\lambda_{kS} = \sqrt{\mu_a}\pi\left(1+k\right)$. In this case, (E.12)'s denominators do not cancel each other so that the $\nu_s \ll 1$ behavior is trivial,

$$\frac{c_\pm^2-1}{\left(c_+^2-c_-^2\right)}\frac{\langle Z\left(\begin{smallmatrix}1\\-1\end{smallmatrix}\right),\tilde{\mathbf{\Phi}}_k(Z)\rangle}{\|\tilde{\mathbf{\Phi}}_k(Z)\|^2}\left(\tilde{\mathbf{\Phi}}_k(Z)\cdot\mathbf{e}_{\begin{smallmatrix}1\\2\end{smallmatrix}}\right) = O\left(\nu_s\right). \quad \text{(E.15)}$$

Combining (E.8)-(E.15) in (E.11), finally leads to [31]'s leading order solution

$$\lim_{\nu_s\to 0}\left(P(Z,\tau)\right) = 2\sum_{k=0}^{\infty}(-1)^k\frac{\sin\left(\lambda_{kF}Z\right)\sin\left(\lambda_{kF}\tau\right)}{\lambda_{kF}}. \quad \text{(E.16)}$$

Appendix F. Analytical analysis of $\frac{\boldsymbol{\beta c_-\kappa_-}}{\boldsymbol{c_+\kappa_+}}$

Let us set up

$$\chi = \frac{1-\frac{2\nu_s\mathcal{D}}{\alpha(2+\alpha)(c_+^2-1)}}{1-\frac{2\nu_s\mathcal{D}}{\alpha(2+\alpha)(c_-^2-1)}}, \quad \text{(F.1)}$$

so that invoking the definition of $\kappa_\pm$ in (68), it leads to

$$\frac{\kappa_-}{\chi\kappa_+} = \frac{1+\frac{2\nu_s}{c_-^2-1}}{1+\frac{2\nu_s}{c_+^2-1}}\frac{1-\frac{2\nu_s\mathcal{D}}{\alpha(2+\alpha)(c_-^2-1)}}{1-\frac{2\nu_s\mathcal{D}}{\alpha(2+\alpha)(c_+^2-1)}}. \quad \text{(F.2)}$$

Reorganizing (F.2) then follows

$$\frac{\kappa_-}{\chi\kappa_+} = \left(\frac{c_+^2-1}{c_-^2-1}\right)^2\left(\frac{c_-^2-1+2\nu_s}{c_+^2-1+2\nu_s}\right)\left(\frac{c_-^2-1-\frac{2\nu_s\mathcal{D}}{\alpha(2+\alpha)}}{c_+^2-1-\frac{2\nu_s\mathcal{D}}{\alpha(2+\alpha)}}\right). \quad \text{(F.3)}$$

Developing the term

$$\left(c_\pm^2-1+2\nu_s\right)\left(c_\pm^2-1-\frac{2\nu_s\mathcal{D}}{\alpha(2+\alpha)}\right) =$$
$$c_\pm^4-c_\pm^2\left[1+\frac{2\nu_s\mathcal{D}}{\alpha(2+\alpha)}+1-2\nu_s\right]+1+\frac{2\nu_s\mathcal{D}}{\alpha(2+\alpha)}-2\nu_s-\frac{4\nu_s^2\mathcal{D}}{\alpha(2+\alpha)}, \quad \text{(F.4)}$$

whilst using relation (14) for dimensionless wave speeds in (F.4) leads to

$$\left(c_{\pm}^2-1+2\nu_s\right)\cdot\left(c_{\pm}^2-1-\frac{2\nu_s\mathcal{D}}{\alpha(2+\alpha)}\right)= \\ -\left(c_{\pm}^2-1\right)\left[1+\frac{2\nu_s\mathcal{D}}{\alpha(2+\alpha)}-2\nu_s-\mathcal{C}_s^2-\frac{4\nu_s^2\mathcal{D}}{\alpha(2+\alpha)}\right], \quad \text{(F.5)}$$

so that using β definition (49) within (F.3) simplifies to

$$\frac{\kappa_-}{\chi\kappa_+}=\frac{c_+^2-1}{c_-^2-1}=\frac{c_+}{\beta c_-}. \quad \text{(F.6)}$$

Finally, one finds

$$\frac{c_-\beta\kappa_-}{c_+\kappa_+}=\chi=\frac{1-\frac{2\nu_s\mathcal{D}}{\alpha(2+\alpha)(c_+^2-1)}}{1-\frac{2\nu_s\mathcal{D}}{\alpha(2+\alpha)(c_-^2-1)}}. \quad \text{(F.7)}$$

Appendix G. Derivation of $\tilde{\mathbf{\Phi}}_k(Z)$ for second configuration (Cf. Fig.1b)

Let us focus on the second configuration boundary matrices (69) along with the homogeneous system upon $\left(\mathbf{\Phi}_k(0),\partial_Z\mathbf{\Phi}_k(0)\right)^T$ in (33). Using (D.1), it follows

$$\begin{pmatrix} 1 & \frac{\beta c_-}{c_+} & 0 & 0 \\ 0 & 0 & \frac{1}{c_-} & \frac{1}{c_+} \\ -\frac{\lambda_k\kappa_-\sin\left(\frac{\lambda_k}{c_-}\right)}{c_-} & -\frac{\lambda_k\kappa_+\sin\left(\frac{\lambda_k}{c_+}\right)}{c_+} & \kappa_-\cos\left(\frac{\lambda_k}{c_-}\right) & \kappa_+\cos\left(\frac{\lambda_k}{c_+}\right) \\ \cos\left(\frac{\lambda_k}{c_-}\right) & \frac{\beta c_-\kappa_-}{c_+\kappa_+}\cos\left(\frac{\lambda_k}{c_+}\right) & \frac{c_-\sin\left(\frac{\lambda_k}{c_-}\right)}{\lambda_k} & \frac{\beta c_-\kappa_-\sin\left(\frac{\lambda_k}{c_+}\right)}{\kappa_+} \end{pmatrix}\begin{pmatrix}\phi_k^-\\ \phi_k^+\\ \partial_Z\phi_k^-\\ \partial_Z\phi_k^+\end{pmatrix}=\mathbf{0}. \quad \text{(G.1)}$$

Using the first two lines simplifies to

$$\begin{pmatrix} -\frac{\lambda_k}{c_-}\left[\sin\left(\frac{\lambda_k}{c_-}\right)-\frac{\kappa_+}{\beta\kappa_-}\sin\left(\frac{\lambda_k}{c_+}\right)\right] & \cos\left(\frac{\lambda_k}{c_-}\right)-\frac{\kappa_+}{\kappa_-}\cos\left(\frac{\lambda_k}{c_+}\right) \\ \cos\left(\frac{\lambda_k}{c_-}\right)-\frac{\kappa_-}{\kappa_+}\cos\left(\frac{\lambda_k}{c_+}\right) & \frac{c_-}{\lambda_k}\left[\sin\left(\frac{\lambda_k}{c_-}\right)-\frac{\beta\kappa_-}{\kappa_+}\sin\left(\frac{\lambda_k}{c_+}\right)\right] \end{pmatrix}\begin{pmatrix}\phi_k^-\\ \partial_Z\phi_k^-\end{pmatrix}=\mathbf{0}, \quad \text{(G.2)}$$

and

$$\phi_k^+=-\frac{c_+}{\beta c_-}\phi_k^- \quad \text{, and, } \quad \partial_Z\phi_k^+=-\frac{c_+}{c_-}\partial_Z\phi_k^-. \quad \text{(G.3)}$$

Let us check out the following relation

$$\frac{\sin\left(\frac{\lambda_k}{c_-}\right)-\frac{\kappa_+}{\beta\kappa_-}\sin\left(\frac{\lambda_k}{c_+}\right)}{\cos\left(\frac{\lambda_k}{c_-}\right)-\frac{\kappa_+}{\kappa_-}\cos\left(\frac{\lambda_k}{c_+}\right)}=-\frac{\cos\left(\frac{\lambda_k}{c_-}\right)-\frac{\kappa_-}{\kappa_+}\cos\left(\frac{\lambda_k}{c_+}\right)}{\sin\left(\frac{\lambda_k}{c_-}\right)-\frac{\beta\kappa_-}{\kappa_+}\sin\left(\frac{\lambda_k}{c_+}\right)}. \tag{G.4}$$

The (G.4) holds only if

$$\begin{aligned}\sin^2\left(\frac{\lambda_k}{c_-}\right)-\left[\frac{\beta\kappa_-}{\kappa_+}+\frac{\kappa_+}{\beta\kappa_-}\right]\sin\left(\frac{\lambda_k}{c_-}\right)\sin\left(\frac{\lambda_k}{c_+}\right)+\sin^2\left(\frac{\lambda_k}{c_+}\right)=\\ -\cos^2\left(\frac{\lambda_k}{c_-}\right)+\left[\frac{\kappa_-}{\kappa_+}+\frac{\kappa_+}{\kappa_-}\right]\cos\left(\frac{\lambda_k}{c_-}\right)\cos\left(\frac{\lambda_k}{c_+}\right)-\cos^2\left(\frac{\lambda_k}{c_+}\right),\end{aligned} \tag{G.5}$$

or otherwise

$$\begin{aligned}\frac{1}{\beta}\left[1+\left(\frac{\kappa_-\beta}{\kappa_+}\right)^2\right]\sin\left(\frac{\lambda_k}{c_-}\right)\sin\left(\frac{\lambda_k}{c_+}\right)+\left[1+\left(\frac{\kappa_-}{\kappa_+}\right)^2\right]\cos\left(\frac{\lambda_k}{c_-}\right)\cos\left(\frac{\lambda_k}{c_+}\right)\\ =\frac{2\kappa_-}{\kappa_+},\end{aligned} \tag{G.6}$$

which is the transcendent spectrum (73) satisfied by λ_k. Introducing ξ_k

$$\xi_k=\frac{\sin\left(\frac{\lambda_k}{c_-}\right)-\frac{\kappa_+}{\beta\kappa_-}\sin\left(\frac{\lambda_k}{c_+}\right)}{\cos\left(\frac{\lambda_k}{c_-}\right)-\frac{\kappa_+}{\kappa_-}\cos\left(\frac{\lambda_k}{c_+}\right)}, \tag{G.7}$$

thus leads to

$$\partial_Z\phi_k^-=\frac{\lambda_k\xi_k}{c_-}\phi_k^-. \tag{G.8}$$

Finally, using the expression of ϕ_k^+, $\partial_Z\phi_k^+$, $\partial_Z\phi_k^-$ versus ϕ_k^- in (G.3)-(G.8) and the equations set (30)-(32) in case of a separate pressure–velocity boundary conditions (i.e $\mathbf{T}\equiv\mathbf{T}_s$ such as transfer matrices order are divided by two) results in

$$\mathbf{\Phi}_k(Z)=\phi_k^-\left[\begin{pmatrix}\cos\left(\frac{\lambda_k}{c_-}Z\right)\\ -\frac{c_+}{\beta c_-}\cos\left(\frac{\lambda_k}{c_+}Z\right)\end{pmatrix}+\xi_k\begin{pmatrix}\sin\left(\frac{\lambda_k}{c_-}Z\right)\\ -\frac{c_+}{c_-}\sin\left(\frac{\lambda_k}{c_+}Z\right)\end{pmatrix}\right], \tag{G.9}$$

so that the reduced form of $\mathbf{\Phi}_k(Z)$, $\tilde{\mathbf{\Phi}}_k(Z)$ is consequently

$$\tilde{\mathbf{\Phi}}_k(Z)=\begin{pmatrix}\cos\left(\frac{\lambda_k}{c_-}Z\right)+\xi_k\sin\left(\frac{\lambda_k}{c_-}\right)\\ -\frac{c_+}{\beta c_-}\left[\cos\left(\frac{\lambda_k}{c_+}Z\right)+\beta\xi_k\sin\left(\frac{\lambda_k Z}{c_+}\right)\right]\end{pmatrix}. \tag{G.10}$$

Chapter 3

Asymptotic analyses of liquid-filled pipe systems

Contents

This chapter aims to reconcile the liquid-filled pipe hydraulic description of water-hammer, i.e. the wall shear stress viscous friction modeling at fluid-solid interface, with mechanical viewpoint, i.e. axial ν_s-driven FSI interactions. For FSI couplings with the thin viscous boundary layer located at the fluid-pipe interface, a rigorous asymptotic-based theoretical framework is established. While the leading order reconciles known undamped four-FSI models, [Tijsseling, 2007], the first order viscous corrections informs on the damping trend, through in-depth description of the FSI shear couplings, and phase shift. A brief literature review is thereafter provided before the new low-Mach number and long-wavelength FSI framework is established in the hereby given article.

3.1 Basic asymptotic concepts

This section is dedicated to the presentation of basics asymptotic method concepts such as: (i) asymptotic expansion, (ii) boundary layer matching theories and, (iii) multi-time scale analysis.

3.1.1 Asymptotic expansion

The basic asymptotic developments rely on an expansion, upon a strategic small parameter δ, of the physical fields of interest. Similar to a Taylor expansion, the regular expansion of any physical field f reads

$$f = f^{(0)} + \delta f^{(1)} + \sum_{n=2}^{\infty} \delta^n f^{(n)}. \tag{3.1}$$

The first r.h.s term of (3.1) is denoted as *leading order* and describes the unperturbed response of the physical system (in our case, without viscous damping). The *first order*, i.e. $f^{(1)}$, and *n-order* n corrections, i.e. $f^{(n)}$, then correct the leading-order dynamics. Asymptotic theories permit to simplify complex problems, from ordering the dominant physical phenomena (often allowing its linearization). Noteworthy the asymptotic sequence is not always regular as (3.1) but may involve several dimensionless small numbers, each of them embodying a distinct physical phenomena.

3.1.2 Boundary layer model

The asymptotic theory of boundary layer consists in dividing the near-wall flow in several regions described by a different physics. Here, we consider this concept from analyzing the velocity profile of an oscillating incompressible flow occurring in a circular, in-extensible, tube. This paragraph closely follows the derivation of [Leal, 2007]. In the complex plane and dimensionless form, the pulsatile Poiseuille problem is governed by (Cf. eq. (3-266) of [Leal, 2007])

$$\left(\partial_\tau - \frac{\partial_R}{R}\left(R\partial_R\right)\right) W^c = e^{iR_\omega \tau}, \tag{3.2}$$

with dimensionless radial R, longitudinal length Z and time τ defined as

$$[r,t] = \left[R_0 R, \frac{R^2}{\nu_f}\tau\right], \tag{3.3}$$

$$W(r,t) = \mathcal{R}\left[W^c(R,\tau)\right], \tag{3.4}$$

where $\mathcal{R}$ stands for the real part contribution and

$$R_\omega = \frac{\omega R_0^2}{\nu_f} \gg 1, \tag{3.5}$$

is the Womersley number, the reciprocal of which is the small parameter herein. The complex axial velocity field W^c, is searched as a separated function of R and τ, i.e. $W^c = H(R)e^{iR_\omega \tau}$, whilst the radial amplitude is expanded following the regular asymptotic sequence in the $R_\omega \gg 1$ limit

$$H(R) = H^0(R) + \frac{1}{R_\omega} H^1(R) + O\left(R_\omega^{-2}\right), \tag{3.6}$$

then yielding

$$\left(iR_\omega - \frac{\partial_R}{R}\left(R\partial_R\right)\right)\left(H^0 + \frac{1}{R_\omega}H^1\right) = 1. \tag{3.7}$$

Combining (3.7) with (3.6) achieves as follows

$$H^0 = 0 \quad \text{, and,} \quad H^1 = -i. \tag{3.8}$$

This solution nevertheless vanishes when $\frac{\partial_R}{R}\left(R\partial_R\right) \sim O\left(R_\omega\right)$ except for a small region close to the wall. This is where the boundary layer comes into play. A re-scaled boundary layer variables and fields thus have to be defined, which accounts for the change of the radial gradient amplitude. Let us introduce the boundary layer coordinate $y = \sqrt{R_\omega}\left(1 - R\right)$, along with the radial amplitude in the boundary layer $h(y) \approx h^0 + \frac{1}{R_\omega}h^1$. The constitutive equation (3.7) in the boundary layer then reads

$$R_\omega\left(i - \partial_y^2 + \frac{1}{\sqrt{R_\omega}}\frac{\partial_y}{1 - \frac{y}{\sqrt{R_\omega}}}\right)\left(h^0 + \frac{1}{R_\omega}h^1\right) = 1, \tag{3.9}$$

the solution of which is

$$h^0 = 0 \quad \text{, and,} \quad h^1 = -i + Ae^{i\sqrt{i}y} + Be^{-i\sqrt{i}y}, \tag{3.10}$$

with (A, B) being integration constants. Since at the not moving fluid-solid interface $W^c = 0$, i.e. $h(0) = 0$, it yields

$$h^1 = i\left[-1 + e^{-i\sqrt{i}y}\right] + A\left[e^{i\sqrt{i}y} - e^{-i\sqrt{i}y}\right]. \tag{3.11}$$

It now remains to match outer, i.e. (3.8), with inner, i.e. (3.11), at boundary layer. One simple rule for matching is here

$$\lim_{R\to 0} H^1 = \lim_{y\to\infty} h^1, \tag{3.12}$$

which is satisfied for $A = 0$, since $i\sqrt{i} = \frac{\sqrt{2}}{2}\left(1 + i\right)$. Here the boundary layer matching is trivial but it sometimes needs the use of a the stretching variable technique [Hinch, 1991]. This method will be later on used in §3.3. Finally, a solution is found

$$W^c(R, Z, \tau) = \frac{e^{iR_\omega\tau}}{R_\omega}\begin{cases} -i \quad \text{, outer region,} \\ -i\left[1 - e^{-i\sqrt{iR_\omega}(1-R)}\right] \quad \text{, inner region,} \end{cases} \tag{3.13}$$

which accounts for the boundary layer structure as depicted in Figure 3.1

3.1.3 Asymptotic multi-time scale concept

Whilst the boundary layer approach delineates space in distinct regions, the asymptotic multi-time method splits the physical time in several time regions. It assumes

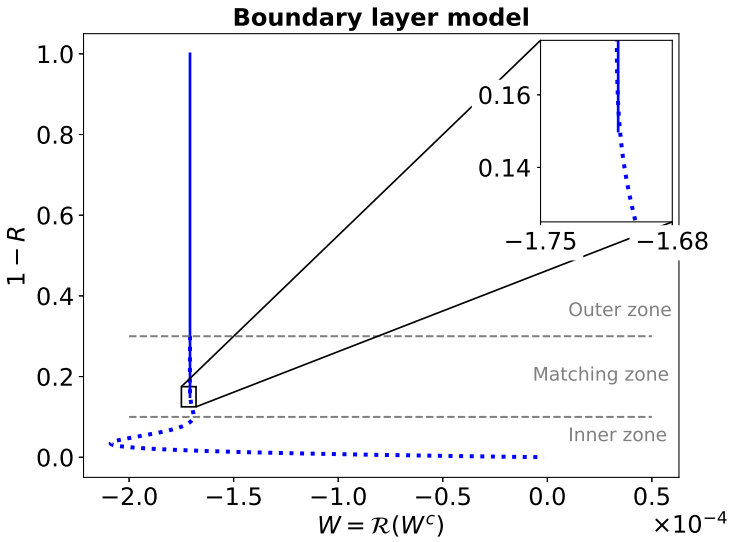

Figure 3.1: *Boundary layer model of a pulsatile incompressible flow in a circular tube, ($R_\omega = 4 \cdot 10^3$, $\tau = 1$).*

that the physical corrections to the leading order solution occurs in a different time-scale. A *fast* time is associated to the leading order development whereas a *slow* time is set up on characteristic corrections time-scales, which informs on the system damping (in our case). The concept of multi-time scale is hereafter introduces regarding the response of a damped oscillator, a study-case investigated in [Hinch, 1991]. The oscillator position, $\theta(t)$, is governed by the time-dependent ODE

$$\left(\partial_t^2 - \gamma\partial_t + 1\right)\theta = 0, \quad \partial_t\theta(0) = 0 \quad \text{, and,} \quad \theta(0) = 1, \tag{3.14}$$

with $\gamma \ll 1$ a small parameter governing the long time damping effects imposed on the oscillator system. Here, an analytical solution is known for (3.14)

$$\theta(t) = e^{-\frac{\gamma t}{2}}\left(\cos\left(\sqrt{\frac{4-\gamma^2}{4}}t\right) + \frac{\gamma}{2}\sqrt{\frac{4}{4-\gamma^2}}\sin\left(\sqrt{\frac{4-\gamma^2}{4}}t\right)\right), \tag{3.15}$$

but its not always true. Let us then define the fast time scale $\tau = t$ and the slow time scale $T = \gamma\tau$ such that

$$\partial_t = \partial_\tau + \gamma\partial_T. \tag{3.16}$$

Expanding the θ variable with respect to γ and taking into account the multi-time scale corrections reads

$$\theta(\tau) = \theta^0(\tau, T) + \gamma\theta^1(\tau, T) + O\left(\gamma^2\right), \tag{3.17}$$

whilst ordering the γ-corrections yields

$$\left(\partial_\tau^2 + 1\right)\theta^0 = 0 \quad \text{, and,} \quad \left(\partial_\tau^2 + 1\right)\theta^1 = -\partial_\tau\left[2\partial_T - 1\right]\theta^0. \tag{3.18}$$

Treating T as constant, the leading order only displays a fast time dependence and is governed by an harmonic oscillator

$$\theta^0(\tau,T) = H^0(T)\cos\Big(\tau+\phi^0(T)\Big) \quad \text{, with,} \quad H^0(0)=1 \quad \text{, and,} \quad \phi^0(0)=0, \tag{3.19}$$

whilst θ^1 is solution of

$$\left(\partial_\tau^2+1\right)\theta^1 = \left(2\partial_T H^0(T) - H^0(T)\right)\underbrace{\sin\left(\tau+\phi^0(T)\right)}_{\text{Resonant term}} + 2H^0(T)\underbrace{\cos\left(\tau+\phi^0(T)\right)}_{\text{Resonant term}}\partial_T\phi^0(T) \tag{3.20}$$

so that

$$\begin{aligned}\theta^1 &= H^1(T)\cos\Big(\tau+\phi^1(T)\Big)\\ &+ H^1(T)\left(2\partial_T H^0(T) - H^0(T)\right)\underbrace{\int_0^\tau \sin\Big(\tau-\tau^{'}+\phi^0(T)\Big)\cos\Big(\tau+\phi^1(T)\Big)\,d\tau^{'}}_{\text{Resonant term}}\\ &+ 2H^1(T)\partial_T\phi^0(T)H^0(T)\underbrace{\int_0^\tau \cos\Big(\tau-\tau^{'}+\phi^0(T)\Big)\cos\Big(\tau+\phi^1(T)\Big)\,d\tau^{'}}_{\text{Resonant term}}\end{aligned} \tag{3.21}$$

The resonant terms display a quadratic form of the l.h.s operator kernel, i.e. (∂_τ^2+1). Their contributions in θ^1, produce a linear divergence with respect to the fast time (accordingly to $\int_0^\tau \cos^2(\tau^{'})d\tau^{'} \sim \tau$), which collapses the asymptotic expansion when $\tau \equiv O\left(\gamma^{-1}\right)$. Then the long-time variable $(H^0(T),\phi^0(T))$ have to be set up in order to cancel out this fast-time divergences. This condition is known as the *secularity* condition and follows regarding (3.21) into

$$2\partial_T H^0(T) - H^0(T) = 0 \quad \text{, and,} \quad \partial_T\phi^0 = 0, \tag{3.22}$$

so that

$$H^0(T) = e^{-\frac{T}{2}} \quad \text{, and,} \quad \phi^0(T) = 0. \tag{3.23}$$

The leading order expression (3.19) along with the analytical solution of (3.14) are depicted in Figure 3.2 so as to provide additional insights on the multi-time scale method.

3.2 Liquid-filled pipe asymptotic analyses

The analysis of pressure wave propagation in pipes is suitable to the use of asymptotic techniques from the presence of the thin near-wall boundary layer as now discussed from a dedicated literature review. One of the first asymptotic approaches can be attributed to [Walker and Phillips, 1977]. The authors indeed performed a very clever asymptotic analysis of the liquid-filled pipe problem, embedding both the radial and axial FSI dynamics. They carried out an asymptotic expansion of the physical fields upon the ratio of the tube inner radius to its length ϵ, assumed to be small. At leading order, they recovered the R-invariant four-FSI equations

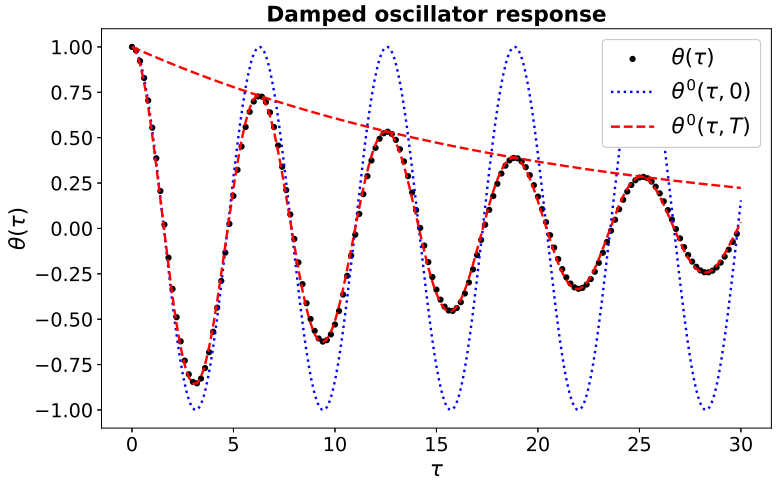

Figure 3.2: *Multi-time scale investigation of a damped oscillator ($\gamma = 0.1$).*

system of [Skalak, 1954, Skalak, 1956] (Cf. (1.28)-(1.31)). Up to order $O(\epsilon^2)$ corrections, they demonstrate the pipe radial inertia has very little effects on the overall dynamics. Considering time scale issues, if one chooses the advective time scale as the reference one, i.e. $t = (c_p/L)\tau$, then the pipe inertial phenomena is expected to develop upon the slow time scale $T = \epsilon^2\tau$. This asymptotic framework is known in the literature framework as the long-wavelength assumption, i.e. $\lambda \gg R_0$ with λ the signal wavelength, and allows to neglect inertial radial phenomena. For very short pipes, i.e. $\epsilon \sim O(1)$, this framework nevertheless vanishes and radial effects have to be considered. Some asymptotic analysis have also been performed from the hydraulic viewpoint, with the search of a viscous fluid wall shear model. The contributions of [Vardy and Brown, 1995, Vardy and Brown, 2004], presented in §1.4.2, thus carried out asymptotic matching upon the fluid axial velocity between the outer acoustic zone and its inner viscous counterpart. These theories follow the matching techniques previously spelled out in §3.1.2, and yielded to the derivation of a convoluted, Reynolds-dependent, kernel to describe the fluid wall shear rate evolution. Nevertheless, these analyses neither consider multi time-scale approach nor tube motion (i.e. zero fluid wall speed assumption). [Corli et al., 2012] focused on the development of fluid hyperbolic equations (1.40), and carried-out an asymptotic expansion upon the re-scaled Mach number $\mathcal{M} = \frac{W_0}{c_p}$. They embedded a Darcy-Weisbach damping term (1.41) to their system. Similarly, a Mach asymptotic expansion was carried out by [Yao et al., 2014] with the distinction of using the IMAB damping model (Cf. §1.4.2). In recent years, the asymptotic [Walker and Phillips, 1977]'s framework was extended by [Kizilova, 2006, Čanić et al., 2006a, Čanić et al., 2006b] for the determination of an oscillating flow-rate and blood pressure responses in visco-elastic blood vessels. Both authors carried out an asymptotic analysis in ϵ for both the solid and the viscous, incompressible, fluid equations. They rigorously managed the fluid-solid interface continuity conditions and considered a three dimensional-based solid rheology. While the one-

dimensional models [Tijsseling, 1993, Tijsseling, 2007] suffer from the need of a closure wall shear rate model (Cf. §1.4.2), the three-dimensional approach yields to a well-posed closed problem. Quoting [Čanić et al., 2006a]: "*The one-dimensional model is obtained by averaging the three-dimensional compressible Navier–Stokes equations over the cross-section of the vessel. In this process of dimension reduction a typical question of "closure" needs to be resolved. More precisely, averaging over the cross-section of the vessel does not lead to a well-posed problem unless extra information is provided*". Each of these analyses furthermore embed both FSI and fluid viscous effects, then making a first attempt to reconcile the hydraulic and mechanic viewpoint of the liquid-filled pipe subject, something which should be highlighted. Despite the evident elegance of the [Kizilova, 2006, Čanić et al., 2006a, Čanić et al., 2006b]'s approaches, the incompressible model used to model the fluid dynamics is not well suited to investigate overpressure waves propagation in liquid-filled pipe systems. Furthermore, [Čanić et al., 2006a] considered the pipe (or more precisely the vessels) as longitudinally tethered, then neglecting the Poisson's coupling effects. More recently, [Mei and Jing, 2016, Mei and Jing, 2018] brilliantly performed an asymptotic analysis of the fluid hyperbolic equations upon parameter δ (1.49). Analyzing up to first order corrections, the authors successfully predicted the overall pressure viscous damping trend and closely match to the [Holmboe and Rouleau, 1967]'s experimental pressure signatures as depicted in Figure 3.3. The key parameter δ, which stands as the dimensionless boundary

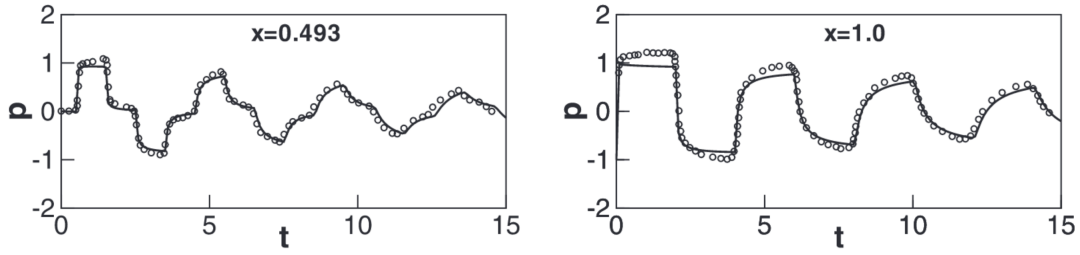

Figure 3.3: *[Mei and Jing, 2016]'s leading and first order dimensionless pressure solution (continuous line) in comparison with the experimental pressure signature of [Holmboe and Rouleau, 1967] (dotted line).*

layer thickness, can hereafter be interpreted as the ratio of the fluid shock-wave advective time-scale by the diffusive viscous one following

$$\delta^2 = \frac{L}{c_p}\frac{\nu_f}{R_0^2}. \tag{3.24}$$

The δ parameter thus seems suited to perform both multi-time scale development and boundary layers modeling. Noteworthy, this parameter was explicitly spelled out by [Holmboe and Rouleau, 1967] when investigating the experimental viscous pressure damping trend and is shown to characterize the wall shear rate order of magnitude in [Zielke, 1968]'s theory (Cf. (1.52) and (1.57)).
Some authors, [Wood and Funk, 1970, Vardy and Brown, 1995, Vardy and Brown,

2004] have conducted asymptotic analysis upon the pre-existing steady-state boundary condition though the use of δ_{st}, defined in (1.58). This distinction stems from a fundamental difference in physical interpretation. While δ_{st} underlies a static distribution of the fluid pressure gradient, the δ parameter is set up to model the dynamical response of the fluid boundary layer to dynamic gradient pressure solicitations.
The use of these models are nevertheless restricted to purely hydraulic analyses, i.e. in the limit $\nu_s \to 0$, since the solid dynamics is not included. Hence it is interesting to reconcile the FSI asymptotic analyses (e.g. [Walker and Phillips, 1977]), with the hydraulic ones (e.g. [Mei and Jing, 2016, Mei and Jing, 2018]) to achieve in a more general FSI-consistent model. This is accomplished in the next section.

3.3 Low Mach number theory of pressure waves inside an elastic tube: Article to *Mathematical Models and Methods in Applied Sciences*

Mathematical Models and Methods in Applied Sciences
© World Scientific Publishing Company

Low–Mach number theory of pressure waves inside an elastic tube

A. Bayle
Institut de Mécanique des Fluides de Toulouse, IMFT, Université de Toulouse, CNRS, Toulouse, France
alexandre.bayle@imft.fr

F. Plouraboué *
Institut de Mécanique des Fluides de Toulouse, IMFT, Université de Toulouse, CNRS, Toulouse, France
fplourab@imft.fr

Received (January 16, 2023)

We consider the pressure wave inside an elastic tube of internal radius R_0, thickness e, length L, shear modulus $\mathcal{G}$ and density ρ_{s_0}, filled with a fluid with kinematic viscosity ν_f. We theoretically analyze the fluid–structure coupling between: (i) the elastic sheath, (ii) the fluid boundary layer, and (iii) the core acoustic pressure and velocity fields. Our analysis provides an asymptotic derivation of the fluid–structure–interactions (FSI) model that recovers known pulse–wave velocities and provides a new theoretical prediction for the exponential time decay of the wave longitudinal attenuation envelope. Taking advantage of highly distinct time–scales between the viscous radial diffusion $\tau_d = R_0^2/\nu_f$ compared with wave–convective time $\tau_c = L/c_p$ as well as the elastic relaxation time $\tau_e = e\sqrt{\rho_s/\mathcal{G}}$, such that $\tau_e \sim \tau_c \ll \tau_d$ we perform a two time–scale asymptotic analysis based on a small parameter $\delta = \sqrt{\tau_c/\tau_d}$. Said parameter is obtained by balancing the momentum acceleration with the inner unsteady boundary–layer viscous damping, the thickness of which being δR_0. The resulting asymptotic sequence provides a unique consistent scaling for solid deformation and velocity fields. It necessitates up–to first–order to obtain the secularity condition associated with the leading–order slow–time scale envelope attenuation. On the one hand our approach reconciles both predictions for the precursive elastic wave and the pulse velocities obtained when considering solid deformation only, and, on the other hand, predictions for the longitudinal attenuation resulting from the effect of boundary layers only. Our analysis also permits the derivation of a new convoluted model for the wall shear stress, which is (FSI)–consistent. The theoretical results are successfully compared with experimental measurements.

Keywords: fluid–structure–interactions; acoustic waves in pipes; multiple time–scale analysis; asymptotic matching; water hammer; blood hammer; Lamé–Clapeyron equations.

*Corresponding author.

1. Introduction

Water–hammer pulsed pressure waves are a well–known, long–standing topic that arises in various practical contexts, such as hydraulic pipes. Examples include gas and petroleum transmission lines ([34,39,35,23,21,3]), blood vessels ([36,47]), fluidic system response ([24,25]), compressor dynamics and hydroelectric power generation, etc... Reviews of this topic are available from ([52,51,44,45,13]), the contents of which are not repeated here. Water–hammer waves are associated with the following three classes of coupling effects: (i) Poisson coupling, (ii) friction coupling, (iii) junction coupling.

Poisson coupling is related to the pipe's successive radial expansion–compression phases (also called pipe's breathing) induced by the fluid overpressure propagation in the solid. This not only generates hoop stress in the tube, but also axial deformation through Poisson's modulus ν_s, thus producing elastic longitudinal compression waves or so–called precursor waves, which have been analyzed by ([40,31,41,50,8]) for thin–walled pipes and by ([42,43]) for thick–walled pipes. These contributions leads to the derivation of four fluid–structure–interactions (FSI) equations for hyperbolic coupled systems ([45]). Additional vibrating modes may occur depending on the considered tube's degree of freedom (e.g. rolling, yawing and swaying; ([29,13])), but these are not consider in this analysis.

When, one considers, in addition to Poisson coupling the influence of junction couplings, i.e. couplings from dead–end tube connections, these four–(FSI) equations are most often solved numerically and more rarely in the frequency domain. The numerical methods are mainly based on the method of characteristics (MOC) in ([53,16,22,10,17]), whilst frequency domain analyses are performed using the transfer matrix method (TMM) framework ([55,28,2]), which displays Fourier peaks associated with the response of specific discrete modes. Time domain solutions of these four–(FSI) equations in simple configurations ([27,4]) display a discrete but infinite set of intrinsic vibrating modes that have distinct and specific wavelengths and frequencies (i.e. a discrete spectrum). On the contrary, when considering infinite, or semi–infinite tubes, then ignoring the junction coupling effects, the continuous propagation of modes with any wavelength and frequency arises (i.e. a continuum spectrum as in ([14,38,24,25])).

As with Poisson coupling, friction coupling occurs over the entire length of a pipe from boundary layer dissipation within the fluid. The transient response of boundary layer, i.e. the near–wall fluid velocity response to a transient solicitation, was studied by ([56]), who considered an axial momentum conservation equation that resulted in a history–dependent shear rate with a time–convolution with the longitudinal pressure gradient. ([56]) also provided an analytical approximation of the convolution kernel. Zielke's model exhibited excellent agreement with experiments by ([5,1]). This fluid friction influence was analyzed in greater depth within a boundary layer theory moving at wave–front speed by ([32,33]), who matched it with the outer fluid region. Furthermore, realizing that the time scale for viscous diffusion

within the boundary layer is comparable with the propagation time of the wave, ([11,32,33]) have proposed a two–time scale asymptotic expansion. This led to the deduction of a slow–time, mode–dependent exponentially amplitude decay of the pulse pressure wave. This approach accounts for the long–time damping of a liquid–filled pipe system.

This overview of various contributions illustrates that although many studies have been performed on the topic, which have provided deep insights into this complex subject as well as reliable predictions compared with measurements, no global and rational theoretical framework exists for re–conciliating the various aspects of water–hammer wave propagation.

This paper presents a systematic asymptotic analysis of classical water–hammer pulsed pressure waves for an elastic tube that exploits the following assumptions: (a) small displacements, (b) weak fluid compressibility, (c) long–wavelengths and (d) a thin viscous boundary layer. The novelty of this study lies into providing a comprehensive and exhaustive analysis of the various couplings established from first principles, using a dimensionless formulation associated with a complete set of dimensionless numbers. Some of them are small, and their relative smallness is clarified.

The aforementioned four assumptions (a–b–c and d) are associated with the following four dimensionless parameters: the tube aspect ratio ϵ, the tube thickness to radius ratio α, the pulse wave Mach number $\mathcal{M}$ and the inverse of the pulse wave–speed Reynolds number $1/Re_p$. From these, a useful dimensionless parameter $\delta = 1/\sqrt{\epsilon Re_p}$ (which is also the square root of the convective to diffusive time–scale as well as the dimensionless boundary layer thickness) is defined, the relative smallness of which is of special interest in our analysis (i.e. $\delta^2 \gg \mathcal{M}$, $\delta \gg \epsilon^2$, $\delta \gg \alpha\mathcal{M}$, and $1 \gg \epsilon \gg \alpha\mathcal{M}$). As discussed in many studies (e.g. ([50,25,43])), the correction to the long–wavelength approximation is $O(\epsilon^2)$. During the course of the derivation this long–wavelength assumption will be seen to also imply negligible radial acceleration of the pipe breathing motion, as well as radially uniform longitudinal displacement inside the solid similar to a planar elastic wave propagation at leading–order. This leading–order planar elastic wave in the solid is coupled with the fluid pressure wave, leading to a set of two coupled propagating waves with two specific propagating velocities, equivalently described by the four aforementioned (FSI) equations. The solution to these leading–order propagating wave problems can be found analytically using an orthogonal base decomposition, as in the study of ([4]). It depends on the applied boundary conditions from the vibrating (FSI) up to some slowly varying (undefined at this order) amplitudes, which are specific for each mode. Conducting an evaluation of the corrections to these leading–order solutions while considering a two–time–scale asymptotic analysis leads to determining the amplitude decay, which depends on viscous effects that arise in boundary layers. Hence, the presented derivation is not only interesting for the asymptotic derivation of the four–(FSI) equations associated with fluid pressure/solid elastic wave coupled propagation. It also permits to determine how viscous effects damp

this propagation, generalizing ([32,33]) from including (FSI) effects. Although applicable to general junction coupling conditions, the hereby derived (FSI) damping is explicitly provided for a specific set of boundary conditions and compared with experimental observations.

The remainder of this paper is organized as follows. Section §2 describes the fundamental dimensionless equations in the three considered distinct regions, namely the fluid bulk, fluid boundary layer, and elastic solid. A consistency condition for small elastic deformation is found, which motivates a more systematic analysis of the asymptotic framework developed in §3. Through defining the various corrections associated with three small parameters, namely the dimensionless thickness of the viscous boundary layer, Mach number, and tube aspect ratio, a systematic asymptotic analysis is presented in §3 and coupled with a two–time scale one. Section §3 involves the derivation of coupled (FSI) leading– and first–order corrections associated with the small parameter of the dimensionless viscous boundary layer thickness, δ , as well as the resolution of their coupling using asymptotic matching. The analysis finally permits the establishment of the (FSI) wave model with two–coupled propagative equations with additional dissipative terms included as corrections. In §4 the (FSI) waves model is solved (both at leading– and first–orders) so as to find the secularity condition for the slow–time amplitude of the leading–order, thus providing the (FSI) wave system's attenuation. Finally §5 compares the proposed low–Mach theory with experimental measurements, considering longitudinal damping predictions in particular.

2. Fundamental equations

A pressure wave having typical velocity c_p propagating on top of a non-zero steady flow, inside a fluid-filled elastic-walled tube is considered. Dimensional fields will be denoted with the superscript *.

2.1. *Definitions overview and problem setting*

We consider an initially circular tube of length L, inner radius R_0, wall thickness e, density ρ_{s_0}, Young's modulus E and Poisson's ratio ν_s. The tube is supposed elastic and isothermal. It is filled with a Newtonian, weakly compressible, and isothermal fluid, having possibly varying density ρ_f^*, isentropic bulk modulus $\mathcal{K}_f$, kinematic viscosity ν_f, dynamic viscosity μ_f, volume viscosity λ_f, and the viscosity ratio $\Gamma = \lambda_f/\mu_f \sim O(1)$. The fluid is supposed initially flowing at the velocity W_{st}^*, under the steady–state pressure P_{st}^*, condition. The constant fluid reference density is denoted ρ_{f_0}. The steady–state flow is taken unidirectional and gravity effects are neglected. The dimensionless tube thickness and aspect ratio are defined as

$$\alpha = \frac{e}{R_0}, \quad \& \quad \epsilon = \frac{R_0}{L} \ll 1. \tag{2.1}$$

Thereafter, α is considered to be an order one quantity, but the thin–wall limit $\alpha \ll 1$ is sometimes discussed in comparison with thin–shell theory. A more precise

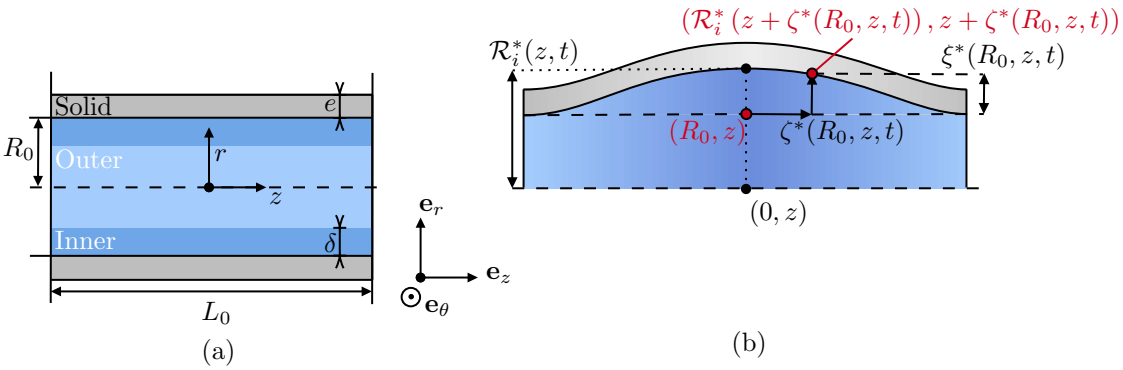

Fig. 1: (a) Geometrical and coordinate variables. (b) Tube's deformation, i.e. pipe *breathing*, induced by the local fluid over-pressure. The initial material point vector (R_0, z), is transported by the solid displacement vector (ξ^*, ζ^*)

condition for large α values will be discussed in section 3. In the following, inner region refers to the near–wall viscous boundary layer whereas outer region stands for the core inviscid flow one. The dimensionless thickness of the boundary layer is referred to as δ, being a central small parameter of the study. Capital letters refer to outer fields in the fluid core, while lowercase letters are associated with the inner boundary layer. The fluid–filled pipe system is axisymmetric and described by cylindrical radial/axial coordinates (r, z), having basis vectors $(\mathbf{e}_r, \mathbf{e}_z)$, and dimensionless counterparts $(R = r/R_0, Z = z/L)$. A dimensionless *fast* time $\tau = c_p\, t/L$, is build upon the wave speed advective time-scale L/c_p. As the pressure waves propagate, the elastic tube deforms and solid material points are transported by solid displacement vector

$$\boldsymbol{\xi}^*(r,z,t) = \xi^*(r,z,t)\mathbf{e}_r + \zeta^*(r,z,t)\mathbf{e}_z, \tag{2.2}$$

where (ξ^*, ζ^*) are the radial and axial solid displacement components, respectively. We then define $(\mathbf{n}_i, \mathbf{n}_o)$ and $(\mathbf{t}_i, \mathbf{t}_o)$ as the unit normal and tangential vectors associated with the inner $\mathcal{R}_i^*(z,t) = R_0\mathcal{R}_i(Z,\tau)$ and outer, $\mathcal{R}_o^*(z,t) = R_0\mathcal{R}_o(Z,\tau)$, tube radius. The tube inner radius depends on the displacement components as

$$\mathcal{R}_i^*(z+\zeta^*(R_0,z,t),t) = R_0 + \xi^*(R_0,z,t). \tag{2.3}$$

All variables are depicted in Figure 1. The outer/inner fluid pressure P_f^*/p_f^*, axial velocity W_f^*/w_f^*, and radial velocity U_f^*/u_f^*, are splitted into steady, denoted with subscript st, and unsteady components (without subscript) following the classical acoustic approach, ([30])

$$P_f^* = P^*(r,z,t) + P_{st}^*(r,z), \qquad p_f^* = p^*(r,z,t) + p_{st}^*(r,z), \tag{2.4}$$

$$W_f^* = W^*(r,z,t) + W_{st}(r,z), \qquad w_f^* = w^*(r,z,t) + w_{st}^*(r,z), \tag{2.5}$$

$$U_f^* = U^*(r,z,t), \qquad u_f^* = u^*(r,z,t). \tag{2.6}$$

As the steady–state is assumed unidirectional, the outer/inner radial velocity components U_f^*/u_f^*, are only unsteady. Finally, the fluid inner stress tensor, unsteady shear stress and unsteady wall shear rate are defined, following a Newtonian rheology, as $\boldsymbol{\sigma}_f^* = \boldsymbol{\sigma}_{st}^* + \boldsymbol{\sigma}^*$, τ_f^*, τ_w^*

$$\boldsymbol{\sigma}_{st}^* = \left(-P_{st}^* + \lambda_f \partial_z W_{st}^*\right)\mathbf{I} + \mu_f \begin{pmatrix} 0 & \cdots & \partial_r W_{st}^* \\ \cdots & 0 & \cdots \\ \partial_r W_{st}^* & \cdots & 0 \end{pmatrix}, \tag{2.7}$$

$$\boldsymbol{\sigma}^* = \left(-p^* + \lambda_f \left[\frac{\partial_r}{r}\left(ru^*\right) + \partial_z w^*\right]\right)\mathbf{I} + 2\mu_f \begin{pmatrix} \partial_r u^* & \cdots & \frac{\partial_r w^* + \partial_z u^*}{2} \\ \cdots & \frac{u^*}{r} & \cdots \\ \frac{\partial_r w^* + \partial_z u^*}{2} & \cdots & \partial_z w^* \end{pmatrix}, \tag{2.8}$$

$$\tau_f^* = -\rho_{f_0}\nu_f \partial_r w^*, \quad \& \quad \tau_w^* = \tau_f^*\left(\mathcal{R}_i^*, z, t\right). \tag{2.9}$$

2.2. *Dimensionless numbers set and hypothesis framework*

When an unsteady fluid velocity perturbation of magnitude W_0, is applied to a liquid–filled pipe system, an acoustic pressure pulse with velocity c_p then propagate, the magnitude of which denoted ΔP_0 is given by ([21])'s law

$$\Delta P_0 = \rho_{f_0} c_p W_0. \tag{2.10}$$

The longitudinal wave speed propagation in the fluid, c_p, and in the solid, c_s, has been provided by ([45,43])

$$c_0 = \sqrt{\frac{\mathcal{K}_f}{\rho_{f_0}}}, \quad \& \quad c_p = \frac{c_0}{\sqrt{1 + \frac{2\mathcal{K}_f}{\alpha E}\left(\frac{2(1-\nu_s^2)}{2+\alpha} + \alpha(1+\nu_s)\right)}}, \quad \& \quad c_s = \sqrt{\frac{E}{\rho_{s_0}}}, \tag{2.11}$$

where c_0 is the speed of sound of acoustic waves into an infinite fluid and α is the dimensionless tube thickness provided in (2.1). The ratios of these speeds are denoted

$$\mathcal{C} = \frac{c_0}{c_p}, \quad \& \quad \mathcal{C}_s = \frac{c_s}{c_p}. \tag{2.12}$$

Since the elastic–walled tube offers resistance to the fluid overpressure, two dimensionless numbers (similar to Cauchy's number) are introduced to compare the wave dynamic pressure, i.e. $\rho_{f_0} c_p^2$, with the tube elastic resistance

$$\mathcal{C}_{\mathcal{G}} = \frac{\rho_{f_0} c_p^2}{\mathcal{G}} \equiv \frac{2\rho_{f_0} c_p^2 (1+\nu_s)}{E}, \quad \& \quad \mathcal{C}_{\lambda_s} = \frac{\rho_{f_0} c_p^2}{\lambda_s} \equiv \frac{\mathcal{C}_{\mathcal{G}}(1-2\nu_s)}{2\nu_s}, \tag{2.13}$$

where

$$\mathcal{G} = \frac{E}{2(1+\nu_s)}, \quad \& \quad \lambda_s = \frac{\nu_s E}{(1+\nu_s)(1-2\nu_s)}, \tag{2.14}$$

are the solid shear modulus and the second Lamé-Clapeyron coefficient, respectively. The overpressure wave velocity c_p, given in (2.11), is thus a corrective formulation of c_0 due to the tube elastic constraints. By introducing parameter

$$\chi = \frac{2\mathcal{K}_f}{\alpha E \mathcal{C}^2}\left(\frac{2(1-\nu_s^2)}{2+\alpha} + \alpha(1+\nu_s)\right) \equiv \frac{2\nu_s \mathcal{C}_{\lambda_s} + (1+\alpha)^2 \mathcal{C}_{\mathcal{G}}}{\alpha(2+\alpha)}, \tag{2.15}$$

the pulse wave speed (2.11) becomes

$$c_p^2 = \frac{c_0^2}{1+\chi\mathcal{C}^2}, \tag{2.16}$$

where $1+\chi\mathcal{C}^2$ is a corrective fluid pulse–wave speed factor. Regarding the definition of c_p in (2.11), it is relevant to highlight that $\mathcal{C}^2 > 1$ which follows from $c_p < c_0$ ([23,40,42,15]). The (FSI) behavior is finally impacted by the fluid to solid density ratio, ([45])

$$\mathcal{D} = \frac{\rho_{f_0}}{\rho_{s_0}}. \tag{2.17}$$

Finally, a set of dimensionless parameters associated with boundary layer thickness δ, Reynolds number Re, pulsed Reynolds number Re_p and Mach number $\mathcal{M}$ is introduced yielding to

$$Re_p = \frac{c_p R_0}{\nu_f} \gg 1, \qquad Re = \frac{W_0 R_0}{\nu_f} = \mathcal{M} Re_p, \tag{2.18}$$

$$\delta^2 = \frac{\nu_f L}{c_p R_0^2} = \frac{1}{\epsilon Re_p} \ll 1, \qquad \mathcal{M} = \frac{W_0}{c_p} \ll 1. \tag{2.19}$$

Low–Mach number ([16,10]), along with the long–wavelength, i.e. $\epsilon \ll 1$ ([26,31,50,43]), asymptotic analyses are simultaneously used in the forthcoming. The following asymptotic framework is assumed, for which boundary layer dissipation effects are dominant compare to compressible and radial solid inertial ones

$$\delta^2 \gg \mathcal{M} > \frac{\mathcal{M}}{\mathcal{C}^2}, \qquad \delta \gg \epsilon^2, \qquad \delta \gg \alpha\mathcal{M}, \qquad 1 \gg \epsilon \gg \alpha\mathcal{M}. \tag{2.20}$$

The hereby asymptotic ordering is in depth discussed and justified in §3, the relevance of which will be shown to provide an asymptotic derivation for known four–(FSI) equations model ([43]). Hence parameter δ being the ratio of viscosity diffusion time–scale ν_f/R_0^2, to advection one L/c_p, is the cornerstone small parameter of the proposed two–times–scale asymptotic analysis ([20,32]). In the inner region a rescaled radial coordinates y, scaling as $O(1/\delta)$, is set up

$$y = \frac{1-R}{\delta}, \tag{2.21}$$

to account for the influence of the radial gradient contributions in the boundary layer. The fluid and solid constitutive, dimensionless, equations are thereafter derived.

2.3. *Dimensionless Navier–Stokes equations*

The unsteady pressure component P^*, is scaled upon ([21])'s overpressure (2.10), whereas the unsteady fluid axial velocity is scaled on the steady–state one, i.e. W_0. In the radial direction, the unsteady fluid velocity is assumed ϵ smaller than the axial one, resulting from long–wavelength assumption, so that

$$P^*_{st} = \rho_{f_0} W_0^2 P_{st}(R,Z), \qquad W^*_{st} = W_0 W_{st}(R,Z), \tag{2.22}$$

$$P^* = \rho_{f_0} c_p W_0 P(R,Z,\tau), \qquad p^* = \rho_{f_0} c_p W_0 p(y,Z,\tau), \tag{2.23}$$

$$W^* = W_0 W(R,Z,\tau), \qquad w^* = W_0 w(y,Z,\tau), \tag{2.24}$$

$$U^* = \epsilon W_0 U(R,Z,\tau), \qquad u^* = \epsilon W_0 u(y,Z,\tau), \tag{2.25}$$

where unsteady outer/inner pressure and velocity field components are identically scaled to match at the boundary layer interface. Relevant at the fluid/solid interface, i.e. inside the boundary layer, the unsteady wall shear stress and wall shear rate responses, defined in (2.7)–(2.9), are scaled as follows

$$\tau_f^* = -\frac{\rho_{f_0}\nu_f W_0}{\delta R_0}\tau_f(y,Z,\tau), \qquad \tau_f = \partial_y w(y,Z,\tau), \tag{2.26}$$

$$\boldsymbol{\sigma}^* = \rho_{f_0} c_p W_0 \boldsymbol{\sigma}, \qquad \boldsymbol{\sigma}^*_{st} = \rho_{f_0} W_0^2 \boldsymbol{\sigma}_{st}, \tag{2.27}$$

$$\boldsymbol{\sigma}_{st} = \left(-P_{st} + \Gamma\frac{(\epsilon\delta)^2}{\mathcal{M}}\partial_Z W_{st}\right)\mathbf{I} + \frac{\epsilon\delta}{\mathcal{M}}\begin{pmatrix} 0 & \cdots & -\partial_y W_{st} \\ \cdots & 0 & \cdots \\ -\partial_y W_{st} & \cdots & \epsilon\delta\partial_Z W_{st}\end{pmatrix}, \tag{2.28}$$

$$\boldsymbol{\sigma} = \left(-p + \Gamma(\epsilon\delta)^2\left(-\frac{\partial_y\left[(1-\delta y)\,u\right]}{\delta(1-\delta y)} + \partial_Z w\right)\right)\mathbf{I} + \epsilon\delta\begin{pmatrix} -2\epsilon\partial_y u & \cdots & -\partial_y w + \epsilon^2\partial_Z u \\ \cdots & 2\epsilon\delta\frac{u}{1-\delta y} & \cdots \\ -\partial_y w + \epsilon^2\partial_Z u & \cdots & 2\epsilon\delta\partial_Z w\end{pmatrix}, \tag{2.29}$$

Using the fluid isentropic compression law, i.e. $\partial_{P_f^*}\left(\rho_f^*\right) = \rho_f^*/\mathcal{K}_f$, the fluid density is subjected to pressure variations following

$$\rho_f^*(r,z,t) = \rho_{f_0} e^{\frac{P_f^*(r,z,t)}{\mathcal{K}_f}} = \rho_{f_0} e^{\frac{P^*(r,z,t)+P^*_{st}(r,z)}{\mathcal{K}_f}}, \tag{2.30}$$

so that by introducing the dimensionless density $\rho_f = \rho_f^*/\rho_{f_0}$, and regarding the scalings provided in (2.22)–(2.25), it yields to

$$[1, \boldsymbol{\nabla}, \partial_\tau]\,\rho_f = e^{\frac{\mathcal{M}}{\mathcal{C}^2}(P+\mathcal{M}P_{st})}\left[1, \frac{\mathcal{M}}{\mathcal{C}^2}\boldsymbol{\nabla}\left(P+\mathcal{M}P_{st}\right), \frac{\mathcal{M}}{\mathcal{C}^2}\partial_\tau P\right], \tag{2.31}$$

with $\boldsymbol{\nabla}$ the dimensionless Nabla operator, $\mathcal{C}^2$ defines in (2.12) and $\mathcal{M}/\mathcal{C}^2 \ll 1$. Obviously, in the inner region (2.31) holds from replacing P by the inner pressure p. The Navier–Stokes equations, which follows from fluid mass and momentum conservations, yield

$$\left(\partial_t + W_f^*\partial_z + U^*\partial_r\right)\rho_f^* + \rho_f^*\left(\partial_z W_f^* + \frac{1}{r}\partial_r\left(r\partial_r U^*\right)\right) = 0, \tag{2.32}$$

$$\begin{aligned}\rho_f^*\left(\partial_t + W_f^*\partial_z + U^*\partial_r\right)W_f^* &= -\partial_z P_f^* \\ &+ \rho_{f_0}\nu_f\left((1+\Gamma)\,\partial_z\left[\partial_z W_f^* + \frac{\partial_r}{r}\left(rU^*\right)\right] + \left(\frac{\partial_r}{r}\left(r\partial_r\right) + \partial_z^2\right)W_f^*\right),\end{aligned} \tag{2.33}$$

$$\rho_f^* \left(\partial_t + W_f^* \partial_z + U^* \partial_r\right) U^* = -\partial_r P_f^* + \rho_{f_0} \nu_f \left((1+\Gamma)\, \partial_r \left[\partial_z W_f^* + \frac{\partial_r}{r} \left(r U^* \right) \right] + \left(\frac{\partial_r}{r} \left(r \partial_r \right) - \frac{1}{r^2} + \partial_z^2 \right) U^* \right), \quad (2.34)$$

and are now investigated though dimensionless variables.

2.3.1. *Dimensionless steady–state fluid equations*

At steady–state, the fluid unsteady components vanish in (2.32)–(2.34), it thus yields

$$\left(\frac{\mathcal{M}}{\mathcal{C}} \right)^2 W_{st} \partial_Z P_{st} + \partial_Z W_{st} = 0, \quad (2.35)$$

$$\mathcal{M} e^{\left(\frac{\mathcal{M}}{\mathcal{C}}\right)^2 P_{st}} W_{st} \partial_Z W_{st} = -\mathcal{M} \partial_Z P_{st} + (\epsilon\delta)^2 (2+\Gamma) \partial_Z^2 W_{st} + \delta^2 \frac{\partial_R}{R} \left(R \partial_R \right) W_{st}, \quad (2.36)$$

$$\frac{\mathcal{M}}{\epsilon^2} \partial_R P_{st} = (1+\Gamma) \delta^2 \partial_R \partial_Z W_{st}, \quad (2.37)$$

Where $(\epsilon Re)^{-1} = \delta^2 / \mathcal{M}$ have been used.

2.3.2. *Dimensionless unsteady bulk fluid equations*

Regarding the relations (2.32)–(2.34) but subtracting the steady–state relations (2.35)–(2.37), it follows regarding the fluid scalings (2.22)–(2.25), the outer dimensionless mass and momentum conservation equations

$$\partial_\tau P + \mathcal{M} \left(\left[W \partial_Z + U \partial_R \right] \left(P + \mathcal{M} P_{st} \right) + W_{st} \partial_Z P \right) + \mathcal{C}^2 \left[\partial_Z W + \frac{1}{R} \partial_R \left(R U \right) \right] = 0, \quad (2.38)$$

$$\begin{aligned} e^{\frac{\mathcal{M}}{\mathcal{C}^2}(P+\mathcal{M}P_{st})} & \left(\partial_\tau W + \mathcal{M} \left(\left[W \partial_Z + U \partial_R \right] \left(W + W_{st} \right) + W_{st} \partial_Z W \right) \right) \\ & + \mathcal{M} e^{\left(\frac{\mathcal{M}}{\mathcal{C}}\right)^2 P_{st}} \left(e^{\frac{\mathcal{M}}{\mathcal{C}^2} P} - 1 \right) W_{st} \partial_Z W_{st} = \\ - \partial_Z P + (\epsilon\delta)^2 (1+\Gamma) \partial_Z & \left[\partial_Z W + \frac{1}{R} \partial_R \left(R U \right) \right] + \delta^2 \left(\frac{\partial_R}{R} R \partial_R + \epsilon^2 \partial_Z^2 \right) W, \end{aligned} \quad (2.39)$$

$$e^{\frac{\mathcal{M}}{\mathcal{C}^2}(P+\mathcal{M}P_{st})} \left(\partial_\tau + \mathcal{M} \left[\left(W + W_{st} \right) \partial_Z + U \partial_R \right] \right) U = -\frac{1}{\epsilon^2} \partial_R P + \delta^2 (1+\Gamma) \partial_R \left[\partial_Z W + \frac{1}{R} \partial_R \left(R U \right) \right] + \delta^2 \left(\frac{\partial_R}{R} \left(R \partial_R \right) - \frac{1}{R^2} + \epsilon^2 \partial_Z^2 \right) U, \quad (2.40)$$

2.3.3. *Dimensionless unsteady fluid boundary layer equations*

In the inner viscous zone, using rescaled coordinate y defined in (2.21) dimensionless Navier–Stokes equations are

$$\partial_\tau p + \mathcal{M}\left(\left[w\partial_Z - \frac{u}{\delta}\partial_y\right](p+\mathcal{M}P_{st}) + W_{st}\partial_Z p\right) + \mathcal{C}^2\left[\partial_Z w - \frac{1}{\delta}\frac{1}{1-\delta y}\partial_y\left((1-\delta y)u\right)\right] = 0, \tag{2.41}$$

$$\begin{aligned} e^{\frac{\mathcal{M}}{\mathcal{C}^2}(p+\mathcal{M}P_{st})}&\left(\partial_\tau w + \mathcal{M}\left(\left[w\partial_Z - \frac{u}{\delta}\partial_y\right](w+W_{st}) + W_{st}\partial_Z w\right)\right) \\ &+ \mathcal{M}e^{\left(\frac{\mathcal{M}}{\mathcal{C}}\right)^2 P_{st}}\left[e^{\frac{\mathcal{M}}{\mathcal{C}^2}p} - 1\right]W_{st}\partial_Z W_{st} \\ &= -\partial_Z p + (\epsilon\delta)^2(1+\Gamma)\partial_Z\left[\partial_Z w - \frac{1}{\delta}\frac{1}{1-\delta y}\partial_y\left((1-\delta y)u\right)\right] \\ &+ \left(\frac{\partial_y}{1-\delta y}\left((1-\delta y)\partial_y\right) + (\epsilon\delta)^2\partial_Z^2\right)w, \end{aligned} \tag{2.42}$$

$$\begin{aligned} e^{\frac{\mathcal{M}}{\mathcal{C}^2}(p+\mathcal{M}P_{st})}&\left(\partial_\tau + \mathcal{M}\left[(w+W_{st})\,\partial_Z - \frac{u}{\delta}\partial_y\right]\right)u = \frac{1}{\delta\epsilon^2}\partial_y p \\ &- (1+\Gamma)\partial_y\left[\delta\partial_Z w - \frac{1}{1-\delta y}\partial_y\left((1-\delta y)u\right)\right] \\ &+ \left(\frac{\partial_y}{1-\delta y}\left((1-\delta y)\partial_y\right) - \frac{\delta^2}{(1-\delta y)^2} + (\epsilon\delta)^2\partial_Z^2\right)u. \end{aligned} \tag{2.43}$$

The fluid steady and unsteady constitutive dimensionless equations are now derived, the solid dynamic is then investigated.

2.4. *The dimensionless Lamé-Clapeyron equations*

From the linearity of the solid elastic rheology, only the unsteady responses of strains and stresses are considered (i.e. the pre–existing steady–state stress–strain does not influence the unsteady one). Furthermore, axial fluid velocity predominance produces a very similar order of magnitude hierarchy within the solid displacement field from kinematic boundary conditions. Consequently, the dimensional unsteady solid displacement vector, $\boldsymbol{\xi}^*$ in (2.2), fulfills as in ([6])

$$\boldsymbol{\xi}^* = \xi_0\xi\mathbf{e}_r + \frac{\xi_0}{\epsilon}\zeta\mathbf{e}_z, \tag{2.44}$$

with ξ_0 the solid radial displacement order of magnitude. The stress $\boldsymbol{\sigma}_s^*$, displacement $\boldsymbol{\xi}^*$, relationships is provided by Hooke's law

$$\boldsymbol{\sigma}_s^* \equiv \begin{pmatrix} \sigma_{rr}^* & \dots & \sigma_{rz}^* \\ \dots & \sigma_{\theta\theta}^* & \dots \\ \sigma_{rz}^* & \dots & \sigma_{zz}^* \end{pmatrix} = \lambda_s\left(\boldsymbol{\nabla}^*\cdot\boldsymbol{\xi}^*\right)\mathbf{I} + \mathcal{G}\left(\boldsymbol{\nabla}^*\boldsymbol{\xi}^* + \boldsymbol{\nabla}^*\boldsymbol{\xi}^{*^T}\right), \tag{2.45}$$

where the superscript T refers to the transpose operation and $\boldsymbol{\nabla}^*$ stands for the dimensional Nabla operator. The solid stress tensor diagonal terms are all identically

scaled so as to match with the pulse overpressure, i.e. $O\left(\rho_{f_0} c_p W_0\right)$, thereby ensuring volumetric stress components of $\mathrm{Tr}\left(\boldsymbol{\sigma}_{\mathrm{s}}^*\right)$ to uniformly respond to this overpressure

$$[\sigma_{rr}^*, \sigma_{\theta\theta}^*, \sigma_{zz}^*] = \rho_{f_0} c_p W_0 \left[\sigma_{rr}, \sigma_{\theta\theta}, \sigma_{zz}\right]. \tag{2.46}$$

From (2.45), the radial and axial deformations then scale as

$$\xi_0 = \alpha R_0 \mathcal{M}. \tag{2.47}$$

The solid displacement magnitudes must ensure the assumptions of small strains and displacements, i.e. $\xi_0 \ll e \;\&\; \xi_0/\epsilon \ll R_0$. The former condition is met in the considered low–Mach number framework, i.e. $\mathcal{M} \ll 1$, whereas the latter necessitates

$$\epsilon \gg \alpha \mathcal{M}. \tag{2.48}$$

At this stage, the as–yet unknown order of magnitude of the solid shear stresses, σ_{rz}^* remains. The latter follows from the axial component of the momentum conservation, or the solid Lamé-Clapeyron equation

$$\rho_{s_0} \partial_t^2 \boldsymbol{\xi}^* = \left(\lambda_s + \mathcal{G}\right) \boldsymbol{\nabla}^* \left(\boldsymbol{\nabla}^* \cdot \boldsymbol{\xi}^*\right) + \mathcal{G} {\nabla^*}^2 \boldsymbol{\xi}^* = \boldsymbol{\nabla}^* \cdot \boldsymbol{\sigma}_s^*. \tag{2.49}$$

Thus, relying on (2.44)–(2.46), one finds the solid stress deviatoric component to be

$$\sigma_{rz}^* = \epsilon \rho_{f_0} c_p W_0 \sigma_{rz}. \tag{2.50}$$

This completes the non–dimensionalisation of the solid stress tensor (2.45),

$$\boldsymbol{\sigma}_s^* = \rho_{f_0} c_p W_0 \boldsymbol{\sigma}_s \quad \text{, where, } \quad \boldsymbol{\sigma}_s = \begin{pmatrix} \sigma_{rr} & \dots & \epsilon\sigma_{rz} \\ \dots & \sigma_{\theta\theta} & \dots \\ \epsilon\sigma_{rz} & \dots & \sigma_{zz} \end{pmatrix}, \tag{2.51}$$

with deviatoric and diagonal components

$$\epsilon^2 \frac{\mathcal{C}_{\mathcal{G}}}{\alpha} \sigma_{rz} = \partial_R \zeta + \epsilon^2 \partial_Z \xi, \tag{2.52}$$

$$[\sigma_{rr}, \sigma_{\theta\theta}, \sigma_{zz}] = \frac{\alpha}{\mathcal{C}_{\lambda_s}} \left(\frac{\partial_R}{R}\left(R\xi\right) + \partial_Z \zeta\right) [1,1,1] + \frac{2\alpha}{\mathcal{C}_{\mathcal{G}}} \left[\partial_R \xi, \frac{\xi}{R}, \partial_Z \zeta\right]. \tag{2.53}$$

From (2.51) dimensionless Lamé-Clapeyron equations (2.49) read as follows

$$\epsilon^2 \frac{\alpha}{\mathcal{D}} \left(\partial_\tau^2 \xi - \partial_Z \sigma_{rz}\right) = \frac{\partial_R}{R}\left(R\sigma_{rr}\right) - \frac{\sigma_{\theta\theta}}{R}, \tag{2.54}$$

$$\frac{\alpha}{\mathcal{D}} \partial_\tau^2 \zeta = \partial_Z \sigma_{zz} + \frac{\partial_R}{R}\left(R\sigma_{rz}\right), \tag{2.55}$$

or using (2.52)–(2.53)

$$\epsilon^2 \left(\partial_\tau^2 - \frac{\mathcal{D}}{\mathcal{C}_{\mathcal{G}}} \partial_Z^2\right) \xi = \mathcal{D} \frac{2\mathcal{C}_{\lambda_s} + \mathcal{C}_{\mathcal{G}}}{\mathcal{C}_{\mathcal{G}} \mathcal{C}_{\lambda_s}} \partial_R \left(\frac{\partial_R}{R}\left(R\xi\right)\right) + \mathcal{D} \frac{\mathcal{C}_{\mathcal{G}} + \mathcal{C}_{\lambda_s}}{\mathcal{C}_{\mathcal{G}} \mathcal{C}_{\lambda_s}} \partial_R \partial_Z \zeta, \tag{2.56}$$

$$\epsilon^2 \left(\partial_\tau^2 - \mathcal{D} \frac{2\mathcal{C}_{\lambda_s} + \mathcal{C}_{\mathcal{G}}}{\mathcal{C}_{\mathcal{G}} \mathcal{C}_{\lambda_s}} \partial_Z^2\right) \zeta = \frac{\mathcal{D}}{\mathcal{C}_{\mathcal{G}}} \frac{\partial_R}{R}\left(R \partial_R \zeta\right) + \epsilon^2 \mathcal{D} \frac{\mathcal{C}_{\mathcal{G}} + \mathcal{C}_{\lambda_s}}{\mathcal{C}_{\mathcal{G}} \mathcal{C}_{\lambda_s}} \partial_Z \left(\frac{\partial_R}{R}\left(R\xi\right)\right). \tag{2.57}$$

Whilst fluid dynamics is governed by the boundary layer dimensionless parameter δ, the solid one is controlled by small parameter ϵ. Neglecting $O(\epsilon^2)$ terms leads to radially time–invariance fields, since a zero (2.54)'s RHS leads to a steady radial stress which is identical with the one found within an elastic tube subjected to a steady internal overpressure. Hence, up to order $O\left(\epsilon^2\right)$ corrections the solid radial deformation quasi–steadily responds to the fluid pressure load, while the axial dynamics are free to propagate as a radially uniform planar wave ([40,50,43]). Furthermore, since the outer radial fluid pressure derivative in (2.40) displays a $O\left(\epsilon^{-2}\right)$ correction, the fluid pressure remains uniform per section within the long–wavelength approximation.

2.5. *Axial boundary conditions*

To set up an axially enclose the problem, a specific set boundary conditions have to be prescribed at the tube's dead ends. The hereby analysis focus on the reservoir–pipe–anchored valve configuration, a very standard study case in hydraulic and biological communities ([43,32]). These boundary conditions influence both the fluid and the solid dynamic as the problem involves (FSI) considerations. Upstream a homogeneous Dirichlet condition is assumed for unsteady pressure, then impeding any pressure fluctuation at this point, whereas downstream an unsteady fluid velocity variation, i.e. a time–dependent–Dirichlet condition, is imposed

$$P\big|_{Z=0} = 0 \quad \text{, and,} \quad W\big|_{Z=1} = -H_{eav}(\tau), \tag{2.58}$$

where H_{eav} is the time–dependent Heaviside distribution. For the steady–state, the upstream and downstream pressure conditions are assumed known and constant. On the other hand, the tube is supposed perfectly anchored at its dead ends, i.e. a homogeneous Dirichlet conditions upon the solid axial displacement field ζ, so that no motion occurs at these specific locations

$$\zeta\big|_{Z=0\&1} = 0. \tag{2.59}$$

The hereby boundary conditions will be clarified in the analysis forthcoming in §4.1.

2.6. *Fluid matching and fluid–solid interface continuity conditions*

The radial boundary conditions in the boundary layer and at the fluid–solid interface are now considered. No additional stress contributions at the external edges is supposed, so that dimensionless stresses and kinematic continuity conditions read

$$\mathbf{n}_i \left(\mathcal{M}\boldsymbol{\sigma}_{s,st}\big|_{\mathcal{R}_i} + \boldsymbol{\sigma}_s\big|_{\mathcal{R}_i} \right) \mathbf{n}_i = \mathbf{n}_i \left(\mathcal{M}\boldsymbol{\sigma}_{st}\big|_{y=\frac{1-\mathcal{R}_i}{\delta}} + \boldsymbol{\sigma}\big|_{y=\frac{1-\mathcal{R}_i}{\delta}} \right) \mathbf{n}_i, \tag{2.60}$$

$$\mathbf{n}_o \left(\mathcal{M}\boldsymbol{\sigma}_{s,st}\big|_{\mathcal{R}_o} + \boldsymbol{\sigma}_s\big|_{\mathcal{R}_o} \right) \mathbf{n}_o = \mathbf{0}, \tag{2.61}$$

$$\mathbf{n}_i \left(\mathcal{M}\boldsymbol{\sigma}_{s,st}\big|_{\mathcal{R}_i} + \boldsymbol{\sigma}_s\big|_{\mathcal{R}_i} \right) \mathbf{t}_i = \mathbf{n}_i \left(\mathcal{M}\boldsymbol{\sigma}_{st}\big|_{y=\frac{1-\mathcal{R}_i}{\delta}} + \boldsymbol{\sigma}\big|_{y=\frac{1-\mathcal{R}_i}{\delta}} \right) \mathbf{t}_i, \tag{2.62}$$

$$\mathbf{n}_o \left(\mathcal{M}\boldsymbol{\sigma}_{s,st}\big|_{\mathcal{R}_o} + \boldsymbol{\sigma}_s\big|_{\mathcal{R}_o} \right) \mathbf{t}_o = \mathbf{0}, \tag{2.63}$$

$$\mathbf{e}_r\boldsymbol{\sigma}_{s,st}\big|_{R=1}\mathbf{e}_r = \mathbf{e}_r\boldsymbol{\sigma}_{st}\big|_{y=0}\mathbf{e}_r, \qquad \mathbf{e}_r\boldsymbol{\sigma}_{s,st}\big|_{R=1+\alpha}\mathbf{e}_r = \mathbf{0}, \tag{2.64}$$

$$\mathbf{e}_r\boldsymbol{\sigma}_{s,st}\big|_{R=1}\mathbf{e}_z = \mathbf{e}_r\boldsymbol{\sigma}_{st}\big|_{y=0}\mathbf{e}_z, \qquad \mathbf{e}_r\boldsymbol{\sigma}_{s,st}\big|_{R=1+\alpha}\mathbf{e}_z = \mathbf{0}, \tag{2.65}$$

$$\mathbf{u}\big|_{\mathcal{R}_i} = \alpha\partial_\tau\boldsymbol{\xi}\big|_{\mathcal{R}_i}, \tag{2.66}$$

where $\boldsymbol{\sigma}_{s,st} = \boldsymbol{\sigma}^*_{s,st}/\rho_{f_0}W_0^2$ is the solid pre–stress tensor associated with the steady–state condition. The solid pre–existing stress tensor is not explicitly defined has it will not impact the solid unsteady dynamic due to the linearity of the solid constitutive equations (2.54)–(2.57) . On the other hand, the unsteady boundary layer inner fields, (p, w, u), are matched to outer ones (P, W, U) using stretched coordinate η

$$\eta = \frac{1-R}{\delta^\gamma} = \frac{y}{\delta^{\gamma-1}} \sim O(1), \tag{2.67}$$

associated with stretching parameter $0 < \gamma < 1$, ([19]), giving matching conditions

$$(P, W, U)\,\big|_{R=1-\delta^\gamma\eta} = (p, w, u)\,\big|_{y=\delta^{\gamma-1}\eta}. \tag{2.68}$$

The asymptotic analysis of the constitutive fluid and solid equations is now carried out.

3. Asymptotic analysis

3.1. *Boundary layer forcing terms and asymptotic framework*

Considering the fluid shear stress (2.27), and expanding (2.42) yields to

$$\begin{aligned} &e^{\frac{\mathcal{M}}{\mathcal{C}^2}(p+\mathcal{M}P_{st})}\left(\partial_\tau w + \mathcal{M}\left((w+W_{st})\,\partial_Z w - \frac{u}{\delta}\left(\tau_f + \partial_y W_{st}\right) + w\partial_Z W_{st}\right)\right) \\ &+\mathcal{M}e^{\left(\frac{\mathcal{M}}{\mathcal{C}}\right)^2 P_{st}}\left[e^{\frac{\mathcal{M}}{\mathcal{C}^2}p} - 1\right]W_{st}\partial_Z W_{st} = -\partial_Z p + (\epsilon\delta)^2(1+\Gamma)\partial_Z\left[\partial_Z w - \frac{1}{\delta}\left(\partial_y u - \delta\frac{u}{1-\delta y}\right)\right] \\ &\qquad + \partial_y^2 w - \delta\frac{\tau_f}{1-\delta y} + (\epsilon\delta)^2\,\partial_Z^2 w. \end{aligned} \tag{3.1}$$

The resulting forced diffusion equation for longitudinal velocity component w provides crucial informations to understand the damping mechanisms. (3.1)'s terms leading to the wave's energy loss are

- $O\left(\frac{\mathcal{M}}{\mathcal{C}^2}\right)$ and $O\left(\left(\frac{\mathcal{M}}{\mathcal{C}}\right)^2\right)$ fluid density compressibility effects (2.31);
- $O\left(\epsilon^2\delta\right)$ radial flow compressibility effects within the inner region;
- $O\left(\epsilon^2\delta^2\right)$ and $O\left(\epsilon^2\delta\right)$ axial diffusion and radial flow compressibility;
- $O\left(\mathcal{M}\right)$ axial inertial corrections;
- $O\left(\frac{\mathcal{M}}{\delta}\right)$ radial inertial transport of viscous shear;
- $O\left(\delta\right)$ radial diffusion transport of viscous shear.

Energy losses in the (FSI) problem are thus related to two distinct phenomena: diffusion and inertia, which may, or may not, simultaneously contribute regarding

their respective orders of magnitude. The presented low–Mach number asymptotic framework, i.e. neglecting inertial over viscous contributions, applies when

$$\delta \gg \frac{\mathcal{M}}{\delta} \gg \mathcal{M}, \tag{3.2}$$

which is consistent with (2.20). The dimensionless numbers ordering spelled out in (2.20) is herein clarified regarding (2.48) and (3.18). The radial diffusion transport of viscous shear is thus the damping mechanism under focus. Further investigations could be conducted out to analyze the impact of distinct asymptotic regimes on the long–time dynamics. A high–Mach number case was asymptotically considered by ([54]) for a practical case of a hydroelectric power plant. Ignoring (FSI), the low–Mach boundary layer theory has been brilliantly investigated by ([32,33]).

3.2. *Multiple time–scale approach*

Next, the time variations of all considered fields are decomposed into fast–time associated with wave propagation and slow–time associated with the damping envelope as well as a phase-shift that arises from friction dissipation, ([19]). Let us note the slow-time scale T. Since the corrections of interest in the axial momentum conservation equation (3.1) are of order $O(\delta)$, this slow time-scale should scale as follows

$$T = \delta\tau, \quad \text{so} \qquad \text{that} \quad \partial_t \equiv \frac{c_p}{L}\left(\partial_\tau + \delta\partial_T\right). \tag{3.3}$$

In this multiple time-scale approach, all previous time–derivatives fulfill a chain-rule correction given by $\partial_\tau + \delta\partial_T$. For the framework being established, one must consider the coupling conditions between the solid and fluid given by stress and kinematic continuity at the fluid–solid interface within this asymptotic scheme.

3.3. *Asymptotic sequence*

In the herein δ–driven asymptotic framework, a regular asymptotic sequence for solid displacement components (ξ, ζ), inner/outer velocity fields $(u, w), (U, W)$, inner/outer pressures $[p, P]$, fluid shear stresses $[\tau_f, \tau_w]$, and solid stress tensor components $[\sigma_{rz}, \sigma_{rr}, \sigma_{\theta\theta}, \sigma_{zz}]$ is searched for

$$[\xi, \zeta] = [\xi, \zeta]^0 + \delta\,[\xi, \zeta]^1 + O(X), \tag{3.4}$$

$$[u, w, U, W] = [u, w, U, W]^0 + \delta\,[u, w, U, W]^1 + O(X), \tag{3.5}$$

$$[p, P] = [p, P]^0 + \delta\,[p, P]^1 + O(X), \tag{3.6}$$

$$[\tau_f, \tau_w] = [\tau_f, \tau_w]^0 + \delta\,[\tau_f, \tau_w]^1 + O(X), \tag{3.7}$$

$$[\sigma_{rz}, \sigma_{rr}, \sigma_{\theta\theta}, \sigma_{zz}] = [\sigma_{rz}, \sigma_{rr}, \sigma_{\theta\theta}, \sigma_{zz}]^0 + \delta\,[\sigma_{rz}, \sigma_{rr}, \sigma_{\theta\theta}, \sigma_{zz}]^1 + O(X), \tag{3.8}$$

with $X \equiv \max\left(\delta^2, \mathcal{M}/\delta, \epsilon^2, \alpha\mathcal{M}\right)$.

3.4. *Steady–state fluid axial velocity leading–order solution*

The steady–state contributions into the unsteady fluid equations (2.38)–(2.43) appear to driven by the Mach number. Despite the hereby asymptotic framework ensures $\delta \gg \mathcal{M}$, it is crucial to ensure that no steady–state contributions arise into the unsteady boundary layer (2.42). Since the leading–order steady–state solution only is hereby investigated, no assumptions are made regarding its asymptotic sequence. The leading–order dimensionless steady solution refers to as $\left(W_{st}^0, P_{st}^0\right)$. Steady–state mass conservation (2.35), follows steady incompressible condition

$$\partial_Z W_{st}^0 = 0. \tag{3.9}$$

On the other hand, $\epsilon^2\delta^2/\mathcal{M} = \epsilon/R_e \ll 1$ follows from the definition of δ, ϵ and $\mathcal{M}$ in (2.18)–(2.19) so that using (2.35), the steady–state leading–order pressure field is found uniform per section

$$\partial_R P_{st}^0 = 0. \tag{3.10}$$

Finally, the steady–state leading–order axial mass conservation equation (2.36) results in equalizing a R–dependent function to a Z–dependent one

$$\mathcal{M}\partial_Z P_{st}^0 = \delta^2 \frac{\partial_R}{R}\left(R\partial_R W_{st}^0\right), \tag{3.11}$$

yielding to

$$W_{st}^0 = \frac{\mathcal{M}}{4\delta^2}\partial_Z P_{st}^0\left[R^2-1\right] = \frac{\mathcal{M}}{4\delta}\partial_Z P_{st}^0\left[\delta y - 2\right] y, \tag{3.12}$$

$$\partial_y W_{st}^0 = \frac{\mathcal{M}}{4\delta}\partial_Z P_{st}^0\left[\delta y - 2\right] + \frac{\mathcal{M}}{4}\partial_Z P_{st}^0 y, \tag{3.13}$$

where the no–slip condition have been used at the fluid/solid interface. The $\mathcal{M}$ pre–factor in (3.13) is $O(\mathcal{M}/\delta)$ and thus smaller than one according to (2.20). Then, there is a (small) one–way coupling of the unsteady fields from steady ones in the boundary layer (2.42), the order of which is $O\left(\frac{\mathcal{M}^2}{\delta}\right) \ll 1$. Furthermore, (3.13) contributes as $O(\epsilon) \ll 1$ in the deviatoric part of the steady–state stress tensor (2.28).

3.5. *Correction on the inner tube radius position, $\mathcal{R}_i^*$*

The fluid–solid interface position, which is characterized by $\mathcal{R}_i^*$ defined in (2.3), is expected to vary as the fluid overpressure wave propagates. Using solid displacement scalings (2.47), one finds

$$\mathcal{R}_i(Z + \alpha\mathcal{M}\zeta(1,Z,\tau),\tau) = 1 + \alpha\mathcal{M}\xi(1,Z,\tau). \tag{3.14}$$

Taylor-expanding (3.14) leads to

$$\mathcal{R}_i(Z+\alpha\mathcal{M}\zeta(1,Z,\tau) = \mathcal{R}_i(Z,\tau) + \alpha\mathcal{M}\zeta(1,Z,\tau)\partial_Z\mathcal{R}_i(Z,\tau) + O\left((\alpha\mathcal{M})^2\right), \tag{3.15}$$

so that combining (3.14) and (3.15), one finally gets

$$\mathcal{R}_i(Z,\tau,T) = 1 + O\left(\alpha\mathcal{M}\right). \tag{3.16}$$

By following the same footsteps, an equivalent relation is achieved for $\mathcal{R}_o^*(z,t)$. The dimensionless normal and tangential vectors, $(\mathbf{n}_i,\mathbf{n}_o)$ and $(\mathbf{t}_i,\mathbf{t}_o)$ respectively then fulfills

$$\mathbf{n}_i = \mathbf{n}_o = \mathbf{e}_r + O\left(\alpha\epsilon\mathcal{M}\right), \qquad \mathbf{t}_i = \mathbf{t}_o = \mathbf{e}_z + O\left(\alpha\epsilon\mathcal{M}\right). \tag{3.17}$$

Thus, in the considered low–Mach number asymptotic framework, the response of the inner and outer tube's radius to overpressure is irrelevant as long as

$$\delta \gg \alpha\mathcal{M} \gg \alpha\epsilon\mathcal{M}. \tag{3.18}$$

These asymptotically unperturbed normal and tangent vectors, combined with the order of magnitudes of the steady–state radial gradient contribution (3.13) into the deviatoric part of $\boldsymbol{\sigma}_{st}$ in (2.28), thus justifies continuity condition (2.60)-(2.63) to be applied to unsteady fluid and solid fields only, i.e. without coupling with steady–state. The stress and velocity continuity conditions in (2.60)-(2.66) thus finally reads

$$\sigma_{rr}\big|_{R=1+O(\alpha\mathcal{M})} = -p\big|_{y=O\left(\frac{\alpha\mathcal{M}}{\delta}\right)} + O\left(\alpha\epsilon\mathcal{M}\right), \tag{3.19}$$

$$\sigma_{rr}\big|_{R=1+\alpha+O(\alpha\mathcal{M})} = O\left(\alpha\epsilon\mathcal{M}\right), \tag{3.20}$$

$$\sigma_{rz}\big|_{R=1+O(\alpha\mathcal{M})} = -\delta\tau_w\big|_{y=O\left(\frac{\alpha\mathcal{M}}{\delta}\right)} + O\left(\alpha\epsilon\mathcal{M}\right), \tag{3.21}$$

$$\sigma_{rz}\big|_{R=1+\alpha+O(\alpha\mathcal{M})} = O\left(\alpha\epsilon\mathcal{M}\right), \tag{3.22}$$

$$\alpha\left(\partial_\tau + \delta\partial_T\right)\xi\big|_{R=1+O(\alpha\mathcal{M})} = u\big|_{y=O\left(\frac{\alpha\mathcal{M}}{\delta}\right)} + O\left(\alpha\epsilon\mathcal{M}\right), \tag{3.23}$$

$$\alpha\left(\partial_\tau + \delta\partial_T\right)\zeta\big|_{R=1+O(\alpha\mathcal{M})} = w\big|_{y=O\left(\frac{\alpha\mathcal{M}}{\delta}\right)} + O\left(\alpha\epsilon\mathcal{M}\right), \tag{3.24}$$

where $[\sigma_{rr},\sigma_{rz}]$ are provided in (2.52)–(2.53), respectively. Thus, in the considerd asymptotic low–Mach framework, the unsteady fluid and solid components decouple each other. In the forthcoming, only the system unsteadiness response will be investigated.

3.6. *Fluid structure interaction equations*

3.6.1. *Stress and kinematic continuity at the tube wall*

The stress and kinematic continuity relationships (2.60)-(2.66) hold at the fluid–solid interface, where $\boldsymbol{\sigma}$ and $\boldsymbol{\sigma}_s$ are defined in (2.29) and (2.51), respectively. Regarding the tangential stress continuity in (2.62)–(2.63) it is noteworthy that the deviatoric dimensionless fluid stress tensor $\boldsymbol{\sigma}$ components scales as $O(\epsilon\delta)$. Moreover, since from (2.50) the dimensionless solid deviatoric part scales as $O(\epsilon)$, there is a $O(\delta)$ mismatch between them. It then result that the boundary layer influence on the solid shear stress is not sensible at leading–order. It only arises at order $O(\delta)$.

The leading– and first– orders kinematic and stress continuity conditions (2.60)-(2.66) thus finally simplify to

$$\sigma^0_{rr}\big|_{R=1} = -p^0\big|_{y=0}, \qquad \sigma^1_{rr}\big|_{R=1} = -p^1\big|_{y=0}, \tag{3.25}$$

$$\sigma^0_{rr}\big|_{R=1+\alpha} = 0, \qquad \sigma^1_{rr}\big|_{R=1+\alpha} = 0, \tag{3.26}$$

$$\sigma^0_{rz}\big|_{R=1} = 0, \qquad \sigma^1_{rz}\big|_{R=1} = -\tau^0_w\big|_{y=0}, \tag{3.27}$$

$$\sigma^0_{rz}\big|_{R=1+\alpha} = 0, \qquad \sigma^1_{rz}\big|_{R=1+\alpha} = 0, \tag{3.28}$$

$$\alpha\partial_\tau\xi^0\big|_{R=1} = u^0\big|_{y=0}, \qquad \alpha\left(\partial_\tau\xi^1\big|_{R=1} + \partial_T\xi^0\big|_{R=1}\right) = u^1\big|_{y=0}, \tag{3.29}$$

$$\alpha\partial_\tau\zeta^0\big|_{R=1} = w^0\big|_{y=0}, \qquad \alpha\left(\partial_\tau\zeta^1\big|_{R=1} + \partial_T\zeta^0\big|_{R=1}\right) = w^1\big|_{y=0}. \tag{3.30}$$

3.6.2. *Solid equations*

The Lamé–Clapeyron equations (2.54)–(2.55), or more explicitly (2.56)–(2.57), along with dimensionless Hooke's law (2.52)–(2.53), provide information on the R-dependence of the solid's fields

$$\partial_R\left(\frac{\partial_R}{R}\left(R\left[\xi^0+\delta\xi^1\right]\right)\right) = -\frac{\mathcal{C}_\mathcal{G}+\mathcal{C}_{\lambda_s}}{\mathcal{C}_\mathcal{G}\mathcal{C}_{\lambda_s}}\partial_R\partial_Z\left[\zeta^0+\delta\zeta^1\right], \tag{3.31}$$

$$\partial_R\left[\zeta^0+\delta\zeta^1\right] = 0, \tag{3.32}$$

$$\sigma^0_{rz} - \frac{\sigma^0_{rz}|_{R=1}}{R} = \frac{1}{R}\int_1^R R\left[\frac{\alpha}{\mathcal{D}}\partial^2_\tau\zeta^0 - \partial_Z\sigma^0_{zz}\right]dr, \tag{3.33}$$

$$\sigma^1_{rz} - \frac{\sigma^1_{rz}|_{R=1}}{R} = \frac{1}{R}\int_1^R R\left[\frac{\alpha}{\mathcal{D}}\left(\partial^2_\tau\zeta^1 + 2\partial_T\partial_\tau\zeta^0\right) - \partial_Z\sigma^1_{zz}\right]dr, \tag{3.34}$$

$$\sigma^0_{zz} + \delta\sigma^1_{zz} = \alpha\frac{2\mathcal{C}_{\lambda_s}+\mathcal{C}_\mathcal{G}}{\mathcal{C}_\mathcal{G}\mathcal{C}_{\lambda_s}}\partial_Z\left[\zeta^0+\delta\zeta^1\right] + \frac{\alpha}{\mathcal{C}_{\lambda_s}}\frac{\partial_R}{R}\left(R\left[\xi^0+\delta\xi^1\right]\right). \tag{3.35}$$

Equation (3.32) highlights the radial uniformity of solid axial displacement at leading– and first–orders. This uniformity along R follows from the long–wavelength assumptions, that is, the irrelevance of radial inertia when discarding $O(\epsilon^2)$ as already discussed in §3.1. This also implies a simplification of (3.31) by enforcing its RHS to equal zeros. After defining six R–invariant functions, namely $H_1^{0,1}$, $H_2^{0,1}$ and $H_3^{0,1}$, the leading– and first–orders displacement fields fulfill

$$\zeta^0+\delta\zeta^1 = H_1^0(Z,\tau,T) + \delta H_1^1(Z,\tau,T), \tag{3.36}$$

$$\xi^0+\delta\xi^1 = \frac{H_2^0(Z,\tau,T)+\delta H_2^1(Z,\tau,T)}{2}R + \frac{H_3^0(Z,\tau,T)+\delta H_3^1(Z,\tau,T)}{R}, \tag{3.37}$$

The relation (3.36) is the first integral of (3.32) and (3.37) the first integral of (3.31)'s LHS. This similarly ensures the uniform behavior of the integrands of both (3.33) and (3.34). The shear continuity conditions in (3.27) and (3.28) then yield to

$$\frac{\alpha}{\mathcal{D}}\left(\partial^2_\tau\left[\zeta^0+\delta\zeta^1\right] + 2\delta\partial_T\partial_\tau\zeta^0\right) - \partial_Z\left[\sigma^0_{zz}+\delta\sigma^1_{zz}\right] = \frac{2\delta\tau^0_w}{\alpha(2+\alpha)}. \tag{3.38}$$

The as–yet–unknown functions $H_2^{0,1}$ and $H_3^{0,1}$ are prescribed by the normal–stress continuity conditions (3.25)–(3.26)

$$H_2^0 + \delta H_2^1 = \frac{\mathcal{C}_{\lambda_s}\mathcal{C}_{\mathcal{G}}}{\mathcal{C}_{\mathcal{G}}+\mathcal{C}_{\lambda_s}}\left(\frac{p^0+\delta p^1}{\alpha^2(2+\alpha)} - \frac{1}{\mathcal{C}_{\lambda_s}}\partial_Z\left[\zeta^0+\delta\zeta^1\right]\right), \tag{3.39}$$

$$H_3^0 + \delta H_3^1 = \frac{\mathcal{C}_{\mathcal{G}}}{\alpha}\frac{(1+\alpha)^2}{2\alpha(2+\alpha)}\left[p^0+\delta p^1\right]. \tag{3.40}$$

Using that $\mathcal{C}_{\mathcal{G}}/(\mathcal{C}_{\mathcal{G}}+\mathcal{C}_{\lambda_s}) = 2\nu_s$, $H_2^{0,1}$ and $H_3^{0,1}$ reduce to

$$H_2^0(Z,\tau,T) + \delta H_2^1(Z,\tau,T) = 2\nu_s\left(\frac{\mathcal{C}_{\lambda_s}}{\alpha}\frac{p^0+\delta p^1}{\alpha(2+\alpha)} - \partial_Z\left[\zeta^0+\zeta^1\right]\right), \tag{3.41}$$

$$H_3^0(Z,\tau,T) + \delta H_3^1(Z,\tau,T) = \frac{\mathcal{C}_{\mathcal{G}}}{\alpha}\frac{(1+\alpha)^2}{2\alpha(2+\alpha)}\left[p^0+\delta p^1\right], \tag{3.42}$$

thus fulfilling the radial displacement expression in (3.37) at each order

$$\xi^0 + \delta\xi^1 = \frac{2\nu_s\mathcal{C}_{\lambda_s}R + \frac{(1+\alpha)^2\mathcal{C}_{\mathcal{G}}}{R}}{\alpha(2+\alpha)}\frac{p^0+\delta p^1}{2\alpha} - \nu_s R\partial_Z(\zeta^0+\delta\zeta^1), \tag{3.43}$$

$$\xi^0\big|_{R=1} + \delta\xi^1\big|_{R=1} = \frac{\chi(p^0+\delta p^1)}{2\alpha} - \nu_s\partial_Z(\zeta^0+\delta\zeta^1), \tag{3.44}$$

with χ given in (2.15). Noting that $2\alpha/\mathcal{C}_{\mathcal{G}} + \alpha(1-2\nu_s)/\mathcal{C}_{\lambda_s} = \alpha\mathcal{C}_s^2/\mathcal{D}$, and considering the dimensionless Hooke stress tensor (2.52)–(2.53), direct relations between the normal solid stress components, p^0 and $\partial_Z\zeta^0$ are found

$$\sigma_{rr}^0(R,Z,\tau,T) + \delta\sigma_{rr}^1(R,Z,\tau,T) = \left[1 - \frac{(1+\alpha)^2}{R^2}\right]\frac{p^0+\delta p^1}{\alpha(2+\alpha)}, \tag{3.45}$$

$$\sigma_{\theta\theta}^0(R,Z,\tau,T) + \delta\sigma_{\theta\theta}^1(R,Z,\tau,T) = \left[1 + \frac{(1+\alpha)^2}{R^2}\right]\frac{p^0+\delta p^1}{\alpha(2+\alpha)}, \tag{3.46}$$

$$\sigma_{zz}^0(Z,\tau,T) + \delta\sigma_{zz}^1(Z,\tau,T) = 2\nu_s\frac{p^0+\delta p^1}{\alpha(2+\alpha)} + \frac{\alpha\mathcal{C}_s^2}{\mathcal{D}}\partial_Z\left[\zeta^0+\delta\zeta^1\right]. \tag{3.47}$$

Thus, (3.45) and (3.46) recover the known radial dependence of stresses in thick pipes ([18]). In the $\alpha \ll 1$ limit, (3.45) also provides the thin–wall shell theory for which the radial stress linearly varies along the radial direction, that is $\sigma_{rr}^0 = p^0(r-(R_0+e))/e + O(\alpha^2)$, from the applied fluid pressure at the inner pipe radius to the zero external pressure at the outer one. Furthermore, as $\alpha \ll 1$, the hoop stress $\sigma_{\theta\theta}$ is found to be constant and thin-wall shell theory (more often named circumferential tension) is recovered (i.e $\sigma_{\theta\theta} = p^0/\alpha + O(\alpha^2)$) since $1/\alpha$ is approximately the ratio of the average radius over the pipe wall thickness up to $O(\alpha^2)$ corrections. It is also interesting to note that σ_{zz}^0 does not exhibit a radial dependence, a feature known in thin-wall shell theory (where σ_{zz}^0 is called longitudinal tension), which extends to thick walls. Finally, the dependence of σ_{zz}^0 with R is found consistent with thin–wall shell theory ([25]).

3.6.3. *Fluid equations in the bulk outer region*

The outer leading– and first–orders fluid behaviors are governed by mass and momentum conservation equations (2.38)–(2.40). Using the asymptotic sequence given in §3.3 along with the multi–time scale decomposition discussed in §3.2 leads to the following

$$\partial_\tau \left[P^0 + \delta P^1\right] + \delta \partial_T P^0 + \mathcal{C}^2 \partial_Z \left[W^0 + \delta W^1\right] = -\mathcal{C}^2 \frac{\partial_R}{R} \left(R \left[U^0 + \delta U^1\right]\right), \tag{3.48}$$

$$\partial_\tau \left[W^0 + \delta W^1\right] + \delta \partial_T W^0 = -\partial_Z \left[P^0 + \delta P^1\right], \tag{3.49}$$

$$\partial_R \left[P^0 + \delta P^1\right] = 0. \tag{3.50}$$

At leading–order since $\partial_R P^0 = 0$ from (3.50), and, from the R derivative of (3.49), $\partial_\tau \partial_R W^0 = 0$. If $\partial_R W^0 = 0$ is initially set at $\tau = 0$, then $\partial_R W^0 = 0$ for all times. The same applies for P^1 and W^1. The radial uniformity of both outer pressure and axial velocity thus arises at leading– and first–orders, so that the LHS of (3.48) does not depend on R. We therefore introduce functions $\mathcal{F}^0(Z, \tau, T)$ and $\mathcal{F}^1(Z, \tau, T)$ so that

$$U^0 + \delta U^1 = -\frac{R}{2} \left[\mathcal{F}^0(Z, \tau, T) + \delta \mathcal{F}^1(Z, \tau, T)\right], \tag{3.51}$$

and consequently from (3.48), it yields

$$\partial_\tau \left[P^0 + \delta P^1\right] + \delta \partial_T P^0 + \mathcal{C}^2 \partial_Z \left[W^0 + \delta W^1\right] = \mathcal{C}^2 \left[\mathcal{F}^0 + \delta \mathcal{F}^1\right]. \tag{3.52}$$

3.6.4. *Fluid equations in the inner boundary layer region*

The inner flow is driven by the boundary layer's rescaled mass and momentum conservation equations, (2.41)–(2.43). Up to first–order, one obtains the following

$$\delta \left(\partial_\tau p^0 + \mathcal{C}^2 \partial_Z w^0\right) = \mathcal{C}^2 \partial_y \left[u^0 + \delta u^1\right] - \delta \mathcal{C}^2 u^0, \tag{3.53}$$

$$\left(\partial_\tau - \partial_y^2\right) \left[w^0 + \delta w^1\right] = -\partial_Z \left[p^0 + \delta p^1\right] - \delta \left(\partial_T w^0 + \tau_f^0\right), \tag{3.54}$$

$$\partial_y \left[p^0 + \delta p^1\right] = 0. \tag{3.55}$$

As in the outer region (3.50), the inner pressure in (3.55) is uniform upon the radial re–scaled variable y, leading to pressure continuity per section at both orders

$$p^0 = P^0, \quad p^1 = P^1. \tag{3.56}$$

At leading–order, the inner mass equation (3.53) gives $\partial_y u^0 = 0$, so that the normal kinematic continuity condition (3.29) reads

$$u^0 = \alpha \partial_\tau \xi^0|_{R=1}, \tag{3.57}$$

or, equivalently, invoking (3.44)

$$u^0 = \frac{\chi}{2} \partial_\tau P^0 - \alpha \nu_s \partial_Z \partial_\tau \zeta^0. \tag{3.58}$$

Furthermore, re–arranging the $O(\delta)$ terms in (3.53) along with the kinematic continuity condition (3.29) leads to

$$u^1 = \frac{y}{\mathcal{C}^2} \partial_\tau P^0 + \partial_Z \int_0^y w^0 dy' + y \alpha \partial_\tau \xi^0\big|_{R=1} + \alpha \left[\partial_\tau \xi^1 + \partial_T \xi^0\right]_{R=1}. \tag{3.59}$$

3.7. *Outer and inner fluid velocity matching*

The as–yet–unknown velocity functions $\mathcal{F}^0(Z,\tau,T)$ and $\mathcal{F}^1(Z,\tau,T)$, defined in (3.51), are fully determined by the asymptotic matching of radial velocities between the inner boundary layer and the outer region, as presented in §2.6. This matching nevertheless requires the knowledge of $\int_0^y w^0 dy^{'}$ accordingly to (3.59). For the sake of simplicity, the analysis is handled in the Laplace domain. The Laplace transform $\mathcal{L}$ with respect to the fast time τ is denoted by a tilde. So far any dependent variable $f(Z,\tau,T)$, we write

$$\tilde{f}(Z,s,T) = \mathcal{L}\left(f(Z,\tau,T)\right) = \int_0^\infty f(Z,\tau^{'},T)e^{-s\tau^{'}}d\tau^{'}. \tag{3.60}$$

With all unsteady fields initially at rest, the Laplace transform will map time derivatives into factors of the transform variable s. The inner leading–order axial velocity, w^0, is governed by a diffusion equation (3.30), so its The Laplace transform leads to

$$\tilde{w}^0 = s\alpha\tilde{\zeta}^0 e^{-\sqrt{s}y} - \frac{1}{s}\partial_Z\tilde{P}^0\left[1-e^{-\sqrt{s}y}\right], \tag{3.61}$$

where the axial kinematic continuity condition at the tube wall have been used. The Laplace transform of (3.49)'s leading–order produces

$$\tilde{W}^0 = -\frac{1}{s}\partial_Z\tilde{P}^0, \tag{3.62}$$

the which implies

$$\lim_{y\to\infty}\tilde{w}^0 = \tilde{W}^0 + E.S.T, \tag{3.63}$$

where E.S.T="exponentially small terms". The asymptotic matching of axial velocities is directly guaranteed since they are far from the wall (i.e. for $y=\frac{1-R}{\delta}\gg 1$). The leading–order shear rate $\tilde{\tau}_f^0$ and wall shear rate $\tilde{\tau}_w^0$ can be deduced from (3.61)

$$\tilde{\tau}_f^0 = \partial_y\tilde{w}^0 = -\sqrt{s}\left[\frac{1}{s}\partial_Z\tilde{P}^0 + s\alpha\tilde{\zeta}^0\right]e^{-\sqrt{s}y}, \tag{3.64}$$

$$\tilde{\tau}_w^0 = -\sqrt{s}\left[\frac{1}{s}\partial_Z\tilde{P}^0 + s\alpha\tilde{\zeta}^0\right]. \tag{3.65}$$

As expected, the leading–order wall shear rate is a linear combination of the leading–order pressure P^0 and solid axial displacement ζ^0 from tangential velocity continuity at the tube wall (3.30). The derived parietal shear rate appears to be a combination of the $s\to 0$ leading contribution of the theoretical parietal shear rate found by ([56]), namely $-\partial_Z\tilde{P}^0/\sqrt{s}$, which provides a convolution kernel in time space as well as a new (FSI) shear rate contribution ($-\alpha s\sqrt{s}\tilde{\zeta}^0$). Noteworthy, ([56]) found other corrective contributions in his Laplace shear rate, which were related to the fact that his analysis did not consider an asymptotic boundary layer. However, neglecting the (FSI) corrections leads to an inconsistency regarding the velocity

continuity condition. The wall shear rate expressed within the time domain falls from a classical solution to the diffusion equation, yielding the following

$$\tau_w^0(Z,\tau,T) = \frac{1}{\sqrt{\pi}} \int_0^\tau \frac{\partial_{\tau'}\left[W^0(Z,\tau',T) - \alpha\partial_{\tau'}\zeta^0(Z,\tau',T)\right]}{\sqrt{\tau-\tau'}} d\tau'. \tag{3.66}$$

The convolution kernel derived herein (i.e. $1/\sqrt{\pi t}$), is identical to the leading–order contribution of ([56])'s kernel while also sharing the same form as that of ([48]). On the other hand, our analysis reveals that the relevant acceleration to be considered in the convolution product must be the *relative* acceleration of the fluid to that of the pipe's wall, for ensuring asymptotic consistency. Suggested by ([8]), the solid contribution to the fluid wall shear rate is hereby rigorously established. The matching condition upon the radial fluid velocities, spelled out in (2.68), reads

$$\left(\tilde{U}^0 + \delta\tilde{U}^1\right)\big|_{R=1-\delta^\gamma\eta} = \left(\tilde{u}^0 + \delta\tilde{u}^1\right)\big|_{y=\delta^{\gamma-1}\eta}, \tag{3.67}$$

where η is the stretched coordinates defined in (2.67). The matching procedure thus constrains the expression of the unknown velocity functions $\mathcal{F}^0_1(Z,\tau,T)$ in (3.51), yielding to

$$\mathcal{F}^0(Z,\tau,T) = -\chi\partial_\tau P^0 + 2\alpha\nu_s\partial_Z\partial_\tau\zeta^0, \tag{3.68}$$

$$\mathcal{F}^1(Z,\tau,T) = -\chi\partial_\tau P^1 + 2\alpha\nu_s\partial_Z\partial_\tau\zeta^1 + \int_0^\tau \left(\partial_T\mathcal{F}^0 + 2\partial_Z\tau_w^0\right) dt. \tag{3.69}$$

The full derivation of these expressions can be found in Appendix A.

3.8. *Discussion on the fluid–filled pipe asymptotic (FSI) scheme*

Based on many relations involved, it seems critical to focus on relations (3.44) and (3.47) as they reveal the radial–axial and axial stress–pressure Poisson coupling discussed many times in the literature (e.g. ([44,45,43])). The Poisson's modulus indeed converts the radial displacement (i.e. pipe breathing and overpressure) into axial displacement and axial stress, respectively. In the limit $\nu_s \to 0$, this coupling vanishes and the only remaining coupling comes from the radial term. In this zero Poisson coupling limit the pipe can consequently be regarded as successive elastic cylindrical rings independent of each other, as proposed by ([23]). Figure 2 depicts the various couplings that occur in this asymptotic framework, thus providing a comprehensive description and detailed inventory. This scheme is completed by a the Table 1 that provides the related mechanical couplings as well as the associated relations in the derivation.

Table 1: Description of the asymptotic scheme for the fluid–structure–interaction that occur within a fluid–filled elastic tube system.

Relation	**Mechanical coupling**	**Asymptotic sequence**
[1,13]	Normal stress continuity	(3.25) + (3.26)
[2,14]	Radial Hooke's law	(2.45) + [1,13] + (3.37) = (3.44)
[3], [15]-[15] & [21]	Normal velocity continuity	(3.29) + (3.53) = (3.57) + (3.59)
[4,16]	Radial fluid velocity matching	(3.67) + Appendix A
[5], [17]-[17]	Outer fluid mass conservation	(3.51) + (3.52)
[6], [18]-[18]	Outer fluid axial momentum conservation	(3.49)
[7],[19]-[19]	Solid axial momentum conservation	(3.27) + (3.28) + (3.33) = (3.38)
[8,20]	Axial Hooke's law	(3.35) + (3.37) = (3.47)
[9]	Tangential velocity continuity	(3.30) + (3.47)
[10]	Fluid pressure matching	(3.50) + (3.55) + (3.56)
[11]	Inner fluid axial momentum conservation	(3.54)
[12]	Definition of the fluid shear stress	(3.64)
[22]	Tangential stress continuity	(3.27) + (3.28) + (3.33) + (3.34)
[23]	Axial fluid velocity matching	(3.63)

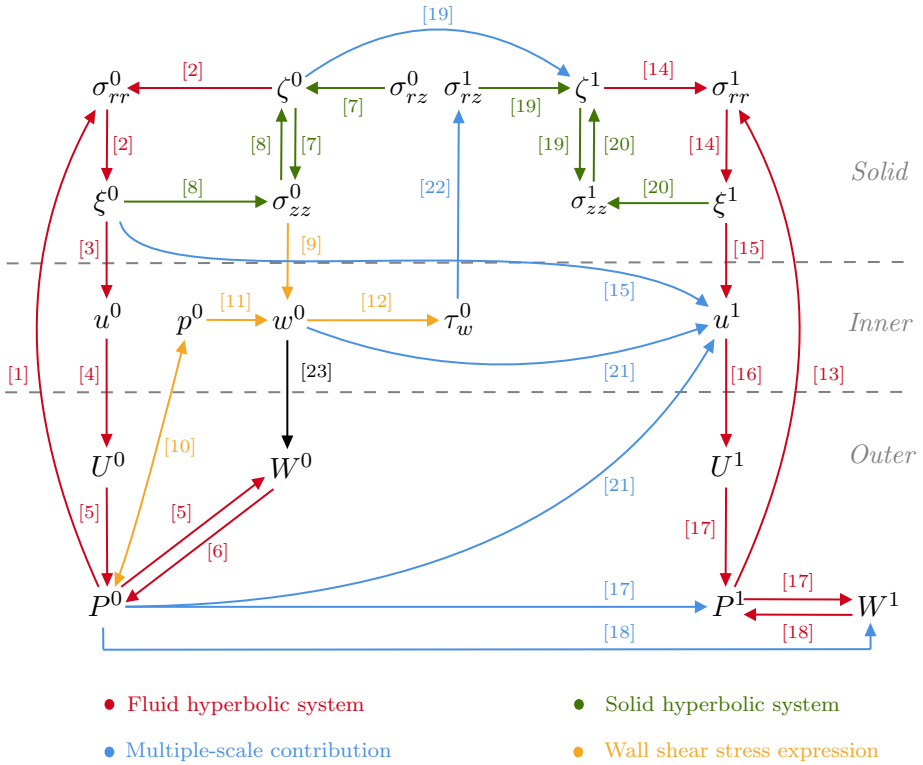

Fig. 2: Asymptotic scheme for fluid–structure–interaction in a fluid–filled elastic tube.

The red loops, (i.e. arrows [1]–[6] and [13]–[18]), in Figure 2 are related to (FSI), resulting in the pulse–wave speed c_p modification occurring from the presence of the surrounding elastic tube. Its mechanism is detailed as follows. First, the pressure pulse is radially transmitted to the solid through stress continuity [1]. Then, the elastic Hooke's rheology transforms this radial stress into solid deformations [2]. The resulting radial velocity displacement should ensure velocity continuity conditions at the tube wall and thus match the inner fluid velocity [3]. A second matching on radial fluid velocity occurs at the boundary layer's interface [4], and the mass conservation equation in the outer region allows one to relate these radial velocity perturbations to the initial pressure pulse and axial velocity [5]. The axial momentum conservation equation [6] provides an outer relation between acceleration and the pressure gradient, which is necessary for closing the model. The red loop is nevertheless slaved to an unknown longitudinal displacement ζ^0 according to [2] which is a consequence of the Poisson coupling effects. Identical successive couplings also apply at first–order, resulting in the second loop (see arrows [13]–[18]).
The green relations, (i.e. [7]–[8] and [19]–[20]), result from the combination of both the axial momentum-conservation equation and elastic Hooke's rheology. This combination produces a hyperbolic system upon ζ^0 and σ_{zz}^0 enslaved by the fluid overpressure p^0. Both hyperbolic systems arising from the red and green loops are consequently coupled through ν_s parameter.
The leading–order fluid shear stress follows from a combination of a pressure uniformity and continuity argument [10], an inner axial momentum conservation equation [11], an axial velocity conservation equation expressed on the axial shear stress, [9], and the fluid shear stress definition [12]. While most damping models ([7], [48], [49], [46]), consider near–wall fluid friction, an additional fluid shear stress occurring from the solid axial dynamic has to be considered. This additional term is nevertheless required in terms of the axial velocity continuity conditions. As the axial velocity matching [23] does not introduce any further information to the coupling scheme, it is omitted from the discussion as a secondary by-product of the analysis.
At first–order, the slow–time contribution and $O(\delta)$ corrections provide additional contributions that must be considered to evaluate the damping of the leading–order. The various contributions are indicated in Figure 2 with blue arrows (i.e. [15], [17], [18], [19], [21] and [22]). At this stage, however the combined effect of these various terms on damping is not easy to summarize, even if it can be re–cast into a highly compact form, as derived later in Section §4.

3.9. *(FSI) coupled hyperbolic system*

The liquid–filled pipe dynamic, at both leading– and first–orders, coupled with (FSI) is governed by a set of two coupled hyperbolic problem systems. The first is related to an elastic solid wave propagation, whereas the second accounts for pulse pressure acoustic wave propagation. Each hyperbolic system is enslaved by either a pressure component for the solid elastic system or the solid axial stress for the fluid

acoustic system. The fluid hyperbolic system is built upon a combination of the axial momentum and the mass conservation equations, or (3.49) and (3.52) respectively, with the expression of the asymptotic matching functions $\mathcal{F}^0$ and $\mathcal{F}^1$ defined in (3.68) and (3.69). The axial momentum conservation equation then achieves in

$$\partial_\tau \left[W^0 + \delta W^1\right] + \delta \partial_T W^0 = -\partial_Z \left[P^0 + \delta P^1\right], \tag{3.70}$$

while the mass conservation equation leads to

$$\partial_\tau \left[P^0 + \delta P^1\right] + \partial_Z \left[W^0 + \delta W^1\right] = 2\alpha\nu_s \partial_Z \left(\partial_\tau \zeta^0 + \delta \left(\partial_\tau \zeta^1 + \partial_T \zeta^0\right)\right) - \delta \partial_T P^0 + 2\delta \int_0^\tau \partial_Z \tau_w^0 dt. \tag{3.71}$$

where the relation $(1 + \chi\mathcal{C}^2)/\mathcal{C}^2 = 1$ from (2.16) have been used. The solid hyperbolic system, in turn, depends on a combination of the axial momentum conservation equation and the derivation with respect to the fast time τ of the axial component of the Hooke's law through combining (3.38), (3.47)

$$\frac{\alpha}{\mathcal{D}} \left(\partial_\tau^2 \zeta^0 + \delta \left(\partial_\tau^2 \zeta^1 + 2\partial_T \partial_\tau \zeta^0\right)\right) - \partial_Z \left[\sigma_{zz}^0 + \delta \sigma_{zz}^1\right] = \frac{2\delta\tau_w^0}{\alpha(2+\alpha)}, \tag{3.72}$$

$$\partial_\tau \left(\sigma_{zz}^0 + \delta \sigma_{zz}^1\right) - \frac{\alpha \mathcal{C}_s^2}{\mathcal{D}} \partial_Z \partial_\tau \left[\zeta^0 + \delta \zeta^1\right] = \frac{2\nu_s}{\alpha(2+\alpha)} \left(P^0 + \delta P^1\right). \tag{3.73}$$

The fast time integration of (3.73)'s leading–order gives

$$-\frac{\alpha \mathcal{C}_s^2}{\mathcal{D}} \partial_Z \zeta^0 = \frac{2\nu_s}{\alpha(2+\alpha)} P^0 - \sigma_{zz}^0, \tag{3.74}$$

then yielding to

$$\partial_\tau \left[\sigma_{zz}^0 + \delta \sigma_{zz}^1\right] - \frac{\alpha \mathcal{C}_s^2}{\mathcal{D}} \partial_Z \left[\partial_\tau \zeta^0 + \delta \left(\partial_\tau \zeta^1 + 2\partial_T \zeta^0\right)\right] = \frac{2\nu_s}{\alpha(2+\alpha)} \partial_\tau \left[P^0 + \delta P^1\right] + 2\delta \partial_T \left(\frac{2\nu_s}{\alpha(2+\alpha)} P^0 - \sigma_{zz}^0\right). \tag{3.75}$$

The equations set of (3.70), (3.71), (3.72) and (3.75) provides the four–(FSI) coupled hyperbolic equations associated with the dynamic of the liquid–filled pipe problem. At leading–order, it is identical to those derived by ([9]) and ([43]). The ([43])'s derivation was based on averaging solid displacement vectors and stress along the radial direction. This approach relies on the hypothesis of no tangential shear stress in the solid (Eq. (2.50) demonstrates that it is indeed $O(\epsilon)$ smaller than the stress spherical components), providing radially uniform stress, which is also a basic assumption of thin–shell models ([40]). The constitutive hyperbolic coupled system is hereby re–organized into a coupled wave equation system that acts upon the pressure and stress variables only. Let us first focus on the pressure wave equation derivation. Combining a fast–time derivative of the outer mass equation (3.71) with the spatial derivative of the outer momentum equation (3.70) leads to the following

$$\left(\partial_\tau^2 - \partial_Z^2\right) \left[P^0 + \delta P^1\right] = 2\alpha\nu_s \partial_Z \partial_\tau \left(\partial_\tau \zeta^0 + \delta \left(\partial_\tau \zeta^1 + \partial_T \zeta^0\right)\right) + \delta \partial_T \left(\partial_Z W^0 - \partial_\tau P^0\right) + 2\delta \partial_Z \tau_w^0. \tag{3.76}$$

The leading–order of (3.71) reads as follows

$$\partial_\tau P^0 + \partial_Z W^0 = 2\alpha\nu_s \partial_Z \partial_\tau \zeta^0, \tag{3.77}$$

while combining (3.77) with (3.72) results in

$$\left(\partial_\tau^2 - \partial_Z^2\right)\left[P^0 + \delta P^1\right] = 2\alpha\nu_s \partial_Z \partial_\tau \left(\partial_\tau \zeta^0 + \delta\left(\partial_\tau \zeta^1 + 2\partial_T \zeta^0\right)\right) - 2\delta\left(\partial_T \partial_\tau P^0 - \partial_Z \tau_w^0\right). \tag{3.78}$$

We now use (3.75) to substitute for $\partial_Z\left(\partial_\tau \zeta^0 + \delta\left(\partial_\tau \zeta^1 + 2\partial_T \zeta^0\right)\right)$ in (3.78). This yields

$$\left(\left[1 + \frac{4\nu_s^2 \mathcal{D}}{\alpha(2+\alpha)\mathcal{C}_s^2}\right]\partial_\tau^2 - \partial_Z^2\right)\left[P^0 + \delta P^1\right] = \frac{2\nu_s \mathcal{D}}{\mathcal{C}_s^2}\partial_\tau^2\left[\sigma_{zz}^0 + \delta\sigma_{zz}^1\right] - 2\delta\left[\partial_T \partial_\tau\left(\left[1 + \frac{4\nu_s^2 \mathcal{D}}{\alpha(2+\alpha)\mathcal{C}_s^2}\right]P^0 - \frac{2\nu_s \mathcal{D}}{\mathcal{C}_s^2}\sigma_{zz}^0\right) - \partial_Z \tau_w^0\right]. \tag{3.79}$$

On the other hand, the solid stress wave equation is revealed by a simple combination of the derivative with respect to τ in (3.75) with the derivative with respect to Z in (3.72), yielding the following

$$\left(\partial_\tau^2 - \mathcal{C}_s^2 \partial_Z^2\right)\left[\sigma_{zz}^0 + \delta\sigma_{zz}^1\right] = \frac{2\nu_s}{\alpha(2+\alpha)}\partial_\tau^2\left[P^0 + \delta P^1\right] - 2\delta\left[\partial_T \partial_\tau\left(\sigma_{zz}^0 - \frac{2\nu_s}{\alpha(2+\alpha)}P^0\right) - \frac{\mathcal{C}_s^2}{\alpha(2+\alpha)}\partial_Z \tau_w^0\right]. \tag{3.80}$$

Both wave–equations can be re–casted into a coupled formulation

$$\left(\partial_\tau^2 - \mathbf{C}_\mathbf{P}^2 \partial_Z^2\right)\left[\mathbf{P}^0 + \delta\mathbf{P}^1\right] = -2\delta\left[\partial_T \partial_\tau \mathbf{P}^0 - \partial_Z \tau_w^0\begin{pmatrix} 1 + \frac{2\nu_s \mathcal{D}}{\alpha(2+\alpha)} \\ \frac{1}{\alpha(2+\alpha)}\left[2\nu_s \mathcal{D} + \mathcal{C}_s^2 + \frac{4\nu_s^2 \mathcal{D}}{\alpha(2+\alpha)}\right]\end{pmatrix}\right], \tag{3.81}$$

where

$$\mathbf{C}_\mathbf{P}^2 = \begin{pmatrix} 1 & 2\nu_s \mathcal{D} \\ \frac{2\nu_s}{\alpha(2+\alpha)} & \frac{4\nu_s^2 \mathcal{D}}{\alpha(2+\alpha)} + \mathcal{C}_s^2 \end{pmatrix} \quad \text{, and, } \quad \mathbf{P}^0 + \delta\mathbf{P}^1 = \begin{pmatrix} P^0 + \delta P^1 \\ \sigma_{zz}^0 + \delta\sigma_{zz}^1 \end{pmatrix}. \tag{3.82}$$

The leading–order of (3.81) displays a parabolic form without dissipation associated with a fast time–scale wave propagation, as opposed to the additional slow–time scale damping that arises when $O(\delta)$ corrections are considered. This short–time behavior appears because the dissipation in the fluid boundary layer does not have time to develop; thus, the coupled system remains purely conservative. The eigenvalues $c_\pm$ of $\mathbf{C}_\mathbf{P}^2$ provide the (FSI)'s impact on the previously defined *intrinsic* wave speeds c_p and c_s. More precisely, since c_p is selected as the reference speed, $c_p c_-$ provides the fluid pulse pressure wave speed mode while $c_p c_+$ provides the elastic wave speed mode. The eigenvalues $c_\pm^2$ are found equal to

$$c_\pm^2 = \frac{1 + \mathcal{C}_s^2 + \frac{4\nu_s^2 \mathcal{D}}{\alpha(2+\alpha)} \pm \sqrt{\left(1 + \mathcal{C}_s^2 + \frac{4\nu_s^2 \mathcal{D}}{\alpha(2+\alpha)}\right)^2 - 4\mathcal{C}_s^2}}{2}. \tag{3.83}$$

In dimensional form, these expressions are identical to those of ([43]). In the latter, and for the sake of brevity, the sum of the squared speed $\overline{c^2}$ is introduced

$$\overline{c^2} = c_+^2 + c_-^2 = 1 + \mathcal{C}_s^2 + \frac{4\nu_s^2\mathcal{D}}{\alpha(2+\alpha)}. \tag{3.84}$$

The asymptotic behavior with respect to the α parameter of all dimensionless (FSI) characteristic wave speeds is provided in Figure 3. As α increases or $\nu_s \to 0$, the dimensionless positive and negative wave speed mode, $c_\pm$, respectively tend to $\mathcal{C}_s$ and one according to (3.83), as depicted in Figures 3b, 3c and 3d. In other words, in the $\nu_s \to 0$ limit the wave-speed remains unhampered by the (FSI) and the pressure pulse propagates at c_p within the fluid while the elastic wave at c_s within the tube. For the wave speed signatures depicted here, the pulse wave speed modifications, (i.e. corrections in c_-, Cf. Figure 3c), remains low and do not exceed 6% (for $\nu_s = 0.35$).

3.10. *Axial gradient of the wall shear rate, $\partial_Z \tau_w^0$*

Let us now derive the previous expression of the parietal shear rate, τ_w^0 with respect to Z in (3.65) to enclose the 2D vector wave equation (3.81). Combining it with the leading–order Laplace transforms of (3.70) and (3.71) leads to

$$\partial_Z \tilde{\tau}_w^0 = -s\sqrt{s}\left(\tilde{P}^0 + \alpha(1-2\nu_s)\partial_Z\tilde{\zeta}^0\right), \tag{3.85}$$

while the use of (3.74) transforms it into

$$\partial_Z \tilde{\tau}_w^0 = -s\sqrt{s}\left(\left[1-(1-2\nu_s)\frac{2\nu_s\mathcal{D}}{\alpha\mathcal{C}_s^2(2+\alpha)}\right]\tilde{P}^0 + (1-2\nu_s)\frac{\mathcal{D}}{\mathcal{C}_s^2}\tilde{\sigma}_{zz}^0\right). \tag{3.86}$$

The axial gradient of the fluid wall shear stress appears to be a linear combination of $\tilde{P}^0$ and $\tilde{\sigma_{zz}^0}$; thus, the vector–wave equation defined in (3.81) ensues in the Laplace domain

$$\left(s^2 - \mathbf{C}_\mathbf{P}^2\partial_Z^2\right)\tilde{\mathbf{P}}^0 = \mathbf{0}, \tag{3.87}$$

$$\left(s^2 - \mathbf{C}_\mathbf{P}^2\partial_Z^2\right)\tilde{\mathbf{P}}^1 = -2s\left[\partial_T + \sqrt{s}\mathbf{E}\right]\tilde{\mathbf{P}}^0, \tag{3.88}$$

where

$$\mathbf{E} = \frac{1}{2\nu_s}\begin{pmatrix} \left(1-(1-2\nu_s)\frac{\overline{c^2}-1}{\mathcal{C}_s^2}\right)\left(1+\frac{2\nu_s\mathcal{D}}{\alpha(2+\alpha)}\right) & \frac{2\nu_s\mathcal{D}(1-2\nu_s)}{\mathcal{C}_s^2}\left(1+\frac{2\nu_s\mathcal{D}}{\alpha(2+\alpha)}\right) \\ \left(1-(1-2\nu_s)\frac{\overline{c^2}-1}{\mathcal{C}_s^2}\right)\frac{\overline{c^2}-(1-2\nu_s)}{\alpha(2+\alpha)} & \frac{2\nu_s\mathcal{D}(1-2\nu_s)}{\mathcal{C}_s^2}\frac{\overline{c^2}-(1-2\nu_s)}{\alpha(2+\alpha)} \end{pmatrix}. \tag{3.89}$$

Supplementary details of this derivation are provided in Appendix B.1.

4. Pressure–stress wave equation solution and secularity condition

4.1. *Leading– and first–order pressure–stress wave equations*

The solutions to (3.87)-(3.88) are sought in the eigenvector basis of $\mathbf{C}_\mathbf{P}^2$, while eigenvalues of $\mathbf{C}_\mathbf{P}^2$ are defined in (3.83). Let us define $\mathbf{\Pi}$ the transition matrix from the

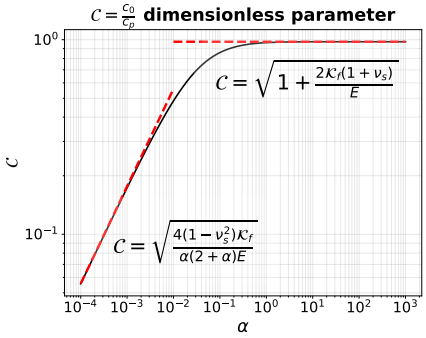

(a) Asymptotic behavior of $\mathcal{C} = \frac{c_0}{c_p}$

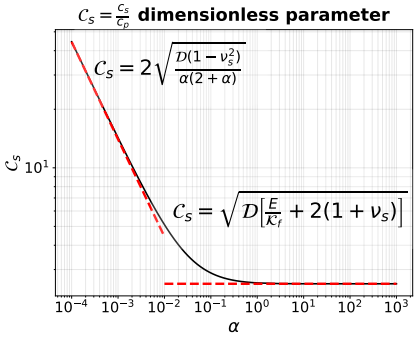

(b) Asymptotic behavior of $\mathcal{C}_s = \frac{c_s}{c_p}$

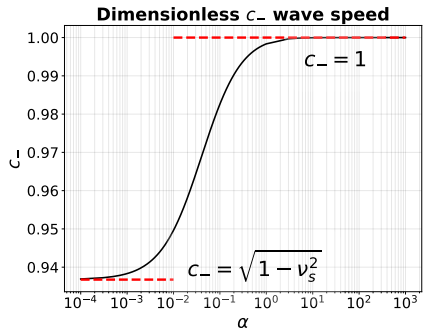

(c) Asymptotic behavior of c_-

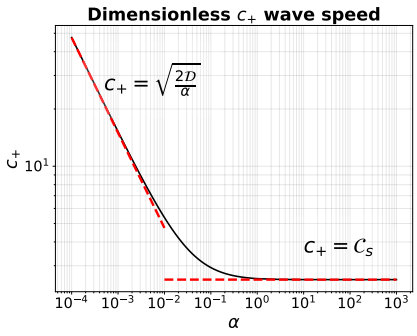

(d) Asymptotic behavior of c_+

Fig. 3: α-dependence ($\alpha = \frac{e}{R_0}$) of the characteristic wave speeds of the (FSI) problem for $\nu_s = 0.35$ and $\mathcal{D} = 0.1122$, $\frac{E}{\mathcal{K}_f} = 54$. The red dashed lines provide information on the asymptotic behavior of the dimensionless wave speeds with respect to α.

canonical basis, $(\mathbf{e}_1, \mathbf{e}_2)$ to the eigenvector basis of $\mathbf{C}^2_{\mathbf{P}}$, $\boldsymbol{\mathcal{C}}^2_{\boldsymbol{\mathcal{P}}}$ the associated diagonal matrix, $\tilde{\boldsymbol{\mathcal{P}}}^0 = \left(\tilde{\mathcal{P}}^0_-, \tilde{\mathcal{P}}^0_+\right)$, $\tilde{\boldsymbol{\mathcal{P}}}^1 = \left(\tilde{\mathcal{P}}^1_-, \tilde{\mathcal{P}}^1_+\right)$ and $\boldsymbol{\mathcal{E}}$ respectively the expression of $\left(\tilde{\mathbf{P}}^0, \tilde{\mathbf{P}}^1\right)$ and $\mathbf{E}$ in the eigenvector basis. Then

$$\boldsymbol{\Pi} = \begin{pmatrix} \frac{2\nu_s\mathcal{D}}{c_-^2-1} & \frac{2\nu_s\mathcal{D}}{c_+^2-1} \\ 1 & 1 \end{pmatrix} \quad \& \quad \boldsymbol{\Pi}^{-1} = \frac{1}{\det(\boldsymbol{\Pi})} \begin{pmatrix} 1 & -\frac{2\nu_s\mathcal{D}}{c_+^2-1} \\ -1 & \frac{2\nu_s\mathcal{D}}{c_-^2-1} \end{pmatrix}, \tag{4.1}$$

$$\boldsymbol{\mathcal{C}}^2_{\boldsymbol{\mathcal{P}}} = \boldsymbol{\Pi}^{-1} \cdot \mathbf{C}^2_{\mathbf{P}} \cdot \boldsymbol{\Pi} = \begin{pmatrix} c_-^2 & 0 \\ 0 & c_+^2 \end{pmatrix}, \tag{4.2}$$

$$\mathbf{E} = \boldsymbol{\Pi}^{-1} \cdot \boldsymbol{\mathcal{E}} \cdot \boldsymbol{\Pi}, \quad \tilde{\mathbf{P}}^0 = \boldsymbol{\Pi} \cdot \tilde{\boldsymbol{\mathcal{P}}}^0 \quad \& \quad \tilde{\mathbf{P}}^1 = \boldsymbol{\Pi} \cdot \tilde{\boldsymbol{\mathcal{P}}}^1. \tag{4.3}$$

Some additional elements regarding the axial boundary conditions, provided in §2.5, are now discussed. In the fluid, the downstream velocity variation (2.58), i.e. $W^0\big|_{Z=1} + \delta W^1\big|_{Z=1} = -H_{eav}(\tau)$, is equivalent, regarding the leading– and first–orders fluid momentum conservation equation (3.70), to impose Neumann condition on the pressure field, then yielding to

$$\partial_Z P^0\big|_{Z=1} = \delta(\tau) \quad \text{, and, } \quad \partial_Z P^1\big|_{Z=1} = 0, \tag{4.4}$$

where $\delta(\tau)$ is the Dirac distribution. Upstream, the homogeneous Dirichlet condition applied on the pressure trivially leads to

$$P^0\big|_{Z=0} = P^1\big|_{Z=0} = 0. \tag{4.5}$$

In the solid, the upstream and downstream homogeneous Dirichlet conditions (2.59), i.e. $\zeta^0\big|_{Z=0\&1} = \zeta^1\big|_{Z=0\&1} = 0$, are equivalent regarding (3.72) to

$$\partial_Z \sigma^0_{zz}\big|_{Z=0\&1} = 0 \quad \text{, and, } \quad \partial_Z \sigma^1_{zz}\big|_{Z=0\&1} = -\frac{2}{\alpha(2+\alpha)} \tau^0_w\big|_{Z=0\&1}. \tag{4.6}$$

For the sake of simplicity and compactness let us introduce four 2×2 matrices $\boldsymbol{\mathcal{N}}$, $\boldsymbol{\mathcal{M}}$, $\boldsymbol{\mathcal{Q}}$, $\boldsymbol{\mathcal{R}}$. Boundary conditions in the diagonalization basis can formally be written as a rectangular 4×8 linear system

$$\begin{pmatrix} \boldsymbol{\mathcal{N}} & \boldsymbol{\mathcal{M}} & \mathbf{0} & \mathbf{0} \\ \mathbf{0} & \mathbf{0} & \boldsymbol{\mathcal{Q}} & \boldsymbol{\mathcal{R}} \end{pmatrix} \left[\begin{pmatrix} \tilde{\boldsymbol{\mathcal{P}}}^0\big|_{Z=0} \\ \partial_Z \tilde{\boldsymbol{\mathcal{P}}}^0\big|_{Z=0} \\ \tilde{\boldsymbol{\mathcal{P}}}^0\big|_{Z=1} \\ \partial_Z \tilde{\boldsymbol{\mathcal{P}}}^0\big|_{Z=1} \end{pmatrix} + \delta \begin{pmatrix} \tilde{\boldsymbol{\mathcal{P}}}^1\big|_{Z=0} \\ \partial_Z \tilde{\boldsymbol{\mathcal{P}}}^1\big|_{Z=0} \\ \tilde{\boldsymbol{\mathcal{P}}}^1\big|_{Z=1} \\ \partial_Z \tilde{\boldsymbol{\mathcal{P}}}^1\big|_{Z=1} \end{pmatrix} \right] =$$

$$\frac{\left(c_-^2 - 1\right)}{2\nu_s \mathcal{D}} \begin{pmatrix} 0 \\ 0 \\ 1 \\ 0 \end{pmatrix} + \delta \left(\frac{2}{\alpha(2+\alpha)\sqrt{s}} \begin{pmatrix} 0 \\ 0 \\ 0 \\ 1 \end{pmatrix} + \begin{pmatrix} \mathbf{0} & \boldsymbol{\mathcal{M}}\boldsymbol{\mathcal{N}} & \mathbf{0} & \mathbf{0} \\ \mathbf{0} & \mathbf{0} & \mathbf{0} & \mathbf{0} \end{pmatrix} \begin{pmatrix} \tilde{\boldsymbol{\mathcal{P}}}^0\big|_{Z=0} \\ \partial_Z \tilde{\boldsymbol{\mathcal{P}}}^0\big|_{Z=0} \\ \tilde{\boldsymbol{\mathcal{P}}}^0\big|_{Z=1} \\ \partial_Z \tilde{\boldsymbol{\mathcal{P}}}^0\big|_{Z=1} \end{pmatrix} \right), \tag{4.7}$$

where

$$\boldsymbol{\mathcal{N}} = \begin{pmatrix} 1 & \frac{c_- \beta}{c_+} \\ 0 & 0 \end{pmatrix}, \quad \boldsymbol{\mathcal{M}} = \begin{pmatrix} 0 & 0 \\ 1 & 1 \end{pmatrix}, \quad \boldsymbol{\mathcal{Q}} = \mathbf{0}, \quad \boldsymbol{\mathcal{R}} = \boldsymbol{\mathcal{N}} + \boldsymbol{\mathcal{M}}, \tag{4.8}$$

and

$$\beta = \frac{c_+ \left(c_-^2 - 1\right)}{c_- \left(c_+^2 - 1\right)}. \tag{4.9}$$

In deriving (4.7), the use have been used of $\partial_Z \tilde{\tau}^0_w\big|_{Z=0\&1} = -\frac{1}{\sqrt{s}} \tilde{P}^0\big|_{Z=0\&1}$ according to (3.65) and the solid boundary conditions. Let us then define the operator $\mathcal{H}$ that acts on the square–integrable 2D–vector field $\boldsymbol{\Psi}(Z)$

$$\forall \boldsymbol{\Psi}(Z) \in L^2(\mathbb{R}) \times L^2(\mathbb{R}), \quad \boldsymbol{\Psi}(Z) \to \mathcal{H}\boldsymbol{\Psi}(Z) = \boldsymbol{\mathcal{C}}^2_{\boldsymbol{\mathcal{P}}} \cdot \partial_Z^2 \boldsymbol{\Psi}(Z), \tag{4.10}$$

with the following homogeneous associated set of spatial boundary conditions

$$\begin{pmatrix} \boldsymbol{\mathcal{N}} & \boldsymbol{\mathcal{M}} & \mathbf{0} & \mathbf{0} \\ \mathbf{0} & \mathbf{0} & \boldsymbol{\mathcal{Q}} & \boldsymbol{\mathcal{R}} \end{pmatrix} \cdot \begin{pmatrix} \boldsymbol{\Psi}(0) \\ \partial_Z \boldsymbol{\Psi}(0) \\ \boldsymbol{\Psi}(1) \\ \partial_Z \boldsymbol{\Psi}(1) \end{pmatrix} = \mathbf{0}. \tag{4.11}$$

The vector–wave equations system (3.87)&(3.88) then become

$$\left(s^2 - \mathcal{H}\right) \left(\tilde{\boldsymbol{\mathcal{P}}}^0 + \delta \tilde{\boldsymbol{\mathcal{P}}}^1\right) = -2s\delta \left[\partial_T + \sqrt{s}\boldsymbol{\mathcal{E}}\right] \tilde{\boldsymbol{\mathcal{P}}}^0. \tag{4.12}$$

4.2. *Strategic decomposition of $\tilde{\boldsymbol{\mathcal{P}}}^0$ and $\tilde{\boldsymbol{\mathcal{P}}}^1$*

Following Duhamel's principle, the vectors $\left(\tilde{\boldsymbol{\mathcal{P}}}^0, \tilde{\boldsymbol{\mathcal{P}}}^1\right)$ are split into homogeneous solutions $\left(\tilde{\boldsymbol{\mathcal{P}}}^0_h, \tilde{\boldsymbol{\mathcal{P}}}^1_h\right)$ (both having homogeneous boundary conditions) and particular ones $\left(\tilde{\boldsymbol{\mathcal{P}}}^0_p, \tilde{\boldsymbol{\mathcal{P}}}^1_p\right)$ taking care–off non–homogeneous boundary conditions. Both leading– and first–orders homogeneous components, $\tilde{\boldsymbol{\mathcal{P}}}^0_h$ and $\tilde{\boldsymbol{\mathcal{P}}}^1_h$, are then decomposed into the eigenvector orthonormal basis, $\boldsymbol{\Phi}_k(Z)$, of the operator $\mathcal{H}$

$$\tilde{\boldsymbol{\mathcal{P}}}^0(Z,s,T) = \sum_{\lambda_k \in \mathbb{R}} \tilde{a}^0_{\lambda_k}(s) A_{\lambda_k}(T) \boldsymbol{\Phi}_{\lambda_k}(Z) + \tilde{\boldsymbol{\mathcal{P}}}^0_p(Z,s), \tag{4.13}$$

$$\tilde{\boldsymbol{\mathcal{P}}}^1(Z,s) = \sum_{\lambda_k \in \mathbb{R}} \tilde{a}^1_{\lambda_k}(s) \boldsymbol{\Phi}_{\lambda_k}(Z) + \tilde{\boldsymbol{\mathcal{P}}}^1_p(Z,s), \tag{4.14}$$

where $A_{\lambda_k}(T)$ is for the long–time attenuation amplitude of each leading–order kth mode associated with $\mathcal{H}$'s eigenvalues, $-\lambda_k^2$. It is shown in Appendix C that the operator $\mathcal{H}$ is self–adjoint for the scalar product

$$\forall \boldsymbol{\Psi}, \boldsymbol{\Psi}^{'} \in L^2(\mathbb{R}) \times L^2(\mathbb{R}), \quad \langle \boldsymbol{\Psi}^{'}, \boldsymbol{\Psi} \rangle = \sum_{j=1}^{2} \eta_j \int_0^1 \Psi^{'}_j(Z) \Psi_j(Z) dZ, \tag{4.15}$$

with $\boldsymbol{\eta} \equiv [\eta_1, \eta_2] = [1, -\beta \left(c_-/c_+\right)^3]$ for a reservoir–pipe–anchored valve system, ([4]). The eigenvectors $\boldsymbol{\Phi}_{\lambda_k}(Z)$ then constitute an orthogonal basis of $\mathcal{H}$. Note that (4.14) displays no dependence on the long–time scale T because $O(\delta T)$ corrections have been discarded. It is also interesting to mention that the choice for the particular solution $\tilde{\boldsymbol{\mathcal{P}}}^0_p(Z,s)$ is not unique even–though it has to fulfill the prescribed non-homogeneous boundary conditions. The general solution in the RHS of (4.13) is thus adapted so as to provide the unique LHS $\tilde{\boldsymbol{\mathcal{P}}}^0(Z,s,T)$. The initial rest conditions of the unsteady fields along with the orthogonal behavior of $\boldsymbol{\Phi}_{\lambda_k}(Z)$ imposes

$$a_{\lambda_k}(0) = -\langle \boldsymbol{\mathcal{P}}^0_p(Z,0), \boldsymbol{\Phi}_{\lambda_k}(Z) \rangle \;\; \& \;\; \partial_\tau a_{\lambda_k}(0) = -\langle \partial_\tau \boldsymbol{\mathcal{P}}^0_p(Z,0), \boldsymbol{\Phi}_{\lambda_k}(Z) \rangle \tag{4.16}$$

The terms $\left(\tilde{\boldsymbol{\mathcal{P}}}_p^{\,0}(Z,s), \tilde{\boldsymbol{\mathcal{P}}}_p^{\,1}(Z,s)\right)$ are regarded as separated space–time variables functions

$$\tilde{\boldsymbol{\mathcal{P}}}_p^0(Z,s) \equiv \tilde{\boldsymbol{\mathcal{P}}}_p^0(Z) = \frac{Z}{\det(\boldsymbol{\Pi})}\begin{pmatrix}1\\-1\end{pmatrix}, \tag{4.17}$$

$$\tilde{\boldsymbol{\mathcal{P}}}_p^1(Z,s) = \frac{1}{\alpha(2+\alpha)\sqrt{s}}\left(\frac{Z^2}{1-\frac{c_+}{c_-\beta}}\begin{pmatrix}1\\-\frac{c_+}{c_-\beta}\end{pmatrix} - \frac{4\nu_s\mathcal{D}\left(\frac{Z^2}{2}-Z\right)}{c_-^2-1}\begin{pmatrix}1 & 0\\ 0 & \frac{c_-\beta}{c_+}\end{pmatrix}\partial_Z\tilde{\boldsymbol{\mathcal{P}}}^0|_{Z=0}\right), \tag{4.18}$$

the which are particular solutions for the boundary condition system (4.7). In the early–stage of the propagation, the fast–time τ is of order $O(1)$ such that $T \sim O(\delta)$ according to the slow–time definition (3.3). Thus, from a fast–time viewpoint, the attenuation function thereby remains at initial condition $A_{\lambda_k}(0) = 1$, set up to one, and leads to

$$A_{\lambda_k}(T) \equiv A_{\lambda_k}(\delta\tau) \approx 1, \quad \text{for,} \quad \tau \ll O\left(\frac{1}{\delta}\right), \text{i.e} \quad T \sim O(1). \tag{4.19}$$

This condition nevertheless holds as long as τ does not exceeds $O(1/\delta)$. In this limit, the attenuation plays an overcoming role, and a secularity condition is required to ensure consistency ([19]). Then, this secularity condition, associated with the resonance condition of the $O(\delta)$ perturbations sets the long–time attenuation amplitude $A_{\lambda_k}(T)$, which is investigated next. Note that since $\boldsymbol{\mathcal{P}}^0$ is real, the LHS of (4.13) is also real when s is real from the definition of the Laplace transform (3.60). Hence the RHS of (4.13) is also real when s is real. Then, from the parity of $\boldsymbol{\Phi}_{\lambda_k} = \boldsymbol{\Phi}_{-\lambda_k}$ detailed in Appendix C, a conjugation of the amplitudes is required for each mode couple $(\lambda_k, -\lambda_k)$: $\tilde{a}^{0\star}_{\lambda_k} A^\star_{\lambda_k} = \tilde{a}^0_{-\lambda_k} A_{-\lambda_k}$ for real s. Furthermore, since this conjugate relation has to hold for every slow–time T and since at $T = 0$ $A_{\lambda_k}(0) = 1$, the conjugate condition extend to both $\tilde{a}^0_{\lambda_k}$ and A_{λ_k}, i.e., $\tilde{a}^{0\star}_{\lambda_k} = \tilde{a}^0_{-\lambda_k}$ for real s and $A^\star_{\lambda_k} = A_{-\lambda_k}$.

4.3. *Solution for 2D–vector wave equation*

4.3.1. *Leading–order fast–time dependent amplitude* $\tilde{a}^0_k(s)$

Combining $\tilde{\boldsymbol{\mathcal{P}}}^0(Z,s,T=0)$ (the $T=0$ is chosen according to condition (4.19)) in expression (4.13) with boundary conditions (4.16) into the constitutive vector-wave equation (4.12) leads to

$$\sum_{\lambda_k\in\mathbb{R}} \left(s^2 - \mathcal{H}\right)\tilde{a}^0_{\lambda_k}(s)\boldsymbol{\Phi}_{\lambda_k}(Z) = -s^2\tilde{\boldsymbol{\mathcal{P}}}^0_p(Z). \tag{4.20}$$

Using (C.4), the orthogonality of the eigenfunction basis as well as its symmetry $\boldsymbol{\Phi}_{\lambda_k} = \boldsymbol{\Phi}_{-\lambda_k}$, one obtains the following

$$\tilde{a}^0_{\lambda_k}(s) + \tilde{a}^0_{-\lambda_k}(s) = \left[\frac{\lambda_k}{2i}\left(\frac{1}{s-i\lambda_k} - \frac{1}{s+i\lambda_k}\right) - 1\right]\langle\tilde{\boldsymbol{\mathcal{P}}}^0_p(Z), \boldsymbol{\Phi}_{\lambda_k}(Z)\rangle. \tag{4.21}$$

An identification using the conjugate relation $\tilde{a}^{0\star}_{\lambda_k} = \tilde{a}^0_{-\lambda_k}$ (for real s) discussed above, thus leads to the following (note that this identification is not unique up to

irrelevant odd functions of λ_k, canceling out in the mode summation)

$$\tilde{a}^0_{\pm\lambda_k}(s) = -\frac{1}{2}\left[\frac{\pm i\lambda_k}{s \mp i\lambda_k} + 1\right] \langle \tilde{\boldsymbol{\mathcal{P}}}^0_p(Z), \boldsymbol{\Phi}_{\lambda_k}(Z)\rangle. \tag{4.22}$$

Finally re–injecting the $\tilde{a}^0_{\lambda_k}(s)$ found in (4.22) within the Laplace transform in (4.13) gives the following

$$\tilde{\boldsymbol{\mathcal{P}}}^0(Z,s,T) = \tilde{\boldsymbol{\mathcal{P}}}^0_p(Z) - \sum_{\lambda_k\in\mathbb{R}} \frac{A_{\lambda_k}(T)}{2}\left[\frac{i\lambda_k}{s - i\lambda_k} + 1\right] \langle \tilde{\boldsymbol{\mathcal{P}}}^0_p(Z), \boldsymbol{\Phi}_{\lambda_k}(Z)\rangle \boldsymbol{\Phi}_{\lambda_k}(Z) \tag{4.23}$$

At this stage, the attenuation $A_{\lambda_k}(T)$ remains the only unknown.

4.3.2. *First–order coupled wave equation and secularity condition*

Next, let us combine the Laplace splitting form of $\tilde{\boldsymbol{\mathcal{P}}}^1(Z,s)$ in (4.14) within the first–order constitutive vector–wave equation (4.12). Regarding the derived expression of $\tilde{\boldsymbol{\mathcal{P}}}^0$ in (4.23), it then yields the following

$$\begin{aligned}\sum_{\lambda_k\in\mathbb{R}} \left(s^2 + \lambda_k^2\right) \tilde{a}^1_{\lambda_k}(s)\boldsymbol{\Phi}_{\lambda_k}(Z) &= -\left(s^2 - \mathcal{H}\right) \tilde{\boldsymbol{\mathcal{P}}}^1_p(Z,s) - 2s\sqrt{s}\boldsymbol{\mathcal{E}}\tilde{\boldsymbol{\mathcal{P}}}^0_p(Z,s)\\ &+ s\sum_{\lambda_k\in\mathbb{R}} \left[\partial_T + \sqrt{s}\boldsymbol{\mathcal{E}}\right] A_{\lambda_k}(T)\left[\frac{i\lambda_k}{s - i\lambda_k} + 1\right] \langle \tilde{\boldsymbol{\mathcal{P}}}^0_p(Z,s), \boldsymbol{\Phi}_{\lambda_k}(Z)\rangle \boldsymbol{\Phi}_{\lambda_k}(Z).\end{aligned} \tag{4.24}$$

A complete derivation of $\left(s^2 - \mathcal{H}\right) \tilde{\boldsymbol{\mathcal{P}}}^1_p(Z,s)$ have been carried out in Appendix D, and is not repeated here. From the orthogonality of $\boldsymbol{\Phi}_{\lambda_k}(Z)$, one finds the following

$$\begin{aligned}\tilde{a}^1_{\lambda_k}(s) + \tilde{a}^1_{-\lambda_k}(s) &= is\lambda_k \frac{\langle \tilde{\boldsymbol{\mathcal{P}}}^0_p(Z,s), \boldsymbol{\Phi}_{\lambda_k}(Z)\rangle}{(s + i\lambda_k)\,(s - i\lambda_k)^2}\left[\partial_T + \sqrt{s}\langle \boldsymbol{\mathcal{E}}\boldsymbol{\Phi}_{\lambda_k}(Z) - \frac{\boldsymbol{\mathcal{J}}_{\lambda_k}(Z,s)}{s^2}, \boldsymbol{\Phi}_{\lambda_k}(Z)\rangle\right] A_{\lambda_k}(T)\\ &- is\lambda_k \frac{\langle \tilde{\boldsymbol{\mathcal{P}}}^0_p(Z,s), \boldsymbol{\Phi}_{\lambda_k}(Z)\rangle}{(s - i\lambda_k)\,(s + i\lambda_k)^2}\left[\partial_T + \sqrt{s}\langle \boldsymbol{\mathcal{E}}\boldsymbol{\Phi}_{\lambda_k}(Z) - \frac{\boldsymbol{\mathcal{J}}_{\lambda_k}(Z,s)}{s^2}, \boldsymbol{\Phi}_{\lambda_k}(Z)\rangle\right] A_{-\lambda_k}(T)\\ -2s\sqrt{s}\frac{\langle \boldsymbol{\mathcal{E}}\tilde{\boldsymbol{\mathcal{P}}}^0_p(Z,s), \boldsymbol{\Phi}_{\lambda_k}(Z)\rangle}{s^2 + \lambda_k^2} &+ s\left[\partial_T + \sqrt{s}\langle \boldsymbol{\mathcal{E}}\boldsymbol{\Phi}_{\lambda_k}(Z), \boldsymbol{\Phi}_{\lambda_k}(Z)\rangle\right]\left(A_{\lambda_k}(T) + A_{-\lambda_k}(T)\right)\frac{\langle \tilde{\boldsymbol{\mathcal{P}}}^0_p(Z,s), \boldsymbol{\Phi}_{\lambda_k}(Z)\rangle}{s^2 + \lambda_k^2}\\ &+ s\sqrt{s}\sum_{\lambda_j\in\mathbb{R}\setminus\{-\lambda_k,\lambda_k\}}\left[\frac{i\lambda_j}{s - i\lambda_j} + 1\right]\frac{\langle \tilde{\boldsymbol{\mathcal{P}}}^0_p(Z,s), \boldsymbol{\Phi}_{\lambda_j}(Z)\rangle\langle \boldsymbol{\mathcal{E}}\boldsymbol{\Phi}_{\lambda_j}(Z), \boldsymbol{\Phi}_{\lambda_k}(Z)\rangle}{(s - i\lambda_k)\,(s + i\lambda_k)} A_{\lambda_j}(T)\\ -\frac{1}{\alpha(2+\alpha)\sqrt{s}\left(s^2 + \lambda_k^2\right)}\langle \frac{s^2Z^2 - 2\mathcal{C}^2_{\boldsymbol{\mathcal{P}}}}{1 - \frac{c_+}{c_-\beta}}\begin{pmatrix}1\\ -\frac{c_+}{c_-\beta}\end{pmatrix} &- \frac{s^2\left(Z^2 - 2Z\right) - 2\mathcal{C}^2_{\boldsymbol{\mathcal{P}}}}{1 - \frac{c_-\beta}{c_+}}\begin{pmatrix}1\\ -\frac{c_-\beta}{c_+}\end{pmatrix}, \boldsymbol{\Phi}_{\lambda_k}(Z)\rangle\\ &- \sum_{\lambda_j\in\mathbb{R}\setminus\{-\lambda_k,\lambda_k\}} i\lambda_j \frac{\langle \tilde{\boldsymbol{\mathcal{P}}}^0_p(Z), \boldsymbol{\Phi}_{\lambda_j}(Z)\rangle\langle \boldsymbol{\mathcal{J}}_{\lambda_j}(Z,s), \boldsymbol{\Phi}_{\lambda_k}(Z)\rangle}{\sqrt{s}\,(s - i\lambda_j)\,(s - i\lambda_k)\,(s + i\lambda_k)} A_{\lambda_j}(T)\\ &- \sum_{\lambda_j\in\mathbb{R}} \frac{\langle \tilde{\boldsymbol{\mathcal{P}}}^0_p(Z), \boldsymbol{\Phi}_{\lambda_j}(Z)\rangle\langle \boldsymbol{\mathcal{J}}_{\lambda_j}(s,Z), \boldsymbol{\Phi}_{\lambda_k}(Z)\rangle}{\sqrt{s}\,(s - i\lambda_k)\,(s + i\lambda_k)} A_{\lambda_j}(T),\end{aligned} \tag{4.25}$$

with

$$\boldsymbol{\mathcal{J}}_{\lambda_k}(Z,s) = \frac{\lambda_k}{\alpha(2+\alpha)\left(1 - \frac{c_-\beta}{c_+}\right)}\begin{pmatrix}\left(s^2\left(\frac{Z^2}{2} - Z\right) - c_-^2\right)\frac{\tan\left(\frac{\lambda_k}{c_-}\right)}{c_-}\\ -\left(s^2\left(\frac{Z^2}{2} - Z\right) - c_+^2\right)\frac{\tan\left(\frac{\lambda_k}{c_+}\right)}{c_+}\end{pmatrix}, \tag{4.26}$$

an even function of λ_k. The secularity contribution lies in every double–pole found in the RHS terms of $\tilde{a}^1_{\lambda_k}(s)$. These double–poles are associated with resonance conditions between the (4.24)'s RHS and the natural frequencies of the (4.24)'s LHS, i.e. $(s \pm i\lambda_k)^2$. These resonance conditions produce a linear divergence term upon the fast time τ of $\tilde{a}^1_{\lambda_k}(s)$, as found from the inverse Laplace transform of the double poles in (4.25), through Cauchy's residue theorem

$$\mathcal{L}^{-1}\left(\frac{1}{(s \pm i\lambda_k)^2}\right)(\tau) = \lim_{s \to \pm i\lambda_k} (\partial_s e^{s\tau}) = \tau e^{\pm i\lambda_k \tau}. \tag{4.27}$$

When τ reaches $O(1/\delta)$, the asymptotic approximation collapses since assumption (4.19) vanishes. To prevent it, the attenuation function is built to cancel the divergent double–pole contributions. In (4.25), double–poles are gathered within the two first RHS terms since $\lambda_j \neq \pm\lambda_k$. The secularity condition therefore reads as follows

$$\lim_{s \to \pm i\lambda_k} \left(\partial_T + \sqrt{s}\langle \boldsymbol{\mathcal{E}}\boldsymbol{\Phi}_{\lambda_k}(Z) - \frac{\boldsymbol{\mathcal{J}}_{\lambda_k}(Z,s)}{s^2}, \boldsymbol{\Phi}_{\lambda_k}(Z)\rangle\right) A_{\pm\lambda_k}(T) = 0, \tag{4.28}$$

leading to

$$A_{\lambda_k}(T) = e^{-\sqrt{i\lambda_k}\frac{T}{\mathcal{T}_{\lambda_k}}}, \tag{4.29}$$

$$\mathcal{T}^{-1}_{\lambda_k} = \langle \boldsymbol{\mathcal{E}}\boldsymbol{\Phi}_{\lambda_k}(Z) + \frac{\boldsymbol{\mathcal{J}}_{\lambda_k}(s = i\lambda_k, Z)}{\lambda_k^2}, \boldsymbol{\Phi}_{\lambda_k}(Z)\rangle, \tag{4.30}$$

$$\boldsymbol{\mathcal{J}}_{\lambda_k}(Z, s = i\lambda_k) = \frac{\lambda_k}{\alpha(2+\alpha)\left(1 - \frac{c_-\beta}{c_+}\right)} \begin{pmatrix} -\left(\left(\frac{Z^2}{2} - Z\right) + \left(\frac{c_-}{\lambda_k}\right)^2\right)\frac{\tan\left(\frac{\lambda_k}{c_-}\right)}{c_-} \\ \left(\left(\frac{Z^2}{2} - Z\right) + \left(\frac{c_+}{\lambda_k}\right)^2\right)\frac{\tan\left(\frac{\lambda_k}{c_+}\right)}{c_+} \end{pmatrix}. \tag{4.31}$$

An explicit expression of the envelope slow–time decay $\mathcal{T}_{\lambda_k}$ is provided in Appendix E. Result (4.30) for the deviation of our prediction from ([32]) given by $\mathcal{T}_{\lambda_k}$ shows that this deviation results from the interaction between (FSI) vibrations modes and dissipation. More precisely this term is the projection of vector $\boldsymbol{\mathcal{E}}\boldsymbol{\Phi}_{\lambda_k}(Z) + \frac{\boldsymbol{\mathcal{J}}_{\lambda_k}(s=i\lambda_k,Z)}{\lambda_k^2}$ which results from wall shear rate longitudinal gradient on each (FSI) modes. Note that with the conjugation conditions $A^\star_{\lambda_k} = A_{-\lambda_k}$ is verified. In the Laplace domain, the leading–order vector $\tilde{\boldsymbol{\mathcal{P}}}^0$ is now fully established. Combining the previous expression of $A_{\lambda_k}(T)$ within $\tilde{\boldsymbol{\mathcal{P}}}^0$ in (4.23) leads to the following

$$\tilde{\boldsymbol{\mathcal{P}}}^0(Z,s,T) = \tilde{\boldsymbol{\mathcal{P}}}^0_p(Z,s) - \frac{1}{2}\sum_{\lambda_k \in \mathbb{R}} e^{-\sqrt{i\lambda_k}\frac{T}{\mathcal{T}_{\lambda_k}}}\left[\frac{i\lambda_k}{s - i\lambda_k} + 1\right]\langle \tilde{\boldsymbol{\mathcal{P}}}^0_p(Z,s), \boldsymbol{\Phi}_{\lambda_k}(Z)\rangle \boldsymbol{\Phi}_{\lambda_k}(Z) \tag{4.32}$$

As often required, the space–time solution associated with the previous expression could be deduced by performing an inverse Laplace transform.

4.3.3. *Laplace inversion and time–dependent solution*

The particular part of $\tilde{\boldsymbol{\mathcal{P}}}^0$, $\tilde{\boldsymbol{\mathcal{P}}}^0_p$ for the hereby reservoir–pipe–anchored valve system examined here under impulse disturbance, does not depend on s as found in (4.17).

The inverse Laplace transform of (4.32) then becomes

$$\boldsymbol{\mathcal{P}}^0(Z,\tau,T) = \boldsymbol{\mathcal{P}}^0_p(Z) - \frac{1}{2}\sum_{\lambda_k\in\mathbb{R}} e^{-\sqrt{i\lambda_k}\frac{T}{\mathcal{T}_{\lambda_k}}}\langle\boldsymbol{\mathcal{P}}^0_p(Z),\boldsymbol{\Phi}_{\lambda_k}(Z)\rangle\boldsymbol{\Phi}_{\lambda_k}(Z)$$
$$+\frac{1}{2i}\sum_{\lambda_k\in\mathbb{R}}\lambda_k\boldsymbol{\Phi}_{\lambda_k}(Z)\mathcal{L}^{-1}\left(\frac{e^{-\sqrt{i\lambda_k}\frac{T}{\mathcal{T}_{\lambda_k}}}}{s-i\lambda_k}\right)(\tau)\langle\boldsymbol{\mathcal{P}}^0_p(Z),\boldsymbol{\Phi}_{\lambda_k}(Z)\rangle. \quad (4.33)$$

Applying Cauchy's residue theorem yields the following

$$\mathcal{L}^{-1}\left(\frac{e^{-\sqrt{i\lambda_k}\frac{T}{\mathcal{T}_{\lambda_k}}}}{s-i\lambda_k}\right) = e^{i\lambda_k\tau-\sqrt{i\lambda_k}\frac{T}{\mathcal{T}_{\lambda_k}}}. \quad (4.34)$$

Using notation $\mathrm{sgn}(\lambda_k)$ for the sign of λ_k, (i.e. $\lambda_k = \mathrm{sgn}(\lambda_k)|\lambda_k|$) and since $\sqrt{i\,\mathrm{sgn}(\lambda_k)|\lambda_k|} = (1+\mathrm{sgn}(\lambda_k)i)\sqrt{\frac{|\lambda_k|}{2}}$, (4.34) results by symmetry

$$\boldsymbol{\mathcal{P}}^0(Z,\tau,T) = \boldsymbol{\mathcal{P}}^0_p(Z) - \sum_{\lambda_k\in\mathcal{S}_p} e^{-\sqrt{\frac{\lambda_k}{2}}\frac{T}{\mathcal{T}_{\lambda_k}}}\cos\left(\sqrt{\frac{\lambda_k}{2}}\frac{T}{\mathcal{T}_{\lambda_k}}\right)\langle\boldsymbol{\mathcal{P}}^0_p(Z),\boldsymbol{\Phi}_{\lambda_k}(Z)\rangle\boldsymbol{\Phi}_{\lambda_k}(Z)$$
$$+\sum_{\lambda_k\in\mathcal{S}_p}\lambda_k e^{-\sqrt{\frac{\lambda_k}{2}}\frac{T}{\mathcal{T}_{\lambda_k}}}\boldsymbol{\Phi}_{\lambda_k}(Z)\sin\left(\lambda_k\tau-\sqrt{\frac{\lambda_k}{2}}\frac{T}{\mathcal{T}_{\lambda_k}}\right)\langle\boldsymbol{\mathcal{P}}^0_p(Z),\boldsymbol{\Phi}_{\lambda_k}(Z)\rangle, \quad (4.35)$$

Here $\mathcal{S}_p$ is the operator $\mathcal{H}$'s discrete spectrum introduced in (C.7). The leading–order pressure–stress vector $\mathbf{P}^0(Z,\tau,T)$ falls from basis change relationships (4.3). The wall shear stress τ^0_w, through combining of (3.66), (3.70), (3.72) and (4.17), achieves the following

$$\tau^0_w(Z,\tau,T) = -\frac{\boldsymbol{\mathcal{D}}\left[\binom{1}{-1}\right]}{\det(\boldsymbol{\Pi})\sqrt{\pi\tau}}$$
$$+\sum_{\lambda_k\in\mathcal{S}_p} e^{-\sqrt{\frac{\lambda_k}{2}}\frac{T}{\mathcal{T}_{\lambda_k}}}\left[\sqrt{2\lambda_k}b_{\lambda_k}(\tau,T)+\frac{\cos\left(\sqrt{\frac{\lambda_k}{2}}\frac{T}{\mathcal{T}_{\lambda_k}}\right)}{\sqrt{\pi\tau}}\right]\frac{\langle Z\binom{1}{-1},\boldsymbol{\Phi}_{\lambda_k}(Z)\rangle\boldsymbol{\mathcal{D}}\left[\partial_Z\boldsymbol{\Phi}_{\lambda_k}(Z)\right]}{\det(\boldsymbol{\Pi})}, \quad (4.36)$$

where,

$$\boldsymbol{\mathcal{D}}[\boldsymbol{\mathcal{X}}] = \left(\begin{pmatrix}1 & \mathcal{D}\\ 1 & \mathcal{D}\end{pmatrix}\boldsymbol{\Pi}\boldsymbol{\mathcal{X}}\right)\cdot\begin{pmatrix}1\\0\end{pmatrix} \quad (4.37)$$

$$b_{\lambda_k} = \cos\left(\lambda_k\tau-\sqrt{\frac{\lambda_k}{2}}\frac{T}{\mathcal{T}_{\lambda_k}}\right)\mathcal{F}_s\left(t_{\lambda_k}\right)-\sin\left(\lambda_k\tau-\sqrt{\frac{\lambda_k}{2}}\frac{T}{\mathcal{T}_{\lambda_k}}\right)\mathcal{F}_c\left(t_{\lambda_k}\right). \quad (4.38)$$

Here, $\mathcal{F}_s$, $\mathcal{F}_c$ are the sine and cosine Fresnel functions, respectively, and $t_{\lambda_k} = \sqrt{\frac{2\lambda_k\tau}{\pi}}$.

5. Comparison with experiments

In this section various quantities are compared with previous theoretical predictions ignoring (FSI) and with experimental observations. All geometrical and physical

properties from experimental articles are provided in Table 2. A reservoir–pipe–anchored valve system has been studied by ([32,33]), but they did not consider (FSI), so an analytical expression for the pressure field and its spectrum has been found

$$P = 2\sum_{k\in\mathbb{N}}(-1)^k \frac{\sin(\lambda_k Z)}{\lambda_k} e^{-\sqrt{\frac{\lambda_k}{2}}T} \sin\left(\lambda_k \tau - \sqrt{\frac{\lambda_k}{2}}T\right) \;\; \& \;\; \lambda_k = \pi\left(\frac{1}{2}+k\right). \quad (5.1)$$

Noteworthy, in the $\nu_s \to 0$ limit and for the impulse response, the predicted pressure attenuation in (4.35) reaches that found by ([32,33]), which is given in (5.1), since $\mathcal{T}_{\lambda_k}^{-1} = 1$ (as $\nu_s \to 0$, $\boldsymbol{\mathcal{E}} \to \mathbf{I}$ and $\boldsymbol{\mathcal{J}}_{\lambda_k}(s = i\lambda_k) \to 0$, whilst the eigenmodes are orthogonal). The pressure signature is compared at different locations in Figure 4

Table 2: Physical and geometrical properties for the analysis of the reservoir pipe anchored valve system. ($\star$) refers to unavailable data in the original article. They were estimated by the authors based up available properties of pure copper tube and water.

Article	**Density** $(kg \cdot m^{-3})$	**Elasticity** $(10^9 Pa)$	ν_f $(m^2 \cdot s^{-1})$	ν_s	**Geometry** (m)
([20])	$\rho^\star_{f_0} = 998.3$ $\rho^\star_{s_0} = 8935.0$	$\mathcal{K}^\star_f = 2.1$ $E^\star = 127.0$	$3.967 \cdot 10^{-5}$	$0.34^\star$	$R = 0.0127$ $e = 0.001651$ $L = 36.088$
([1])	$\rho_{f_0} = 1000.0$ $\rho_{s_0} = 8890.0$	$\mathcal{K}_f = 2.1$ $E = 120.0$	$9.493 \cdot 10.0^{-7.0}$	0.35	$R = 0.008$ $e = 0.001$ $L = 98.11$
([5])	$\rho^\star_{f_0} = 1000.0$ $\rho^\star_{s_0} = 8960.0$	$\mathcal{K}^\star_f = 2.1$ $E^\star = 130.0$	$1.182 \cdot 10^{-6.0}$	$0.3^\star$	$R = 0.01105$ $e = 0.00163$ $L = 37.23$
([37])	$\rho^\star_{f_0} = 1000.0$ $\rho^\star_{s_0} = 8960.0$	$\mathcal{K}^\star_f = 2.1$ $E^\star = 130.0$	$10^{-6.0}$	$0.3^\star$	$R = 0.01$ $e = 0.001$ $L = 15.22$

from ([1])'s data set. The special case $\nu_s \to 0$ or that of ([32]) is again depicted. Each analytical solutions exhibits excellent agreement for both amplitude and phase for every considered pipe's locations with experimental observations. No parameter fit is used. The variety of observed patterns of the pressure signal depicted in Figure 4 and the surprisingly precise predictions provided by the theory results from the complex mode decomposition $\boldsymbol{\Phi}_{\lambda_k}(Z)$, each with its own phase. In Figure (4a), a deeper analysis of the pressure signature reveals that ([32])'s theory leads to a better agreement with experimental data in the early times, i.e. $\tau \ll O(1/\delta)$. At longer times, both models correctly describe the attenuation, ([32])'s theory under–attenuating, whist the hereby developed one slightly over–attenuating. In Figure (4b) however, the present analysis shows excellent agreement with experimental

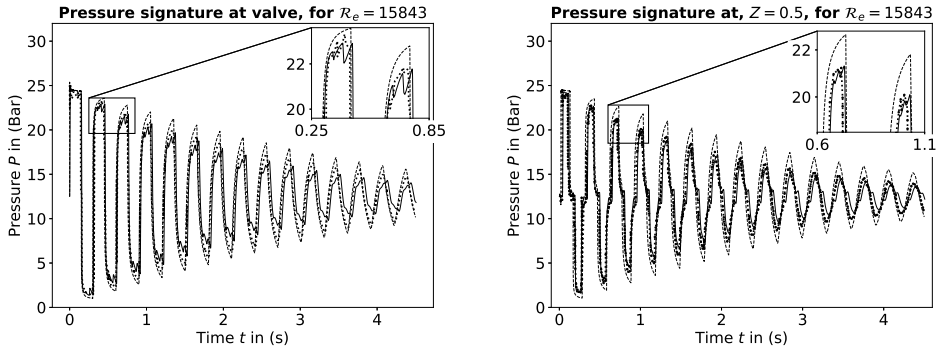

(a) (b)

Fig. 4: Pressure signature compared with experimental data of ([1]). Experimental data are depicted with black dotted lines while theoretical results from (4.35) are depicted with continuous lines. ([32])'s solution (no-FSI) is provided with dashed line. Dimensionless numbers are $\mathcal{M} = 7.2 \cdot 10^{-4}$, $\epsilon = 8.2 \cdot 10^{-5}$, $\alpha = 0.125$, $\delta = 3.3 \cdot 10^{-2}$ and $\mathcal{D} = 0.11$.

data at long time, ([32])'s theory again under–attenuating. It is worth noting that these differences are minor in both configurations as the (FSI) coupling has little influences in these experimental data set.

To deepen the analysis of the new prediction for (FSI) damping, Figures (5a)–(5d) then focus on the damping envelope of the first exponential mode. A comparison with four sets of experiments is provided. For each experiment, the pressure of the envelope peaks are extracted, non–dimensionalized, and compared with the theoretical damping trend. Figures (5a)–(5d) reveal as very good agreement between the predictions and experiments for laminar and transitional Reynolds numbers. As the first mode damping is dominant over others at long time, the match between predictions and observations becomes better with time, as expected. Furthermore, to more accurately quantify how much this preferential damping dominates others, Figure (6a) and (7a) depict and compare the ratio of ([32]) first damping mode (i.e. $\sqrt{\pi/4}$) with the present asymptotic theory (i.e. $\sqrt{\lambda_0}/\sqrt{2}\mathcal{T}_{\lambda_0}$) for a various set of iso–α and iso–E. This ratio appears to be less than unity within the entire ν_s range between zero and one–half, which demonstrates that (FSI) liquid–filled pipe systems attenuate faster than those where no–(FSI) is considered, which is an expected effect. It is also interesting to note that the thinner the pipe (i.e. the lower the α), the stronger the damping, which is also expected due to the increasing importance of (FSI) effects in thin–shell. In Figure (6b) and (7b), the ratio of the second to first exponential damping rate (i.e. $\frac{\mathcal{T}_{\lambda_0}}{\mathcal{T}_{\lambda_1}}\sqrt{\frac{\lambda_1}{\lambda_0}}$) is analyzed. Whereas no–(FSI) modes gradually attenuate, liquid–filled pipe systems that incorporate (FSI) do not neces-

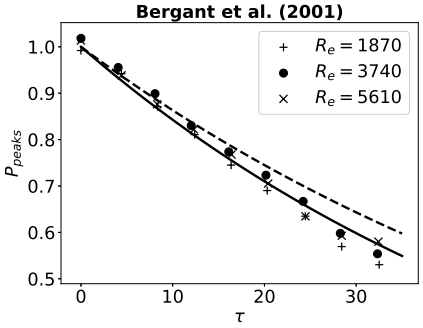

(a) $\mathcal{M} = [7.65^{(+)}, 15.3^{(\bullet)}, 23^{(\times)}] \cdot 10^{-5}$, $\epsilon = 3 \cdot 10^{-4}$, $\alpha = 0.146$, $\delta = 1.7 \cdot 10^{-2}$

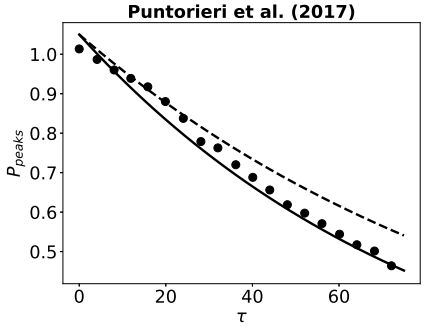

(b) $\mathcal{M} = 1.53 \cdot 10^{-4}$, $\epsilon = 6.57 \cdot 10^{-4}$, $\alpha = 0.1$, $\delta = 1.1 \cdot 10^{-2}$

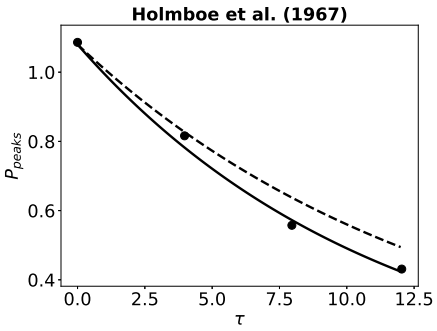

(c) $\mathcal{M} = 1.88 \cdot 10^{-4}$, $\epsilon = 3.5 \cdot 10^{-4}$, $\alpha = 0.13$, $\delta = 8.2 \cdot 10^{-2}$

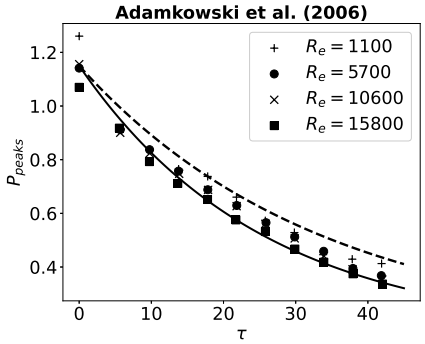

(d) $\mathcal{M} = [5.05^{(+)}, 26.0^{(\bullet)}, 48.3^{(\times)}, 72.0^{(\blacksquare)}] \cdot 10^{-5}$, $\epsilon = 8.2 \cdot 10^{-5}$, $\alpha = 0.125$, $\delta = 3.3 \cdot 10^{-2}$

Fig. 5: First exponential damping mode comparison with experimental dimensionless pressure peaks, P_{peaks}. The present theory is depicted with a continuous line while ([32])'s theory ($\nu_s \to 0$) is depicted by a dashed line.

sarily follow this pattern. Depending on the dimensionless numbers' relative values, the second attenuation mode could attenuates slower than the first, possibly leading to a distinct long–time behavior. This can be observed for the chosen parameters in Figure (6b) and (7b) when the computed ratio is smaller than one for increasing ν_s values; thus, in this special case, the second mode drives the long–time dynamics. For extremely thin tubes (i.e. $\alpha \sim 10^{-2}$), lying within a shell theory framework, such behaviors should therefore be expected.

The wall shear stress (4.36) is provided in Figure 8 and 9 using ([1])'s experimental parameters. The solution in the $\nu_s \to 0$ limit is again depicted to illustrate the possible contribution of the solid axial displacement acceleration in the convolution

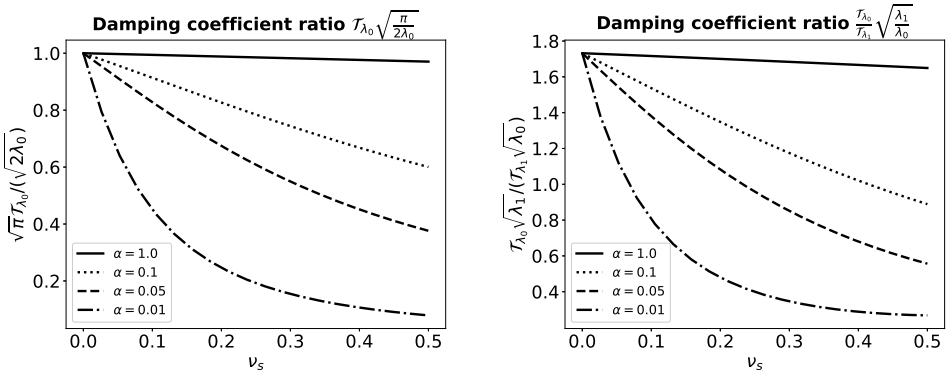

(a) (b)

Fig. 6: Exponential damping coefficient analysis: (a) Analysis of $\mathcal{T}_0\sqrt{\frac{\pi}{2\lambda_0}}$, (b) Analysis of $\frac{\mathcal{T}_0}{\mathcal{T}_1}\sqrt{\frac{\lambda_1}{\lambda_0}}$. Iso–$\alpha$ lines are represented based on ([1])'s data from Table 2.

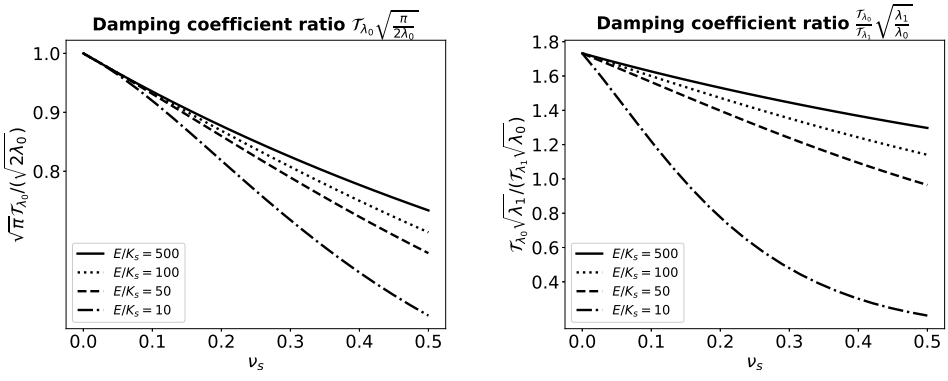

(a) (b)

Fig. 7: Exponential damping coefficient analysis: (a) Analysis of $\mathcal{T}_0\sqrt{\frac{\pi}{2\lambda_0}}$, (b) Analysis of $\frac{\mathcal{T}_0}{\mathcal{T}_1}\sqrt{\frac{\lambda_1}{\lambda_0}}$. Iso–$E$ lines are represented based on ([1])'s data from Table 2.

term (3.65), i.e. $\partial_\tau[W - \alpha\dot{\zeta}]$. Since Figure 8 and 9 consider the wall shear stress under impulse disturbance, one can observe the successive peaks associated with the back–and–forth pulse propagating wave at a given position. Obviously, these peaks should be smoothed by convolution with the applied valve closure law for non–impulse disturbances. The observed difference between the (FSI) wall shear stress and the one computed without including (FSI) effects are rising with time, but also increasing for larger density ratio $\mathcal{D}$. This difference is systematically in-

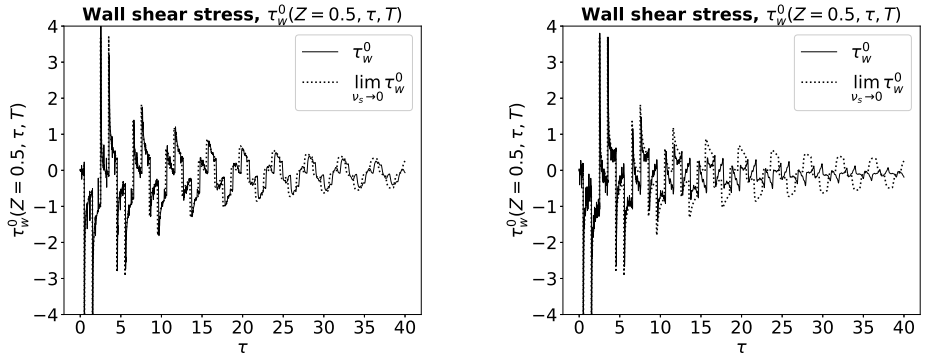

(a) $\alpha = 0.125$, $\mathcal{D} = 0.11$ (b) $\alpha = 0.125$, $\mathcal{D} = 1$

Fig. 8: Dimensionless fluid wall shear stress τ_w^0 at middle's pipe location. ([1])'s data from Table 2 are used with (a) unmodified density ratio $\mathcal{D}$, (b) modified density ratio $\mathcal{D} = 1$.

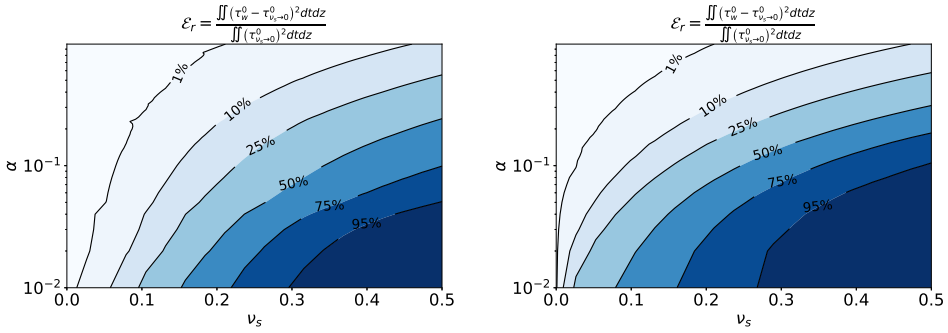

(a) $\mathcal{D} = 0.11$ (b) $\mathcal{D} = 1$

Fig. 9: Relative difference $\mathcal{E}_r$ between (FSI) and no–(FSI) ($\nu_s \to 0$) fluid wall shear rate. ([1])'s data from Table 2 are used with (a) unmodified density ratio $\mathcal{D}$, (b) modified density ratio $\mathcal{D} = 1$.

vestigated in Figure (9a) and (9b) where the influence of the thickness of the tube wall and the Poisson coefficient are provided. These plots permit to realize that the prediction of the (FSI) wall shear stress differ by a factor two or more from the one omitting (FSI), for ν_s larger than 0.25 for usual relative wall thickness (i.e. $\alpha < 0.1$). From this, one can infer that this very important quantity in the blood–hammer context (for which $\mathcal{D} \approx 1$, $\alpha \in [0.05-0.2]$, $\nu_s \in [0.45-0.5]$) deserves to be examined from an (FSI) viewpoint. Since many studies have demonstrated the importance of the wall shear stress in bio–mechanics (e.g., ([12])) this theoretical prediction is thus

worth considering.

Conclusion

This contribution investigated a low–Mach number theory of (FSI) pulsed waves in a pipe. The asymptotic analysis included three small parameters, namely the dimensionless viscous boundary layer thickness $\delta = 1/\sqrt{\epsilon Re_p}$, the Mach number $\mathcal{M}$, and the tube aspect ratio ϵ, which were chosen within the framework of $\delta^2 \gg \mathcal{M},\ \delta \gg \epsilon^2,\ \delta \gg \alpha\mathcal{M}$ (or equivalently $1/Re_p \gg \max\left(\epsilon\mathcal{M}, \epsilon^5, \alpha^2\epsilon\mathcal{M}^2\right)$) and $1 \gg \epsilon \gg \alpha\mathcal{M}$, consistent with the parameter ranges of many relevant studies. The resulting (FSI) problem was then analyzed considering three distinct and coupled regions, namely the elastic solid, inner boundary layer, and outer pipe region, as well as two time scales, namely a fast one associated with wave propagation along the tube and a slow one associated with momentum diffusion within the boundary layer. The couplings between the various pressures, velocity components, stress components, and elastic displacement fields were studied in detail to produce a complete asymptotic understanding, as depicted in Figure 2.

Within this framework, the leading–order four–(FSI) equations were recovered, exhibiting a pulsed velocity consistent with ([43])'s average analysis predictions. Furthermore, at this leading–order, the resulting shear stress was found to be equally consistent with the leading–order long time behavior found by ([56]), except for a missing (FSI) coupling term, which is small in the limit of thick–wall, but can be significantly different for thin–wall and solid/fluid density ratio close to one. Seeking a prediction for the slow–time damping of the leading–order wave propagation, a secularity condition was developed, which was found by analyzing first–order perturbations. The resulting longitudinal, mode–dependent, exponential damping generalized the $\nu_s \to 0$ theory of ([32,33]), which now includes (FSI). This damping not only depended on the fluid and solid properties through a newly defined tensor $\boldsymbol{\mathcal{E}}$ associated with dissipation but also on the considered boundary conditions though a damping vector $\boldsymbol{\mathcal{J}}_{\lambda_k}$. This is because it was directly related to $(\boldsymbol{\mathcal{E}}, \boldsymbol{\mathcal{J}}_{\lambda_k})$'s double contraction over the vibration eigenmodes as well as to the corresponding eigenvalue, both of which were strongly connected with the set of axial boundary conditions. The resulting damping predictions were successfully compared with various experimental measurements, providing convincing evidence for the presented theory.

Appendix A. Matching procedure for the radial velocity field

The leading–order inner axial velocity $\tilde{w}^0$ found in (3.61) can be y–integrated and Z–derived, such that

$$\partial_Z \int_0^y \tilde{w}^0 dy' = \alpha\sqrt{s}\left(1 - e^{-\sqrt{s}y}\right)\partial_Z\tilde{\zeta}^0 - \frac{1}{s}\partial_Z^2\tilde{P}^0\left[y - \frac{1}{\sqrt{s}}\left(1 - e^{-\sqrt{s}y}\right)\right] \quad \text{(A.1)}$$

The radial velocity matching procedure presented in (2.68) is detailed as follows. Invoking the expressions $\tilde{U}^0$, $\tilde{u}^0$, and $\tilde{u}^1$ in (3.51), (3.57) and (3.59), respectively,

leads to the following

$$-\frac{1}{2}\tilde{\mathcal{F}}^0+\frac{1}{2}\delta^\gamma\eta\tilde{\mathcal{F}}^0+\delta\left(-\frac{1}{2}\tilde{\mathcal{F}}^1+\frac{1}{2}\delta^\gamma\eta\tilde{\mathcal{F}}^1\right)=s\alpha\tilde{\xi}^0\big|_{R=1}+\frac{s}{\mathcal{C}^2}\tilde{P}^0\delta^\gamma\eta+s\alpha\delta^\gamma\tilde{\xi}^0\big|_{R=1}$$
$$+\alpha\delta\left(s\tilde{\xi}^1\big|_{R=1}+\partial_T\tilde{\xi}^0\big|_{R=1}\right)+\alpha\sqrt{s}\partial_Z\tilde{\zeta}^0\big|_{\mathcal{R}_i}\left(\delta-E.S.T\right)$$
$$-\frac{1}{s}\partial_Z^2\tilde{P}^0\left[\delta^\gamma\eta-\frac{1}{\sqrt{s}}\left(\delta-E.S.T\right)\right], \quad (A.2)$$

or, reorganising terms

$$-\frac{1}{2}\tilde{\mathcal{F}}^0+\frac{1}{2}\delta^\gamma\eta\tilde{\mathcal{F}}^0-\frac{\delta}{2}\tilde{\mathcal{F}}^1=s\alpha\tilde{\xi}^0\big|_{R=1}+\frac{s}{\mathcal{C}^2}\tilde{P}^0\delta^\gamma\eta+s\alpha\delta^\gamma\eta\tilde{\xi}^0\big|_{R=1}$$
$$+\alpha\delta\left(s\tilde{\xi}^1\big|_{R=1}+\partial_T\tilde{\xi}^0\big|_{R=1}\right)+\delta\alpha\sqrt{s}\partial_Z\tilde{\zeta}^0\big|_{R=1}$$
$$-\frac{1}{s}\partial_Z^2\tilde{P}^0\left[\delta^\gamma\eta-\frac{\delta}{\sqrt{s}}\right]+O\left(\delta^{\gamma+1}\right). \quad (A.3)$$

The asymptotic sequence reads as follows

- $O\left(1\right)$

$$\tilde{\mathcal{F}}^0=-2s\alpha\tilde{\xi}^0\big|_{R=1}, \quad (A.4)$$

- $O\left(\delta^\gamma\right)$

$$\frac{1}{2}\tilde{\mathcal{F}}^0=s\alpha\xi^0\big|_{R=1}+\frac{1}{s\mathcal{C}^2}\left(s^2-\mathcal{C}^2\partial_Z^2\right)\tilde{P}^0. \quad (A.5)$$

Combining (3.70) and (3.71) considered at leading–order and in the Laplace domain yields

$$\left(s^2-\mathcal{C}^2\partial_Z^2\right)\tilde{P}^0=s\mathcal{C}^2\tilde{\mathcal{F}}^0, \quad (A.6)$$

such that

$$\tilde{\mathcal{F}}^0=-2s\alpha\xi^0\big|_{R=1}, \quad (A.7)$$

which is identical to (A.4).

- $O\left(\delta\right)$

$$-\frac{1}{2}\tilde{\mathcal{F}}^1=s\alpha\tilde{\xi}^1\big|_{R=1}+\alpha\partial_T\tilde{\xi}^0\big|_{R=1}+\frac{1}{\sqrt{s}}\left[\frac{1}{s}\partial_Z^2\tilde{P}^0+\alpha s\partial_Z\tilde{\zeta}^0\big|_{R=1}\right]. \quad (A.8)$$

Using the definition of the parietal shear rate in (3.65) leads to the following

$$\tilde{\mathcal{F}}^1=-2s\alpha\tilde{\xi}^1\big|_{R=1}-2\alpha\partial_T\tilde{\xi}^0\big|_{R=1}+\frac{2}{s}\partial_Z\tilde{\tau}_w^0. \quad (A.9)$$

Through using (3.44), the matching functions $\mathcal{F}^0(Z,\tau,T)$ and $\mathcal{F}^1(Z,\tau,T)$ are fully determined from the inverse Laplace transform of (A.4) and (A.9)

$$\mathcal{F}^0(Z,\tau,T) = -\chi\partial_\tau P^0 + 2\alpha\nu_s\partial_Z\partial_\tau\zeta^0, \tag{A.10}$$

$$\mathcal{F}^1(Z,\tau,T) = -\chi\partial_\tau P^1 + 2\alpha\nu_s\partial_Z\partial_\tau\zeta^1 + \int_0^\tau \left(\partial_T\mathcal{F}^0 + 2\partial_Z\tau_w^0\right) d\tau^{'}. \tag{A.11}$$

Appendix B. Comparative analysis with Tijsseling's thick–wall theory

One starts from the four–(FSI) coupled equation system derived by ([43])

$$\partial_t W^* + \frac{1}{\rho_{f_0}}\partial_z P^* = 0, \tag{B.1}$$

$$\partial_z W^* + \left[\frac{1}{\mathcal{K}_f} + \frac{2}{E}\left(\frac{1}{\alpha} + \frac{1+\alpha}{2+\alpha} + \nu_s\right)\right]\partial_t P^* = \frac{2\nu_s}{E}\partial_t\sigma_{zz}^*, \tag{B.2}$$

$$\partial_t\dot{\zeta}^* - \frac{1}{\rho_{s_0}}\partial_z\sigma_{zz}^* = 0, \tag{B.3}$$

$$\partial_z\dot{\zeta}^* - \frac{1}{E}\partial_t\sigma_{zz}^* = -\frac{2\nu_s}{\alpha E\,(2+\alpha)}\partial_t P^*. \tag{B.4}$$

Invoking the scaling from §2.3.2 and §2.4, leads to

$$\partial_\tau W + \partial_Z P = 0, \tag{B.5}$$

$$\partial_Z W + \rho_{f_0}c_p^2\left[\frac{1}{\mathcal{K}_f} + \frac{2}{E}\left(\frac{1}{\alpha} + \frac{1+\alpha}{2+\alpha} + \nu_s\right)\right]\partial_\tau P = \frac{2\nu_s\rho_{f_0}c_p^2}{E}\partial_\tau\sigma_{zz}, \tag{B.6}$$

$$\partial_\tau\dot{\zeta} - \frac{\mathcal{D}}{\alpha}\partial_Z\sigma_{zz}, = 0, \tag{B.7}$$

$$\frac{\alpha E}{\rho_{f_0}c_p^2}\partial_Z\dot{\zeta} - \partial_\tau\sigma_{zz} = -\frac{2\nu_s}{\alpha\,(2+\alpha)}\partial_\tau P. \tag{B.8}$$

Using (2.11), (2.12), and (2.17), one finds

$$\frac{E}{\rho_{f_0}c_p^2} = \frac{\mathcal{C}_s^2}{\mathcal{D}}, \tag{B.9}$$

and

$$\partial_\tau W + \partial_Z P = 0, \tag{B.10}$$

$$\partial_Z W + \rho_{f_0}c_p^2\left[\frac{1}{\mathcal{K}_f} + \frac{2}{E}\left(\frac{1}{\alpha} + \frac{1+\alpha}{2+\alpha} + \nu_s\right)\right]\partial_\tau P = \frac{2\nu_s\mathcal{D}}{\mathcal{C}_s^2}\partial_\tau\sigma_{zz}, \tag{B.11}$$

$$\partial_\tau\dot{\zeta} - \frac{\mathcal{D}}{\alpha}\partial_Z\sigma_{zz} = 0, \tag{B.12}$$

$$\frac{\alpha\mathcal{C}_s^2}{\mathcal{D}}\partial_Z\dot{\zeta} - \partial_\tau\sigma_{zz} = -\frac{2\nu_s}{\alpha\,(2+\alpha)}\partial_\tau P. \tag{B.13}$$

One is left with an expression of the term $\rho_{f_0} c_p^2 \left[\frac{1}{\mathcal{K}_f} + \frac{2}{E}\left(\frac{1}{\alpha} + \frac{1+\alpha}{2+\alpha} + \nu_s\right)\right]$ versus dimensionless parameters. Using the definition of acoustic fluid wave speed $c_0 = \sqrt{\mathcal{K}_f/\rho_{f_0}}$ while invoking (2.11), (2.12), and (2.17) leads to

$$\rho_{f_0} c_p^2 \left[\frac{1}{\mathcal{K}_f} + \frac{2}{E}\left(\frac{1}{\alpha} + \frac{1+\alpha}{2+\alpha} + \nu_s\right)\right] = 1 + \frac{4\nu_s^2 \mathcal{D}}{\alpha(2+\alpha)\mathcal{C}_s^2}. \tag{B.14}$$

Now, combining (B.11) within (B.13) result in

$$\partial_\tau \sigma_{zz} - \frac{\alpha \mathcal{C}_s^2}{\mathcal{D}} \partial_Z \dot{\zeta} = \frac{2\nu_s}{\alpha(2+\alpha)} \partial_\tau P, \tag{B.15}$$

$$\partial_\tau \dot{\zeta} = \frac{\mathcal{D}}{\alpha} \partial_Z \sigma_{zz}, \tag{B.16}$$

$$\partial_\tau P + \partial_Z W = 2\alpha\nu_s \partial_Z \dot{\zeta}, \tag{B.17}$$

$$\partial_\tau W = -\partial_Z P. \tag{B.18}$$

The four–(FSI) dimensionless equation system derived by ([43]) is thus identical to the one asymptotically defined in §3.9.

B.1. *Vector–wave system in the Laplace domain*

The first–order dynamic is governed by the equations (3.79) and (3.80) expressed within the Laplace domain

$$\left(\left[1 + \frac{4\nu_s^2 \mathcal{D}}{\alpha(2+\alpha)\mathcal{C}_s^2}\right] s^2 - \partial_Z^2\right)\left[\tilde{P}^0 + \delta \tilde{P}^1\right] = \frac{2\nu_s \mathcal{D}}{\mathcal{C}_s^2} s^2 \left[\tilde{\sigma}_{zz}^0 + \delta \tilde{\sigma}_{zz}^1\right] - 2\delta \left[s\partial_T \left(\left[1 + \frac{4\nu_s^2 \mathcal{D}}{\alpha(2+\alpha)\mathcal{C}_s^2}\right] \tilde{P}^0 - \frac{2\nu_s \mathcal{D}}{\mathcal{C}_s^2} \tilde{\sigma}_{zz}^0\right) - \partial_Z \tilde{\tau}_w^0\right], \tag{B.19}$$

and

$$\left(s^2 - \mathcal{C}_s^2 \partial_Z^2\right)\left[\tilde{\sigma}_{zz}^0 + \delta \tilde{\sigma}_{zz}^1\right] = \frac{2\nu_s}{\alpha(2+\alpha)} s^2 \left[\tilde{P}^0 + \delta \tilde{P}^1\right] - 2\delta \left[s\partial_T \left(\tilde{\sigma}_{zz}^0 - \frac{2\nu_s}{\alpha(2+\alpha)} \tilde{P}^0\right) - \frac{\mathcal{C}_s^2}{\alpha(2+\alpha)} \partial_Z \tilde{\tau}_w^0\right]. \tag{B.20}$$

By combining the previous relations with the derived expression of $\partial_Z \tilde{\tau}_w(Z,s)$ in (3.86), it follows

$$\left(\mathbf{A}s^2 - \mathbf{B}\partial_Z^2\right)\left(\tilde{\mathbf{P}}^0 + \delta \tilde{\mathbf{P}}^1\right) = -2s\delta \left(\mathbf{A}s^2 + \sqrt{s}\mathbf{D}\right) \tilde{\mathbf{P}}^0, \tag{B.21}$$

with $\mathbf{A}$, $\mathbf{B}$, $\mathbf{D}$ and $\left(\tilde{\mathbf{P}}^0, \tilde{\mathbf{P}}^1\right)$ defined as

$$\mathbf{A} = \begin{pmatrix} 1 + \frac{4\nu_s^2 \mathcal{D}}{\alpha \mathcal{C}_s^2 (2+\alpha)} & -\frac{2\nu_s \mathcal{D}}{\mathcal{C}_s^2} \\ -\frac{2\nu_s}{\alpha(2+\alpha)} & 1 \end{pmatrix} \ , \ \mathbf{B} = \begin{pmatrix} 1 & 0 \\ 0 & \mathcal{C}_s^2 \end{pmatrix} \ , \ \tilde{\mathbf{P}}^0 = \begin{pmatrix} \tilde{P}^0 \\ \tilde{\sigma}_{zz}^0 \end{pmatrix} \ , \ \tilde{\mathbf{P}}^1 = \begin{pmatrix} \tilde{P}^1 \\ \tilde{\sigma}_{zz}^1 \end{pmatrix}, \tag{B.22}$$

$$\mathbf{D} = \begin{pmatrix} 1-(1-2\nu_s)\frac{2\nu_s\mathcal{D}}{\alpha\mathcal{C}_s^2(2+\alpha)} & \frac{(1-2\nu_s)\mathcal{D}}{\mathcal{C}_s^2} \\ \\ \frac{\mathcal{C}_s^2}{\alpha(2+\alpha)}\left(1-(1-2\nu_s)\frac{2\nu_s\mathcal{D}}{\alpha\mathcal{C}_s^2(2+\alpha)}\right) & \frac{(1-2\nu_s)\mathcal{D}}{\alpha(2+\alpha)} \end{pmatrix}. \tag{B.23}$$

Since $\mathbf{A}$ is a unitary matrix, its inverse reads as follows

$$\mathbf{A}^{-1} = \begin{pmatrix} 1 & \frac{2\nu_s\mathcal{D}}{\mathcal{C}_s^2} \\ \\ \frac{2\nu_s}{\alpha(2+\alpha)} & 1+\frac{4\nu_s^2\mathcal{D}}{\alpha\mathcal{C}_s^2(2+\alpha)} \end{pmatrix}. \tag{B.24}$$

Let us define the matrix $\mathbf{E} = \mathbf{A}^{-1}\cdot\mathbf{D}$. Noting that $\mathbf{C}_\mathbf{P}^2 = \mathbf{A}^{-1}\cdot\mathbf{B}$, and using the definition of $\overline{c^2}$ in (3.84), one yields

$$\mathbf{E} = \frac{1}{2\nu_s}\begin{pmatrix} \left(1-(1-2\nu_s)\frac{\overline{c^2}-1}{\mathcal{C}_s^2}\right)\left(1+\frac{2\nu_s\mathcal{D}}{\alpha(2+\alpha)}\right) & \frac{2\nu_s\mathcal{D}(1-2\nu_s)}{\mathcal{C}_s^2}\left(1+\frac{2\nu_s\mathcal{D}}{\alpha(2+\alpha)}\right) \\ \\ \left(1-(1-2\nu_s)\frac{\overline{c^2}-1}{\mathcal{C}_s^2}\right)\frac{\overline{c^2}-(1-2\nu_s)}{\alpha(2+\alpha)} & \frac{2\nu_s\mathcal{D}(1-2\nu_s)}{\mathcal{C}_s^2}\frac{\overline{c^2}-(1-2\nu_s)}{\alpha(2+\alpha)} \end{pmatrix}, \tag{B.25}$$

such that

$$\left(s^2-\mathbf{C}_\mathbf{P}^2\partial_Z^2\right)\left[\tilde{\mathbf{P}}^0+\delta\tilde{\mathbf{P}}^1\right] = -2s\delta\left(\partial_T+\sqrt{s}\mathbf{E}\right)\tilde{\mathbf{P}}^0. \tag{B.26}$$

Appendix C. Self–adjointness of the $\mathcal{H}$ operator and eigenvector decomposition

([4]) developed a solution for the leading–order vector–wave equation (4.12) associated with boundary conditions (4.7)–(4.9) using the orthonormal decomposition basis arising from the eigenvectors $\mathbf{\Phi}_{\lambda_k}(Z)$ of the operator $\mathcal{H}$, whereby $\tilde{\boldsymbol{\mathcal{P}}}^0$ and $\tilde{\boldsymbol{\mathcal{P}}}^1$ were projected. To achieve this decomposition, one must set $\mathcal{H}$'s self–adjointness. Defining the scalar product

$$\forall\mathbf{\Psi},\mathbf{\Psi}^{'}\in L^2(\mathbb{R})\times L^2(\mathbb{R}),\quad \forall\eta_1,\eta_2\in\mathbb{R},\quad \langle\mathbf{\Psi}^{'},\mathbf{\Psi}\rangle = \sum_{j=1}^{2}\eta_j\int_0^1\Psi_j^{'}(Z)\Psi_j(Z)dZ, \tag{C.1}$$

with $\boldsymbol{\eta}\equiv(\eta_1,\eta_2)\in\mathbb{R}^2$ an as yet unknown real vector that is adapted to each specific boundary condition set. From the self–adjoint property $\langle\mathcal{H}\mathbf{\Psi},\mathbf{\Psi}^{'}\rangle = \langle\mathbf{\Psi},\mathcal{H}\mathbf{\Psi}^{'}\rangle$, one finds from (C.1) condition

$$\sum_{j=1}^{2}\eta_j c_j^2\left[\partial_Z\Psi_j(Z)\Psi_j^{'}(Z)-\Psi_j(Z)\partial_Z\Psi_j^{'}(Z)\right]_0^1 = 0. \tag{C.2}$$

Denoting $-\lambda_k^2$, the k^{th} eigenvalue is real negative in accordance with the well–known Laplacian eigenvalues. Its related eigenfunction $\mathbf{\Phi}_{\lambda_k}$, fulfills the following eigenvalue problem

$$\mathcal{H}\mathbf{\Phi}_{\lambda_k}(Z) = -\lambda_k^2\mathbf{\Phi}_{\lambda_k}(Z), \tag{C.3}$$

or, using (4.10)

$$\partial_Z^2 \mathbf{\Phi}_{\lambda_k}(Z) = -\lambda_k^2 \boldsymbol{\mathcal{C}}_{\boldsymbol{\mathcal{P}}}^{-2} \mathbf{\Phi}_{\lambda_k}(Z), \quad \text{with} \quad \boldsymbol{\mathcal{C}}_{\boldsymbol{\mathcal{P}}}^{-2} = \begin{pmatrix} c_-^{-2} & 0 \\ 0 & c_+^{-2} \end{pmatrix}. \tag{C.4}$$

The solution to (C.4) reads as follows

$$\begin{pmatrix} \mathbf{\Phi}_{\lambda_k}(Z) \\ \partial_Z \mathbf{\Phi}_{\lambda_k}(Z) \end{pmatrix} = \begin{pmatrix} \partial_Z \mathbf{T}_{\lambda_k}(Z) & \mathbf{T}_{\lambda_k}(Z) \\ -\lambda_k^2 \boldsymbol{\mathcal{C}}_{\boldsymbol{\mathcal{P}}}^{-2} \mathbf{T}_{\lambda_k}(Z) & \partial_Z \mathbf{T}_{\lambda_k}(Z) \end{pmatrix} \begin{pmatrix} \mathbf{\Phi}_{\lambda_k}(0) \\ \partial_Z \mathbf{\Phi}_{\lambda_k}(0) \end{pmatrix}, \tag{C.5}$$

where

$$\mathbf{T}_{\lambda_k}(Z) = \frac{1}{\lambda_k} \begin{pmatrix} c_- \sin\left(\frac{\lambda_k Z}{c_-}\right) & 0 \\ 0 & c_+ \sin\left(\frac{\lambda_k Z}{c_+}\right) \end{pmatrix}, \tag{C.6}$$

and $(\mathbf{\Phi}_{\lambda_k}(0), \partial_Z \mathbf{\Phi}_{\lambda_k}(0))^T$ represent the modal-dependent amplitudes of $\mathbf{\Phi}_{\lambda_k}(Z)$, each of which is associated with the Dirichlet or Neumann condition imposed at $Z = 0\&1$. Furthermore $\mathbf{\Phi}_{\lambda_k}(Z)$ should ensures the homogeneous boundary condition system (4.11). Finding a non trivial solution leads to the following condition

$$\begin{vmatrix} \boldsymbol{\mathcal{N}} & \boldsymbol{\mathcal{M}} \\ \boldsymbol{\mathcal{Q}} \partial_Z \mathbf{T}_k(1) - \lambda_k^2 \boldsymbol{\mathcal{R}} \boldsymbol{\mathcal{C}}_{\boldsymbol{\mathcal{P}}}^{-2} \mathbf{T}_k(1) & \boldsymbol{\mathcal{Q}} \mathbf{T}_k(1) + \boldsymbol{\mathcal{R}} \partial_Z \mathbf{T}_k(1) \end{vmatrix} = 0. \tag{C.7}$$

This transcendental equation upon λ_k fully prescribes the system's spectrum $\mathcal{S}_{\mathcal{P}}$. While the radial boundary condition (i.e., the stress and velocity continuity conditions) informs about the wave-speed propagations of pulses within both fluid and solid, the axial boundary conditions located at the pipe's dead-end, in-turn, specify the system's spectrum

$$\mathcal{S}_{\mathcal{P}} = \{-\lambda_k^2 \ \mid \ \lambda_k \in \mathbb{R}^+\}. \tag{C.8}$$

Combining the boundary matrix expressions provided in (4.8) with the spectrum equation (C.7) yields the following (simplified) transcendental equation,

$$\beta \tan\left(\frac{\lambda_k}{c_-}\right) = \tan\left(\frac{\lambda_k}{c_+}\right), \tag{C.9}$$

where β was provided in (4.9). ([4]) found the following analytical expression for the eigenvectors $\mathbf{\Phi}_{\lambda_k}(Z)$

$$\mathbf{\Phi}_{\lambda_k}(Z) = \frac{\tilde{\mathbf{\Phi}}_{\lambda_k}(Z)}{\|\tilde{\mathbf{\Phi}}_{\lambda_k}(Z)\|}, \tag{C.10}$$

$$\tilde{\mathbf{\Phi}}_{\lambda_k}(Z) = \begin{pmatrix} \cos\left(\frac{\lambda_k}{c_-} Z\right) + \tan\left(\frac{\lambda_k}{c_-}\right) \sin\left(\frac{\lambda_k}{c_-} Z\right) \\ -\frac{c_+}{\beta c_-} \left[\cos\left(\frac{\lambda_k}{c_+} Z\right) + \tan\left(\frac{\lambda_k}{c_+}\right) \sin\left(\frac{\lambda_k}{c_+} Z\right)\right] \end{pmatrix}, \tag{C.11}$$

$$\|\tilde{\mathbf{\Phi}}_{\lambda_k}(Z)\|^2 = \frac{c_+ \beta \cos^2\left(\frac{\lambda_k}{c_+}\right) - c_- \cos^2\left(\frac{\lambda_k}{c_-}\right)}{2 c_+ \beta \cos^2\left(\frac{\lambda_k}{c_+}\right) \cos^2\left(\frac{\lambda_k}{c_-}\right)}, \tag{C.12}$$

$$\boldsymbol{\eta} = \begin{pmatrix} \eta_1 \\ \eta_2 \end{pmatrix} = \begin{pmatrix} 1 \\ -\beta \left(\frac{c_-}{c_+}\right)^3 \end{pmatrix}. \tag{C.13}$$

Appendix D. Simplification of $\left(s^2-\mathcal{H}\right)\tilde{\boldsymbol{\mathcal{P}}}_p^1(s,Z)$

Let us combine the definition of the operator $\mathcal{H}$ in (4.10) with the expression of $\tilde{\boldsymbol{\mathcal{P}}}_p^1(s,Z)$ in (4.14), it follows

$$\left(s^2-\mathcal{H}\right)\tilde{\boldsymbol{\mathcal{P}}}_p^1(s,Z)=\frac{s^2Z^2-2\boldsymbol{\mathcal{C}}_{\boldsymbol{\mathcal{P}}}^2}{\alpha(2+\alpha)\sqrt{s}\left(1-\frac{c_+}{c_-\beta}\right)}\begin{pmatrix}1\\-\frac{c_+}{c_-\beta}\end{pmatrix}-\frac{4\nu_s\mathcal{D}\left(s^2\left(\frac{Z^2}{2}-Z\right)-\boldsymbol{\mathcal{C}}_{\boldsymbol{\mathcal{P}}}^2\right)}{\alpha(2+\alpha)\sqrt{s}\left(c_-^2-1\right)}\begin{pmatrix}1&0\\0&\frac{c_-\beta}{c_+}\end{pmatrix}\partial_Z\tilde{\boldsymbol{\mathcal{P}}}^0\big|_{Z=0}. \quad \text{(D.1)}$$

The expression of $\partial_Z\tilde{\boldsymbol{\mathcal{P}}}^0\big|_{Z=0}$, which is easily deduced from (4.13) and (4.17), then yields to

$$\left(s^2-\mathcal{H}\right)\tilde{\boldsymbol{\mathcal{P}}}_p^1(s,Z)=\frac{s^2Z^2-2\boldsymbol{\mathcal{C}}_{\boldsymbol{\mathcal{P}}}^2}{\alpha(2+\alpha)\sqrt{s}\left(1-\frac{c_+}{c_-\beta}\right)}\begin{pmatrix}1\\-\frac{c_+}{c_-\beta}\end{pmatrix}$$
$$-\frac{4\nu_s\mathcal{D}}{\alpha(2+\alpha)\sqrt{s}\left(c_-^2-1\right)}\sum_{\lambda_k\in\mathbb{R}}\tilde{a}_{\lambda_k}^0(s)A_{\lambda_k}(T)\left(s^2\left(\frac{Z^2}{2}-Z\right)-\boldsymbol{\mathcal{C}}_{\boldsymbol{\mathcal{P}}}^2\right)\begin{pmatrix}1&0\\0&\frac{c_-\beta}{c_+}\end{pmatrix}\partial_Z\boldsymbol{\Phi}_{\lambda_k}\big|_{Z=0}$$
$$-\frac{4\nu_s\mathcal{D}\left(s^2\left(\frac{Z^2}{2}-Z\right)-\boldsymbol{\mathcal{C}}_{\boldsymbol{\mathcal{P}}}^2\right)}{\alpha(2+\alpha)\sqrt{s}\det\left(\boldsymbol{\Pi}\right)\left(c_-^2-1\right)}\begin{pmatrix}1\\-\frac{c_-\beta}{c_+}\end{pmatrix}, \quad \text{(D.2)}$$

or otherwise since $\det\left(\boldsymbol{\Pi}\right)=\frac{2\nu_s\mathcal{D}}{c_-^2-1}\left(1-\frac{c_-\beta}{c_+}\right)$

$$\left(s^2-\mathcal{H}\right)\tilde{\boldsymbol{\mathcal{P}}}_p^1(s,Z)=\frac{1}{\alpha(2+\alpha)\sqrt{s}}\left(\frac{s^2Z^2-2\boldsymbol{\mathcal{C}}_{\boldsymbol{\mathcal{P}}}^2}{1-\frac{c_+}{c_-\beta}}\begin{pmatrix}1\\-\frac{c_+}{c_-\beta}\end{pmatrix}-2\frac{s^2\left(\frac{Z^2}{2}-Z\right)-\boldsymbol{\mathcal{C}}_{\boldsymbol{\mathcal{P}}}^2}{1-\frac{c_-\beta}{c_+}}\begin{pmatrix}1\\-\frac{c_-\beta}{c_+}\end{pmatrix}\right)$$
$$-\frac{2}{\alpha(2+\alpha)\sqrt{s}\left(1-\frac{c_-\beta}{c_+}\right)}\sum_{\lambda_k\in\mathbb{R}}\tilde{a}_{\lambda_k}^0(s)A_{\lambda_k}(T)\left(s^2\left(\frac{Z^2}{2}-Z\right)-\boldsymbol{\mathcal{C}}_{\boldsymbol{\mathcal{P}}}^2\right)\begin{pmatrix}1&0\\0&\frac{c_-\beta}{c_+}\end{pmatrix}\partial_Z\boldsymbol{\Phi}_{\lambda_k}\big|_{Z=0}. \quad \text{(D.3)}$$

Regarding the definition of $\partial_Z\boldsymbol{\Phi}_{\lambda_k}\big|_{Z=0}$ provided in (C.11), it follows

$$\left(s^2\left(\frac{Z^2}{2}-Z\right)-\boldsymbol{\mathcal{C}}_{\boldsymbol{\mathcal{P}}}^2\right)\begin{pmatrix}1&0\\0&\frac{c_-\beta}{c_+}\end{pmatrix}\partial_Z\boldsymbol{\Phi}_{\lambda_k}\big|_{Z=0}=\frac{\lambda_k}{c_-}\begin{pmatrix}\left(s^2\left(\frac{Z^2}{2}-Z\right)-c_-^2\right)\tan\left(\frac{\lambda_k}{c_-}\right)\\-\frac{c_-}{c_+}\left(s^2\left(\frac{Z^2}{2}-Z\right)-c_+^2\right)\tan\left(\frac{\lambda_k}{c_+}\right)\end{pmatrix}. \quad \text{(D.4)}$$

whilst injecting the expression of $\tilde{a}_{\lambda_k}^0(s)$ derived in (4.22) into (D.3), it results

$$\left(s^2-\mathcal{H}\right)\tilde{\boldsymbol{\mathcal{P}}}_p^1(s,Z)=\frac{1}{\alpha(2+\alpha)\sqrt{s}}\left(\frac{s^2Z^2-2\boldsymbol{\mathcal{C}}_{\boldsymbol{\mathcal{P}}}^2}{1-\frac{c_+}{c_-\beta}}\begin{pmatrix}1\\-\frac{c_+}{c_-\beta}\end{pmatrix}-\frac{s^2\left(Z^2-2Z\right)-2\boldsymbol{\mathcal{C}}_{\boldsymbol{\mathcal{P}}}^2}{1-\frac{c_-\beta}{c_+}}\begin{pmatrix}1\\-\frac{c_-\beta}{c_+}\end{pmatrix}\right)$$
$$+\sum_{\lambda_k\in\mathbb{R}}\left[\frac{i\lambda_k}{s-i\lambda_k}+1\right]\frac{\langle\tilde{\boldsymbol{\mathcal{P}}}_p^0(Z),\boldsymbol{\Phi}_{\lambda_k}(Z)\rangle}{\sqrt{s}}A_{\lambda_k}(T)\boldsymbol{\mathcal{J}}_{\lambda_k}(Z,s), \quad \text{(D.5)}$$

with

$$\boldsymbol{\mathcal{J}}_{\lambda_k}(Z,s)=\frac{\lambda_k}{\alpha(2+\alpha)\left(1-\frac{c_-\beta}{c_+}\right)}\begin{pmatrix}\left(s^2\left(\frac{Z^2}{2}-Z\right)-c_-^2\right)\frac{\tan\left(\frac{\lambda_k}{c_-}\right)}{c_-}\\-\left(s^2\left(\frac{Z^2}{2}-Z\right)-c_+^2\right)\frac{\tan\left(\frac{\lambda_k}{c_+}\right)}{c_+}\end{pmatrix}. \tag{D.6}$$

Appendix E. Further investigation of $\boldsymbol{\mathcal{T}}_{\boldsymbol{\lambda_k}}^{-1}$

Let us define $\mathcal{E}_{i,j}$, $i,j\in\{1,2\}$ as the matrix elements of $\boldsymbol{\mathcal{E}}=\boldsymbol{\Pi}^{-1}\cdot\mathbf{E}\cdot\boldsymbol{\Pi}$. Invoking the definition of $\boldsymbol{\Pi}$ and $\boldsymbol{\Pi}^{-1}$ in (4.1) along with that of $\mathbf{E}$ in (B.25) leads to the following

$$\mathcal{E}_{11}=\frac{\mathcal{D}\left[\frac{1-(1-2\nu_s)\frac{\overline{c^2}-1}{\mathcal{C}_s^2}}{c_-^2-1}+\frac{1-2\nu_s}{\mathcal{C}_s^2}\right]\left[1+\frac{2\nu_s\mathcal{D}}{\alpha(2+\alpha)}\left(1-\frac{\overline{c^2}-(1-2\nu_s)}{c_+^2-1}\right)\right]}{\det\boldsymbol{\Pi}}, \tag{E.1}$$

$$\mathcal{E}_{12}=\frac{\mathcal{D}\left[\frac{1-(1-2\nu_s)\frac{\overline{c^2}-1}{\mathcal{C}_s^2}}{c_+^2-1}+\frac{1-2\nu_s}{\mathcal{C}_s^2}\right]\left[1+\frac{2\nu_s\mathcal{D}}{\alpha(2+\alpha)}\left(1-\frac{\overline{c^2}-(1-2\nu_s)}{c_+^2-1}\right)\right]}{\det\boldsymbol{\Pi}}, \tag{E.2}$$

$$\mathcal{E}_{21}=\frac{\mathcal{D}\left[\frac{1-(1-2\nu_s)\frac{\overline{c^2}-1}{\mathcal{C}_s^2}}{c_-^2-1}+\frac{1-2\nu_s}{\mathcal{C}_s^2}\right]\left[\frac{2\nu_s\mathcal{D}}{\alpha(2+\alpha)}\left(\frac{\overline{c^2}-(1-2\nu_s)}{c_-^2-1}-1\right)-1\right]}{\det\boldsymbol{\Pi}}, \tag{E.3}$$

$$\mathcal{E}_{22}=\frac{\mathcal{D}\left[\frac{1-(1-2\nu_s)\frac{\overline{c^2}-1}{\mathcal{C}_s^2}}{c_+^2-1}+\frac{1-2\nu_s}{\mathcal{C}_s^2}\right]\left[\frac{2\nu_s\mathcal{D}}{\alpha(2+\alpha)}\left(\frac{\overline{c^2}-(1-2\nu_s)}{c_-^2-1}-1\right)-1\right]}{\det\boldsymbol{\Pi}} \tag{E.4}$$

where $1/\det\boldsymbol{\Pi}$ is obtained regarding (4.1). Invoking both the scalar product definition in (C.1) with the definition of $\mathcal{T}_{\lambda_k}^{-1}$ in (4.30) while introducing the 2D-function $\boldsymbol{\Phi}_{\lambda_k}(Z)=[\Phi_{\lambda_k}^-,\Phi_{\lambda_k}^+](Z)$ achieves the following

$$\int_0^1\left[\Phi_{\lambda_k}^-\right]^2Zdz=\frac{\lambda_k+c_-\cos\left(\frac{\lambda_k}{c_-}\right)\sin\left(\frac{\lambda_k}{c_-}\right)}{2\lambda_k\|\tilde{\boldsymbol{\Phi}}_{\lambda_k}(Z)\|\cos^2\left(\frac{\lambda_k}{c_-}\right)}, \tag{E.5}$$

$$\int_0^1\left[\Phi_{\lambda_k}^+\right]^2Zdz=\left(\frac{c_+}{\beta c_-}\right)^2\frac{\lambda_k+c_+\cos\left(\frac{\lambda_k}{c_+}\right)\sin\left(\frac{\lambda_k}{c_+}\right)}{2\lambda_k\|\tilde{\boldsymbol{\Phi}}_{\lambda_k}(Z)\|^2\cos^2\left(\frac{\lambda_k}{c_+}\right)}, \tag{E.6}$$

$$\int_0^1\Phi_{\lambda_k}^-(Z)\Phi_{\lambda_k}^+(Z)dz=\frac{c_+^2\left[c_+\tan\left(\frac{\lambda_k}{c_-}\right)-c_-\tan\left(\frac{\lambda_k}{c_+}\right)\right]}{\lambda_k\|\tilde{\boldsymbol{\Phi}}_{\lambda_k}(Z)\|^2\beta\left(c_-^2-c_+^2\right)}. \tag{E.7}$$

Then the $\langle \boldsymbol{\mathcal{E}}\boldsymbol{\Phi}_{\lambda_k}(Z), \boldsymbol{\Phi}_{\lambda_k}(Z)\rangle$ contributes to

$$\langle \boldsymbol{\mathcal{E}}\boldsymbol{\Phi}_{\lambda_k}(Z), \boldsymbol{\Phi}_{\lambda_k}(Z)\rangle = \mathcal{E}_{11}\int_0^1 \left[\Phi^-_{\lambda_k}(z)\right]^2 dz + \eta_2\mathcal{E}_{22}\int_0^1 \left[\Phi^+_{\lambda_k}(z)\right]^2 dz + \left[\mathcal{E}_{12}+\eta_2\mathcal{E}_{21}\right]\int_0^1 \Phi^-_{\lambda_k}(z)\Phi^+_{\lambda_k}(z)dz, \quad \text{(E.8)}$$

in the expression of $\mathcal{T}^{-1}_{\lambda_k}$ in (4.30). Furthermore, by definition of $\boldsymbol{\mathcal{J}}_{\lambda_k}$ in (D.6)

$$\frac{\boldsymbol{\mathcal{J}}_{\lambda_k}(s=i\lambda_k, Z)}{\lambda_k^2} = \frac{\lambda_k}{\alpha(2+\alpha)\left(1-\frac{c_-\beta}{c_+}\right)}\begin{pmatrix} -\left(\left(\frac{Z^2}{2}-Z\right)+\left(\frac{c_-}{\lambda_k}\right)^2\right)\frac{\tan\left(\frac{\lambda_k}{c_-}\right)}{c_-} \\ \left(\left(\frac{Z^2}{2}-Z\right)+\left(\frac{c_+}{\lambda_k}\right)^2\right)\frac{\tan\left(\frac{\lambda_k}{c_+}\right)}{c_+}\end{pmatrix}, \quad \text{(E.9)}$$

then $\langle \frac{\boldsymbol{\mathcal{J}}_{\lambda_k}(s=i\lambda_k,Z)}{\lambda_k^2}, \boldsymbol{\Phi}_{\lambda_k}(Z)\rangle$ contributes to

$$\langle \frac{\boldsymbol{\mathcal{J}}_{\lambda_k}(s=i\lambda_k, Z)}{\lambda_k^2}, \boldsymbol{\Phi}_{\lambda_k}(Z)\rangle = -\frac{\lambda_k\tan\left(\frac{\lambda_k}{c_-}\right)}{\alpha(2+\alpha)c_-\left(1-\frac{c_-\beta}{c_+}\right)}\left(\int_0^1\left[\frac{Z^2}{2}-Z\right]\Phi^-_{\lambda_k}(Z)dz+\left(\frac{c_-}{\lambda_k}\right)^2\int_0^1\Phi^-_{\lambda_k}(Z)dz\right) - \frac{\eta_2\lambda_k\tan\left(\frac{\lambda_k}{c_+}\right)}{\alpha(2+\alpha)c_+\left(1-\frac{c_-\beta}{c_+}\right)}\left(\int_0^1\left[\frac{Z^2}{2}-Z\right]\Phi^+_{\lambda_k}(Z)dz+\left(\frac{c_+}{\lambda_k}\right)^2\int_0^1\Phi^+_{\lambda_k}(Z)dz\right), \quad \text{(E.10)}$$

in $\mathcal{T}^{-1}_{\lambda_k}$ with

$$\int_0^1\left[\frac{Z^2}{2}-Z\right]\Phi^+_{\lambda_k}(Z)dz = -\frac{c_+^3}{c_-\beta\lambda_k^3\|\tilde{\boldsymbol{\Phi}}_{\lambda_k}(Z)\|}\left(\lambda_k - c_+\tan\left(\frac{\lambda_k}{c_+}\right)\right), \quad \text{(E.11)}$$

$$\int_0^1\left[\frac{Z^2}{2}-Z\right]\Phi^-_{\lambda_k}(Z)dz = \frac{c_-^2}{\lambda_k^3\|\tilde{\boldsymbol{\Phi}}_{\lambda_k}(Z)\|}\left(\lambda_k - c_-\tan\left(\frac{\lambda_k}{c_-}\right)\right), \quad \text{(E.12)}$$

$$\int_0^1\Phi^+_{\lambda_k}(Z)dz = -\frac{c_+^2}{c_-\beta\lambda_k\|\tilde{\boldsymbol{\Phi}}_{\lambda_k}(Z)\|}\tan\left(\frac{\lambda_k}{c_+}\right), \quad \text{(E.13)}$$

$$\int_0^1\Phi^-_{\lambda_k}(Z)dz = \frac{c_-}{\lambda_k\|\tilde{\boldsymbol{\Phi}}_{\lambda_k}(Z)\|}\tan\left(\frac{\lambda_k}{c_-}\right). \quad \text{(E.14)}$$

Acknowledgments

This work was supported by the collaborative ANRT Grant CIFRE 2019/1453 co-funded by SETOM, dedicated society of Veolia for the public drinking water service of Toulouse Métropole operating under the brand Eau de Toulouse Métropole. F. P. also warmly acknowledge discussions with Pr. E. J. Hinch the influence of who whispered and possibly silently infused this work, the familiarity of which he might recognize as a modest legacy.

The authors have no competing interests to declare.

References

1. A. Adamkowski and M. Lewandowski, Experimental Examination of Unsteady Friction Models for Transient Pipe Flow Simulation, *J. Fluids Eng.* **128**.
2. H. K. Aliabadi, A. Ahmadi and A. Keramat, Frequency response of water hammer with fluid-structure interaction in a viscoelastic pipe, *Mech. Syst. Signal Process.* **144** (2020) 106848.
3. L. Allievi, Teoria del colpo d'ariete, Atti Collegio Ing. Arch.(English translation by Halmos E.E. 1929), The Theory of Waterhammer, *Tipografia della R. Accademia dei Lincei* .
4. A. Bayle and F. Plouraboué, Spectral properties of Fluid Structure Interaction pressure/stress waves in liquid filled pipe, *Wave Motion* **116** (2023) 103081.
5. A. Bergant, A. Simpson and J. Vìtkovsky, Developments in unsteady pipe flow friction modelling, *J. Hydraul. Res.* **39** (2001) 249–257.
6. C. Boutin and K. Viverge, Generalized plate model for highly contrasted laminates, *Eur. J. Mech. A/Solids* **55** (2016) 149–166.
7. B. Brunone, U. Golia and M. Greco, Modelling of fast transients by numerical methods, in *Proceedings of the 9th International Conference on Hydraulic Transients with Water Column Separation, Valencia, Spain* (1991), pp. 273–281.
8. D. D. Budny, D. C. Wiggert and F. J. Hatfield, The Influence of Structural Damping on Internal Pressure During a Transient Pipe Flow, *J. Fluids Eng.* **113** (1991) 424–429.
9. W. Bürmann, Longitudinal motion of coaxial pipes due to water hammer, *3R International* **19** (1980) 398 – 404.
10. M. H. Chaudhry, *Applied Hydraulic Transients* (Springer-Verlag, 2014), 3 edition.
11. A. Corli, I. Gasser, M. Lukacova-Medvid'Ova, A. Roggensack and U. Teschke, A multiscale approach to liquid flows in pipes I: The single pipe, *Appl. Math. Comput.* **219** (2012) 856–874.
12. N. Duraiswamy, R. T. Schoephoerster, M. R. Moreno and J. E. Moore, Jr., Stented artery flow patterns and their effects on the artery wall, *Annu. Rev. Fluid Mech.* **39** (2007) 357–382.
13. D. Ferras, P. Manso, A. Schleiss and D. Covas, One-Dimensional Fluid–Structure Interaction Models in Pressurized Fluid-Filled Pipes: A Review, *Appl. Sci.* **8** (2018) 1844.
14. P. Flaud, D. Geiger, C. Oddou and D. Quemada, Ecoulements pulsés dans les tuyaux visco-élastiques. Application à l'étude de la circulation sanguine., *J. de Physique* **35** (1974) 869–882.
15. F. Gaultier, J. Gilbert, J. Dalmont and R. Picó, Wave propagation in a fluid filled rubber tube: Theoretical and experimental results for Korteweg's wave, *Acta Acust. United Ac.* **93** (2007) 333–344.
16. M. Ghidaoui, M. Zhao, D. McInnis and D. Axworthy, A review of Water Hammer Theory and Practice, *Appl. Mech. Rev.* **58**.
17. A. Ghodhbani and E. Haj Taïeb, A four-equation friction model for water hammer calculation in quasi-rigid pipelines, *Int. J. Press. Vessel. Pip.* **151** (2017) 54–62.
18. J. F. Harvey, *Theory and Design of Modern Pressure Vessels* (Van Nostrand Reinhold, 1974).
19. E. J. Hinch, *Perturbation Methods*, Cambridge Texts in Applied Mathematics (Cambridge University Press, 1991).
20. E. L. Holmboe and W. T. Rouleau, The Effect of Viscous Shear on Transients in Liquid Lines, *J. Basic Eng.* **89** (1967) 174–180.
21. N. Joukowski, Memoirs of the imperial academy society of St.–Petersburg, *Proceedings*

of the American Water Works Association **24** (1898) 341–424.
22. A. Keramat, A. Tijsseling, Q. Hou and A. Ahmadi, Fluid–structure interaction with pipe-wall viscoelasticity during water hammer, *J. Fluids Struct.* **28** (2011) 434–455.
23. D. Korteweg, Ueber die Fortpflanzungsgeschwindigkeit des Schalles in elastischen Röhren (On the speed of sound propagation in elastic tubes), *Annalen der Physik* **241** (1878) 525–542.
24. G. Kuiken, Approximate dispersion equations for thin-walled liquid-filled tubes, *Appl. Sci. Res.* **4** (1984) 37–53.
25. G. Kuiken, Wave propagation in a thin-walled liquid-filled initially-stressed tube, *J. Fluid Mech.* **141** (1984) 289–308.
26. H. Lamb, On the velocity of sound in a tube, as affected by the elastic of the walls., *Memoirs of the Manchester Literary and Philosophical Society, Manchester, (UK)* **42** (1898) 1–16.
27. Q. Li, K. Yang and L. Zhang, Analytical Solution for Fluid-Structure Interaction in Liquid-Filled Pipes Subjected to Impact-Induced Water Hammer, *J. Eng. Mech. - ASCE* **129** (2003) 1408–1417.
28. Q. S. Li, K. Yang, L. Zhang and N. Zhang, Frequency domain analysis of fluid–structure interaction in liquid-filled pipe systems by transfer matrix method, *Int. J. Mech. Sci.* **44** (2002) 2067–2087.
29. S. Li, B. W. Karney and G. Liu, FSI research in pipeline systems – A review of the literature, *J. Fluids Struct.* **57** (2015) 277–297.
30. J. Lighthill, *Waves in fluids* (Cambridge university press, 2001).
31. T. Lin and G. W. Morgan, Wave propagation through fluid contained in a cylindrical, elastic shell, *J. Acoust. Soc. Am.* **28** (1956) 1165–1176.
32. C. Mei and H. Jing, Pressure and wall shear stress in blood hammer – Analytical theory, *Math. Biosci.* **280** (2016) 62–70.
33. C. C. Mei and H. Jing, Effects of thin plaque on blood hammer—An asymptotic theory, *Eur. J. Mech. B Fluids* **69** (2018) 62–75.
34. L. F. Menabrea, *Note sur les effets du choc de l'eau dans les conduites* (Mallet-Bachelier, 1858).
35. J. Michaud, Coups de bélier dans les conduites. Étude des moyens employés pour en atténuer les effects, *Bulletin de la Société Vaudoise des Ingénieurs et des Architectes* **4** (1878) 4.
36. T. Pedley, *The Fluid Mechanics of Large Blood Vessels* (Cambridge University Press, 1980).
37. P. Puntorieri, G. Barbaro, N. Martins, D. Covas and V. Fiamma, Hydraulic Transient Experimental Study in a Copper Pipe, in *Proceedings of the Multiphase Flow 2017* (2017), pp. 27–33.
38. S. I. Rubinow and J. B. Keller, Wave propagation in a viscoelastic tube containing a viscous fluid, *J. Fluid Mech.* **88** (1978) 181–203.
39. H. Résal, Note sur les petits mouvements d'un fluide incompressible dans un tuyau élastique., *Journal de Mathematiques Pures et Appliquées* **2** (1876) 342–344.
40. R. Skalak, An extension of the theory of waterhammer, *J. Fluids Eng. Trans. ASME* **78** (1956) 105–116.
41. A. R. D. Thorley, Pressure Transients in Hydraulic Pipelines, *J. Basic Eng.* **91** (1969) 453–460.
42. A. Tijsseling, Fluid-structure interaction in case of waterhammer with cavitation, Ph.D. thesis, Delft University of Technology, 1993.
43. A. Tijsseling, Water hammer with fluid-structure interaction in thick-walled pipes, *Comput. Struct.* **85** (2007) 844–851.

44. A. Tijsseling and C. Lavooij, Waterhammer with fluid-structure interaction, *Appl. Sci. Res.* **44** (1990) 273–285.
45. A. S. Tijsseling, FLUID-STRUCTURE INTERACTION IN LIQUID-FILLED PIPE SYSTEMS: A REVIEW, *J. Fluids Struct.* **10** (1996) 109–146.
46. K. Urbanowicz, Fast and accurate modelling of frictional transient pipe flow, *Z Angew Math Mech* **98**.
47. F. N. Van De Vosse and N. Stergiopulos, Pulse wave propagation in the arterial tree, *Annu. Rev. Fluid Mech.* **43** (2011) 467–499.
48. A. Vardy and J. Brown, Transient turbulent friction in smooth pipe flows, *J. Sound Vib.* **259** (2003) 1011–1036.
49. A. Vardy and J. Brown, Transient turbulent friction in fully rough pipe flows, *J. Sound Vib.* **270** (2004) 233–257.
50. J. S. Walker and J. W. Phillips, Pulse Propagation in Fluid-Filled Tubes, *J. Appl. Mech.* **44** (1977) 31–35.
51. D. C. Wiggert, Coupled transient flow and structural motion in liquid-filled piping systems : a survey., in *Proceedings of the ASME Pressure Vessels and Piping Conference* (Chicago, 1986), pp. 86–PVP–4.
52. D. C. Wiggert, F. J. Hatfield and S. Stuckenbruck, Analysis of Liquid and Structural Transients in Piping by the Method of Characteristics, *J. Fluids Eng.* **109** (1987) 161–165.
53. E. Wylie, V. Streeter and L. Suo, *Fluid Transients in Systems*, volume 1 (Prentice Hall Englewood Cliffs, NJ, 1993).
54. E. Yao, G. Kember and D. Hansen, Water Hammer Analysis and Parameter Estimation in Polymer Pipes with Weak Strain–Rate Feedback, *J. Eng. Mech.* **142** (2016) 04016052.
55. L. Zhang, A. Tijsseling and A. Vardy, FSI analysis of liquid-filled pipes, *J. Sound Vib.* **224** (1999) 69–99.
56. W. Zielke, Frequency-Dependent Friction in Transient Pipe Flow, *J. Basic Eng.* **90** (1968) 109–115.

Chapter 4

The liquid-filled-visco-elastic pipe problem

Contents

The increasing number of polymeric ducts in water distribution networks goes hand-in-hand with its modernization. Although traditional pipe raw materials (e.g. ductile iron, steel) suffer from time chemical and mechanical deterioration, polymeric materials offer a stronger time resiliency for a low-cost installation. Furthermore, where carbonaceous materials rapidly propagate shock waves ($c_p \approx 1200m/s$), the polymeric materials reduce the water hammer wave speed ($c_p \approx 300 - 400m/s$), which drops-down the generated overpressure accordingly to the [Joukowsky, 1904]'s law (Cf. (1.6)), as well as strongly attenuates the pressure signal. Despite their clear operational interest, the rheological characterization of polymeric pipes is non-trivial and still suffers from a lack of understanding. This chapter aims developing a new rheological-based, FSI-consistent, to model the liquid-filled visco-elastic pipe dynamic. A brief literature review of the current models along with some of the existing visco-elastic knowledge is provided. Then, a new model is established, the implications of which are in-depth analyzed and compared with other pre-existing models.

4.1 Linear visco-elastic pipe rheology

4.1.1 Terminology of visco-elastic materials

Unlike the elastic materials, the visco-elastic fluid or solid do not instantaneously respond to stress or strain solicitations. A time-delay response is observed along with possible hysteretic behaviors. The creep response corresponds to the strain evolution when the solid is submitted to a constant stress. On the other hand, the relaxation behavior depicts the stress evolution when the solid is submitted to a constant strain deformation. Several models exist to characterize the visco-elastic behavior of a solid (or a fluid), one-dimensional ones being the most popular. The Maxwell and Kelvin-Voigt models are the most widely spread 1D visco-elastic models, generally described by a combination of dashpot and spring responses as depicted in Figure 4.1.

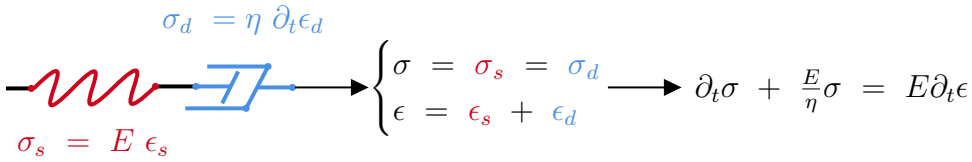

(a) *Maxwell's visco-elastic model (single element).*

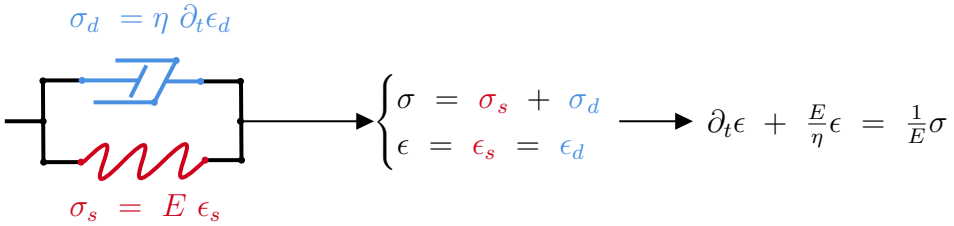

(b) *Kelvin-Voigt's visco-elastic model (single element).*

Figure 4.1: *Schematic interpretation of the Maxwell and Kelvin-Voigt rheological models. A single element is depicted.*

- **Maxwell's model** is one of the simplest existing model to describe the visco-elastic response of a fluid or a solid. It is mechanically analogous to a spring and a damper in a row (Cf. Figure 4.1a). While the spring describes the instantaneous elastic response, the damper enslaves the long time dynamic. This model nevertheless fails to describe the material creep behavior.
- **Kelvin-Voigt's model** consists in a spring set up in parallel to a damper (Cf. Figure 4.1b). This model fails to describe the material relaxation behavior.

According to [Covas, 2003]: "*These models describe the behavior of simple systems and do not provide a good approximations to the visco-elastic behavior of polymers*".

Then, the 1D models are generalized, using a combination of several Maxwell or Kelvin-Voigt single elements added in series. The generalized 1D Kelvin-Voigt model is depicted in Figure 4.2. Let us now introduce the creep function $J(t)$

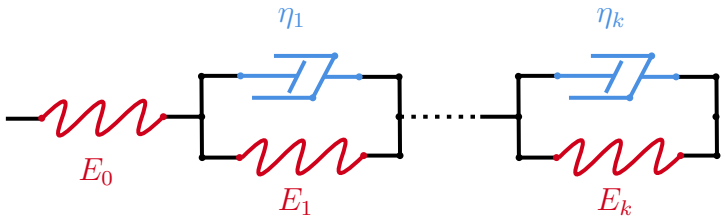

Figure 4.2: *Generalized Kelvin-Voigt model*

resulting from a constant axial stress perturbation of amplitude σ_0. For the generalized Kelvin-Voigt model, following [Covas et al., 2004b, Keramat et al., 2011], it yields

$$J(t) = J_0 + \sum_{k=1}^{N} J_k \left(1 - e^{-\frac{t}{\tau_k}}\right) \quad \text{, with,} \quad J_k = 1/E_k \quad \text{, and,} \quad \tau_k = \frac{\eta_k}{E_k}. \tag{4.1}$$

The stress perturbation is nevertheless not always constant but can vary in time. In this case, the Boltzmann superposition principle is used to express the instantaneous strain response versus the time-dependent stress following [Shaw and MacKnight, 2018]

$$\epsilon(t) = \underbrace{J_0\sigma(t)}_{\text{Instantaneous response}} + \underbrace{\int_0^t \sigma(t-t')\frac{d}{dt'}J(t')dt'}_{\text{Retarded response}}. \tag{4.2}$$

4.1.2 Visco-elastic fluid pulse wave speed: hydraulic analysis of water hammer in visco-elastic materials

The presence of a retarded stress-strain relation in the solid rheology 4.2 perturbs the fluid dynamic. In this subsection the pipe axial dynamic is discarded, i.e. $\nu_s = 0$, and the fluid will be considered inviscid. The fluid is thus governed by its mass and momentum conservation equations, which are forced by hoop-stress response associated with the pipe breathing [Meißner, 1977, Suo and Wylie, 1990, Covas et al., 2004b]

$$\left[\partial_t + \begin{pmatrix} 0 & \mathcal{K}_f \\ -\frac{1}{\rho_f} & 0 \end{pmatrix} \partial_z\right] \begin{pmatrix} P \\ W \end{pmatrix} = -2\mathcal{K}_f \partial_t \epsilon_{\theta\theta} \begin{pmatrix} 1 \\ 0 \end{pmatrix}. \tag{4.3}$$

From (4.2) whilst re-organizing (4.3), it yields the visco-elastic forced pressure wave equation

$$\left(\partial_t^2 - \frac{\mathcal{K}_f}{\rho_f}\partial_Z^2\right) P = -2\mathcal{K}_f \partial_t^2 \left(J_0\sigma_{\theta\theta}(t) + \int_0^t \sigma_{\theta\theta}(t-t')\frac{d}{dt'}J(t')dt'\right). \tag{4.4}$$

For a circular tube, when the influence of the Poisson's modulus is discarded, the force equilibrium provides a straightforward relation between the radial solid stress and the pressure $\sigma_{\theta\theta} = P/\alpha$, which has been spelled out in (1.11) (Cf. §1.4.1). From this one gets

$$\left(\partial_t^2 - \frac{\mathcal{K}_f}{\rho_f}\partial_Z^2\right) P = -\frac{2\mathcal{K}_f}{\alpha}\partial_t^2 \left(J_0 P + \int_0^t P(t-t')\frac{d}{dt'}J(t')dt'\right). \tag{4.5}$$

Performing a Fourier transform (4.6) leads to

$$\left(\omega^2 + \underbrace{\frac{\frac{\mathcal{K}_f}{\rho_f}}{1 + \frac{2\mathcal{K}_f}{\alpha}\left(J_0 + i\omega\tilde{J}(\omega)\right)}}_{\text{Frequency-dependent wave speed, } \tilde{c}_p} \partial_Z^2\right)\tilde{P} = 0. \tag{4.6}$$

Noteworthy, the visco-elastic pulse wave speed is frequency-dependent and displays a similar form with the elastic Korteweg's wave speed, defined in (1.2), but for the elastic Young modulus replaced by a complex, frequency-dependent one [Meißner, 1977, Suo and Wylie, 1990, Mitosek and Chorzelski, 2003, Covas et al., 2004b]. An example of time-varying pulse-wave speed is depicted in Figure 4.3 associated with the experiment measurements of [Mitosek and Chorzelski, 2003]. The visco-

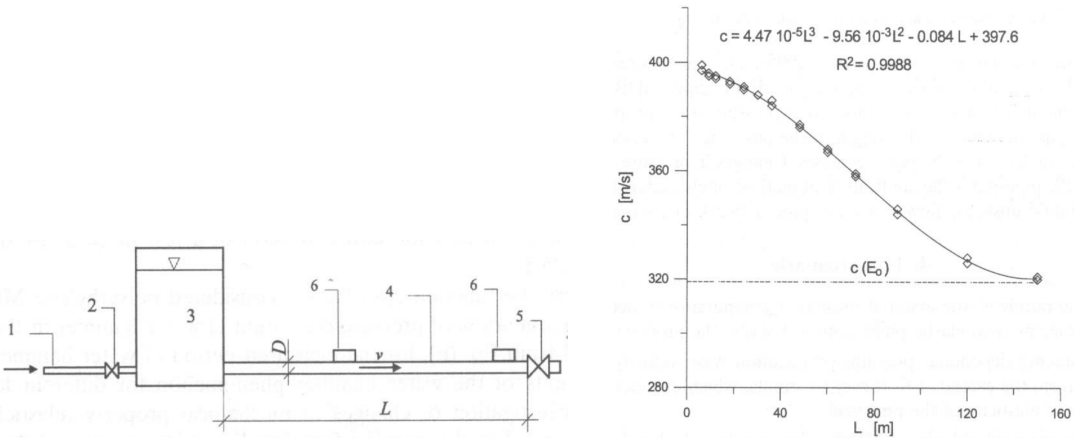

(a) *Experimental setup* **(b)** *Wave speed measurement*

Figure 4.3: *Fluid pulse wave speed time variation in an (MDPE) pipe, [Mitosek and Chorzelski, 2003].*

elastic rheology is thus modeled as a simple extension of the elastic framework from only considering complex solid rheological parameters, [Rubinow and Keller, 1971, Rubinow and Keller, 1978, Barez et al., 1979]. Let us discuss the physical consequences of a complex wave speed. Following the analysis of [Suo and Wylie,

1990], writing the pressure field as a plane-wave, leads to

$$P = P_0 e^{i\omega\left(t-\frac{z}{\tilde{c}_p(\omega)}\right)} = P_0 \underbrace{e^{-\frac{\omega z I_m(\tilde{c}_p(\omega))}{\|c_p(\omega)\|^2}}}_{\text{Rheological damping}} e^{i\omega\left(t-\frac{z R_e(\tilde{c}_p(\omega))}{\|c_p(\omega)\|^2}\right)}. \tag{4.7}$$

The real part of the fluid complex visco-elastic pulse wave speed drives the phase-shift of the pressure signature. Its imaginary counterpart is responsible for the wave damping. It is interesting to note that this complex velocity component is directly related with the imaginary part of the creeping-law response according to (4.6). The rheological-based damping appears to be dominant over the fluid viscous one (Cf. §3.3) as demonstrated by [Lee et al., 2013], the results of which are depicted in Figure 4.4. The comparison between the fluid boundary layer viscous dissipation, and visco-elastic damping trend was performed by [Ramos et al., 2004] and merges with [Lee et al., 2013]'s conclusions. [Urbanowicz et al.,

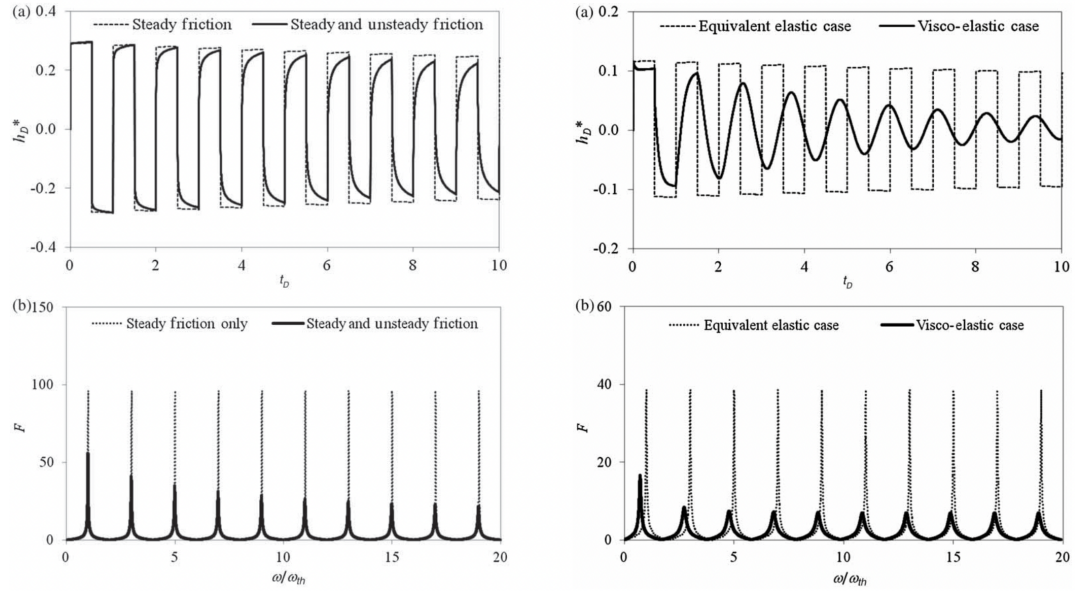

Figure 4.4: *Time- and frequency-response of a reservoir-pipe-valve system. Fluid friction along with visco-elastic effects have been considered, [Lee et al., 2013].*

2016, Urbanowicz and Firkowski, 2018] surveyed the main models, along with their numerical implementation, used to describe the visco-elastic liquid-filled pipe dynamic (restricted at $\nu_s = 0$). Some authors furthermore extended the $\nu_s = 0$ restricted framework to account for the solid axial coupled dynamic.

4.1.3 Visco-elastic FSI systems

[Barez et al., 1979] extended the elastic work of [Walker and Phillips, 1977], by considering a visco-elastic, Maxwell-driven, rheology for the pipe. The authors then investigates the resulting FSI coupled wave speeds and conclude that: "*the*

viscosity of the fluid has negligible influence on the pulse propagation in the system, although it is well known that it has a significant effect on the flow characteristics". The asymptotic approach of [Walker and Phillips, 1977] was also revisited by the breakthrough contributions of [Čanić et al., 2006a, Čanić et al., 2006b, Kizilova, 2006] (already presented in §3.2), the which performed an asymptotic expansion in ϵ of both the incompressible, viscous, Navier-Stokes equations and the visco-elastic pipe wall ones. The strength of these theories lies in the incorporation of three-dimensional models to describe the pipe visco-elastic rheology, i.e. by the generalization of the elastic Hooke's law to visco-elastic materials, thus considerably extending the one-dimensional scope proposed so far. More recently, [Keramat et al., 2011] delivered an insightful work by extended the four-FSI elastic framework of [Tijsseling, 2007] to one-dimensional visco-elastic Kelvin-Voigt-based, materials. The authors spelled out a four-equations hyperbolic system, which displays a mathematical structure similar to the elastic one, but where additional visco-elastic, convoluted-based, terms are found. [Achouyab and Bahrar, 2011] used a very similar approach but considered a visco-elastic shell model for the solid. [Keramat et al., 2011]'s model now stands has a reference study in the literature and was largely used for pipe anomaly detection [Zanganeh et al., 2020] or for the analysis of junction couplings [Hosseini et al., 2020, Aliabadi et al., 2020]. Very recently, [Andrade et al., 2023] proposed a quasi-2D model to investigate the effects of visco-elastic FSI and fluid dissipation in liquid-filled pipe systems. The authors combined the continuum theory of mixtures to describe the viscous fluid dynamics (previously derived for elastic material in [Andrade et al., 2022]) with the internal variable constitutive theory to model the solid visco-elastic response. For the fluid, the continuum theory of mixtures consists in splitting the fluid into a succession of concentrically-shell-shaped constituents (similarly done by [Vardy and Hwang, 1991] but without FSI) and to ensure mass and momentum conservation equations in each fluid rings. The fluid viscous dissipation is then incorporated to the model by using an idealize turbulent kinematic viscosity distribution and by invoking the *frozen-viscosity* assumption (Cf. [Vardy and Brown, 2003, Vardy et al., 2015] and §1.4.2). In the solid, the thermodynamics viewpoint is adopted by the definition of potentials that portray the reversible and irreversible character of the visco-elastic material, the latter being associated with dissipative phenomena. A linear generalized Kelvin-Voigt visco-elastic rheological model was adopted then providing relationships between the thermodynamics potential and the Kelvin-Voigt elements, i.e. shear elastic constants E_i and viscosity coefficients η_i on Figure 4.2. Finally, the set of hyperbolic fluid-solid governing equations was numerically solved and compared with the experiments of [Gally et al., 1979, Covas, 2003]. A very close agreement was found between numerical predictions and experimental measurements when only two and five Kelvin-Voigt cells were used to describe [Gally et al., 1979]'s and [Covas, 2003]'s experiments, respectively. Through a rigorous, thermodynamics-based, energetic analysis, [Andrade et al., 2023] estimated the rate of energy dissipation (separately in the fluid and the solid) and yielded to the conclusions that the: "*energy dissipation in the pipe has superior magnitudes*

compared to those found in the fluid"" and that "*the alteration of the visco-elastic characteristics of the pipe affects the fluid hydrodynamics*".

4.1.4 Creep characterization

The visco-elastic models nevertheless remain difficult to use without a proper creep function model. A significant visco-elastic HDPE solid creep characterization was for instance carried out by [Covas et al., 2004a, Covas et al., 2005, Covas et al., 2004b]. The authors indeed investigated the presence of hysteretic responses in the material and analyzed the temperature influence on the visco-elastic behavior, which can have an important impact on parameter estimation [Thorley, 1969, Williams, 1977], as depicted in Figure 4.5 Overpressure measurement in sev-

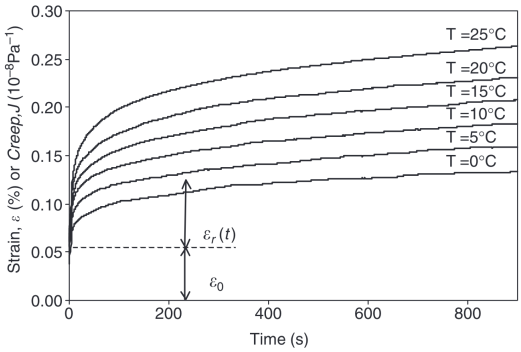

Figure 4.5: *Influence of the temperature on the creep characterization, [Covas et al., 2004a].*

eral locations, of water hammer waves were used to spelled out an optimal set of Kelvin-Voigt's visco-elastic parameters. Such estimation, i.e. the minimization of the error between experimental data and the model, is quasi-systematic in the literature subject an often limit the model scope to the experiment setup, [Urbanowicz et al., 2016]. [Weinerowska-Bords, 2006] delivered an in-depth discussion on the modeling problems encountered in visco-elastic pipes from the model choice (e.g. pros and cons of the use of generalized Kelvin-Voigt and Maxwell models) to the complex wave speed implications. [Soares et al., 2008] followed the work of [Covas et al., 2005] and embedded several fluid viscous damping models (Cf. §1.4.2), the pressure signatures of which were confronted to experimental measurements on a PVC tube.

The current four-FSI equations systems, restricted to the long-wavelength asymptotic framework, appears to be FSI-inconsistent when 3D visco-elastic effects are taken into account because the visco-elastic variations of the Poisson modulus are discarded. On the other hand, the two-equations fluid models fails to handle junction couplings. Thus, there is a need to develop an FSI-consistent, rheological-based model, to reconcile the classical approaches with the Poisson

coupling effects.

4.2 Rheology-based fluid-structure-interactions water-hammer wave propagation in liquid-filled visco-elastic pipes: Article to *Journal of Sound and Vibration*.

Abstract

This contribution proposes a new rheology-based model for water-hammer wave propagation in visco-elastic pipes. Using a long wavelength analysis and a generalized frequency-dependent Hooke-law for the stress/strain relation, the pressure/longitudinal stress coupled wave system is derived. In this general framework, a visco-elastic Fluid-Structure Interaction (FSI) four equations model is derived by having four visco-elastic kernels associated with the non-local time response of the visco-elastic solid. The explicit dependence of these kernels with the material creep function and the pipe dimension is found. Considering a general linear visco-elastic rheology, the four visco-elastic kernels, and the corresponding creep function are explicitly derived in frequency and time-domain versus four visco-elastic parameters. For a given set of boundary conditions, a general analytical solution for the pressure/stress water hammer wave is obtained in frequency domain. The model's predictions are successfully compared with experimental measurements as well as with other models adjusted to the same experimental data set by calibrating the model's parameter. The proposed model can be used in many other contexts with the specific ability to distinguish the intrinsic visco-elastic rheology from the considered pipe geometry and boundary conditions.

Highlights

Frequency varying rheology-based fluid-structure-interactions waves in liquid-filled visco-elastic pipes.

A.Bayle, F.Rein, F.Plouraboué

- A fluid-structure-interaction water-hammer model for linear visco-elastic rheology is derived.
- It involves new history-dependent visco-elastic response through time-convolution kernels.
- It does not need Kelvin-Voigt calibrated parameters, but rheological ones.
- The dispersive wave velocity is also obtained explicitly versus rheological parameters.

Frequency varying rheology-based fluid-structure-interactions waves in liquid-filled visco-elastic pipes.

A.Bayle[a], F.Rein[a,b], F.Plouraboué[a]

[a]*Institut de Mécanique des Fluides de Toulouse, IMFT, Université de Toulouse, CNRS, Toulouse, 31400, France*
[b]*Institut de Recherche sur les Phénomène Hors Equilibre, IRPHE, Université d'Aix-Marseille, CNRS, Marseille, 13013, France*

Keywords: visco-elastic rheology, Kelvin-Voigt, water-hammer, creeping-law, fluid-structure-interactions, polymer pipes, dispersive waves

1. Introduction

Pressure waves in visco-elastic tubes is a topic of importance in many hydraulic contexts [1] as well as biomechanical ones [2, 3, 4, 5, 6]. It is known for a long time that when a water-hammer wave propagates into a filled-fluid pipe, the visco-elastic properties of the solid wall drastically modifies the nature and characteristic of its motion. More precisely, the importance of visco-elastic stress-strain response of the pipe wall in the water-hammer waves propagation was first raised by [7]. A few years later some experiments from the same team [8] complemented with a 1D theoretical model [9] confirmed the relevance and interest of these effects on water-hammer waves propagation. As opposed to the situation of a purely elastic solid tube, the wave velocity becomes dispersive when a visco-elastic wall is present [2, 10, 11]. Secondly, not only the wave velocity depends on the considered frequency, but it also acquires an imaginary component associated with visco-elastic dissipation resulting in exponential damping [12, 13, 14, 15]. Such exponential damping is also present in water-hammer wave propagation within elastic filled-fluid pipes but for a very distinct mechanism: the viscous dissipation arises only within the liquid boundary layers [16]. Nevertheless, compared to this viscous damping, the visco-elastic one turns out to be dominant in many configurations, resulting in the filtering of high-frequency bouncing elastic waves. Recently, [17] indeed analysed the energy rates of energy dissipation in the fluid and the pipe for visco-elastic water-hammer.

Since most aspects of water-hammer wave propagation have been found material dependant, the pioneering studies of [7, 8, 9] inspired many others, following the similar footsteps, combining experimental measurements with one-dimensional two-equations modelling associated with pressure

(hydraulic head) and axial velocity coupled propagation coupled with solid creep-functions displaying Kelvin-Voigt behaviour (Cf [18, 13, 14, 19] among others). The applicative interest and the relevance of the topic motivated many further studies whereby one could enrich the Kelvin-Voigt model [20, 21] to better fit with observations. Alternatively, some authors also included both solid visco-elastic damping and fluid one, through time-convolution shear-stress models [22, 23, 24]. Because the modelling relies on many parameters, combined with time-convolution many approaches are possible to match experiments raising a number of questions including wave-speed calibration in visco-elastic pipes [19, 25]. The influence of the visco-elastic stress response has been more recently considered in a Fluid-Structure-Interaction (FSI) context as more extensively discussed in the recent review of [26]. In this context Kelvin-Voigt solid responses of the creep function have also been used in FSI four-equations models [27, 28] in order to improve the relevance of the modelling. Furthermore, for improving data fitting, a series of Kelvin-Voigt units are often considered [27, 29, 28, 30]. However, in these previous modelling, the creep-function parameters are calibrated [31] not only to describe the visco-elastic properties of the solid but also the considered pipe configuration associated with a specific length, thickness, diameter and boundary conditions. Nevertheless, Kelvin-Voigt units leading to a thermodynamic consistent framework of internal stress-strain theory have recently been proposed in [30] so as to improve their mechanical background.

In this contribution we pursue in this direction with the aim of stepping aside from Kelvin-Voigt models from considering rheology-based visco-elastic modelling of water-hammer propagation within a visco-elastic solid. The aim of this contribution is thus to distinguish and clarify the respective contribution of the visco-elastic response within pressure/stress wave propagation from the considered boundary conditions and pipe configuration. This permits to propose a new rheology-based visco-elastic FSI four equations model which can be used in many configurations (pipe's and boundary conditions) with material dependent only, visco-elastic kernels. The parameters of this model evidently need calibration. One option undertaken in this contribution is to use the existing pressure measurements of the water-hammer wave dynamic for inverse transient analysis of the model's parameter [32]. Another possible option opened by our contribution is to perform the parameter calibration/estimation from rheological measurements of the pipe material. The advantage of such rheology-based parameter calibration is to precisely focus the model estimation independently of the specific configuration at the end for water-hammer use (hence not

depending on the configuration geometry, pipe supports, flow conditions, boundary conditions, etc...). Whilst the latter is interesting, it is beyond the scope of the present contribution to the lack of existing data. The details of the protocol for this rheological-based parameter calibration are nevertheless presented in Appendix A.

The paper is organised as follows. Section S.2 provides a first overview of notations and considered problems. Using a long wavelength analysis and a generalised frequency-dependent Hooke-law for the stress/strain relation the pressure/longitudinal stress coupled wave system (equivalent to the classical four-equations Fluid-Structure Interaction (FSI) description) is derived in section S.3. The resulting set of equations involves four visco-elastic kernels directly related to the generalised frequency-dependent Hooke-law, the visco-elastic dispersive speed wave being solved as an explicit function of those. Considering specific visco-elastic rheology in S. 4.1, a specific set of boundary conditions in S.4.2, an explicit solution for the resulting visco-elastic FSI is derived in section S.4.2. It is then compared with previously proposed models as well as with experimental observations in section S. 4.5.

2. General considerations concerning visco-elastic material and their FSI waves.

2.1. Physical analysis overview

We consider the axi-symmetric propagation of a pressure/stress wave inside a Newtonian liquid filling a visco-elastic cylindrical tube. The circular visco-elastic-walled pipe tube has a thickness e, an inner radius R_0, and a length L_0 whilst its density is set constant equal to ρ_s. The solid has both an elastic Poisson's modulus ν_e and Young modulus E_e. The fluid is assumed isothermal and inviscid of constant density ρ_f, bulk modulus $\mathcal{K}_f$ and crossed by an acoustic overpressure P^*, the elastic wave speed of which is set to c_p^e ([33, 34])

$$c_p^e = \frac{c_0}{\sqrt{1+\chi_e \mathcal{C}^2}}, \qquad c_0 = \sqrt{\frac{\mathcal{K}_f}{\rho_f}}, \qquad \chi_e = \frac{2\mathcal{K}_f}{\alpha E_e \mathcal{C}^2}\left(\frac{2(1-\nu_e^2)}{2+\alpha} + \alpha\,(1+\nu_e)\right), \qquad \mathcal{C} = \frac{c_0}{c_p^e}, \qquad (1)$$

which depends on the dimensionless pipe thickness $\alpha = e/R_0$ and the bulk fluid acoustic velocity c_0. From this definition of χ_e, one can find a trivial but important relation $\mathcal{C}^2 = 1 + \chi_e \mathcal{C}^2$ (pulse speed wave $c_p^e = c_0/\mathcal{C}$ from definition of $\mathcal{C}$ in (1)) which is also important to consider for the simplification of the visco-elastic model provided in Appendix Appendix B.

In the solid, a deformation occurs due to the propagation of the acoustic fluid overpressure

waves, the displacement of which is

$$\boldsymbol{\xi}^* = \xi^* \mathbf{e}_r + \zeta^* \mathbf{e}_z. \tag{2}$$

where (ξ^*, ζ^*) are respectively the radial and axial displacements, whereas $(\mathbf{e}_r, \mathbf{e}_z)$ are the cylindrical coordinates unit vectors in the radial and axial directions. These deformations are associated with solid stress tensor

$$\boldsymbol{\sigma}_s^* = \begin{pmatrix} \sigma_{rr}^* & 0 & \sigma_{rz}^* \\ 0 & \sigma_{\theta\theta}^* & 0 \\ \sigma_{rz}^* & 0 & \sigma_{zz}^* \end{pmatrix}. \tag{3}$$

The wave advective time-scale L/c_p^e is chosen as a reference for the physical time t, whilst the length of the pipe L and radius R_0 as a reference length-scale in the longitudinal and radial direction (r, z), respectively, so that dimensionless time and coordinates are set

$$\tau = \frac{c_p^e}{L} t, \quad Z = \frac{z}{L}, \quad R = \frac{r}{R_0}, \quad \text{and} \quad \epsilon = \frac{R_0}{L}, \tag{4}$$

where we also introduce the tube aspect-ratio being a small parameter $\epsilon \ll 1$ as one key feature of the problem on which a long wavelength approximation is based. In the following the Fourier transform of a causal function $f^*(t)$, i.e. $f^*(t) = 0$ if $t < 0$, is denoted $\tilde{f}(\omega^*)$ from

$$\tilde{f}^*(\omega^*) = \int_{-\infty}^{\infty} f^*(t) e^{-i\omega^* t} dt \equiv \int_0^{\infty} f^*(t) e^{-i\omega^* t} dt, \tag{5}$$

with associated pulsation ω^*. When a dimensionless system is regarded, the pulsation ω^* has to be substituted by the dimensionless pulsation ω such that

$$\omega^* = \frac{c_p^e}{L} \omega. \tag{6}$$

2.2. Visco-elastic solid rheology

2.2.1. General linear dynamical rheological model

In Fourier space, the dimensional form of the 3D solid rheology is a frequency-dependent generalized Hooke-law [3]

$$\tilde{\boldsymbol{\sigma}}_s^* = \tilde{\lambda}_s^*(\omega^*) \, \mathrm{Tr}\left(\tilde{\boldsymbol{\epsilon}}_s^*\right) \mathbf{I} + 2\tilde{\mu}_s^*(\omega^*) \tilde{\boldsymbol{\epsilon}}_s^* \quad , \text{and,} \quad \tilde{\boldsymbol{\epsilon}}_s^* = \frac{1}{2}\left(\boldsymbol{\nabla}\tilde{\boldsymbol{\xi}}^* + \boldsymbol{\nabla}^T \tilde{\boldsymbol{\xi}}^*\right). \tag{7}$$

where Tr is trace, $\tilde{\lambda}_s^*, \tilde{\mu}_s^*$ are the generalized Lamé coefficients, dependent on pulsation ω^*. These coefficients provide the respective spherical and deviatoric response of the elastic deformation, depending on the considered pulsation ω^*, i.e. the response to oscillating compression and oscillating shear stress. From them, one can deduce the generalized Poisson and Young coefficients

$$2\tilde{\nu}_s^*(\omega^*) = \frac{\tilde{\lambda}_s^*(\omega^*)}{\tilde{\lambda}_s^*(\omega^*) + \tilde{\mu}_s^*(\omega^*)}, \quad \tilde{E}_s^*(\omega^*) = \frac{\tilde{\mu}_s^*(\omega^*)\left[3\tilde{\lambda}_s(\omega^*) + 2\tilde{\mu}_s^*(\omega^*)\right]}{\tilde{\lambda}_s^*(\omega^*) + \tilde{\mu}_s^*(\omega^*)}. \tag{8}$$

Subscript s stands thereafter for solid generalized physical fields or quantities. Also, from these relations one can deduce the reverse Lamé coefficients versus Poisson and Young coefficients

$$\tilde{\lambda}_s^*(\omega^*) = \frac{\tilde{\nu}_s^*(\omega^*)\tilde{E}_s^*(\omega^*)}{(1+\tilde{\nu}_s^*(\omega^*))(1-2\tilde{\nu}_s^*(\omega^*))}, \qquad \tilde{\mu}_s^*(\omega^*) = \frac{\tilde{E}_s^*(\omega^*)}{2(1+\tilde{\nu}_s^*(\omega^*))}. \tag{9}$$

This notation embeds both elastic and visco-elastic contributions. In this general context, one needs to specify the functional dependence of generalized Lamé coefficients on pulsation ω^*. Nevertheless, it is not easy to deduce them from experimental measurements as discussed in Appendix A. This is the reason for considering explicit rheological constitutive laws as later on considered in S.4.

2.3. Dimensionless parameters and physical fields scaling

The general Lamé-Clapeyron rheological parameters (8)-(9) are scaled to their elastic counterparts [3]

$$2\nu_e = \frac{\lambda_e}{\lambda_e + \mu_e} \text{ , and, } E_e = \frac{\mu_e\,(3\lambda_e + 2\mu_e)}{\lambda_e + \mu_e}, \tag{10}$$

so that

$$\tilde{\nu}_s^*(\omega^*) = \nu_e\tilde{\nu}_s(\omega), \qquad \tilde{E}_s^*(\omega^*) = E_e\tilde{E}_s(\omega), \tag{11}$$

$$\tilde{\lambda}_s^*(\omega^*) = \lambda_e\tilde{\lambda}_s(\omega), \qquad \tilde{\mu}_s^*(\omega^*) = \mu_e\tilde{\mu}_s(\omega). \tag{12}$$

The couple $\left(\tilde{\nu}_s, \tilde{E}_s\right)$ then corresponds to the re-scaled Poisson and Young visco-elastic modulus, respectively. The solid axial visco-elastic and elastic propagating wave speeds are furthermore set up regarding these dimensionless functions [1]

$$\tilde{c}_s^*(\omega^*) = \sqrt{\frac{\tilde{E}^*(\omega^*)}{\rho_s}} = c_s^e\sqrt{\tilde{E}_s(\omega)} \text{ , with } c_s^e = \sqrt{\frac{E_e}{\rho_s}}, \tag{13}$$

so that their dimensionless ratios to c_p^e of are

$$\mathcal{C}_s^e = \frac{c_s^e}{c_p^e} \quad \text{, and} \quad \tilde{\mathcal{C}}_s(\omega) = \mathcal{C}_s^e \sqrt{\tilde{E}_s(\omega)}. \tag{14}$$

Four dimensionless Cauchy numbers are associated with the solid elastic and visco-elastic responses to the acoustic pulse pressure one [35]

$$\mathcal{C}_{\mu_e} = \frac{\rho_f c_p^{e2}}{\mu_e}, \qquad \mathcal{C}_{\lambda_e} = \frac{\rho_f c_p^{e2}}{\lambda_e}, \tag{15}$$

$$\tilde{\mathcal{C}}_{\mu_s}(\omega) = \frac{\rho_f c_p^{e2}}{\mu_e \tilde{\mu}_s(\omega)} \equiv \frac{\mathcal{C}_{\mu_e}}{\tilde{\mu}_s(\omega)}, \qquad \tilde{\mathcal{C}}_{\lambda_s}(\omega) = \frac{\rho_f c_p^{e2}}{\lambda_e \tilde{\lambda}_s(\omega)} \equiv \frac{\mathcal{C}_{\lambda_e}}{\tilde{\lambda}_s(\omega)}. \tag{16}$$

Leading to the dimensionless parametrisation of $\tilde{\lambda}_s^*(\omega^*)$ and $\tilde{\mu}_s^*(\omega^*)$

$$\tilde{\lambda}_s(\omega) = \frac{\mathcal{C}_{\lambda_e}}{\tilde{\mathcal{C}}_{\lambda_s}(\omega)} \qquad \tilde{\mu}_s(\omega) = \frac{\mathcal{C}_{\mu_e}}{\tilde{\mathcal{C}}_{\lambda_s}(\omega)}, \tag{17}$$

and finally, the fluid-solid density ratio is introduced

$$\mathcal{D} = \frac{\rho_f}{\rho_s}. \tag{18}$$

The reference longitudinal fluid velocity is chosen has W_0. From Joukowsky's theory, [36] a reference pressure $\rho_f c_p^e W_0$ is built. This Joukowsky reference pressure is also chosen as reference stresses in the fluid and the solid, so that

$$\mathbf{W}^* = W_0 W \cdot \mathbf{e}_z, \tag{19}$$

$$P^* = \rho_f c_p^e W_0 P. \tag{20}$$

$$\left[\sigma_{rr}, \sigma_{\theta\theta}, \sigma_{zz}, \sigma_{rz}\right]^* = \rho_f c_p^e W_0 \left[\sigma_{rr}, \sigma_{\theta\theta}, \sigma_{zz}, \epsilon\sigma_{rz}\right]. \tag{21}$$

Finally, it has been shown in [34] that the solid displacements are related to fluid typical velocity because of kinematic boundary conditions to be applied at the fluid/solid interface. From choosing L/c_p^e as a reference time it results in the appearance of the dimensionless ratio $W_0/c_p^e \equiv \mathcal{M}$ defined as the Mach number, in the solid displacement $\boldsymbol{\xi}^*$ (2) scaling, so that

$$\boldsymbol{\xi}^* = \alpha R_0 \mathcal{M} \left(\xi \mathbf{e}_r + \frac{\zeta}{\epsilon} \mathbf{e}_z \right), \tag{22}$$

3. Dimensionless governing equations

3.1. Solid's equations

In dimensionless form, frequency domain, in cylindrical coordinates (4), the visco-elastic governing equation (7) using (17) reads

$$\tilde{\sigma}_{rr} = \alpha\left[\frac{2}{\tilde{\mathcal{C}}_{\mu_s}(\omega)}+\frac{1}{\tilde{\mathcal{C}}_{\lambda_s}(\omega)}\right]\partial_R\tilde{\xi}+\frac{\alpha}{\tilde{\mathcal{C}}_{\lambda_s}(\omega)}\left[\partial_Z\tilde{\zeta}+\frac{\tilde{\xi}}{R}\right], \tag{23}$$

$$\tilde{\sigma}_{\theta\theta} = \alpha\left[\frac{2}{\tilde{\mathcal{C}}_{\mu_s}(\omega)}+\frac{1}{\tilde{\mathcal{C}}_{\lambda_s}(\omega)}\right]\frac{\tilde{\xi}}{R}+\frac{\alpha}{\tilde{\mathcal{C}}_{\lambda_s}(\omega)}\left[\partial_Z\tilde{\zeta}+\partial_R\tilde{\xi}\right], \tag{24}$$

$$\tilde{\sigma}_{zz} = \alpha\left[\frac{2}{\tilde{\mathcal{C}}_{\mu_s}(\omega)}+\frac{1}{\tilde{\mathcal{C}}_{\lambda_s}(\omega)}\right]\partial_Z\tilde{\zeta}+\frac{\alpha}{\tilde{\mathcal{C}}_{\lambda_s}(\omega)}\frac{\partial_R}{R}\left(R\tilde{\xi}\right), \tag{25}$$

$$\epsilon^2\frac{\tilde{\mathcal{C}}_{\mu_s}(\omega)}{\alpha}\tilde{\sigma}_{rz} = \partial_R\tilde{\zeta}+\epsilon^2\partial_Z\tilde{\xi}, \tag{26}$$

where it takes the form of a generalised frequency-dependent Hooke-law (form the linearity of the visco-elastic rheological model (59)). The advantage of these dimensionless forms is to show that some terms are small as they involve the small parameter $\epsilon \ll 1$ [37, 38, 39, 33, 34]. The dimensionless form of Lamé-Clapeyron equations in frequency domain are [40]

$$-\epsilon^2\left(\omega^2\tilde{\xi}+\partial_Z\tilde{\sigma}_{rz}\right) = \frac{\partial_R}{R}\left(R\tilde{\sigma}_{rr}\right)-\frac{\tilde{\sigma}_{\theta\theta}}{R}, \tag{27}$$

$$-\frac{\alpha}{\mathcal{D}}\omega^2\tilde{\zeta} = \partial_Z\tilde{\sigma}_{zz}+\frac{\partial_R}{R}\left(R\tilde{\sigma}_{rz}\right). \tag{28}$$

Inserting the visco-elastic rheology (23)-(26) into the dimensionless Lamé-Clapeyron equations (27)-(28) leads to the solid dynamical governing equations

$$-\epsilon^2\left(\omega^2+\frac{\mathcal{D}}{\tilde{\mathcal{C}}_{\mu_s}(\omega)}\partial_Z^2\right)\tilde{\xi} = \mathcal{D}\frac{2\tilde{\mathcal{C}}_{\lambda_s}(\omega)+\tilde{\mathcal{C}}_{\mu_s}(\omega)}{\tilde{\mathcal{C}}_{\mu_s}(\omega)\tilde{\mathcal{C}}_{\lambda_s}(\omega)}\partial_R\left(\frac{\partial_R}{R}\left(R\tilde{\xi}\right)\right)+\mathcal{D}\frac{\tilde{\mathcal{C}}_{\mu_s}(\omega)+\tilde{\mathcal{C}}_{\lambda_s}(\omega)}{\tilde{\mathcal{C}}_{\mu_s}(\omega)\tilde{\mathcal{C}}_{\lambda_s}(\omega)}\partial_R\partial_Z\tilde{\zeta}, \tag{29}$$

$$-\epsilon^2\left(\omega^2+\mathcal{D}\frac{2\tilde{\mathcal{C}}_{\lambda_s}(\omega)+\tilde{\mathcal{C}}_{\mu_s}(\omega)}{\tilde{\mathcal{C}}_{\mu_s}(\omega)\tilde{\mathcal{C}}_{\lambda_s}(\omega)}\partial_Z^2\right)\tilde{\zeta} = \frac{\mathcal{D}}{\tilde{\mathcal{C}}_{\mu_s}(\omega)}\frac{\partial_R}{R}\left(R\partial_R\right)\tilde{\zeta}+\epsilon^2\mathcal{D}\frac{\tilde{\mathcal{C}}_{\mu_s}(\omega)+\tilde{\mathcal{C}}_{\lambda_s}(\omega)}{\tilde{\mathcal{C}}_{\mu_s}(\omega)\tilde{\mathcal{C}}_{\lambda_s}(\omega)}\partial_Z\left(\frac{\partial_R}{R}\left(R\tilde{\xi}\right)\right) \tag{30}$$

3.2. Fluid equations

In the fluid region, the dimensionless low-Mach, long-wavelength mass conservation and momentum balance lead to the following outer/core region fluid equations [31, 33, 34]

$$\partial_\tau P + \mathcal{C}^2 \partial_Z W = -2\alpha \mathcal{C}^2 \partial_\tau \xi\big|_{R=1}, \tag{31}$$

$$\partial_\tau W = -\partial_Z P. \tag{32}$$

From the r.h.s of (31) and the long-wavelength approximation, continuity relations of the radial velocity at the wall is automatically satisfied. Moving to the frequency domain gives

$$i\omega \tilde{P} + \mathcal{C}^2 \partial_Z \tilde{W} = -2i\alpha\omega \mathcal{C}^2 \tilde{\xi}\big|_{R=1}, \tag{33}$$

$$i\omega \tilde{W} = -\partial_Z \tilde{P}. \tag{34}$$

3.3. Fluid/solid interface boundary conditions

Ignoring external constraints applying to the solid radial direction (supposing a zero external normal stress), and using definition of $\tilde{\sigma}_{rr}$ in (23), the continuity of the normal and tangential stress as well as axial velocity reads (Cf [34] for more details)

$$\tilde{\sigma}_{rr} = -\tilde{P} \ \text{, at} \ \ R = 1 \qquad\qquad \tilde{\sigma}_{rr} = 0 \ \text{, at} \ \ R = 1 + \alpha \tag{35}$$

$$\tilde{\sigma}_{rz} = 0 \ \text{, at} \ \ R = 1 \qquad\qquad \tilde{\sigma}_{rz} = 0 \ \text{, at} \ \ R = 1 + \alpha \tag{36}$$

Note that, for dimensionless radial distance r, since the dimensionless thickness of the pipe is α, the outer wall is reached as $R = 1 + \alpha$.

$$\tilde{w} = i\alpha\omega\tilde{\zeta} \ \text{, at,} \ \ R = 1. \tag{37}$$

3.4. FSI four-equations dimensionless visco-elastic problem derivation

From the combination of the fluid, solid and the fluid-solid interface governing equations, a set of four coupled hyperbolic equations system is obtained upon $(\tilde{P}, \tilde{W}, \tilde{\sigma}_{zz}, \tilde{\zeta})$. Its complete

derivation is provided in Appendix B and achieves as follows [33, 27, 34]

$$
\begin{aligned}
i\omega\tilde{P} + \partial_Z\tilde{W} - 2i\omega\alpha\nu_e\partial_Z\tilde{\zeta} &= -i\omega\chi_e\tilde{\mathcal{I}}_P^F\tilde{P} + \frac{2\mathcal{D}\nu_e}{\mathcal{C}_s^{e2}}i\omega\tilde{\mathcal{I}}_\sigma^F\tilde{\sigma}_{zz}, && (38)\\
i\omega\tilde{W} &= -\partial_Z\tilde{P} && (39)\\
i\omega\tilde{\sigma}_{zz} - \frac{2\nu_e}{\alpha(2+\alpha)}i\omega\tilde{P} - i\omega\frac{\alpha\mathcal{C}_s^{e2}}{\mathcal{D}}\partial_Z\tilde{\zeta} &= -i\omega\tilde{\mathcal{I}}_\sigma^S\tilde{\sigma}_{zz} + \frac{2\nu_e}{\alpha(2+\alpha)}i\omega\tilde{\mathcal{I}}_P^S\tilde{P}, && (40)\\
\frac{\alpha}{\mathcal{D}}\omega^2\tilde{\zeta} + \partial_Z\tilde{\sigma}_{zz} &= 0, && (41)
\end{aligned}
$$

where the hereby introduced visco-elastic extra terms $\tilde{\mathcal{I}}_P^F$, $\tilde{\mathcal{I}}_\sigma^F$, $\tilde{\mathcal{I}}_P^S$ and $\tilde{\mathcal{I}}_\sigma^S$ read

$$
\begin{aligned}
\tilde{\mathcal{I}}_P^F &= \left(\frac{\mathcal{C}_s^e}{\tilde{\mathcal{C}}_s}\right)^2\frac{1-\nu_e^2\tilde{\nu}_s+\frac{\alpha(2+\alpha)}{2}(1+\nu_e\tilde{\nu}_s)}{1-\nu_e^2+\frac{\alpha(2+\alpha)}{2}(1+\nu_e)} - 1 \equiv \frac{1}{\tilde{E}_s(\omega)}\frac{1-\nu_e^2\tilde{\nu}_s(\omega)+\frac{\alpha(2+\alpha)}{2}(1+\nu_e\tilde{\nu}_s(\omega))}{1-\nu_e^2+\frac{\alpha(2+\alpha)}{2}(1+\nu_e)} - 1, && (42)\\
\tilde{\mathcal{I}}_\sigma^F &= \left(\frac{\mathcal{C}_s^e}{\tilde{\mathcal{C}}_s}\right)^2(\tilde{\nu}_s(\omega)-1) \equiv \frac{\tilde{\nu}_s(\omega)-1}{\tilde{E}_s(\omega)}, && (43)\\
\tilde{\mathcal{I}}_P^S &= \tilde{\nu}_s - 1 + \tilde{\nu}_s\frac{\mathcal{C}_s^{e2}-\tilde{\mathcal{C}}_s^2}{\tilde{\mathcal{C}}_s^2} \equiv -\left(1-\frac{\tilde{\nu}_s(\omega)}{\tilde{E}(\omega)}\right), && (44)\\
\tilde{\mathcal{I}}_\sigma^S &= \frac{\mathcal{C}_s^{e2}-\tilde{\mathcal{C}}_s^2}{\tilde{\mathcal{C}}_s^2} \equiv \frac{1-\tilde{E}_s(\omega)}{\tilde{E}_s(\omega)}. && (45)
\end{aligned}
$$

In (42)-(45), the relation $\tilde{\mathcal{C}}_s^2 = \mathcal{C}_s^{e2}\tilde{E}_s$ have been used according to (14). The dimensionless visco-elastic Young modulus ratio in (42)-(45) are directly connected to the dimensionless, frequency-dependent, creep function $\tilde{J}_s(\omega)$, defined as

$$
\tilde{J}_s(\omega) - 1 = \frac{1-\tilde{E}_s}{\tilde{E}_s}, \quad \text{or} \quad \tilde{J}_s(\omega) = \frac{1}{\tilde{E}_s}, \tag{46}
$$

so that, each visco-elastic kernel in (42)-(45) is linearly related to the creep function $\tilde{J}_s(\omega)$ which encapsulates part of their material rheology dependence. Nevertheless, (42)-(45) display supplementary frequency dependence of these kernels related to the visco-elastic Poisson coefficient $\tilde{\nu}_s(\omega)$ and the dimensionless Young modulus $\tilde{E}_s(\omega)$ defined in (11). Finally, it is interesting to state that the time-domain version of (39)-(41), i.e the inverse Fourier transform of (39)-(41) is the FSI four-equations formulation used for the method of characteristics since all l.h.s terms display constant convective hyperbolic operators associated with a constant travelling velocity. This choice has been set in order to provide the easiest comparison with previous formulations, such as [27]. However, the next section details another popular approach for visco-elastic propagation, i.e. the evaluation

of a dispersive frequency-dependent visco-elastic velocity with its associated, wave propagation operator in the Fourier domain.

3.5. Pressure-stress coupled visco-elastic wave propagation

Let us now consider the three equations (38)-(39)-(40)-, which, from the elimination of $\tilde{\zeta}$ and $\tilde{W}$ produces the following forced wave equation for the pressure perturbation

$$\omega^2 \left[1 + \chi_e \tilde{\mathcal{I}}_P^F + \frac{4\nu_e^2 \mathcal{D}}{\alpha(2+\alpha)\mathcal{C}_s^{e2}} \left(1 + \tilde{\mathcal{I}}_P^S\right)\right] \tilde{P} + \partial_Z^2 \tilde{P} = \frac{2\nu_e \mathcal{D}}{\mathcal{C}_s^{e2}} \left(1 + \tilde{\mathcal{I}}_\sigma^S + \tilde{\mathcal{I}}_P^F\right) \tilde{\sigma}_{zz}. \tag{47}$$

This wave equation can then be rewritten using (40) and (41) on the right-hand-side of (47), whilst also using (43) and (45) to simplify the kernel's dependance

$$\omega^2 \tilde{P} + [\tilde{c}_p^v]^2 \partial_Z^2 \tilde{P} = 2\alpha \nu_e \tilde{\nu}_s \omega^2 [\tilde{c}_p^v]^2 \partial_Z \tilde{\zeta} \tag{48}$$

where the effective frequency-dependent corrective visco-elastic pulsed-wave speed $\tilde{c}_p^v(\omega)$ has been introduced

$$\tilde{c}_p^v(\omega) = \frac{1}{\sqrt{1 + \chi_e \tilde{\mathcal{I}}_P^F - \frac{4\mathcal{D}\nu_e^2}{\alpha(2+\alpha)\mathcal{C}_s^{e2}} \tilde{\mathcal{I}}_\sigma^F \frac{1+\tilde{\mathcal{I}}_P^S}{1+\tilde{\mathcal{I}}_\sigma^S}}}. \tag{49}$$

On the other hand, the coupled equations (40) and (41) give rise to the coupled stress/pressure wave equation in the solid

$$\left[1 + \tilde{\mathcal{I}}_\sigma^S\right] \omega^2 \tilde{\sigma}_{zz} + \mathcal{C}_s^{e2} \partial_Z^2 \tilde{\sigma}_{zz} = \frac{2\nu_e \omega^2}{\alpha(2+\alpha)} \left[1 + \tilde{\mathcal{I}}_P^S\right] \tilde{P}. \tag{50}$$

The wave system resulting from the FSI four equations hyperbolic problem (39)-(41) can thus be recast into two coupled waves propagating system associated with a two-component pressure/stress vector $\tilde{\mathbf{P}} \equiv [\tilde{P}, \tilde{\sigma}_{zz}]$ following [34]

$$\omega^2 \tilde{\mathbf{P}} + [\tilde{c}_p^v]^2 \begin{pmatrix} 1 & 2\nu_e \mathcal{D} \frac{1+\tilde{\mathcal{I}}_\sigma^S + \tilde{\mathcal{I}}_\sigma^F}{1+\tilde{\mathcal{I}}_\sigma^S} \\ \frac{2\nu_e}{\alpha(2+\alpha)} \frac{1+\tilde{\mathcal{I}}_P^S}{1+\tilde{\mathcal{I}}_\sigma^S} & \mathcal{C}_s^{e2} \frac{1+\chi_e \tilde{\mathcal{I}}_P^F}{1+\tilde{\mathcal{I}}_\sigma^S} + \frac{4\nu_e^2 \mathcal{D}}{\alpha(2+\alpha)} \frac{1+\tilde{\mathcal{I}}_P^S}{1+\tilde{\mathcal{I}}_\sigma^S} \end{pmatrix} \partial_Z^2 \tilde{\mathbf{P}} = \mathbf{0}. \tag{51}$$

The characteristic equation associated with this propagating operator is

$$\left(\frac{\tilde{c}_\pm}{\tilde{c}_p^v}\right)^4 - \left(\frac{\tilde{c}_\pm}{\tilde{c}_p^v}\right)^2 \left[1 + \mathcal{C}_s^{e2}\frac{1+\chi_e\tilde{\mathcal{I}}_P^F}{1+\tilde{\mathcal{I}}_\sigma^S} + \frac{4\nu_e^2\mathcal{D}}{\alpha(2+\alpha)}\frac{1+\tilde{\mathcal{I}}_P^S}{1+\tilde{\mathcal{I}}_\sigma^S}\right] + \mathcal{C}_s^{e2}\frac{1+\chi_e\tilde{\mathcal{I}}_P^F}{1+\tilde{\mathcal{I}}_\sigma^S} + \frac{4\nu_e^2\mathcal{D}}{\alpha(2+\alpha)}\frac{1+\tilde{\mathcal{I}}_P^S}{1+\tilde{\mathcal{I}}_\sigma^S}\left(1 - \frac{1+\tilde{\mathcal{I}}_\sigma^S+\tilde{\mathcal{I}}_\sigma^F}{1+\tilde{\mathcal{I}}_\sigma^S}\right) = 0, \quad (52)$$

the root of which can then be explicitly found

$$\tilde{c}_\pm^2 = [\tilde{c}_p^v]^2\frac{\hat{c} \pm \sqrt{\hat{c}^2 - 4\left[\mathcal{C}_s^{e2}\frac{1+\chi_e\tilde{\mathcal{I}}_P^F}{1+\tilde{\mathcal{I}}_\sigma^S} + \frac{4\nu_e^2\mathcal{D}}{\alpha(2+\alpha)}\frac{1+\tilde{\mathcal{I}}_P^S}{1+\tilde{\mathcal{I}}_\sigma^S}\left(1 - \frac{1+\tilde{\mathcal{I}}_\sigma^S+\tilde{\mathcal{I}}_\sigma^F}{1+\tilde{\mathcal{I}}_\sigma^S}\right)\right]}}{2}, \quad (53)$$

$$\hat{c} = 1 + \mathcal{C}_s^{e2}\frac{1+\chi_e\tilde{\mathcal{I}}_P^F}{1+\tilde{\mathcal{I}}_\sigma^S} + \frac{4\nu_e^2\mathcal{D}}{\alpha(2+\alpha)}\frac{1+\tilde{\mathcal{I}}_P^S}{1+\tilde{\mathcal{I}}_\sigma^S} \equiv \frac{\tilde{c}_+^2 + \tilde{c}_-^2}{[\tilde{c}_p^v]^2}. \quad (54)$$

The diagonalisation matrix of (51) operator along with the change of basis relations are

$$\tilde{\mathbf{\Pi}}(\omega) = \begin{pmatrix} \frac{2\nu_e\mathcal{D}[\tilde{c}_p^v]^2}{\tilde{c}_-^2-[\tilde{c}_p^v]^2}\frac{1+\tilde{\mathcal{I}}_\sigma^S+\tilde{\mathcal{I}}_\sigma^F}{1+\tilde{\mathcal{I}}_\sigma^S} & \frac{2\nu_e\mathcal{D}[\tilde{c}_p^v]^2}{\tilde{c}_+^2-[\tilde{c}_p^v]^2}\frac{1+\tilde{\mathcal{I}}_\sigma^S+\tilde{\mathcal{I}}_\sigma^F}{1+\tilde{\mathcal{I}}_\sigma^S} \\ 1 & 1 \end{pmatrix}, \text{ and } \tilde{\boldsymbol{\mathcal{P}}} = \tilde{\mathbf{\Pi}}^{-1}\tilde{\mathbf{P}} = \begin{pmatrix} \tilde{\mathcal{P}}^- \\ \tilde{\mathcal{P}}^+ \end{pmatrix}. \quad (55)$$

The wave-vector system (51) then becomes diagonal

$$\left[\omega^2 + \begin{pmatrix} \tilde{c}_-^2 & 0 \\ 0 & \tilde{c}_+^2 \end{pmatrix}\partial_Z^2\right]\tilde{\boldsymbol{\mathcal{P}}} = \mathbf{0}. \quad (56)$$

From (56) it is then possible to find the explicit (Z,ω) dependence of $\tilde{\boldsymbol{\mathcal{P}}}(Z,\omega)$ (as well as its gradient) which depends upon the prescribed boundary condition $\left(\tilde{\mathcal{P}}^\pm(0,\omega), \partial_Z\tilde{\mathcal{P}}^\pm(0,\omega)\right)$ as

$$\tilde{\mathcal{P}}^\pm(Z,\omega) = \cos\left(\frac{\omega}{\tilde{c}_\pm}Z\right)\tilde{\mathcal{P}}^\pm(0,\omega) + \sin\left(\frac{\omega}{\tilde{c}_\pm}Z\right)\left[\frac{\tilde{c}_\pm}{\omega}\partial_Z\tilde{\mathcal{P}}^\pm(0,\omega)\right], \quad (57)$$

$$\partial_Z\tilde{\mathcal{P}}^\pm(Z,\omega) = -\frac{\omega}{\tilde{c}_\pm}\sin\left(\frac{\omega}{\tilde{c}_\pm}Z\right)\tilde{\mathcal{P}}^\pm(0,\omega) + \cos\left(\frac{\omega}{\tilde{c}_\pm}Z\right)\partial_Z\tilde{\mathcal{P}}^\pm(0,\omega). \quad (58)$$

4. Analysis of an experimental configuration using explicit visco-elastic rheology

The herein rheology-based model is now explicitly derived for a single pipe closed valve configuration, also known as the reservoir-pipe-anchored valve problem. Hereafter, general visco-elastic rheology is considered which allows the analytical derivation of the pressure-stress vector solution

$\tilde{\mathbf{P}}$, along with explicit expressions for visco-elastic convolution kernels (42)-(45).

4.1. Generalized 3D visco-elastic rheology

Various Kelvin-Voigt models have been previously considered in the literature [41, 31, 20, 21, 22, 28]. Nevertheless, for a real solid a 3D rheological model is necessary to take care of the solid's shape (not necessarily 1D/isotropic/spherical) and the considered boundary conditions. A general form of 3D visco-elastic rheology reads

$$a\left(1+\tau_r\partial_t\right)\boldsymbol{\sigma}_s^* = \lambda_e\left(1+\tau_\lambda\partial_t\right)\left(\boldsymbol{\nabla}\cdot\boldsymbol{\xi}^*\right)\mathbf{I} + \mu_e\left(1+\tau_\mu\partial_t\right)\left(\boldsymbol{\nabla}\boldsymbol{\xi}^* + \boldsymbol{\nabla}^T\boldsymbol{\xi}^*\right), \tag{59}$$

where six parameters $a, \tau_r, \tau_\lambda, \tau_\mu, \lambda_e, \mu_e$ can be used as constitutive ones, whilst (λ_e, μ_e) being the elastic Lamé coefficients and $(\tau_r, \tau_\lambda, \tau_\mu)$ are characteristic times, all independent from ω^*. Various 3D visco-elastic rheological laws have indeed been considered in the literature [3, 15, 42, 43, 44, 45, 46], (59) encapsulating all of those. More precisely, all model parameters of the cited references, are provided in table 1. It is important to note that most of the visco-elastic models proposed in literature did not consider the relaxation parameter τ_r associated with the instantaneous elastic response. Only [15] consider this term for an incompressible material. Now, from the Fourier

	a	τ_r	λ_e	τ_λ	μ_e	τ_μ
Carcione et al. [42]			✓	✓	✓	✓
Eringen, Canic et al.[43, 3]			✓	✓	✓	✓
Kisilova et al. [15]		✓			✓	✓
Bland [44]			✓		✓	
Ieşan [45]			✓	✓	✓	✓
Sharma et al. [46]			✓	✓	✓	✓

Table 1: Comparative table of 3D rheological parameters taken from literature.

transform of (59) and identification with (7) the generalized Lamé coefficients can be deduced for this rheology

$$\tilde{\lambda}_s^*(\omega^*) = \lambda_e\frac{1+i\omega^*\tau_\lambda}{a\left(1+i\omega^*\tau_r\right)} \quad \text{, and} \quad \tilde{\mu}_s^*(\omega^*) = \mu_e\frac{1+i\omega^*\tau_\mu}{a\left(1+i\omega^*\tau_r\right)}. \tag{60}$$

Generalized Poisson and Young modulus can also be found from these rheological parameters

$$\tilde{\nu}_s^*\left(\omega^*\right) = \nu_e\frac{1+i\omega^*\tau_\lambda}{1+i\omega^*\tau_\nu} \quad \text{, and} \quad \tilde{E}_s^*\left(\omega^*\right) = \frac{E_e(1+i\omega^*\tau_\mu)(1+i\omega^*\tau_E)}{a(1+i\omega^*\tau_r)(1+i\omega^*\tau_\nu)}, \tag{61}$$

where the above introduced times-scale τ_ν and τ_E are given by

$$\tau_\nu = \frac{\lambda_e\tau_\lambda + \mu_e\tau_\mu}{\lambda_e + \mu_e} \quad \text{, and} \quad \tau_E = \frac{3\lambda_e\tau_\lambda + 2\mu_e\tau_\mu}{3\lambda_e + 2\mu_e}. \tag{62}$$

Also, the dimensionless creep function $\tilde{J}_s(\omega)$ (46) reads regarding (6) and (9)

$$\tilde{J}_s(\omega) = \frac{1}{\tilde{E}_s} = a\frac{\left(1+i\omega\tau_r\frac{c_p^e}{L}\right)\left(1+i\omega\tau_\nu\frac{c_p^e}{L}\right)}{\left(1+i\omega\tau_\mu\frac{c_p^e}{L}\right)\left(1+i\omega\tau_E\frac{c_p^e}{L}\right)}. \tag{63}$$

4.1.1. Explicit form of visco-elastic extra-terms kernels

As discussed in S.2.2, the motivation of this study is to built a rheology-based model dependent on the material visco-elastic properties but not on the specific wave problem and/or its boundary conditions. For this the visco-elastic kernels are now explicitly derived versus rheological parameters. In the 3D visco-elastic rheology model framework, the rheological parameters $\left(\tilde{\nu}_s^*, \tilde{E}_s^*\right)$ presented in (11) and (61), are explicit function of the characteristic times $(\tau_\lambda, \tau_\mu, \tau_\nu, \tau_E, \tau_r)$ presented in (62) as well as elastic parameters. The convolution visco-elastic kernels (42)-(45) can thus be explicitly found

$$\tilde{\mathcal{I}}_P^F = a\frac{\left(1+i\omega\tau_r\frac{c_p^e}{L}\right)\left(1+i\omega\tau_\nu\frac{c_p^e}{L}\right)}{\left(1+i\omega\tau_\mu\frac{c_p^e}{L}\right)\left(1+i\omega\tau_E\frac{c_p^e}{L}\right)}\frac{\nu_e^2\frac{1+i\omega\tau_\lambda\frac{c_p^e}{L}}{1+i\omega\tau_\nu\frac{c_p^e}{L}} - 1 - \frac{\alpha(2+\alpha)}{2}\left(1+\nu_e\frac{1+i\omega\tau_\lambda\frac{c_p^e}{L}}{1+i\omega\tau_\nu\frac{c_p^e}{L}}\right)}{\nu_e^2 - 1 - \frac{\alpha(2+\alpha)}{2}(1+\nu_e)} - 1, \tag{64}$$

$$\tilde{\mathcal{I}}_\sigma^F = a\frac{\left(1+i\omega\tau_r\frac{c_p^e}{L}\right)\left(1+i\omega\tau_\nu\frac{c_p^e}{L}\right)}{\left(1+i\omega\tau_\mu\frac{c_p^e}{L}\right)\left(1+i\omega\tau_E\frac{c_p^e}{L}\right)}\left(\frac{1+i\omega\tau_\lambda\frac{c_p^e}{L}}{1+i\omega\tau_\nu\frac{c_p^e}{L}} - 1\right), \tag{65}$$

$$\tilde{\mathcal{I}}_P^S = -\left(1 - a\frac{\left(1+i\omega\tau_r\frac{c_p^e}{L}\right)\left(1+\omega\tau_\lambda\frac{c_p^e}{L}\right)}{\left(1+i\omega\tau_\mu\frac{c_p^e}{L}\right)\left(1+i\omega\tau_E\frac{c_p^e}{L}\right)}\right), \tag{66}$$

$$\tilde{\mathcal{I}}_\sigma^S = -\left(1 - a\frac{\left(1+i\omega\tau_r\frac{c_p^e}{L}\right)\left(1+i\omega\tau_\nu\frac{c_p^e}{L}\right)}{\left(1+i\omega\tau_\mu\frac{c_p^e}{L}\right)\left(1+i\omega\tau_E\frac{c_p^e}{L}\right)}\right). \tag{67}$$

Using the inverse Fourier transform, their time-domain form read

$$\mathcal{I}_P^F = \frac{\frac{a}{\mathcal{C}_\nu}\tau_r\left[\nu_e\tau_\lambda\left(\nu_e-\frac{\alpha(2+\alpha)}{2}\right)-\tau_\nu\left(\frac{\alpha(2+\alpha)}{2}+1\right)\right]-\tau_E\tau_\mu}{\tau_E\tau_\mu}\delta(\tau)$$
$$+\frac{aL(\tau_E-\tau_r)\left(\nu_e(\tau_\lambda-\tau_E)\left(\frac{\alpha(2+\alpha)}{2}-\nu_e\right)+(\tau_\nu-\tau_E)\left(\frac{\alpha(2+\alpha)}{2}+1\right)\right)}{c_p^e\tau_E^2\mathcal{C}_\nu(\tau_E-\tau_\mu)}e^{-\frac{\tau L}{\tau_E c_p^e}}H(\tau)$$
$$+\frac{aL(\tau_\mu-\tau_r)\left(\nu_e(\tau_\mu-\tau_\lambda)\left(\frac{\alpha(2+\alpha)}{2}-\nu_e\right)+(\tau_\mu-\tau_\nu)\left(\frac{\alpha(2+\alpha)}{2}+1\right)\right)}{c_p^e\tau_\mu^2\mathcal{C}_\nu(\tau_E-\tau_\mu)}e^{-\frac{\tau L}{\tau_\mu c_p^e}}H(\tau), \quad (68)$$

$$\mathcal{I}_\sigma^F = \frac{a\tau_r(\tau_\lambda-\tau_\nu)}{\tau_E\tau_\mu}\delta(\tau)-\frac{aL(\tau_\lambda-\tau_\nu)}{c_p^e\tau_E^2\tau_\mu^2(\tau_E-\tau_\mu)}\left(\tau_\mu^2(\tau_E-\tau_r)e^{-\frac{\tau L}{\tau_E c_p^e}}-\tau_E^2(\tau_\mu-\tau_r)e^{-\frac{\tau L}{\tau_\mu c_p^e}}\right)H(\tau), \quad (69)$$

$$\mathcal{I}_P^S = \frac{a\tau_\lambda\tau_r-\tau_E\tau_\mu}{\tau_E\tau_\mu}\delta(\tau)+\frac{aL}{c_p^e(\tau_E-\tau_\mu)}\left(\frac{(\tau_E-\tau_r)(\tau_E-\tau_\lambda)}{\tau_E}\frac{e^{-\frac{\tau L}{\tau_E c_p^e}}}{\tau_E}-\frac{(\tau_\mu-\tau_r)(\tau_\mu-\tau_\lambda)}{\tau_\mu}\frac{e^{-\frac{\tau L}{\tau_\mu c_p^e}}}{\tau_\mu}\right)H(\tau), \quad (70)$$

$$\mathcal{I}_\sigma^S = \frac{a\tau_\nu\tau_r-\tau_E\tau_\mu}{\tau_E\tau_\mu}\delta(\tau)+\frac{aL}{c_p^e(\tau_E-\tau_\mu)}\left(\frac{(\tau_E-\tau_r)(\tau_E-\tau_\nu)}{\tau_E}\frac{e^{-\frac{\tau L}{\tau_E c_p^e}}}{\tau_E}-\frac{(\tau_\mu-\tau_r)(\tau_\mu-\tau_\nu)}{\tau_\mu}\frac{e^{-\frac{\tau L}{\tau_\mu c_p^e}}}{\tau_\mu}\right)H(\tau), \quad (71)$$

where $\delta(\tau)$ and $H(\tau)$ stands for the Dirac distribution and its primitive, the Heaviside function. Relations (68)-(71) have been cross-checked using formal calculus software. It is interesting to note that every r.h.s of(68)-(71) display a Dirac distribution term resulting in a *local* visco-elastic response thus modifying the elastic one. In other words, these terms being independent of ω in Fourier space (the Fourier transform of the Dirac distribution is equal to one) they act as a modification of the non-dispersive elastic wave-speed. We will more explicitly examine how this provides an additional visco-elastic contribution to the elastic velocity in the next section. However it is interesting to mention that the choice for defining kernels $\tilde{\mathcal{I}}_P^F, \tilde{\mathcal{I}}_\sigma^F, \tilde{\mathcal{I}}_P^S, \tilde{\mathcal{I}}_\sigma^S$ has been done in order to permit a better comparison with previous models. However, local terms could have been recast into some elastic-like behaviour resulting from visco-elastic effects and left aside the kernels.

4.2. The reservoir-pipe-anchored valve problem

As depicted in Figure 1, the single visco-elastic pipe anchored upstream to a reservoir and downstream to an instantaneous closure valve, is now investigated. In the following the experimental data of Covas et al. ([18, 13]) and Pezinga et al. [32] are investigated, the details of which are given in Table 2. The perturbed flow rate is set to $Q_0 = 1.01\ l/s$ and $Q_0 = 4.03\ l/s$ for the experiments of Covas et al., [18, 13] and Pezinga et al., [32], respectively. For the investigated systems, the elastic fluid pulse wave speed is found equal to $c_p^e = 394.6m/s$ and $c_p^e = 360.05m/s$ respectively for Covas et al. ([18, 13]) and Pezzinga et al. [32] experimental set up. Upstream, the reservoir impedes the pressure to fluctuate whereas downstream, a sudden velocity perturbation

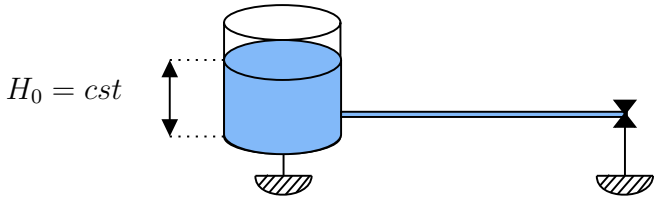

Figure 1: Constant head H_0 reservoir-pipe-anchored valve configuration

Article	Material	Density ($\mathrm{kg \cdot m^{-3}}$)	Elasticity (Pa)	ν_f ($\mathrm{m^2 \cdot s^{-1}}$)	ν_e	Geometry (m)
Covas et al., [18, 13]	$HDPE$	$\rho_f = 998.3$ $\rho_s = 960.0$	$\mathcal{K}_f = 2.1 \cdot 10^9$ $E_e = 1.43 \cdot 10^9$	$3.967 \cdot 10^{-5}$	0.46	$R = 2.53 \cdot 10^{-2}$ $e = 6.3 \cdot 10^{-3}$ $L = 277.0$
Pezinga et al., [32]	$HDPE$	$\rho_f = 998.3$ $\rho_s = 960.0$	$\mathcal{K}_f = 2.1 \cdot 10^9$ $E_e = 1.56 \cdot 10^9$	10^{-6}	0.45	$R = 4.67 \cdot 10^{-2}$ $e = 8.1 \cdot 10^{-3}$ $L = 200.0$

Table 2: Physical and geometrical properties for the experimental visco-elastic analysis of the reservoir-pipe-anchored valve system of Covas et al. ([18, 13]) and Pezinga et al. [32].

is imposed, the result of which is a pressure gradient variation according to (39). Downstream, the velocity variation associated with an impulse response is thus $W(1,t) = -H(t)$(here again $H(t)$ is the Heaviside function), being minus one for positive time. This transient closure law is set to compensate steady-state velocity (being one at time zero) with initial transient conditions $W(Z, t = 0) = 0$. The Fourier transform of $W(1,t)$ for $\omega > 0$ is thus precisely $\tilde{W}(1,\omega) = -i/\omega$ leading to $\partial_Z \tilde{P}(1,\omega) = 1 \equiv i\omega\tilde{W}(1,w)$ from (34). The pipe is supposed anchored at both ends so that no solid motion occurs, i.e. $\tilde{\zeta}(Z = 0,\omega) = \tilde{\zeta}(Z = 1,\omega) = 0$, which is equivalent to cancel-out the solid stress gradient according to (41). In the original basis, the boundary conditions read

$$\tilde{P}(0,\omega) = 0 \quad , \partial_Z \tilde{P}(1,\omega) = 1, \quad \partial_Z \tilde{\sigma}_{zz}(0,\omega) = \partial_Z \tilde{\sigma}_{zz}(1,\omega) = 0. \tag{72}$$

Introducing

$$\tilde{\beta}(\omega) = \frac{\tilde{c}_+}{\tilde{c}_-} \cdot \frac{\tilde{c}_-^2 - \left(\tilde{c}_p^v\right)^2}{\tilde{c}_+^2 - \left(\tilde{c}_p^v\right)^2}, \tag{73}$$

the diagonal-space vector boundary conditions can be deduced from (55), (58) and (72)

$$\tilde{\mathcal{P}}^-(0,\omega) = -\frac{\tilde{c}_-\tilde{\beta}}{\tilde{c}_+}\tilde{\mathcal{P}}^+(0,\omega), \tag{74}$$

$$\partial_Z\tilde{\mathcal{P}}^-(0,\omega) = -\partial_Z\tilde{\mathcal{P}}^+(0,\omega), \tag{75}$$

$$\partial_Z\tilde{\mathcal{P}}^-(1,\omega) = -\frac{\omega}{\tilde{c}_-}\sin\left(\frac{\omega}{\tilde{c}_-}\right)\tilde{\mathcal{P}}^-(0,\omega) + \cos\left(\frac{\omega}{\tilde{c}_-}\right)\partial_Z\tilde{\mathcal{P}}^-(0,\omega) = \frac{\tilde{c}_-^2 - \left(\tilde{c}_p^v\right)^2}{2\nu_e\mathcal{D}\left(\tilde{c}_p^v\right)^2\left(1-\frac{\tilde{c}_-\tilde{\beta}}{\tilde{c}_+}\right)}\frac{1+\tilde{\mathcal{I}}_\sigma^S}{1+\tilde{\mathcal{I}}_\sigma^S+\tilde{\mathcal{I}}_\sigma^F}, \tag{76}$$

$$\partial_Z\tilde{\mathcal{P}}^+(1,\omega) = \frac{\omega}{\tilde{c}_-\tilde{\beta}}\sin\left(\frac{\omega}{\tilde{c}_+}\right)\tilde{\mathcal{P}}^-(0,\omega) - \cos\left(\frac{\omega}{\tilde{c}_+}\right)\partial_Z\tilde{\mathcal{P}}^-(0,\omega) = -\frac{\tilde{c}_-^2 - \left(\tilde{c}_p^v\right)^2}{2\nu_e\mathcal{D}\left(\tilde{c}_p^v\right)^2\left(1-\frac{\tilde{c}_-\tilde{\beta}}{\tilde{c}_+}\right)}\frac{1+\tilde{\mathcal{I}}_\sigma^S}{1+\tilde{\mathcal{I}}_\sigma^S+\tilde{\mathcal{I}}_\sigma^F}. \tag{77}$$

Defining matrix $\tilde{\mathbf{M}}(\omega)$ as

$$\tilde{\mathbf{M}}(\omega) \equiv \begin{pmatrix} -\frac{\omega}{\tilde{c}_-}\sin\left(\frac{\omega}{\tilde{c}_-}\right) & \cos\left(\frac{\omega}{\tilde{c}_-}\right) \\ \frac{\omega\sin\left(\frac{\omega}{\tilde{c}_+}\right)}{\tilde{c}_-\tilde{\beta}} & -\cos\left(\frac{\omega}{\tilde{c}_+}\right) \end{pmatrix}. \tag{78}$$

The boundary condition system (74)-(77) can be expressed in the following matrix form

$$\tilde{\mathbf{M}}(\omega)\cdot\begin{pmatrix}\tilde{\mathcal{P}}^- \\ \partial_Z\tilde{\mathcal{P}}^-\end{pmatrix}(0,\omega) = \frac{\tilde{c}_-^2 - \left(\tilde{c}_p^v\right)^2}{2\nu_e\mathcal{D}\left(\tilde{c}_p^v\right)^2\left(1-\frac{\tilde{c}_-\tilde{\beta}}{\tilde{c}_+}\right)}\frac{1+\tilde{\mathcal{I}}_\sigma^S}{1+\tilde{\mathcal{I}}_\sigma^S+\tilde{\mathcal{I}}_\sigma^F}\begin{pmatrix}1\\-1\end{pmatrix}. \tag{79}$$

Multiplying (79) by $\tilde{\mathbf{M}}^{-1}(\omega)$ leads to

$$\begin{pmatrix}\tilde{\mathcal{P}}^- \\ \partial_Z\tilde{\mathcal{P}}^-\end{pmatrix}(0,\omega) = -\frac{\tilde{c}_-^2 - \left(\tilde{c}_p^v\right)^2}{2\nu_e|\tilde{\mathbf{M}}|\mathcal{D}\left(\tilde{c}_p^v\right)^2\left(1-\frac{\tilde{c}_-\tilde{\beta}}{\tilde{c}_+}\right)}\frac{1+\tilde{\mathcal{I}}_\sigma^S}{1+\tilde{\mathcal{I}}_\sigma^S+\tilde{\mathcal{I}}_\sigma^F}\begin{pmatrix}\cos\left(\frac{\omega}{\tilde{c}_+}\right)-\cos\left(\frac{\omega}{\tilde{c}_-}\right) \\ \frac{\omega}{\tilde{c}_-}\left[\frac{\sin\left(\frac{\omega}{\tilde{c}_+}\right)}{\tilde{\beta}}-\sin\left(\frac{\omega}{\tilde{c}_-}\right)\right]\end{pmatrix}, \tag{80}$$

with $|\tilde{\mathbf{M}}|(\omega) \equiv \det\left(\tilde{\mathbf{M}}\right)$ given by

$$|\tilde{\mathbf{M}}|(\omega) = \frac{\omega}{\tilde{c}_-}\left[\sin\left(\frac{\omega}{\tilde{c}_-}\right)\cos\left(\frac{\omega}{\tilde{c}_+}\right) - \frac{1}{\tilde{\beta}}\sin\left(\frac{\omega}{\tilde{c}_+}\right)\cos\left(\frac{\omega}{\tilde{c}_-}\right)\right]. \tag{81}$$

Combining (80), (81) and (74) in (57) close the diagonal wave solution in Fourier domain reading

$$\tilde{\boldsymbol{\mathcal{P}}}(Z,\omega) = \tilde{\mathcal{P}}^-(0,\omega)\begin{pmatrix}\cos\left(\frac{\omega Z}{\tilde{c}_-}\right) \\ -\frac{\tilde{c}_+}{\tilde{c}_-\tilde{\beta}}\cos\left(\frac{\omega Z}{\tilde{c}_+}\right)\end{pmatrix} + \frac{\partial_Z\tilde{\mathcal{P}}^-(0,\omega)}{\omega}\begin{pmatrix}\tilde{c}_-\sin\left(\frac{\omega Z}{\tilde{c}_-}\right) \\ -\tilde{c}_+\sin\left(\frac{\omega Z}{\tilde{c}_+}\right).\end{pmatrix} \tag{82}$$

Or, in a more explicit and compact form

$$\tilde{\boldsymbol{\mathcal{P}}}(Z,\omega) = -\frac{\tilde{c}_-^2 - \left(\tilde{c}_p^v\right)^2}{2\nu_e|\tilde{\mathbf{M}}|\mathcal{D}\left(\tilde{c}_p^v\right)^2\left(1-\frac{\tilde{c}_-\tilde{\beta}}{\tilde{c}_+}\right)}\frac{1+\tilde{\mathcal{I}}_\sigma^S}{1+\tilde{\mathcal{I}}_\sigma^S+\tilde{\mathcal{I}}_\sigma^F}\begin{pmatrix}\left[\cos\left(\frac{\omega}{\tilde{c}_+}\right)-\cos\left(\frac{\omega}{\tilde{c}_-}\right)\right]\cos\left(\frac{\omega Z}{\tilde{c}_-}\right)+\frac{\sin\left(\frac{\omega}{\tilde{c}_+}\right)-\tilde{\beta}\sin\left(\frac{\omega}{\tilde{c}_-}\right)}{\tilde{\beta}}\sin\left(\frac{\omega Z}{\tilde{c}_-}\right)\\ -\frac{\tilde{c}_+}{\tilde{c}_-\tilde{\beta}}\left(\left[\cos\left(\frac{\omega}{\tilde{c}_+}\right)-\cos\left(\frac{\omega}{\tilde{c}_-}\right)\right]\cos\left(\frac{\omega Z}{\tilde{c}_+}\right)+\left[\sin\left(\frac{\omega}{\tilde{c}_+}\right)-\tilde{\beta}\sin\left(\frac{\omega}{\tilde{c}_-}\right)\right]\sin\left(\frac{\omega Z}{\tilde{c}_+}\right)\right)\end{pmatrix}. \tag{83}$$

4.3. Numerical Fast Fourier Transform (FFT) inversion procedure

The pressure-stress solution (83) has a simple pole in $\omega = 0$ associated with the trivial zero of $|\tilde{\mathbf{M}}|$ (81), the contribution of which is equal to average signal in the time domain. The solution in the time domain is difficult to obtain first because of the discrete non-trivial set of poles from condition $|\tilde{\mathbf{M}}| = 0$, and second from the square-root dependence of velocity $\tilde{c}_+$ (Cf (53)) leading to a branch-cut. Hence, the inverse Fourier transform of (83) is numerically computed with a homemade *Python* code and the use of the *Scipy.fft* library.

Experimental data analysis. The steady-pressure time-dependent experimental variations have been disregarded withdrawing the initial static head value to the pressure signal. The transient component has been scaled according to Joukowsky's theory [36] (Cf. eq.(20)) and the physical time on the water-hammer advective one (Cf. eq.(4)). Then, the signal linear time-drift between the beginning and the end of the experimental pressure measurements is removed so as to analyse the effect of perturbations only, removing the change in the steady-state provided by the valve aperture. A Fast-Fourier-Transform (FFT) of the experimental time-dependent signal is performed providing their frequency-dependent counterpart. This FFT analysis is useful for the establishment of a suitable frequency threshold ensuring the Nyquist criterium, i.e. frequency truncation, value to perform the inverse numerical FFT of (83). A cutoff frequency of $f_c = 2000Hz$ is found for both the experimental data sets.

Inverse Fast Fourier Transform (IFFT) of the theoretical pressure-stress solution. The dimensionless pulsation and time resolution are set equal to $\Delta\omega = 10^{-3}$ and $\Delta\tau = 2.5 \cdot 10^{-4}$, respectively, providing a frequency cutoff at $f_c = 2000Hz$. At this stage, the direct inverse Fourier transform of (83) cannot be performed from the ignorance of the rheological parameters $[a, \tau_r, \tau_\mu, \tau_\lambda]$. This is where the calibration procedure enters into play so as to minimise the quadratic error (using *"Scipy.optimize.curve_fit" Pyhton*'s library) between (83)'s IFFT and the experimental data in time domain, at the very same time-located points. If needed, a linear interpolation of (83)'s

IFFT is used to perfectly match experimental time and numerical one. The calibration results are given below (for dimensionless parameters, as dicussed above) for the datasets of Covas et al. and Pezzinga et al.

$$[a, \tau_r, \tau_\mu, \tau_\lambda] \approx [1.3017, 0.1963, 0.3008, 0.1291] \quad \text{for Covas et al., [18, 13] data,} \tag{84}$$

$$[a, \tau_r, \tau_\mu, \tau_\lambda] \approx [1.1771, 0.1963, 0.2709, 0.1299] \quad \text{for Pezzinga et al., [32] data.} \tag{85}$$

It is interesting to observe that these calibrated dimensionless visco-elastic parameters are quite close although the two experiments were performed by two distinct teams in two distinct publications. However this can be understood from realising that the considered materials (HDPE) had closed mechanical properties, as provided in table 2. The calibration procedure is thus comforted by this coherent estimation.

4.4. Comparison between fluid viscous dissipation, elastic FSI effects and visco-elastic effects

As mentioned in the introduction, viscous dissipation in the fluid boundary-layers is a supplementary source of damping, eventually less dissipative than visco-elastic effects as discussed in [14]. To illustrate this point, this section compares the fluid viscous dissipation with various visco-elastic models and the one observed in experiments. The fluid viscous dissipation brilliantly investigated by [16] without considering FSI effects is used for this purpose. Furthermore, to complement this comparison this section also analyses the influence of FSI effects in visco-elastic models. In the case of a reservoir-pipe-anchored valve system, Mei et al. [16] derived an analytical exponential decay $H_{k,Mei}$, both mode and time dependent, for the pressure time domain variation

$$H_{k,Mei} = e^{-\sqrt{\frac{\lambda_k}{2}}\delta\tau} \text{ , with, } \quad \lambda_k = \pi\left(\frac{1}{2} + k\right) \text{for, } \quad k \in \mathbf{N}, \tag{86}$$

so that Mei et al. [16] rediscover the cornerstone role of the small dimensionless parameter $\delta = \sqrt{\nu_f L / c_p^e R_0^2}$ in the viscous boundary-layers exponential damping (this parameter was known of importance from many other previous studies). Recently, [34] provided a time-dependent solution for the elastic liquid-filled pipe FSI elastic response on the very same reservoir-pipe-anchored valve configuration but disregarded the effect of fluid viscosity. [34] derived a spectral transcendental equation governing the elastic resonant frequencies, the structure of which is found close to (81) when elastic parameters are considered only. The visco-elastic pressure at the valve, i.e. $Z = 1$,

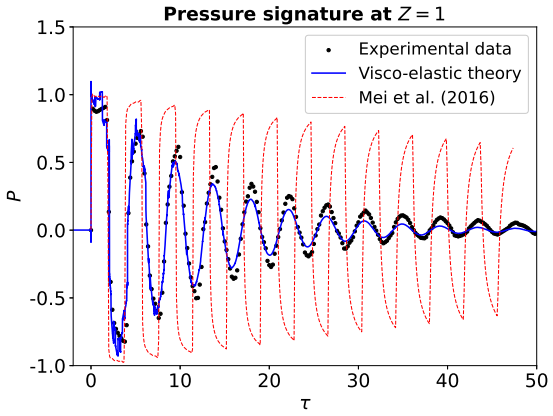

(a) Time-dependent pressure signal at the valve compared to the non-FSI Mei et al. [16]'s theory.

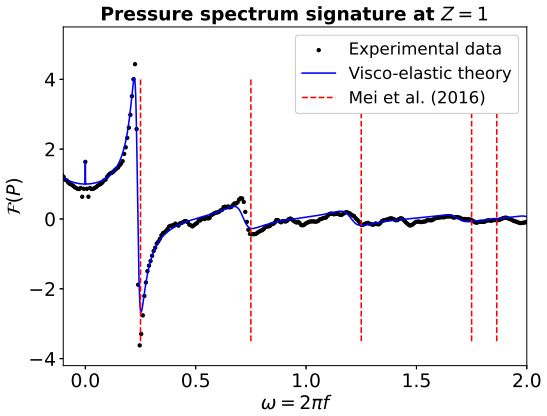

(b) Positive-half pressure signal spectrum at the valve. The Mei et al. [16]'s resonant frequencies are depicted by dotted red lines.

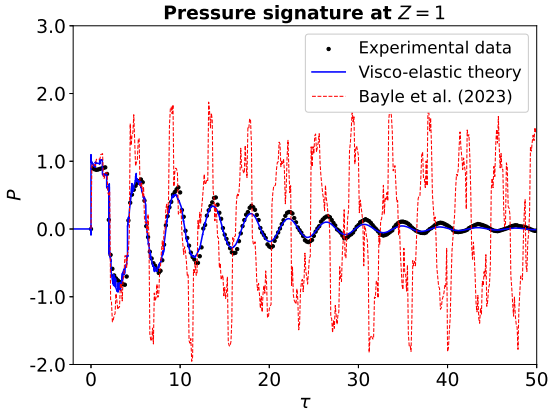

(c) Time-dependent pressure signal at the valve compared to the FSI, fluid non-viscous Bayle et al. [34]'s theory.

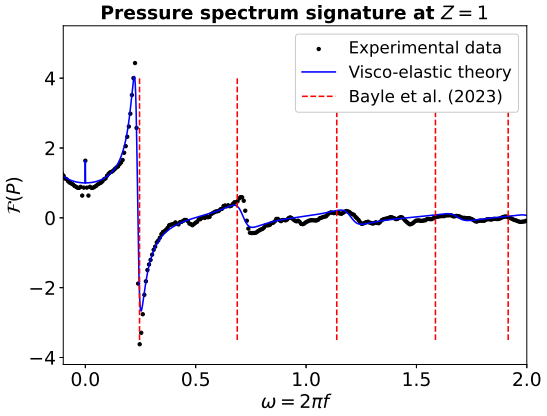

(d) Positive-half pressure signal spectrum at the valve. The Bayle et al. [34]'s resonant frequencies are depicted by dotted red lines.

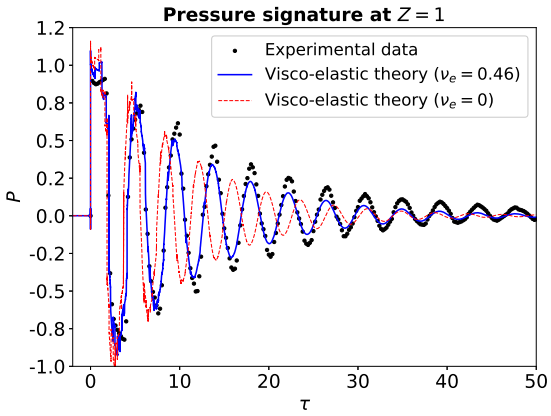

(e) Limit in $\nu_e \to 0$ of the visco-elastic solution.

Figure 2: Dimensionless time (using (4)) and frequency (using (6)) pressure signature at the valve comparing model's prediction with the experiment of Pezinga et al., [32]. The elastic signature is also depicted to point-out (a) the fluid viscous damping without FSI in the elastic pipe (b) the associated resonant frequencies and (c) the elastic FSI effects without fluid viscous damping (d) the associated resonant frequencies. Figure (e) displays the limit $\nu_e \to 0$ of (83)'s IFFT compared to Pezinga et al. [32]'s experiment.

for the experiment of Pezinga et al., [32] is depicted in Figure 2a along with its elastic counterpart where fluid viscous damping and FSI effects have been evaluated using the analytical solution of Mei et al. [16] (figures 2a-2b) and Bayle et al. [34] (figures 2c-2d), respectively. On can observe in figures 2a that the fluid viscous damping is small compared to the observed visco-elastic one, as previously stated. Furthermore, the purely elastic FSI effect illustrated in figures 2c produces high-frequency response to the signal that are not visible in Pezinga et al., [32] experimental observations. Also, these high-frequencies are not clearly visible in the frequency domain either, as illustrated in figure 2d. Nevertheless both elastic non-FSI (figure 2b) and FSI predictions figure 2d accurately capture the first-two lowest frequency observed in Pezinga et al. [32]'s signal. Finally it is interesting to observe that visco-elastic FSI effects are interesting to consider in order to more accurately describe Pezinga et al. [32] pressure time variations as illustrated in figure 2e. Hence figure 2 illustrates the strong impact of the visco-elastic response to the pressure signal which displays a much stronger decay than the one found from viscous dissipation in the fluid [14]. This figure shows that the proposed visco-elastic theory permits a convincing description of the experimental pressure signature both in time and frequency domains. For longer times, the elastic and visco-elastic predictions rapidly diverge from each other. This is also consistent with the fact that for this long time, i.e smallest frequency, the corrective velocity $\tilde{c}_p^v$ is dissipative and strongly depends on frequency (as latter-on reported in figure 4a). As expected, the visco-elastic FSI response much more strongly attenuates high-frequency oscillations than the elastic one. More precisely, the signal's high frequencies arising from FSI-couplings quickly attenuate from the influence of visco-elastic kernel convolution and are barely discernible after the wave's first back and forth. The spectrum analysis provided in Figure 2b reveals how much the visco-elastic response smoothens high-frequencies so that only the first three harmonics appear relevant. A small shift of the visco-elastic resonant frequency compared to the elastic ones provided by the red dotted lines of figure 2b is also found as previously noted in [47]. However, in the early stage of the signal the proposed theoretical model fails to accurately reproduce the observed pressure variations by $\approx 18\%$, so that the Joukowsky [36] over-pressure is not exactly recovered from visco-elastic FSI effects at this position $Z = 1$. Nevertheless, the overall damping trend and phase seem correctly represented. The comparison of the proposed visco-elastic rheology-based model with previous Kelvin-Voigt models is now discussed.

4.5. Comparison with previous theoretical models.

In Fourier-domain, the dimensionless form of models proposed by Covas et al. [13], on the left, and Keramat et al. [27], on the right, reads

$$i\omega\tilde{W} = -\partial_Z\tilde{P}, \qquad i\omega\tilde{W} = -\partial_Z\tilde{P}, \tag{87}$$

$$i\omega\tilde{P} + \partial_Z\tilde{W} = -\frac{2\mathcal{D}}{\alpha\mathcal{C}_s^{e2}}i\omega\tilde{\mathcal{I}}_{Cov}\tilde{P}, \qquad i\omega\tilde{P} + \partial_Z\tilde{W} - 2i\omega\alpha\nu_e\partial_Z\tilde{\zeta} = -\frac{2\mathcal{D}\left(1-\nu_e^2\right)}{\alpha\mathcal{C}_s^{e2}}i\omega\tilde{\mathcal{I}}_{Ker}\tilde{P}, \tag{88}$$

$$i\omega\tilde{\sigma}_{zz} - i\omega\frac{\nu_e}{\alpha}\tilde{P} - i\omega\frac{\alpha\mathcal{C}_s^{e2}}{\mathcal{D}}\partial_Z\tilde{\zeta} = -i\omega\tilde{\mathcal{I}}_{ker}\tilde{\sigma}_{zz} + \frac{\nu_e}{\alpha}i\omega\tilde{\mathcal{I}}_{Ker}\tilde{P}, \tag{89}$$

$$\frac{\alpha}{\mathcal{D}}\omega^2\tilde{\zeta} + \partial_Z\tilde{\sigma}_{zz} = 0, \tag{90}$$

where $\tilde{\mathcal{I}}_{Cov}$ –resp. $\tilde{\mathcal{I}}_{Ker}$– is the Fourier transform of kernels proposed in Covas et al. [13] (resp. Keramat et al. [27]). The Covas et al. [13]'s model stands as a limit when ν_e tends to zeros of the Keramat et al. [27]'s one as the Poisson coupling vanishes, resulting in decoupling fluid axial dynamic to the solid's one. The dimensionless derivation of the Keramat et al. [27]'s model is provided in Appendix C. Both authors consider N_{kv} Kelvin-Voigt elements to build their convolution kernel interpreted as a creeping law, each having its own exponential times-decay τ_k, amplitudes J_k, to model their convolution kernels, [29]

$$\left(\tilde{\mathcal{I}}_{Cov}, \tilde{\mathcal{I}}_{Ker}\right) = \sum_{k=1}^{N_{kv}} \frac{E_e J_k}{1 + i\omega\frac{c_p^e\tau_k}{L}}. \tag{91}$$

The values of (τ_k, J_k) for both models are provided in Table 3 for the experimental set-up of [13]. It is very interesting to note that Covas et al. [13]'s and Keramat et al. [27]'s models both display a very similar form compared to (39)-(41). Qualitatively, the visco-elastic material response can indeed be recasted into similar convolution products with pressure and axial stress. In order to make this comparison more precise it is interesting to consider the very same hypothesis that the generalized Young modulus ν_s^* equals the elastic one ν_e, i.e. $\tilde{\nu}_s = 1$, and the dimensionless tube's thickness is small, i.e. $\alpha \ll 1$, in which case the visco-elastic kernels (42)-(45) in frequency-domain simplify to

$$\tilde{\mathcal{I}}_P^F = \tilde{\mathcal{I}}_P^S = \tilde{\mathcal{I}}_\sigma^S = \tilde{J}_s(\omega) - 1 \quad \text{, and } \tilde{\mathcal{I}}_\sigma^F = 0. \tag{92}$$

k	τ_k(s)	$J_k(10^{-10}$Pa)
1	0.05	1.060
2	0.5	0.933
3	1.5	1.120

(a) Model [13]

k	$\tau_k(s)$	$J_k(10^{-10}Pa)$
1	0.05	1.057
2	0.5	1.054
3	1.5	0.9051
4	5	0.2617
5	10	0.7456

(b) Model [27]

Table 3: Covas et al.[13] and Keramat et al. [27]'s convolution kernels parameters for the experimental data of Covas et al. [18, 13].

This simplified framework indeed provides a simple condition for the equivalence of formulation according, to (46) and (91)

$$\tilde{J}_s(\omega) \equiv 1 + \sum_{k=1}^{N_{kv}} \frac{E_e J_k}{1 + i\omega \frac{c_p^e \tau_k}{L}}. \tag{93}$$

Hence, within $\tilde{\nu}_s = 1$ ($\tilde{\nu}_s^* = \nu_e$) and $\alpha \to 0$ hypothesis, it is nice to observe that the l.h.s of (38)

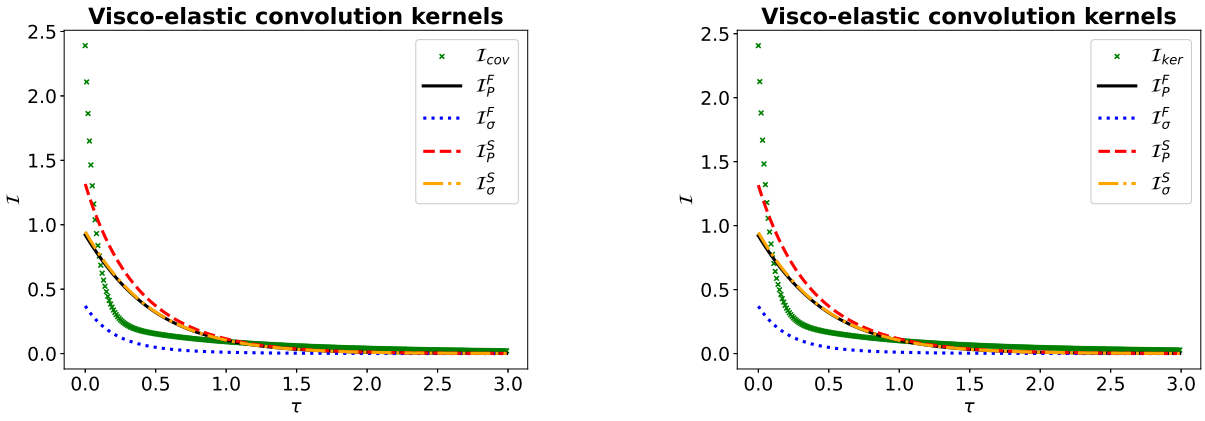

(a) (b)

Figure 3: Comparison to (a) Covas et al. [13]'s and (b) Keramat et al. [27]'s visco-elastic convolution kernels for the experimental data of Covas et al. [18, 13]. Dimensionless time τ (using (4)) has been used.

display a convolution product with the pressure only, as so does (43) when $\mathcal{I}_\sigma^F = 0$ as provided by (92). Furthermore, the kernel associated with $\tilde{\mathcal{I}}_P^F$, $\tilde{\mathcal{I}}_P^S$ and $\tilde{\mathcal{I}}_\sigma^S$ is the same, so that both r.h.s terms of (40) share the same kernel respectively applied to the pressure and the axial stress. The very same feature is satisfied by the r.h.s of (89). Hence, the visco-elastic rheological based model (39)-(41) is similar with Keramat et al. (2011) (87)-(90) when using the $\tilde{\nu}_s = 1$ and $\alpha \to 0$ hypothesis. In other words, in the limit of thin-wall and without visco-elastic contribution to the

Poisson coupling, the proposed rheological model produces convolution kernels directly provided by the creep function, as previously done in [13, 27]. The various visco-elastic convolution kernels are compared in Figure 3 for the experimental data of [13] presented in Table 2. Each kernel family has been fitted with the same pressure field time variation coming from [18, 13]. Even though they present similar exponential decay family types, $\tilde{\mathcal{I}}_{Cov}$ and $\tilde{\mathcal{I}}_{Ker}$ display faster attenuation that the various kernels $\mathcal{I}_P^F, \mathcal{I}_\sigma^F, \mathcal{I}_P^S, \mathcal{I}_\sigma^S$ of the proposed model. Also, both $\mathcal{I}_P^F$ and $\mathcal{I}_\sigma^S$ are very similar for the obtained visco-elastic parameters.

Concerning the velocity dispersivity prediction provided in figure 4, it is interesting to mention that every models display a similar trend for the norm of complex velocities: it varies from a minimum value at $\omega = 0$ within a narrow low-frequency region (associated with a long time behaviour) so as to reach a constant plateau for large $|\omega|$ values. Hence, at short-time/large $|\omega|$ most dispersivity of the wave velocity is lost and the visco-elastic response is very much like the elastic one, [48, 49]. This allows to define a 'dispersive' frequency gap band depicted within vertical orange dotted lines for which visco-elastic effects are important. The 'dispersive' frequency gap band $\Delta\omega_v$ is more precisely define as the 95% difference velocity region from the asymptotic high-frequency regime, as exemplified in the inset of figure 4a. The larger this dispersive gap-band, and the deeper the $\omega = 0$ velocity, the larger visco-elastic effects are. It is interesting to observe in figure 4 that the dispersive gap is wider for Covas et al. [13] and Keramat et al. [27] models than for the hereby model (in black) for parameters obtained from the same data set [18, 13]. Considering specifically the corrective visco-elastic velocity $\tilde{c}_p^v(\omega)$ predictions analysed in figure 4a it can be observed that for the Covas [13] and Keramat [27] models the corrective visco-elastic velocity $\tilde{c}_p^v(\omega)$ tends to one in the $|\omega| \gg 1$ limit. Noteworthy, this is not the case for our model for which the high-frequency limit of $\tilde{c}_p^v(\omega)$ is approximately 6.5% above one as can be observed in figure 4a. Combining this limit with the $\tilde{c}_- \to 1$ as $|\omega| \gg 1$ found in figure 4c produces a slight over-visco-elastic-velocity of about 6.5% larger than the elastic one. These additional contributions to the elastic velocity from visco-elastic effects result from local terms in the visco-elastic kernels (as previously mentioned at the end of S.4.1.1). The vertical dotted line, depicted in the zoom inset of Figure 4a, reports the time-scale range for which the complex corrective velocity factor $\tilde{c}_p^v$ evaluated with the same visco-elastic parameter display a non-dissipative behaviour, i.e very weakly depends on frequency. This result is interesting per-see since it affects the predicted Joukowsky over-pressure which should be higher in visco-elastic materials

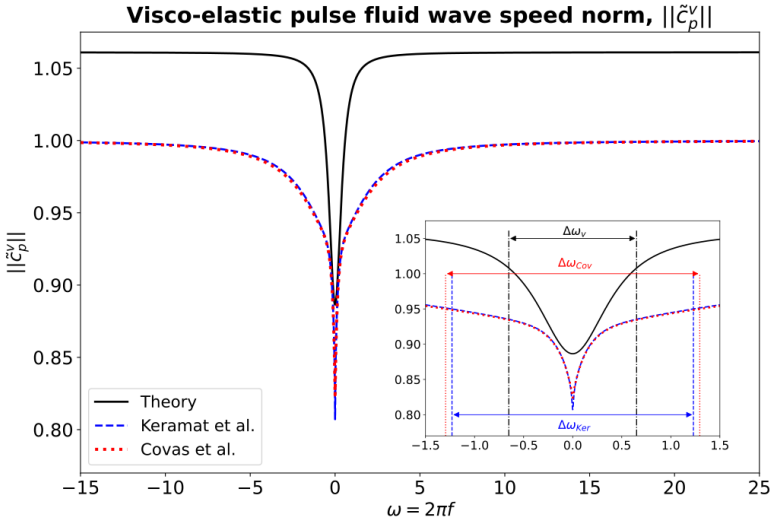

(a)

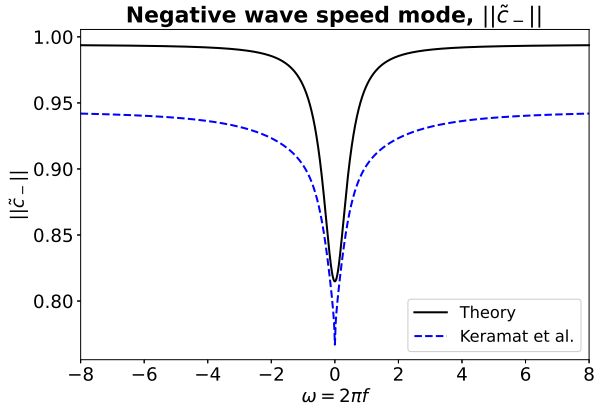

(b)

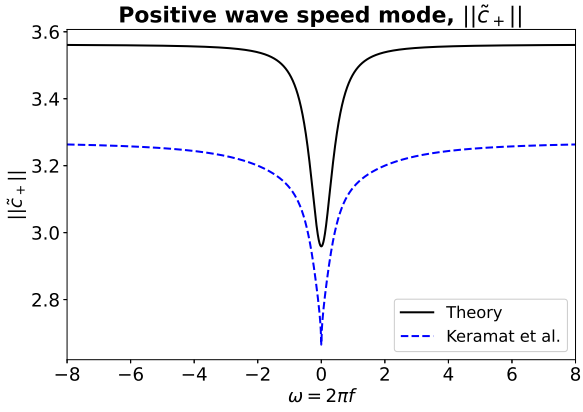

(c)

Figure 4: Comparison of frequency domain dependence of dimensionless visco-elastic velocities obtained from fitting parameters to the experimental data of [18, 13]. (a) $\tilde{c}_p^v(\omega)$ (49), (b) $\tilde{c}_+$ (53), (c) $\tilde{c}_-$ (53). Dimensionless pulsation ω using (6) have been used.

when taking into account their elastic properties only. This 6.5% over-velocity of our prediction compared to Covas et al. [13] and Keramat et al. [27] models is also observable for $\tilde{c}_+$ in figure 4c. Previous studies, e.g. [18, 41, 50], had indeed pointed-out some difficulties in correctly estimating the effective wave speed in visco-elastic materials, consequently, leading to bad predictions for the first pressure overshoot according to Joukowsky's theory. The visco-elastic wave-speed correction (approximately evaluated between $10\% - 25\%$ in [18, 41, 50]) is of practical consequence. It should be taken into account in the modelling from using rheology-based visco-elastic dispersive velocities such as (49) and (53). This can be implemented using the transfer matrix method [51] recently extended to visco-elastic materials [52]. Such theoretical method which is very useful for leakage

detection in pipes [53, 54, 55], could suffer from an approximated wave speed modelling that our contribution might improve. For now, we did only compared subsequent quantities not easy to

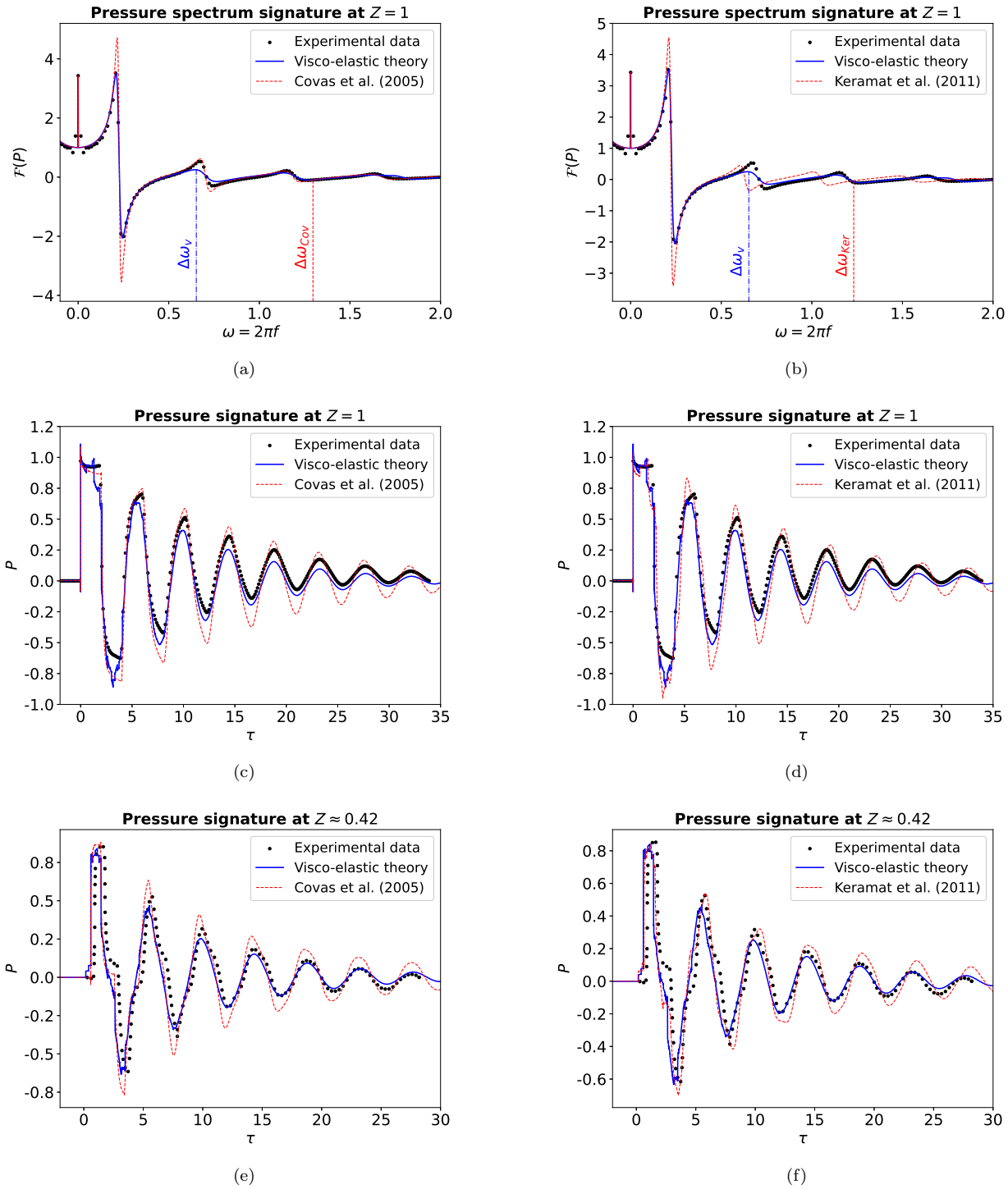

Figure 5: Comparison between the proposed rheology-based model and [13] and [27] ones for the pressure signal at various location for the reservoir-pipe-anchored valve configuration. Dimensionless pulsation ω using (6) have been used in (a) and (b), dimensionless time using (4) in (c), (d), (e) and (f).

measure experimentally i.e. visco-elastic kernels and the dispersive velocities. It is nevertheless interesting to compare predictions for the pressure signature to [13] and [27] ones. This comparison is illustrate in Figure 5 for the pressure signal at the valve. Whilst Covas's model slightly overshoot its prediction for the first pressure mode, it succeeds in nicely capturing the second and third one as illustrated in figure 5a. In time-domain, this first frequency overshoot manifests itself from a systematic over-pressure prediction at long times as illustrated in figures 5c and 5e although more markedly noted in the case associated with dimensionless distance $Z = 0.42$. For these long-time behavior the proposed visco-elastic model in blue provides a better fit to the pressure dynamics. Nevertheless, at small time, the opposite can be observed in figure 5c for capturing the first peak. A similar behavior is observed with Keramat's model in 5b with an overshoot prediction for the first Fourier's peak, but for a less accurate fitting for the further second and third peaks. In time-domain, this again explains why Keramat's model over-predicts the pressure at long-time. It is interesting to observe that, at short time, both Keramat's model and the proposed visco-elastic one nicely match together, especially for providing high-frequency peaks which are absent in Covas's model prediction in figure 5a. These high-frequency peaks result from the FSI interaction from bouncing elastic waves in the solid obviously not considered in Covas's model. They are not observed in the experiments from high-frequency filtering of the measurement's sensors. Also of interest in figure 5a and 5b are the reported dispersive frequency band $\Delta\omega$ evaluated in figure 4a indicating which frequency range is associated with the elastic response (on the left) and the visco-elastic one (on the right). Overall our proposed visco-elastic model provides a convincing comparison to the pressure signal measured at various positions, comparable with other previous models.

4.6. Sensitivity analysis

This section considers the sensitivity analysis of visco-elastic kernels to parameters in the four-dimensional parameter-space of $(a, \tau_r, \tau_\lambda, \tau_\mu)$ –in general the elastic parameters (λ_e, μ_e) are supposed known material properties–. More precisely, any method (e.g. steepest-descent, Newton method, etc..) for minimizing the distance/the error between measurements and model's predictions needs the evaluation of visco-elastic kernel gradients in the parameter space. It is interesting to mention that the analytical relations between kernels $\tilde{\mathcal{I}}_P^F, \tilde{\mathcal{I}}_\sigma^F, \tilde{\mathcal{I}}_P^S, \tilde{\mathcal{I}}_\sigma^S$ and parameters $(a, \tau_r, \tau_\lambda, \tau_\mu)$ has been obtained in 64-67, permitting the explicit analytical evaluation of the kernel's Jacobian in parameter space if needed.

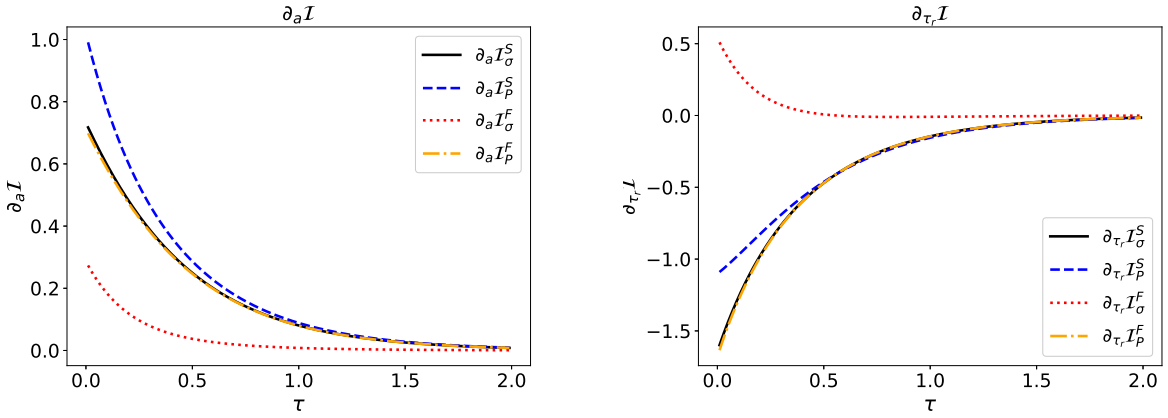

(a) (b)

Figure 6: Dispersive behaviour of the visco-elastic corrective pulse wave speed, $\tilde{c}_p^v$ versus dimensionless time (using (4)).

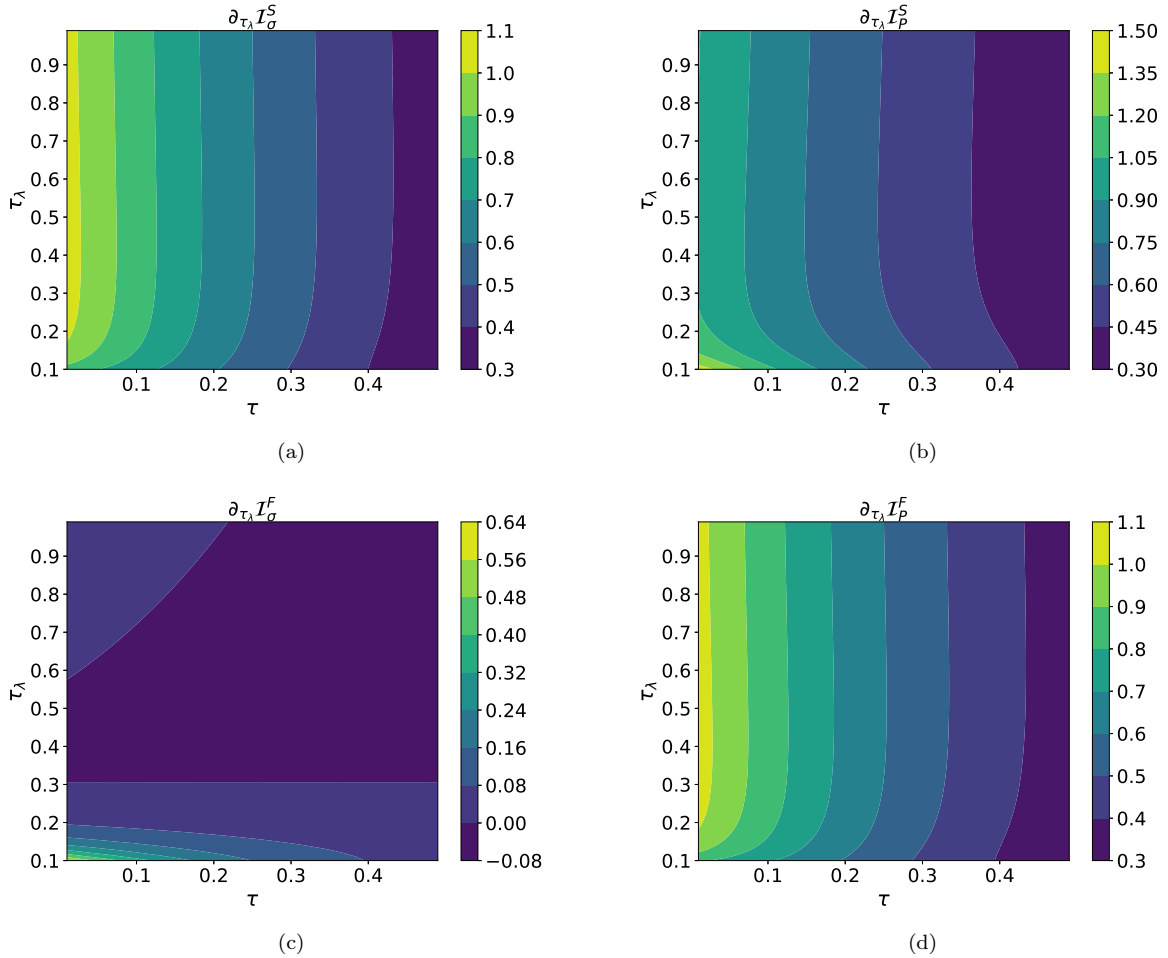

(a) (b)

(c) (d)

Figure 7: Visco-elastic kernels derivatives with respect to parameter τ_λ versus dimensionless time (using (4)).

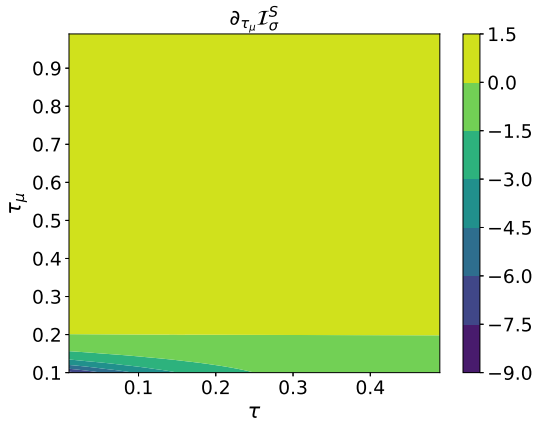

(a)

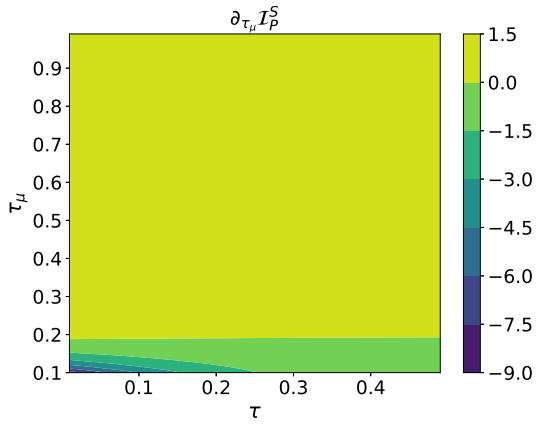

(b)

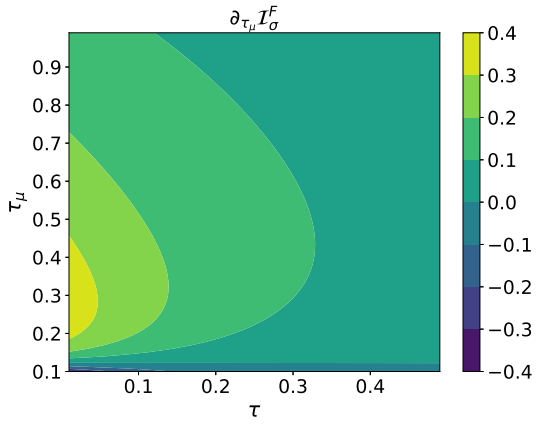

(c)

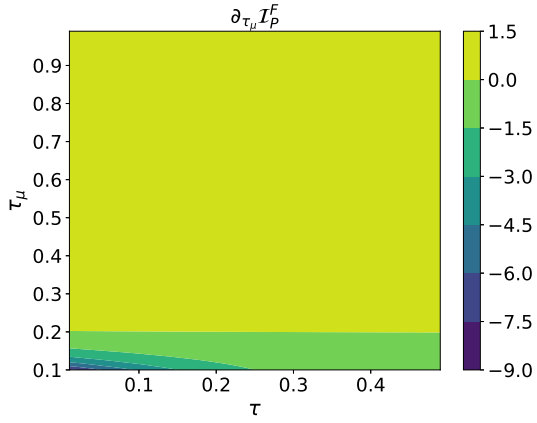

(d) Visco-elastic kernels derivatives with respect to τ_μ versus dimensionless time (using (4)).

Figure 8: Visco-elastic kernels derivatives with respect to τ_μ versus dimensionless time (using (4)).

In order to simplify the picture, it is first interesting to realize from the definition of the visco-elastic kernels $\tilde{\mathcal{I}}^F_P, \tilde{\mathcal{I}}^F_\sigma, \tilde{\mathcal{I}}^S_P, \tilde{\mathcal{I}}^S_\sigma$ in 64-67 that these kernels are all linear functions of parameter a and τ_r. Thus the derivative of visco-elastic kernels in the $a - \tau_r$ space does not depend on these parameters and decays in time as illustrated in figures 6a and 6b. Considering the other parameters (τ_λ, τ_μ) being chosen at their optimal value, it is interesting to observe that the kernel derivatives in the $a - \tau_r$ sub-space is very moderate. In other words, visco-elastic kernels are poorly sensitive to a and τ_r parameters. Similarly the derivative of the kernels with respect to τ_λ are also moderate, with a significant decay in time, as illustrated in figure 7a -7d. On the contrary, the derivative of the kernels with respect to τ_μ reach much higher values as shown in figures 8a-8d where, at short time, the kernels derivatives are an order of magnitude more sensitive to τ_μ that all other parameters. Hence, from the four dimensional parameters, the most sensitive one to visco-elastic kernels is τ_μ,

meaning that its precise evaluation is of clear significance in the parametric estimation. This result is consistent with the fact that the visco-elastic kernels exponential decay are directly related to τ_μ in (64)-(67).

5. Conclusion

A rheology-based model for water-hammer wave propagation in a visco-elastic pipe has been proposed. Using a long wavelength analysis and a generalized frequency-dependent Hooke-law for the stress/strain relation the pressure/longitudinal stress coupled wave system has been derived. In this general framework, a visco-elastic FSI four equations model having four visco-elastic kernels and the corresponding pressure/longitudinal stress wave equation system have been established. This has first permitted us to find the generalized visco-elastic dispersive propagating velocity as explicit functions of the visco-elastic kernels. For a general linear visco-elastic rheology, the four visco-elastic kernels, and the corresponding creep function have been derived explicitly. They can be used to find visco-elastic rheology parameters in any specific pipe/boundary conditions configuration (e.g. from numerically solving the corresponding FSI-four equation problem, i.e. using a time-domain version of (39)-(41), with kernels (68)-(71) and creep function (63)). Furthermore, for specific boundary conditions, an explicit analytical solution in Fourier domain for the pressure/stress wave has been derived and used so as to estimate the visco-elastic parameters from experimental water-hammer time-domain pressure measurements from numerical inverse Fourier transform.

The model's predictions have then been successfully compared to the experimental measurements as well as with other models adjusted to the same experimental data set. Also, the model's parameter sensitivity has been quantified by computing the four visco-elastic kernels derivative with parameters, showing a stronger influence of the viscous relaxation time τ_μ over all other parameters. This contribution has shown that the proposed rheology-based visco-elastic model provides a convincing description of the water-hammer wave propagation in the visco-elastic pipe. It can be used in many other contexts with the specific ability to distinguish the intrinsic visco-elastic rheology from the considered pipe geometry and boundary conditions.

Let us finally discuss the practical relevance and usefulness of this contribution. Even if the proposed model needs parameter calibration exactly as previous other visco-elastic Kelvin-Voigt models, it nevertheless presents two distinct features. First, as opposed to other models which need

the numerical computation of the water-hammer wave system problem, our Fourier-domain analytical solution permits getting the time-domain pressure solution from a simple Fourier transform only. This is more simple and more useful than being able to accurately compute the wave equations (a hyperbolic problem necessitates devoted numerical schemes and methods). Furthermore, the minimisation between observation and model for parameter calibration could also be performed in frequency-domain, from a simple Fourier transform of the pressure observations themselves as done in this paper in Figures 5a and 5b. In this case, the parameter calibration could directly benefit from our analytical solution as well as from the analytical sensitivity matrix computation, the derivative of which is needed in the calibration numerical procedure. This is a simplified procedure over the state of the art. Secondly, because our parameters are rheology-based, they can be estimated before-end from applied mechanical stress-strain response tests. These mechanical stress-strain tests might be of various kinds (e.g. oscillatory, shear, compression, mixed, etc..) so as to increase the parameter estimation step robustness. In this case, the presented model could provide water-hammer time-domain pressure prediction without the need for parameter calibration on water-hammer tests. A distinct path which is beyond the scope of the present paper but might motivate future investigations.

Acknowledgement

This work was supported by the collaborative ANRT Grant CIFRE 2019/1453 co-funded by SETOM, a dedicated society of Veolia for the public drinking water service of Toulouse Métropole operating under the brand Eau de Toulouse Métropole. The authors thank Pr. D. Covas from Lisbon University for sharing her data on visco-elastic damped waves.
The authors have no competing interests to declare.

References

[1] A. S. Tijsseling, Fluid-Structure Interaction in liquid-filled pipe systems: a review, J. Fluids Struct. 10 (2) (1996) 109–146.

[2] P. Flaud, D. Geiger, C. Oddou, D. Quemada, Ecoulements pulsés dans les tuyaux visco-élastiques. application à l'étude de la circulation sanguine., J. de Physique 35 (1974) 869–882.

[3] S. Čanić, J. Tambača, G. Guidoboni, A. Mikelić, C. J. Hartley, D. Rosenstrauch, Modeling Viscoelastic Behavior of Arterial Walls and Their Interaction with Pulsatile Blood Flow, SIAM J. Appl. Math. 67 (1) (2006) 164–193, publisher: Society for Industrial and Applied Mathematics.

[4] D. Bessems, C. Giannopapa, M. Rutten, F. Van De Vosse, Experimental validation of a time-domain-based wave propagation model of blood flow in viscoelastic vessels, J. Biomech. 41 (2) (2008) 284–291.

[5] N. Duraiswamy, R. T. Schoephoerster, M. R. Moreno, J. E. Moore, Jr., Stented artery flow patterns and their effects on the artery wall, Annu. Rev. Fluid Mech. 39 (2007) 357–382.

[6] F. N. Van De Vosse, N. Stergiopulos, Pulse wave propagation in the arterial tree, Annu. Rev. Fluid Mech. 43 (2011) 467–499.

[7] E. Rieutord, A. Blanchard, Influence d'un comportement viscoélastique de la conduite dans le phénomène du coup de bélier, C. R. Acad. Sci. 274 (1972) 1963–1966.

[8] M. Gally, M. Güney, E. Rieutord, An investigation of pressure transients in viscoelastic pipes, J. Fluids Eng. 101 (4) (1979) 495–499.

[9] E. Rieutord, A. Blanchard, Pulsating viscoelastic pipe flow - water-hammer, J. Hydraul. Res. 17 (3) (1979) 217–229.

[10] G. Kuiken, Wave propagation in a thin-walled liquid-filled initially-stressed tube, J. Fluid Mech. 141 (1984) 289–308.

[11] R. P. Sawatzky, M. B., On the propagation of pressure pulses through a viscous fluid contained in a visco-elastic tube, Q. J. Mech. Apppl. Math. 41 (1) (1988) 33–50.

[12] L. Suo, E. B. Wylie, Complex Wavespeed and Hydraulic Transients in Viscoelastic Pipes, J. Fluid Eng. 112 (4) (1990) 496–500.

[13] D. Covas, I. Stoianov, J. F. Mano, H. Ramos, N. Graham, C. Maksimovic, The dynamic effect of pipe-wall viscoelasticity in hydraulic transients. Part II model development, calibration and verification, J. Hydraul. Res. 43 (1) (2005) 56–70.

[14] H. Ramos, D. Covas, A. Borga, D. Loureiro, Surge damping analysis in pipe systems: modelling and experiments, J. Hydraul. Res. 42 (4) (2004) 413–425.

[15] N. Kizilova, Pressure Wave Propagation in Liquid-Filled Tubes of Viscoelastic Material, Fluid Dyn. 41 (2006) 434–446.

[16] C. C. Mei, H. Jing, Pressure and wall shear stress in blood hammer – Analytical theory, Math. Biosci. 280 (2016) 62–70.

[17] T. Khudayarov, Mathematical simulation of nonlinear oscillations of viscoelastic pipelines conveying fluid, Appl. Math 66 (2019) 662–679.

[18] D. Covas, I. Stoianov, H. Ramos, N. Graham, C. Maksimovic, The dynamic effect of pipe-wall viscoelasticity in hydraulic transients. Part I Experimental analysis and creep characterization, J. Hydraul. Res. 42 (2004) 517–532.

[19] K. Weinerowska-Bords, Viscoelastic model of waterhammer in single pipeline problems and questions, Arch. Hydroengineering Environ. Mech. 53 (4) (2006) 331–351.

[20] A. K. Soares, D. Covas, L. F. Reis, Analysis of PVC Pipe-Wall Viscoelasticity during Water Hammer, J. Hydraul. Eng. 134 (9) (Sep. 2008).

[21] S. Meniconi, B. Brunone, M. Ferrante, Water-hammer pressure waves interaction at cross-section changes in series in viscoelastic pipes, J. Fluids Struct. 33 (2012) 44–58.

[22] K. Urbanowicz, M. Firkowski, Z. Zarzycki, Modelling water hammer in viscoelastic pipelines: short brief, J. Phys. Conf. Ser. 760 (2016) 012037.

[23] K. Urbanowicz, D. Huan-Feng, A. Bergant, Transient flow of liquid in plastic pipes, J. Mech. Eng. Res. 66 (2) (2020) 77–90.

[24] Z. Duan, T. Li, Comprehensive application analyses of elastic models and viscoelastic models in transient flows in polymeric pipelines, J. Hydroinformatics 24 (5) (2022) 1020–1052.

[25] K. Weinerowska-Bords, Alternative approach to convolution term of viscoelasticity in equations of unsteady pipe flow, J. Fluids Eng. 137 (5) (2015) 054501.

[26] S. Li, B. W. Karney, G. Liu, FSI research in pipeline systems – A review of the literature, J. Fluids Struct. 57 (2015) 277–297.

[27] A. Keramat, A. Tijsseling, Q. Hou, A. Ahmadi, Fluid–structure interaction with pipe-wall viscoelasticity during water hammer, J. Fluids Struct. 28 (2011) 434–455.

[28] R. S. Hosseini, A. Ahmadi, R. Zanganeh, Fluid-structure interaction during water hammer in a pipeline with different performance mechanisms of viscoelastic supports, J. Sound Vib. 487 (2020) 115527.

[29] M. T. Shaw, W. J. MacKnight, Introduction to polymer viscoelasticity, 4^{th} edition, John Wiley & Sons, 2018.

[30] A. Monteiro, A. Freitas Rachid, Tijsseling, Fluid transients in viscoelastic pipes via an internal variable constitutive theory, Appl. Math 114 (2023) 846–869.

[31] D. Covas, I. Stoianov, H. Ramos, N. G., C. Maksimović, D. Butler, Water hammer in pressurized polyethylene pipes: conceptual model and experimental analysis, Urban Water J. 1 (2) (2004) 177–197.

[32] G. Pezinga, B. Brunone, M. S., Relevance of Pipe Period on Kelvin-Voigt Viscoelastic Parameters : 1d and 2d Inverse Transient Analysis, J. Hydraul. Eng. 142 (12) (2016) 04016063.

[33] A. Tijsseling, Water hammer with fluid-structure interaction in thick-walled pipes, Comput. Struct. 85 (2007) 844–851.

[34] A. Bayle, F. Plouraboué, Spectral properties of Fluid Structure Interaction pressure/stress waves in liquid filled pipes, Wave motion 116 (2023) 103081.

[35] J. Massey, B. S.; Ward-Smith, Mechanics of Fluids, 7th ed. Cheltenham: Nelson Thornes, 1998.

[36] N. Joukowski, Memoirs of the imperial academy society of St.-Petersburg, J Am Water Works Assoc. 24 (1898) 341–424.

[37] R. Skalak, An extension of the theory of waterhammer, J. Fluids Eng. Trans. ASME 78 (1956) 105–116.

[38] T. Lin, G. W. Morgan, Wave propagation through fluid contained in a cylindrical, elastic shell, J. Acoust. Soc. Am. 28 (1956) 1165–1176.

[39] J. S. Walker, J. W. Phillips, Pulse Propagation in Fluid-Filled Tubes, J. Appl. Mech. 44 (1) (1977) 31–35.

[40] A. E. H. Love, A treatise on the mathematical theory of elasticity., Dover, 1944.

[41] M. Mitosek, M. Chorzelski, Influence of visco-elasticity on pressure wave velocity in polyethylene MDPE pipe, Arch. Hydroengineering Environ. Mech. Vol. 50 (2) (2003) 127–140.

[42] J. M. Carcione, F. Poletto, D. Gei, 3-D wave simulation in anelastic media using the Kelvin–Voigt constitutive equation, J. Comput. Phys. 196 (1) (2004) 282–297.

[43] A. Eringen, Mechanics of Continua, R. E. Krieger Publishing Company, 1980.

[44] D. Bland, The Theory of Linear Viscoelasticity, Dover Books on Physics, Dover Publications, 2016.

[45] D. Annie, On a Theory of Thermoviscoelastic Materials with Voids, J. Elast. 104 (2011) 369–384.

[46] J. Sharma, M. I. Othman, Effect of rotation on generalized thermo-viscoelastic Rayleigh–Lamb waves, Int. J. Solids Struct. 44 (13) (2007) 4243–4255.

[47] J. Gong, A. C. Zecchin, M. F. Lambert, A. R. Simpson, Determination of the Creep Function of Viscoelastic Pipelines Using System Resonant Frequencies with Hydraulic Transient Analysis, J. Hydraul. Eng. 142 (9) (2016) 04016023.

[48] F. Barez, W. Goldsmith, J. L. Sackman, Longitudinal waves in liquid-filled tubes—I: Theory, Int. J. Mech. Sci. 21 (4) (1979) 213–221.

[49] M. Prek, Analysis of wave propagation in fluid-filled viscoelastic pipes, Mech Syst Signal Process 21 (2007) 1907–1916.

[50] K. Weinerowska-Bords, Viscoelastic Model of Waterhammer in Single Pipeline–Problems and Questions, Arch. Hydroengineering Environ. Mech. 53 (2006) 331–351.

[51] L. Zhang, A. Tijsseling, E. Vardy, FSI Analysis of Liquid-Filled Pipes, J. Sound Vib. 224 (1999) 69–99.

[52] H. K. Aliabadi, A. Ahmadi, A. Keramat, Frequency response of water hammer with fluid-structure interaction in a viscoelastic pipe, Mech Syst Signal Process 144 (2020) 106848.

[53] A. Keramat, H.-F. Duan, Spectral based pipeline leak detection using a single spatial measurement, Mech Syst Signal Process 161 (2021) 107940.

[54] A. Keramat, B. Karney, M. S. Ghidaoui, X. Wang, Transient-based leak detection in the frequency domain considering fluid-structure interaction and viscoelasticity, Mech Syst Signal Process 153 (2021) 107500.

[55] X. Wang, G. A. Camino, T.-C. Che, M. S. Ghidaoui, Factorized wave propagation model in tree-type pipe networks and its application to leak localization, Mech Syst Signal Process 147 (2021) 107116.

[56] F. Khan, C. Yeakle, Experimental investigation and modeling of non-monotonic creep behavior in polymers, Int. J. Plast. 27 (4) (2011) 512–521.

[57] E. Kontou, S. Katsourinis, Application of a fractional model for simulation of the viscoelastic functions of polymers, J. Appl. Polym. Sci. 133 (23) (2016).

[58] S. Neidigk, C. Salas, E. Soliman, D. Mercer, M. Reda Taha, Creep and relaxation of osteoporotic bones, in: Society for Experimental Mechanics - SEM Annual Conference and Exposition on Experimental and Applied Mechanics 2009, Vol. 4, 2009, pp. 1–4.

Appendix A. Visco-elastic parameters estimation from creep and stress relaxation methods

In this appendix, the rheological parameters identification within a 3D linear rheological model is discussed. Most common rheological models are based upon a mechanical approach, where

springs and dashpot are associated in order to establish differential equations describing media's deformation. The Kelvin-Voigt, Maxwell, and Zener models are built within this approach and represent 1D models involving parameters either directly fitted to pressure signals [31, 27] or to mechanical measurements [56, 57]. A wide variety of techniques (e.g. creep and stress relaxation, free oscillation methods, resonance methods, and wave propagation methods) based on different solicitation frequencies can be used to quantify visco-elastic models and estimate their parameters. Here, the details of the rheological parameters determination of 3D models 59 based on the creep and stress relaxation methods are presented. In index form model 59 reads

$$a(1+\tau_r\partial_t)\sigma^*_{ij} = \lambda_e(1+\tau_\lambda\partial_t)\epsilon^*_{ll}\delta_{ij} + 2\mu_e(1+\tau_\mu\partial_t)\epsilon^*_{ij}, \tag{A.1}$$

δ_{ij} being the Kronecker's symbol. In rheological studies, one applies stress (either constant or oscillating) to the visco-elastic media and measures the associated strain. Hence, the strain field components ϵ^*_{ij}, have to be written versus the stress fields ones σ^*_{ij}, thus inverting (A.1). Let us first focus on the non-diagonal part of (A.1). The strain non-diagonal components achieve as follows

$$\epsilon^*_{ij}(t) = \frac{1}{2\mu_e}\,\frac{a}{\tau_\mu}\int_0^t (1+\tau_r\partial_T)\sigma^*_{ij}(T)\; e^{\frac{T-t}{\tau_\mu}}\; dT + \epsilon^*_{ij}(0)\; e^{-t/\tau_\mu}, \tag{A.2}$$

whilst performing an integration by parts of (A.2)'s r.h.s, yields

$$\epsilon^*_{ij}(t) = \underbrace{\frac{a}{2\mu_e}\left(1-\frac{\tau_r}{\tau_\mu}\right)\frac{1}{\tau_\mu}\int_0^t \sigma^*_{ij}(T)e^{\frac{T-t}{\tau_\mu}}\; dT}_{\text{Visco-elastic component}} + \underbrace{\frac{\tau_r}{\tau_\mu}\frac{a}{2\mu_e}\sigma^*_{ij}(t)}_{\text{Elastic component}} + \underbrace{\left(\epsilon^*_{ij}(0) - \frac{\tau_r}{\tau_\mu}\frac{a}{2\mu_e}\sigma_{ij}(0)\right)}_{\text{Initial conditions}}\; e^{-t/\tau_\mu}. \tag{A.3}$$

The ϵ^*_{ij} strain field components are therefore composed of three terms. A visco-elastic component whose dynamics is only driven by the characteristic shear-time τ_μ, an elastic component whose response is instantaneous and an exponentially decaying initial conditions contribution. The inversion of (A.1)'s diagonal terms is now considered. Introducing the stress $\boldsymbol{\sigma}^*_d$ and strain $\boldsymbol{\epsilon}^*_d$ vector field

$$\boldsymbol{\sigma}^*_d = \left(\sigma^*_{xx}(t), \sigma^*_{yy}(t), \sigma^*_{zz}(t)\right)^T \quad \text{, and} \quad \boldsymbol{\epsilon}^*_d = \left(\epsilon^*_{xx}(t), \epsilon^*_{yy}(t), \epsilon^*_{zz}(t)\right)^T. \tag{A.4}$$

From considering the applied stress configurations of figure A.9b, it yields

$$\lambda_e\;\left[\tau_\lambda\partial_t + \mathbf{A^{-1}B}\right]\boldsymbol{\epsilon}^*_d = a\mathbf{A}^{-1}\left(1+\tau_r\partial_t\right)\boldsymbol{\sigma}^*_d, \tag{A.5}$$

with $\mathbf{A}$ and $\mathbf{B}$ defined by

$$\mathbf{A} = \begin{pmatrix} 1+\frac{\mu_e}{\lambda_e}\frac{\tau_\mu}{\tau_\lambda} & 1 & 1 \\ 1 & 1+\frac{\mu_e}{\lambda_e}\frac{\tau_\mu}{\tau_\lambda} & 1 \\ 1 & 1 & 1+\frac{\mu_e}{\lambda_e}\frac{\tau_\mu}{\tau_\lambda} \end{pmatrix} \text{ , and, } \mathbf{B} = \begin{pmatrix} 1+2\frac{\mu_e}{\lambda_e} & 1 & 1 \\ 1 & 1+2\frac{\mu_e}{\lambda_e} & 1 \\ 1 & 1 & 1+2\frac{\mu_e}{\lambda_e} \end{pmatrix}. \tag{A.6}$$

To obtain the strain evolution, $\mathbf{A^{-1}B}$ is diagonalized. In the eigenvector basis, it follows

$$(\partial_t + \mathbf{\Omega})\,\hat{\boldsymbol{\epsilon}}_d^* = \frac{a(1+\nu_e)}{E_e}\ \ \mathbf{F}\ \ (1+\tau_r\partial_t)\,\hat{\boldsymbol{\sigma}}_d^*, \tag{A.7}$$

with $\mathbf{\Omega}$ and $\mathbf{F}$ defined by

$$\mathbf{\Omega} = \begin{pmatrix} 1/\tau_\mu & 0 & 0 \\ 0 & 1/\tau_\mu & 0 \\ 0 & 0 & 1/\tau_E \end{pmatrix} \text{ , and, } \mathbf{F} = \begin{pmatrix} 1/\tau_\mu & 0 & 0 \\ 0 & 1/\tau_\mu & 0 \\ 0 & 0 & \frac{1}{\tau_E}\ \frac{1-2\nu_e}{1+\nu_e} \end{pmatrix}, \tag{A.8}$$

whilst $\hat{\boldsymbol{\epsilon}}_d$ and $\hat{\boldsymbol{\sigma}}_d$ vectors are defined by

$$\boldsymbol{\epsilon}_d^* = \mathbf{\Pi}\ \hat{\boldsymbol{\epsilon}}_{\mathbf{d}}^* \text{ , and, } \boldsymbol{\sigma}_{\mathbf{d}}^* = \mathbf{\Pi}\ \hat{\boldsymbol{\sigma}}_{\mathbf{d}}^* \text{ , where } \mathbf{\Pi} = \begin{pmatrix} -1 & -1 & 1 \\ 0 & 1 & 1 \\ 1 & 0 & 1 \end{pmatrix}. \tag{A.9}$$

Using the base change matrix $\mathbf{\Pi}$, we found the strain components as

$$\begin{aligned} \epsilon_i^*(t) =& \frac{a(1+\nu_e)}{E_e}\left[\underbrace{\int_0^t \sum_j \Pi_{ij}F_{jj}\hat{\sigma_j}^*(T)\ e^{(T-t)\Omega_{jj}}\ (1-\tau_r\Omega_{jj})dT}_{\text{Visco-elastic component}} + \underbrace{\sum_j \tau_r\Pi_{ij}F_{jj}\hat{\sigma_j}^*(t)}_{\text{Elastic component}}\right] \\ &+ \underbrace{\sum_j \Pi_{ij}\left(\hat{\epsilon_i}^*(0) - \frac{(1+\nu_e)}{E_e}\hat{\sigma_j}^*(0)\right)e^{-t\Omega_{jj}}}_{\text{Initial conditions}}. \end{aligned} \tag{A.10}$$

Similarly to the shear case, the strain field can be expressed with three contributions: (i) a visco-elastic one the dynamics of which is driven by the characteristic times resulting from matrix $\mathbf{\Omega}$ and $\mathbf{F}$ (ii) an elastic one, not depending of time, having an instantaneous contribution (iii) an

exponentially decaying initial conditions contribution, the characteristic time of which results from matrix $\mathbf{\Omega}$. Using the model previously developed in the context of stress or creep relaxation tests, it

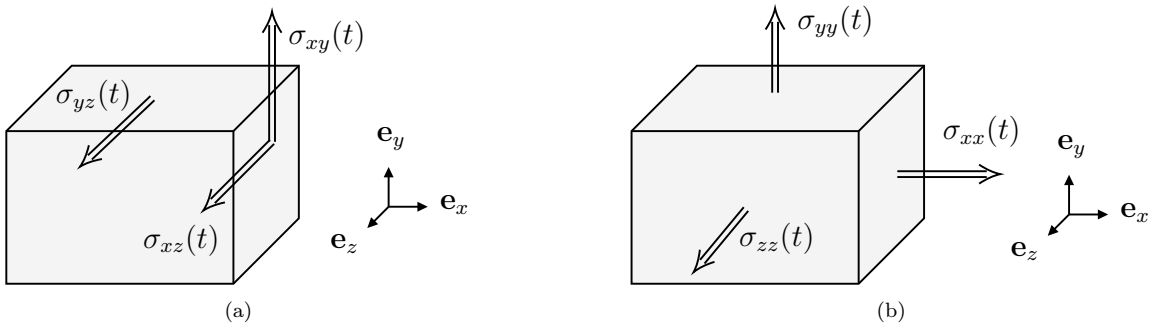

Figure A.9: Sketch of (a) shear, and (b) creep applied mechanical stress configurations on a visco-elastic material.

is possible to determine parameters $(a, \tau_r, \tau_\mu, \tau_\lambda)$ for various visco-elastic materials. Unfortunately, all model's parameters cannot be determined through a single experiment. Indeed, for a creep test, the characteristic stress relaxation time τ_r does not appear. It is, therefore, necessary to carry out two independent tests, a creep one and a stress relaxation one so as to determine all model parameters. However, for a given material it is not easy to find all the necessary mechanical stress configurations in the literature to close the parameter estimations. We perform some of those from the data sets found in the literature to further exemplified the approach.

Appendix A.1. Creep

In the framework of a single step loading of a stress σ_0^*, the model predicts the strain from (A.10), so that the creep compliance $J^*(t) = \epsilon^*(t)/\sigma_0^*$ is

$$J^*(t) = J^*(0)\left[a - \frac{1-a}{3}\left(2(1+\nu_e)e^{-t/\tau_\mu} + (1-2\nu_e)e^{-t/\tau_E}\right)\right]. \tag{A.11}$$

This test allows to determine parameters $(a, \tau_\mu, \tau_\lambda)$.

Appendix A.2. Stress relaxation

Similarly to the creep test, for a single step strain ϵ_0^*, the model involves stress from (A.3) and therefore Young modulus $E_{(t)} = \sigma^*(t)/\epsilon_0^*$

$$E(t) = \frac{E_e}{a}\left(1 + (a-1)e^{-at/\tau_r}\right). \tag{A.12}$$

This test allows finding parameters (a, τ_r). Note that in both experiments, the a value can be evaluated, thus providing a cross-checked evaluation.

An example of parameter estimation based on creep and stress relaxation tests on femur bones experiments carried out by [58] is illustrated inA.10. The parameter estimation has been carried out using a least square method in order to find the minimum error between the model and data. Figure A.10 display the stress and strain time variations respectively associated with stress relaxation and creep tests. Parameters $a = 1.77$ and $\tau_r = 4.42h$ for the stress relaxation test and $a = 1.41$, $\tau_\mu = 4.32\ min$ and $\tau_\lambda = 33.8\ min$ for the creep test have been found. These results

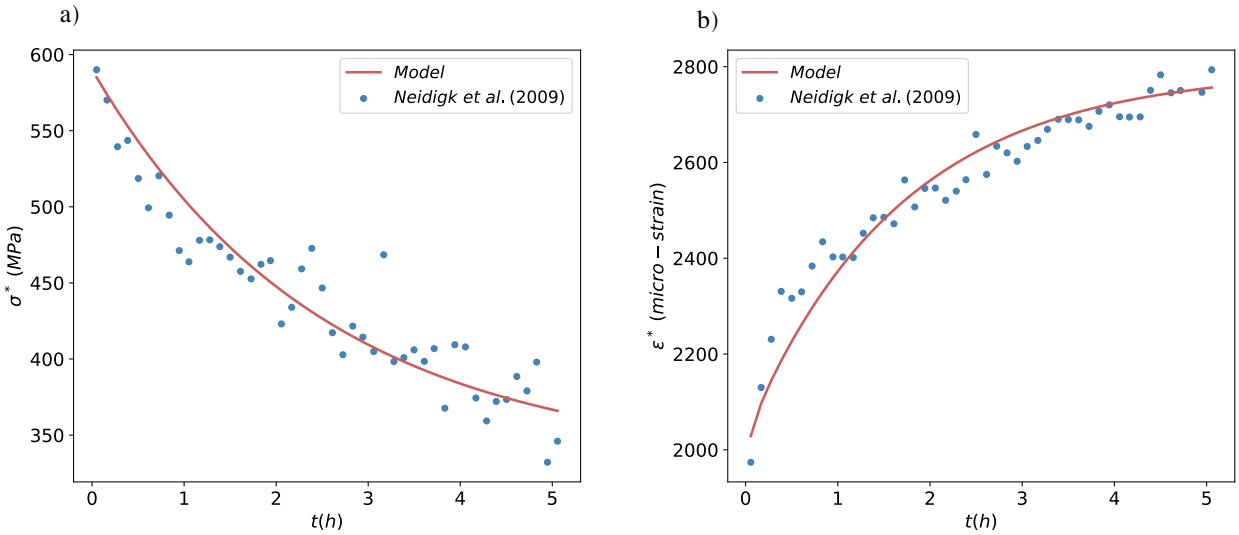

Figure A.10: Plot of the stress (a) and strain (b) evolution with time based on the femur bones media.

show a good agreement between the model with the experimental measurements. Also, the a value estimate lies within the 25% difference between both tests. The a parameter is then allowed to characterize the visco-elastic strain of a material, which is added to its elastic strain. It is thus necessarily larger than one. Furthermore the larger parameter a, the more visco-elastic the media.

Appendix B. Theoretical derivation of the visco-elastic FSI four-equations model

Keeping $O(1)$ terms and neglecting $O(\epsilon^2)$ in (29)-(30), it is possible to find that, to leading order, the displacements fields fulfils (Cf [34] for more details)

$$\tilde{\zeta} = \tilde{H}_1(Z, \omega) \quad \text{, and, } \quad \tilde{\xi} = \frac{\tilde{H}_2(Z, \omega)}{2} R + \frac{\tilde{H}_3(Z, \omega)}{R}, \tag{B.1}$$

where $\tilde{H}_{[1,2,3]}$ are functions of ω and Z given by the boundary conditions associated with axial velocity and radial constraint (Cf [34]). Note that this analysis is a long wavelength approach which neglects $O(\epsilon^2)$ so that (B.1) is in fact consistent with (26). Following [34], combining boundary conditions (35)-(36) with $\tilde{\xi}$ expression in (B.1) whilst using visco-elastic Poisson modulus (8) and (11) leads to

$$\tilde{H}_2(Z,\omega) = 2\nu_e\tilde{\nu}_s(\omega)\left(\tilde{\mathcal{C}}_{\lambda_s}(\omega)\frac{\tilde{P}}{\alpha^2(2+\alpha)} - \partial_Z\tilde{\zeta}\right) \quad \text{, and,} \quad \tilde{H}_3(Z,\omega) = \tilde{\mathcal{C}}_{\mu_s}(\omega)\frac{(1+\alpha)^2}{2\alpha^2(2+\alpha)}\tilde{P}. \quad \text{(B.2)}$$

The deformation vector field at the solid wall is necessary in order to close fluid momentum equation (33). It can be found from replacing results (B.2) in (B.1)

$$\tilde{\xi}\big|_{R=1} = \frac{\tilde{\chi}_s(\omega)\tilde{P}}{2\alpha} - \nu_e\tilde{\nu}_s(\omega)\partial_Z\tilde{\zeta}, \quad \text{(B.3)}$$

$$\tilde{\chi}_s(\omega) = \frac{2\nu_e\tilde{\nu}_s(\omega)\tilde{\mathcal{C}}_{\lambda_s}(\omega) + (1+\alpha)^2\tilde{\mathcal{C}}_{\mu_s}(\omega)}{\alpha(2+\alpha)} \quad \text{(B.4)}$$

where $\tilde{\chi}_s(\omega)$ generalizes the elastic effective velocity parameters χ_e, introduced in (1). Now, considering the leading-order solid stress, from $\tilde{\sigma}_{rz}$ in (28), whilst using (B.1) as well as $\tilde{\sigma}_{zz}$ in (25), the shear-stress boundary conditions (35)-(36) leads to find zero shear-stress everywhere inside the solid (at leading order, neglecting $O(\epsilon^2)$), as in the elastic case [33, 34]

$$\tilde{\sigma}_{rz} = 0. \quad \text{(B.5)}$$

It is noteworthy that this zero-shear stress in the solid is also a hypothesis of thin-shell approximation, hence consistent with this result. Using (B.2) in (B.1) to replace the $\tilde{\xi}$ field in the axial constraint $\tilde{\sigma}_{zz}$ visco-elastic rheology expression (25) yields

$$\tilde{\sigma}_{zz} = 2\nu_e\tilde{\nu}_s\frac{\tilde{P}}{\alpha(2+\alpha)} + \frac{\alpha\tilde{\mathcal{C}}_s^2}{\mathcal{D}}\partial_Z\tilde{\zeta}, \quad \text{(B.6)}$$

whilst simplification $\alpha\left[\frac{2}{\tilde{\mathcal{C}}_{\mu_s}} + \frac{1-2\nu_e\tilde{\nu}_s}{\tilde{\mathcal{C}}_{\lambda_s}}\right] \equiv \frac{\alpha\tilde{\mathcal{C}}_s^2}{\mathcal{D}}$ has also been used. Finally, combining (28) and (B.5), one gets

$$\frac{\alpha}{\mathcal{D}}\omega^2\tilde{\zeta} + \partial_Z\tilde{\sigma}_{zz} = 0. \quad \text{(B.7)}$$

By, using (33), (34), (B.3), (B.6) and (B.7), the dimensionless visco-elastic FSI four equation model can be derived

$$
\begin{aligned}
i\omega\tilde{W} &= -\partial_Z\tilde{P} && \text{(B.8)}\\
i\omega\tilde{P}+\mathcal{C}^2\partial_Z\tilde{W} &= -i\omega\mathcal{C}^2\left[\tilde{\chi}_s\tilde{P}-2\alpha\nu_e\tilde{\nu}_s\partial_Z\tilde{\zeta}\right], && \text{(B.9)}\\
\tilde{\sigma}_{zz} &= 2\nu_e\tilde{\nu}_s\frac{\tilde{P}}{\alpha(2+\alpha)}+\frac{\alpha\tilde{\mathcal{C}}_s^2}{\mathcal{D}}\partial_Z\tilde{\zeta}, && \text{(B.10)}\\
\frac{\alpha}{\mathcal{D}}\omega^2\tilde{\zeta}+\partial_Z\tilde{\sigma}_{zz} &= 0. && \text{(B.11)}
\end{aligned}
$$

Injecting (B.10) in (B.9) permits to express the r.h.s of (B.9) versus pressure and axial stress, i.e.

$$
i\omega\tilde{P}+\partial_Z\tilde{W}-2\alpha i\omega\nu_e\partial_Z\tilde{\zeta}=-i\omega\left[\left(\tilde{\chi}_s-\chi_e+\frac{4\nu_e^2\tilde{\nu}_s\left(\tilde{\nu}_s-1\right)\mathcal{D}}{\alpha(2+\alpha)\tilde{\mathcal{C}}_s^2}\right)\tilde{P}-2\mathcal{D}\frac{\nu_s^e\left(\tilde{\nu}_s-1\right)}{\tilde{\mathcal{C}}_s^2}\tilde{\sigma}_{zz}\right], \quad \text{(B.12)}
$$

or equivalently

$$
i\omega\tilde{P}+\partial_Z\tilde{W}-2\alpha i\omega\nu_e\partial_Z\tilde{\zeta}=-i\omega\left[\chi_e\left(\frac{\tilde{\chi}_s-\chi_e}{\chi_e}+\frac{4\nu_e^2\tilde{\nu}_s\left(\tilde{\nu}_s-1\right)\mathcal{D}}{\alpha(2+\alpha)\chi_e\tilde{\mathcal{C}}_s^2}\right)\tilde{P}-2\mathcal{D}\frac{\nu_e\left(\tilde{\nu}_s-1\right)}{\tilde{\mathcal{C}}_s^2}\tilde{\sigma}_{zz}\right]. \quad \text{(B.13)}
$$

The elastic and visco-elastic velocity parameters $(\chi_e,\tilde{\chi}_s)$ introduced in (1) and (B.4) respectively, can be revised regarding the solid acoustic wave speeds (13), their ratio to the acoustic fluid wave speed (14) and the density ratio (18). It thus follows

$$
\begin{aligned}
\chi_e &= \frac{4\mathcal{D}}{\alpha(2+\alpha)\mathcal{C}_s^{e2}}\left[1-\nu_e^2+\frac{\alpha(2+\alpha)}{2}(1+\nu_s^e)\right], && \text{(B.14)}\\
\tilde{\chi}_s &= \frac{4\mathcal{D}}{\alpha(2+\alpha)\tilde{\mathcal{C}}_s^2}\left[1-\nu_e^2{\tilde{\nu}_s}^2+\frac{\alpha(2+\alpha)}{2}(1+\nu_e\tilde{\nu}_s)\right], && \text{(B.15)}
\end{aligned}
$$

so one found the relation

$$
\frac{\tilde{\chi}_s-\chi_e}{\chi_e}+\frac{4\nu_e^2\tilde{\nu}_s\left(\tilde{\nu}_s-1\right)\mathcal{D}}{\alpha(2+\alpha)\chi^e\tilde{\mathcal{C}}_s^2}=\left(\frac{\mathcal{C}_s^e}{\tilde{\mathcal{C}}_s}\right)^2\frac{1-\nu_e^2\tilde{\nu}_s^2+\frac{\alpha(2+\alpha)}{2}(1+\nu_e\tilde{\nu}_s^s)+\nu_e^2\tilde{\nu}_s(\tilde{\nu}_s-1)}{1-\nu_e^2+\frac{\alpha(2+\alpha)}{2}(1+\nu_e)}-1, \quad \text{(B.16)}
$$

or equivalently

$$
\frac{\tilde{\chi}_s-\chi_e}{\chi_e}+\frac{4\nu_e^2\tilde{\nu}_s\left(\tilde{\nu}_s-1\right)\mathcal{D}}{\alpha(2+\alpha)\chi^e\tilde{\mathcal{C}}_s^2}=\left(\frac{\mathcal{C}_s^e}{\tilde{\mathcal{C}}_s}\right)^2\frac{1-\nu_e^2\tilde{\nu}_s+\frac{\alpha(2+\alpha)}{2}(1+\nu_e\tilde{\nu}_s^s)}{1-\nu_e^2+\frac{\alpha(2+\alpha)}{2}(1+\nu_e)}-1. \quad \text{(B.17)}
$$

Finally, the relation (B.13) results in

$$i\omega\tilde{P}+\partial_Z\tilde{W}-2\alpha i\omega\nu_e\partial_Z\tilde{\zeta}=2\mathcal{D}i\omega\frac{\nu_e(\tilde{\nu}_s-1)}{\tilde{\mathcal{C}}_s^2}\tilde{\sigma}_{zz}-\chi_e i\omega\left(\left(\frac{\mathcal{C}_s^e}{\tilde{\mathcal{C}}_s}\right)^2\frac{\nu_e^2\tilde{\nu}_s-1-\frac{\alpha(2+\alpha)}{2}(1+\nu_e\tilde{\nu}_s^s)}{\nu_e^2-1-\frac{\alpha(2+\alpha)}{2}(1+\nu_e)}-1\right)\tilde{P}. \quad \text{(B.18)}$$

Likewise, the (B.10) r.h.s is modified to bring out elastic contributions in its l.h.s

$$\tilde{\sigma}_{zz}-2\nu_e\frac{\tilde{P}}{\alpha(2+\alpha)}-\frac{\alpha\mathcal{C}_s^{e2}}{\mathcal{D}}\partial_Z\tilde{\zeta}=2\nu_e\left(\tilde{\nu}_s-1\right)\frac{\tilde{P}}{\alpha(2+\alpha)}+\frac{\alpha}{\mathcal{D}}\left(\tilde{\mathcal{C}}_s^2-\mathcal{C}_s^{e2}\right)\partial_Z\tilde{\zeta}, \quad \text{(B.19)}$$

so that re-injecting the $\partial_Z\tilde{\zeta}$ term of (B.10) yields

$$\tilde{\sigma}_{zz}-2\nu_e\frac{\tilde{P}}{\alpha(2+\alpha)}-\frac{\alpha\mathcal{C}_s^{e2}}{\mathcal{D}}\partial_Z\tilde{\zeta}=\frac{\tilde{\mathcal{C}}_s^2-\mathcal{C}_s^{e2}}{\tilde{\mathcal{C}}_s^2}\tilde{\sigma}_{zz}+\frac{2\nu_e}{\alpha(2+\alpha)}\left(\tilde{\nu}_s-1-\tilde{\nu}_s\frac{\tilde{\mathcal{C}}_s^2-\mathcal{C}_s^{e2}}{\tilde{\mathcal{C}}_s^2}\right)\tilde{P}. \quad \text{(B.20)}$$

Finally, (B.8), (B.9),(B.18) and (B.10) lead to

$$\begin{aligned}
i\omega\tilde{W} &= -\partial_Z\tilde{P} && \text{(B.21)}\\
i\omega\tilde{P}+\partial_Z\tilde{W}-2i\omega\alpha\nu_e\partial_Z\tilde{\zeta} &= -i\omega\chi_e\tilde{\mathcal{I}}_P^F\tilde{P}+\frac{2\mathcal{D}\nu_e}{\mathcal{C}_s^{e2}}i\omega\tilde{\mathcal{I}}_\sigma^F\tilde{\sigma}_{zz}, && \text{(B.22)}\\
i\omega\tilde{\sigma}_{zz}-\frac{2\nu_e}{\alpha(2+\alpha)}i\omega\tilde{P}-i\omega\frac{\alpha\mathcal{C}_s^{e2}}{\mathcal{D}}\partial_Z\tilde{\zeta} &= -i\omega\tilde{\mathcal{I}}_\sigma^S\tilde{\sigma}_{zz}+\frac{2\nu_e}{\alpha(2+\alpha)}i\omega\tilde{\mathcal{I}}_P^S\tilde{P}, && \text{(B.23)}\\
\frac{\alpha}{\mathcal{D}}\omega^2\tilde{\zeta}+\partial_Z\tilde{\sigma}_{zz} &= 0, && \text{(B.24)}
\end{aligned}$$

where the hereby introduced visco-elastic extra terms $\tilde{\mathcal{I}}_P^F$, $\tilde{\mathcal{I}}_\sigma^F$, $\tilde{\mathcal{I}}_P^S$ and $\tilde{\mathcal{I}}_\sigma^S$ read

$$\begin{aligned}
\tilde{\mathcal{I}}_P^F &= \left(\frac{\mathcal{C}_s^e}{\tilde{\mathcal{C}}_s}\right)^2\frac{1-\nu_e^2\tilde{\nu}_s+\frac{\alpha(2+\alpha)}{2}(1+\nu_e\tilde{\nu}_s)}{1-\nu_e^2+\frac{\alpha(2+\alpha)}{2}(1+\nu_e)}-1, && \text{(B.25)}\\
\tilde{\mathcal{I}}_\sigma^F &= \left(\frac{\mathcal{C}_s^e}{\tilde{\mathcal{C}}_s}\right)^2\left(\tilde{\nu}_s-1\right), && \text{(B.26)}\\
\tilde{\mathcal{I}}_P^S &= \tilde{\nu}_s-1+\tilde{\nu}_s\frac{\mathcal{C}_s^{e2}-\tilde{\mathcal{C}}_s^2}{\tilde{\mathcal{C}}_s^2}, && \text{(B.27)}\\
\tilde{\mathcal{I}}_\sigma^S &= \frac{\mathcal{C}_s^{e2}-\tilde{\mathcal{C}}_s^2}{\tilde{\mathcal{C}}_s^2}. && \text{(B.28)}
\end{aligned}$$

Appendix C. Dimensionless formulation of Keramat et al.'s model

The model of Keramat et al. [27] reads

$$\partial_t W^* = -\partial_z P^*, \tag{C.1}$$

$$\partial_t P^* + \partial_z W^* - 2\nu_e \partial_z \dot{\zeta}^* = \frac{2\left({\nu_e}^2 - 1\right)}{\alpha} \partial_t \int_0^t \mathcal{I}^*_{ker}(t^{'}) P^*(t - t^{'}) dt^{'}, \tag{C.2}$$

$$\partial_\tau \sigma^*_{zz} - \frac{\nu_e}{\alpha} \partial_\tau P^* - \rho_s {c_s^e}^2 \partial_z \dot{\zeta}^* = -\rho_s {c_s^e}^2 \partial_t \int_0^t \mathcal{I}^*_{ker}(t^{'}) \sigma^*_{zz}(t - t^{'}) dt^{'} + \frac{\nu_e}{\alpha} \partial_t \int_0^t \mathcal{I}^*_{ker}(t^{'}) P^*(t - t^{'}) dt^{'}, \tag{C.3}$$

$$\rho_s \partial_\tau \dot{\zeta}^* - \partial_z \sigma^*_{zz} = 0, \tag{C.4}$$

where the original hydraulic head H terms have been substituted by the pressure $P = \rho_f g H$, and

$$\mathcal{I}^*_{ker} = \frac{d}{dt} J^*(t), \tag{C.5}$$

the time derivative of the [27]'s Fourier creep function. The equations set (C.1)-(C.4) are now regarded under dimensionless form according to the scaling provided from (19) to (22) and by assuming the creep function to scale as the inverse of the elastic Young modulus, i.e. $J^*(t) = J(\tau)/E_e$. It then yields

$$\partial_t \int_0^t \mathcal{I}^*_{ker}(t^{'}) P^*(t - t^{'}) dt^{'} = \frac{\mathcal{D}}{\mathcal{C}_s^{e2}} \frac{W_0}{L} \partial_\tau \int_0^\tau \mathcal{I}_{ker}(\tau^{'}) P(\tau - \tau^{'}) d\tau^{'}, \tag{C.6}$$

$$\partial_t \int_0^t \mathcal{I}^*_{ker}(t^{'}) \sigma^*_{zz}(t - t^{'}) dt^{'} = \frac{\mathcal{D}}{\mathcal{C}_s^{e2}} \frac{W_0}{L} \partial_\tau \int_0^\tau \mathcal{I}_{ker}(\tau^{'}) \sigma_{zz}(\tau - \tau^{'}) d\tau^{'}, \tag{C.7}$$

so that

$$\partial_\tau W = -\partial_Z P, \tag{C.8}$$

$$\partial_\tau P + \partial_Z W - 2\alpha\nu_e \partial_Z \dot{\zeta} = \frac{2\mathcal{D}\left({\nu_e}^2 - 1\right)}{\alpha \mathcal{C}_s^{e2}} \partial_\tau \int_0^\tau \mathcal{I}_{ker}(\tau^{'}) P(\tau - \tau^{'}) d\tau^{'}, \tag{C.9}$$

$$\partial_\tau \sigma_{zz} - \frac{\nu_e}{\alpha} \partial_\tau P - \frac{\alpha \mathcal{C}_s^{e2}}{\mathcal{D}} \partial_z \dot{\zeta} = -\partial_\tau \int_0^\tau \mathcal{I}_{ker}(\tau^{'}) \sigma_{zz}(\tau - \tau^{'}) d\tau^{'} + \frac{\nu_e}{\alpha} \partial_\tau \int_0^\tau \mathcal{I}_{ker}(\tau^{'}) P(\tau - \tau^{'}) d\tau^{'}, \tag{C.10}$$

$$\frac{\alpha}{\mathcal{D}} \partial_\tau \dot{\zeta} - \partial_Z \sigma_{zz} = 0. \tag{C.11}$$

Finally, in the frequency-domain (C.8)-(C.11) achieve as follows

$$
\begin{aligned}
i\omega\tilde{W} &= -\partial_Z\tilde{P}, && \text{(C.12)}\\
i\omega\tilde{P}+\partial_Z\tilde{W}-2i\omega\alpha\nu_e\partial_Z\tilde{\zeta} &= -\frac{2\mathcal{D}\left(1-\nu_e^2\right)}{\alpha\mathcal{C}_s^{e2}}i\omega\tilde{\mathcal{I}}_{ker}(\omega)\tilde{P}(\omega), && \text{(C.13)}\\
i\omega\tilde{\sigma}_{zz}-\frac{\nu_e}{\alpha}i\omega\tilde{P}-\frac{\alpha\mathcal{C}_s^{e2}}{\mathcal{D}}\partial_z\tilde{\zeta} &= -i\omega\tilde{\mathcal{I}}_{ker}(\omega)\tilde{\sigma}_{zz}(\omega)+\frac{\nu_e}{\alpha}i\omega\tilde{\mathcal{I}}_{ker}(\omega)\tilde{P}(\omega), && \text{(C.14)}\\
\frac{\alpha}{\mathcal{D}}\omega^2\tilde{\zeta}+\partial_Z\tilde{\sigma}_{zz} &= 0, && \text{(C.15)}
\end{aligned}
$$

which is equal to (87)-(90).

Chapter 5

Numerical solutions using the Method Of Characteristics

Contents

This chapter focuses on the development of a network-oriented numerical tool to model the water hammer wave propagation phenomena. The numerical solver handles the resolution of the hyperbolic fluid equations (disregarding FSI effects i.e. in the limit $\nu_s \to 0$), using the very standard Method Of Characteristics (MOC). The WDN are usually burred, which strongly suggests the simplification of disregarding the signal's high-frequencies (e.g. Poisson coupling) in the modeling and consider the fluid mass and momentum conservation equations only [Chaudhry, 2014]. At the network nodes, specific boundary conditions have to be ensured, the latter depending of the type of hydraulic component being modeled (e.g. valve,

Institution	Software Name	Solution Method	Friction Model
Applied Flow Technology	AFT Impulse	MoC	Quasisteady
Flow Science Inc.	FLOW 3-D	TruVOF	Steady
Hydromantis Inc.	ARTS	MoC	Steady
University of Auckland	HYTRAN	MoC	Vítkovský
BHR Group	FLOWMASTER 2	MoC	Steady
Bentley Systems, Inc.	HAMMER	MoC	Vítkovský
Stoner Associates, Inc.	LIQT	MoC	Steady
DHI	HYPRESS	Finite-Difference Method	Steady
University of Cambridge	PIPENET	MoC	Steady
University of Kentucky	SURGE	Wave Method (WM)	Steady
University of Texas at Austin	TSNet	MoC	Vítkovský
University of Toronto	TRANSAM	MoC	Steady
University Politécnica de Valencia	DYAGATS	MoC	Steady
University Politécnica de Valencia	ALLIEVI	MoC	Steady
Deltares	WANDA	MoC	Quasisteady
US Army Corps Engineers	WHAMO	Finite-Difference Method	Steady
DHI	MIKE URBAN	MoC	Steady
Innovyze	H_2O SURGE	WM	Steady
KYPIPE	SURGE	WM	Steady
EPA	EPA SURGE	WM	Steady
Unisont Engineering, Inc.	uSLAM	MoC	Steady

Figure 5.1: *Overview of the open-source and commercial water hammer software, source [Abdeldayem et al., 2021]*

.

pump, reservoir), [Covas, 2003]. A first part of this section is dedicated to provide a brief overview of the numerical methods used to model water hammer waves. Then the MOC formalism, i.e. governing equations discretization, is discussed and detailed. The solver is validated by simple comparisons with numerical or experimental benchmarks before being extended, at scale one, to a realistic on-field test case.

5.1 Overview of the existing models

Several numerical schemes exist to model pressure waves in WDN. The forthcoming brief literature review relies on the excellent review of [Pal et al., 2021]. While the MOC numerical scheme is worldly spread as shown in Figure 5.1, other techniques as the Finite Volume Method (FVM) or Finite Difference Method (FDM) are also used.

The FVM is a well known numerical technique which consists in considering flux balance (for mass, momentum, energy, temperature) upon elementary volume-cells (thus, by definition, FVM are conservative). Well-suited for the analysis of hyperbolic problems [Toro, 1997], FVM provides a fine description of the shock interactions and discontinuities, [Zhao and Ghidaoui, 2004]. Some insights on the practical application of FVM for water hammer applications can be found in [Guinot, 2010]. In the low-Mach number framework, i.e. neglecting the influence of the inertial Navier's terms in the Navier-Stokes equations, the hyperbolic system

(1.40) can be recasted in the following form

$$\partial_t \mathbf{X} + \underbrace{\mathbf{J}\partial_z \mathbf{X}}_{\text{Flux}} = \mathbf{0}, \tag{5.1}$$

where $\mathbf{J}$ is the Jacobian matrix and $\mathbf{X}$ unknown fields discretized into the mesh grid. When discontinuities propagate along the pipe domain, such problems are called *Riemann problems*. Numerical methods and approaches to solve *Riemann problems* are called *Riemann solvers*. The eigenvectors directions of the Jacobian matrix provide the shock-wave propagation directions and are known as the *Riemann invariant*. These invariants characterize the diagonal basis of (5.1), which is a key-issue in MOC procedure too, as later-on discussed. Let us discretize a pipe domain in equal volumes. Assuming the field $\mathbf{X}$ being equally distributed in each pipe sub–domain, the time integration procedure results in estimating the flux across each cell interface. The entire FVM numerical scheme lies in the flux determination for which several specific formulations exist [Pal et al., 2021]. Despite the numerical advantages of the FVM (e.g. stability for Courant–Friedrichs–Lewy less than one [Zhao and Ghidaoui, 2004], easy embedding of cavitation phenomena [Zhou et al., 2018]), this scheme is not used much to handle large-scale water distributions networks for which MOC-like or MOC-based methods are preferred, [Nault et al., 2018, Jensen et al., 2018, Meng et al., 2019, Xing and Lina, 2020, Guo et al., 2021, Riaño-Briceño et al., 2022].
The FDM discretizes both space and time derivatives of (5.1) following an explicit (or implicit) scheme [Chaudhry, 2014]. The [Maccormack, 1969]'s procedure, which is second order accurate in both time and space, is commonly used despite its inherent dissipative behavior [Chaudhry, 2014]. It consists in the succession of predicative (e.g. forward finite difference) and a corrective (e.g. backward finite difference) steps to determine the numerical optimal solution. The method was recently used by [Wan and Huang, 2018, Malesińska et al., 2021] to analyze the transient response of in-line connected pipes. Despite its implementation simplicity and second order accuracy, this approach surfers from a dispersive behavior and some difficulties to properly handle boundary conditions, which needs to combine finite difference method with characteristics equations [Chaudhry, 2014].

5.2 The Method of Characteristics (MOC) formalism

5.2.1 Numerical scheme

The MOC, [Chaudhry, 2014, Jensen et al., 2018, Xing and Lina, 2020], consists in describing a set of hyperbolic equations along their characteristics, i.e. parametric curves $(t, z(t))$, along which the solutions are conserved. For one-dimensional hyperbolic systems, it results in an eigenvalue problem where each eigenvalues depict the propagation wave speed solution, [Tijsseling, 2007]. The fluid hyperbolic two

equations set (1.40) (Cf. §1.4.2) displays trivial eigenvalues being $\pm c_p$ associated with characteristic curves $z(t) = \pm c_p t$ the slopes of which are

$$\frac{dz(t)}{dt} = \pm c_p. \tag{5.2}$$

The fluid hyperbolic equations set (1.40) is now re-organized to display a dependence upon the hydraulic head H and the flow-rate Q

$$\left[\partial_t + \begin{pmatrix} 0 & \frac{c_p^2}{gS} \\ gS & 0 \end{pmatrix} \partial_z\right] \begin{pmatrix} H \\ Q \end{pmatrix} = \left[gS\sin(\theta) - \frac{4\tau_w S}{\rho_f D}\right] \begin{pmatrix} 0 \\ 1 \end{pmatrix}, \tag{5.3}$$

$$P = \rho_f g\left(H + x\sin(\theta)\right), \tag{5.4}$$

$$W = \frac{Q}{S}, \tag{5.5}$$

where θ is the pipe slope, S its section, D its inner diameter and x the altitude. Then, along the characteristic curves (5.2), i.e. in the hyperbolic system diagonalization basis, the hyperbolic fluid system (5.3) reads

$$\frac{D}{Dt}\left(H \pm \frac{c_p}{gS}Q\right) = \mp\frac{4c_p\tau_w}{\rho_{f_0} gD} \pm c_p\sin(\theta) \quad \text{, along, } \quad \frac{dz(t)}{dt} = \pm c_p, \tag{5.6}$$

where $\frac{D}{Dt} \equiv \partial_t \pm c_p\partial_z$ is the Lagrangian derivative, which depends on the characteristic curve slope sign.

5.2.2 Governing equation discretization

Let us introduce (N_z, N_t) the number of space and time grid points. In the following the discrete expression of physical fields is denoted

$$H(z,t) \equiv H(i\Delta_z, n\Delta_t) \equiv H_i^n, \tag{5.7}$$

with $(i,n) \in [\![0, N_z - 1]\!] \times [\![0, N_t - 1]\!]$. Some insights on the MOC discretization scheme is provided in Figure 5.2. Integrating (5.6) along the characteristic lines (5.2) leads to

$$\frac{H_i^{n+1} - H_{i-1}^n}{\Delta_t} + \frac{c_p}{gS}\frac{Q_i^{n+1} - Q_{i-1}^n}{\Delta_t} = -\frac{4c_p\tau_{w,i-1}^n}{\rho_f gD} + c_p\sin(\theta) \quad \text{, on, } \quad z_i = z_{i-1} + c_p\Delta_t, \tag{5.8}$$

$$\frac{H_i^{n+1} - H_{i+1}^n}{\Delta_t} - \frac{c_p}{gS}\frac{Q_i^{n+1} - Q_{i+1}^n}{\Delta_t} = \frac{4c_p\tau_{w,i+1}^n}{\rho_f gD} - c_p\sin(\theta) \quad \text{, on, } \quad z_i = z_{i+1} - c_p\Delta_t, \tag{5.9}$$

whilst combining (5.8)-(5.9) in

$$H_i^{n+1} = \frac{1}{2}\left(H_{i+1}^n + H_{i-1}^n - \frac{c_p}{gS}\left(Q_{i+1}^n - Q_{i-1}^n\right) + \frac{4c_p\Delta_t}{\rho_f gD}\left(\tau_{w,i+1}^n - \tau_{w,i-1}^n\right)\right), \tag{5.10}$$

$$Q_i^{n+1} = \frac{1}{2}\left(Q_{i+1}^n + Q_{i-1}^n - \frac{gS}{c_p}\left(H_{i+1}^n - H_{i-1}^n\right) - \frac{4S\Delta_t}{\rho_f D}\left(\tau_{w,i+1}^n + \tau_{w,i-1}^n\right) + 2gS\sin(\theta)\right). \tag{5.11}$$

The wall shear rate, $\tau_w(z,t)$ is thereafter discretized, at grid points, as the boundary conditions, permitting to close the model.

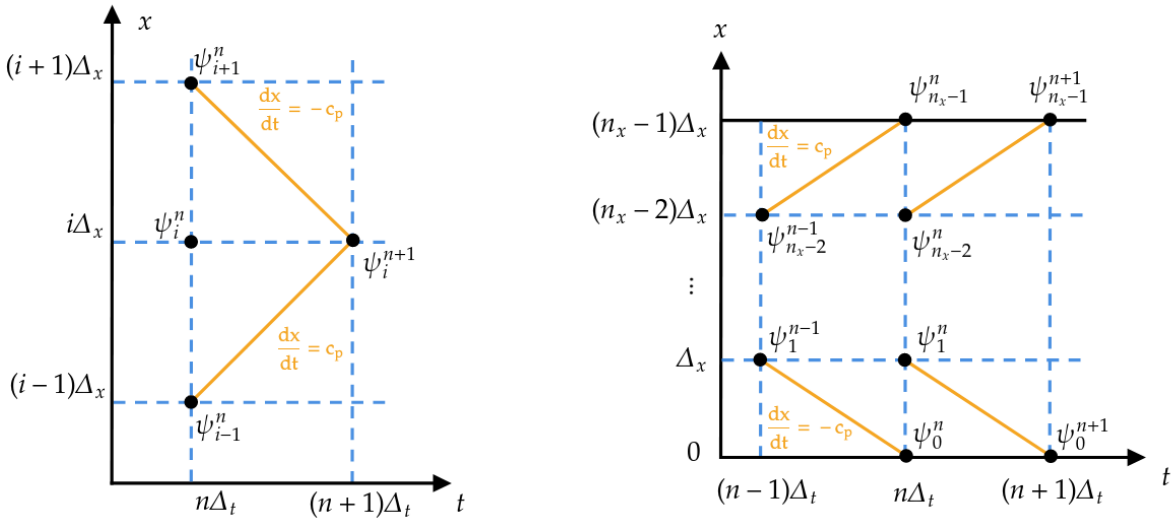

(a) *MOC grid-discretization, inner points*

(b) *MOC grid-discretization, boundary points*

Figure 5.2: *Fixed MOC grid discretization formalism.*

5.2.3 Wall shear rate discretization

The quasi-steady shear stress (1.41) is easily discretized following [Chaudhry, 2014]

$$\tau_{qst,i}^n = \frac{\rho_f f_{DW,i}^n Q_i^n |Q_i^n|}{8S^2}. \tag{5.12}$$

Depending on the transient shear rate model (Instantaneous material acceleration-based (IMAB) or Weighting function-based (WFB) (Cf. (1.4.1)), the numerical implementation of the MOC greatly differs. Indeed, the IMAB discretization remains a matter of debate. [Ramos et al., 2004] considers the impact of the time-space derivative within the hyperbolic operator. In such implementation, the pulse wave speed c_p is Reynolds dependent, via the deviation parameter k_3 introduced in (1.46)-(1.47), then modifying the hyperbolic eigenvalues. The invariant space-time behavior of the MOC discretization grid thus enforces the use of grid interpolations [Ghidaoui et al., 2005, Pal et al., 2021], which gives rise to numerical diffusion. On the other hand, [Vítkovský et al., 2006, Xing and Lina, 2020] have considered the space and time inertial derivatives of the IMAB's models as source terms. In these approaches, the original hyperbolic structure (5.3) remains, and so does its eigenvalues. Grid interpolations are therefore unnecessary. [Tiselj and Gale, 2008] analyzed both approaches for second order accurate characteristic upwind scheme. The authors concluded that the source term approach is relevant as long as the inertial contributions do not *severely* affect the eigen-structure of the hyperbolic system. Then, in the hereby low-Mach number asymptotic framework, this approach is adopted for IMAB models. In addition, the results inaccuracy introduced by the source term implementation method can be reduced by using

a thinner discretization grid, which is however computationally expensive (≈ 5 times more CPU than for the scheme used in [Tiselj and Gale, 2008]). Considering a time-explicit first-order Euler discretization of space-time derivatives in (1.44) yields

$$\tau^n_{tr,i+1} = \frac{\rho_f D k_3}{4S}\left(\frac{Q^n_{i+1}-Q^{n-1}_{i+1}}{\Delta_t} + c_p \cdot sgn\left(Q^n_{i+1}\right)\left|\frac{Q^n_{i+1}-Q^n_i}{\Delta_x}\right|\right), \quad (5.13)$$

$$\tau^n_{tr,i-1} = \frac{\rho_f D k_3}{4S}\left(\frac{Q^n_{i-1}-Q^{n-1}_{i-1}}{\Delta_t} + c_p \cdot sgn\left(Q^n_{i-1}\right)\left|\frac{Q^n_{i-1}-Q^n_i}{\Delta_x}\right|\right). \quad (5.14)$$

The WFB wall shear rate models have the major disadvantage of being computationally costly since the full flow history have to be conserved to handle the convolution product. To avoid this hindrance, [Trikha, 1975] proposed an exponential fitting decomposition of the convolution kernel, which then simplify the convolution product (1.52)

$$\tau_{tr}(z,t) = \sum_{j=1}^{N_k} y_j(z,t), \quad (5.15)$$

$$y_j(z,t) = \frac{4\rho_f \nu_f}{DS}\int_0^t \partial_u Q(z,u)\mathcal{W}_j(t-u)du, \quad (5.16)$$

$$\mathcal{W}_j(t) = m_j e^{-\frac{4\nu_f n_j t}{D^2}}, \quad (5.17)$$

with N_k the number of exponential fitting terms. [Kagawa et al., 1983, Schohl, 1993] further improved the [Trikha, 1975]'s method by reconsidering the kernel fitting, i.e. by increasing N_k, and the integration procedure for laminar flows. [Vardy and Brown, 2007], relying on the re-scaled weighing function approach detailed in [Vitkovsky et al., 2004], proposed a Reynolds-dependent scaling for the convolution kernel delivered in (1.62) and (1.65). The authors used the relation

$$\frac{A^* e^{-B^*(Re)\frac{4\nu_f t}{D^2}}}{\sqrt{\frac{4\nu_f t}{D^2}}} \approx \sum_{j=1}^{N_k} m_j e^{-\frac{4\nu_f n_j t}{D^2}}, \quad (5.18)$$

so that

$$\frac{1}{\sqrt{\frac{4\nu_f t}{D^2}}} \approx \sum_{j=1}^{N_k} m^*_j e^{-n^*_j \frac{4\nu_f t}{D^2}}, \quad (5.19)$$

where the general, Reynolds independent, fitting coefficients

$$m^*_j = \frac{m_j}{A^*} \text{ , and, } n^*_j = n_j - B^*(Re), \quad (5.20)$$

have been defined. These coefficients are tabulated in Table 5.1. Finally the (A^*, B^*) coefficients are determined using (1.62) and (1.65), which fully determine the kernel fitting parameters (m_j, n_j) values. Once the [Vardy and Brown, 2007]'s model parametric estimation overcomes, the [Trikha, 1975]'s integration is performed. The procedure is denoted as the Trikha-Vardy-Brown (TVB) procedure

$\Psi < 10^{-8}$		$10^{-8} \leq \Psi < 10^{-7}$		$10^{-7} \leq \Psi < 10^{-6}$		$10^{-6} \leq \Psi < 10^{-5}$		$10^{-5} \leq \psi < 10^{-4}$		$10^{-4} \leq \Psi$	
m_j^*	n_j^*	m_j^*	n_j^*	m_j^*	n_j^*	m_j^*	n_j^*	m_j^*	n_j^*	m_j^*	n_j^*
9.08	10	9.08	10	9.08	10	9.08	10	9.08	10	9.08	10
-4.23	$10^{1.5}$	-4.23	$10^{1.5}$	-4.23	$10^{1.5}$	-4.23	$10^{1.5}$	-4.23	$10^{1.5}$	-4.23	$10^{1.5}$
13.2	10^2	13.2	10^2	13.2	10^2	13.2	10^2	13.2	10^2	13.2	10^2
40.1	10^3	40.1	10^3	40.1	10^3	40.1	10^3	40.1	10^3	40.1	10^3
124.	10^4	124.	10^4	124.	10^4	124.	10^4	124.	10^4	124.	10^4
397.	10^5	397.	10^5	397.	10^5	397.	10^5	397.	10^5		
1250.	10^6	1250.	10^6	1250.	10^6	1250.	10^6				
3960.	10^7	3960.	10^7	3960.	10^7						
12500.	10^8	12500.	10^8								
39600.	10^9										

Table 5.1: *WFB's kernel exponential coefficients, for the Trikha-Vardy-Brown (TVB) integration procedure,* $\Psi \equiv \frac{4\nu_f t}{D^2}$.

in the subject literature. It is interesting to mention that the convolution kernel found in [Bayle and Plouraboué, 2022]'s (Cf. §3.3) can be exponentially fitted following the TVB approach since this kernel scales in $1/\sqrt{\frac{4\nu_f t}{D^2}}$ (Cf. §1.4.2), i.e. by canceling out the B^* contribution in (5.18)-(5.20). More recently, [Urbanowicz, 2018] enriched the integration procedure in the early convolution time by setting up a corrective parameter η defined as follows

$$\eta = \frac{\int_0^{\frac{4\nu_f \Delta_t}{D^2}} \mathcal{W}_{analytic}(u)du}{\int_0^{\frac{4\nu_f \Delta_t}{D^2}} \mathcal{W}_{fitted}(u)du}. \tag{5.21}$$

Several values of η are thereafter provided depending on the WFB model used. Let us define the dimensionless viscous time step, $\Delta_t^* = \frac{4\nu_f \Delta_t}{D^2}$, then it yields:

- for laminar flow, [Bayle and Plouraboué, 2022]

$$\eta(\Delta_t^*) = \frac{2z_1\sqrt{\Delta_t^*}}{\sum_{j=1}^{N_k}\left(\frac{m_j}{n_j}\left(1-e^{-n_j\Delta_t^*}\right)\right)}, \tag{5.22}$$

with $z_1 = \frac{1}{2\sqrt{\pi}} \equiv A^*$.

- for laminar flow, [Zielke, 1968], $\Delta_t^* \leq 0.02$

$$\eta(\Delta_t^*) = \frac{2z_1\sqrt{\Delta_t^*} + z_2\Delta_t^* + \frac{2}{3}z_3\left(\Delta_t^*\right)^{\frac{3}{2}} + \frac{z_4}{2}\left(\Delta_t^*\right)^2 + \frac{2}{5}z_5\left(\Delta_t^*\right)^{\frac{5}{2}} + \frac{z_6}{3}\left(\Delta_t^*\right)^3}{\sum_{j=1}^{N_k}\left(\frac{m_j}{n_j}\left(1-e^{-n_j\Delta_t^*}\right)\right)}, \tag{5.23}$$

with $z_2 = -\frac{5}{4}$, $z_3 = \frac{15}{16\cdot\Gamma\left(\frac{3}{2}\right)}$, $z_4 = \frac{15}{16}$, $z_5 = \frac{135}{256\cdot\Gamma\left(\frac{5}{2}\right)}$ and $z_6 = -\frac{45}{128}$ and where Γ stands for the gamma function (Cf. (1.53)).

- for laminar flow, [Zielke, 1968], $\Delta_t^* \geq 0.02$

$$\eta(\Delta_t^*) = \frac{(5.23)(\Delta_t^* \equiv 0.02) + \sum_{j=1}^{5} \frac{e^{r_j \Delta_t^*} - e^{0.02 \cdot r_j}}{r_j}}{\sum_{j=1}^{N_k} \left(\frac{m_j}{n_j} \left(1 - e^{-n_j \Delta_t^*} \right) \right)}. \tag{5.24}$$

with $r_1 = -26.3744$, $r_2 = -70.8463$, $r_3 = -135.0198$, $r_4 = 218.9216$, $r_5 = 322.5544$ (Cf. (1.54)).

- for turbulent flow [Vardy and Brown, 2003]

$$\eta(\Delta_t^*) = \frac{erf\left(\sqrt{\Delta_t^* B^*(Re)} \right)}{2\sqrt{B^*(Re)} \sum_{j=1}^{N_k} \left(\frac{m_j}{n_j} \left(1 - e^{-n_j \Delta_t^*} \right) \right)}. \tag{5.25}$$

The [Urbanowicz, 2018] integration procedure, i.e. the approximation of the convolution product (5.15)-(5.17), finally results in

$$\tau_{tr,i}^{n+1} = \sum_{j=1}^{N_k} y_{j,i}^{n+1} \tag{5.26}$$

$$y_{j,i}^{n+1} \approx \frac{4\rho_f \nu_f}{DS} \left[E_j y_{j,i}^n + \eta F_j \left(Q_i^{n+1} - Q_i^n \right) + [1 - \eta] E_j F_j \left(Q_i^n - Q_i^{n-1} \right) \right], \tag{5.27}$$

$$E_j = e^{-\frac{4\nu_f n_j \Delta_t}{D^2}}, \quad F_j = \frac{m_j D^2}{4\nu_f \Delta_t n_j} \left[1 - E_j \right], \tag{5.28}$$

where in the limit, $\mathcal{W}_{fitted} \equiv \mathcal{W}_{analytic}$, the parameter η tends to one, which recovers the results of [Schohl, 1993].

5.2.4 Optimal time-step discussion

The MOC scheme stability is ensured by the Courant–Friedrichs–Lewy C_{fl}, criteria [Chaudhry, 2014], which is defined by

$$C_{fl} = \frac{\delta_t c_p}{\delta_x} \leq 1. \tag{5.29}$$

When the C_{fl} is not equal to one, some grid interpolations are necessary to perform the computation, introducing numerical dispersion and/or artificial damping [Pal et al., 2021]. When an undamped scheme is considered, i.e. by setting $\tau_w \equiv 0$ in (5.10)-(5.11), this condition follows from analytical considerations. In contrast, when damping terms are considered, the use of an analytical determination is no longer possible and the stability must be handled by numerical simulation [Chaudhry, 2014]. For IMAB models, [Tiselj and Gale, 2008] indicated that the C_{fl} number should be reduced of nearly 2% (due to the hyperbolic eigenvalues modification by k_3), to respect the stability condition criteria. The author criteria was nevertheless not established by considering neither space-time derivatives of equation (1.44) as source terms, nor the sign variations in the spatial gradient. From a network standpoint, all pipes should respond to the very same time step, $\Delta_t = \min_{i \in Pipes} \delta_t$ so as to ensure the boundary conditions. For $C_{fl} = 1$, the local space step, Δ_z, hence have to be modified as to ensure the local stability criteria.

Let N_{cr} be the number of space sample points in the time step most restrictive pipe. The global time and local space steps then achieve in

$$\Delta_t = \min_{i \in Pipes} \left(\frac{L_i}{c_{p,i}} \right) \frac{1}{N_{cr} - 1} \quad \text{, and,} \quad \Delta_z = c_p \Delta_t. \tag{5.30}$$

This choice of time step introduces some space discretization errors, Δ_ϵ, intrinsic to the numerical method, in each pipe of the network, the amplitude of which are given by

$$\Delta_\epsilon(\%) = 100 \cdot \left| 1 - E\left(\frac{L}{\Delta_x} \right) \frac{\Delta_z}{L} \right|, \tag{5.31}$$

where E is the integer part function. The update local number of grid point in each pipe then follows from

$$n_z = 1 + E\left(\frac{c_p \Delta_t}{L} \right). \tag{5.32}$$

The N_{cr} parameter is representative of the cut-off frequency of the numerical method in the most restrictive pipe. The higher the cut-off frequency, the higher the number of grid points in every pipe, and thus a considerable increase in computation time.

5.2.5 Boundary condition management

Boundary conditions are one of the arduous points to deal with in numerical analyses since they directly influence the simulation results. For the classical case-study of a pipe-reservoir-valve (RPV) connected system, [Cao et al., 2020] provided a recent in-depth analysis of the impact of boundary condition upon the general pressure damping. While the boundary conditions at the regular network nodes result in ensuring both the hydraulic head and flow-rate conservation, for specific hydraulic organs (e.g pumps, throttle valve or pressure reducing valves) additional boundary conditions have to be set up [Tijsseling, 1993, Covas, 2003, Zecchin, 2010]. Some specific boundary conditions are hereafter provided.

Regular nodes

Let us introduce (N_e, N_s) being respectively the number of incoming and outgoing flows connection to a node, and Q_d the steady-state flow demand. The connection configuration is depicted in Figure 5.3. The head/flow-rate conservation conditions then read

$$\sum_{k=1}^{N_e} Q^{n+1}_{k,n_{(z,k)}-1} - \sum_{l=1}^{N_s} Q^{n+1}_{l,0} = Q^{n+1}_d, \tag{5.33}$$

$$H^{n+1}_{1,n_{(z,1)}-1} \cdots H^{n+1}_{N_e,n_{(z,N_e)}-1} = H^{n+1}_{1,0} \cdots H^{n+1}_{N_s,0} \equiv H^{n+1}_{inc}. \tag{5.34}$$

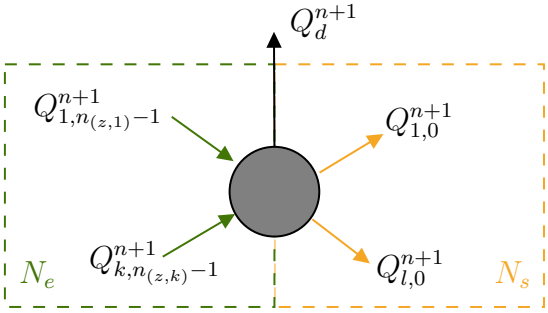

Figure 5.3: *Flow rate conservation at a regular network node.*

As depicted in Figure 5.2b, the use of the negative characteristic (5.9) for incoming pipes to the node, respectively the positive characteristic (5.8) for outgoing pipes, yields to

$$Q_{l,0}^{n+1} = Q_{l,1}^{n} + \frac{gS_l}{c_{p,l}}\left(H_{inc}^{n+1} - H_{l,1}^{n} - \frac{4c_{p,l}\Delta_t\tau_{w,l,1}^{n}}{\rho_{f_0}gD_l} + c_{p,l}\Delta_t\sin(\theta_l)\right), \tag{5.35}$$

$$Q_{k,n_{(z,k)}-1}^{n+1} = Q_{k,n_{(z,k)}-2}^{n} - \frac{gS_k}{c_{p,k}}\left(H_{inc}^{n+1} - H_{k,n_{(z,k)}-2}^{n} + \frac{4c_{p,k}\Delta_t\tau_{w,k,n_{(z,k)}-2}^{n}}{\rho_{f_0}gD_k} - c_{p,k}\Delta_t\sin(\theta_k)\right) \tag{5.36}$$

Finally, combining the equations (5.33) and (5.35)-(5.36) results in

$$H_{inc}^{n+1} = -\frac{\gamma^n}{\beta}, \tag{5.37}$$

with

$$\gamma^n = Q_d^{n+1} - \sum_{k=1}^{N_e}\left(Q_{k,n_{(x,k)}-2}^{n} - \frac{gS_k}{c_{p,k}}\left(-H_{k,n_{(x,k)}-2}^{n} + \frac{4c_{p,k}\Delta_t\tau_{w,k,n_{(x,k)}-2}^{n}}{\rho_{f_0}gD_k} - c_{p,k}\Delta_t\sin(\theta_k)\right)\right) + \sum_{l=1}^{N_s}\left(Q_{l,1}^{n} + \frac{gS_l}{c_{p,l}}\left(-H_{l,1}^{n} - \frac{4c_{p,l}\Delta_t\tau_{w,l,1}^{n}}{\rho_{f_0}gD_l} + c_{p,l}\sin(\theta_l)\right)\right), \tag{5.38}$$

and β the node impedance transmission coefficient

$$\beta = g\left(\sum_{k=1}^{N_e}\frac{S_k}{c_{p,k}} + \sum_{l=1}^{N_s}\frac{S_l}{c_{p,l}}\right). \tag{5.39}$$

The updated flow-rates simply follow from (5.35)-(5.36).

Reservoir nodes

The reservoir impedes any head variation over time so that

$$H_{inc}^{n+1} = H_{res}. \tag{5.40}$$

The updated boundary condition flow-rates are thus prescribed by (5.35)-(5.36).

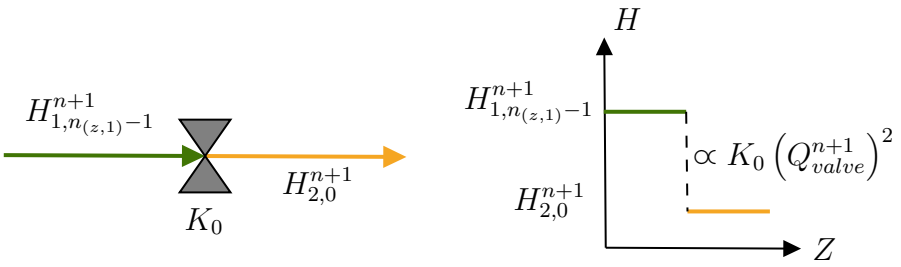

Figure 5.4: *Singular head loss at a valve.*

Valve law

Under steady-state flow conditions, a valve is known to produce a local hydraulic head loss, as depicted in Figure 5.4, which is proportional to the valve squared flow-rate according to [Chaudhry, 2014]

$$H^0_{1,n_{(z,1)}-1} - H^0_{2,0} = K_0 \left(Q^0_{valve}\right)^2, \tag{5.41}$$

where K_0 is the quasi-steady valve head loss coefficient. For transient analyses, this relation is supposed to hold, [Tijsseling, 1993], so that a valve device is modeled as

$$K_0 \left(Q^{n+1}_{valve}\right)^2 = |H^{n+1}_{1,n_{(z,1)}-1} - H^{n+1}_{2,0}|. \tag{5.42}$$

The valve flow-rate then follows from the combination of the positive characteristic (5.8) with (5.42)

$$K_0 \left(Q^{n+1}_{valve}\right)^2 - \left| -\frac{1}{g}\left(\frac{c_{p,1}}{S_1} + \frac{c_{p,2}}{S_2}\right) Q^{n+1}_{valve} + H^n_{1,n_{z,1}-2} - H^n_{2,1} + \frac{1}{g}\left(\frac{c_{p,1}Q^n_{1,n_z-2}}{S_1} + \frac{c_{p,2}Q^n_{2,1}}{S_2}\right) - \frac{4\Delta_t}{\rho_f g}\left(\frac{c_{p,1}\tau^n_{w,n_x-2}}{D_1} + \frac{c_{p,2}\tau^n_{w,2,1}}{D_2}\right) + \Delta_t \left(c_{p,1}\sin(\theta_1) + c_{p,2}\sin(\theta_2)\right)\right| = 0. \tag{5.43}$$

5.2.6 Wave-speed model

It is known that the fluid pulse wave speed is a function of the fluid physical (usually water), solid geometrical and rheological properties (Cf. §1.4.2). These properties are not always known at the network scale and data interpolation are needed, e.g. the tube's thickness per its inner radius ratio, α. The α ratio depends on the pipe materials and should be consequently adjusted. Some generics α-laws are hereafter provided in Figures 5.5a-5.5e. The SETOM's collaborators gathered, for the pipes installed in the Toulouse's WDN, the pipe thickness (provided by the pipe's manufacturers) with respect to the pipe radius R_0, the discrete ratio of which is depicted by blue dotted points in Figures 5.5a-5.5e. An error minimization procedure is thus performed between the tabulated $\alpha \equiv \frac{e}{R_0}$ and some general dependence laws evaluated at the very same set of discrete radius, finally providing a generic α dependence trend with respect to the pipe radius, for several pipe materials.

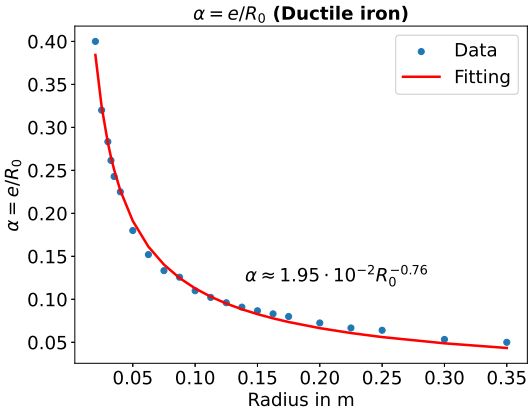

(a) *Ductile iron*

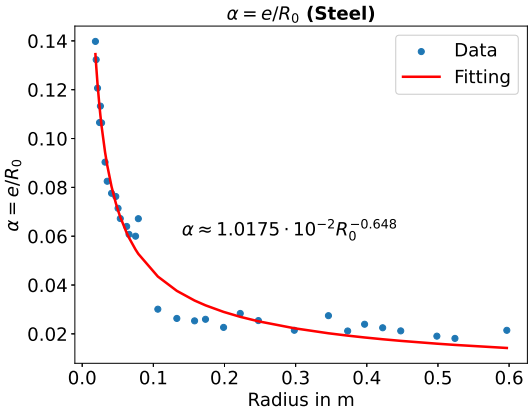

(b) *Steel*

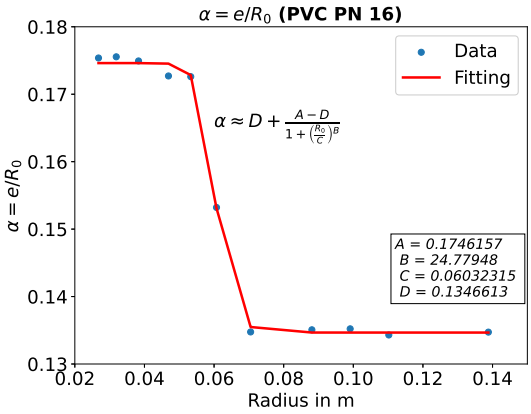

(c) *PVC*

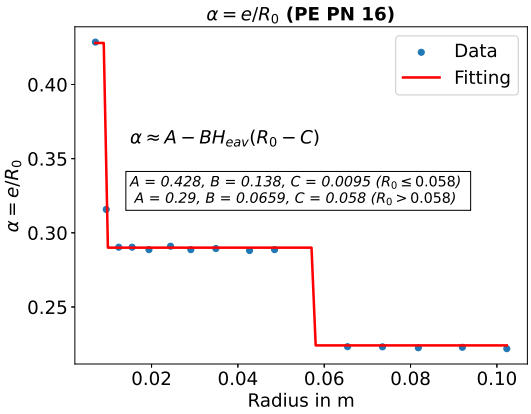

(d) *PE, LDPE, HDPE*

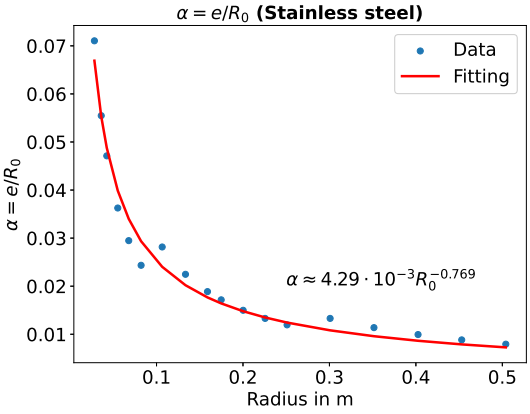

(e) *Stainless steel*

Figure 5.5: *Tube's thickness to its inner radius ratio, $\alpha \equiv \frac{e}{R_0}$, in function of the pipe materials.*

5.2.7 Solver overview

The herein numerical MOC solver is a home-made Python code operating with the open source Python package WNTR, [Klise et al., 2017], to optimize the network management of the original EPANET's data, [Rossman et al., 2020]. The oriented-object solver architecture is thereafter provided in Figure 5.6.

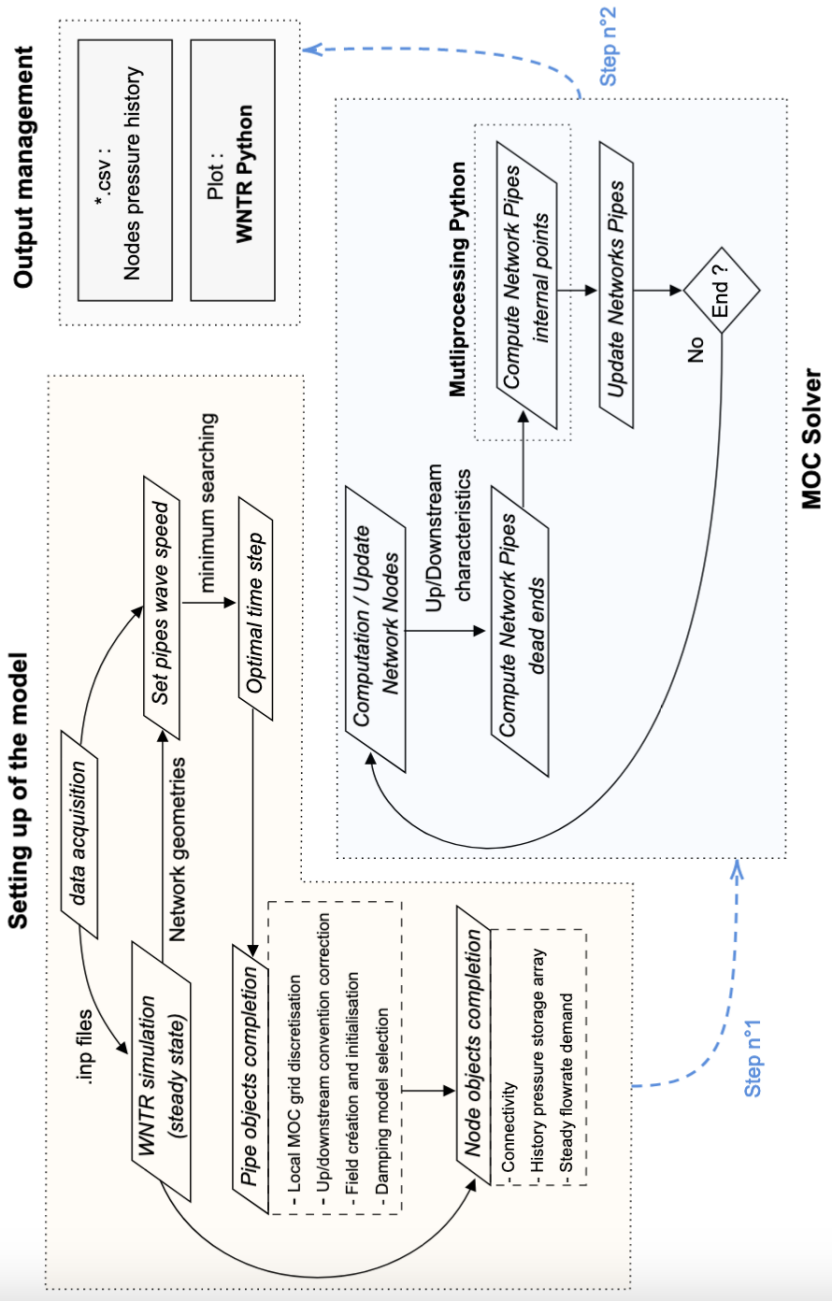

Figure 5.6: *Method of characteristic solver's MOC architecture.*

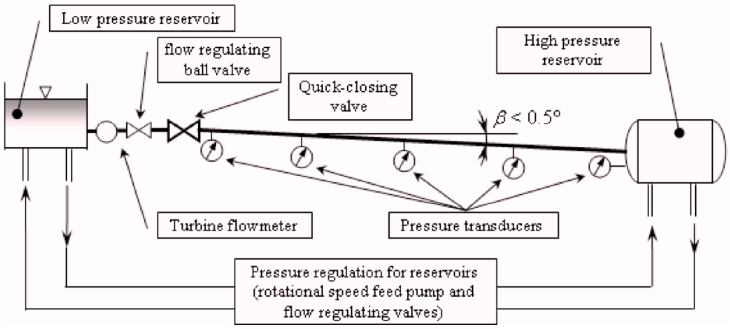

Figure 5.7: *[Adamkowski and Lewandowski, 2006]'s experimental setup.*

Density $(kg \cdot m^{-3})$	Elasticity (Pa)	ν_f $(m^2 \cdot s^{-1})$	ν_s	Geometry (m)
$\rho_f = 1000.$	$\mathcal{K}_f = 2.1 \cdot 10^9$	$9.493 \cdot 10^{-5}$	0.35	$R = 0.008$
	$E = 120.0 \cdot 10^9$			$e = 0.001$
				$L = 98.11$

Table 5.2: *Physical and geometrical properties for the analysis of the RPV system, [Adamkowski and Lewandowski, 2006].*

5.3 Numerical to experimental validations

The numerical code, along with the implementation of the viscous wall shear rate models, is validated and analyzed with respect to the experiments of [Adamkowski and Lewandowski, 2006], [Malesińska et al., 2021] and the numerical analysis of [Kim, 2022]. In the forthcoming, notations $(DW), (TVB), (BP), (Z), (Bru)$ are adopted to refers to the Darcy-Weisbach, [Vardy and Brown, 2007], [Bayle and Plouraboué, 2022], [Zielke, 1968] and [Brunone et al., 1991] models, respectively.

5.3.1 Comparison with [Adamkowski and Lewandowski, 2006]'s experiment

The [Adamkowski and Lewandowski, 2006]'s experimental setup dimensions are provided in Table 5.2 along with the Figure 5.7. Two different initial flows are investigated, $W_0 = 0.066m/s$ and $W_0 = 0.940m/s$, the respective laminar and turbulent Reynolds being $Re = 1100$ and $Re = 15843$. For the low-Reynolds number study case, i.e. Figures 5.8a-5.8c&5.8e, the WFB models are found close to each-other and better represent the signal attenuation and sharpness than other wall shear rate models (quasi-steady and IMAB). The quasi-steady model fails to describe the pressure patterns while the IMAB struggles to represent the peak's sharpness. This is an expected result since WFB models have been analytically established for laminar flows by [Zielke, 1968, Bayle and Plouraboué, 2022]. However, at $Re = 15843$, i.e. Figures 5.8b-5.8d&5.8f, the IMAB model better represents the

Wall shear rate models	$Re = 1100$	$Re = 15843$
Darcy-Weisbach	88.48%	17.63%
[Vardy and Brown, 2007]	5.98%	9.91%
[Zielke, 1968]	5.23%	8.83%
[Bayle and Plouraboué, 2022]	5.8%	10.87%
[Brunone et al., 1991]	16.22 %	5.50 %

Table 5.3: *Relative Δ_{L^2} norm between the MOC's models and the [Adamkowski and Lewandowski, 2006]'s experiment.*

signal attenuation and phase shift than WFB ones, which under estimates the pressure peak's amplitudes but correctly depicts peak's sharpness. For the very same Reynolds number, the quasi-steady model surprisingly matches with the experimental data and seems to provide a better description of the peaks attenuation than WFB ones. In the water hammer early-stage, a line packing phenomena, i.e. the linear pressure increase due to fluid accumulation [Chaudhry, 2014], slightly modified the expected [Joukowsky, 1904]'s overpressure by nearly 5%. The relative Δ_{L^2} norm, defined as

$$\Delta_{L^2}(\%) = 100 \frac{\int_0^t ||P_{exp} - P_{MOC}||^2 dt}{\int_0^t ||P_{exp}||^2 dt}, \tag{5.44}$$

is also investigated for the different models as an accuracy indicator. This indicator is thereby used to assess the numerical to experimental errors at several pipe locations. This approach nevertheless fails to provide an exhaustive description of the energetic losses, i.e. along the whole pipe, since only space-located error are considered. This limit can be overcome following [Duan et al., 2017], who have extended the energetic balance approach of [Karney, 1990] to characterize the global energetic variations induced by the fluid viscosity, versus the wall shear rate model. Despite the hereby analysis only assesses the error between experiment and numerical predictions, this point deserves to be emphasized. The corresponding values of Δ_{L^2} are presented in Table 5.3. The analysis of the relative L^2-norm goes along with our previous conclusions. The relevance of the WFB's model to characterize the laminar flow regime is degrading when the regime is turbulent, for the benefit of IMAB's models. To provide additional insights on the observed slight Reynolds-dependent differences between the models, the wall shear rate at the middle pipe location is investigated, the results of which are provided in Figure 5.9. For laminar flow, the wall shear rate is poorly affected by the quasi-steady contributions, the main viscous damping arising from the transient response of the boundary layer, i.e. WFB or IMAB modes. In contrast, for $Re = 15843$, the contributions of the transient WFB and IMAB models to the overall damping appear weak. This justifies the relevance of the Darcy-Weisbach model, a striking

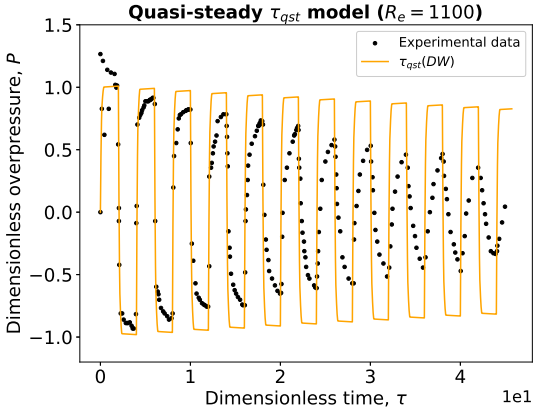

(a) *Quasi-steady model ($Re = 1100$)*

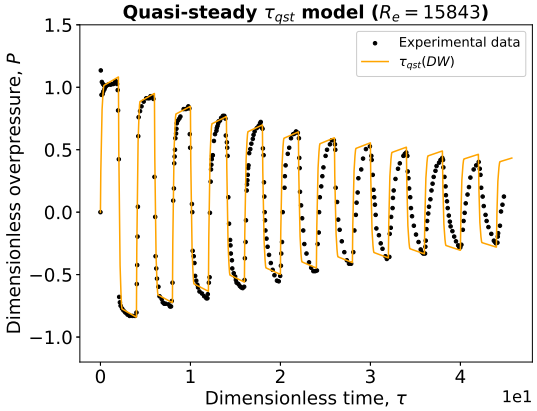

(b) *Quasi-steady model ($Re = 15843$)*

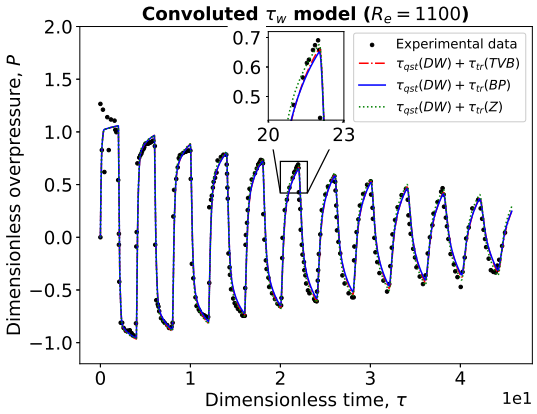

(c) *WFB models ($Re = 1100$)*

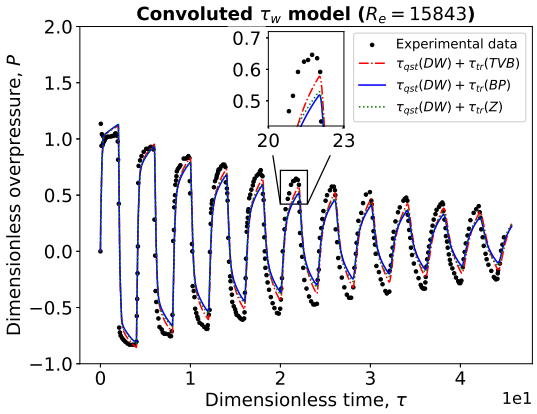

(d) *WFB models ($Re = 15843$)*

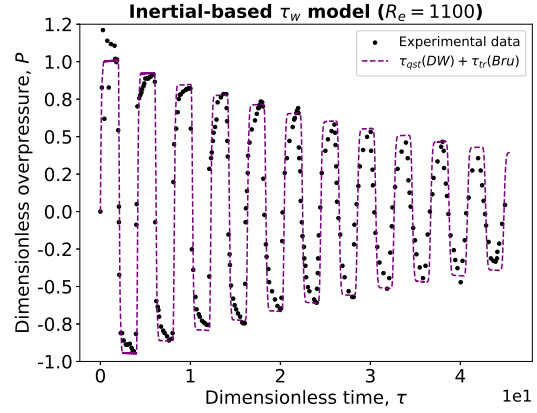

(e) *IMAB model ($Re = 1100$)*

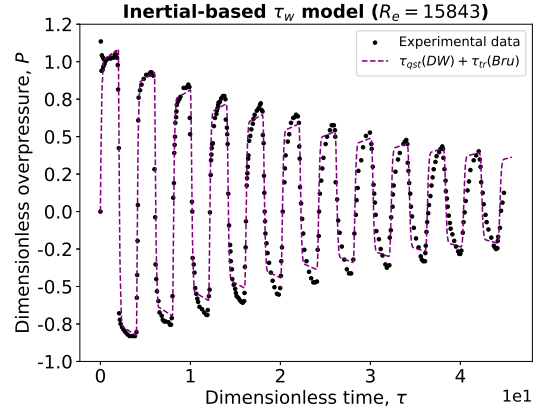

(f) *IMAB model ($Re = 15843$)*

Figure 5.8: *MOC numerical prediction compared with the experimental data of [Adamkowski and Lewandowski, 2006].*

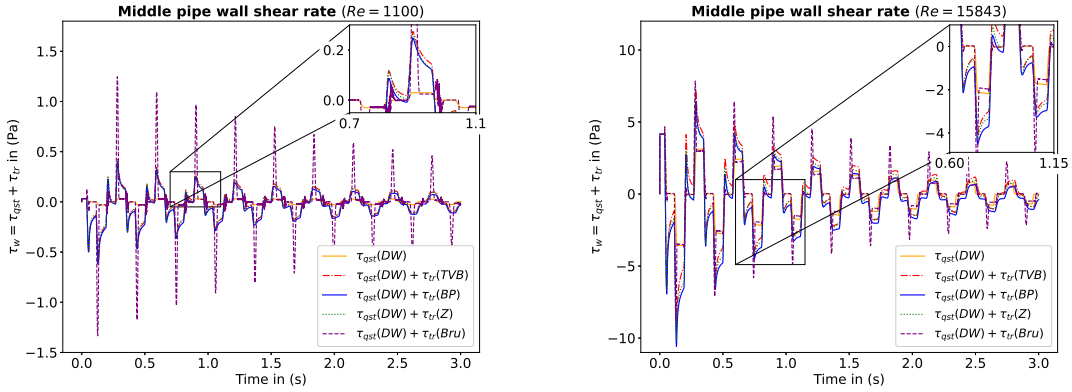

(a) τ_w *at* $Re = 1100$. **(b)** τ_w *at* $Re = 15843$.

Figure 5.9: *Wall shear rate model comparison for the [Adamkowski and Lewandowski, 2006]'s experiment.*

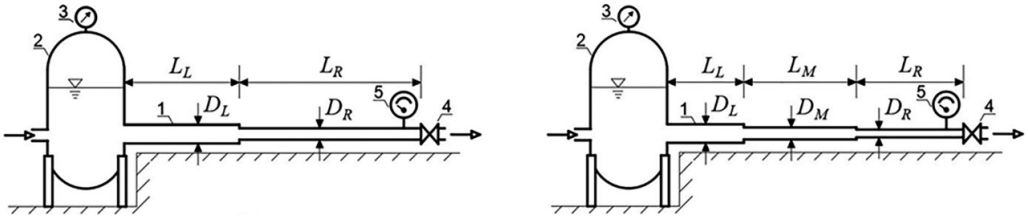

(a) *One narrowing* **(b)** *Two narrowing*

Figure 5.10: *[Malesińska et al., 2021]'s experimental setup*

observation also reported by [Ferrari and Vento, 2020]. The peaks depicted in the IMAB's wall shear rate models arise from numerical difficulties to handle the flow-rate time derivative in (1.44), which are found close to the Dirac distribution when instantaneous perturbations are considered. Very similar peak patterns occurs in the WFB models but are smoothen by the convolution product. This preliminary numerical validation is now extended to the analysis of in-line connected pipe branch with diameter heterogeneity, experimentally studied in [Malesińska et al., 2021].

5.3.2 Comparison with [Malesińska et al., 2021]'s experiment

The [Malesińska et al., 2021]'s experimental setup dimensions are provided in Table 5.4 along with the Figure 5.10. Two configurations are hereafter analyzed: (i) one narrowing and, (ii) two narrowing, the result of which are provided in Figures 5.11a-5.11f. The experimental measurements are performed at the downstream end of the in-line hydraulic configuration. For the one narrowing configuration, i.e. Figures 5.11a-5.11c and 5.11e, the numerical simulations show close agreements

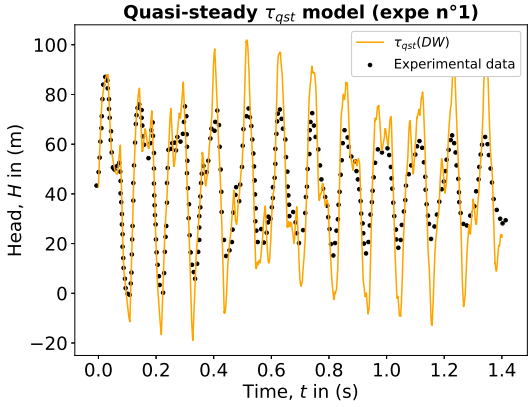

(a) *Quasi-steady model, one narrowing*

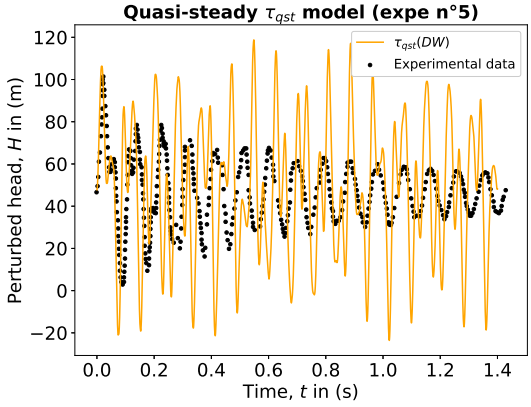

(b) *Quasi-steady model, two narrowing*

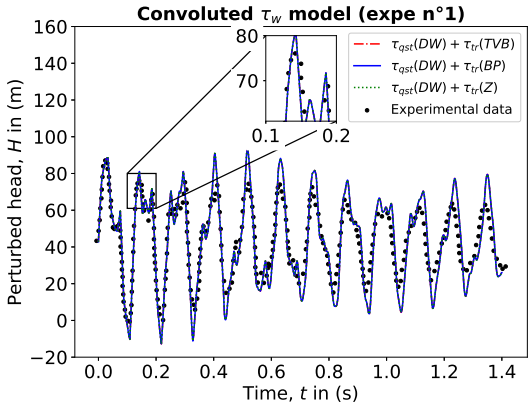

(c) *WFB models, one narrowing*

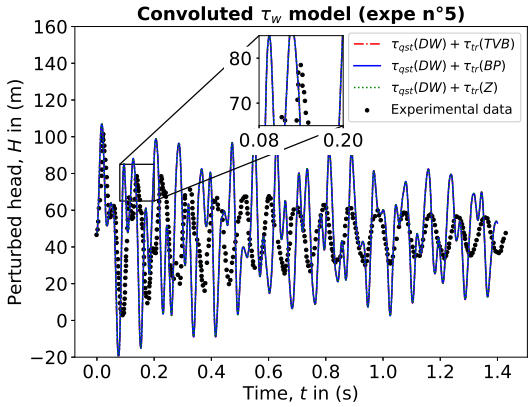

(d) *WFB models, two narrowing*

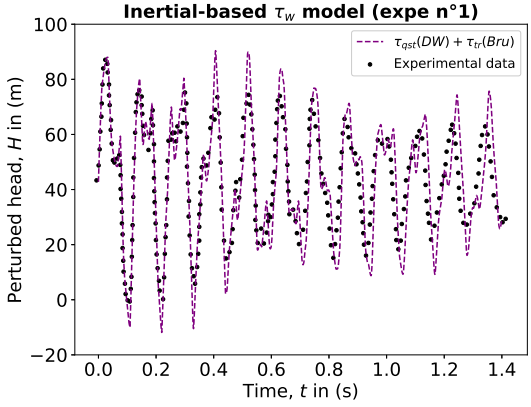

(e) *IMAB model, one narrowing*

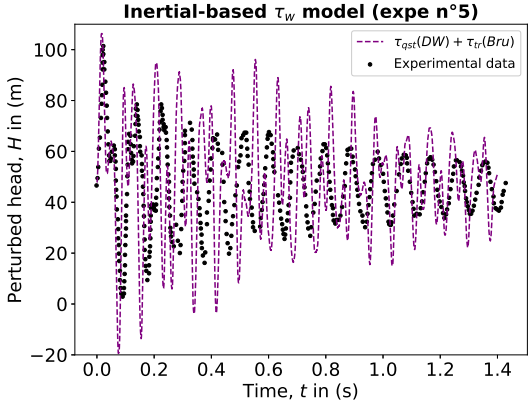

(f) *IMAB model, one narrowing*

Figure 5.11: *MOC numerical predictions compared with the experimental data of [Malesińska et al., 2021].*

Density $(kg \cdot m^{-3})$	Elasticity (Pa)	ν_f $(m^2 \cdot s^{-1})$	ν_s
$\rho_f^\star = 1000.$	$\mathcal{K}_f^\star = 2.1 \cdot 10^9$	$9.493^\star \cdot 10^{-5}$	$0.3^\star$
	$E^\star = 120.0 \cdot 10^9$		

(a) *Physical properties.*

Pipe	Diameter	Thickness	Length
n^o1	$42mm$	$2.6^\star mm$	$26.45m$
n^o2	$26.5mm$	$2.2^\star mm$	$21.2m$

(b) *One narrowing geometries*

Pipe	Diameter	Thickness	Length
n^o1	$42mm$	$2.6^\star mm$	$13.3m$
n^o2	$35mm$	$2.4^\star mm$	$14.15m$
n^o3	$21mm$	$2^\star mm$	$12.2m$

(c) *Two narrowing geometries*

Table 5.4: *Physical and geometrical properties for the analysis of the experimental setup of, [Malesińska et al., 2021]. (⋆) refers to unavailable data in the original article.*

Wall shear rate models	One narrowing	Two narrowing
Darcy-Weisbach	7.70%	53.34%
[Vardy and Brown, 2007]	3.46%	36.30%
[Zielke, 1968]	3.44%	36.27%
[Bayle and Plouraboué, 2022]	3.42%	36.24%
[Brunone et al., 1991]	4.49%	29.22%

Table 5.5: *Relative Δ_{L^2} norm between the MOC's models and the [Malesińska et al., 2021]'s experiment.*

with the experimental data for all the considered wall shear rate models. The WFB's models once again provide pressure signatures close to each-others despite the steady Reynolds number in the downstream pipe is estimated at $Re \approx 5 \cdot 10^3$. Since no fitting parameters have been used, the pressure signature phase is surprisingly well described, and so does the fluid pulse wave speeds. All the models nevertheless suffer from a poor description of the long-time damped dynamic, the quasi-steady model being the less accurate. The analysis of the second configuration, i.e. Figures 5.11b-5.11d and 5.11f, degrades these conclusions. While the short-time signal remains relatively well described by the numerical analysis, all the models rapidly fail to provide a relevant description of the signal characteristics, i.e. its amplitude and phase. The relative Δ_{L^2} norms, for both configurations, are provided in Table 5.5. The use of transient wall shear rate models, even for the second configuration, diminish the error between the MOC predictions and the experimental pressure signals.

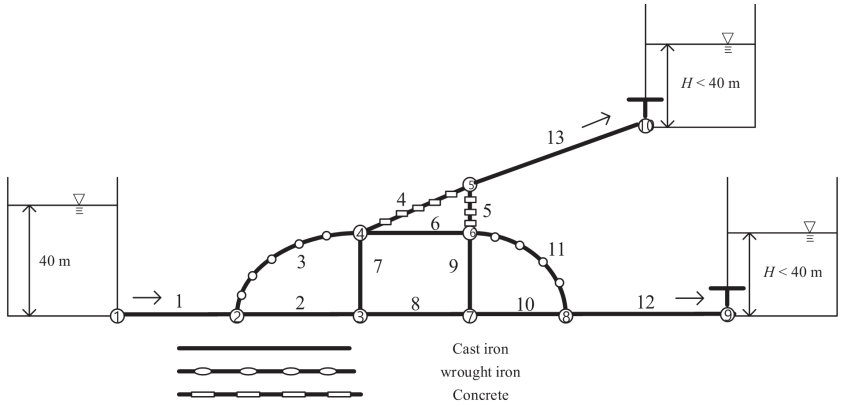

Figure 5.12: *[Kim, 2022]'s network topology.*

5.3.3 Comparison with [Kim, 2022]'s numerical analysis

[Kim, 2022] implemented the impedance matrix method, previously developed by [Zecchin, 2010], and applied it to the analysis of transient in a small idealize network, which is depicted in Figure 5.12 along with its geometrical properties in Table 5.6. Only a quasi-steady viscous damping model was considered by [Kim, 2022], so that no transient wall shear- ate model is used in the forthcoming comparison. The pressure signature at node n^o9 (Cf. Fig. 5.12) is provided in Figure 5.13 for both approaches. The herein MOC numerical code reveals a close agreement with the prediction of [Kim, 2022] despite slight differences in the wave speed model. These differences nevertheless introduce some signal high-frequencies mismatch, having small amplitudes. Furthermore, the observed differences may arise from a different modeling of the Darcy-Weisbach friction factor. While [Kim, 2022]'s considered a constant initial-Reynolds-based friction coefficient factor f_{DW}, the present MOC procedure both updates, in time and space, the value of f_{DW} to match with the local flow conditions according to the steady-state EPANET, [Rossman et al., 2020] correlations. These set of experimental and numerical comparisons validate the MOC approach and provide reliable base for further analyses. An on-field, realistic, study case has been set up on a small sub-network of the Toulouse's WDN, the results of which are hereafter discussed.

5.4 On-field networks investigation

In order to further investigate the MOC solver ability to model operational hydraulic network transient life, a on-field test has been carried out. First, a strategic zone has been identified, so as to have a low connectivity to the rest of the network and mainly composed of carbon materials (e.g. ductile iron, stain). Then, the hydraulic flow condition and pressure distribution are investigated and some hydraulic components are simplified (e.g. simplification of pressure regulation valves and connection to households). Finally, the valve head loss coefficient K_0 defined in (5.42) is determined and the MOC predictions to the on-field measurements

Pipe	Length (m)	Diameter (m)	[Kim, 2022]'s c_p (m/s)	MOC's c_p (m/s)	c_p relative error
$n°1$	100	40	1431.13	1392.90	2.67%
$n°2$	60	40	1431.13	1392.90	2.67%
$n°3$	80	32	1451.53	1398.90	3.63%
$n°4$	60.42	25	1247.34	1367.97	9.67%
$n°5$	25	25	1247.34	1367.97	9.67%
$n°6$	55	40	1431.13	1392.90	2.67%
$n°7$	40	40	1431.13	1392.9	2.67%
$n°8$	55	40	1431.13	1392.9	2.67%
$n°9$	40	40	1431.13	1392.9	2.67%
$n°10$	50	40	1431.13	1392.9	2.67%
$n°11$	70	32	1451.53	1398.90	3.63%
$n°12$	150	40	1431.13	1392.9	2.67%
$n°13$	100	40	1431.13	1392.9	2.67%

Table 5.6: *[Kim, 2022]'s network geometries*

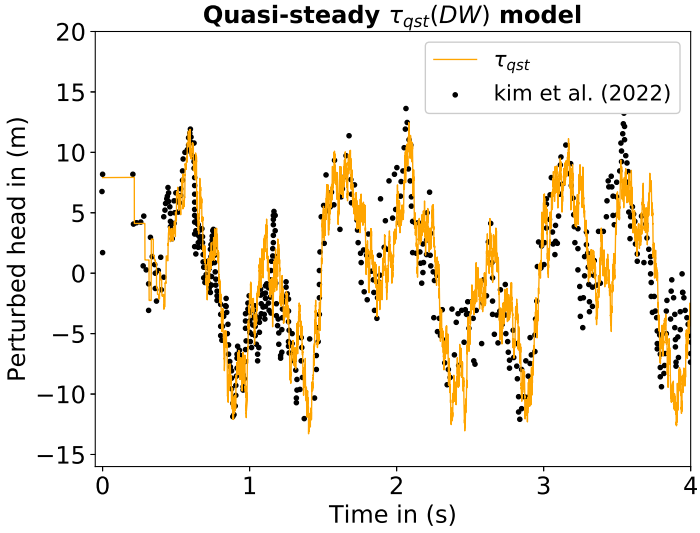

Figure 5.13: *Comparison to the numerical predictions, based on the impedance matrix technique, of [Kim, 2022].*

are analyzed. Few studies have reported the comparison between some numerical predictions and on-field transient response of WDN, [Ebacher et al., 2011], although a crucial step for practical relevance of modeling approaches. The test network is composed of 198 pipes and fed upstream by a constant head reservoir, the value of which has been settled to match with the mean daily head variation at this point. An overview of the investigated sub-network is depicted in Figure 5.14. The opened and closed PRV valve, depicted on Figure 5.14a, have been respectively modeled by a simple node (i.e. fully open valve without head loss) and a dead-end configuration. The network skeletonization simply follows from the available EPANET model, provided by SETOM, while the minor connection to users have been disregarded. At the input node, an hydrant have been opened and its flow-rate controlled by a control valve. Then a new steady-state is reached from the hydrant opening condition and once re-stabilized, the valve is suddenly, manually, closed by an operator. The resulting pressure transient signature is recorded at two output nodes in the network (Cf. Fig. 5.14). The pressure sensors have a frequency sample rate of 100 Hz (which allows the analyses of the low frequency transient response band), a resolution of ± 150 mBar, and a measurement range of $0 - 30$ Bar. The pressure sensors time synchronization was manually handled by clocking the sensors on the internal clock of a computer a few moment before the experiment began. It latter appears a poor synchronization due to manufacturer technical issues, then leading to a residual incertitude on the time localization of the pressure signatures. In the forthcoming numerical to experimental comparisons, the experimental signals are consequently time shifted to match with the first pressure rise at each measurement locations. The pressure input impulse at the valve is also recorded, to provide a measurement of the initial overpressure generation. The network diameter and material distributions have been regarded from the perceptive of inducing fluid pulse wave speed variations in the network. It appears, regarding the test network theoretical wave speed distribution in Figure 5.15a, that the wave speed is quasi-constant across the whole network as its mainly composed of ductile iron material (Cf. Fig. 5.15b) and the diameter heterogeneity is weak (Cf. Fig. 5.15c). The strategic set of small dimensionless parameters introduced in §3, i.e. $\left(\delta = \sqrt{\frac{\nu_f L}{c_p R_0}},\ \mathcal{M} = \frac{W_0}{c_p},\ \epsilon = \frac{R_0}{L}\right)$, have also been investigated as depicted in Figure 5.16. The asymptotic low-Mach framework and long-wavelength framework established in §3 stipulates the need of $\delta \gg \epsilon^2$ and $\delta^2 \gg \mathcal{M}$ conditions to be ensured in order that viscous corrections to prevail over inertial ones. While the first conditions is unquestionably satisfied regarding the Figure 5.16e, then satisfying the long-wavelength framework, the second low-Mach conditions is not always ensured regarding the values of the ratio $\delta^2/\mathcal{M}$ provided in Figure 5.16f. Then, some additional inertial corrections may occur in the network, which are expected to couple the transient response of the system to its preexisting flow conditions according to the non-linear Navier's term in the Navier-Stokes equations (Cf. §3.3 or [Bayle and Plouraboué, 2022]). Despite the Mach number is small, as illustrated in Figure 5.16d, its impact on the network

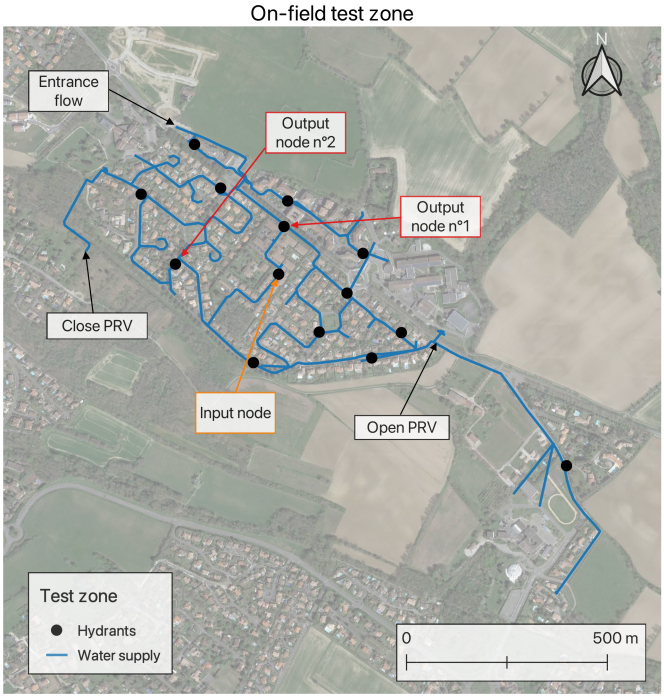

(a) *On-field test network characteristics.*

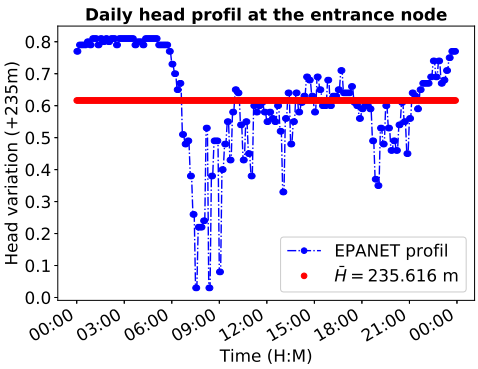

(b) *Input head daily variations.*

(c) *Input hydrant perturbation.*

Figure 5.14: *Test zone overview.*

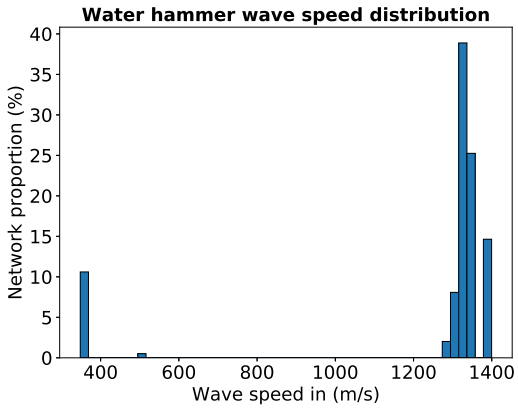

(a) *Theoretical wave speed distribution in the test network.*

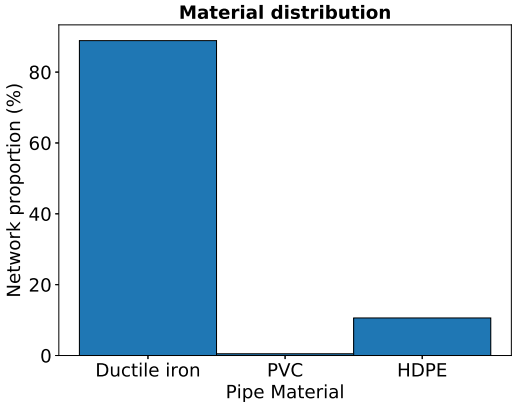

(b) *Pipe's material distribution in the test network.*

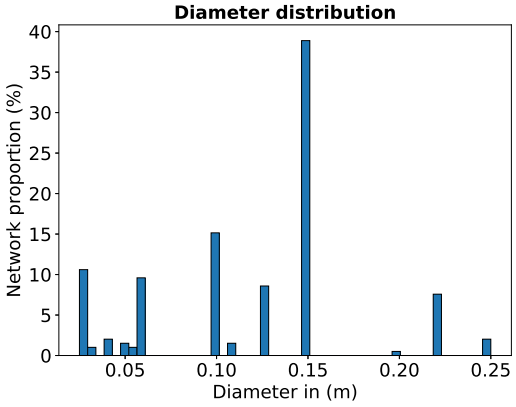

(c) *Pipe's diameter distribution in the test network.*

Figure 5.15: *Characteristic parameter distributions for the investigated test network.*

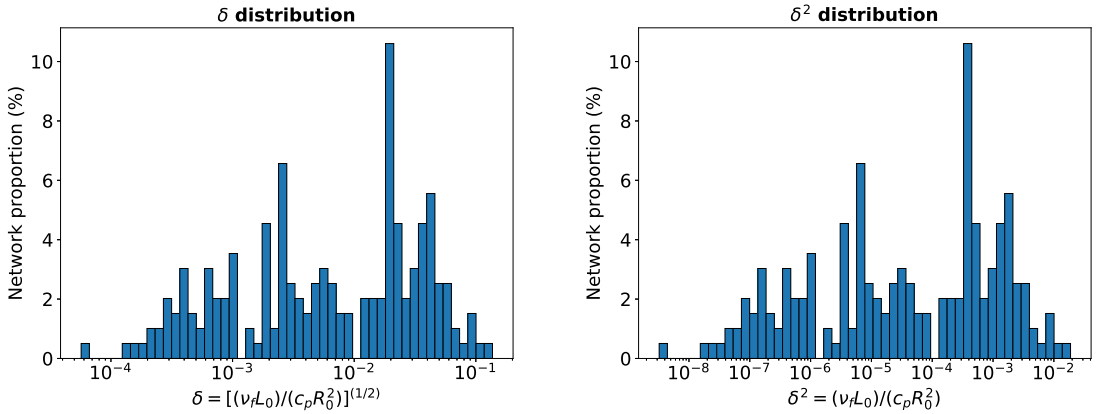

(a) δ *distribution.*

(b) δ^2 *distribution.*

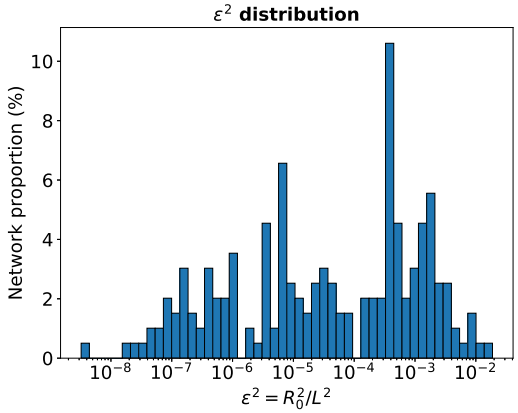

(c) ϵ^2 *distribution.*

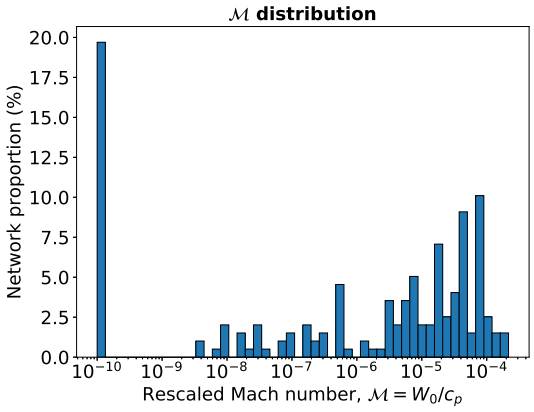

(d) $\mathcal{M}$ *distribution.*

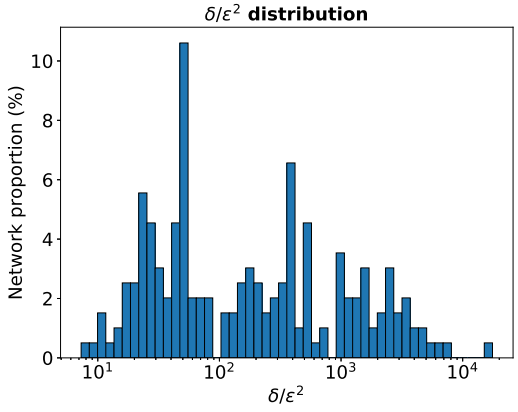

(e) δ/ϵ^2 *distribution.*

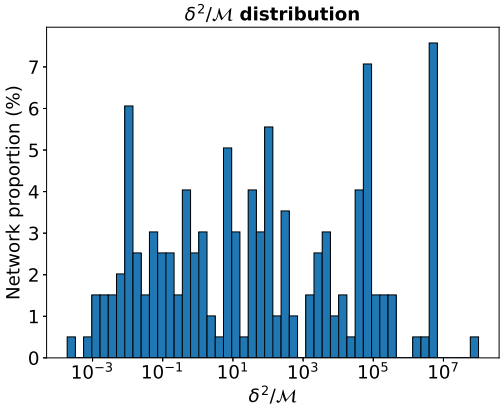

(f) $\delta^2/\mathcal{M}$ *distribution.*

Figure 5.16: *Small dimensionless asymptotic number distributions for the investigated test network. The hydrant input flow-rate is equal to* $10m^3/h$ *for the herein distributions.*

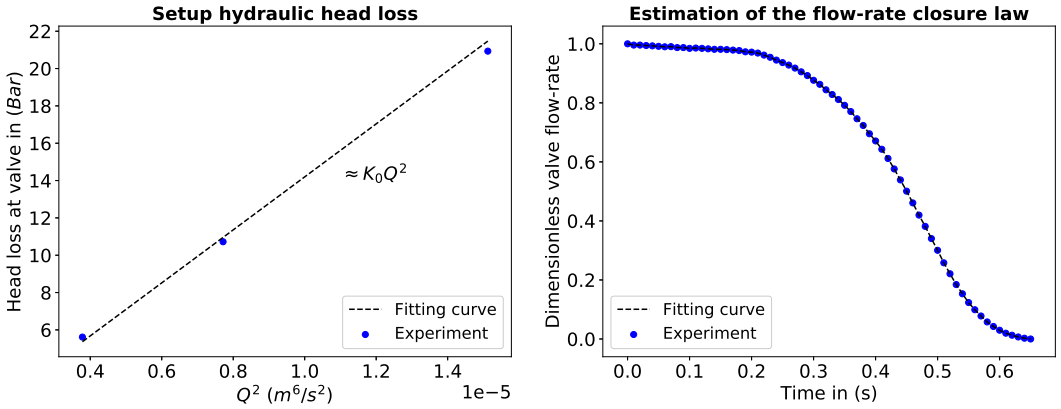

(a) *On-field valve setup head loss law.* **(b)** *Experimental closure flow-rate.*

Figure 5.17: *Experimental valve and closure properties*

transient may be important in some of the network's subareas. The herein MOC procedure nevertheless does not account for inertial effects and we then assume a model simplification. At the input node, the valve generates a singular head loss following relation (5.41). The steady-state head loss valve coefficient K_0, is hereafter estimated. This is accomplished from measuring the pressure upstream to the valve and the flow-rate through it. By squaring the flow-rate, a linear relation is obtained between the head loss and the flow-rate according to (5.42), the slope of which is a function of K_0. For the hereby experimental configuration, K_0 was experimentally measured at $K_0 \approx 0.257 m^{-5} \cdot s^2$, the experimental data used for the estimation being shown in Figure 5.17a. The closure law trend is finally provided in Figure 5.17b, along with its flow-rate fitting curve. The simulation results are hereafter provided, for two tests realized with an initial perturbation amplitude of $\Delta Q \approx 10 m^3/h$ and $\Delta Q \approx 14 m^3/h$, in Figure 5.18. In both tests, the pressure increase at the input and output n°2 nodes are well described by the model, so does their first harmonic. Nevertheless, its seems clear that the results are unsatisfactory for longer time as the model fails to reproduce the damping following the pressure increase at the input node. The results at the output node n°1 are even more unexpected. The pressure increase is poorly described and a second pressure increase is observed just after the first initial pressure front. This sudden secondary increase is unexpected regarding the sub-network topology. Several operational conclusions are reached from the on-field investigations.

The control valve damping effects on the first pressure decrease phase ($\approx 0.6s$ in Figure 5.18a and $\approx 1s$ in Figure 5.18b) is numerically lower than the one experimentally observed. The numerical second overpressure peaks then propagates and is found in both output responses, as displayed in Figures 5.18c to 5.18f. The valve closure, which has been manually operated, may also interferes with the results. The closure time, of the second order of magnitude in each test case, does

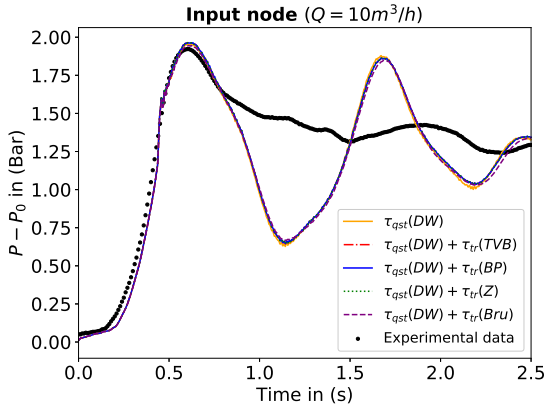

(a) *Comparison at the input node,* $\Delta Q = 10m^3/h$.

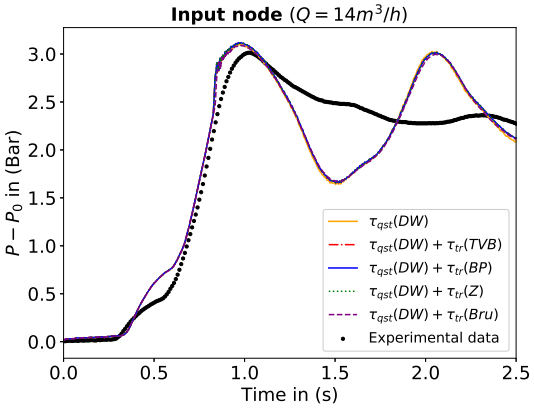

(b) *Comparison at the input node,* $\Delta Q = 14m^3/h$

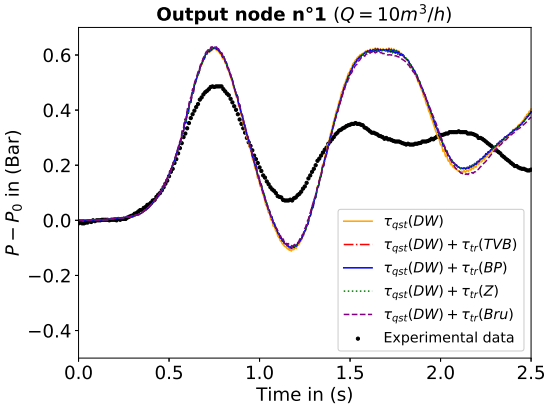

(c) *Comparison at the output node n°1,* $\Delta Q = 10m^3/h$

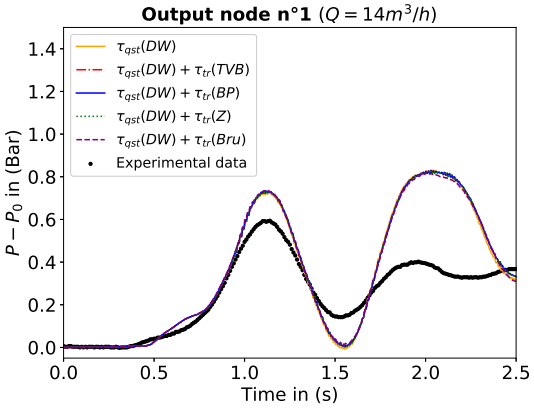

(d) *Comparison at the output node n°1,* $\Delta Q = 14m^3/h$

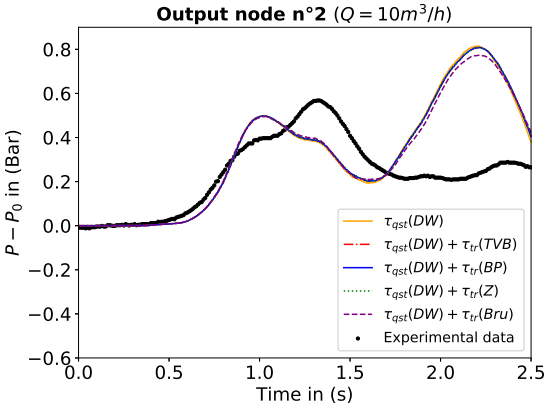

(e) *Comparison at the output node n°2,* $\Delta Q = 10m^3/h$

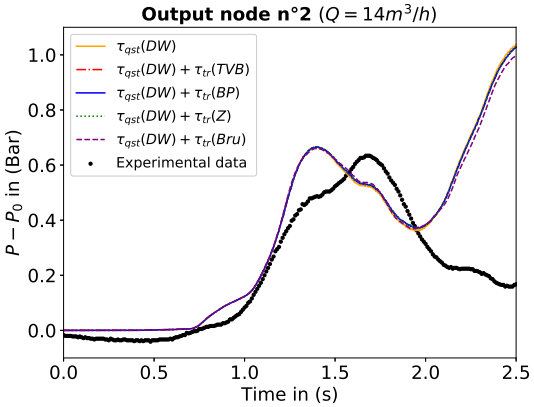

(f) *Comparison at the output node n°2,* $\Delta Q = 10m^3/h$

Figure 5.18: *Comparison between MOC simulations and on-field recorded pressure signals.*

not allow the generation of proper water hammer waves. The non-instantaneous valve closure causes a coupling between the water hammer (fast) network transient response and its slow steady-state head re-establishment one. This point is nevertheless crucial at the pipe narrowing. While the water hammer boundary condition does not account for the local head losses occurring at pipe narrowing, i.e. perfect acoustic reflection conditions, the network slow response is enslaved by these energetic losses. This point should analyzed in further investigations. Regarding the closure signals in Figures 5.18a and 5.18b, the head profile indeed seems to step up from the initial steady-state head profile to a new one, the small amplitude pressure overshoot being associated with the water hammer effect, which does not match with the [Joukowsky, 1904]'s criteria. Furthermore, the presence of minor branches in polymeric materials may plays an important role in the overall network dynamic response as recently addressed by [Meniconi et al., 2018]. These materials are mainly of small diameters and are located at the network dead-ends but they are not considered in the herein analysis. However, such rheology behavior is known to produce higher damping effects than elastic ones (Cf. §4), which may be an important point to consider in further analysis. From an operative viewpoint, the repetition of closure and opening tests, i.e. a loss of water in the network, leads to a head re-establishment in the sub-network though automatic consign transmitted to the upstream PRV valve (Cf. Fig. 5.14a), the variations of which have perturbed the transient measurement by adding supplemantary uncontrolled flow and head variations. The complex influence of *active end users* and water consumption on the water hammer predictions have recently been investigated by [Marsili et al., 2021, Meniconi et al., 2022], then pointed out the relevance of such operative behavior. All the wall shear rate models furthermore fail to predict the overpressure damping. The water hammer waves seem to attenuate much faster than what its theoretically and numerically predicted. The presence of inertial, Mach-driven, corrections, not considered in the herein MOC simulations, but relevant from the asymptotic standpoint (Cf. Fig. 5.16f), might be one possible reason for the observed mismatch. Nevertheless it remains allusive which effect is the more influential in these reported on-field measures among the various mentioned ones (discarding small visco-elastic pipes, "active" networks changes associated with the demand during the test, influence of $\delta^2 \ll \mathcal{M}$ corrections).

Chapter 6

Geolocalization of water-waves origin within urban hydraulic networks using time reversal of first event detection: Article to *Water Research*.

Several detection methods have been provided in §1. While these detection methods rely on complex signal analyses techniques and often need an in-depth knowledge of the network before any anomaly occurs, an operational efficient network anomaly detection procedure is hereafter provided. This technique, already investigated by [Pinto et al., 2012, Shen et al., 2016], only focuses on the first transient event signature, i.e. the initial transient pressure gradient, to backtrack the potential source. This method may suffers from pressure wave front refocusing errors [Waqar et al.,], i.e. the water hammer wave speed frequency dispersion due to FSI, polymeric and fluid viscous effects which does not allow an exact wave backpropagation. To overcome this limitation, a strategic operative concept of Region Of Interest (ROI) is defined and characterized, then distinguishing our approach from [Shen et al., 2016]'s one and enriching the classical anomaly detection framework.
In the forthcoming chapter, the high frequency pressure sensors were pre-installed by the operative company SETOM, while time synchronization was ensured through embedded GPS ships in each sensor. The frequency acquisition was set to 128 Hz, then being slightly different from the previous transient pressure acquisitions presented in the §5.

Geolocalization of water-waves origin within water distribution networks using time reversal of first event detection

R. Guibert, A. Bayle and F. Plouraboué

Institut de Mécanique des Fluides de Toulouse, IMFT, Université de Toulouse, CNRS, Toulouse, France

Abstract

Drinking water distribution networks in urban areas are daily subject to fast propagating pressure waves resulting from routine operations. These water-hammer waves lead to structural aging and facility damages, the origin of which is not easy to find but are sometimes of high managerial interest. In this contribution, we demonstrate that using a reasonable number of high-frequency pressure detectors distributed within the network combined with a proper post-processing method permits a close geolocalization of the damaging wave origin. The method is first tested and validated on a real water distribution network having approximately 26 000 pipes, whereas considering a known, prescribed waveorigin, so that the sensitivity to sensor number (sensor spatial density), sensor location and signal-to-noise ratio on the geolocalization robustness are analyzed in detail. It is then applied and illustrated over real sensor recordings the result of which are validated on the field from history matching. This paper thus presents the first field-scale geolocalization of water-hammer events origin test as well conditions for which, given sensor density and signal-to-noise ratio, the geolocalization success is to be expected.

Keywords: water distribution network, water-hammer, high-frequency detector, geolocalization

2010 MSC: 00-01, 99-00

*Fully documented templates are available in the elsarticle package on CTAN.

1. Introduction

Water hammer waves within Water Distribution Networks (WDNs) are a common hindrance resulting from many possible routine operations, either organized, voluntary or accidental. Not only these waves are responsible for structure wear, but they are also capable of facility damage. Intermittent water supply operations have indeed been correlated to incident damages in WDNs (Agathokleous and Christodoulou, 2016) pin-pointing both the detrimental influence of quasi-steady WDN dynamic but also the generated transients associated with related operations (e.g. valve opening and closure, pumps starting).

Since the water-hammer wave speed in WDNs is very fast (between for 350 m/s for the softest plastic pipes to 1200 m/s for cast iron pipes) having a rather slow attenuation, the wave generated at a given location can propagate over a large portion of the entire urban network within a few seconds before decaying in less than a minute. It results in a myriad of reverberation causing as much disorder and possible breakages as pre-existing weaknesses. Since the lifetime of these events inside the network is short, and since they are not numerous within a day (e.g less than a few per day in the considered city of about half a million people), the dynamic of each water-hammer event can be considered separately. Being able to find the origin of a cascade of reverberating waterwaves events is interesting from various viewpoints: patrimonial management, security, insurance, etc...

Nevertheless, this topic has not been developed in real WDNs because it necessitates overcoming several challenges, not been fully addressed yet. Firstly, urban WDNs are, in many cases, not sufficiently and reliably detected and observed in detail for precise modeling of transient waves into them to be relevant. Secondly, localizing the origin of water-hammer waves necessitates real-time high-frequency monitoring with widely distributed detectors, rarely deployed in WDNs. Thirdly, the computational cost of direct transient wave modeling in water distribution networks is very challenging either using the Method Of Characteristics (Wang et al., 2014; Nault et al., 2018; Meniconi et al., 2021; Moosavian and Lence, 2020; Riaño-Briceño et al., 2022), or finite volumes e.g (Pal et al., 2021; Zhang et al., 2021). Fourthly, an inverse method capable of identifying the origin of a reverberating water hammer

wave over a large network, solving as many direct problems as tentative tries for possible origin, is even more challenging. Last but not least, from a more fundamental viewpoint, even if the uniqueness of the wave origin from detecting reverberation waves has been established on discrete wave models on arbitrary networks (Caputo et al., 2019; Plouraboué et al., 2022), it is still a pending issue for continuum ones.

Hence, even if the idea of using the entire timecourse of signal reverberation within the network at the sensor location to enlarge as much as possible data collection is appealing, in practice, this approach is still very difficult to develop at the present state of the art (Che et al., 2021). As part of the European "Surge-Net" project, Ferrante et al. (2009) carried out leakage location tests using echo analysis, by combining Lagrangian and wavelet transforms signal analysis, in the Lintrahen's (Scotland) WDN main trunk. Shucksmith et al. (2012) performed leakage tests on Bradford's (Yorkshire, UK) WDN. The authors operated at the neighborhood scale (about 100m of weakly branched pipe) using spectral analysis for the leak echo-localization (cepstrum analysis) and with a wide variety of pipe materials (PVC, cast iron, asbestos–cement). Recently, Meniconi et al. (2015) also combined a wavelet transform analysis with a Lagrangian method to preliminary examine one of the main pressure transmission lines of Milan's (Italy) WDN. Although achievable on a district scale or the main supply pipes of a water distribution network, the implementation of such leak detection techniques is questionable for large-scale analysis. Indeed, techniques based on leak wave reflection suffer from a high sensitivity to propagation speed uncertainties and surrounding noise (Wang et al., 2021). Moreover, an idealized test case without leakage or blockage is required for allowing direct comparison with the field pressure signal in the absence of transients generated by users' consumption variations unavoidably present within WDN. In order to improve the matching between transient predictions and experimental observations laboratory experiments within controlled networks are thus interesting and useful, e.g (Meniconi et al., 2022a). However, such benchmark case is often not operationally possible or prone to modeling errors (e.g. cross-section pressure interactions, wave attenuation, incorrect network topology, etc...) as in other contexts such as quality event detection (Kessler et al., 1998).

This is why an approximate alternative method avoiding the cost of a complete timecourse of wave propagation evaluation is proposed and developed in this contribution, following (Meniconi et al., 2022b). Rather than trying to exploit the entire signal complexity recorded at each sensor location, we take advantage of the first arrival time only. This already permits back-track wave origin using a time-reversal method. Time reversal methods, either at the individual pipe level (Grigoropoulos et al., 2021) or at the network one (Shen et al., 2016) have already permit computationaly efficient source identification. This method has been used to develop noise-tolerant pipeline defect detection (Wang and Ghidaoui, 2018; Wang and Xie, 2018; Meniconi et al., 2021) in the precise context of water-hammer waves. This contribution aims to demonstrate that combining first-event detection with timereversal is an interesting strategy to geolocalize water-hammer events in real WDN.

The paper is organized as follows. Section 2.1 describes the material related to the urban network and the pressure sensors used within the study. Section 2.2 details the algorithm of the first event detection, time reversal method, and candidate order. Section 3.1 discusses the localization of prescribed events in a real WDN to test and validate the method efficiency and its sensitivity to detectors number (more precisely the sensor "density", the sensor number divided by the total node number in the network). Section 3.2 finally describes the application of the proposed method to the field's data to geolocalize real events and discuss the obtained results.

2. Materials and Methods

2.1. Materials

The materials consist in WDN data within which high-frequency pressure detectors are disposed of.

2.1.1. Water distribution network data

The entire network from the city of Toulouse (France) illustrated in figure 1a is composed of a total of 26 094 pipes. It has been formatted in Epanet format providing the pipe lengths, structural properties and diameters. The distinct pipe's composition within the network is

84 detailed in table 1, showing a great majority of cast iron material. The heterogeneity of pipe
85 diameters and lengths is illustrated in figure 1b and c showing a great diversity of diameter
86 and length over more than a decade.

Material	**Quantity (%)**	**Length (%)**
Iron	87.66	89.28
Steel	1.97	4.04
PVC	1.01	1.22
Others	2.15	1.46
Unknown	7.21	4.00

Table 1: Distribution of pipe materials. Other materials are inox, fiber, PE, and PVD.

87

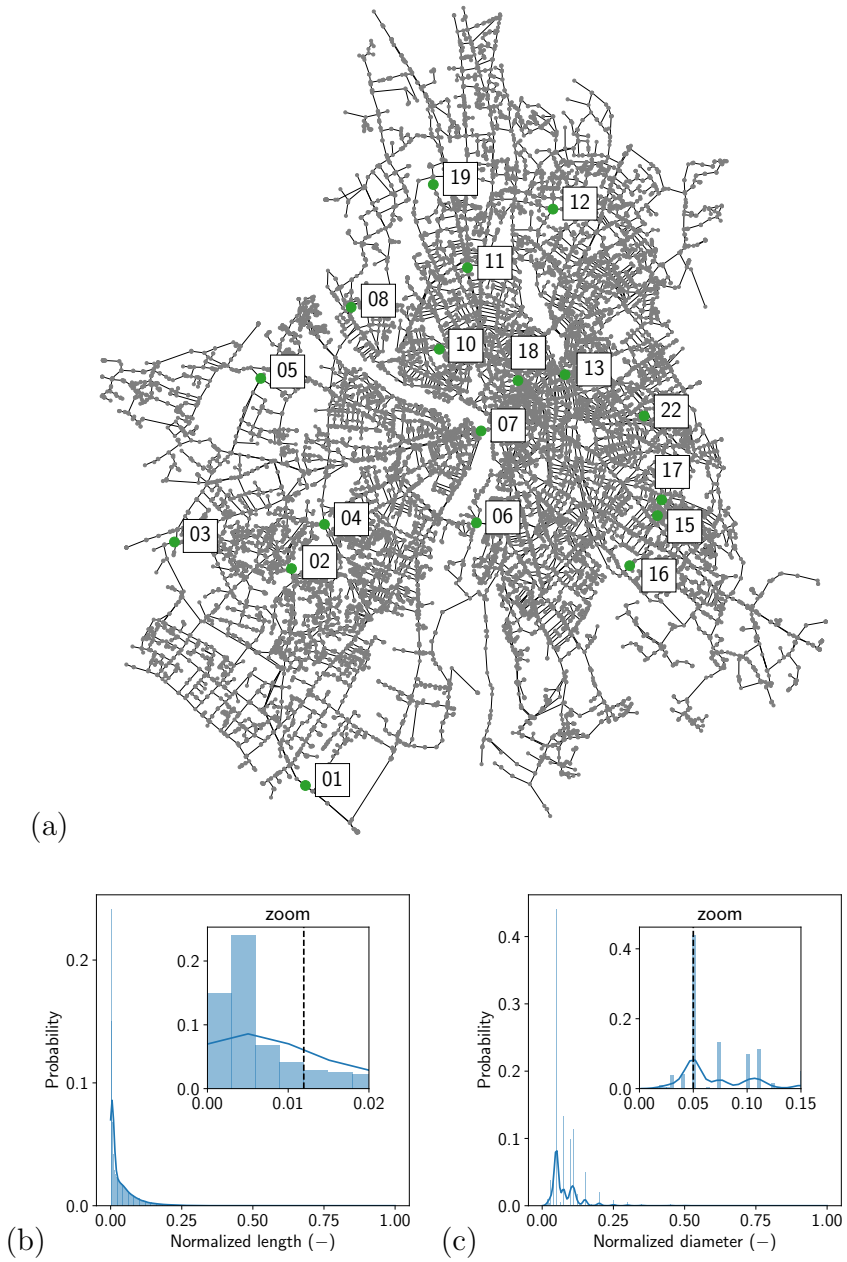

Figure 1: (a) Topography of the considered water distribution network. The network is composed of 23 784 nodes, 26 094 pipes for a total pipe distance close to 1 200 km. The positions of high-frequency pressure detectors (from 1 to 18), arranged within the network are illustrated with green dots. (b) Probability Density Functions (PDF) (with the corresponding histogram in zoom's inset) of dimensionless lengths (median 0.012 indicated with vertical dotted lines) normalized by maximal length. (c) same as (b) for dimensionless diameters (median 0.05) normalized with maximal diameter.

This result in wave-propagation heterogeneity to be taken care-off of considering the adapted velocity in each pipe. Local wave-hammer wave velocity indeed depends on the pipe diameter, length, thickness, Young modulus, and material density. It is estimated from known validated formulas (cf Appendix). Furthermore, the chosen location for high-frequency pressure sensors (18 in total) is depicted in Figure 1a with green dots, each described by a label between 1 to 18, being spatially uniformly distributed over the urban network.

2.1.2. High-frequency pressure detectors

Pressure detectors record at 128 Hz frequency with a $5000Pa$ accuracy. The recording mode is triggered by an awaking threshold which is empirically set from the base signal. These thresholds are chosen as a multiple (in-between 2 and 3) of the WDN time-variation base-signal. They are empirically chosen by the network manager, so as to have a reasonable number (about twenty) of ascents per day. Each sensor threshold lies in the range 1 ± 0.5bar over the local base-line average pressure. This precautionary procedure avoids recording embarrassing irrelevant signal series in the detection event database, also needed from the limited capabilities of the used sensors technology.

Since the event amplitude is expected within the range of $[0.8, 2]10^5$Pa, the relative precision on the detected peak amplitude is of the order of 6.25%. Also, only the time-arrival of the first peak is critical for the chosen method. Each detector has been primarily submitted to a pressure calibration test using a prescribed static pressure before field deployment. Each sensor has its own embarked battery and RAM. Once triggered to awaken mode, the detectors acquire at full high-frequency (i.e. 128Hz) during 300 seconds. The resulting collected data are then transmitted latelly with a standard GSM 3G protocol keeping each signal associated with each detector identifier.

2.2. Methods

The method decomposes into various steps : (i) first event detection into each detectors, (ii) back-propagation from detectors to potential source of detected event using the time-

reversal method and (iii) calibration of time-reversal method on the network and detector set. The methods associated with these three steps are now detailed. An additional noise sensitivity check of the method has also been used, the details of which is also given in 2.2.3.

2.2.1. First event detection and time reversal method

First event detection is performed using offline change point detection method (Truong et al., 2020). The detection criteria are associated with a functional minimization associated with the local gradient of the noisy signal. More precisely we use a binary change point detection to perform a fast signal segmentation, coupled with a L^2 cost function that detects meanshifts in the signal. The determination of the arrival times is illustrated for a real signal in figure 2.

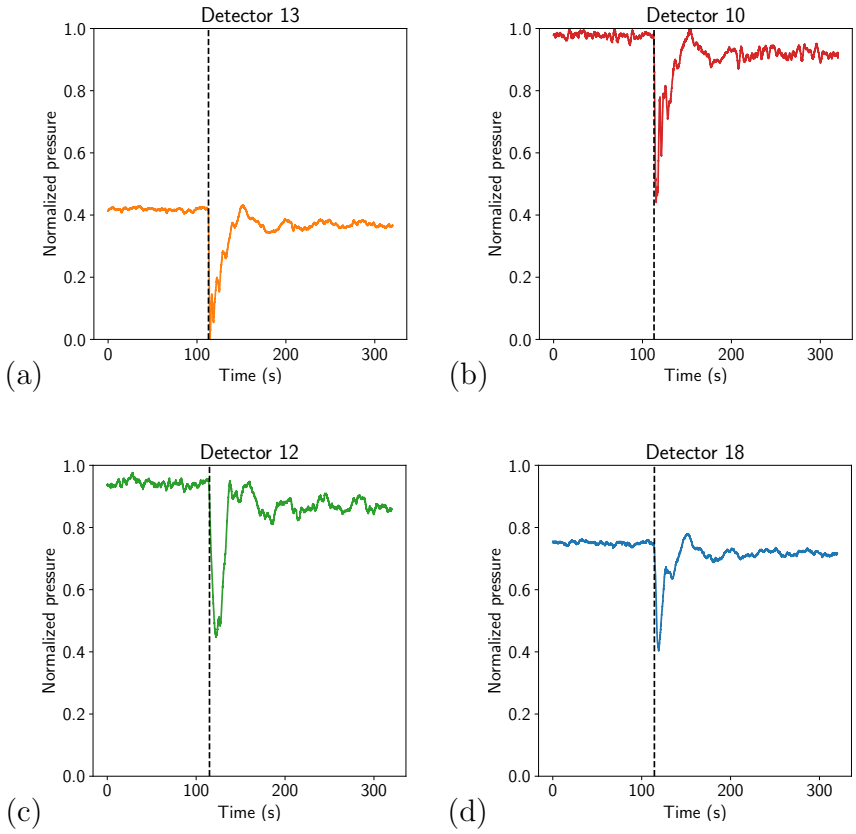

Figure 2: Illustration of change point detection applied to a real pressure signal detected on the considered WDN (figure 1a) using high-frequency detectors. The illustrated event is discussed in subsection 3.2. For each signal related to the event, the normalized pressure is reported versus time (cf figure 7). The obtained arrival time is represented by the vertical dashed line. The signal is captured almost simultaneously at detectors #13 and #10 (respectively at time 112.92 and 112.96 s), then at detector #12 (at time 114.29 s), and finally at detector #18 (115.00 s).

Time reversal of first event detection within the network follows the approach proposed in Shen et al. (2016). The method principle is detailed in Figure 3. As a prerequisite, each pipe is associated with a time propagation resulting from computing the ratio between pipe length and velocity evaluated following the Appendix formula. Then the signal processing starts when an event has been detected, resulting in a first-time arrival (denoted t_i, $i = 1, 2, 3$ in figure 3a) of the signal at various awaken detectors (denoted d_i, $i = 1, 2, 3$). For each pair

of detector/non-detector nodes in the network, a totaltime is evaluated by computing the sum of each time propagation within each pipe along the shortest path between those within the network, as depicted in figure 3b. Performing this total time of propagation between each node and one detector results in the detector back-propagation cartography depicted in figure 3c for detector d_1, figure 3d for detector d_2 and figure 3e for detector d_3. Now using the first-time arrival component vector t_i, $i = 1, 2, 3$, results in back-propagating-time vectors at each node (each time is colored with the same color as the detector with which it is associated in figure 3f). In Shen et al. (2016) the source node is the one with minimum variance back-propagating-time vector as illustrated in figure 3f. Note, however, that depending on the recorded time, several source nodes are possibly found with this method as depicted in figure 3e. Hence, in the case of noisy recordings one can infer that, in this case, the true source might not necessarily be the one having the minimum variance. Hence, to give more robustness to the method (but less sensitivity) we extend the search for the true source by considering the sorted list of back-propagating-time vector variances to find the "best" source candidates. This sorted list has to be closed, keeping with a "reasonable" number of possible candidates. This is what we call the method "calibration" as detailed in the next section.

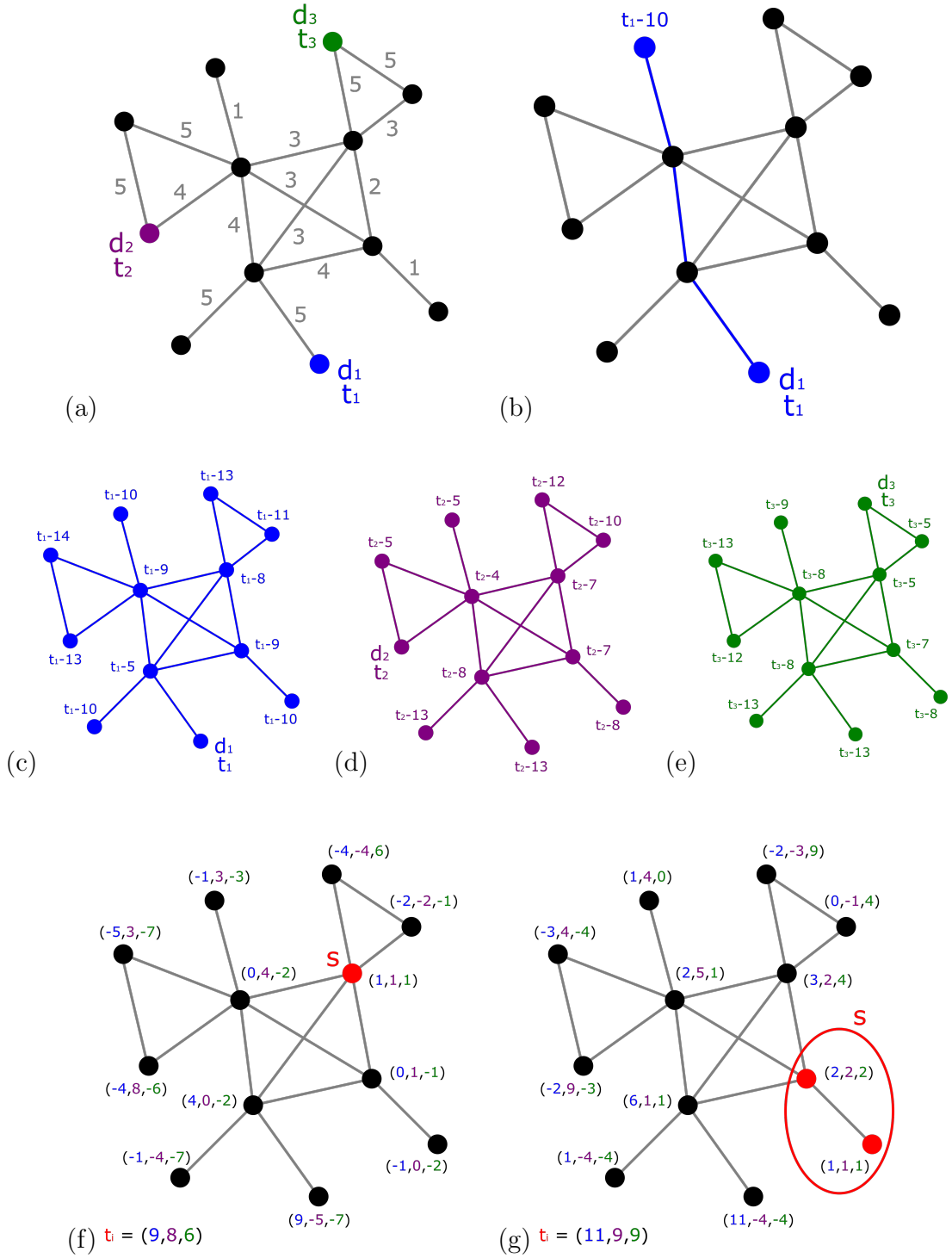

Figure 3: Time-reversal propagation method principle. (a) awaiken detectors d_i, $i = 1, 2, 3$ at first passage time t_i, $i = 1, 2, 3$ (b) Shortest-path between detector d_1 and one node. (c,d,e) Back-propagation cartography for detector d_1-d_2-d_3. (f) For a given arrival time vector, the source node is the one having a back-propagation vector with minimum variance. (g) Depending on the first passage time t_i, the resulting time arrival time vector can lead to several possible source nodes.

149

150 *2.2.2. Calibration of the time reversal method*

151 In the original research (Shen et al., 2016), the locality condition is widely discussed. Two
152 main aspects are highlighted: (i) all edge spreading times must be sufficiently different and
153 (ii) nodes with a single neighbor disrupt this condition. Consequently, the success rate (i.e.
154 exact source location) of the method depends on the topology of the considered network and
155 the number of detectors. In our approach, the signals are real and uncertainties necessarily
156 exist in the signal measurements. Moreover, it is currently not possible to deploy sensors
157 on 20% of the nodes in the city networks, as suggested by Shen et al. (2016); the current
158 order of magnitude is less than one percent. In response to this, the method has been
159 adapted to achieve interesting success rates with a limited number of sensors. The resulting
160 variance of each source candidate is sorted to produce a tentative hierarchy of the best
161 source candidate. Nevertheless, this priority list is not always relevant: the source having
162 the minimum variance, i.e. the first source in the sorted list of variances, is not always the
163 true source. Hence, a list of potentially successful sources, i.e. "the best choice" among
164 the entire variance list has to be defined. This "best choice" needs a potentially successful
165 source number to be defined. For this, a dedicated "calibration" of the method needs to be
166 performed to find the most sensible potentially successful source number. This potentially
167 successful source number has to be chosen from a trade-off between *accuracy* and *selectivity*,
168 i.e. maximizing the probability of finding the true source whilst, on the order hand, not
169 increasing too much the number of potential sources.

170 This "calibration" is highly sensitive to the specific network at hand, the detector number,
171 and their positions, as well as to the wave velocity variability among the pipes. Hence,
172 this calibration is empirically evaluated using the real network data and the exact detector
173 positions and numbers. For this, we randomly chose sources in the network, perform the
174 time-reversal approach in each case, and built the success-rate histogram of finding the true
175 source at each rank of the variance list. The success probability is thus empirically evaluated
176 from the ratio between successfull tries (those where the true source is part of the source

candidates) and the total number of tries. This is what we called the "calibration" of the method.

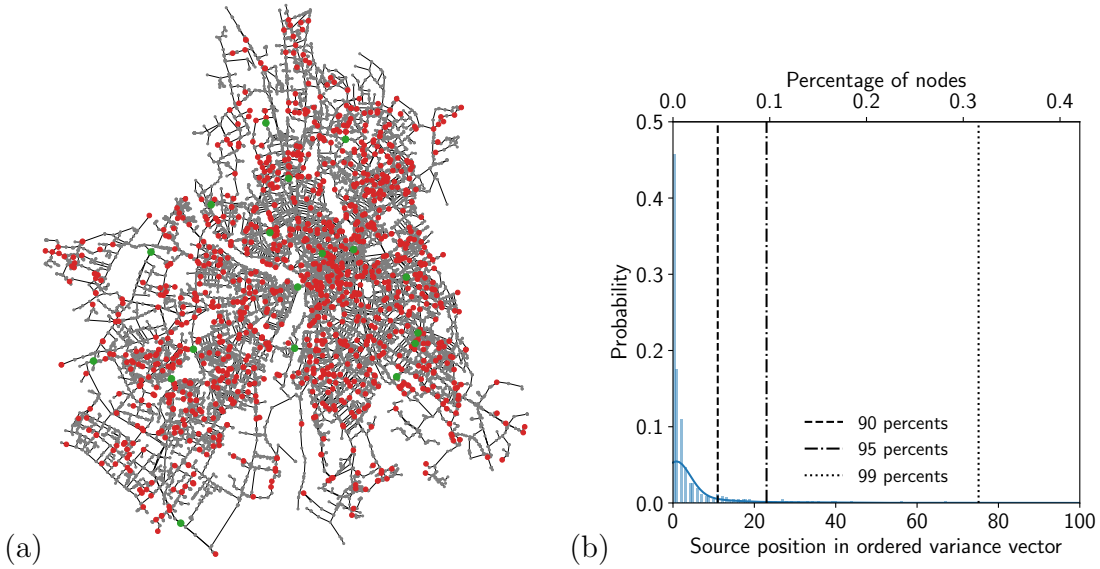

Figure 4: Calibration of the method for the city network and the 18 real sensors (cf. figure 1a). 5% of the network nodes are chosen independently and randomly as sources. (a) network with random sources in red. (b) Calibration histogram and probability density function.

One calibration example is illustrated in figure 4a where all tested sources (used for building statistics) have been colored in red (they represent 5% of the total network). Figure 4b depicts the probability of each candidate being a true source versus its rank in the potentially successful source list. The closest to one, the most probable being the true source. Once adding together all potentially successful source probability in the list result in the probability of having the true source versus rank, i.e. versus the chosen potentially successful source number. The 0.9, 0.95, and 0.99 probabilities have been depicted with vertical dotted lines in figure 4b. They are "calibrated" in this case by a potentially successful source number of 11, 23, and 75 respectively.

2.2.3. Time reversal method with noisy data

To test the influence of noise in the first event detection time, some noise is added to the celerity wave in each pipe. This noise is modeling the uncertainty associated with

structural or geometrical parameters both influencing the wave velocity. We chose to impose a multiplicative noise, i.e. a noise being a small fraction (between 0 to 5%) of the local value of wave time-travel within each pipe. In this framework, first event detection times become random variables to be evaluated a large number of times to access the reliability and sensitivity of the source identification to noise. Obviously, for a given configuration (i.e. fixed network topology, wave celerity field, detector number, and locations) the calibration procedure is performed only once so that for each set of random sources, the noise distribution is applied in a randomly and differently . Increasing the noise amplitude permits quantifying the degradation of the method performance, to be able to extrapolate it for increasing noise and/or uncertainty.

3. Results

3.1. Influence of detector density and signal-to-noise ratio

As discussed in section 2.2.2, the success rate, i.e. the capability of finding the true source among the potentially selected ones depends both upon the sensor spatial density and on the signal-to-noise ratio. We hereby analyze both from randomly chosen detector locations within the network.

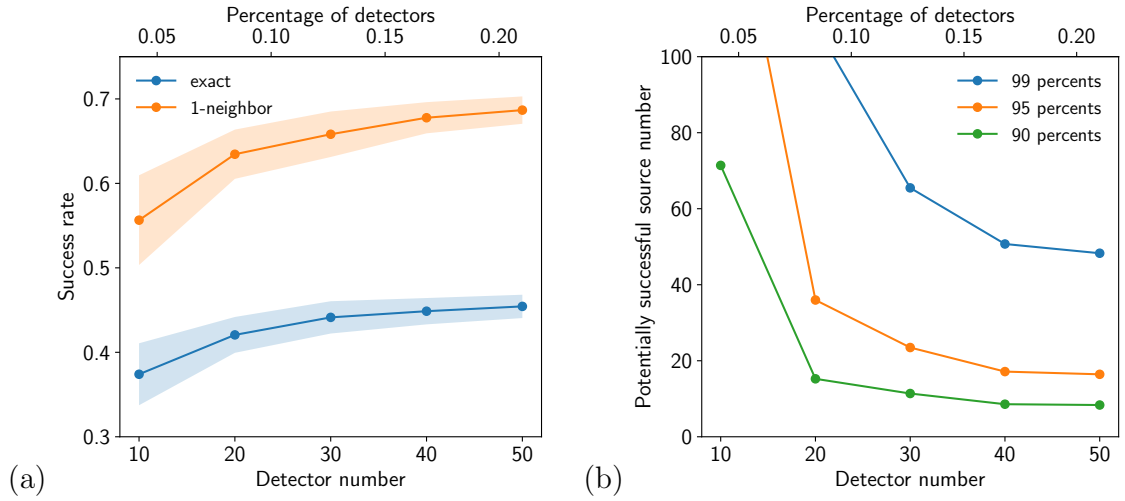

Figure 5: Influence of detector number on the selectivity and success rate of the source geolocalisation. For each detector number, 30 random sets are calibrated, using 5% of temptative randomly chosen true sources among all nodes (1189). (a) Exact and one-neighbor detection function of detector number. In each case, the average behavior is plotted with bold continuous lines where respective colored zone displays ± the standard deviation around it. (b) Average values of the potentially successful source number versus detector number.

The detector density influence is first analyzed without noise, i.e. supposing that the wave velocity is perfectly evaluated within each pipe. In this case, 30 randomly chosen detector configurations are analyzed for each varying number of detectors between 10 to 50. This corresponds to a detector "density" (i.e. the percentage of the detector within the total node number of the network) between 0.05% to 0.22%. Note that these detector densities have been voluntarily chosen in a much modest range than the ones tested in Shen et al. (2016), in line with what is currently deployed and what will be deployed soon. This is motivated by the practical constraint that detectors deployment within the network is costly. Hence it is required to test how the method performs for weak detector density. For such low detector density, it is not expected that the method could provide a highly reliable success rate. Nevertheless, Figure 5a shows that the success rate associated with the best source in the variance list can reach 45.5% of exact detection for the highest detector density (with

50 detectors). This is already an interesting performance from the practical point of view considering the poor detector deployment effort. Moreover, when relaxing/extending the identification success to a one-neighbor distance within the network, i.e. considering one node distance to the best source of the variance list is a success, then the success rate can reach 68.7% as illustrated in Figure 5a. This means that the obtained geolocalization of the best source positions in the network is useful to locate the true source in its vicinity in case of an unsuccessful search. Hence, it is interesting to relax the *selectivity* of the method (which is the maximum for a single choice associated with the best variance in the potentially successful source list) to study how increasing the sensor density with a given calibration (from varying the list success rate from 0.9 to 0.99) impacts its *selectivity*. This calibration sensitivity to detector density is is shown in figure 5b. Whereas increasing the detector density had a weak impact on the success rate of the best source candidate in the list, on the contrary, one can observe in figure 5b that it has a strong impact on the potentially successful source number which strongly decays as the detector number increases from 10 to 50. This is true for every level of calibration (i.e. for every prescribed success rate from 0.9 to 0.99). Hence, even if the method *accuracy* is poorly sensitive to sensor density, it is *selectivity* is strongly influenced by it. For this reason, we also evaluate the convex hull of potentially successful source positions to provide a Region Of Interest (ROI) for the source location. This convex hull is not only useful from the practical viewpoint to delineate the research ROI. It is also useful as a possibly expandable region to increase research success, in case of unsuccessful research within it. This convex hull will be exemplified in two practical cases in the next section.

We now turn to the analysis of noise impact on success rate. To analyze the expected precision of the geolocalization produced by the first event detection method in the presence of noise, we analyze the performance of the method with the same number of detectors as the one used on the field (18) for a large number of randomly chosen sources when considering a relative uncertainty between 0 to 5% for each local wave velocity in pipes. As expected, the larger the noise amplitude, the lower the success rate. Interestingly enough, the performance

degradation scales linearly with the noise amplitude as found in figure 6a and 6b. This linear behavior permits an easy extrapolation of the method's performance for larger noise, resulting from many possible networks defects, aging, breakages, etc.... Hence this permits us to predict the method performances in different contexts for which the uncertainty of the wave velocity is larger.

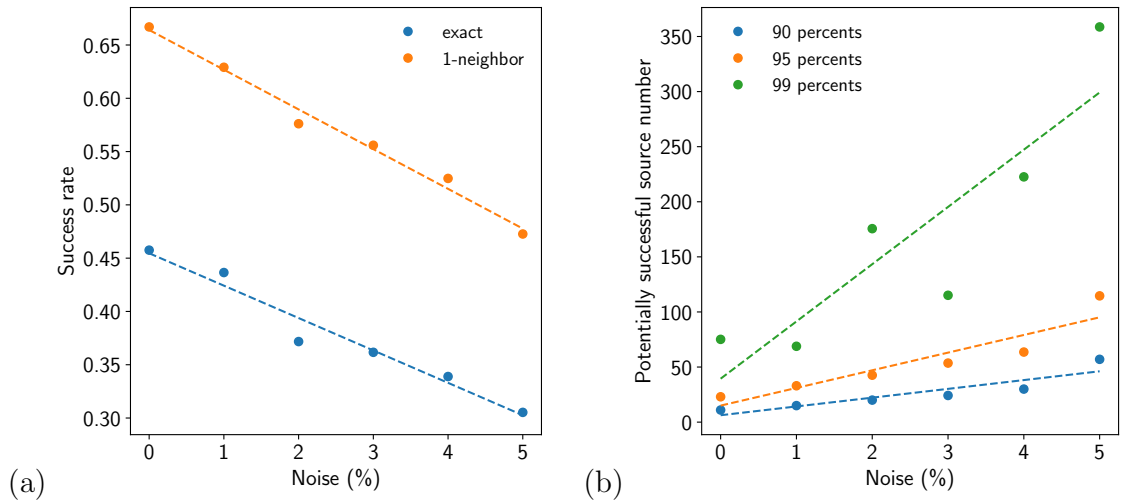

Figure 6: Noise influence on the geolocalization (a) *accuracy* and (b) *selectivity*. Using the 18 detector locations provided in figure 1a, the calibration is performed by randomly adding a multiplicative noise to each pipe travel time, for each tested random source. Evolutions of (a) success rates and (b) potentially successful source number versus noise amplitude. Dashed lines display linear regressions.

3.2. Real events geolocalization

The method is now applied to two real field data analyes denoted case 1 and case 2. For case 1, figure 7a shows the time variation of the high-frequency pressure signal from the awaken detectors (four of those, # $10, 12, 13, 18$ whose location is given in figure 1) of one event. The geolocalization of the source is provided in figure 7b using various convex-hull of potentially successful source positions associated with various calibrations as previously explained in section 3.1. The physical motivation for the convex-hull evaluation is to provide a hierarchy of investigated sites within the network, to be exploted by operators as well as quantity the surface area of possible source candidate sites. As quantified in table 2, the

ROI area provided by the convex hull represents a small fraction (a few percent) of the total network area. This area varies depending on the calibration level.

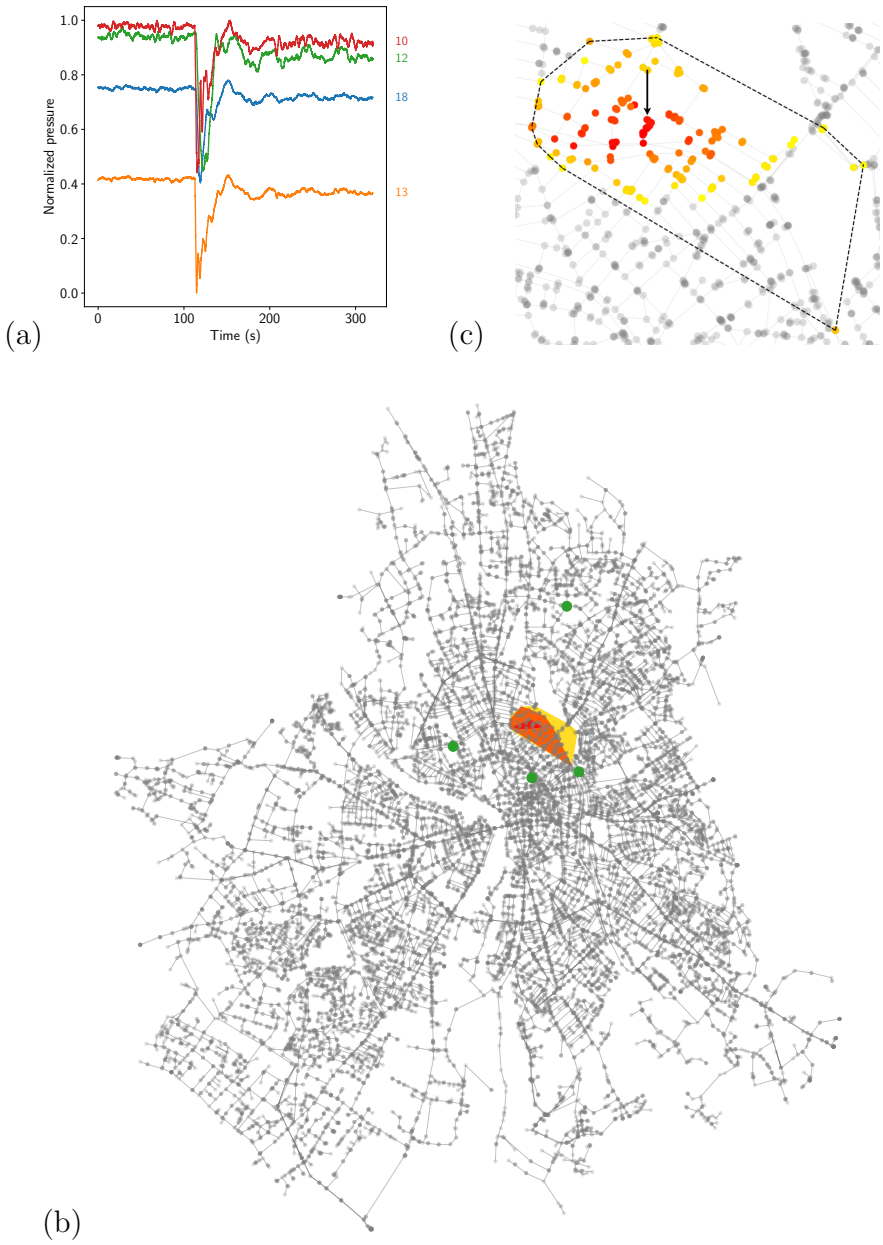

Figure 7: Case 1 illustrating real event detection from the field's data recordings. (a) Normalized pressure signals recorded by high-frequency detectors. (b) Geolocalization of the source with three convex hulls associated with three calibration levels : (yellow) 0.75 %, (orange) 0.5 %, and (red) 0.1 % of potentially successful source number in overall nodes. The four detectors that awaken during this event are depicted in green. (c) Zoom on ROI with the largest hull in dashed lines and nodes colorized versus their variance level from yellow to red for increasing probability of being the source.

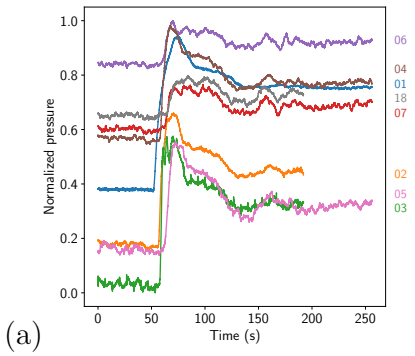

(a)

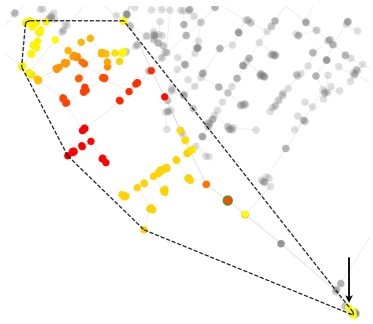

(c)

(b)

Figure 8: Same conventions as figure 7 for case 2.

Case #	% of pot. suc. source number	Hull area (%)	Pipe length (%)
Case 1	0.75	7.97	0.67
	0.5	7.27	0.40
	0.1	2.39	0.05
Case 2	0.75	15.92	0.77
	0.5	10.05	0.52
	0.1	4.24	0.08

Table 2: Hull areas (normalized by the total area of the network) and subgraph pipe lengths (normalized by the total pipe length of the network) versus the node proportion kept in the potentially successful source list for the real events illustrated in figure 7 and 8.

It decreases as the potentially successful source number used also levels down. The proportion of pipe length within the convex hull for the case 1 is also provided in table 2. It shows that (in the less selective choice) only 0.6% of the total pipe length is worth of investigating for finding the source. This shows that the methods already permit a huge screening over the total pipe length inside the network, a result of high operational interest. This is the geolocalized illustration of the method's *selectivity*. Figure 7c also provides a zoom into the ROI region to better visualize the convex hull as well as the true source location. In the considered event, history matching has indeed permitted us to find the true location of the responsible event associated with a pipe breakage. The black arrow of figure 7c indicates that the breakage location indeed lies inside the ROI prediction of the method. This a posteriori confirmation is a supplementary demonstration that the proposed method is relevant for the field's water-hammer source identification.

Another geolocalization example associated with case 2 is illustrated in figure 8 for which the event responsible for the water-hammer wave has been identified as the start-up of one boost pump inside a drinking water production plant. In this case height detectors have been awakened (# $1, 2, 3, 4, 5, 6, 7, 18$) all showing a sudden uprising from base-state illustrated in figure 8a as opposed to the sudden depression found in figure 7a. This is indeed the

expected behavior from a pressure injection event associated with a boost pump turn-on. The location of the pump is however found (figure 8c arrow) at the very edge of the ROI in this case. This might be related to the presence of high-diameter pipe connections of the drinking water production plant into the distribution system for which the associated wave velocity is perhaps roughly approximated. Concerning the quantitative figures obtained for the case 2 provided in table 2 a similar conclusion to case 1 can be raised. Also, in this case, the method permits a huge screening over the total pipe length worth investigating from the overall network.

4. Conclusions

This work has investigated the geolocalization of water-hammer events sources within a water distribution network from the use of high-frequency pressure detectors distributed within it. Combining first event detection with a time-reversal method, the *accuracy* and *selectivity* of the method have been analyzed within real network configurations, considering the very low density of pressure detectors. In this context, we demonstrate from a dedicated calibration procedure the relevance of the proposed method to perform a very good screening of potentially successful sources. The effect of noise either associated with the detector signal or the network uncertainty has also been analyzed. Performance degradation of the method has also been quantified for a noise range between 1 to 5% of the base signal. Finally, the relevance of the proposed method is illustrated in two field cases for which history-matching analysis provides a true source location consistent with the method's prediction.

Hence the proposed method has demonstrated the proof-of-concept that water-hammer events geolocalization is possible with a combination of rather sparing computational and technological tools. Considering the possible managerial interest of such localization in insurance issues and/or repairing investigations, this contribution can lead to significant operational consequences in the field.

Uncertainties about the pipe's properties as well as network topological reliability could hamper a direct application of the method in some urban networks. Nevertheless, some more

involved sensors and/or a more elaborated use of the signal beyond first-event detection might be interesting to develop in the future to partly overcome these uncertainties.

Declaration of Competing Interest

The authors have no competing interests to declare.

Acknowledgments

This work was supported by the collaborative ANRT Grant CIFRE 2019/1453 co-funded by SETOM, a dedicated society of Veolia for the public drinking water service of Toulouse Métropole operating under the brand Eau de Toulouse Métropole. The authors gratefully acknowledge F. Nospelle, from SETOM, for sharing his network knowledge and for his contribution in gathering the on-field information necessary to confirm the sources of the transient events herein analyzed.

Appendix. Local water-hammer wave velocity

Given the Young modulus E of the pipe, the Poisson coefficient ν_s, the pipe's density ρ_s, the dimensionless thickness $\alpha = e/R$ (e being the pipe thickness and R its radius), the acoustic water velocity c_0, K the isothermal fluid bulk modulus, the water-hammer wave speed is given by

$$c = c_- \cdot c_p, \tag{.1}$$

with,

$$c_p^2 = \frac{c_0^2}{1 + \frac{2K}{\alpha E}\left(\frac{2(1-\nu_s^2)}{2+\alpha} + \alpha(1+\nu_s)\right)}. \tag{.2}$$

$$c_-^2 = \frac{1 + \mathcal{C}_s^2 + \frac{4\nu_s^2\mathcal{D}}{\alpha(2+\alpha)} - \sqrt{\left(1 + \mathcal{C}_s^2 + \frac{4\nu_s^2\mathcal{D}}{\alpha(2+\alpha)}\right)^2 - 4\mathcal{C}_s^2}}{2} \tag{.3}$$

with $\mathcal{C}_s = E/\rho_s c_p$ being the pulse wave velocity ratio, whilst $\mathcal{D} = \rho_f/\rho_s$ being the fluid to solid density one. These expressions can be found in Zhang et al. (1999); Tijsseling (2007).

References

Agathokleous, A., Christodoulou, S., 2016. Vulnerability of urban water distribution networks under intermittent water supply operations. Water Resour Manage 30, 4731–4750.

Caputo, J.G., Hamdi, A., Knippel, A., 2019. Inverse source problem in a forced network. Inverse Probl. 35, 055006.

Che, T.C., Duan, H.F., Lee, P.J., 2021. Transient wave-based methods for anomaly detection in fluid pipes: A review. Mech. Syst. Signal Process. 160. doi:10.1016/j.ymssp.2021.107874.

Ferrante, M., Brunone, B., Meniconi, S., 2009. Leak detection in branched pipe systems coupling wavelet analysis and a Lagrangian model. J. Water. Supply. Res. T. 58, 95–106. doi:10.2166/aqua.2009.022.

Grigoropoulos, G., Ghidaoui, M.S., Louati, M., Nasraoui, S., 2021. Time reversal of waves in hydraulics: experimental and theoretical proof with applications. Journal of Hydraulic Research 60, 1–24.

Kessler, A., Ostfeld, A., Sinai, G., 1998. Detecting accidental contaminations in municipal water networks. Journal of Water Resources Planning and Management 124, 192–198.

Meniconi, S., Brunone, B., Ferrante, M., Capponi, C., Carrettini, C., Chiesa, C., Segalini, D., Lanfranchi, E., 2015. Anomaly pre-localization in distribution-transmission mains by pump trip: Preliminary field tests in the Milan pipe system 17, 377. doi:10.2166/hydro.2014.038.

Meniconi, S., Capponi, C., Frisinghelli, M., Brunone, B., 2021. Leak detection in a real transmission main through transient tests: Deeds and misdeeds. Water Resources Research 57, e2020WR027838.

Meniconi, S., Maietta, F., Alvisi, S., Capponi, C., Marsili, V., Franchini, M., Brunone, B., 2022a. Consumption change-induced transients in a water distribution network: Laboratory tests in a looped system. Water Resources Research 58, e2021WR031343.

Meniconi, S., Maietta, F., Alvisi, S., Capponi, C., Marsili, V., Franchini, M., Brunone, B., 2022b. A quick survey of the most vulnerable areas of a water distribution network due to transients generated in a service line: A lagrangian model based on laboratory tests. Water 14, 2741.

Moosavian, N., Lence, B., 2020. Unified matrix frameworks for water hammer analysis in pipe networks. Int. J. Civ. Eng 18.

Nault, J.D., Karney, B.W., Jung, B.S., 2018. Generalized flexible method for simulating transient pipe network hydraulics. Journal of Hydraulic Engineering 144, 04018031.

Pal, S., Hanmaiahgari, P.R., Karney, B.W., 2021. An overview of the numerical approaches to water hammer modelling: The ongoing quest for practical and accurate numerical approaches. Water 13.

Plouraboué, F., Uszes, P., Guibert, R., 2022. Source identification of propagating waves inside a network. IEEE Trans. Netw. Sci. Eng 9, 1437–1450.

Riaño-Briceño, G., Sela, L., Hodges, B.R., 2022. Distributed and vectorized method of characteristics for fast transient simulations in water distribution systems. Computer-Aided Civil and Infrastructure Engineering 37, 163–184.

Shen, Z., Cao, S., Wang, W.X., Di, Z., Stanley, H.E., 2016. Locating the source of diffusion in complex networks by time-reversal backward spreading. Phys. Rev. E 93, 032301.

Shucksmith, J.D., Boxall, J.B., Staszewski, W.J., Seth, A., Beck, S.B., 2012. Onsite leak location in a pipe network by cepstrum analysis of pressure transients. J. Water. Supply. Res. T. 104, E457–E465. doi:10.5942/jawwa.2012.104.0108.

Tijsseling, A., 2007. Water hammer with fluid-structure interaction in thick-walled pipes 85, 844–851. doi:10.1016/j.compstruc.2007.01.008.

Truong, C., Oudre, L., Vayatis, N., 2020. Selective review of offline change point detection methods. Signal Processing 167, 107299.

Wang, R., Wang, Z., Wang, X., Yang, H., Sun, J., 2014. Pipe burst risk state assessment and classification based on water hammer analysis for water supply networks. Journal of Water Resources Planning and Management 140, 04014005.

Wang, X., Camino, G.A., Che, T., Ghidaoui, M.S., 2021. Factorized wave propagation model in tree-type pipe networks and its application to leak localization. Mech. Syst. Signal Process. 147, 107116. doi:10.1016/j.ymssp.2020.107116.

Wang, X., Ghidaoui, M.S., 2018. Pipeline leak detection using the matched-field processing method. Journal of Hydraulic Engineering 144, 04018030.

Wang, X., Xie, H., 2018. A review on applications of remote sensing and geographic information systems (gis) in water resources and flood risk management. Water 10.

Zhang, C., Zhang, J.J., Ma, C.B., Korobkov, G.E., 2021. Algorithm for detecting multiple partial blockages in liquid pipelines by using inverse transient analysis. SPE 26, 1337–1342.

Zhang, L., Tijsseling, A., Vardy, E., 1999. FSI Analysis of Liquid-Filled Pipes. J. Sound Vib. 224, 69–99.

Chapter 7

Conclusion

Contents

7.1 PhD highlights

This PhD thesis has been dedicated to the **Modeling of transient pressure waves in water distribution networks (WDN).** The literature review of §1 has permitted to describe the distinct aspects of transient modeling: on the one-hand water-hammer considered from the hydraulic viewpoint, i.e. by neglecting the axial response of the pipe and focusing on the near-wall viscous fluid modeling, or, on the other hand, the mechanical one considering an inviscid fluid associated with fluid-structure interactions (FSI). The presence of FSI-couplings, especially the Poisson's coupling, give rise to a complex structure of resonant modes for elastic pipes, the dynamics of which is non-dispersive in the long-wavelength asymptotic framework. In such framework, the radial pipe inertial response to overpressure transients can be neglected, i.e. transverse pipe vibrations are not considered, and yields to the derivation of the well-known four-FSI hyperbolic equations set to describe the behavior of liquid-filled pipe systems.

The coupled four-FSI equations have been investigated, for specific hydraulic configurations, using the Transfer Matrix Method (TMM). Since this frequency-dependent method suffers from practical limitations (e.g. the need to perform an inverse Laplace transform in complex hydraulic networks), a new theoretical, operator-based framework was derived in §2. This new dynamical analysis of the coupled four-FSI equations allows a direct time-domain treatment from selecting a strategic orthogonal decomposition basis for the pressure-stress solutions, providing a complete description of the resonant modes. This operator-based theory has been successfully compared with previously published numerical FSI-analyses,

recovering well-established results derived using TMM's method.

In order to include the fluid viscosity effects into the overall liquid-filled pipe transient modeling so as to reconcile both hydraulic and mechanical viewpoints, a multi-time scale asymptotic analysis has been carried out in §3. The FSI couplings were investigated in a low-Mach number, $M = \frac{W_0}{c_p} \ll 1$, and long-wavelength, $\epsilon = \frac{R_0}{L} \ll 1$, asymptotic framework, seeking for a small parameter $\delta = \sqrt{\frac{\nu_f L}{c_p R_0}}$ (the dimensionless boundary layer thickness defined in (1.49)) expansion solution. This parameter has been shown to play a cornerstone role in the system's exponential damping. A rigorous asymptotic framework associated with condition $\delta^2 \gg \mathcal{M}$, $\delta \gg \epsilon^2$ and $\epsilon \gg \mathcal{M}$, has been spelled out to ensure the dominance of the viscous wall shear rate effects at first order, thus discarding the influence of both fluid and solid radial inertia. From analyzing corrections up to first order, an FSI-consistent asymptotic scheme has been spelled out bringing significant insights on the description of the coupling mechanisms. Regarding the liquid-filled pipe system $O(\delta)$ corrections (Cf. secularity condition in §3.1.3) a mode-dependent exponential damping has been found to characterize the FSI viscous energetic losses in liquid-filled pipe systems. Finally, this chapter stresses the relevance of considering the relative fluid to solid acceleration at the pipe's inner wall, i.e. $\partial_\tau \left(W - \alpha\dot{\zeta}\right)$, for FSI-consistent convoluted wall shear rate model (Cf. WFB models in §1.4.2). This issue is relevant in bio-mechanical applications, whereby relative errors up to 75% have been found between the FSI and the no-FSI wall shear rate models, confirming the necessity of further investigations.

Even if the asymptotic multi-time scale analysis provides significant insights on the liquid-filled pipe behavior description, this analysis is restricted to elastic pipes. An extension of the four-FSI equations to visco-elastic pipes has been proposed in §4, at leading order (discarding $O(\delta)$ corrections). It permits to promote a new rheology-based, FSI-model. The investigation has been successfully handled and permitted to derive new visco-elastic-kernels associated with the non-local response in time of convolution terms generalizing previous model such as [Keramat et al., 2011] one. The proposed kernels dependence in both pipe mechanical properties (rheological behavior) and geometrical properties (pipe's thickness to its inner radius ratio, α) have been found explicitly. The new model's predictions were successfully confronted with previous theories as well as experiments both in time and frequency domains. While the pipe visco-elasticity smooths the signal's high-frequencies and increases the damping (compared to purely elastic materials), the dispersion band on the coupled wave speed modes is found to be weak.

By focusing only on the numerical modeling of the transient response of WDN, the FSI-high frequencies can be discarded to deal only with fluid coupled hyperbolic equations. An in-house numerical solver has then been set-up in §5, fully coupled to the steady-state EPANET's solver, [Rossman et al., 2020], using the

MOC method. Several wall shear rate models have been implemented, i.e. quasi-steady, convoluted- and inertial- based ones, and confronted with respect to experimental and numerical previously published investigations. The analysis of the relative L^2 norm error between MOC-predictions reveals very little differences between all the proposed convoluted models. Furthermore, while convoluted models better represent the transient signal peaks sharpness and phase, the inertial-based one better depicts the amplitudes. In the low to transitional Reynolds number range, the convoluted-based wall shear rate models are shown to be more accurate than inertial-based one, the quasi-steady model always being the less accurate. For higher Reynolds number, the inertial-based model nevertheless increases the predictions accuracy to experimental observations, the convoluted models being slightly less accurate. Noteworthy, the quasi-steady wall shear rate model describes surprisingly well the high Reynolds transient responses and then can stands as a good operational compromise between accuracy and efficiency. To go further in the wall shear rate models description, an on-field test has been set up in a sub-network of the Toulouse's water distribution network. The comparisons with the on-field measurements nevertheless remain unsatisfactory up to now [Meniconi et al., 2018, Marsili et al., 2021], for all considered damping models.

Finally, a new anomaly detection method in WDN, relying on the backtracking of the overpressure waves first front, has been developed in §6. This method is simple to implement, CPU-efficient and has already permitted to geolocalize several anomalies in the Toulouse's water distribution network. The method is pipe material sensitive and then requires the full-knowledge of the network. No need are nevertheless made to dispose of an idealize test benchmark as classically needed for other detection methods (Cf §1.4.4). The method is also sensitive to the sensor density but shown good robustness to noise, then allowing the detection of anomalies despite uncertainties in the theoretical prediction of water hammer wave speeds.

7.2 Research perspectives

The research on the modeling of overpressure waves in WDN is obviously still an ongoing work. Relying on the work that have been accomplished in this PhD, several enhancements can be accomplished:

- First, the herein one-pipe restricted FSI-models should be extended to the network scale. The self-operator-based theory developed in §2 must be enlarged to network analyses, classically by following the step of the transfer matrix method or the impedance matrix method (Cf. the notable contributions of [Zecchin, 2010, Zecchin et al., 2012]). Such advances will provide a full theoretical, time-dependent, transient network description.

- Second, relying on the first above-mentioned point, the multi-time scale analysis performed in §3 should also be extended to the network scale. This is expected to provide a theoretical description of FSI-viscous damping occurring in WDN. The wall shear rate convoluted structure can be expected to remain so that the global network multi-time scale asymptotic method should provides a suitable alternative to the classical MOC-numerical schemes (Cf. §5).

- The promising new first front backtracking anomaly detection method (Cf. §6) can also be improved. The relevance of the method indeed depends on several surrounding variables such as the completeness of the water distribution network data (e.g. material, diameter or length distributions) along with the position of the sensors. Several data analyses, along with the definition of a strategic sensor positioning procedure, can then be envisioned to overcome these technical barriers. Furthermore, the herein method does not account for the daily network connectivity evolution, i.e. the daily modification of water fluxes in the district metered areas (DMA) (Cf. section 1.2).

Bibliography

[Abdeldayem et al., 2021] Abdeldayem, O., Ferras, D., Zwan, S., and Kennedy, M. (2021). Analysis of Unsteady Friction Models Used in Engineering Software for Water Hammer Analysis: Implementation Case in WANDA. *Water*, 13(4):495.

[Abu-Mahfouz et al., 2019] Abu-Mahfouz, A. M., Hamam, Y., Page, P. R., Adedeji, K. B., Anele, A. O., and Todini, E. (2019). Real-Time Dynamic Hydraulic Model of Water Distribution Networks. *Water*, 11(3):470.

[Abuiziah et al., 2013] Abuiziah, I., Ahmed, O., Karima, S., and Driss, O. (2013). Sizing the Protection Devices to Control Water Hammer Damage. *Int. J. Civ. Eng. Archit. Eng.*, 7(11):415–420.

[Achouyab and Bahrar, 2011] Achouyab, E. H. and Bahrar, B. (2011). Numerical modeling of phenomena of waterhammer using a model of fluid–structure interaction. *C. R. - Mec.*, 339(4):262–269.

[Adamkowski and Lewandowski, 2004] Adamkowski, A. and Lewandowski, M. (2004). Unsteady friction modelling in transient pipe flow simulation. *Transactions of the Institute of Fluid-Flow Machinery*, 115:83–97.

[Adamkowski and Lewandowski, 2006] Adamkowski, A. and Lewandowski, M. (2006). Experimental Examination of Unsteady Friction Models for Transient Pipe Flow Simulation. *J. Fluids Eng. Trans. ASME*, 128(6):1351–1363.

[Al-Khomairi, 2008] Al-Khomairi, A. (2008). Leak detection in long pipelines using the least squares method. *J. Hydraul. Res.*, 46(3):392–401.

[Aliabadi et al., 2020] Aliabadi, H. K., Ahmadi, A., and Keramat, A. (2020). Frequency response of water hammer with fluid-structure interaction in a viscoelastic pipe. *Mech. Syst. Signal Process.*, 144:106848.

[Allievi, 1913] Allievi, L. (1913). *Teoria del colpo d'ariete*. Tipografia della R. Accademia dei Lincei.

[Andrade et al., 2022] Andrade, D., Freitas Rachid, F., and Tijsseling, A. (2022). A new model for fluid transients in piping systems taking into account the fluid–structure interaction. *J. Fluids Struct.*, 114:103720.

[Andrade et al., 2023] Andrade, D., Freitas Rachid, F., and Tijsseling, A. (2023). Fluid transients in viscoelastic pipes via an internal variable constitutive theory. *Appl. Math. Model.*, 114:846–869.

[Armand et al., 2018] Armand, H., Stoianov, I., and Graham, N. (2018). Impact of network sectorisation on water quality management. *J. Hydroinformatics*, 20(2):424–439.

[Artl, 1993] Artl, H. (1993). Experimented Untersuchungen uber das instationare, turbulente Reibungsverhalten bei aufgepragten Druckimpulsen in einer Rohrleitung mit kreisquerchnitt (Experimented investigations on the unsteady, turbulent friction behaviour with applied pressure pulses in a circular cross-section pipeline). Technical report, Mitteilung Nr 102, Institut fur Wasserbau und Wasserwirtschaft, Technische Universitat Berlin.

[Avitia and Deniss, 2011] Avitia, E. and Deniss, C. (2011). Multi-leak detection with wavelet analysis of pressure sensitivities in water distribution networks. Master's thesis, Instituto Tecnológico y de Estudios Superiores de Monterrey, Monterrey, Mexico.

[Bakhtawar and Zayed, 2021] Bakhtawar, B. and Zayed, T. (2021). Review of Water Leak Detection and Localization Methods through Hydrophone Technology. *J. Pipeline Syst. Eng. Pract.*, 12(4):03121002.

[Barez et al., 1979] Barez, F., Goldsmith, W., and Sackman, J. L. (1979). Longitudinal waves in liquid-filled tubes—I: Theory. *Int. J. Mech. Sci.*, 21(4):213–221.

[Bayle and Plouraboué, 2022] Bayle, A. and Plouraboué, F. (2022). Low Mach number theory of pressure waves inside an elastic tube. *submitted to J. Fluid Mech.*

[Bentoumi et al., 2017] Bentoumi, M., Chikouche, D., Mezache, A., and Bakhti, H. (2017). Wavelet DT method for water leak-detection using a vibration sensor: an experimental analysis. *IET Signal Process.*, 11(4):396–405.

[Bergant et al., 2001] Bergant, A., Ross Simpson, A., and Vìtkovski, J. (2001). Developments in unsteady pipe flow friction modelling. *J. Hydraul. Res.*, 39(3):249–257.

[Brown, 2002] Brown, G. O. (2002). The History of the Darcy-Weisbach Equation for Pipe Flow Resistance. In *Environmental and Water Resources History Sessions at ASCE Civil Engineering Conference*.

[Brunone, 1999] Brunone, B. (1999). Transient Test-Based Technique for Leak Detection in Outfall Pipes. *J. Water Resour. Plan. Manag.*, 125(5):302–306.

[Brunone et al., 1991] Brunone, B., Golia, U., and Greco, M. (1991). Some remarks on the momentum equation for fast transients. In *Proc. Int. Conf. on Hydr. Transients With Water Column Separation*, pages 201–209.

[Brunone et al., 2018] Brunone, B., Meniconi, S., and Capponi, C. (2018). Numerical analysis of the transient pressure damping in a single polymeric pipe with a leak. *Urban Water J.*, 15(8):760–768.

[Budny et al., 1991] Budny, D. D., Wiggert, D. C., and Hatfield, F. J. (1991). The Influence of Structural Damping on Internal Pressure During a Transient Pipe Flow. *J. Fluids Eng.*, 113(3):424–429.

[Bürmann, 1975] Bürmann, W. (1975). Water hammer in coaxial pipe systems. *J. Hydraul. Div.*, 101(6):699–715.

[Camichel et al., 1917] Camichel, C., Eydoux, D., and Gariel, M. (1917). étude théorique et expérimentale des coups de bélier. *Annales de la Faculté des sciences de Toulouse : Mathématiques*, 9:1–145.

[Campisano et al., 2016] Campisano, A., Modica, C., Reitano, S., Ugarelli, R., and Bagherian, S. (2016). Field-Oriented Methodology for Real-Time Pressure Control to Reduce Leakage in Water Distribution Networks. *J. Water Resour. Plan. Manag.*, 142(12):04016057.

[Cao et al., 2020] Cao, H., Nistor, I., and Mohareb, M. (2020). Effect of Boundary on Water Hammer Wave Attenuation and Shape. *J. Hydraul. Eng.*, 146(3):04020001.

[Capponi et al., 2018] Capponi, C., Ferrante, M., Zecchin, A. C., and Gong, J. (2018). Experimental validation of the admittance matrix method on a Y-system. *J. Hydraul. Res.*, 56(4):439–450.

[Capponi et al., 2020] Capponi, C., Meniconi, S., Lee, P. J., Brunone, B., and Cifrodelli, M. (2020). Time-domain Analysis of Laboratory Experiments on the Transient Pressure Damping in a Leaky Polymeric Pipe. *Water Resour. Manag.*, 34:501–514.

[Chaudhry, 2014] Chaudhry, M. H. (2014). *Applied Hydraulic Transients*. Springer-Verlag, 3 edition.

[Che et al., 2021] Che, T.-C., Duan, H.-F., and Lee, P. J. (2021). Transient wave-based methods for anomaly detection in fluid pipes: A review. *Mech. Syst. Signal Process.*, 160:107874.

[Corli et al., 2012] Corli, A., Gasser, I., Lukáčová-Medvid'ová, M., Roggensack, A., and Teschke, U. (2012). A multiscale approach to liquid flows in pipes I: The single pipe. *Appl. Math. Comput.*, 219(3):856–874.

[Courant and Friedrichs, 1999] Courant, R. and Friedrichs, K. O. (1999). *Supersonic Flow and Shock Waves*, volume 21. Springer New York, NY.

[Covas, 2003] Covas, D. (2003). *INVERSE TRANSIENT ANALYSIS FOR LEAK DETECTION AND CALIBRATION OF WATER PIPE SYSTEMS MODELLING SPECIAL DYNAMIC EFFECTS*. PhD thesis, Imperial College London (University of London).

[Covas and Ramos, 2001] Covas, D. and Ramos, H. (2001). Hydraulic Transients used for Leakage Detection in Water Distribution Systems. In 4^{th} *Int. Conf. on Water Pipe-line Systems*, pages 227–241. BHR Group.

[Covas and Ramos, 2010] Covas, D. and Ramos, H. (2010). Case Studies of Leak Detection and Location in Water Pipe Systems by Inverse Transient Analysis. *J. Water Resour. Plan. Manag.*, 136(2):248–257.

[Covas et al., 2005] Covas, D., Stoianov, I., Mano, J. F., Ramos, H., Graham, N., and Maksimovic, C. (2005). The dynamic effect of pipe-wall viscoelasticity in hydraulic transients. Part II—model development, calibration and verification. *J. Hydraul. Res.*, 43(1):56–70.

[Covas et al., 2004a] Covas, D., Stoianov, I., Ramos, H., Graham, N., and Maksimovic, C. (2004a). The dynamic effect of pipe-wall viscoelasticity in hydraulic transients. Part I - Experimental analysis and creep characterization. *J. Hydraul. Res.*, 42:517–532.

[Covas et al., 2004b] Covas, D., Stoianov, I., Ramos, H., Graham, N., Maksimovic, C., and Butler, D. (2004b). Water hammer in pressurized polyethylene pipes: conceptual model and experimental analysis. *Urban Water J.*, 1(2):177–197.

[Creaco et al., 2019] Creaco, E., Campisano, A., Fontana, N., Marini, G., Page, P. R., and Walski, T. (2019). Real time control of water distribution networks: A state-of-the-art review. *Water Res.*, 161:517–530.

[Creaco and Walski, 2018] Creaco, E. and Walski, T. (2018). Operation and Cost-Effectiveness of Local and Remote RTC. *J. Water Resour. Plan. Manag.*, 144(11):04018068.

[Dai et al., 2012] Dai, H. L., Wang, L., Qian, Q., and Gan, J. (2012). Vibration analysis of three-dimensional pipes conveying fluid with consideration of steady combined force by transfer matrix method. *Appl. Math. Comput.*, 219(5):2453–2464.

[Daily et al., 1955] Daily, J. W., Hankey, J., Olive, R. W., and Jordaan, J. (1955). Resistance Coefficients for Accelerated and Decelerated Flows Through Smooth Tubes and Orifices. Technical report, MASSACHUSETTS INST OF TECH CAMBRIDGE.

[Datta and Sarkar, 2016] Datta, S. and Sarkar, S. (2016). A review on different pipeline fault detection methods. *J. Loss. Prev. Process. Ind.*, 41:97–106.

[Daubechies, 1992] Daubechies, I. (1992). *Ten lectures on wavelets*. Society for Industrial and Applied Mathematics, Springer-Verlag, Philadelphia.

[DeArmond and Rouleau, 1972] DeArmond, R. P. and Rouleau, W. T. (1972). Wave Propagation in Viscous, Compressible Liquids Confined in Elastic Tubes. *J. Basic Eng.*, 94(4):811–816.

[Duan et al., 2011] Duan, H., Lee, P. J., Ghidaoui, M. S., and Tung, Y. (2011). Leak detection in complex series pipelines by using the system frequency response method. *J. Hydraul. Res.*, 49(2):213–221.

[Duan et al., 2012a] Duan, H., Lee, P. J., Ghidaoui, M. S., and Tung, Y. (2012a). Extended Blockage Detection in Pipelines by Using the System Frequency Response Analysis. *J. Water Resour. Plan. Manag.*, 138(1):55–62.

[Duan et al., 2012b] Duan, H., Lee, P. J., Ghidaoui, M. S., and Tung, Y. (2012b). System Response Function–Based Leak Detection in Viscoelastic Pipelines. *J. Hydraul. Eng.*, 138(2):143–153.

[Duan and Lee, 2016] Duan, H. F. and Lee, P. J. (2016). Transient-Based Frequency Domain Method for Dead-End Side Branch Detection in Reservoir Pipeline-Valve Systems. *J. Hydraul. Eng.*, 142(2):04015042.

[Duan et al., 2014] Duan, H. F., Lee, P. J., Ghidaoui, M. S., and Tuck, J. (2014). Transient wave-blockage interaction and extended blockage detection in elastic water pipelines. *J. Fluids Struct.*, 46:2–16.

[Duan et al., 2013] Duan, H.-F., Lee, P. J., Kashima, A., Lu, J., Ghidaoui, M. S., and Tung, Y. (2013). Extended Blockage Detection in Pipes Using the System Frequency Response: Analytical Analysis and Experimental Verification. *J. Hydraul. Eng.*, 139(7):763–771.

[Duan et al., 2017] Duan, H. F., Meniconi, S., Lee, P. J., Brunone, B., and Ghidaoui, M. S. (2017). Local and Integral Energy-Based Evaluation for the Unsteady Friction Relevance in Transient Pipe Flows. *J. Hydraul. Eng.*, 143(7):04017015.

[Duan et al., 2020] Duan, H.-F., Pan, B., Wang, M., Chen, L., Zheng, F., and Zhang, Y. (2020). State-of-the-art review on the transient flow modeling and utilization for urban water supply system (UWSS) management. *J. Water Supply: Res. Technol. - AQUA*, 69(8):858–893.

[D'Souza and Oldenburger, 1969] D'Souza, A. F. and Oldenburger, R. (1969). Dynamic Response of Fluid Lines. *J. Basic Eng.*, 86(3):589–598.

[EauFrance, 2022] EauFrance (2022). Le service public d'information sur l'eau. https://www.eaufrance.fr/.

[Ebacher et al., 2011] Ebacher, G., Besner, M.-C., Lavoie, J., Jung, B. S., Karney, B. W., and Prévost, M. (2011). Transient Modeling of a Full-Scale Distribution System: Comparison with Field Data. *J. water resour. plan. manag.*, 137(2):173–182.

[Farley, 2001] Farley, M. (2001). *Leakage management and control: a best practice training manual*. World Health Organization.

[Ferrante and Brunone, 2003] Ferrante, M. and Brunone, B. (2003). Pipe system diagnosis and leak detection by unsteady-state tests. 2. Wavelet analysis. *Adv. Water Resour.*, 26(1):107–116.

[Ferrante et al., 2009a] Ferrante, M., Brunone, B., and Meniconi, S. (2009a). Leak-edge detection. *J. Hydraul. Res.*, 47(2):233–241.

[Ferrante et al., 2009b] Ferrante, M., Brunone, B., and Meniconi, S. (2009b). Leak detection in branched pipe systems coupling wavelet analysis and a Lagrangian model. *J. Water. Supply. Res. T.*, 58(2):95–106.

[Ferrari and Vento, 2020] Ferrari, A. and Vento, O. (2020). Influence of Frequency-Dependent Friction Modeling on the Simulation of Transient Flows in High-Pressure Flow Pipelines. *J. Fluids. Eng.*, 142(8):081205.

[Ferras et al., 2018] Ferras, D., Manso, P. A., Schleiss, A. J., and Covas, D. I. C. (2018). One-Dimensional Fluid–Structure Interaction Models in Pressurized Fluid-Filled Pipes: A Review. *Appl. Sci.*, 8(10):1844.

[Flügge, 1960] Flügge, W. (1960). *Stresses in Shells*. Springer Berlin, Heidelberg.

[Fontana et al., 2018] Fontana, N., Giugni, M., Glielmo, L., Marini, G., and Zollo, R. (2018). Real-Time Control of Pressure for Leakage Reduction in Water Distribution Network: Field Experiments. *J. Water Resour. Plan. Manag.*, 144(3):04017096.

[Gally et al., 1979] Gally, M., Güney, M., and Rieutord, E. (1979). An investigation of pressure transients in viscoelastic pipes. *J. Fluids. Eng.*, 101:495–499.

[Ghidaoui et al., 2002] Ghidaoui, M. S., Mansour, S. G. S., and Zhao, M. (2002). Applicability of Quasisteady and Axisymmetric Turbulence Models in Water Hammer. *J. Hydraul. Eng.*, 128(10):917–924.

[Ghidaoui et al., 2005] Ghidaoui, M. S., Zhao, M., McInnis, D. A., and Axworthy, D. H. (2005). A Review of Water Hammer Theory and Practice. *Applied Mechanics Reviews*, 58(1):49–76.

[Guinot, 2010] Guinot, V. (2010). *Wave Propagation in Fluid: Models and Numerical Techniques (2^{nd} edition)*. John Wiley & Sons, Inc.

[Guo et al., 2021] Guo, W., Wang, B., and Zhao, L. (2021). A Visual Software Implementation of Numerical Simulation for Transient Process of Pipeline Network System of Water Supply Project. *Energies*, 14(15):4606.

[Hinch, 1991] Hinch, E. J. (1991). *Perturbation Methods*. Cambridge Texts in Applied Mathematics. Cambridge University Press.

[Holmboe and Rouleau, 1967] Holmboe, E. L. and Rouleau, W. T. (1967). The Effect of Viscous Shear on Transients in Liquid Lines. *J. Basic Eng.*, 89(1):174–180.

[Hosseini et al., 2020] Hosseini, R. S., Ahmadi, A., and Zanganeh, R. (2020). Fluid-structure interaction during water hammer in a pipeline with different performance mechanisms of viscoelastic supports. *J. Sound Vib.*, 487:115527.

[IPCC Working Group II, 2022] IPCC Working Group II (2022). Climate Change 2022: Impacts, Adaptation and Vulnerability. Summary for Policymakers. Technical Report Sixth Assessment Report, section B.4.2, Intergovernmental Panel on Climate Change, IPCC.

[Jensen et al., 2018] Jensen, R. K., Larsen, J. K., Lassen, K. L., Mandø, M., and Andreasen, A. (2018). Implementation and validation of a free open source 1d water hammer code. *Fluids*, 3(3):64.

[Jönsson and Larson, 1992] Jönsson, L. and Larson, M. (1992). Leak detection through hydraulic transient analysis. In *Pipeline systems*, pages 273–286. Springer.

[Joukowsky, 1904] Joukowsky, N. (1904). Uber den hydraulischen Stoss in Wasserleitungsro hren. (on the hydraulic hammer in water supply pipes) Mémoires de l'Académie Impériale des Sciences de St.-Petersbourg. *English translation, partly, by Simin*, 9(5).

[Kagawa et al., 1983] Kagawa, T., Lee, I., Kitagawa, A., and Takenaka, T. (1983). High Speed and Accurate Computing Method of Frequency-Dependent Friction in Laminar Pipe Flow for Characteristics Method. *J. Jpn. Soc. Mech. Eng. Series B*, 49(447):2638–2644.

[Kapelan et al., 2003] Kapelan, Z. S., Savic, D. A., and Walters, G. A. (2003). A hybrid inverse transient model for leakage detection and roughness calibration in pipe networks. *J. Hydraul. Res.*, 41(5):481–492.

[Karney, 1990] Karney, B. (1990). Energy relations in transient closed-conduit flow. *J. Hydraul. Eng.*, 116(10):1180–1196.

[Keramat and Duan, 2021] Keramat, A. and Duan, H. (2021). Spectral based pipeline leak detection using a single spatial measurement. *Mech. Syst. Signal Process.*, 161:107940.

[Keramat et al., 2011] Keramat, A., Tijsseling, A., Hou, Q., and Ahmadi, A. (2011). Fluid–structure interaction with pipe-wall viscoelasticity during water hammer. *J. Fluids Struct.*, 28:434–455.

[Kim, 2005] Kim, S. (2005). Extensive Development of Leak Detection Algorithm by Impulse Response Method. *J. Hydraul. Eng.*, 131(3):201–208.

[Kim, 2007] Kim, S. (2007). Impedance matrix method for transient analysis of complicated pipe networks. *J. Hydraul. Res.*, 45(6):818–828.

[Kim, 2022] Kim, S. (2022). Hydraulic transient evaluation via fabricable impedance matrix for pipe networks. *J. Hydraul. Res.*, 60(2):326–340.

[Kizilova, 2006] Kizilova, N. (2006). Pressure Wave Propagation in Liquid-Filled Tubes of Viscoelastic Material. *Fluid Dyn.*, 41:434–446.

[Klise et al., 2017] Klise, K., Bynum, M., Moriarty, D., and Murray, R. (2017). A software framework for assessing the resilience of drinking water systems to disasters with an example earthquake case study. *Environ. Model. Softw.*, 95:420–431.

[Korteweg, 1878] Korteweg, D. (1878). Ueber die Fortpflanzungsgeschwindigkeit des Schalles in elastischen Rohren, On the speed of sound propagation in elastic tubes. *Annalen der Physik*, 241(12):525–542.

[Kousiopoulos et al., 2020] Kousiopoulos, G., Papastavrou, G., Kampelopoulos, D., Karagiorgos, N., and Nikolaidis, S. (2020). Comparison of Time Delay Estimation Methods Used for Fast Pipeline Leak Localization in High-Noise Environment. *Technologies*, 8(2):27.

[Kuiken, 1984a] Kuiken, G. (1984a). Approximate dispersion equations for thin-walled liquid-filled tubes. *Appl. Sci. Res.*, 41:37–53.

[Kuiken, 1984b] Kuiken, G. (1984b). Wave propagation in a thin-walled liquid-filled initially-stressed tube. *J. Fluid Mech.*, 141:289–308.

[Kuiken, 1984c] Kuiken, G. (1984c). *WAVE PROPAGATION IN INITIALLY STRESSED ORTHOTROPIC COMPLIANT TUBES CONTAINING A COMPRESSIBLE, VISCOUS AND HEAR-CONDUCTING FLUID.* PhD thesis, Delft University of Technology.

[Lamb, 1898] Lamb, H. (1898). On the velocity of sound in a tube, as affected by the elastic of the walls. *Memoirs of the Manchester Literary and Philosophical Society, Manchester, (UK)*, 42(9):1–16.

[Laucelli et al., 2017] Laucelli, D. B., Simone, A., Berardi, L., and Giustolisi, O. (2017). Optimal Design of District Metering Areas for the Reduction of Leakages. *J. Water Resour. Plan. Manag.*, 143(6):04017017.

[Laufer, 1953] Laufer, J. (1953). The structure of turbulence in fully developed pipe flow. Technical report, NTRS - NASA Technical Reports Server.

[Leal, 2007] Leal, L. G. (2007). *Advanced Transport Phenomena: Fluid Mechanics and Convective Transport Processes*, chapter 4, pages 204–293. Cambridge Series in Chemical Engineering. Cambridge University Press, Cambridge.

[Lee et al., 2008] Lee, P., Vítkovský, J., Lambert, M., Simpson, A., and Liggett, J. (2008). Discrete blockage detection in pipelines using the frequency response diagram. *J. Hydraul. Eng.*, 134(5):658–663.

[Lee et al., 2013] Lee, P. J., Duan, H., Ghidaoui, M., and Karney, B. (2013). Frequency domain analysis of pipe fluid transient behaviour. *J. Hydraul. Eng.*, 51(6):609–622.

[Lee et al., 2006] Lee, P. J., Lambert, M. F., Simpson, A. R., Vítkovský, J. P., and Liggett, J. (2006). Experimental verification of the frequency response method for pipeline leak detection. *J. Hydraul. Res.*, 44(5):693–707.

[Lee et al., 2007] Lee, P. J., Vítkovský, J. P., Lambert, M. F., Simpson, A. R., and Liggett, J. (2007). Leak location in pipelines using the impulse response function. *J. Hydraul. Res.*, 45(5):643–652.

[Lee et al., 2005] Lee, P. J., Vítkovský, J. P., Lambert, M. F., Simpson, A. R., and Liggett, J. A. (2005). Leak location using the pattern of the frequency response diagram in pipelines: a numerical study. *J. Sound Vib.*, 284(3-5):1051–1073.

[Lesmez, 1989] Lesmez, M. (1989). *MODAL ANALYSIS OF VIBRATIONS IN LIQUID-FILLED PIPING SYSTEMS*. PhD thesis, Michigan State University.

[Lesmez et al., 1990] Lesmez, M. W., Wiggert, D. C., and Hatfield, F. J. (1990). Modal Analysis of Vibrations in Liquid-Filled Piping Systems. *J. Fluids. Eng.*, 112(3):311–318.

[Li et al., 2002] Li, Q. S., Yang, K., Zhang, L., and Zhang, N. (2002). Frequency domain analysis of fluid–structure interaction in liquid-filled pipe systems by transfer matrix method. *Int. J. Mech. Sci.*, 44(10):2067–2087.

[Li et al., 2015] Li, S., Karney, B. W., and Liu, G. (2015). FSI research in pipeline systems – A review of the literature. *J. Fluids Struct.*, 57:277–297.

[Li et al., 2014] Li, S.-j., Liu, G.-m., and Kong, W.-t. (2014). Vibration analysis of pipes conveying fluid by transfer matrix method. *Nucl. Eng. Des.*, 266:78–88.

[Liemberger and Wyatt, 2019] Liemberger, R. and Wyatt, A. (2019). Quantifying the global non-revenue water problem. *Water Supply*, 19(3):831–837.

[Liggett and Chen, 1994] Liggett, J. A. and Chen, L. (1994). Inverse Transient Analysis in Pipe Networks. *J. Hydraul. Eng.*, 120(8):934.

[Lighthill, 2001] Lighthill, J. (2001). *WAVES IN FLUIDS*. Cambridge university press.

[Lin and Morgan, 1956] Lin, T. and Morgan, G. W. (1956). WAVE PROPAGATION THROUGH FLUID CONTAINED IN A CYLINDRICAL, ELASTIC SHELL. *J. Acoust. Soc. Am.*, 28:1165–1176.

[Liu and Li, 2011] Liu, G. and Li, Y. (2011). Vibration analysis of liquid-filled pipelines with elastic constraints. *J. Sound Vib.*, 330(13):3166–3181.

[Liu and Kleiner, 2013] Liu, Z. and Kleiner, Y. (2013). State of the art review of inspection technologies for condition assessment of water pipes. *Measurement*, 46(1):1–15.

[Lockwood et al., 2005] Lockwood, A., Murray, T., Stuart, G., and Scudder, L. (2005). Locating leaks from water supply pipes using the passive acoustic method. *J. Water Supply: Res. Technol. - AQUA*, 54(8):519–530.

[Louati and Ghidaoui, 2017] Louati, M. and Ghidaoui, M. S. (2017). Eigenfrequency shift mechanism due to variation in the cross sectional area of a conduit. *J. Hydraul. Res.*, 55(6):829–846.

[Louati and Ghidaoui, 2018] Louati, M. and Ghidaoui, M. S. (2018). Eigenfrequency Shift Mechanism due to an Interior Blockage in a Pipe. *J. Hydraul. Eng.*, 144(1):04017055.

[Maccormack, 1969] Maccormack, R. (1969). The effect of viscosity in hypervelocity impact cratering. In 4^{th} *Aerodynamic Testing Conference*, Aerodynamic Testing Conference. American Institute of Aeronautics and Astronautics.

[Malesińska et al., 2021] Malesińska, A., Kubrak, M., Rogulski, M., Puntorieri, P., Fiamma, V., and Barbaro, G. (2021). Water Hammer Simulation in a Steel Pipeline System With a Sudden Cross Section Change. *J. Fluids. Eng.*, 143(9):091204.

[Marsili et al., 2021] Marsili, V., Meniconi, S., Alvisi, S., Brunone, B., and Franchini, M. (2021). Experimental analysis of the water consumption effect on the dynamic behaviour of a real pipe network. *J. Hydraul. Res.*, 59(3):477–487.

[Martins et al., 2017] Martins, N. M. C., Brunone, B., Meniconi, S., Ramos, H. M., and Covas, D. I. C. (2017). CFD and 1D Approaches for the Unsteady Friction Analysis of Low Reynolds Number Turbulent Flows. *J. Hydraul. Eng.*, 143(12):04017050.

[Mei and Jing, 2016] Mei, C. C. and Jing, H. (2016). Pressure and wall shear stress in blood hammer - Analytical theory. *Math Biosci.*, 280:62–70.

[Mei and Jing, 2018] Mei, C. C. and Jing, H. (2018). Effects of thin plaque on blood hammer — An asymptotic theory. *Eur. J. Mech. B Fluids*, 69:62–75.

[Meißner, 1977] Meißner, E. (1977). Berechnung pulsierender Strömung in Systemen aus Kunststoffleitungen mit Berücksichtigung von Reibungsverlusten. *Forschung im Ingenieurwesen A*, 43(2):53–63.

[Menabrea, 1858] Menabrea, L. F. (1858). *Note sur les effets du choc de l'eau dans les conduites*. Mallet-Bachelier.

[Meng et al., 2019] Meng, W., Cheng, Y., Wu, J., Yang, Z., Zhu, Y., and Shang, S. (2019). GPU Acceleration of Hydraulic Transient Simulations of Large-Scale Water Supply Systems. *Appl. Sci.*, 9(1):91.

[Meniconi et al., 2012] Meniconi, S., Brunone, B., and Ferrante, M. (2012). Water-hammer pressure waves interaction at cross-section changes in series in viscoelastic pipes. *J. Fluids Struct.*, 33:44–58.

[Meniconi et al., 2015] Meniconi, S., Brunone, B., Ferrante, M., Capponi, C., Carrettini, C., Chiesa, C., Segalini, D., and Lanfranchi, E. (2015). Anomaly pre-localization in distribution-transmission mains by pump trip: Preliminary field tests in the milan pipe system. *J. Hydroinformatics*, 17(3):377–389.

[Meniconi et al., 2018] Meniconi, S., Brunone, B., and Frisinghelli, M. (2018). On the role of Minor Branches, Energy Dissipation, and Small Defects in the Transient Response of Transmission Mains. *Water*, 10(2):187.

[Meniconi et al., 2021] Meniconi, S., Capponi, C., Franchini, M., and Brunone, B. (2021). Leak Detection in a Real Transmission Main Through Transient Tests: Deeds and Misdeeds. *Water Resour. Res.*, 57(3):e2020WR027838.

[Meniconi et al., 2022] Meniconi, S., Maietta, F., Alvisi, S., Capponi, C., Marsili, V., Franchini, M., and Brunone, B. (2022). Consumption change-induced transients in a water distribution network: Laboratory tests in a looped system. *Water Resour. Res.*, 58(10):e2021WR031343.

[Michaud, 1878] Michaud, J. (1878). Coups de bélier dans les conduites. Étude des moyens employés pour en atténuer les effects. *Bulletin de la Société Vaudoise des Ingénieurs et des Architects*, 4(3):4.

[Mitosek and Chorzelski, 2003] Mitosek, M. and Chorzelski, M. (2003). Influence of visco-elasticity on pressure wave velocity in polyethylene MDPE pipe. *Arch. Hydroengineering Environ. Mech.*, 50:127–140.

[Nault et al., 2018] Nault, J. D., Karney, B. W., and Jung, B.-S. (2018). Generalized Flexible Method for Simulating Transient Pipe Network Hydraulics. *J. Hydraul. Eng.*, 144(7):04018031.

[Nguyen et al., 2018] Nguyen, S. T. N., Gong, J., Lambert, M. F., Zecchin, A. C., and Simpson, A. R. (2018). Least squares deconvolution for leak detection with a pseudo random binary sequence excitation. *Mech. Syst. Signal Process.*, 99:846–858.

[Nixon et al., 2006] Nixon, W., Ghidaoui, M. S., and Kolyshkin, A. A. (2006). Range of Validity of the Transient Damping Leakage Detection Method. *J. Hydraul. Eng.*, 132(9):944–957.

[Ohmi and Usui, 1976] Ohmi, M. and Usui, T. (1976). Pressure and velocity distributions in pulsating turbulent pipe flow part 1 theoretical treatments. *Bulletin of JSME*, 19(129):307–313.

[Paidoussis, 2003] Paidoussis, M. P. (2003). *Fluid-Structure Interactions, Volume 2: Slender Structures and Axial Flow*. Elsevier.

[Pal et al., 2021] Pal, S., Hanmaiahgari, P. R., and Karney, B. W. (2021). An Overview of the Numerical Approaches to Water Hammer Modelling: The Ongoing Quest for Practical and Accurate Numerical Approaches. *Water*, 13(11):1597.

[Pan et al., 2021] Pan, B., Duan, H., Meniconi, S., and Brunone, B. (2021). FRF-based transient wave analysis for the viscoelastic parameters identification and leak detection in water-filled plastic pipes. *Mech. Syst. Signal Process.*, 146:107056.

[Pezzinga, 2000] Pezzinga, G. (2000). Evaluation of Unsteady Flow Resistances by Quasi-2D or 1D Models. *J. Hydraul. Eng.*, 126(10):778–785.

[Pinto et al., 2012] Pinto, P. C., Thiran, P., and Vetterli, M. (2012). Locating the Source of Diffusion in Large-Scale Networks. *Phys. Rev. Lett.*, 109(6):068702.

[Ramos et al., 2004] Ramos, H., Covas, D., Borga, A., and Loureiro, D. (2004). Surge damping analysis in pipe systems: modelling and experiments. *J. Hydraul. Res.*, 42(4):413–425.

[Résal, 1876] Résal, H. (1876). Note sur les petits mouvements d'un fluide incompressible dans un tuyau élastique. *Journal de Mathematiques Pures et Appliquées*, 2:342–344.

[Riaño-Briceño et al., 2022] Riaño-Briceño, G., Sela, L., and Hodges, B. R. (2022). Distributed and vectorized method of characteristics for fast transient simulations in water distribution systems. *Comput.-Aided Civ. Infrastruct. Eng.*, 37(2):163–184.

[Riedelmeier et al., 2014] Riedelmeier, S., Becker, S., and Schlücker, E. (2014). Measurements of junction coupling during water hammer in piping systems. *J. Fluids Struct.*, 48:156–168.

[Rossman et al., 2020] Rossman, L., Woo, H., Tryby, M., Shang, F., Janke, R., and Haxton, T. (2020). EPANET 2.2 User Manual. Technical Report EPA/600/R-20/133, U.S. Environmental Protection Agency, Washington, DC.

[Rubinow and Keller, 1971] Rubinow, S. and Keller, J. (1971). Wave Propagation in a Fluid-Filled Tube. *Journal of the Acoustical Society of America*, 50:198–223.

[Rubinow and Keller, 1978] Rubinow, S. I. and Keller, J. B. (1978). Wave propagation in a viscoelastic tube containing a viscous fluid. *J. Fluid Mech.*, 88(1):181–203.

[Sarkamaryan et al., 2018] Sarkamaryan, S., Haghighi, A., and Adib, A. (2018). Leakage detection and calibration of pipe networks by the inverse transient analysis modified by Gaussian functions for leakage simulation. *J. Water Supply: Res. Technol. - AQUA*, 67(4):404–413.

[Schohl, 1993] Schohl, G. A. (1993). Improved Approximate Method for Simulating Frequency-Dependent Friction in Transient Laminar Flow. *J. Fluids. Eng.*, 115(3):420–424.

[Shamloo and Haghighi, 2009] Shamloo, H. and Haghighi, A. (2009). Leak detection in pipelines by inverse backward transient analysis. *J. Hydraul. Res.*, 47(3):311–318.

[Shaw and MacKnight, 2018] Shaw, M. T. and MacKnight, W. J. (2018). *Introduction to polymer viscoelasticity,* 4^{th} *edition.* John Wiley & Sons.

[Shen et al., 2016] Shen, Z., Cao, S., Wang, W., Di, Z., and Stanley, H. E. (2016). Locating the source of diffusion in complex networks by time-reversal backward spreading. *Phys. Rev. E*, 93(3):032301.

[Shucksmith et al., 2012] Shucksmith, J. D., Boxall, J. B., Staszewski, W. J., Seth, A., and Beck, S. B. (2012). Onsite leak location in a pipe network by cepstrum analysis of pressure transients. *J. Water. Supply. Res. T.*, 104(8):E457–E465.

[Skalak, 1954] Skalak, R. (1954). *AN EXTENSION OF THE THEORY OF WATER HAMMER.* PhD thesis, Columbia University.

[Skalak, 1956] Skalak, R. (1956). An extension of the theory of waterhammer. *Transactions of the ASME*, 78(1):105–115.

[Soares et al., 2008] Soares, A. K., Covas, D. I., and Reis, L. F. (2008). Analysis of PVC Pipe-Wall Viscoelasticity during Water Hammer. *J. Hydraul. Eng.*, 134(9):1389–1394.

[Soares et al., 2011] Soares, A. K., Covas, D. I. C., and Reis, L. F. R. (2011). Leak detection by inverse transient analysis in an experimental PVC pipe system. *J. Hydroinformatics*, 13(2):153–166.

[Stephens et al., 2002] Stephens, M., Simpson, A., Lambert, M., Vítkovský, J., and Nixon, J. (2002). The Detection of Pipeline Blockages Using Transients in the Field. In *South Australian Regional Conf.* Australian Water Association.

[Stephens et al., 2013] Stephens, M. L., Lambert, M. F., and Simpson, A. R. (2013). Determining the Internal Wall Condition of a Water Pipeline in the Field Using an Inverse Transient. *J. Hydraul. Eng.*, 139(3):310–324.

[Storli and Nielsen, 2011] Storli, P. and Nielsen, T. K. (2011). Transient Friction in Pressurized Pipes. II: Two-Coefficient Instantaneous Acceleration–Based Model. *J. Hydraul. Eng.*, 137(6):679–695.

[Suo and Wylie, 1990] Suo, L. and Wylie, E. B. (1990). Complex Wavespeed and Hydraulic Transients in Viscoelastic Pipes. *J. Fluids. Eng.*, 112(4):496–500.

[Taghvaei et al., 2006] Taghvaei, M., Beck, S. B. M., and Staszewski, W. J. (2006). Leak detection in pipelines using cepstrum analysis. *Meas. Sci. Technol.*, 17(2):367–372.

[Thorley, 1969] Thorley, A. R. D. (1969). Pressure Transients in Hydraulic Pipelines. *J. Basic Eng.*, 91(3):453–460.

[Thual, 1997] Thual, O. (1997). *Introduction à la Mécanique des milieux continus déformables*. Cépadués-Editions.

[Tijsseling, 1993] Tijsseling, A. (1993). *FLUID-STRUCTURE INTERACTION IN CASE OF WATERHAMMER WITH CAVITATION*. PhD thesis, Delft University of Technology.

[Tijsseling, 2007] Tijsseling, A. (2007). Water hammer with fluid-structure interaction in thick-walled pipes. *Comput. Struct.*, 85(11-14):844–851.

[Tijsseling and Anderson, 2012] Tijsseling, A. and Anderson, A. (2012). A. Isebree Moens and D.J. Korteweg: On the speed of propagation of waves in elastic tubes. In 11^{th} *International Conferences on Pressure Surges*, pages 227–245. BHR Group.

[Tijsseling and Lavooij, 1990] Tijsseling, A. and Lavooij, C. S. W. (1990). Waterhammer with fluid-structure interaction. *Appl. Sci. Res.*, 47(3):273–285.

[Tijsseling, 1996] Tijsseling, A. S. (1996). FLUID-STRUCTURE INTERACTION IN LIQUID-FILLED PIPE SYSTEMS: A REVIEW. *J. Fluids Struct.*, 10(2):109–146.

[Tiselj and Gale, 2008] Tiselj, I. and Gale, J. (2008). Integration of unsteady friction models in pipe flow simulations. *J. Hydraul. Res.*, 46(4):526–535.

[Toro, 1997] Toro, E. F. (1997). *Riemann Solvers and Numerical Methods for Fluid Dynamics*. Springer, Berlin, Heidelberg.

[Trikha, 1975] Trikha, A. K. (1975). An Efficient Method for Simulating Frequency-Dependent Friction in Transient Liquid Flow. *J. Fluids. Eng.*, 97(1):97–105.

[Urbanowicz, 2018] Urbanowicz, K. (2018). Fast and accurate modelling of frictional transient pipe flow. *J. Appl. Math. Mech.*, 98(5):802–823.

[Urbanowicz and Firkowski, 2018] Urbanowicz, K. and Firkowski (2018). Modelling Water Hammer with Quasi-Steady and Unsteady Friction in Viscoelastic Pipelines. In *Dynamical Systems in Applications*, pages 385–399. Springer International Publishing.

[Urbanowicz et al., 2016] Urbanowicz, K., Firkowski, M., and Zarzycki, Z. (2016). Modelling Water Hammer with Quasi-Steady and Unsteady Friction in Viscoelastic Pipelines. In *J. Phys.: Conf. Ser.*, 760, page 012037.

[Vardy and Fan, 1986] Vardy, A. and Fan, D. (1986). Water hammer in a closed tube. In 5^{th} *International Conference on the Pressure Surge*. BHRA.

[Vardy and Brown, 2007] Vardy, A. E. and Brown, J. M. (2007). Approximation of Turbulent Wall Shear Stresses in Highly Transient Pipe Flows. *J. Hydraul. Eng.*, 133(11):1219–1228.

[Vardy and Brown, 1995] Vardy, A. E. and Brown, J. M. B. (1995). Transient, turbulent, smooth pipe friction. *J. Hydraul. Res.*, 33(4):435–456.

[Vardy and Brown, 2003] Vardy, A. E. and Brown, J. M. B. (2003). Transient turbulent friction in smooth pipe flows. *J. Sound Vib.*, 259(5):1011–1036.

[Vardy and Brown, 2004] Vardy, A. E. and Brown, J. M. B. (2004). Transient turbulent friction in fully rough pipe flows. *J. Sound Vib.*, 270(1-2):233–257.

[Vardy et al., 2015] Vardy, A. E., Brown, J. M. B., He, S., Ariyaratne, C., and Gorji, S. (2015). Applicability of Frozen-Viscosity Models of Unsteady Wall Shear Stress. *J. Hydraul. Eng.*, 141(1):04014064.

[Vardy and Hwang, 1991] Vardy, A. E. and Hwang, K. (1991). A characteristics model of transient friction in pipes. *J. Hydraul. Res.*, 29(5):669–684.

[Vardy and Hwang, 1993] Vardy, A. E. and Hwang, K. (1993). A weighting function model of transient turbulent pipe friction. *J. Hydraul. Res.*, 31(4):533–548.

[Vicente et al., 2016] Vicente, D. J., Garrote, L., Sánchez, R., and Santillán, D. (2016). Pressure Management in Water Distribution Systems: Current Status, Proposals, and Future Trends. *J. Water Resour. Plan. Manag.*, 142(2):04015061.

[Vitkovsky et al., 2000] Vitkovsky, J., Lambert, M., Simpson, A., and Bergant, A. (2000). Advances in unsteady friction modelling in transient pipe flow. In 8^{th} *Int. Conf. on Pressure Surges*, pages 471–482. BHR Group.

[Vitkovsky et al., 2004] Vitkovsky, J., Stephens, M., Bergant, A., Lambert, M., Simpson, A., and Simpson, A. (2004). Efficient and accurate calculation of Zielke and Vardy-Brown unsteady friction in pipe transients. In 9^{th} *International Conference on Pressure Surges*.

[Vítkovský et al., 2006] Vítkovský, J. P., Bergant, A., Simpson, A. R., and Lambert, M. F. (2006). Systematic Evaluation of One-Dimensional Unsteady Friction Models in Simple Pipelines. *J. Hydraul. Eng.*, 132(7):696–708.

[Vítkovský et al., 2007] Vítkovský, J. P., Lambert, M. F., Simpson, A. R., and Liggett, J. A. (2007). Experimental Observation and Analysis of Inverse Transients for Pipeline Leak Detection. *J. Water Resour. Plan. Manag.*, 133(6):519–530.

[Vítkovský et al., 2000] Vítkovský, J. P., Simpson, A. R., and Lambert, M. F. (2000). Leak Detection and Calibration Using Transients and Genetic Algorithms. *J. Water Resour. Plan. Manag.*, 126(4):262–265.

[Walker and Phillips, 1977] Walker, J. S. and Phillips, J. W. (1977). Pulse Propagation in Fluid-Filled Tubes. *J. Appl. Mech.*, 44(1):31–35.

[Wan and Huang, 2018] Wan, W. and Huang, W. (2018). Water hammer simulation of a series pipe system using the MacCormack time marching scheme. *Acta Mech.*, 229(7):3143–3160.

[Wang et al., 2021] Wang, X., Camino, G. A., Che, T., and Ghidaoui, M. S. (2021). Factorized wave propagation model in tree-type pipe networks and its application to leak localization. *Mech. Syst. Signal Process.*, 147(5):107116.

[Wang and Ghidaoui, 2018a] Wang, X. and Ghidaoui, M. S. (2018a). Pipeline Leak Detection Using the Matched-Field Processing Method. *J. Hydraul. Eng.*, 144(6):04018030.

[Wang and Ghidaoui, 2018b] Wang, X. and Ghidaoui, M. S. (2018b). Identification of multiple leaks in pipeline: Linearized model, maximum likelihood, and super-resolution localization. *Mech. Syst. Signal Process.*, 107:529–548.

[Wang et al., 2019] Wang, X., Ghidaoui, M. S., and Lin, J. (2019). Identification of multiple leaks in pipeline III: Experimental results. *Mech. Syst. Signal Process.*, 130:395–408.

[Wang et al., 2002] Wang, X., Lambert, . F., Simpson, A. R., Liggett, J. A., and Vitkovský, J. P. (2002). Leak Detection in Pipelines using the Damping of Fluid Transients. *J. Hydraul. Eng.*, 128(7):697–711.

[Wang et al., 2005] Wang, X., Lambert, M. F., and Simpson, A. R. (2005). Detection and Location of a Partial Blockage in a Pipeline Using Damping of Fluid Transients. *J. Water Resour. Plan. Manag.*, 131(3):244–249.

[Waqar et al.,] Waqar, M., Louati, M., and M.S., G. Time-reversal of water-hammer waves. *J. Hydraul. Res.*, 60(1):25–45.

[Weinerowska-Bords, 2006] Weinerowska-Bords, K. (2006). Viscoelastic Model of Waterhammer in Single Pipeline–Problems and Questions. *Arch. Hydroengineering Environ. Mech.*, 53(4):331–351.

[Wiggert and Tijsseling, 2001] Wiggert, D. and Tijsseling, A. (2001). Fluid transients and fluid-structure interaction in flexible liquid-filled piping. *Applied Mechanics Reviews*, 54(5):455–481.

[Williams, 1977] Williams, D. J. (1977). Waterhammer in Non-Rigid Pipes Precursor Waves and Mechanical Damping. *J. Mech. Eng. Sci.*, 19(6):237–242.

[Wood and Funk, 1970] Wood, D. J. and Funk, J. E. (1970). A Boundary-Layer Theory for Transient Viscous Losses in Turbulent Flow. *J. Basic Eng.*, 92(4):865–873.

[World Health Organization, 2022] World Health Organization (2022). Drinking-water. https://www.who.int/news-room/fact-sheets/detail/drinking-water.

[Wylie et al., 1993] Wylie, E. B., Streeter, V. L., and Suo, L. (1993). *Fluid Transients in Systems*, volume 1. Prentice Hall Englewood Cliffs, NJ.

[Xing and Lina, 2020] Xing, L. and Lina, S. (2020). Transient simulations in water distribution networks: TSNet python package. *Adv. Eng. Softw.*, 149:102884.

[Yang et al., 2004] Yang, K., Li, Q. S., and Zhang, L. (2004). Longitudinal vibration analysis of multi-span liquid-filled pipelines with rigid constraints. *J. Sound Vib.*, 273(1-2):125–147.

[Yao et al., 2014] Yao, E., Kember, G., and Hansen, D. (2014). Analysis of water hammer attenuation in the Brunone model of unsteady friction. *Quart. Appl. Math.*, 72(2):281–290.

[Zaman et al., 2020] Zaman, D., Tiwari, M. K., Gupta, A. K., and Sen, D. (2020). A review of leakage detection strategies for pressurised pipeline in steady-state. *Eng. Fail. Anal.*, 109:104264.

[Zanganeh et al., 2020] Zanganeh, R., Jabbari, E., Tijsseling, A., and Keramat, A. (2020). Fluid-Structure Interaction in Transient-Based Extended Defect Detection of Pipe Walls. *J. Hydraul. Eng.*, 146(4):04020015.

[Zecchin, 2010] Zecchin, A. (2010). *Laplace-Domain Analysis of Fluid Line Networks with Applications to Time-Domain Simulation and System Parameter Identification*. PhD thesis, University of Adelaide.

[Zecchin et al., 2012] Zecchin, A. C., Lambert, M. F., and Simpson, A. R. (2012). Inverse Laplace Transform for Transient-State Fluid Line Network Simulation. *J. Eng. Mech.*, 138(1):101.

[Zhang et al., 2018] Zhang, C., Gong, J., Zecchin, A., Lambert, M., and Simpson, A. (2018). Faster Inverse Transient Analysis with a Head-Based Method of Characteristics and a Flexible Computational Grid for Pipeline Condition Assessment. *J. Hydraul. Eng.*, 144(4):04018007.

[Zhang et al., 1999] Zhang, L., Tijsseling, A., and Vardy, A. (1999). FSI analysis of liquid-filled pipes. *J. Sound Vib.*, 224(1):69–99.

[Zhao and Ghidaoui, 2004] Zhao, M. and Ghidaoui, M. S. (2004). Godunov-Type Solutions for Water Hammer Flows. *J. Hydraul. Eng.*, 130(4):341–348.

[Zhou et al., 2018] Zhou, L., Wang, H., Bergant, A., Tijsseling, A., Liu, D., and Guo, S. (2018). Godunov-Type Solutions with Discrete Gas Cavity Model for Transient Cavitating Pipe Flow. *J. Hydraul. Eng.*, 144(5):04018017.

[Zielke, 1966] Zielke, W. (1966). *FREQUENCY DEPENDENT FRICTION IN TRANSIENT PIPE FLOW*. phdthesis, The University of Michigan.

[Zielke, 1968] Zielke, W. (1968). Frequency-Dependent Friction in Transient Pipe Flow. *J. Basic Eng.*, 90(1):109–115.

[Čanić et al., 2006a] Čanić, S., Hartley, C. J., Rosenstrauch, D., Tambaca, J., Guidoboni, G., and Mikelić, A. (2006a). Blood Flow in Compliant Arteries: An Effective Viscoelastic Reduced Model, Numerics, and Experimental Validation. *Annu. Rev. Biomed. Eng*, 34(4):575–592.

[Čanić et al., 2006b] Čanić, S., Tambača, J., Guidoboni, G., Mikelić, A., Hartley, C. J., and Rosenstrauch, D. (2006b). Modeling Viscoelastic Behavior of Arterial Walls and Their Interaction with Pulsatile Blood Flow. *SIAM J. Appl. Math.*, 67(1):164–193.